

The Sheet of Impact Melt at West Clearwater Lake, Northern Quebec

Daniel F. Rosa

A dissertation submitted to The McGill University in conformity with the
requirements for the degree of doctor of Philosophy.

Montreal, Quebec, Canada

2011

© Daniel F. Rosa 2011

All rights reserved, all wrongs reversed.

Abstract

The meteorite impact that formed the 32-km-wide Upper Pennsylvanian (285 ± 23 Ma) West Clearwater structure, situated about 125 km east of the Hudson Bay arc, northern Quebec, formed a sheet of impact melt now exposed on a central ring of islands. Crater-fill deposits exposed on the ring of islands can be divided into three major successive units, which are, in ascending order: 1) a red, friable impact-melt-bearing fragmental breccia 0 to 20 m thick cut by small (cm to dm) dykes of impact melt; 2) a red, massive, clast-rich impact-generated melt about 18 meters thick containing up to 25% clasts > 1 mm in size, and 3) a massive poorly jointed clast-poor impact-generated melt containing $< 15\%$ clasts greater than 1 mm in size, at least 85 m thick, with a matrix that shows an ophitic to subophitic texture. The average composition of the West Clearwater Lake impact melt, which has a bulk composition similar to that of a trachyandesitic volcanic rock, can be modeled by mixing the average chemical compositions of three types of lithologies present in the vicinity of the impact structure: 1) granitic rocks, 2) granodioritic, enderbitic and tonalitic rocks, and 3) mafic and ultramafic rocks, according to the following proportions: 1) 31%, 2) 62% and 3) 6%. The order of crystallization of the melt was plagioclase + Fe-Ti oxides + clinopyroxene + sanidine + apatite + quartz. The initial clast content in the clast-poor melt, before the onset of crystallization, must have been much higher. This conclusion is supported by the widespread occurrence in the clast-poor impact melt rock of plagioclase grains with an irregular, partially resorbed relict core. In thin section, plagioclase xenocrysts now form $\sim 5\%$ to $\sim 15\%$ of the clast-poor impact melt rock, depending on the thin section. The preferential preservation of plagioclase as a clast implies that the melt quickly equilibrated to temperatures below the liquidus and within the range of plagioclase crystallization. Two-feldspar thermometry calculations suggest that the last plagioclase and the first alkali feldspar crystallized at temperatures of about 781 to 816°C ($\pm 44^\circ\text{C}$). Quartz, the last phase to crystallize in the clast-poor impact melt rock, formed at temperatures of 700 to 730°C, with an activity of Ti in quartz between 0.5 and 0.6. This study is the first to employ Ti-in-quartz geothermometry to estimate the temperature of solidification of a melt sheet created by a meteoritic impact. Because the melt crystallized anhydrous minerals, it is possible that the melt was highly undersaturated at the liquidus but had achieved H₂O saturation at the solidus.

Sommaire

Le cratère du Lac à l'Eau Claire Ouest, une structure de 32 km de diamètre, a été formé pendant le Pennsylvanien supérieur, il y a 285 ± 23 Ma; il se trouve environ 125 km à l'est de l'arc de la Baie d'Hudson. L'impact météoritique à l'origine de ce cratère a produit une nappe de magma, et les roches qui en résultent se trouvent maintenant exposées dans un anneau d'îles occupant le centre du cratère. Ces roches peuvent être divisées en trois unités, qui sont, en ordre ascendant, 1) une brèche de base rougeâtre et friable (0 – 20 m d'épaisseur) infiltrée par d'étroits dykes d'impactite, 2) une ignimbrite d'impacte rougeâtre massive, épaisse de 18 m, contenant jusqu'à 25% de débris clastiques > 1 mm, et 3) une impactite massive épaisse d'au moins 85 m, pauvre en débris clastiques ($< 15\%$), montrant une matrice de texture ophitique à sub-ophitique. La composition moyenne trachyandésitique du magma d'impact à l'Eau Claire Ouest peut être modélisée en mélangeant trois unités présentes dans le voisinage immédiat du cratère: 1) 31% granites, 2) 62% granodiorites, enderbites et tonalites, et 3) 6% roches mafiques et ultramafiques. La cristallisation de l'impactite a suivi la séquence plagioclase + oxydes de Fe-Ti + clinopyroxène + sanidine + apatite + quartz. La quantité de débris clastiques présente dans l'impactite avant le début de la cristallisation était plus élevée que celle qui est maintenant observée, ce que confirme la présence dans l'impactite de nombreux grains de plagioclase ayant des noyaux composés de xénocristaux partiellement résorbés. Ces xénocristaux forment présentement $\sim 5\%$ à 15% de l'impactite. La préservation de ces xénocristaux suggère que le refroidissement du magma a été rapide ; des températures en dessous du liquidus plaçant le magma en équilibre avec les températures de cristallisation du plagioclase ont dû être rapidement atteintes. Des calculs de thermométrie fondée sur la coexistence de deux feldspaths indiquent que le dernier plagioclase et le premier feldspath potassique ont cristallisé à $781 - 816^{\circ}\text{C}$ ($\pm 44^{\circ}\text{C}$). Le quartz, dernier minéral à cristalliser, s'est formé à $700 - 730^{\circ}\text{C}$; l'activité du Ti dans le quartz a été estimée à 0.5 - 0.6. Dans cette étude, la géothermométrie du Ti dans le quartz a été employée pour la première fois pour estimer la température de cristallisation d'un magma créé par un impact météoritique. Parce que le magma a cristallisé des minéraux anhydres, il est probable que le magma était fortement sous saturé en H_2O au liquidus, mais avait atteint saturation en H_2O au solidus.

Contents

Abstract.....	I
Sommaire.....	II
Table of contents.....	III
List of figures.....	VII
List of tables.....	XII
Chapter 1 Introduction and Previous Studies.....	2
1.1) Introduction.....	2
1.2) The West Clearwater Lake Impact Structure.....	3
1.3) Previous Studies.....	5
Chapter 2 Geology of the West Clearwater Lake Impact Structure.....	12
2.1) Archean Units.....	12
2.1.1) The granites and granodiorites of the Desbergères Suite..	16
2.1.2) The enderbites, diorites, granodiorites and tonalites of the Loups Marins Complex.....	17
2.1.3) The leucotonalites of the Favard Suite.....	18
2.1.4) The mafic and ultramafic rocks of the Qullinaaraaluk Suite.....	21
2.2) Proterozoic Units.....	22
2.3) Ordovician Units (West Clearwater Lake Carbonates).....	22
2.4) Pennsylvanian Units (Impact-Related Lithologies).....	24
2.5) Summary of chapter 2.....	26
Chapter 3 Impact Cratering.....	28
3.1) Contact and Compression.....	28

3.2)	Excavation.....	30
3.3)	Modification.....	32
3.4)	The Production of Impact Melt.....	34
3.5)	Estimation of the volume of melt produced by the West Clearwater Lake impact.....	37
3.6)	Can impact cratering generate volcanic eruptions?.....	38
Chapter 4	The Drill Core.....	42
4.1)	The drill core.....	42
4.2.1)	Overview of the core extracted from Drill Hole 1-63.....	45
4.2.2)	Overview of the core extracted from Drill Hole 3-63.....	48
4.2.3)	Overview of the core extracted from Drill Hole 4-63.....	52
4.2.4)	Overview of the core extracted from Drill Hole 4A-63.....	55
4.2.5)	Overview of the core extracted from Drill Hole 5-63.....	57
4.3)	Summary of chapter 4.....	60
Chapter 5	The Fractured Basement.....	63
5.1)	Composition of the target rocks.....	63
5.2)	Deformation and fracturing of target rocks.....	66
5.3)	Granitic Rocks.....	70
5.4)	Granodioritic, enderbitic and tonalitic rocks.....	79
5.5)	Mafic rocks.....	86
5.6)	Diabase.....	94
5.7)	Comparison of the lithologies described in Simard et al. (2004) with those described in this study.....	99

Chapter 6	Fragmental Breccia, Infiltration Dykes and Glass Spheroids.....	103
6.1)	The impact related lithologies of the West Clearwater Lake impact structure.....	103
6.2)	Fragmental breccia.....	108
6.3)	Infiltration dykes.....	118
6.4)	Glass Spheroids in glass of the West Clearwater Lake impact structure.....	126
6.4.1)	Petrography of the glass spheroids.....	126
6.4.2)	Chemical composition of the glasses.....	130
6.5)	Summary of chapter 6.....	152
Chapter 7	Clast-rich impact melt rock and clast-poor impact melt rock....	153
7.1)	Clast-rich impact melt rock.....	153
7.2)	Clast-poor impact melt rock.....	163
7.2.1)	Feldspars.....	167
7.2.2)	Pyroxenes.....	182
7.2.3)	Quartz and its titanium content.....	188
7.2.4)	Iron-Titanium Oxides.....	195
7.2.5)	Apatite.....	203
7.2.6)	Fine-grained aggregates of quartz and feldspars.....	203
7.3)	Summary of chapter 7	
Chapter 8	Titanium-in-quartz thermometry.....	206
8.1)	Calculating the temperatures.....	207
8.2)	Limitations imposed by the absence of rutile.....	210
8.3)	Results.....	211

8.4)	Two-feldspar thermometry.....	216
8.4.1)	Results.....	219
8.4.2)	Estimating a_{TiO_2} from two-feldspar temperatures.....	223
8.5)	Summary of chapter 8.....	226
Chapter 9	Discussion and Conclusions.....	228
9.1)	Mixing model.....	228
9.2)	On the origin of the glass spheroids.....	232
9.3)	Plagioclase-sanidine intergrowths (comb texture).....	238
9.4)	On the presence of H_2O during the crystallization of the West Clearwater impact melt sheet.....	243
9.5)	Estimating liquidus and solidus temperatures of the clast-poor impact melt sheet with MELTS.....	246
9.5.1)	Addendum: Estimating liquidus and solidus temperatures of the clast-poor impact melt sheet with Rhyolite-MELTS.....	248
9.6)	Final thoughts regarding impact cratering and the differentiation of impact melts.....	248
9.7)	Topics for future research.....	259
9.8)	Summary and conclusions.....	261
	Acknowledgements.....	264
Appendix A	Chemical compositions of rock samples obtained from the core drilled at the West Clearwater impact structure.....	6 pages
Appendix B	Chemical compositions of rock samples obtained from the surface of the inner ring of islands at the West Clearwater impact structure.....	21 pages
Appendix C	Approximate locations of surface samples.....	17 pages

Appendix D	Electron-microprobe-derived compositions.....	42 pages
-------------------	---	----------

Appendix E	A Spurrite-, Merwinite- and Srebrodolskite-bearing skarn Assemblage, West Clearwater Lake impact crater, northern Quebec.....	14 pages
-------------------	---	----------

List of Figures

1.1	Location of the West Clearwater impact structure.....	4
1.2	Location of the West Clearwater impact structure.....	4
1.3	Location map for the West Clearwater Lake islands.....	6
1.4	Cross section of the West Clearwater impact structure.....	7
2.1	Maximum and minimum ranges of MgO vs. SiO ₂ compositions of the basement rocks present in the Clearwater Lakes region.....	15
2.2	Simplified geology of the West Clearwater Lake region.....	19
2.3	Stratigraphy of the impact melt sheet at the West Clearwater impact structure.....	25
3.1	Growth of a crater.....	31
3.2	Schematic illustration of the formation of complex craters.....	33
4.1	Photographs of core sections.....	43
4.2	Stratigraphic section of basement lithologies at West Clearwater Lake impact structure: drill hole 1-63, drill hole 3-63 and drill hole 4-63.....	61
4.3	Stratigraphic section of basement lithologies at West Clearwater Lake impact structure: drill hole 4A-63, and drill hole 5-63.....	62
5.1	Target rocks (MgO vs. SiO ₂).....	65
5.2	Back-scattered electron images of a rock with a granitic composition.....	71

VIII

5.3	Mineral compositions of feldspars in the granites at West Clearwater...	76
5.4	Back-scattered electron images of thin sections of partially melted rocks with a granitic composition.....	77
5.5	Two back-scattered electron images of thin sections of samples with a granodioritic composition.....	80
5.6	Mineral compositions of feldspars in the tonalites and diorites at West Clearwater.....	84
5.7	Mineral compositions of pyroxene in the tonalites and diorites at West Clearwater.....	84
5.8	Back-scattered electron images of polished thin sections of rock samples with a gabbroic composition.....	88
5.9	Mineral compositions of feldspar in the gabbros found at West Clearwater Lake.....	92
5.10	Mineral compositions of pyroxene in the gabbro at West Clearwater Lake.....	93
5.11	Back-scattered electron images of a polished thin section of a sample of a diabase dyke of Proterozoic age.....	95
5.12	Mineral compositions of feldspar in the diabase found at West Clearwater Lake.....	97
5.13	Mineral compositions of pyroxene in the diabase at West Clearwater Lake.....	98
6.1	Compositional variation in samples of fragmental breccia matrix from the West Clearwater Lake impact structure.....	113
6.2	Two back-scattered electron images of fragmental breccia exemplifying the textures typical of this unit.....	116
6.3	Two back-scattered electron images of infiltration dykes.....	122
6.4	Compositional variation in samples of infiltration dykes from the West Clearwater Lake impact structure.....	123
6.5	Frequency vs. diameter of the glass spheroids.....	129

6.6	Matrix glass compositions: MgO vs. SiO ₂	140
6.7	Matrix glass compositions: Al ₂ O ₃ vs. SiO ₂	140
6.8	Matrix glass compositions: MgO vs. Al ₂ O ₃	141
6.9	Matrix glass compositions: alkalis vs. SiO ₂	141
6.10	Glass spheroid compositions: MgO vs. SiO ₂	142
6.11	Glass spheroid compositions: Al ₂ O ₃ vs. SiO ₂	142
6.12	Glass spheroid compositions: MgO vs. Al ₂ O ₃	143
6.13	Glass spheroid compositions: alkalis vs. SiO ₂	143
6.14	Back-scattered electron images of glass spheroids within samples of fragmental breccia.....	147
6.15	Back-scattered electron images of glass spheroids within samples of fragmental breccia.....	148
6.16	Back-scattered electron images of glass spheroids within samples of fragmental breccia.....	149
6.17	Back-scattered electron images of glass spheroids within samples of fragmental breccia.....	150
6.18	Back-scattered electron images of glass spheroids within samples of fragmental breccia.....	151
7.1	Composition of feldspar microlites from the matrix of the clast-rich impact melt rock.....	159
7.2	Range of feldspar compositions in the very fine-grained matrix of the clast-rich impact melt rock of the West Clearwater impact structure.....	159
7.3	Back-scattered electron images of clast-rich impact melt rock.....	160
7.4	Compositional variation in samples of clast-rich impact melt rock from the West Clearwater Lake impact structure.....	161
7.5	Compositional variation in samples of clast-poor impact melt rock from the West Clearwater Lake impact structure.....	165
7.6	Range of mineral compositions for all feldspars in the clast-poor impact melt unit of the West Clearwater Lake impact structure.....	169

7.7	Range of compositions in confirmed relict xenocrysts in the clast-poor impact melt unit of the West Clearwater Lake impact structure.....	171
7.8	Range of compositions for confirmed melt-derived plagioclase in the clast-poor impact melt unit of the West Clearwater Lake impact structure.....	171
7.9	Back-scattered electron images of clast-poor impact melt rock.....	173
7.10	Range of compositions for confirmed transition-zone plagioclase margins in the clast-poor impact melt unit of the West Clearwater Lake impact structure.....	174
7.11	Range of compositions of confirmed primary sanidine feldspar rims in the clast-poor impact melt unit of the West Clearwater Lake impact structure.....	174
7.12	Range of compositions of confirmed plagioclase laths in the clast-poor impact melt unit of the West Clearwater Lake impact structure.....	175
7.13	Variation in An/(An+Ab) content in microprobe traverses across a feldspar grain in sample DCW-77-33 of the clast-poor impact melt rock of the W.C.L. impact structure	176
7.14	Variation in An/(An+Ab) content in microprobe traverses across a poikilitic feldspar grain in sample DCW-77-61 of the clast-poor impact melt rock of the W.C.L. impact structure.....	177
7.15	Variation in An/(An+Ab) content in microprobe traverses across a feldspar grain in sample DCW-77-61 of the clast-poor impact melt rock of the West Clearwater Lake impact structure.....	178
7.16	Variation in An/(An+Ab) content in microprobe traverses across a feldspar grain in sample DCW-77-53 of the clast-poor impact melt rock of the West Clearwater Lake impact structure.....	179
7.17	A cathodoluminescence (CL) image and a back-scattered electron image of the same area of a thin section of sample DCW-77-36.....	181
7.18	Range of mineral compositions of the pyroxenes in the clast-poor impact melt rock of the W.C.L. impact structure.....	184
7.19	Back-scattered electron images of pyroxene in clast-poor impact melt rock samples of the W.C.L. impact structure.....	185

7.20	A cathodoluminescence (CL) image and a back-scattered electron (BSE) image of a thin section of sample DCW-77-7.....	191
7.21	Variations in Ti content in quartz according to sample and estimated relative stratigraphic position of samples above lake level. This plot includes all values.....	193
7.22	Variations in Ti content in quartz according to sample and estimated relative stratigraphic position of samples above lake level. This plot excludes very high and very low values.....	193
7.23	Back-scattered electron images of Fe-Ti oxides found within the clast-poor melt (thin sections DCW-77-35 and DCW-77-28).....	196
7.24	Back-scattered electron images of Fe-Ti oxides found within the clast-poor melt (thin sections DCW-77-8 and DCW-77-35).....	197
7.25	Back-scattered electron images of Fe-Ti oxides found within the clast-poor melt (thin sections DCW-77-51 and DR-10).....	198
8.1	Temperature estimated with the Ti content of quartz from the clast-poor impact melt rock of the West Clearwater impact structure. The temperature (°C) was calculated using the equation of Wark and Watson (2006), with an activity of TiO ₂ in quartz equal to one.....	212
8.2	Temperature estimated with the Ti content of quartz from the clast-poor impact melt rock of the West Clearwater impact structure. T (°C) was calculated using the equation of Wark and Watson (2006) employing a number of activities for TiO ₂ in quartz.....	213
8.3	Temperature estimated with the Ti content of quartz from the clast-poor impact melt rock of the West Clearwater impact structure. T (°C) calculated using the equation of Thomas et al. (2010) with activity of TiO ₂ in quartz equal to one.....	215
8.4	Temperature estimated with the Ti content of quartz from the clast-poor impact melt rock of the West Clearwater impact structure. T (°C) calculated using the equation of Thomas et al. (2010) employing various of activities for TiO ₂ in quartz.....	215
8.5	Two-feldspar temperatures determined using equation (7); calculations made with the software of Putirka (2008a).....	222
8.6	Two-feldspar temperatures determined using equation (8); calculations made with the software of Putirka (2008a).....	222

8.7	Two-feldspar temperatures determined using global regression analysis; calculations made with the software of Putirka (2008a).....	223
9.1	The ratio between the mass melted in an impact into gabbroic anorthosite and the mass displaced from a crater is plotted against crater diameter on the Earth and the Moon.....	256
9.2	As crater diameter increases the volume of melt and vaporized material may eventually approach the volume of the crater itself.....	257

List of Tables

2.1	Average compositions (major element oxides) of the target rocks of the Clearwater Lakes region (Simard et al. 2004).....	13
2.2	Average composition (trace elements) of the target rocks of the Clearwater Lakes region	14
4.1	Drill core locations and depth of sampling.....	44
5.1	Average composition of the target rocks (this study).....	66
5.2	Representative compositions of the minerals found in the granitic rocks of the W. C. L. impact structure.....	75
5.3	Representative compositions of feldspars and glassy rims (partial melt)..	78
5.4	Representative compositions of the minerals found in the granodioritic, enderbitic and tonalitic rocks of the W. C. L. impact structure.....	81
5.5	Representative compositions of the minerals found in the mafic rocks of the West Clearwater Lake Impact Structure.....	90
5.6	Representative compositions of the minerals found in the diabasic rocks of the West Clearwater Lake Impact Structure.....	96
5.7	Comparison between the main lithologies described by Simard et al. (2004) in the Clearwater Lakes region and the lithologies observed in the basement of the West Clearwater Lake impact structure.....	102
6.1	Average major-element composition of impact lithologies at West Clearwater obtained in previous studies.....	105

6.2	Average major-element composition of impact lithologies at West Clearwater obtained by the author.....	107
6.3	Average abundances of trace-elements of impact lithologies at West Clearwater obtained by the author.....	107
6.4	Major-element compositions of selected samples of fragmental breccia from West Clearwater Lake.....	111
6.5	Trace-element abundances in chosen fragmental breccia samples from West Clearwater.....	111
6.6	Major-element compositions of the infiltration dyke samples from West Clearwater obtained by the author.....	120
6.7	Trace element concentrations in the infiltration dykes samples from West Clearwater obtained by the author.....	120
6.8	Average compositions of the glassy matrix in the samples that contain glass spheroids.....	132
6.9	Individual compositions of the glassy matrix in the samples that contain glass spheroids.....	133
6.10	Average compositions of the glass spheroids.....	136
6.11	Individual compositions of the glass spheroids.....	137
6.12	Comparison of a high-MgO glass spheroid composition with saponite.....	146
7.1	Major element compositions of chosen clast-rich impact melt rock samples from West Clearwater Lake.....	156
7.2	Trace element compositions of chosen clast-rich impact melt rock samples from West Clearwater Lake.....	157
7.3	Representative compositions of the feldspars found in the clast-poor impact melt rocks of the West Clearwater Lake impact structure.....	168
7.4	Representative compositions of the pyroxenes found in the clast-poor impact melt rocks of the West Clearwater Lake Impact Structure.....	186
7.5	Samples chosen for cathodoluminescence (CL) imaging and Ti-in-quartz analysis, with their approximate relative stratigraphic location.....	189

7.6	Representative levels of titanium in the quartz found in the clast-poor impact melt rocks of the West Clearwater Lake Impact Structure.....	192
7.7	Ti contents in the quartz in selected samples from the clast-poor melt impact rock of the West Clearwater Lake impact structure.....	194
7.8	Representative compositions of the iron-titanium oxides found in the clast-poor impact melt rocks of the W. C. L. impact structure.....	201
8.1	Average temperatures per sample and their variation with decreasing a_{TiO_2} estimated with the equation of Wark and Thompson (2006).....	214
8.2	Average temperatures per sample and their variation with decreasing a_{TiO_2} estimated with the equation of Thomas et al. (2010).....	216
8.3	Two-feldspar temperatures determined using the software of Putirka (2008a).....	220
8.4	Average two-feldspar temperatures determined using the software of Putirka (2008a).....	221
8.5	Minimum values for the activities of TiO_2 in quartz estimated from two-feldspar temperatures obtained using equation (7), (8) and global regression.....	225
9.1	Least-squares modeling of sources to account for melt-rock compositions at West Clearwater Lake.....	230
9.2	Composition of the clays formed by the alteration of clinopyroxene vs. the composition of the material presently filling some of the glass spheroids.....	234

Chapter 1:

Introduction and Previous Studies

1.1 Introduction

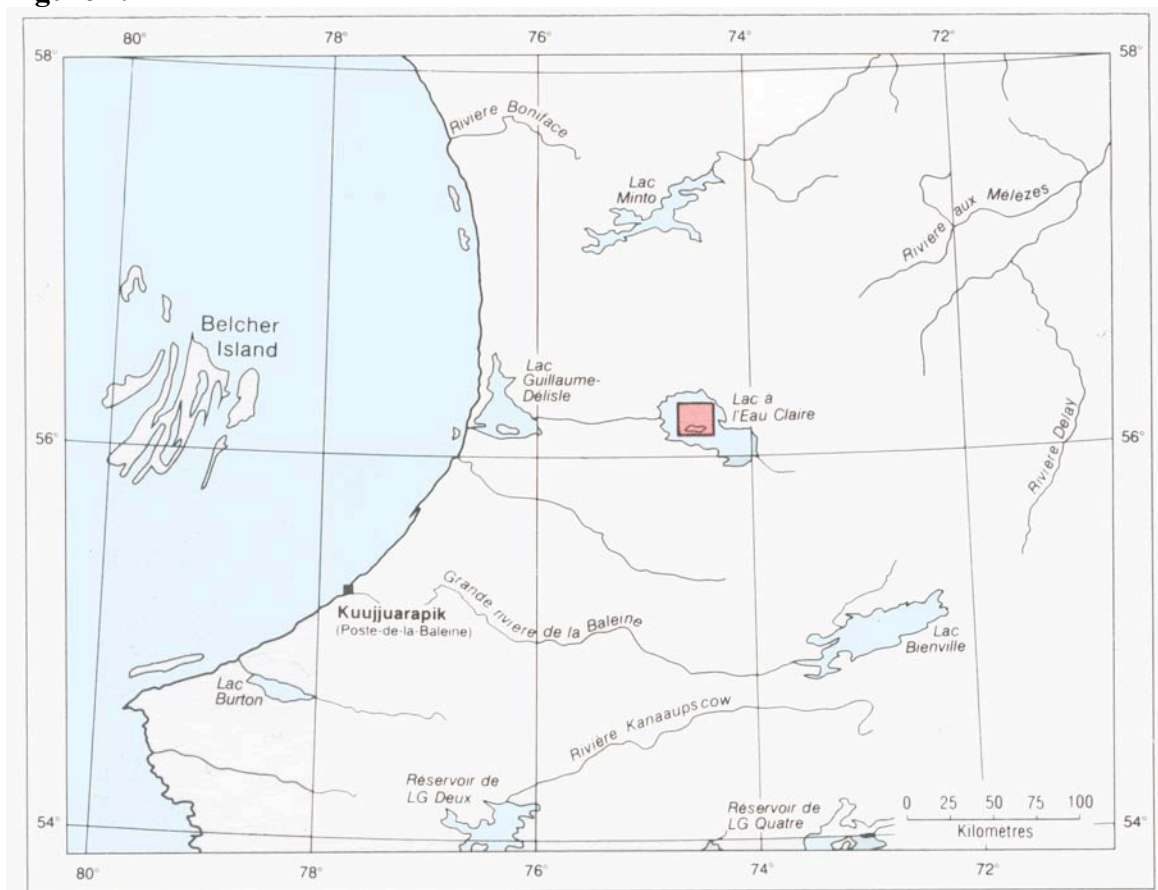
Large meteorite impacts into crystalline igneous and metamorphic rocks on the Earth, Moon and, presumably, other rocky bodies of the Solar System characteristically produce impact melts. Thus bodies of impact melt and impact-generated glass are common and important constituents of impact structures. Their presence has been well documented at many impact structures on Earth (Grieve and Cintala, 1992), and there is evidence for their existence elsewhere in the solar system.

Relative to other large terrestrial bodies of magma, the conditions of formation of an impact melt are relatively simple: impact melts are created by the massive, nearly instantaneous fragmentation of the target rocks, which is then followed by the complete or partial flash melting of the impact-generated breccias. Impact melts differ from “normal” eruptive melts in at least two aspects: their very variable clast content, caused by mixing during crater excavation, and the wide range of initial temperatures ranging from the melting to the boiling point of rock material. Thus, the solidification of a sheet of impact melt is not a simple process. The central area of West Clearwater Lake is one of the rare locations at the surface of the Earth where it is possible to observe and study the products of such an impact event. Careful examination of this uncommon body of magma can lead to important insights into the igneous processes involved in the formation of impact-generated melts. Thus, the main objective of this Ph.D. project is to understand how the impact melt sheet of the West Clearwater Lake impact crater, a crater

of intermediate size comparable to other craters on Earth and elsewhere in the Solar System, has formed, cooled and solidified.

1.2 The West Clearwater Lake Impact Structure

The centre of the West Clearwater Lake structure, located at 56°14'N 74°30'W, in northern Quebec, about 125 km east of the Hudson Bay arc, forms the western portion of twin circular lakes known as Lac à l'Eau Claire (that is, Clearwater Lake). The two large roughly circular lakes are separated by a barrier of islands (Figures 1.1 and 1.2). Clearwater Lake can clearly be seen in satellite images: it appears as a large lake with two circular regions or lobes. This lake has been considered, since at least the mid-sixties, to be the partially eroded and flooded remains of two craters that owe their origin to a simultaneous, or almost simultaneous, impact of two meteorites (or one fragmented meteorite) during the Upper Pennsylvanian (Dence et al., 1965; Phinney et al., 1978; Reimold et al., 1981; Simonds et al., 1978b). The eastern lobe is referred to as East Clearwater Lake. It is ~24 km in diameter, with an island-studded shoreline and an uninterrupted central surface; there are no islands far from shore. The western lobe is known as West Clearwater Lake, and is approximately 25 km in diameter. Like the eastern lake, its indented irregular shoreline contains numerous small islands. As one advances toward the hinterland (that is, away from the site of impact) the land rises from lake level (about 240 m above sea level) to a poorly defined concentric rim 5 to 10 km from the shore. This rim has a maximum elevation of about 425 m above lake level, and it is considered to be the limit of the West Clearwater crater, thus giving an approximate diameter of 32 km to the impact structure (Grieve, 2006).

Figure 1.1**Figure 1.2**

Figures 1.1 and 1.2 Location of the West Clearwater Lake impact structure. The figures are adapted from Simonds et al. (1978) and Rondot et al. (1993). The pink square refers to the area covered by Figure 1.3.

Within West Clearwater Lake, a number of large islands protruding to a maximum elevation of ~340 m above lake level (Figures 1.3 and 1.4) form a ring ~16 km in diameter. A few small islands less than 100 m across occupy the centre of the western lake. These central islands are the tip of an elliptical topographic uplift measuring ~5 x 8 km (Hische, 1995). In between the central uplift and the ring of islands, there is a poorly defined trough, with depths of about 50 m below lake level, whereas an annular trough at least 100 m deep occupies the region between the shore and the ring of islands.

The original form of the western crater is not known. The structure has been heavily eroded by glacial action. Whether the ring of islands, which is partially covered by impact-generated melt rocks, is what is left of a topographically elevated ring, or whether the ring has been created by erosional processes, is not clear. Grieve (2006) and others have assumed that the ring of islands is the remnant of an elevated ring (Figure 1.4); he has therefore classified the structure as a complex crater with a peak-ring form.

1.3 Previous Studies

The first extensive study of the Clearwater Lake area was carried out by H.H. Bostock in the summer of 1963 under the auspices of Operation Leaf River, an airborne reconnaissance project of the Geological Survey of Canada. His work, which comprised geological mapping, major-element analyses of basement and melt rocks, and petrological observations, was later published as a bulletin of the Geological Survey of Canada (Bostock, 1969), and is the first detailed geological report of the area.

According to Bostock, the first Europeans to visit the Clearwater Lake area were two Hudson's Bay Company employees, George Atkinson II and James Clouston, who

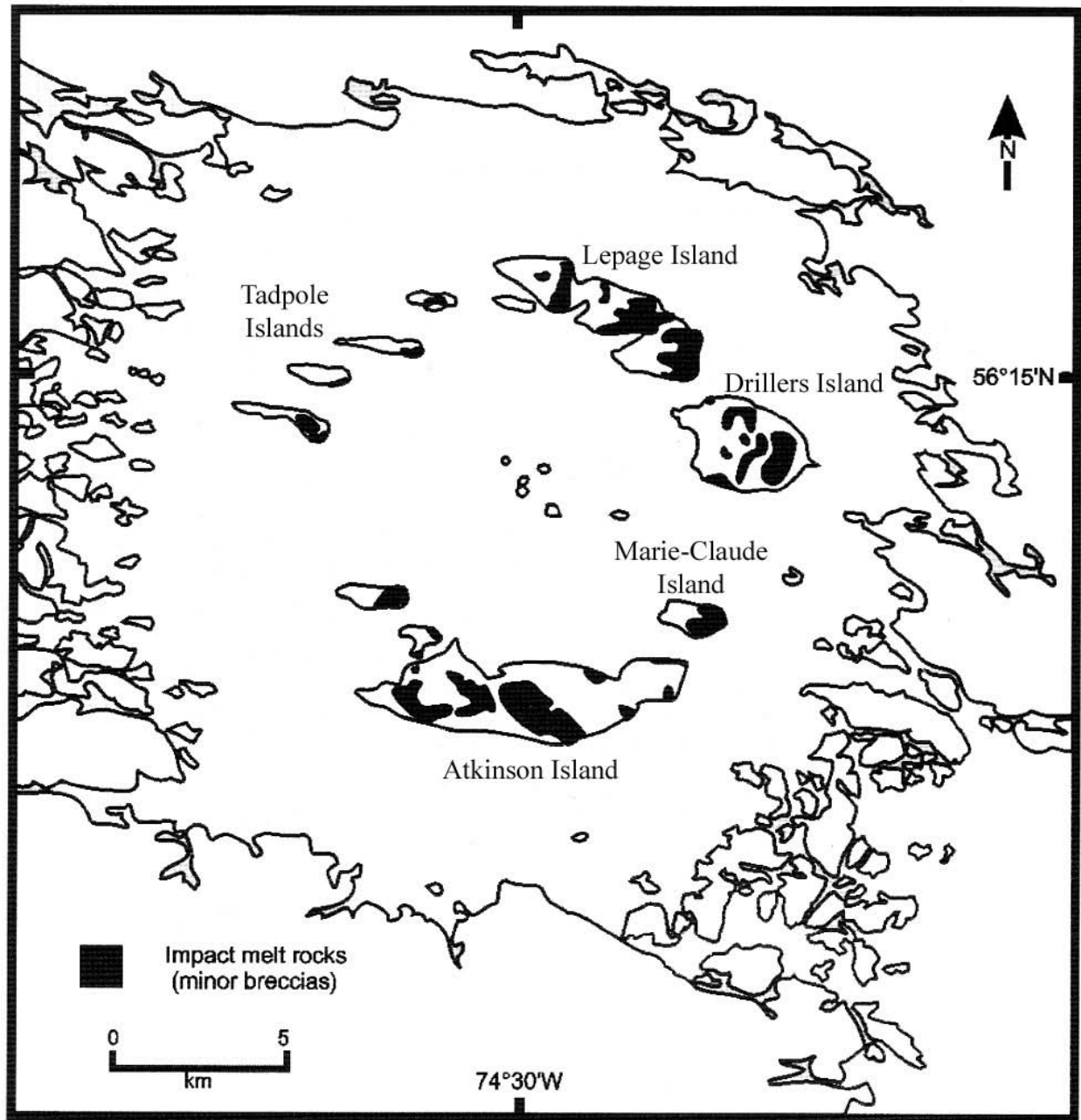


Figure 1.3 Location of major outcrops of impact melt rocks at the West Clearwater impact structure (adapted from Grieve 2006).

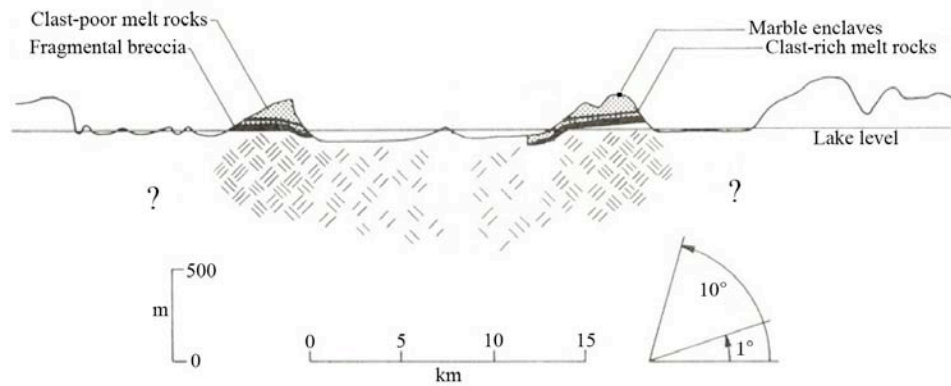


Figure 1.4 Generalized and vertically exaggerated cross-section of the West Clearwater impact structure (adapted from Simonds et al. 1978).

paddled across the lake in 1818 and 1820, respectively. Clouston remarked on the shape of the lake, which was, in his words, “like two circles joined”; both men commented on the clarity of the lake waters. No other visits to the region are recorded until 1888 when, as Bostock wrote, A.P. Low surveyed the Clearwater River to the outlet of Clearwater Lake, making some geological observations along the way. No one followed up on Low’s explorations, and as far as I know (H.H. Bostock concurs), no other accounts of visits to Clearwater Lake were published until the 1950s.

With the onset of the Second World War, newly available techniques of aerial photography were used to produce comprehensive maps of northern Quebec. These maps and photographs were made available to the staff of the Dominion Observatory, who rediscovered the peculiar twin rounded shape of the Clearwater Lake structure and included it in a list of possible Canadian meteorite craters (Beals et al., 1960). In 1958, the lake was visited by a party from the Dominion Observatory and by J.R. Woodcock of Kennco Explorations (Canada) Limited. Woodcock spent an hour at one of the islands in the ring, where he noticed the presence of both unaltered glass and rocks of volcanic

appearance. The Dominion Observatory party noted that the ring of islands mainly consisted of microbreccia of volcanic appearance (Bostock, 1969).

S.H. Krank spent six days on the islands of the West Clearwater Lake during the summer of 1959. Because of bad weather, his exploration concentrated on the large southern island, now known as Atkinson Island (Figure 1.3), which he named “Volcano Island”. He was the first to note the presence of maskelynite on the central islands, and he collected a number of fossils of Ordovician age found in limestone present on Atkinson Island (Krank and Sinclair, 1963).

The structure was also explored by M.R. Dence of the Earth Physics Branch of the Dominion Observatory, who first visited Clearwater Lake in the summer of 1962. Dence observed both the presence of maskelynite in drill core from the centre of the lake and numerous shatter cones, both in the small central islands and in the ring islands. Most importantly for this thesis, Dence supervised a drilling program there the following winter, which was completed in the winter of 1963-64. Results of this drilling program and of a related gravity study are given in Dence (1964), Dence (1981) and Dence et al. (1965).

Because at the time the formation of craters through meteor impact was not well understood and still controversial, both Bostock (1969) and Krank and Sinclair (1963) believed that the Clearwater structure was of volcanic origin. Dence, however, favoured the hypothesis of an impact origin. The impact hypothesis was further supported by petrographic descriptions of impact-induced shock-metamorphic features found in West Clearwater breccia fragments made by McIntyre (1968), Bunch (1968) and Robertson et al. (1968).

Using Bostock's data, Grieve (1978) was able to recreate the average composition of the melt rocks that form most of the impact-related units at the West Clearwater structure. He established that the average composition of the impact melt could be obtained from a mixture of the local basement Archean rocks, without additions of volcanic, sedimentary or meteoritic components. The samples drilled by the Dominion Observatory team in 1963-1964 were analyzed for siderophile trace elements by Palme et al. (1978): no evidence of contamination by meteoritic material was found. However, Grieve (1978), Palme et al. (1978) and Grieve et al. (1980) estimated that there could be about 6% contamination by a carbonaceous chondrite in the eastern crater of the Clearwater Lake structure. This finding was disputed by McDonald (2002) who, using new data on the levels of the platinum-group elements in meteorites, estimated that the structure was most probably formed by the impact of an asteroid composed of material similar to ordinary chondrites. Evidence of nickel enrichment in East Clearwater melt rocks was also mentioned by Currie (1971).

The first estimated ages for the Western Clearwater crater were obtained by K-Ar whole-rock analyses of the impact melt from the crater's ring of islands; the ages obtained were 300 ± 24 Ma and 285 ± 23 Ma (Bostock, 1969; Wanless et al., 1964). Later work on East Clearwater crater produced an age of 287 ± 26 Ma using the Rb-Sr method (Reimold et al., 1981). These ages agree with those found by fission-track annealing studies on glassy samples of melt (Fleischer et al., 1969; Storzer and Wagner, 1977).

A detailed field-based study focusing on the melt rocks, breccia and their contacts with the basement was done in the summer of 1977 by C.H. Simonds and W.C. Phinney, geologists at the time associated with NASA's geological branch. Whereas Simonds et

al. (1978) described the field geology, structure and composition of the West Clearwater crater, Phinney et al. (1978) covered the petrology of the impact melt and breccias. Of all the publications on the Clearwater structure released so far, these two articles cover the geology of the West Clearwater crater in the greatest detail. M.R. Dence accompanied the NASA party to the western crater, where he collected a number of samples from all the impact-related units present there. These samples form the bulk of the material studied in this thesis.

In the last 30 years, the publications relating to the Clearwater structure have been relatively scarce: besides the article on contamination by meteoritic components at East Clearwater mentioned above (McDonald, 2002), I found only two other articles and a conference abstract directly concerned with the Clearwater impact structures: Plante et al. (1990) published the results of a gravimetric study; Rondot et al. (1993), from the Direction Générale de l'Exploration Géologique et Minérale of the Ministère des Ressources Naturelles du Québec, published a guidebook with geological maps of the western ring of islands; Scott et al. (1995) described the magnetic properties of the Clearwater Lake impact craters. Jehan Rondot published a book on Quebec impact structures addressed to the general public in which he provided a short description of the Clearwater double impact structure (Rondot, 1995). Both Ciesielski and Plante (1990) and Simard et al. (2004) provided detailed descriptions of the geology of the vicinity of the Clearwater craters, but neither group described the impact structure. The area around the impact structure was mapped by the Services Géologiques of the Ministère des Ressources Naturelles du Québec in the summer of 2002 (Simard and Sharma, 2004). R.A.F. Grieve dedicated a chapter to the Clearwater structure in his monograph on Impact Structures in Canada (Grieve, 2006), which is a synthesis of knowledge on

Canadian impact structures published by the Geological Association of Canada. Finally, the West Clearwater structure has been the subject of two recent graduate theses: a detailed doctoral study of the shock metamorphism present in the core drilled by Dence's group in 1963-1964 done by R. Hische, then at Westfälischen Wilhelms University, Münster, Germany (Hische, 1995), and my own M. Sc. thesis, in which I studied the contact metamorphism of limestone enclaves enclosed in the impact melt (Rosa, 2005; Rosa and Martin, 2010). For convenience, the latter article is reproduced here as Appendix E, with permission.

Chapter 2: Geology of West Clearwater Lake Impact Structure

2.1 Archean Units

The Clearwater Lake impact structure is situated, according to Ciesielski and Plante (1990) and Simard et al. (2004), in the northwestern most part of the Bienville Subprovince of the Superior craton. The target rocks are mostly of Archean age, and they are dominated by metamorphosed biotite-bearing granites and granodiorites, and by orthopyroxene-bearing enderbites and diorites. Smaller domains of clinopyroxene-bearing tonalites and diorites, and ultramafic lithologies, are also present northwest of the crater. In addition, clinopyroxene-bearing granodiorite, along with gabbro and gabbro-norite, have also been observed in the islands that separate West Clearwater Lake from the eastern lake. Simard et al. (2004) have roughly divided these units into three major lithologies: the Desbergère Suite of granites and granodiorites, the Loups Marins Complex of enderbites, diorites and tonalites, and finally the Qullinaaraaluk Suite of mafic and ultramafic rocks (Figure 2.2). Most of what is presented in the following sections is a summary of the findings of Simard et al. (2004). Unfortunately (and inexplicably), Simard et al. (2004) did not provide mineral compositions in their report. They did, however, report compositions of the rock types encountered; averages and ranges are reported in Tables 2.1 and 2.2.

The mineral assemblages present in these rocks indicate that they were subjected to metamorphism at amphibolite and granulite facies (Ciesielski and Plante, 1990; Simard and Sharma, 2004). The regional orientation of major structures is roughly

Table 2.1 Average composition, and minimum and maximum range of compositions (major element oxides) of the target rocks of the Clearwater Lakes region

Rock Unit	Desbergères suite granite/ granodiorite	Loup Marins complex tonalite/diorite	Loup Marins complex granodiorite	Loup Marins complex enderbite/ OPX diorite	Quilinaarakluk Suite Ultramafic intrusions	Quilinaarakluk Suite Mafic intrusions	Diabase (E-W)							
n	43	7	4	5	19	9	21							
	aver.	min.-max.	aver.	min.-max.	aver.	min.-max.	aver.	min.-max.						
SiO ₂ (%)	70.71	63.80-74.78	58.39	49.93-70.68	67.82	66.72-68.49	60.73	53.82-67.52	50.05	42.87-55.01	47.97	44.17-52.47	49.18	46.25-53.26
TiO ₂	0.28	0.11-0.59	1.05	0.54-2.26	0.48	0.43-0.60	0.62	0.45-0.87	0.61	0.29-1.50	1.58	0.68-3.79	1.69	0.77-2.85
Al ₂ O ₃	14.35	13.03-16.20	16.84	15.51-18.82	15.34	14.97-15.74	17.02	15.06-18.85	14.35	13.03-16.20	14.48	8.34-17.69	14.05	12.30-16.70
Fe ₂ O ₃	2.65	1.06-5.06	7.65	2.46-12.41	3.70	3.35-4.19	6.22	4.66-9.58	12.25	8.90-19.82	13.10	9.72-16.26	12.51	4.95-16.49
MnO	0.03	0.01-0.08	0.08	0.04-0.14	0.05	0.04-0.05	0.08	0.04-0.12	0.18	0.11-0.25	0.15	0.10-0.20	0.16	0.04-0.23
MgO	0.93	0.29-2.68	2.65	0.85-4.50	1.10	0.96-1.26	3.08	1.57-6.21	13.66	5.98-24.25	7.04	4.52-12.35	6.76	4.24-10.68
CaO	1.96	0.64-3.94	5.72	3.79-7.69	3.05	2.94-3.20	5.52	3.08-6.82	10.76	4.71-15.00	8.67	5.63-14.10	7.69	0.78-11.57
Na ₂ O	3.41	2.53-4.08	4.15	3.38-4.46	3.70	3.46-4.06	4.04	3.32-4.71	1.41	0.54-3.15	2.79	1.48-4.14	2.31	0.97-4.85
K ₂ O	4.22	2.80-6.12	1.76	1.17-2.39	3.34	2.76-3.74	1.57	0.88-2.07	0.94	0.31-2.02	1.56	0.49-2.50	1.14	0.22-2.52
P ₂ O ₅	0.08	0.01-0.24	0.47	0.10-1.02	0.17	0.13-0.27	0.30	0.09-0.82	0.16	0.02-0.64	0.39	0.06-1.50	0.22	0.06-0.44
Mg #	0.36	0.19-0.49	0.36	0.31-0.41	0.32	0.30-0.36	0.44	0.35-0.51	0.64	0.43-0.75	0.46	0.32-0.65	0.46	0.31-0.75

Simard et al. (2004): results obtained with inductively coupled plasma-mass-spectrometry (ICP-MS) and inductively coupled plasma emission spectroscopy (ICP-ES). Analyses done at the Acme Analytical Laboratories, Vancouver.

Table 2.2 Average composition, and minimum and maximum range of compositions (trace elements) of the target rocks of the Clearwater Lakes region.

Rock Unit	Desbergères suite granite/granodiorite	Loup Marins comp. tonalite/diorite	Loup Marins comp. granodiorite	Loup Marins comp. enderbite/ OPX diorite	Ultramafic intrusions hornblende/ pyroxenite	Mafic intrusions gabbro/ gabbroiorite	Diabase (E-W)							
n	43	7	4	5	19	9	21							
	aver.	min.-max.	aver.	min.-max.	aver.	min.-max.	aver.							
Ba (ppm)	1015	469-2559	655	232-990	871	729-1235	663	330-813	238	46-1010	455	212-962	678	42-4747
Rb	135	86-263	69	41-98	101	67-131	44	10-64	37	7-116	58	6-107	38	3-121
Cs	1.1	0.1-4.4	0.5	0.1-1.1	0.3	0.1-0.5	0.1	0.1-0.2	0.6	0.1-3.5	0.6	0.1-1.5	0.5	0.1-3.2
Th	18.0	0.9-51.9	2.9	1.5-7.7	4.0	1.7-5.7	1.1	0.3-2.3	1.9	0.5-10.3	2.0	0.7-5.0	1.6	0.2-3.8
U	1.6	0.1-6.4	0.6	0.1-1.4	0.3	0.1-0.7	0.2	0.1-0.4	0.3	0.1-1.3	0.5	0.1-0.8	0.3	0.1-1.4
Ta	0.4	0.1-1.8	0.5	0.2-1.0	0.2	0.1-0.2	0.3	0.1-0.6	0.2	0.1-0.5	0.5	0.1-1.1	0.7	0.1-1.7
Nb	5.5	1.3-16.0	10.0	2.8-24.2	5.0	4.7-5.9	6.1	3.7-10.4	2.6	0.5-7.2	7.8	1.7-17.6	10.7	2.1-25.9
Sr	370	176-645	653	451-864	478	359-627	584	410-772	269	90-1424	601	286-908	248	70-461
Zr	138	83-301	279	114-501	175	118-251	178	98-250	51	21-193	96	22-300	124	41-223
Hf	4.3	2.5-8.9	7.2	3.0-12.0	5.3	3.5-6.8	4.8	2.5-6.9	1.6	0.5-4.8	2.7	0.5-8.0	3.5	1.4-6.3
Y	8.7	1.5-29.2	20.6	4.9-40.7	8.6	7.0-10.5	13.5	5.9-18.9	16.1	8.4-31.3	19.1	5.6-32.8	31.8	13.6-52.0
La	39.2	7.0-85.0	49.9	22.0-78.9	44.4	29.4-70.7	39.2	17.2-66.7	17.9	4.2-60.8	28.1	6.9-86.1	17.8	5.3-35.7
Ce	69.7	10.4-147.6	103.2	38.9-182.1	79.1	53.4-130.5	75.1	30.8-139.0	41.6	12.3-130.2	62.9	16.5-182.6	38.1	11.7-69.6
Nd	24.5	3.2-55.4	52.5	14.8-105.0	31.2	22.5-52.5	33.6	12.0-65.3	24.1	9.2-60.6	35.2	8.3-93.1	22.4	8.3-36.5
Sm	3.6	0.5-9.4	9.1	2.4-18.1	4.8	3.6-7.9	5.7	2.1-10.2	5.0	2.2-10.2	6.9	1.8-15.9	5.1	2.1-8.4
Eu	0.8	0.4-1.5	1.8	0.8-3.8	1.1	0.9-1.6	1.3	0.7-1.9	1.1	0.5-1.8	1.7	0.6-2.9	1.6	0.8-2.4
Yb	0.8	0.2-2.6	1.7	0.4-3.2	0.6	0.6-0.7	1.2	0.6-1.7	1.5	0.7-3.2	1.7	0.6-2.9	3.1	1.4-5.5
Lu	0.1	<0.1-0.4	0.2	<0.1-0.4	0.1	0.1-0.1	0.2	0.1-0.3	0.2	0.1-0.5	0.2	0.1-0.4	0.5	0.2-0.8
V	34	6-91	129	25-203	54	41-65	88	63-127	251	112-931	294	133-506	323	167-471
Ni	6	2-16	15	7-36	7	4-10	24	8-71	157	32-1347	64	3-225	41	21-102
Co	5	1-12	19	6-31	7	6-9	18	10-34	74	40-139	50	31-68	46	25-60

Simard et al. (2004): results obtained with inductively coupled plasma-mass-spectrometry (ICP-MS) and inductively coupled plasma emission spectroscopy (ICP-ES). Analysis done at the Acme Analytical Laboratories, Vancouver.

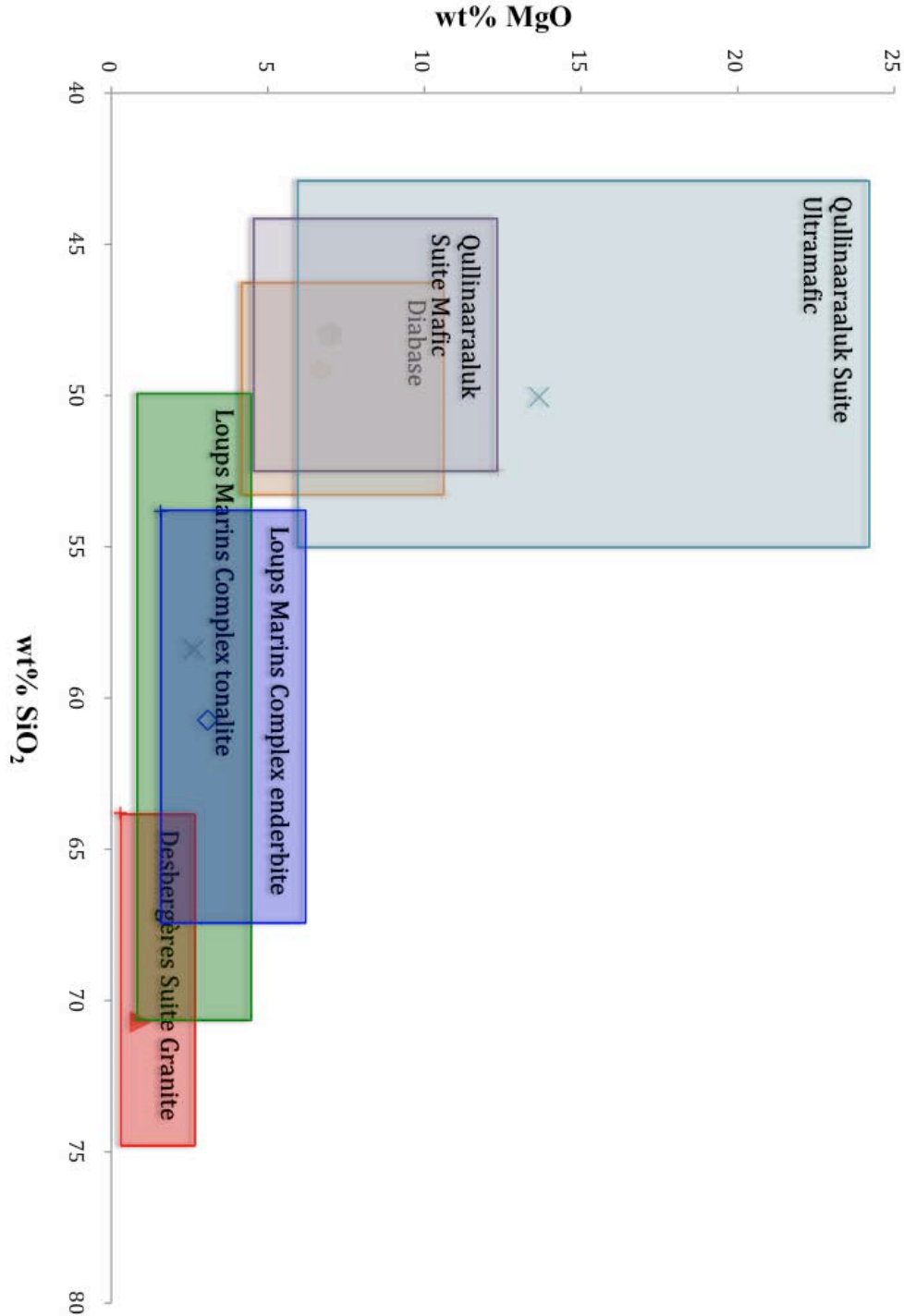


Figure 2.1 Maximum and minimum ranges of MgO vs. SiO₂ compositions of the basement rocks present in the Clearwater Lakes region. Average compositions are showed by an X mark within the rectangles. Results obtained with inductively coupled plasma mass spectrometry (ICP-MS) and inductively coupled plasma emission spectroscopy (ICP-ES). Analyses done at the Acme Analytical Laboratories, Vancouver. Adapted from Simard et al. (2004).

NNW-SSE, as delimited by strong positive aeromagnetic anomalies in the basement (Card and Ciesielski, 1986; Percival et al., 1992).

2.1.1 The granites and granodiorites of the Desbergères Suite

The biotite-bearing granites and granodiorites of the West Clearwater Lake region [which correspond to the “Bienville orthogneiss” of Ciesielski and Plante (1990)] are believed to belong to the Desbergères Suite, a lithostratigraphic unit introduced by Simard et al. (2001) to describe a geographically extensive rock unit of generally granodioritic composition containing both biotite and hornblende found to the east and southeast of the Clearwater Lakes area, in the Maricourt and Lac Bienville regions.

The granites and granodiorites of the Desbergères Suite are typically pale pink to grayish pink and medium- to coarse-grained, with a poorly developed foliation. The mineral composition is rather constant, showing 30 to 65% plagioclase, 20 to 30% quartz and 10 to 35% alkali feldspar. The proportion of mafic minerals varies from 2 to 10%: the most common mafic mineral is biotite, but hornblende is also present locally. In fact, Simard et al. (2004) divided the Desbergères Suite rocks of the West Clearwater Lake area in two compositionally similar units based on the presence or the absence of hornblende. They mentioned that zircon U-Pb ages of 2714 ± 12 Ma and 2711 ± 4 Ma have been obtained for the Desbergères Suite rocks of the Clearwater Lakes region. It should be noted that the “Bienville orthogneiss” around the Clearwater Lake area (which, as already mentioned, correspond to the biotite-bearing granites and granodiorites described above) have yielded a Rb-Sr age of 2562 ± 121 Ma (Reimold et al., 1981), whereas zircon found in the orthogneiss from the southwestern Bienville domain give imprecise discordia U-Pb ages of 2797 to 2818 Ma (Mortensen and Ciesielski, 1987).

The Desbergères Suite of granites and granodiorites includes a cogenetic porphyritic rock that shows a gradational contact with the main Desbergères Suite units. The mineral composition of this porphyritic rock is similar to that of the Desbergères Suite rocks: it is generally granitic, with some granodioritic and, more rarely, monzodioritic, components. Its porphyritic texture is due to the presence of 15 to 35% alkali feldspar crystals 1 to 5 cm long. Simard et al. (2004) distinguished porphyritic biotite granite and granodiorite from porphyritic biotite-hornblende granite and granodiorite on their map.

2.1.2 The enderbites, diorites, granodiorites and tonalites of the Loups Marins Complex

Massive to weakly foliated orthopyroxene-bearing enderbites and diorites form inclusions up to kilometres across in the granites and granodiorites of the Desbergères Suite. The West Clearwater Lake enderbites and diorites were placed by Simard et al. (2004) within the Loups Marins Complex, a lithological group of intrusive and metamorphic clinopyroxene- and orthopyroxene-bearing rocks first described by Gosselin et al. (2001) in the Lacs des Loups Marins area to the east of the Clearwater Lakes impact structure. Dating of the diorite in the Lacs des Loups Marins area has yielded a U-Pb zircon age of 2694 ± 3 Ma (Gosselin et al., 2001).

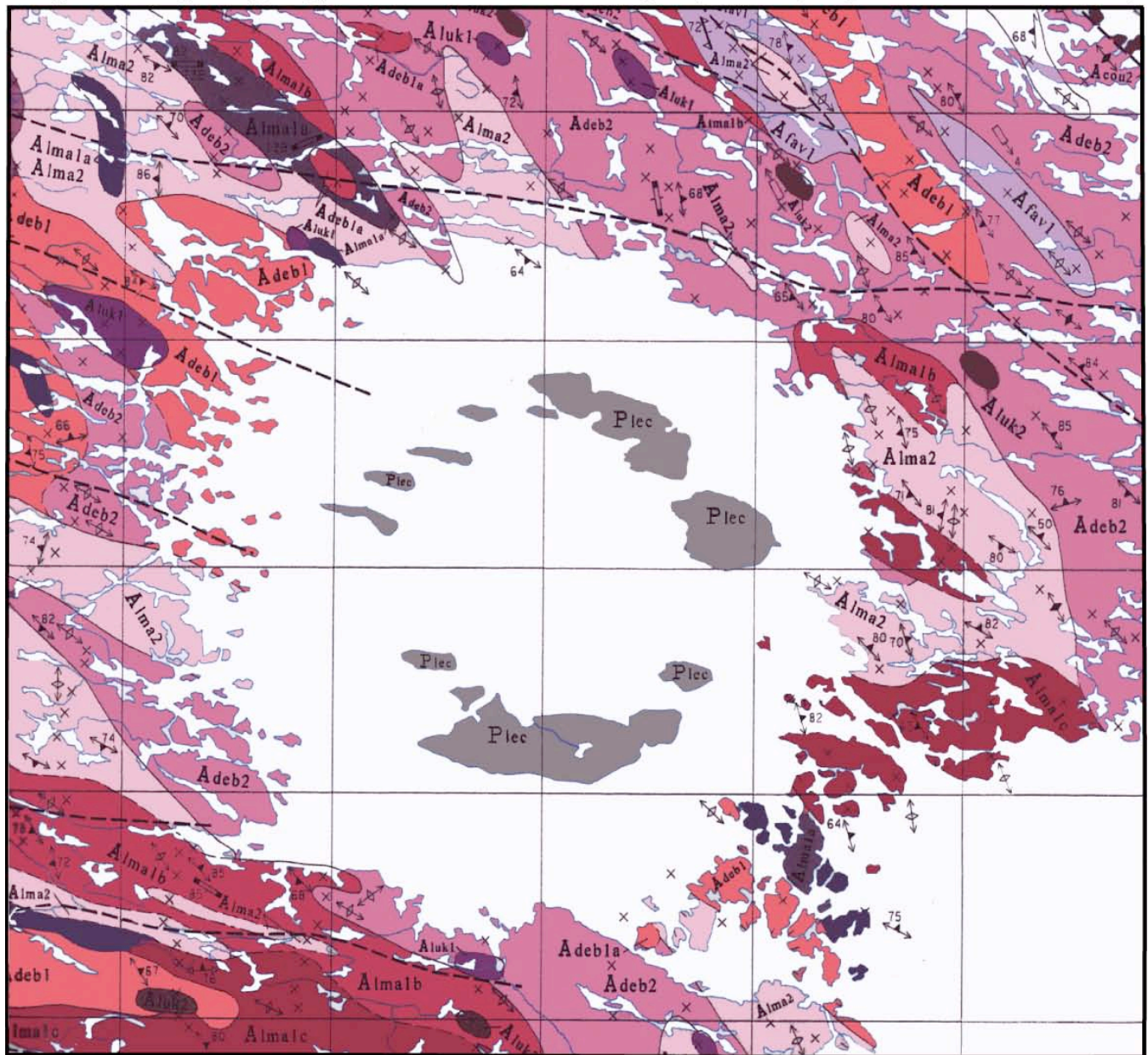
The West Clearwater Lake orthopyroxene-bearing enderbites and diorites are fine to medium grained, with a greenish or brownish tint; they are mostly composed of plagioclase (55 to 80%), with some quartz (2 to 35%) and mafic minerals (3 to 30%). Their mafic minerals comprise a variable proportion of reddish biotite (1 to 15%), clinopyroxene (1 to 10%) and orthopyroxene (1 to 5%), with rare green hornblende

occasionally present; the orthopyroxene is generally strongly altered to talc, serpentine, carbonate and chlorite. Xenomorphic magnetite (1 to 3%) is commonly associated with the mafic minerals. These enderbites and diorites also contain mafic enclaves (1 to 10%, 5 cm up to 1 meter long) stretched along the foliation plane; these enclaves are composed of foliated, dark-colored, fine-grained amphibolite and diorite (Simard et al. 2004).

The West Clearwater Lake area also includes other units placed by Gosselin et al. (2001) within the Loups Marins Complex. These rocks are characterized by the presence of clinopyroxene, reddish biotite and wine-red (or salmon-colored) plagioclase, giving the rock a pink or violet tint. Gosselin et al. (2002) have subdivided these clinopyroxene-bearing rocks in three subunits: 1) a massive to slightly foliated medium- to coarse-grained tonalite containing clusters of mafic minerals (5 to 25%), 2) a massive to slightly foliated medium- to coarse-grained granodiorite, in some cases slightly porphyritic, and 3) a pinkish gray to brownish gray porphyritic granodiorite and monzodiorite containing 10 to 25% alkali feldspar phenocrysts 1 to 5 cm long. Like the orthopyroxene enderbites described above, these rocks contain foliated amphibolitic and dioritic enclaves, in the centimeter to meter size-range and representing about 1 to 10% of the rock volume.

2.1.3 The leucotonalites of the Favard Suite

Rocks of the Favard Suite do not seem to be present in the units involved in the impact structure. However, the presence of a significant areal extent of Favard Suite biotite tonalite mapped by Simard et al. (2004) to the northeast of the crater requires that this suite be briefly described. The Favard Suite was first identified southeast of the Clearwater Lakes impact structure, in the region of Lac Gayot, by Gosselin and Simard

Figure 2.2 Simplified geology of the West Clearwater Lake region (1:250 000, adapted from Simard et al. 2004)**Pennsylvanian Units**

Plec Rock units created by impact cratering

Archean Units**Desbergères Suite**

Adeb1 Biotite-hornblende granite and granodiorite

Adeb2 Biotite granite and granodiorite

Loups Marins Complex

Alma1a CPX tonalite and diorite

Alma1b CPX granodiorite

Alma1c Porphyritic CPX granodiorite and monzodiorite

Alma2 OPX enderbite and diorite

Quillinaaraaluk Suite

Aluk1 Ultramafic rock; gabbro and gabbro-norite

Aluk2 Gabbro and gabbro-norite

Favard Suite

Afav1 Biotite tonalite

10 km

(2000), and is also present in the Maricourt (Simard et al. 2001), Lac des Loups Marins (Gosselin et al. 2001) and Lac Bienville regions (Gosselin et al. 2002). These authors have reported U-Pb dates obtained for samples taken in each of these regions between about 2730 and 2749 Ma (Gosselin and Simard, 2000); Simard et al. 2001; Gosselin et al. 2001; Gosselin et al. 2002). In addition, a sample of biotite leucotonalite from the Clearwater Lakes region gave a preliminary zircon U-Pb age of about 3020-3040 Ma (Simard et al. 2004).

In the Clearwater Lakes region, Simard et al. (2004) have identified a main biotite leucotonalite unit, and a biotite leucotonalite subunit with wine-red plagioclase. This rock is light gray where fresh, and whitish to pinkish where altered. Its grain size varies from fine to medium grained, and it has a massive to slightly foliated aspect. It generally contains about 5% enclaves consisting of centimeter to meter-sized fine-grained, strongly foliated diorite and amphibolite with a well-developed granoblastic texture. These enclaves are generally stretched parallel to the plane of foliation, and described as strongly assimilated by the leucotonalite, commonly showing a cm- to dm-wide hornblende-rich reaction rim at the contact with the leucotonalite (Simard et al. 2004).

Rocks of the biotite leucotonalite unit have a relatively homogeneous medium-grained equigranular texture. They are composed mainly of quartz (20 to 35%) showing a wavy extinction, and plagioclase (50 to 57%), commonly partially altered to white mica and showing signs of exsolution of K-feldspar. This rock generally has a low proportion of alkali feldspar (1 to 8%), and less than 10% greenish biotite altered to chlorite, and usually disseminated in the rock. According to Simard et al. (2004), some rare green

hornblende crystals were observed in a small number of samples (the authors did not provide compositional data).

2.1.4 The mafic and ultramafic rocks of the Qullinaaraaluk Suite

These rocks comprise massive partially or totally metamorphosed mafic and ultramafic rocks, comprising gabbro, gabbronorite, hornblendite, pyroxenite and even some peridotite, they form small homogeneous intrusions emplaced in the granites and granodiorites of the Desbergères Suite near the Clearwater Lake impact structure. Simard et al. (2004) placed these rocks within the Qullinaaraaluk Suite, a series of mafic to ultramafic intrusions first recognized to the north of the Clearwater Lake structure, near the area of Lac Vernon (Parent et al., 2002). These mafic and ultramafic units are cut by numerous white veins of tonalitic or granodioritic composition, centimeters to decimeters thick, giving them a brecciated aspect.

The ultramafic rocks are dark green to black, medium to coarse grained, and some show a cumulus texture. They consist of hornblendite, pyroxenite and some peridotite. Simard et al. (2004) mentioned the presence of 5 to 15% coarse-grained (1 to 3 cm) hornblende crystals that give the rocks a spotted appearance. The ultramafic units are generally in gradual or abrupt contact with gabbros and gabbronorites: Simard et al. (2004) speculated that some of these intrusions could be layered. The gabbro and gabbronorites are medium to coarse grained, greenish gray to black. These rocks contain 30 to 70% plagioclase, together with variable amounts of pyroxene (both clinopyroxene and orthopyroxene), biotite and up to 3% magnetite. It should be noted that Simard et al. (2004) tended to described rocks that have obviously undergone metamorphism as if they

were unaltered, so that a gabbro containing large quantities of secondary amphibole is still called a gabbro.

2.2 Proterozoic Units

Sets of altered diabase dykes trending N-S, NE-SW and NW-SE have been observed in two of the Tadpole Islands (also known as Wiskichanikw Islands), in the exterior margin of the ring of islands and in the region between the western and eastern impact sites (Bostock, 1969; Plante, 1986). According to Ciesielski and Plante (1990), the dykes are fine grained and have small phenocrysts of plagioclase and pyroxene, nodules of plagioclase-augite-pyrite (1-2 mm diameter), and well-developed chilled margins.

The diabase dykes visible in the ring of islands have been strongly affected by shock metamorphism, and they were subjected to the same extensive fracturing as the impacted Archean bedrock. Some fragments of these dykes have been observed within the impact-related rock-types of the Western crater (Rondot et al., 1993). The dykes thus clearly predate the impact. According to Ciesielski and Plante (1990), their orientation suggests that they may correlate with the Mistassini (N-S and NW-SE trends) and Preissac (NE-SW trends) swarms of early Proterozoic age observed in the vicinity of the impact structure. Simard et al. (2004), however, correlated the dykes having N-S and NW-SE orientations with the Minto swarm, and the dykes with a NE-SW trend with the Maguire swarm. Both these suites have been studied by Buchan et al. (1998).

2.3 Ordovician Units (West Clearwater Lake Carbonates)

As far as I know, all the carbonate-rich sedimentary units in the Clearwater Lake region are restricted to the ring of islands in the western crater. These carbonates are found

either as gray fossiliferous limestone float, in blocks of variable size on the external side of the ring of islands, or as partially to totally recrystallized enclaves in the impact melt, the largest of which is about 100 x 15 m. The enclaves of recrystallized carbonate were subjected to contact-metamorphism by the impact melt, and they are remarkable for the presence of relatively rare sanidinite-facies (high-temperature, low-pressure) minerals such as spurrite $[\text{Ca}_5(\text{SiO}_4)_2(\text{CO}_3)]$, merwinite $[\text{Ca}_3\text{Mg}(\text{SiO}_4)_2]$, monticellite $[\text{CaMgSiO}_4]$ and srebrodolskite $[\text{Ca}_2(\text{Fe}^{3+}, \text{Al})_2\text{O}_5]$. These enclaves were the subject of the author's M.Sc. thesis (Rosa, 2005).

These showings of limestone occur far within the Canadian Shield; I know of no record of equivalent outcrops in this part of Quebec (Sanford, 1987; Sanford and Grant, 1990). Although they are stratigraphically isolated, the limestone blocks in the West Clearwater area are attributed to the succession of lower Palaeozoic sedimentary rocks that cover most of the Hudson Bay platform. Krank and Sinclair (1963) attempted to correlate the Clearwater carbonates with other successions in the Hudson Bay region, but the stratigraphy of the region was less well known then than it is now, and they were unable to assign the carbonates to a known formation. They did, however, give middle to upper Ordovician ages (Edenian or Maysvillian) to the fossil assemblages found in the carbonates. By comparing their findings to the known stratigraphy of the area, I came to the conclusion that the carbonates are probably correlated with the second member of the Portage Chute Formation of the Bad Cache Rapids Group, a Middle Ordovician formation that extends from the Foxe Basin and Hudson Strait area southward to the western Ontario interior.

Considering the geographical extent of Bad Cache Rapids Group, it is then, I believe, quite possible that the Clearwater Lake area was, at the time of the impact,

partially covered with a veneer of Bad Cache Rapids Group sediments, and that this sediment cover was later removed by erosion. Glaciers, however, probably pushed parts of this cover into the annular graben that formed as a result of the Clearwater double impact event, preserving it. Other blocks were also preserved as enclaves in the impact melt.

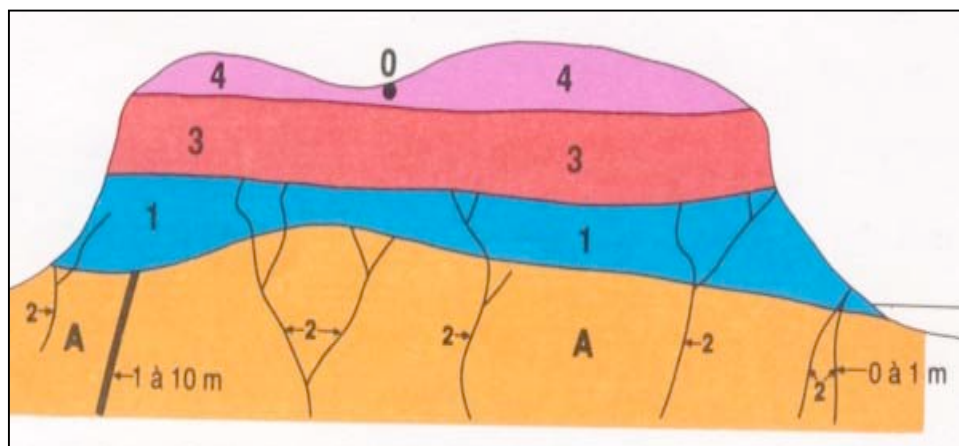
2.4 Pennsylvanian Units (Impact-Related Lithologies)

According to Simonds et al. (1978b), the crater-fill deposits exposed on the ring of islands at the center of the western crater can be divided into three major successive units, which are, in ascending order:

- 1) a red, friable impact-melt-bearing fragmental breccia 0 to 20 m thick cut by small (cm to dm) dykes of impact melt;
- 2) a red, massive and well-jointed clast-rich impact-generated melt (also called impact-ignimbrite) about 18 meters thick containing up to 25% clasts greater than 1 mm in size, with a matrix showing an ophitic to subophitic texture;
- 3) a massive, poorly jointed clast-poor impact-generated melt (also called impactite) containing <15% clasts greater than 1 mm in size, red at the base and grayish at the top, at least 85 m thick, with a matrix that shows, like that of the clast-rich impact-melt, an ophitic to subophitic texture.

The “clast-rich” melt and “clast-poor” melt designations are those used by Simonds et al. (1978) and Phinney et al. (1978), whereas impact-ignimbrite and impactite are used in Rondot et al. (1993). Although the terminology of Rondot et al. is more accurate, I prefer to use that of Simonds and Phinney, which I find more informative.

According to Simonds et al. (1978), the average composition of the impact melt is 59.1% SiO₂, 1.0% TiO₂, 16.2% Al₂O₃, 5.2% FeO, 2.8% MgO, 3.7% CaO, 3.9% Na₂O and 4.1% K₂O; to them, the melt was, therefore, roughly granodioritic in composition.



Pennsylvanian Units Thickness

Unit 4	> 85 m
Unit 3	15 to 20 m
Unit 2	< 1 m
Unit 1	0 to 30 m

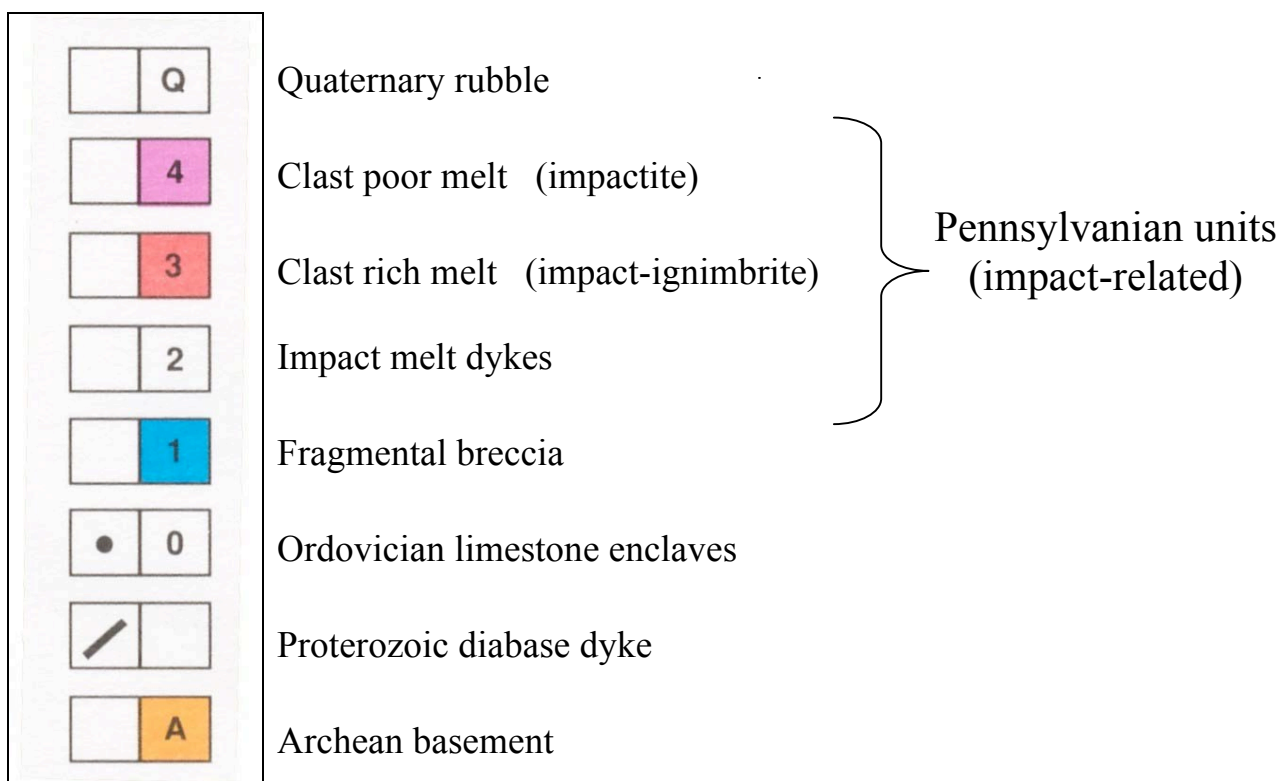


Figure 2.3 Cross-section of the impact melt sheet at the West Clearwater impact structure. Adapted from Simonds et al. (1978) and Rondot et. al. (1993).

The preserved volume of the impact-generated melt rocks was estimated by Grieve et al. (1976) to range from 34 to 50 km³, whereas Phinney and Simonds (1977) estimated the preserved volume to be ~40 km³ and the original (pre-erosion) volume to have been ~80 km³. These impact-related units are the main topic of this thesis and will therefore be described in greater detail later in this work.

Crustal xenoliths up to 100 m across are recognizable as clasts in the impact-related units, but most of the clast-size population is in the centimeter to meter range. The clasts are most abundant in the fragmental breccia (unit 1 mentioned above) and at the bottom of the clast-rich melt (unit 2); they become increasingly rare above the bottom of the clast-rich melt. The clasts generally consist of Archean target rocks, but at least seven of the larger clasts observed at West Clearwater Lake are blocks of the Middle Ordovician limestone mentioned above, considered to represent remnants of a post-cratonic cover present at the time of impact and preserved by enclosure in the impact melt. The contact metamorphism that took place when these carbonate enclaves were engulfed in the superheated impact melt shortly after the formation of the crater reached the sanidinite facies, but this was evidently a very brief event (Rosa, 2005; Rosa and Martin, 2010).

2.5 Summary of chapter 2

According to Simard et al. (2004), by order of importance, the rock lithologies found in the vicinity of the West Clearwater Lake impact structure are:

- The Archean clinopyroxene granodiorites, diorites and tonalites of the Loups Marins complex, which also includes orthopyroxene enderbites;

- The Archean biotite-hornblende and biotite granites and granodiorites of the Desbergère Suite;
- The gabbro and gabbro-norites of the Qullinaaraaluk Suite, which also include a small number of ultramafic units (hornblendite, pyroxenite), probably all of Archean age;
- The country rock is also cut by a number of diabase dykes of Proterozoic age.

Simonds et al. (1978b) divided the crater-fill deposits exposed on the ring of islands at the center of the western crater into three major successive units, which are, in ascending order:

- A red, friable fragmental breccia 0 to 20 m thick cut by small (cm to dm) dykes of impact melt;
- A red, massive and well-jointed clast-rich impact-generated melt (also called impact-ignimbrite) about 18 meters thick containing up to 25% clasts greater than 1 mm in size, with a matrix showing an ophitic to subophitic texture;
- A massive poorly jointed clast-poor impact-generated melt (also called impactite) containing <15% clasts greater than 1 mm in size, red at the base and grayish at the top, at least 85 m thick, with a matrix that shows, like that of the clast-rich impact-melt, an ophitic to subophitic texture.

Chapter 3:

Impact Cratering

When a meteorite moving at tens of kilometers per second hits a planetary surface, it initiates a rapid sequence of events that eventually produces the final crater. This sequence of events controls the initial shape, temperature and composition of the impact melt: it is important, therefore, to spend some time describing the event in some detail.

Although the formation of an impact crater is a continuous process, without clearcut breaks within the sequence of events, it has become common practice to separate the impact sequence into at least three successive sections: 1) contact and compression, 2) excavation, and 3) modification. This sequence has been established as a result of a combination of theoretical studies, analog experiments (including nuclear explosions), and the study of both terrestrial and extraterrestrial impact craters. These stages do not have precise boundaries: it is possible that one stage partially overlaps with the beginning (or the end) of another: this separation into episodes is used to reflect the dominant mechanisms acting during each stage. The general pattern is explained, very thoroughly, by H.J. Melosh in his monograph “Impact Cratering: A Geological Process” (1989). I know of no other publication that treats this subject with comparable detail and clarity, and this chapter will be, in essence, a summary of the chapters in Melosh’s book that focus on the events that take place during an impact.

3.1 Contact and compression

If one neglects the pre-impact interaction with the atmosphere, the first stage of impact cratering commences when the projectile strikes the Earth’s surface. The minimum velocity of impact between a planet and a meteorite is the planet’s escape velocity;

assuming that the incoming meteorite is part of the solar system, the maximum velocity of impact is given by a combination of the planet's escape velocity, its orbital velocity and the velocity of an object just barely within the gravitational pull of the Sun at the planet's orbital position. For the Earth, the minimum velocity of impact is taken to be 11.2 km/s, and the maximum is 72.8 km/s (Melosh, 1989). At contact, the projectile rapidly decelerates, pushing target material out of its path, compressing and accelerating it to a large fraction of the impact velocity. Strongly shocked material is ejected out of the contact area at high speed. The underlying material in the contact zone between the projectile and target is strongly compressed: shock pressures involved in the early stages of most impacts generally reach hundreds of GPa, which creates shock waves at the boundary between compressed and uncompressed material. These shock waves propagate outward from the point of impact (or points of impact, in the case of irregular projectiles), into both the target rock and the projectile. As the pressures generated far exceed the yield strength of the materials involved, both the projectile and the target rock in the immediate vicinity of the point of impact are usually melted or vaporized upon unloading, that is, after the shock wave has passed and left a zone of rarefaction in its wake.

The contact-and-compression stage ends as soon as the shock wave has passed through the projectile, releasing it from high pressure. The duration of the contact-and-compression stage depends upon the projectile's composition, size and initial velocity. For instance, Melosh (1989) estimated that for a silicate meteorite 10 meters across striking at 10 km/s, the contact-and-compression stage lasts approximately 10^{-3} seconds, whereas it will last 100 times as long (10^{-1} seconds) for a projectile 1 km across

approaching at the same speed (Melosh, 1989). It is, therefore, only for the largest impacts that this stage may last a second or more.

3.2 Excavation

As the contact-and-compression stage fizzles out, the excavation stage begins. During this stage, the approximately hemispherical shock wave and the following rarefaction front propagate into the target rock, setting the melted and fractured target material in motion. A subsonic excavation-related flow opens a cavity that is initially hemispherical. Its rate of growth in depth ceases before its radial expansion, producing, in the ideal case, a cavity that is approximately paraboloidal in vertical cross-section (Figure 3.1). It should be noted, however, that in many computer-generated simulations, the floor of the transient crater begins rising while the radius of the transient cavity is still increasing (Melosh and Ivanov, 1999), flattening the ideal paraboloid shape. The opening cavity is lined with impact-generated melt and the most highly shocked material. Upward in the crater, vaporized material expands outward in a plume; some melted and fractured material is either ejected, or displaced out of the crater, deforming the adjacent rocks, uplifting the surface near the crater rim and infiltrating the rocks located beneath the crater.

Gravitational collapse alters the shape of the cavity almost as soon as it ceases to grow; the paraboloid shape described above does not correspond to the final shape of the crater; the temporary paraboloid cavity is thus known as the transient crater. The diameter of the transient crater is many times larger than the projectile that produced it: this is the major difference between high-velocity impacts and the more familiar low-velocity craters made by, for instance, falling rocks or non-explosive military ordinance.

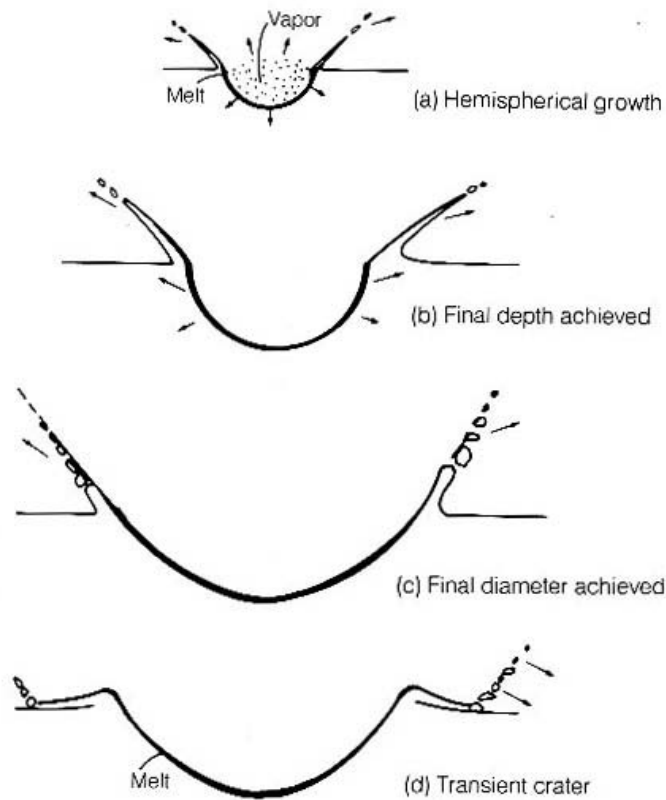


Figure 3.1 Growth of a crater. The crater becomes hemispherical shortly after the impact and initially expands at a fraction of the impact velocity (a). Its rate of growth in depth slows and finally ceases (b) before its radial growth halts (c). The resulting crater (d) is called a transient crater because it is subject to further gravitational collapse. At all stages of its expansion the crater is lined with melt of highly shocked rocks originally produced near the site of the impact (figure and caption adapted from Melosh 1989).

The diameter of the transient crater is considered to be equivalent to the rim-to-rim diameter of the final post-gravitational collapse crater (estimated to be about 32 km for the West Clearwater crater). Furthermore, according to experimental results and several extensively studied natural craters on Earth, ejected material is excavated from a maximum depth that is equal to about 1/3 of the transient crater depth, or 1/10 of its

diameter (Melosh, 1989). The excavation stage lasts much longer than the contact-and-compression stage. As the duration of excavation is, naturally, proportional to crater size, the excavation of smaller craters is considered to require seconds, whereas, for the largest craters, the excavation process can take minutes to reach completion.

3.3 Modification

The modification stage begins around the time the transient crater reaches its maximum excavated volume. In small craters such as Meteor Crater, Arizona (1.2 km across), this stage involves slumping of the crater walls, with loose debris sliding down the steep interior walls and accumulating at the bottom of the final depression. Terrestrial craters larger than about 4 km across collapse in a more complex and spectacular manner: their rims cave-in along a series of large concentric faults, forming slump terraces on their walls. The transition between small crater slumping and large crater cave-in depends on gravity: on Earth, the transition happens at diameters of 2–4 km, whereas the threshold diameter is about 7 km on Mercury and 10–20 km on the Moon (Melosh, 1989). Moreover, in large impact events, the floor of the crater rebounds, producing a structural uplift resulting in the formation of a central peak (as at Manicouagan, Quebec) or a peak-ring, as is considered to have occurred at West Clearwater Lake (Grieve, 2006) (Figure 3.2). It should be noted that the mechanism that produces central peaks and peak-rings is still poorly understood. Attempts at modeling their uplift usually involve some kind of momentary decrease in the strength of the target rocks, allowing them to rapidly flow and deform without melting, in a way similar to that of a liquid, that is, a strengthless fluid (Melosh and Ivanov, 1999). It has been difficult, however, to directly correlate the

structural features predicted by these models with field observations of the geological structure of central uplifts and peak-rings (Kenkmann et al., 2005).

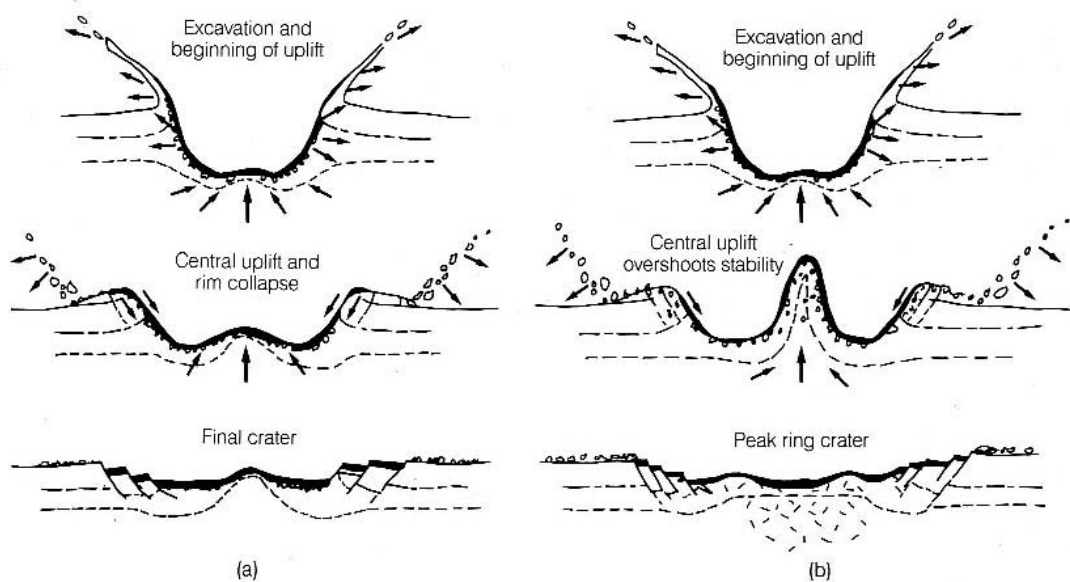


Figure 3.2 Schematic illustration of the formation of complex craters with either (a) central peaks or (b) peak rings. Uplift of the crater floor begins even before the rim is fully formed. As the floor rises further, rim collapse creates a wreath of terraces surrounding the crater. In smaller craters, the central uplift “freezes” to form a central peak. In larger craters, the central peak collapses and creates a peak ring before motion ceases (figure and caption adapted from Melosh 1989).

Grieve and Pilkington (1996) gave, for the relationship between crater diameter and observed amount of structural uplift (SU) undergone by the deepest unit exposed at the center of complex craters on Earth, the relationship:

$$SU = 0.086D^{1.03}$$

where SU is the amount of structural uplift (in km), and D is the rim diameter of the structure (in km). According to the authors, this empirical formula is based on observations from a total of 24 terrestrial impact structures. From this, we can assume that the structural uplift at the central uplift in the West Clearwater Lake impact structure (~32 km in diameter) must have been ~3 km.

Because all materials are fluid over sufficiently long timescales, large craters experience structural adjustments (i.e., isostatic rebound) that tend to flatten their topographic features over scales of thousands of years. Melosh (1989) provided a formula for the relaxation time T_r for a crater of diameter D in a medium of viscosity μ and density ρ ; g is the gravitational constant of acceleration.

$$T_r \cong \frac{8\mu}{\rho g D}$$

If I consider the terrestrial lithosphere to have a viscosity of 10^{22} poises (Fowler, 1990) and a density of approximately 3 g/cm^3 , a crater 32 km in diameter like at West Clearwater Lake would have a relaxation time of about 27 000 years. This time is probably longer than the time taken for the crystallization of the West Clearwater Lake sheet of impact melt. Structural adjustments were thus taking place while the impact melt was cooling and solidifying.

3.4 The Production of Impact Melt

As briefly mentioned before, shock generated by an impact first compresses the underlying target rock, doing irreversible work on this material, and then releases the target rock adiabatically to a low pressure. If the shock is strong enough (the minimum shock pressure necessary is considered to be around 50 GPa), the released rock may be molten or even vaporized. In other words, when silicate rocks are subjected to shock pressures above approximately 50 GPa, individual shocked minerals trap enough waste-heat to melt or vaporize during decompression from the shocked state (Grieve, 2006). Because shock waves strong enough to vaporize and melt rock are only generated very close to the impact site, most of the melt stays within the crater, moving into the

expanding transient cavity as the crater opens and later collapses: with the possible exception of a few deeply injected dikes, impact melt does not mix into the target rocks below the crater floor. Therefore, most impact-generated melt is generally found as coherent or semicoherent sheets of melt lining the crater floor; some is also present in ejecta deposits inside the crater or in the crater rim region, where it is present either as individual clasts (i.e., suevite) or in the groundmass of impact breccias; distal deposits of high-velocity ejecta such as tektites (Wünnemann et al., 2008) are also considered to be impact melt.

Obviously, the production of an impact-generated melt has never been observed in nature, and it is not presently possible to generate, under controlled laboratory conditions, the impact velocities needed to produce significant amounts of melting and vaporization. Consequently, the laws of physics involved in the production of impact melt can only be studied with computer-based simulations and theoretical studies, which are then tested, where possible, against field observations. These computer-based approaches typically use powerful hydrocode simulations to estimate the amount of melt produced for various impact events (note: hydrocode refers to any of several computer programs that model the behaviour of fluid flow systems by breaking down the system into a three-dimensional matrix of cells and calculating the forces etc. affecting each one). One of the main objectives of this approach is the determination of appropriate scaling laws in order to generalize these simulations to all cases, allowing the estimation of melt production for any impact event of interest. I shall not attempt to describe here in any detail these theoretical studies, but if the reader wishes to find relevant information pertaining to this subject, I recommend reading Pierazzo et al. (1997), Pierazzo and Melosh (2000), and Wünnemann et al. (2008). Pierazzo et al. (1997), in particular, have

tested the accuracy of their melt production calculations against a terrestrial dataset compiled by Grieve and Cintala (1992): their melt volumes, produced by hydrocode simulation, are in good agreement with the observed volumes of melt in craters developed on crystalline basement.

Nevertheless, it should be pointed out that computer-based models and calculations are usually based on poorly constrained variables. In order to simplify calculations, a number of simplifying assumptions must be made: for instance, the target rocks are often assumed to be homogeneous, entirely composed of a single silicate rock (e.g., dunite), considered nonporous and dry. Furthermore, limited exposure and extensive erosion, generally combined with incomplete field-based data, only permit a very rough approximation of the amount of melt produced during a particular impact event. It is particularly difficult, for instance, to estimate the melt volume present in the glass fragments deposited within and outside the crater, especially in the case of very widely dispersed and easily eroded ejecta deposits (e.g., tektites, glass spherules and spherule beds).

Convincing melt-production models for impact structures in porous multilayered target rocks have been particularly difficult to achieve: for sedimentary rocks, observed volumes of impact melt are typically inferior to volumes estimated by computer models. This disparity has been usually explained by the dispersion of sediment-derived shock melt by the associated release of considerable amounts of volatiles (Artemieva, 2007; Kieffer and Simonds, 1980; Wünnemann et al., 2008). Another possibility is that the low volumes of melt observed in impact structures in sedimentary targets may simply result from difficulties in recognizing impact melts derived from sedimentary targets (Osinski et al., 2008). For example, considerable volumes of impact-generated carbonate melt

have been recently estimated for the Chicxulub impact structure (Jones et al., 2000), the Ries structure (Graup, 1999), and the Haughton crater (Osinski and Spray, 2001). In light of this, estimates of melt volume at Haughton and revised estimates of melt volume for the Ries structure, based on a re-interpretation of the Ries impactites, are much closer to some models of melt production in porous targets (Wünnemann et al., 2008).

3.5 Estimation of the volume of melt produced by the West Clearwater Lake impact

As mentioned before, the preserved volume of the impact-generated melt rocks present at the West Clearwater Lake impact structure was estimated by Grieve et al. (1976) to range from 34 to 50 km³, which is a minimum estimate, whereas Phinney and Simonds (1977) estimated the preserved volume to be ~40 km³. Nevertheless, this must be smaller than the original volume: the Clearwater Lakes region has been extensively glaciated, and the impact melt rocks, which are considered to be the remnants of a continuous sheet of impact melt, now occur as separated outcrops out to a radial distance of about 13 km from the center of the structure (Phinney and Simonds, 1977).

The thickest preserved outcrop of impact melt is ~130 meters. Assuming a vertical cylinder geometry ($v = \pi r^2 h$, where $r = 13000$ meters and $h = 130$ meters) gives a volume of melt (pre-erosion) of about 69 km³. It is likely, however, that the central uplifted area did not contain much melt, and that the original geometry of the sheet of impact melt was closer to that of a hollow cylinder. Also, the bottom of the impact melt sheet cannot have been perfectly flat, and the maximum radial extent of the original melt sheet is uncertain. Finally, the grain size of the matrix feldspars in the melt rock progressively increases with height in the exposures of melt rock (Phinney et al., 1978), suggesting that the melt sheet was originally much thicker than what remains of it today. It is therefore not

unreasonable to assume that the melt sheet was at least twice as thick as at present (Phinney and Simonds 1977), giving a pre-erosional estimate of ~ 70 to $\sim 100 \text{ km}^3$. This must be considered to be uncertain by at least a factor of two.

The totality of the melted volume estimated here is assumed to have been entirely produced by shock-generated melting. As explained below, I have not considered the “impact triggered volcanism” possibility, that is, that partially melted material could have been produced by the uplift of hot interior rocks and consequent release of pressure (i.e., decompression melting).

3.6 Can impact cratering generate volcanic eruptions?

The idea that impacts may initiate volcanic eruptions on Earth or the Moon has been proposed by several authors over the years: one of the first was Ronca (1966); more recent relevant papers were written in the context of the debate concerning the formation of Large Igneous Provinces (LIPs), e.g., Glickson (1999), Jones et al. (2002). The majority of these articles echo the views of Ronca (1966), who proposed that impact-induced volcanism could be induced by decompression melting beneath the impact crater.

As made clear above, during the crater-excavation stage, large volumes of target country-rock are removed from the immediate vicinity of the point of impact. However, the shape and depth of the final crater are quite different from the crater formed during the initial excavation. During this initial “transient crater” excavation phase, the crater attains its maximum depth, but this only lasts a brief period of time: the rock shattered during impact is too weak to sustain the transient crater, and the structure starts collapsing under gravity soon after it reaches its maximum excavated volume. On Earth, transient craters with an initial diameter larger than about 4 km collapse and get

reconfigured (forming the central peak and concentric ring-features typical of complex craters) by uplifting the crater floor, but this happens as the transient crater rim slides inward. Consequently, the pressure relief under the crater is much smaller than expected. Numerical simulations of crater formation performed by Ivanov and Melosh (2003) suggest that even in the case of the formation of an impact crater with a final diameter of 250 to 300 km on a target with a steep thermal gradient, melt is mainly produced by the shock compression and pressure release associated with the impact, not by decompression melting. In other words, even a large impact is not enough to raise significant amounts of mantle material above the peridotite solidus due to decompression alone. Also, although the amounts of rock melted during such an impact event are considerable, they are not comparable to the volumes involved in a Large Igneous Province: according to Ivanov and Melosh (2003), net production of melt for a crater 250 to 300 km in diameter ($\sim 10^4 \text{ km}^3$) is one to three orders of magnitude smaller than the typical estimated volumes of Large Igneous Provinces (10^5 to 10^7 km^3).

The theoretical arguments of Ivanov and Melosh (2003) are partially supported by geochemical studies of the Sudbury Igneous Complex (SIC), the eroded and tectonically deformed remains of an impact structure ~ 200 km wide (Grieve, 2006). The SIC was initially considered to have a purely terrestrial origin, the result of the intrusion of a large amount of mantle-derived magma massively contaminated by upper crust rocks. Even after it became accepted that the SIC was generated by a meteoritic impact, the mantle-derivation idea was regularly invoked to explain the geochemical peculiarities of the SIC: it was proposed that large amounts of mantle-derived magma brought up via large fractures in the crust and formed by decompression melting had mixed with the impact melt. However, recent developments argue against this idea: $^{87}\text{Sr}/^{86}\text{Sr}$ and Nd isotopic

systematics are considered to be incompatible with a significant mantle-derived contribution to the composition of the SIC (Dickin et al., 1999; Faggart et al., 1985); Cohen et al. (2000) analyzed the Re-Os isotopes in the ultramafic inclusions in the sublayer of the SIC and concluded they are consistent with melting of pre-existing lithologies; high-precision Os isotopic studies of sulfides from several mines in the Sudbury area have confirmed their crustal origin from a binary mixture of Superior Province and Huronian metasedimentary rocks (Morgan et al., 2002).

Finally, it should be noted that impact events capable of producing craters larger than 200 km in diameter are extremely rare: according to lunar crater chronology and comparisons with the frequency of large craters on the surface of other terrestrial planets, impact craters larger than 200 km are considered to form on Earth at a rate of about four to eight craters per billion years; estimates for larger craters give two to four craters with a diameter larger than 250 km and one to two craters with a diameter larger than 300 km per billion years (Ivanov, 2001; Neukum et al., 2001). In contrast, approximately 30 magmatic events large enough to qualify as a Large Igneous Province are known to have happened during the last 250 million years (Coffin and Eldholm, 2001). Thus, most, if not all, of the known large igneous provinces must have a purely terrestrial origin.

Therefore, if a numerical simulation of the formation of a crater 250 to 300 km wide over a target rock with a steep thermal gradient fails to produce significant amounts of magma by decompression melting, and if there is no evidence that decompression melting is responsible for the geochemical particularities of the Sudbury structure, it is most unlikely that decompression melting happened at the West Clearwater Lake impact structure, which is a mere ~32 km in diameter and situated on a cratonic terrane.

3.7 Summary of chapter 3

- An impact event can be divided into three successive episodes, which grade into each other:

- 1) Contact and compression, when the meteorite strikes the Earth;
- 2) Excavation, during which the transient crater is opened;
- 3) Modification, during which the transient crater collapses, giving rise to the final impact structure.

- The preserved volume of melt presently extant at the West Clearwater impact structure is estimated to be $\sim 40 \text{ km}^3$. The pre-erosional volume of melt generated by the impact is thought to have been about ~ 70 to $\sim 100 \text{ km}^3$. This must be considered to be uncertain by at least a factor of two.

- It is unlikely, not to say impossible, that any of this volume originated by the addition of purely terrestrial magma created by decompression melting triggered by the impact.

Chapter 4: The Drill Core

In order to study the impact melt properly, it is necessary to know what has been melted by the impact. Fortunately, a large amount of core sampling the various lithologies below the crater was readily available for study, thanks to the efforts of M.R. Dence who, under the auspices of the Dominion Observatory, supervised a drilling program in West Clearwater Lake in the winter of 1963-1964 (Table 4.1). This core is presently at the sample depository facilities of the Planetary and Space Science Centre (PASSC) of the University of New Brunswick, in Fredericton, New Brunswick, Canada. This chapter will essentially consist of a description, at the hand sample scale, of this PASSC core. A more detailed study of the basement rock, which will bring together core samples and surface samples of the basement rocks, will be presented in chapter 5.

4.1 The drill core

The core was described and sampled in two stays in Fredericton during the summers of 2006 and 2007. Because the core had already been sampled and described in great detail by Hische (1995), I decided that it would be redundant to do the same. Moreover, the core is not the focus of attention in this work. Nevertheless, Hische did not assign his rocks to regionally known map units, and none of his observations have been published. Therefore, twenty-six core samples were cut in order to verify and compare my findings with those of Hische (1995).

The core was photographed in its entirety with a high-resolution digital camera (Figure 4.1). Brief visual descriptions were also written *in situ*. These photo-

Figure 4.1 Photographs of core sections from the West Clearwater impact structure. A) Pink medium-grained biotite-hornblende granite from a depth of ~310 m in drill hole 3-63. B) Medium- to coarse-grained hornblende-biotite gabbro (375 m, drill hole 1-63). C) Fine-grained gray biotite tonalite cut by veins of pseudotachylite (~30 m, drill hole 3-63). D) Fragmental breccia matrix (~50 m, drill hole 4-63).



A



B



C



D

graphs and their accompanying written descriptions were then organized and expanded, allowing me to produce a visual core log. This core log was subsequently used to decide where to sample. I tried to cut samples that are as representative as possible of particular

lithological units, but some samples were also cut in order to clear up ambiguities and unknowns.

Bulk chemical data was obtained using the facilities at the Trace Element Analysis Laboratories (TEAL), which operates within the Department of Earth and Planetary Sciences at McGill University. Major oxides and trace-element concentrations were measured using X-ray fluorescence (XRF) analysis conducted with a Philips PW2440 4kW X-ray fluorescence spectrometer system with a PW2540 VRC 168 sample autochanger. All the chemical data obtained with XRF pertaining to the drill core is given in Appendix A.

The observations below are condensed from the data obtained in a comparative study of my photographs and descriptions, Hische's observations, and the results of my own sampling. Note that, because Simard et al. (2004) described geographically extensive units showing a large range of chemical compositions and mineralogy without providing mineral compositions, it was not possible to establish an unambiguous

Table 4.1 Drill core locations and depth of sampling.

Drill core	Approximate location	Depth of sampling (m)
1-63	Center of the West Clearwater Lake	Begins at 19 m below lake level, ends at 397 m below lake level
3-63	600 m to the ENE of hole 1-63	Begins at 36 m below lake level, ends at 119 m below lake level
4-63	Western margin of Drillers Island, 6 km east of the center of West Clearwater Lake	Begins at 7.6 m below lake level, ends at 384 m below lake level
4A-63	Drilled after hole 4-63, nearly in the same emplacement	Begins at 42 m below lake level, ends at 65 m below lake level
5-63	SW tip of Drillers Island, about 600 m to the ENE of hole 4-63	Begins at 29 m below lake level, ends at 220 m below lake level

correspondence between the rocks I have observed and the lithologies they described.

Dating the basement rocks of the Clearwater Lake impact structure would probably help

in establishing a clearer correspondence between lithologies. A comparative table of the rocks described by Simard et al. (2004) and the rocks studied in this thesis is given at the end of Chapter 5, section 5.7. A stratigraphic section of basement lithologies at West Clearwater Lake impact structure will be presented in section 4.3 at the end of this chapter (Figures 4.2 and 4.3).

Core samples are identified the following way: the first number designates drill hole, the second is the year of drilling, the third is the box containing the core section, and the fourth is the approximate depth in feet at which the sample was obtained. Therefore, 4-63-930-290 designates a sample taken from the fourth core drilled in 1963, box 930, at a depth of 290 feet. However, depths in the text and in figures will be given in the proper S.I. unit, that is, in meters. Since the box number is redundant, it will be omitted on occasion.

4.2.1 Overview of the core extracted from Drill Hole 1-63 (Box 833 to Box 878)

Drill hole 1-63 was sunk vertically near the center of the western crater, piercing the top of the central uplift of the West Clearwater impact structure. The drill core has a diameter of 3.2 cm, and it begins at a depth of 19 m below lake level (the lake level was 237 m above sea level at the time), ending at a depth of 397 meters.

At a depth of 19 meters, the hole starts in medium- to coarse-grained pink granite (not in impact-melt rock), becoming fine- to medium-grained pink and gray granodiorite at 21 m.

At 30 meters, it gradually becomes fine- to medium-grained gray diorite. The core was sampled at about 34 meters (sample 1-63-113): its composition (determined using X-ray fluorescence) resembles that of a Loups Marins Complex diorite or tonalite;

the thin section, which I used to classify the sample as a clinopyroxene-biotite monzodiorite, is strongly fractured, containing numerous very fine-grained regions generally forming vein-like anastomosing structures, probably the result of local mylonitization.

At about 38 meters, the rock becomes strongly brecciated, showing numerous cm- to dm-wide veins filled with a dark gray to black glassy aphanitic groundmass associated with numerous fragments of variable size. These fragments are generally similar to the diorite described at 34 meters. Hische (1995) mentioned observing, at this depth, a well-defined flow texture, which I did not encounter. I sampled one of the thicker aphanitic veins present at this depth (sample 1-63-125): not surprisingly, given the numerous clasts embedded in the vein, its whole-rock composition is similar to that of the monzodiorite sampled at 34 meters (sample 1-63-113). Under the microscope, the texture resembles a clast-rich impact melt rock, with numerous angular clasts of variable size (the largest is a lithic fragment about 5 mm wide) that, in contrast to most of the melt rock samples I have observed, do not seem to be partially melted or resorbed. This thin section could represent a vein of impact melt (see Chapter 6) that infiltrated below the section of basement rock sampled at 30 meters.

Starting at 39 meters, the core mostly consists of patches of medium-grained pinkish gray biotite granite alternating with gray fine- to medium-grained sections in which plagioclase predominates over alkali feldspar, that is, where the composition becomes granodioritic or monzodioritic. However, from a depth of about 58 meters down to around 64 meters, most of the core consists of medium-grained pinkish gray biotite-rich granite.

From 64 meters down to about 130 meters, the core consists of an interlayering of medium- to coarse-grained gray clinopyroxene-bearing granodiorite and tonalite. This lithology was sampled at a depth of 86 meters (sample 1-63-281): its whole-rock composition is similar to that of a Loups Marins Group rock. In thin section, the sample resembles a medium-grained biotite-hornblende-clinopyroxene granodiorite.

Close to 130 m, the mafic mineral content gradually increases: quartz and alkali feldspars virtually disappear, and clinopyroxene and plagioclase become the dominant minerals, with variable amounts of orthopyroxene, amphibole, biotite and oxides present. The core was sampled at the 132 meters mark (sample 1-63-434): the sample's whole-rock composition is similar to that of a Qullinaaraaluk gabbro or gabbro-norite. About 1/3 of the thin section is clinopyroxene, biotite and iron oxides, the rest is plagioclase: I classified this rock as a leucocratic biotite gabbro. Sampling at 181 meters (sample 1-63-593) provided once again a whole-rock chemical composition similar to that of a Qullinaaraaluk Suite mafic intrusion; in thin section, the sample looks like a fine- to medium-grained biotite gabbro-norite. A visual inspection of the core from 130 meters downward indicates that the drill hole intersected a single relatively homogeneous rock unit mostly composed of gabbros. However, the thin section of sample 1-63-910, which was cut from a sample at about 277 meters, contains some primary quartz, which would seem at first to dispel this impression of homogeneity. But the whole-rock chemical composition of sample 1-63-910 is comparable to that of the mafic rocks above and below (49.70 wt.% SiO₂, 14% MgO), and its texture and mafic mineralogy are quite similar to those of the rocks above and below. This otherwise relatively homogeneous mafic rock unit thus must be cut by narrow veins of a more felsic composition that are small enough to not affect the overall chemical composition. In fact, if I assume that I

am looking at rocks from the Qullinaaraaluk Suite, Simard et al. (2004) mentioned that rocks from this suite are commonly cut by cm- to dm-wide whitish injections of a granitic or tonalitic nature. Further sampling was done at around a depth of 354 meters: again, the whole-rock composition recalls that of the Qullinaaraaluk Suite, except that total FeO is a bit low; the respective thin section contains abundant clinopyroxene and orthopyroxene, and some green amphibole. I classified this rock as a medium- to coarse-grained hornblende-biotite gabbro. It should be noted that the section from 130 meters downward, which essentially is composed of gabbro and gabbro, was described as an interlayering of fine-grained dark gray amphibolites, monzodiorites and quartz monzodiorites by Hische (1995). However, in the samples I have studied, amphibole is invariably subordinate to pyroxene, and primary quartz is rare, only appearing in sample 1-63-910, at about 277 meters. It is probable that Hische overestimated the amount of quartz.

Down to the end of the drill hole, at a depth of 397 meters, the core consists of a homogeneous fine-grained dark gray mafic rock, different from the rock sampled below 130 meters by its finer grain-size. The core was sampled near its end, at about 397 meters (sample 1-63-1303): as expected, the whole-rock composition is similar to that of a member of the Qullinaaraaluk Suite; in thin section, compared to samples higher up, the rock is relatively unaltered, and its mineralogy is clearly that of a fine- to medium-grained melanocratic gabbro. Here again, it should be noted that Hische (1995) classified this rock as a quartz monzodiorite.

4.2.2 Overview of the core extracted from Drill Hole 3-63 (Box 879 to Box 924)

Drill hole 3-63 was sunk vertically about 600 m to the ENE of hole 1-63. The core has a diameter of 3.2 cm, and it begins at a depth of 7.6 m below lake level (the lake level was 237 m above sea level), ending at a depth of 384 meters.

The first 30 meters of core correspond to fine-grained quartz- and plagioclase-rich gray rock showing, in some places, a distinct gneissic texture (irregular felsic and mafic layers), with some dm-sized fine-grained pinkish patches probably containing a larger amount of alkali feldspar. The core was sampled at a depth of about 20 meters (sample 3-63-65): its whole-rock composition is similar to that of a Loups Marins Group tonalite or diorite; in thin section, the sample is mostly composed of fine-grained plagioclase and quartz, with some biotite and abundant iron oxides. I did not observe any clinopyroxene, which tends to be ubiquitous in Loups Marins Group rocks. Nevertheless, the mineral assemblage and bulk composition lead me to believe that this rock is akin to a Loups Marins Group biotite tonalite or granodiorite.

From 30 meters downward, the core becomes medium grained, and pale gray to pink, the color varying with alkali feldspar content. There is an obvious gneissic texture, with dm-thick layers often displaying a high content of mafic minerals. At a depth of about 70 meters, the rock shows clumps of cm-sized mafic minerals, which give the core a speckled appearance. This lithology was sampled at a depth of about 99 meters (sample 3-63-325): the whole-rock composition is close to that of a Desbergères Suite granite or granodiorite. However, its SiO_2 content is a bit lower (60.42 compared to a minimum of 63.80 wt.% for typical Desbergères Suite rocks, according to Simard et al. 2004, Table 2.1), whereas TiO_2 , Al_2O_3 and CaO contents are slightly higher. In thin section, the sample clearly appears to be an altered granite or granodiorite, and it is

crisscrossed by thin veins of melt 0.5 mm wide or less. I called this sample a brecciated hornblende-biotite granite.

At about 139 meters, the medium-grained rocks similar to the granites described above are sharply interrupted by a finer-grained dark gray rock with a granodioritic or dioritic composition containing abundant biotite and hornblende. Although I have not sampled this section of the core, the presence of whitish porphyritic alkali feldspar leads me to believe that this layer could be an enclave of porphyritic granodiorite similar to those observed by Simard et al. (2004) within the Desbergères Suite. At about 144 meters, this dark gray granodioritic layer grades into medium- to fine-grained light gray to pink granites. From this depth downward to 241 meters, the core mostly consists of pink, medium-grained granites resembling the Desbergères Suite, occasionally interrupted by mm-wide veins of black aphanitic material (probably pseudotachylite) and a few gray meter-wide sections containing porphyritic alkali feldspar and richer in fine-grained mafic minerals, usually in gradational contact with the pink granites. The core was sampled at a depth of about 206 meters (sample 3-63-677): its whole-rock composition is similar to that of a Desbergères Suite granitic rock; its mineral content is that of a biotite granite or granodiorite.

The granites continue down to about 241 meters. From about 241 to about 247 meters, a medium-grained dark gray gneiss grades into a fine-grained, dark gray mafic-mineral-rich layer. The layer itself is about 9 meters thick. This lithology was sampled at 254 meters (sample 3-63-832): the whole-rock composition is gabbroic, similar to that of a mafic intrusive rock; in thin section, the rock is dark green, with a texture similar to that of a breccia, with abundant fluidal-textured opaque oxides, and plentiful chlorite,

indicating strong alteration. Hische (1995) called this rock a diabase dike; I believe it to be strongly metasomatized gabbro, which could well have had a diabasic texture.

At about 257 meters, the mafic layer described above rapidly grades into medium-grained pale pink chalky-looking rock of probable granitic composition, which is interrupted by finer-grained dark gray mafic-mineral-rich rock at 273 meters. The core is extensively broken-up; the numerous fractures mask the contact between the mafic-mineral-rich layer and the granite above. At a depth of 277 meters, the mafic-mineral-rich layer grades into chalky-looking pale gray to pink granitic rock displaying a clear gneissic texture. This whole section, from 257 meters downward, displays numerous thin (cm-sized) veins filled with black aphanitic material (possibly pseudotachylite), but these veins are particularly abundant in the dark gray mafic-mineral-rich rock. The chalky-looking granites continue down to 286 meters, where the core material is a breccia-like dark gray rock that becomes more homogeneous and finer grained at 287 meters. The core was sampled at a depth of about 288 meters (sample 3-63-944): its whole-rock composition is close to that of a Qullinaaraaluk Suite amphibolite; in thin section, the sample shows a thin layer rich in biotite and brown amphibole sandwiched between two clinopyroxene- and orthopyroxene-rich sections. Most of the plagioclase is strongly altered to epidote, and there also is a pseudomorphic greenish brown alteration assemblage after the mafic minerals, with a texture similar to that of serpentinite.

At about 296 meters, the mafic layer described above grades back into homogeneous pale pink to light gray medium-grained rock of granitic composition. The core was sampled at a depth of about 298 meters (sample 3-63-977): its whole-rock composition is similar to that of a Desbergères Suite granite. This pale pink to light gray medium-grained lithology continues without interruption down to 316 meters, where

it grades into fine-grained dark gray gneissic gabbroic rock. The transition zone contains numerous mm- to cm-wide black veins surrounding patches of felsic material. At about 320 meters, this dark mafic-mineral-rich gneiss grades back into a 2-m-thick pale pink to light gray medium-grained layer of granitic composition, which then, after a sharp contact, is juxtaposed with a homogeneous fine-grained dark gray mafic-mineral-rich rock. Below 324 meters, the core becomes a gray, medium-grained rock displaying sharp dm-wide bands richer in felsic minerals, which, at 328 meters, become alternating patches and bands of gray and pale pink medium-grained gneisses that may grade into each other, but may also display a sharp contact. This gneissic section terminates at 335 meters: below this depth, down to its end at 384 meters, the core consists of pink medium-grained felsic rock of probable granitic composition, occasionally interrupted by a few mm- to cm-wide veins of black aphanitic material. A sample of this section, taken at a depth of 371 meters, has a composition similar to that of a Desbergères Suite granite or granodiorite. The thin section shows coarse-grained quartz and perthitic alkali feldspar in a fine-grained groundmass of feldspar and quartz, with some rare grains of altered biotite and hornblende. I called this rock a biotite-hornblende granite.

4.2.3 Overview of the core extracted from Drill Hole 4-63 (Box 925 to Box 934)

Drill hole 4-63 was sunk vertically about 200 m off the southwestern shore of Drillers Island, the large northeastern island of the island ring, 6 km east of the center of West Clearwater Lake (Figure 1.3). The core has a diameter of 3.2 cm, and it begins at a depth of 36 m below lake level, ending at a depth of 119 meters.

The core first penetrates pale pink medium-grained rock, possibly granitic, which appears heavily altered: all mafic minerals have a rusty aspect, and the rock is porous and

chalky. At a depth of about 43 meters, the core traverses porous very heterogeneous black and rust-red impact-melt rock containing numerous white fragments of medium-grained clasts with visible reaction rims, embedded in a black and rust-red fine-grained groundmass showing a flow texture. The core is extensively fractured, and a number of fragments are missing. At about 54 meters, the clast content of the impact melt increases considerably, to the point where there are more clasts than melt: it is possible that this part of the section represents the transition from fragmental breccia to basement rock. At 60 meters, the drill hole intersects porous, pale pink, medium-grained and heavily altered rock with a probable granitic composition that contains, starting at about 62 meters, several irregular patches of rust-red impact melt rock. One of these patches was sampled at a depth of 65 meters (sample 4-63-214): its whole-rock composition is similar to that of average impact melt (see Chapter 5), but containing more MgO (6.1 wt.% versus about 2.5 to 3 wt.% in the average impact melt rock). The thin section is indistinguishable from other clast-rich impact melt rocks: the rock consists of a large number (over 50% of the thin section) of angular to subangular fragments of variable size and composition (mostly granitic lithic fragments, quartz, plagioclase and alkali feldspar fragments) in a very fine-grained dark groundmass filled with tiny oxide grains and very small clasts. The groundmass has a few more homogeneous-looking nearly isotropic rounded areas (the largest is about 3 mm wide) that may be glassy.

At a depth of 66 meters, the core consists of a medium-grained dark-red equigranular rock; the core section at the contact point between the units above and this dark-red rock is broken and missing. Down to about a depth of 100 meters, this unit consists of heavily altered medium-grained dark red rock, with a few mud-colored segments around 94 meters that could either be covered in clay, or be very fine-grained

and altered. The rock has numerous “rusted” minerals, and the lighter-colored minerals have been smeared by the rusty alteration. Numerous thin cracks and veins (mm or cm wide), filled by a rust-red or black aphanitic material are visible throughout the section. The core was sampled at a depth of 88 meters (sample 4-63-290): its whole-rock composition is similar to that of a Loups Marins Group tonalite or diorite. In thin section, the sample appears quite altered and fragmented, its plagioclase is heavily altered to white mica, and most of the mafic minerals are now pseudomorphic chlorite.

The core was again sampled at a depth of 93 meters (sample 4-63-306): its chemical composition is not close to that of any of the usual units (i.e., Desbergère Suite, Loups Marins Complex and Qullinaaraaluk Suite). The composition is, however, more mafic than that of the rock sampled at 88 meters. In thin section, the rock is extensively fractured, and divided into alternating mafic and felsic areas two or so cm thick. The felsic areas are porphyritic, with coarse-grained alkali feldspar in a fine-grained groundmass of quartz, plagioclase and alkali feldspar. The mafic-mineral-rich areas contain abundant biotite and pyroxene, and a few brown amphibole grains. This thin section reveals a thinly layered gneissic rock.

Another sample was taken at a depth of 98 meters (sample 4-63-322): the whole-rock composition is similar to that of a Desbergères Suite granite; the thin section reveals a equigranular coarse-grained quartz and alkali feldspar, with less than 2% clinopyroxene, largely chloritized.

Although the section from 66 meters down to 100 meters appears, to the naked eye, to be a relatively homogeneous medium-grained dark red rock, the sampling above clearly shows that a heavy overprint due to alteration has hidden the presence of various

lithologies. I assume, however, that this core section consists, for the most part (from 66 meters down to 98 meters) of rocks similar to the Loups Marins Group.

At a depth of about 100 meters, the rock clearly becomes granitic: it is pink and medium-grained, and abundant quartz and alkali feldspar are clearly recognizable. This rock is probably same as the granites described at 98 meters. The same lithology continues down to 106 meters, where it gradually becomes more mafic, becoming a medium-grained “salt-and-pepper” gabbro at around 109 meters. As usual, numerous mm-wide pseudotachylitic cracks and veins filled with rust-red aphanitic material are visible throughout the core section. The core was sampled at a depth of 109 meters (sample 4-63-358): its whole-rock composition is similar to that of a Qullinaaraaluk Suite gabbro; in thin section, the rock is composed of abundant (at least 70%) medium- to fine-grained plagioclase, with medium-grained biotite and pyroxene (ortho- and clinopyroxene) clustered together. Mafic minerals are usually somewhat altered. This unit continues down to about 111 meters, where it gradually becomes a medium-grained pink rock with a possible granitic composition alternating with darker fine-grained cm- to dm-wide mafic-mineral-rich layers: the whole section displays a clearly gneissic texture. It is probable that the layer with the gabbroic composition sample at 109 meters represents a thick mafic-rich layer in a gneissic rock. This unit continues down to the end of the core, at a depth of about 119 meters.

4.2.4 Overview of the core extracted from Drill Hole 4A-63 (Box 935 to Box 936)

Drill hole 4A-63 was drilled after hole 4-63, nearly in the same emplacement. It is only 23 meters long, and it repeats part of the section penetrated by hole 4-63 (Dence et al.,

1974). It has a diameter of 3.2 cm, and it begins at a depth of 42 m below lake level (the lake level was 237 m above sea level), and ends at a depth of 65 meters.

The core first samples porous rust-red impact-melt rock, with a fine-grained rust-red groundmass and a variety of angular clastic debris of variable size and colour. There are a few black irregular patches probably made of relatively fresh glass around the 46-meter mark. The core is extensively fractured, and a number of fragments are missing. This lithology continues down to about 59 meters, where large segments of porous medium-grained pinkish white rock appear. Numerous irregular rust-red melt veins cut these rock segments; the rock seems to be a highly altered fragmental breccia. The core is very fractured, and large sections of its last couple of meters are missing. The core was sampled at a depth of 59 meters (sample 4A-63-195): curiously, its whole-rock composition is quite different from that of an average impact melt rock (see Chapter 6): the sample is significantly poorer in SiO_2 (51% vs. about 61%), and richer in MgO (9% vs. about 3%) and Fe_2O_3 (10.3% vs. 6%). In other words, the sample is notably more mafic than regular impact melt rock. As expected, over half of the thin section consists of angular to subangular rock fragments of variable size: mostly lithic fragments of felsic composition and single feldspar and quartz clasts; mafic minerals are rare, and they are usually heavily altered. In plane light, its groundmass is almost clear, nearly transparent, and it contains numerous small opaque oxide granules. However, back-scattered electron imaging under the microprobe shows that what looked like groundmass with the optical microscope is, in fact, a porous mass of very fine-grained angular to subangular fragments, mostly quartz and feldspar, with a few iron oxide grains. As no chlorite or other minerals containing significant amounts of magnesium were seen, it is unclear what is responsible for the high MgO reading.

Below 59 meters, to the end of the core, the rock consists of fragmented segments of porous medium-grained pinkish white rock. There are still some patches of rust-red melt in the pinkish white rock. The core is very broken-up, and the last two meters or so of the core section are very incomplete.

4.2.5 Overview of the core extracted from Drill Hole 5-63 (Box 937 to Box 954)

Drill hole 5-63 was sunk vertically near the SW tip of Drillers Island (Figure 1.3), about 600 m to the ENE of hole 4-63. It has a diameter of 3.2 cm, and it begins at a depth of 29 m below lake level (the lake level was about 237 m above sea level), and ends at a depth of 220 m.

The core first traverses reddish white fine-grained porous impact breccia that, at a depth of about 35 meters, becomes dark-red impact-melt rock showing a well-defined flow texture. This section was sampled at a depth of 38 meters (sample 5-63-124): its whole-rock composition is close to that of average impact melt rock (see Chapter 6). The thin section contains numerous clasts, once probably partially resorbed and showing a fluidal texture, encased in a microcrystalline dark-colored, nearly opaque groundmass. At the 39-meter mark, the core penetrates porous light-pink medium-grained rock with a granitic composition that appears to be heavily altered. This rock becomes pinkish white, with some dark-red hues, around 59 meters; the core is, at this depth, cut by numerous mm- and cm-wide veins of rust-colored aphanitic material.

The core was sampled at a depth of 50 meters (sample 5-63-174): its whole-rock composition is similar to that of a Desbergères Suite granite; the thin section is mostly composed of coarse-grained quartz displaying shock-metamorphic textures (planar deformation features, or PDFs) and coarse-grained, heavily altered feldspars, with a few

rare grains of pseudomorphic chlorite. This lithology continues down to 80 meters, where the core becomes very broken-up, forming a jumble of diverse segments. Most of these segments seem to consist of medium-grained granitic rock like that above, occasionally appearing chalky owing to alteration. There are, however, numerous cm-sized bands and patches of finer-grained dark gray gneiss rich in mafic minerals, and abundant mm-wide rust-colored veins of aphanitic material (presumably pseudotachylite). The core was sampled at a depth of 89 meters (sample 5-63-293): its whole-rock composition does not clearly fall within any of the general groups defined in Simard et al. (2004); its SiO_2 content is rather low (49 wt. %), and the MgO content (6 wt %) is higher than that of the granites above. The thin section is mostly composed of very fractured, heavily altered plagioclase, with some rare biotite and about 10% chloritized minerals. Quartz and alkali feldspars are rare or absent. The core was again sampled at a depth of 91 meters (sample 5-63-298): its whole-rock composition is similar to that of sample 5-63-293 described above. The rock is highly fractured, and divided in two regions: a rust-red area of coarse-grained to fine-grained felsic minerals, and a finer-grained greenish area rich in chlorite. A cm-sized vein of brown melt (probably a pseudotachylite vein) cuts the red area, and a mm-wide vein of pseudotachylitic melt separates the green and red areas.

From 91 meters downward, the core mostly consists of pale pink to red medium-grained felsic rock with a probable granitic composition, abundantly interspersed with finer-grained patches and bands richer in mafic minerals: the rock is, in other words, clearly gneissic. The rock is occasionally marked with mm-wide rust-red cracks (as in the interval between 125 meters and 136 meters), and there are sections that appear

chalky-white and porous (around 138 meters), or clay-rich (around 148 meters, for instance), probably owing to strong alteration.

Starting at about 145 meters, the core becomes quite broken-up, and large segments of the core section seem to be missing. Although most of the core seems to be of a composition similar to that of the lithology immediately above, there are, at about 150 meters, several segments of black aphanitic rock over a thickness of about 30 cm, and a dm-wide rust-coloured vein cuts one of them. This narrow vein was sampled along with part of the rock immediately next to it (sample 5-63-493): half of the thin section consists of a groundmass containing abundant angular clasts of variable size and composition, whereas the other half is essentially composed of numerous 0.1 mm long altered plagioclase laths with oxide grains and smaller grains of blocky chlorite, crisscrossed by thin black and rust-red veins of extremely fine-grained material, possibly pseudotachylite. The clast-rich section corresponds to the vein, whereas the very fine-grained crystallized section corresponds to the black aphanitic rock. The whole-rock composition of this sample is low in SiO_2 (51%) and quite high in MgO (12%), and it obviously does not correlate with that of the nearby felsic rock.

Around 152 meters, there are traces of epidote, which shows that the rock at this depth underwent low-grade hydrothermal re-equilibration. This observation fits with the pervasive alteration observed throughout the core.

The core was again sampled at a depth of 157 meters (sample 5-63-514): its whole-rock composition is consistent with that of a Desbergères Suite granite or granodiorite. The thin section is mostly composed of coarse-grained quartz and heavily altered feldspar, with some pseudomorphic chlorite; the rock is cut by numerous tiny fractures and areas of ground-up, brecciated, angular grains. I have called this sample

a brecciated and altered granite. This lithology steadily continues downward, with variations in grain size (coarse to medium) and state of alteration (which nevertheless tends to be quite pervasive) to about 197 meters, with only a short interruption from 160 to 163 meters, where the core gradually becomes a finer-grained gray rock slightly richer in mafic minerals, possibly granodioritic or tonalitic, and then it gradually reverts to the altered granites described above.

At about 197 meters, the core shows alternating patches and irregular bands grading into each other of medium-grained porous granitic rock and fine-grained mafic-mineral-rich rock. At 208 meters, the core becomes a homogeneous fine-grained dark gray rock rich in mafic minerals, with red hues visible in fractured sections. The core was sampled at a depth of 212 meters (sample 5-63-696): its whole-rock composition is similar to that of a gabbro. Strong alteration gives the thin section a greenish tint, but it is still clear that the thin section is mostly composed of heavily altered fine-grained plagioclase laths, with some euhedral pleochroic green hornblende and oxide granules. The composition and texture of the sample lead me to believe that this rock is probably a diabase. The core terminates at 220 meters: the last box is partially filled with broken fragments, mostly of diabasic composition, but there is a felsic rock fragment resembling a medium-grained granite at the end of the section.

4.3 Summary of chapter 4

The observations and descriptions given above are summarized in five stratigraphic columns, one for each drill hole, below, in Figures 4.2 and 4.3.

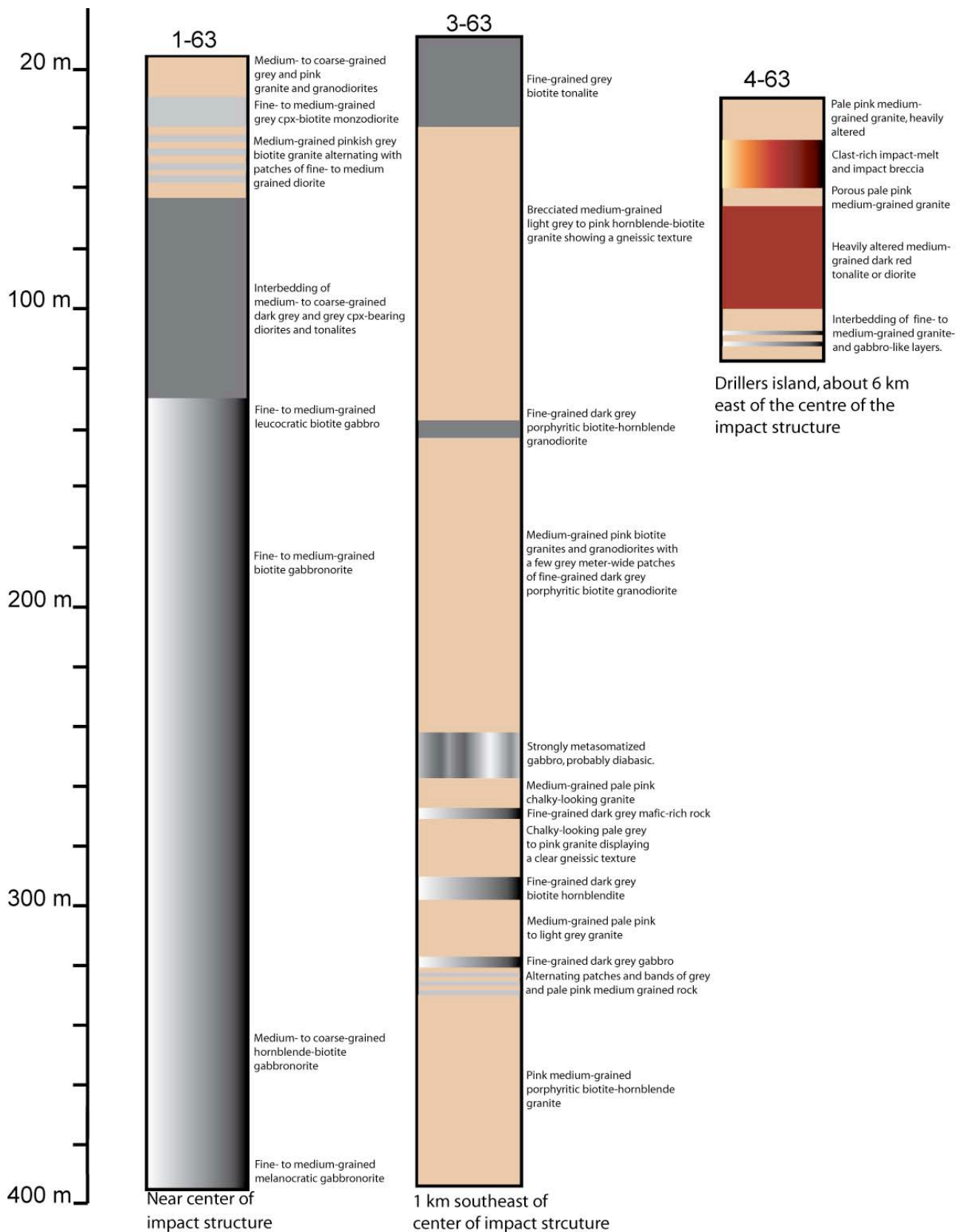


Figure 4.2 - Stratigraphic section of basement lithologies at West Clearwater Lake impact structure: drill hole 1-63, drill hole 3-63 and drill hole 4-63.

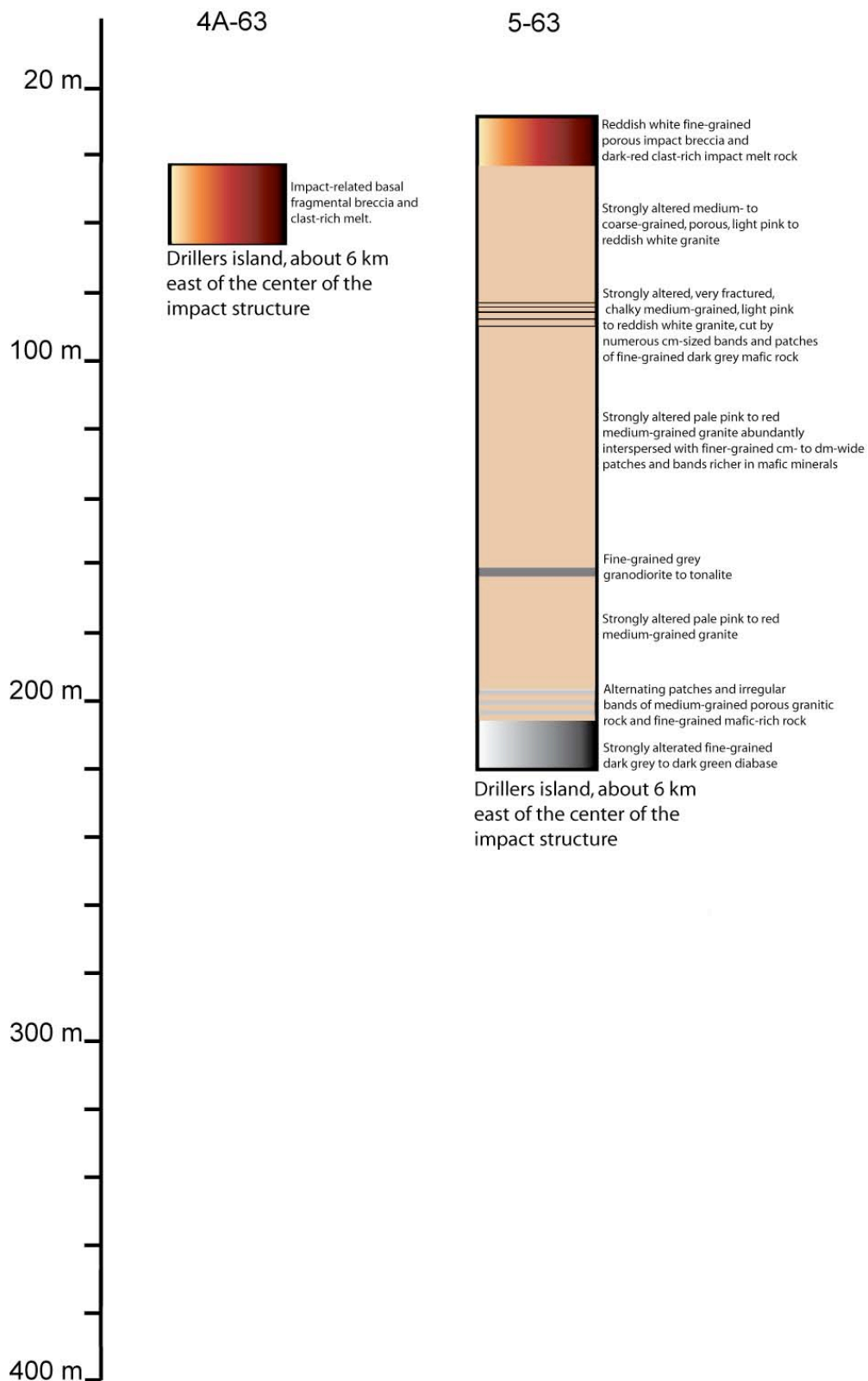


Figure 4.3 - Stratigraphic section of basement lithologies at West Clearwater Lake impact structure: drill hole 4A-63, and drill hole 5-63.

Chapter 5:

The Fractured Basement

In order to describe the basement rocks affected by the impact at West Clearwater lake, I have studied two groups of samples: the first group comprises all the drill core samples collected M.R. Dence who, as mentioned in Chapter 4, supervised a drilling program in West Clearwater Lake in the winter of 1963-64; M.R. Dence also obtained the second group of samples, when he, C.H. Simonds and W.C. Phinney visited the central ring of islands of the West Clearwater Lake impact structure in the summer of 1977 (Simonds et al., 1978b). Both sets of samples are presently stored at the sample depository facility of the Planetary and Space Science Centre (PASSC) of the University of New Brunswick, in Fredericton, New Brunswick, Canada. This chapter provides an overview of the composition and mineralogy of these rocks. It will start with a section dedicated to their composition, followed by a short description of the impact-related deformation and fracturing of the rocks. The rest of the chapter will consist of a study of the individual units. Finally, a comparison between my findings and those of Simard et al. (2004) will be presented. A table at the end of the chapter (p. 102) summarizes both my findings and those of Simard et al. (2004).

5.1 Composition of the target rocks

I have grouped my samples of the target rocks (that is, the rocky material that was vaporized, melted, fractured and shocked by the meteorite impact that created the West Clearwater impact structure) in three major categories, and a minor one: 1) granitic rocks; 2) dioritic and tonalitic rocks; 3) mafic rocks; 3a) diabasic rocks (see Figure 5.1 and

Table 5.1). This particular arrangement loosely follows the approach of Simard et al. (2004) (see Chapter 2), who divided the major units in the vicinity of the West Clearwater Lake into the Desbergères Suite (largely granitic rocks), the Loups Marins Complex (tonalites, enderbites and diorites), and the Qullinaaraaluk Suite (which corresponds to gabbros and ultramafic rocks).

Bulk chemical data were obtained using the facilities at the Trace Element Analysis Laboratories (TEAL), at the Department of Earth and Planetary Sciences, McGill University. Major oxide and trace-element concentration were measured using X-ray fluorescence (XRF) analysis conducted with a Philips PW2440 4 kW X-ray fluorescence spectrometer system with a PW2540 VRC 168 sample autochanger. All the chemical data obtained with XRF are given in Appendixes A and B.

The analysis of minerals was done by wavelength-dispersion spectroscopy (WDS) with a JEOL 8900 electron microprobe using the ZAF correction method and operated by Shi Lang, at McGill University. Both natural and synthetic standards were selected to minimize the correction factors. The accelerating voltage was 15 keV for all analyses, and the beam current was 20 nA. Counting intervals were 20 seconds, and the beam diameter was kept mostly in the 10 to 15 μm range, with the occasional analysis done at 5 μm for small grains. The estimated precision is $\pm 1\%$ for major elements. Microprobe results were tested for the volatilization of alkali cations by analyzing an appropriate feldspar standard and comparing the results with those obtained with X-ray fluorescence (XRF).

Figure 5.1 - Target Rocks (MgO vs. SiO₂)

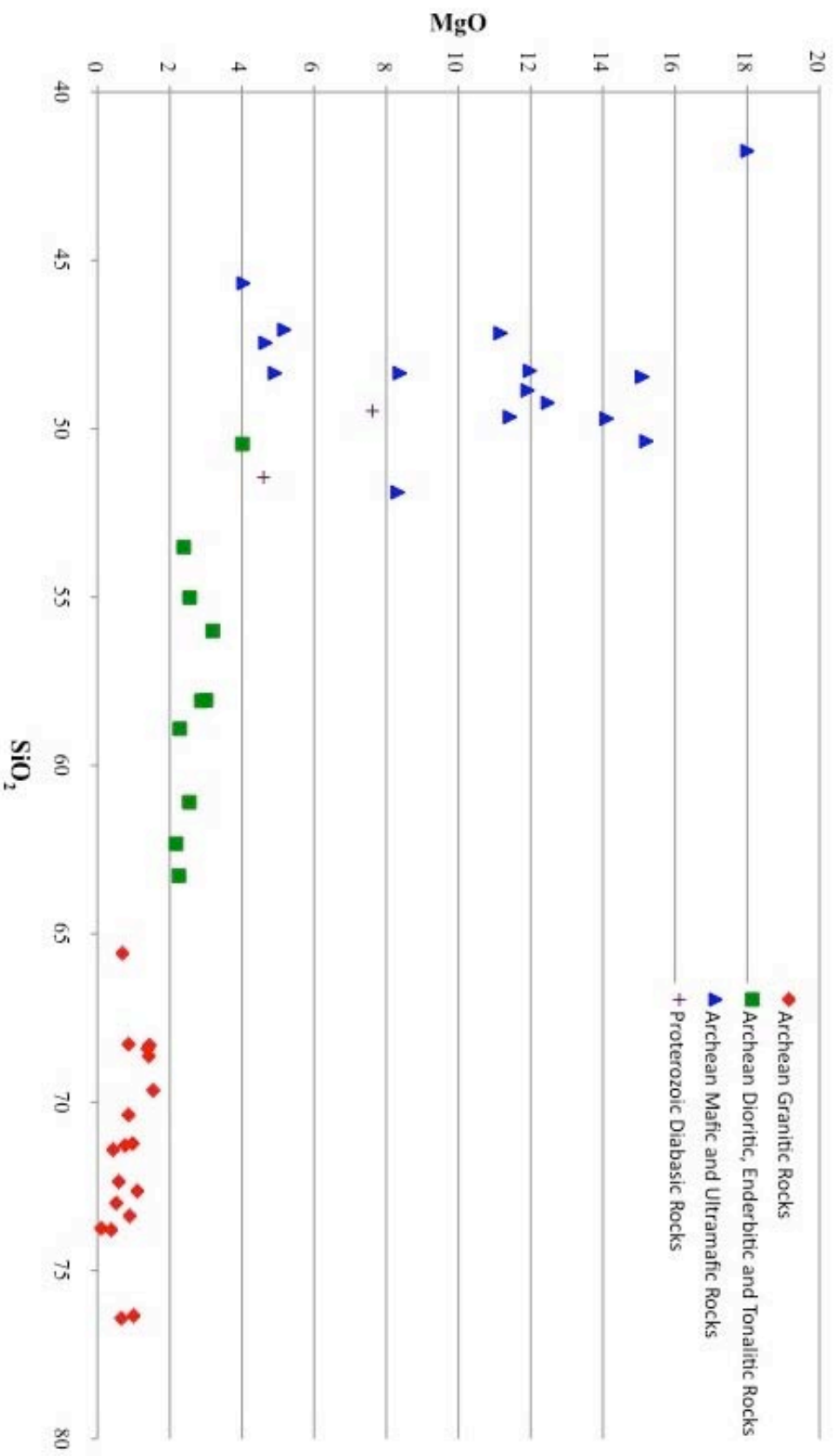


Table 5.1 - Average composition, and minimum and maximum range of compositions of the target rocks beneath the W.C.L. impact structure.

Rock Unit	Granitic Rocks		Granodioritic, Enderbititic and Tonalitic Rocks		Mafic and Ultramafic Rocks		Diabase	
n	18		10		15		2	
	aver.	min.-max.	aver.	min.-max.	aver.	min.-max.	aver.	min.-max.
SiO ₂ (%)	71.38	65.58 - 76.42	57.67	50.45 - 63.28	48.15	41.75 - 51.89	50.46	49.47 - 51.44
TiO ₂	0.29	0.03 - 0.66	1.02	0.61 - 1.77	1.03	0.42 - 3.40	1.71	1.08 - 2.35
Al ₂ O ₃	14.17	12.00 - 16.25	17.07	15.50 - 19.47	12.71	7.10 - 17.87	13.79	12.50 - 15.08
Fe ₂ O ₃	2.65	1.04 - 5.51	7.48	5.04 - 10.78	11.55	8.70 - 15.43	14.21	12.83 - 15.59
MnO	0.04	0.01 - 0.14	0.09	0.04 - 0.22	0.17	0.11 - 0.29	0.18	0.17 - 0.18
MgO	0.87	0.10 - 1.54	2.73	2.18 - 4.01	10.46	4.05 - 18.01	6.11	4.60 - 7.62
CaO	1.96	0.70 - 3.44	5.20	4.57 - 6.85	10.07	5.30 - 14.85	8.00	5.81 - 10.19
Na ₂ O	3.59	2.25 - 4.74	4.17	3.70 - 5.26	2.48	0.44 - 4.98	2.92	2.38 - 3.46
K ₂ O	3.82	1.11 - 5.96	2.63	1.23 - 4.60	1.05	0.44 - 2.42	1.10	0.76 - 1.43
P ₂ O ₅	0.09	0.02 - 0.27	0.46	0.21 - 0.89	0.40	0.04 - 2.29	0.26	0.12 - 0.40
Ba (ppm)	1165	135 - 3172	1270	528 - 3710	375	151 - 985	416	282 - 551
Ce	19	<d/l - 141	77	33 - 144	56.5	<d/l - 340	17.2	<d/l - 34
Co	<d/l	<d/l - 16	11.6	<d/l - 22	52.6	33 - 120	36.9	34 - 40
Cr	92	40 - 190	166	82 - 248	1761	148 - 11454	257	142 - 368
Cu	39	5 - 334	79.6	23 - 467	155	32 - 290	47.6	40 - 55
Ni	18	7 - 86	31.6	24 - 44	296	41 - 1958	54	39 - 69
Sc	<d/l	<d/l - <d/l	<d/l	<d/l - 10	30.9	15 - 54	26.4	20 - 33
V	24	<d/l - 88	123.4	81 - 165	187.3	133 - 286	266	242 - 291
Zn	<d/l	<d/l - 10	24.5	<d/l - 54	180.2	12 - 1720	53	35 - 71

5.2 Deformation and fracturing of target rocks

The most common sign that the rocks in the Clearwater Lake area were subjected to a meteoritic impact is the extensive fracturing of the samples and the presence of abundant veins of pseudotachylite. The intensity (that is, the amount of fracturing per volume) of the fracturing, deformation and even alteration is quite variable along the drill-core sections: in drill cores 1-63 and 3-63, which go through the structural uplift at the center of the impact structure, the shallower sections of the core are severely fractured, deformed and altered, but the intensity of the fracturing decreases with depth, to the point where the deepest sections of core, below 350 m, are nearly unaffected. Also, as one goes deeper, the intensity of the fracturing becomes strongly focused in bands meters to tens of meters thick, which alternate with bands that are much less

affected. The contact between the two can be either sharp or gradational over a few centimeters. Owing to the presence of these relatively pristine intervals, there is little difficulty in indentifying the rock.

In contrast, the fracturing, deformation and alteration in the drill cores sunk 6 km from the center of the impact structure are both more intense and more evenly distributed. There are virtually no bands of unaffected rock in the peripheral cores. In hole 5-63, 6 km from the central region, for instance, there is an epidote-bearing section about 20 meters thick that is severely broken up and jumbled, to the point that I have been unable to classify the rock.

The difference in the intensity of alteration may be due to the fact that the drill core that was sunk 6 km from the center is mostly penetrating material that, during crater formation and collapse, had a greater horizontal component to its movement than the material near the center of the crater, which essentially moved vertically. A vertical drill hole sunk parallel to most of the rock displacement will sample a smaller amount of deformed rock than a drill hole oriented almost perpendicularly to the direction of rock displacement.

Under the optical microscope, the extensive fracturing typically leads to abundant anastomosing cracks cutting through individual grains, and regions with fine-grained abraded, ground-up crystals surrounded by less deformed areas. Quartz almost invariably shows undulatory extinction; where present, biotite is kinked and strongly altered to chlorite. Samples generally display features characteristic of impact-related shock metamorphism, such as planar features and planar deformation features (PDFs in quartz) and maskelynite (diaplectic glass with a composition similar to plagioclase), but they are not common. This is probably due to the fact that the majority of the rocks were

collected in the ring of islands six kilometers from the center of the structure: because the development of PDFs in quartz requires pressures of 1-10 to ~35 GPa and shock pressures of at least ~30-35 GPa are needed to transform quartz and feldspar to diaplectic glass (Stöffler, 1974; 1984), rocks subjected to these pressures are expected near the center of the structure, where pressures near or above these values were achieved immediately upon impact. The samples noted for the presence of maskelynite come from the small islands near the center of the impact structure. Also, most of my samples are strongly affected by both pre-impact regional metamorphism and by post-impact metasomatism and hydrothermal alteration: feldspar grains are generally clouded and replaced by very fine-grained micas, and mafic minerals are generally replaced by chlorite. It is therefore possible that the minerals altered before the impact took place were not shock-metamorphosed in the expected manner. For instance, it is possible that shock-metamorphism will not convert hydrothermally altered plagioclase to maskelynite. Furthermore, I suspect that widespread post-impact alteration might have partially or completely erased the shock metamorphic features that usually affect plagioclase (e.g. maskelynite), mafic minerals (e.g. kink bands in biotite) and quartz [e.g., PDFs, see for instance Trepmann and Spray (2006)].

Pseudotachylite veins (dykes formed by frictional melting) in the drill holes show a variety of colors, going from very dark, nearly black to dark green to dark brownish red. This variation is related to post-impact alteration, the reddish veins being strongly oxidized and laden with hematite. Most are a few mm thick, but their thickness is variable. For instance, where veins cross, their thickness can increase to as much as 1 cm at the intersection; single veins can be about 1 mm thick for a certain distance, and then gradually widen to several mm, narrowing back to about 1 mm. The thickest veins of

pseudotachylite are nearly one decimeter wide, and they contain abundant clastic fragments, appearing almost breccia-like. The narrower veins typically show well-defined, straight margins: under the optical microscope: this appears as a sharp contact between dark-colored glassy material and country rock. Thicker veins, however, show a greater variety of contact types: some have irregular crack-filled margins with a great number of clasts near the contact that gradually decrease in number away from the country rock; in others, the country rock in contact with the glassy vein material appears to form irregular embayments. In some cases, a lighter-colored glassy material separates the darker vein material from the country rock, as if a reaction rim had formed.

The narrower veins typically are filled with featureless aphanitic material. Under the optical microscope, this material is now mostly cryptocrystalline and opaque. Under the microprobe, this featureless material appears scaly, apparently mostly consisting of extremely fine-grained flaky minerals and dot-like bright iron oxides, both probably the result of alteration.

Thicker veins (over 1 mm across) generally show flow textures, with minute elongate mineral clasts arranged along flow lines roughly parallel to the margins of the vein. Clast concentration usually decreases toward the margin, where larger and less-deformed fragments appear to have been sheared off the country rock. In these larger veins, the matrix is similar to that of the narrower veins. I have attempted to use the microprobe to obtain chemical compositions of this matrix, but the totals of my analyses are quite low, in the 70 to 50% range, possibly because the material appears to have been severely altered by hydrothermal activity combined with the fact that the microprobe was not appropriately calibrated for these compositions.

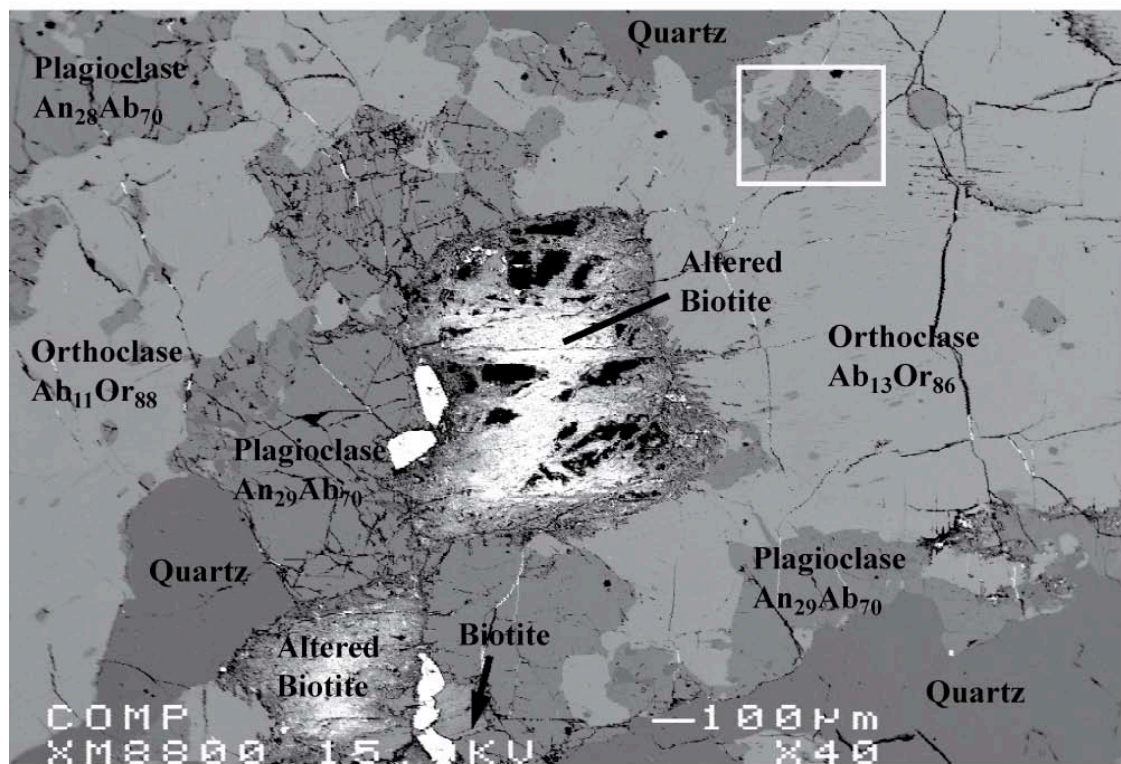
5.3 Granitic Rocks

Rocks with a granitic composition are the most common target rock in samples collected at West Clearwater Lake: they are documented on all the islands visited by Dence in 1977; eighteen of the forty-five target rock samples are classed as being granitic. Granitic rocks are also by far the most abundant rock-type along holes 3-63 and 5-63, and they form about one third of the core in holes 1-63 and 4-63. Among the rocks with a granitic composition in the West Clearwater Lake impact structure, I recognize three varieties: 1) a medium-grained unfoliated granite, 2) a fine- to medium-grained slightly foliated granitic gneiss, and 3) an unusual rock with a granitic composition and mineralogy that I have interpreted to be the result of partial melting.

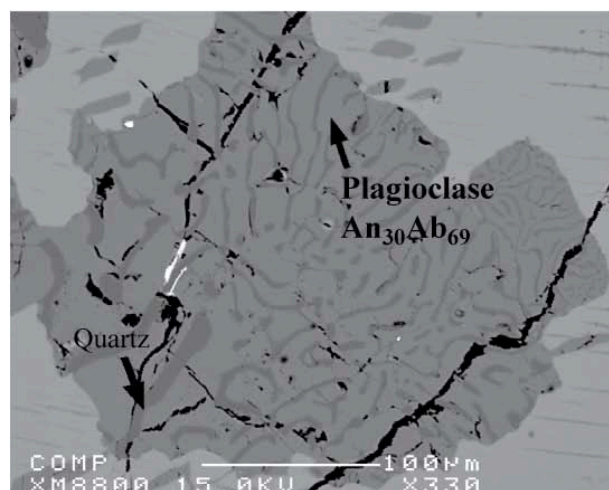
The unfoliated granite, present both in the core and in surface samples, generally displays a pinkish gray to reddish hue on freshly broken surfaces, and is medium-grained hypidiomorphic, equigranular, with average grain-sizes varying from ~1 mm up to ~3 mm. The granite is composed of varying amounts of pale red to pinkish white alkali feldspar, white to yellowish plagioclase and light gray quartz. Subhedral to anhedral alkali feldspar is the most common mineral in the granite samples examined, comprising ~30 to ~50% of their volume, whereas subhedral to anhedral plagioclase make-up ~10 to ~15% of the examined samples. Anhedral quartz makes-up ~20% to ~40%. Quartz also appears as small rounded inclusions less than 0.1 mm across in the alkali feldspar, as wormy intergrowths in symplectite and, on occasion, as a secondary mineral along cracks, which are common in all granitic samples. In at least one sample (DCW-77-11), alkali feldspar also forms antiperthitic rods and beads ranging in length from 50 to 100 μm within coarse-grained plagioclase.

Figure 5.2 A and B Sample with a granitic composition. Surface sample DCW-77-11 was collected in the fractured basement of Marie-Claude Island (Figure 1.3), close to the contact with the overlying impact melt.

Rock samples with a granitic composition:



A) Back-scattered electron image of a polished thin section of sample DCW-77-11, an unfoliated granite. The square area shows a grain of myrmekite, of which a more detailed image is given below, in figure B.



B) Detail of figure A above: back-scattered electron image of a myrmekite texture contained in a grain of orthoclase. This is a two-dimensional image of a three-dimensional arrangement, therefore it is likely that the myrmekite was at the periphery of a grain of plagioclase before this thin section was cut.

Small domains (up to 0.3 mm wide) of myrmekite are present in the margins of larger alkali feldspar grains, at the contact between alkali feldspar and quartz and alkali feldspar and plagioclase (Figures 5.2 A and B), a clear indication of local low-temperature metasomatism of the granites. Feldspar alteration is pervasive: very-fine white mica occurs along cracks and in clusters within the crystals. Plagioclase is more strongly altered than the alkali feldspar: alteration typically takes place along grain margins and cleavage cracks; in some cases, whole plagioclase crystals have been replaced by fine-grained scaly white micas.

Subhedral dark mica is usually associated with finer-grained opaque phases, generally near the margins of the larger mica crystals. The proportion of mafic minerals is low, in the <1 to ~5% range. Common accessory minerals comprise fine-grained apatite, zircon (as inclusions in biotite) and the opaque minerals magnetite (altered to hematite) and ilmenite. Grains of mica are usually strongly chloritized, and only a few isolated small relics of biotite are still preserved. Finely disseminated hematite makes some of the samples reddish.

Compared to the granites described above, the granitic gneisses have roughly similar proportions of alkali feldspar, plagioclase and quartz, with some rare biotite and green amphibole also present. However, the grain size is on average finer (the rocks are fine to medium grained), and they usually show poorly defined, roughly parallel layers of mica and green amphibole. Under the microscope, the granitic gneisses have a granoblastic texture and seem massive, such that the weak foliation seen megascopically is not apparent. Mafic minerals, however, usually appear together; this may delineate the weak foliation observed at the hand-sample scale.

Grains of alkali feldspars range in size from about 0.5 mm up to, in some cases, porphyroblastic crystals 2 mm in size; these grains usually have numerous inclusions of small, rounded quartz grains. Like in the granites described above, alteration to white micas is pervasive.

Plagioclase grains varying in size from 0.2 mm up to about 1 mm are distributed irregularly throughout the thin sections. Their characteristic polysynthetic twinning is usually poorly developed and, like the plagioclase in the unfoliated granite, they are usually quite altered, in some cases even completely replaced. Breakdown usually begins at the center of the grains, and it extends to the margins along cleavage cracks, which implies that originally the plagioclase was normally zoned.

Biotite usually occurs in association with green amphibole, but it also appears dispersed through the section. It can reach up to 1 mm, but its grain size is usually in the 0.3 to 0.5 mm range. It is commonly completely or partially altered to chlorite.

Green amphibole is the more common mafic mineral. It typically represents less than 1% of the composition of the gneissic granites, and it forms crystals about 0.5 mm in size, usually strongly altered. In the rare occasions where a relatively unaltered crystal is found, it displays a distinct green pleochroism, going from deep green to lighter, yellowish green.

Hypidiomorphic opaque oxides consisting of altered magnetite and ilmenite, ranging in size from 0.1 to 0.3 mm, usually occur together with the mafic minerals, and may even be the result of the alteration of these minerals. Very fine-grained hematite stains the sections rust-red, particularly the alkali feldspar grains. It fills tiny cracks in and between grains.

The plagioclase composition in both the regular granite and the deformed granite is rather narrow: it falls near the oligoclase-andesine boundary ($\text{An}_{30-25}\text{Ab}_{71-64}\text{Or}_{8-1}$) (Table 5.2, Figure 5.3).

As expected, the K-rich feldspars in granite samples are potassium-rich. They are close to the end member; sample DCW-77-11 contains up to Or_{92} ($\text{Or}_{92-84}\text{Ab}_{15-13}\text{An}_{1-0}$). However, the K-feldspar composition of the other samples is poorer in potassium: $\text{Or}_{77-62}\text{Ab}_{35-22}\text{An}_{4-1}$ (Table 5.2 and Figure 5.3). Such more sodic compositions may well indicate local homogenization of Or + Ab assemblages following impact.

The most conspicuous feature of the granitic rocks interpreted as being partial melts is the presence of resorbed quartz crystals. Quartz represents about 20 to 40% of the mineral content of these rocks, both as large single crystals and as polycrystalline aggregates, ranging in size from 1 mm up to 5 mm across. The minerals usually display rounded margins with concave contacts (or embayments) curving into cusp-shaped tips (see Figure 5.4 A). A glassy-looking rim ranging in thickness from a 100 μm up to nearly 1 mm is generally visible in immediate contact with the resorbed quartz margin. Under the microscope, in plane light, this rim is brownish in color and may contain small acicular crystals that are perpendicular to the resorbed quartz margin, recalling the axiolitic texture created by devitrification of volcanic glasses. Where thicker, the rim contains what appear to be skeletal crystals with a square cross-section. None of these structures can be seen on back-scattered electron pictures, where the rim appears as a featureless lighter-colored band separating quartz from the feldspathic groundmass (Figures 5.4 A and B).

It should be noted that the resorbed quartz (usually single crystals) locally displays planar deformation features (PDFs), whereas the polycrystalline aggregates

Table 5.2 Representative compositions of the minerals found in the granitic rocks of the West Clearwater Lake impact structure. **DCW-77-11-Region 2-Kspar 6** : DCW-77-11 is the sample designation (Dence Clearwater West, 1977, sample 11), Region 2 refers to the emplacement studied within the thin section and Kspar 6 is the name of the point analysis, that is, the sixth alkali feldspar of region 2 analyzed with the microprobe.

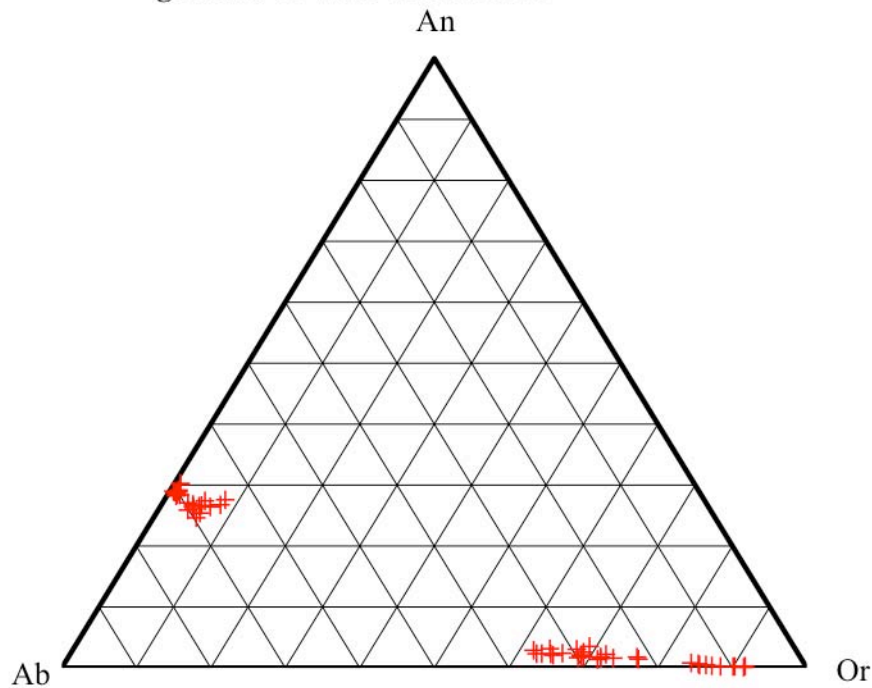
	DCW-77-11- Region 2- Kspar 6 (<i>Antiperthite</i>)	DCW-77-11- Region2- Kspar 1 (<i>Sanidine</i>)	DCW-77-27- Region 2- Kspar 1 (<i>Sanidine</i>)	DCW-77-27- Region 2- Plagioclase 3 (<i>Oligoclase</i>)	DCW-77-27- Region2-Px 1 (<i>Biotite</i>)
SiO ₂ wt. %	64.73	64.71	65.41	61.75	40.87
TiO ₂	0.05	0.01	0.01	0.03	0.21
Cr ₂ O ₃	0.00	0.00	0.00	0.00	0.012
Al ₂ O ₃	18.40	18.47	18.70	23.50	11.53
FeO	0.03	0.02	0.09	0.18	10.32
MnO	0.01	0.00	0.01	0.00	0.03
MgO	0.00	0.00	0.00	0.01	20.60
CaO	0.02	0.07	0.47	5.38	0.01
Na ₂ O	0.94	1.40	3.78	8.05	0.40
K ₂ O	15.47	14.68	11.13	0.70	10.28
P ₂ O ₅	0.00	0.00	0.00	0.00	0.00
Total	99.33	99.36	99.60	99.60	94.26

Number of cations on the basis of X (O)

	X = 8	X = 8	X = 8	X = 8	X = 22 O ⁽¹⁾
Si <i>apfu</i>	2.995	2.994	2.986	2.756	6.044
Ti	0.001	0.000	0.000	0.001	0.023
Cr	0.000	0.000	0.000	0.000	0.001
Al	1.003	1.007	1.006	1.236	2.010
Fe	0.001	0.001	0.003	0.007	1.276
Mn	0.000	0.000	0.000	0.000	0.004
Mg	0.000	0.000	0.000	0.001	4.541
Ca	0.001	0.003	0.023	0.257	0.001
Na	0.084	0.125	0.334	0.697	0.115
K	0.913	0.867	0.648	0.040	1.939
P	0.000	0.000	0.000	0.000	0.000
Total Cation	5.000	4.998	5.002	4.993	15.954
Or mol. %	91.46	87.07	64.47	3.98	---
Ab	8.44	12.58	33.23	70.12	---
An	0.10	0.35	2.30	25.90	---

⁽¹⁾ As neither H₂O nor F were determined, the calculation was done on an anhydrous basis by replacing 4(OH, F)⁻ by two O²⁻.

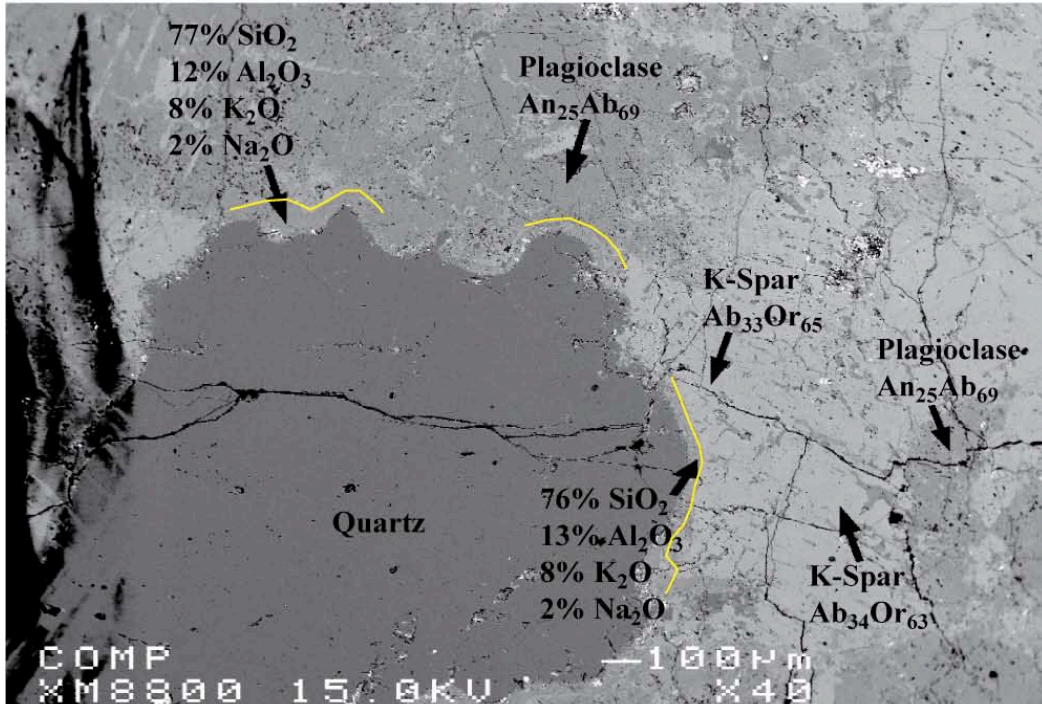
Figure 5.3 Mineral compositions for feldspar in the granites at West Clearwater.



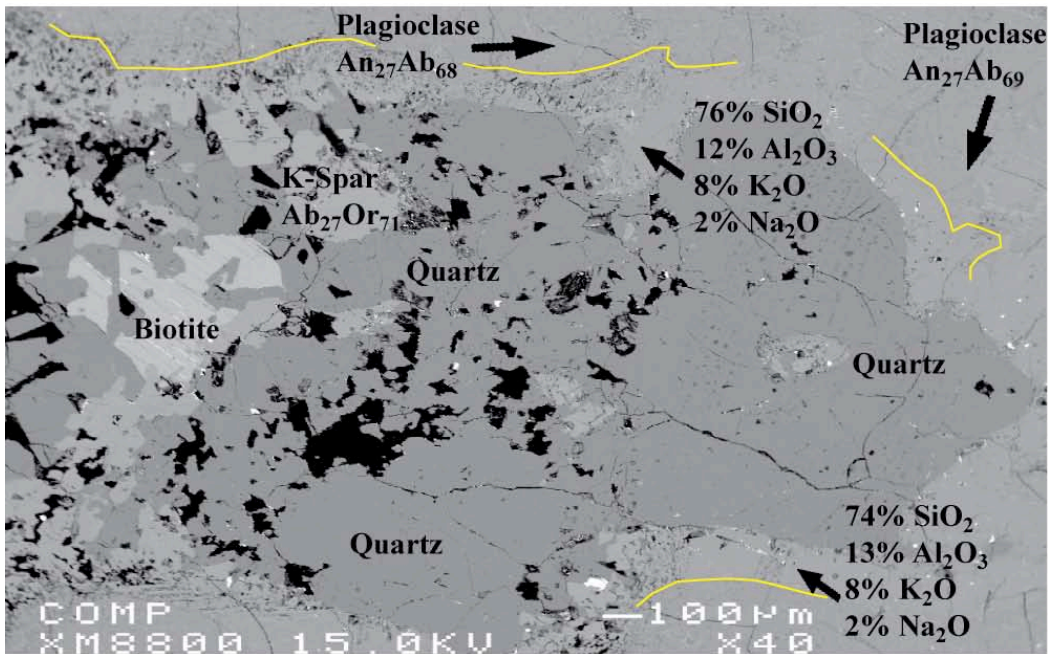
may show inclusions of other minerals (biotite and alkali feldspar, fig. 5.3 B) and numerous cracks and holes. Many of the quartz grains also have an abnormally high birefringence (first-order yellow), and their conoscopic figure is marginally biaxial. Feldspars represent about 60 to 70% of the mineral content of these rocks. Under the optical microscope, alkali feldspars are quite difficult to distinguish from plagioclase: the telltale plagioclase twinning is almost entirely absent. In sample DCW-77-20, where quartz forms coarse-grained crystals, the surrounding feldspars grains are generally fine-grained, under 0.5 mm wide, and they look altered, covered in a very-fine grained diffuse grayish clay-like material, and show poorly defined crystal margins. In sample DCW-77-27, however, most feldspars are coarse-grained, with sizes comparable to quartz.

Figures 5.4 A and B Back-scattered electron images of thin sections of partially melted rocks with a granitic composition. Note the resorbed margins of the quartz crystals and the reaction rim separating the resorbed quartz from the surrounding feldspar. The yellow lines were added in order to make the rims, nearly featureless in back-scattered electron images, clearer to the reader.

Partially melted rock samples with a granitic composition:



A) Back-scattered electron image of a polished thin-section of sample DCW-77-27.



B) Back-scattered electron image of a polished thin-section of sample DCW-77-20.

In plane light, the difference between quartz and feldspars is quite striking: the feldspars look murky, fractured and have indistinct borders, whereas quartz is limpid and has margins clearly defined by the reaction rims described above. The composition of the plagioclase in the vicinity of the resorbed quartz crystals is in the range $An_{25-27}Ab_{67-70}Or_{3-6}$, whereas the alkali feldspar has a composition $An_{1-6}Ab_{26-35}Or_{62-71}$.

Table 5.3 below shows that rim regions surrounding quartz have a composition that is similar to that of the neighboring alkali feldspars, but containing much more SiO_2 (~76% SiO_2 in the rim vs. ~66% in K-feldspar). I suspect that the rims are similar to the axiolites found in devitrified volcanic glass, that is, they are composed of very fine parallel crystals of acicular feldspar and quartz (which might have originally have been cristobalite): the electron beam presumably sampled both minerals, giving an intermediate composition.

Table 5.3 Representative compositions of feldspars and glassy rims (partial melt), both found at the outer margins of resorbed quartz present in partially melted rocks with a granitic composition from the West Clearwater Lake Impact Structure.

	DCW-77-20- Region 1-Rim	DCW-77-27- Region 1-Rim	DCW-77-27- Region 1-Kspar 1	DCW-77-27- Region 1-Plag 1
SiO ₂ wt. %	76.39	75.84	65.91	61.86
TiO ₂	0.07	0.04	0.03	0.02
Cr ₂ O ₃	0.00	0.00	0.00	0.00
Al ₂ O ₃	12.31	12.67	18.59	23.34
FeO	0.12	0.19	0.08	0.07
MnO	0.02	0.00	0.01	0.01
MgO	0.00	0.00	0.00	0.01
CaO	0.21	0.48	0.43	5.22
Na ₂ O	1.82	2.06	3.73	7.80
K ₂ O	8.06	7.89	11.15	1.01
P ₂ O ₅	0.00	0.00	0.00	0.00
Total	99.00	99.18	99.93	99.34

5.4 Granodioritic, enderbitic and tonalitic rocks

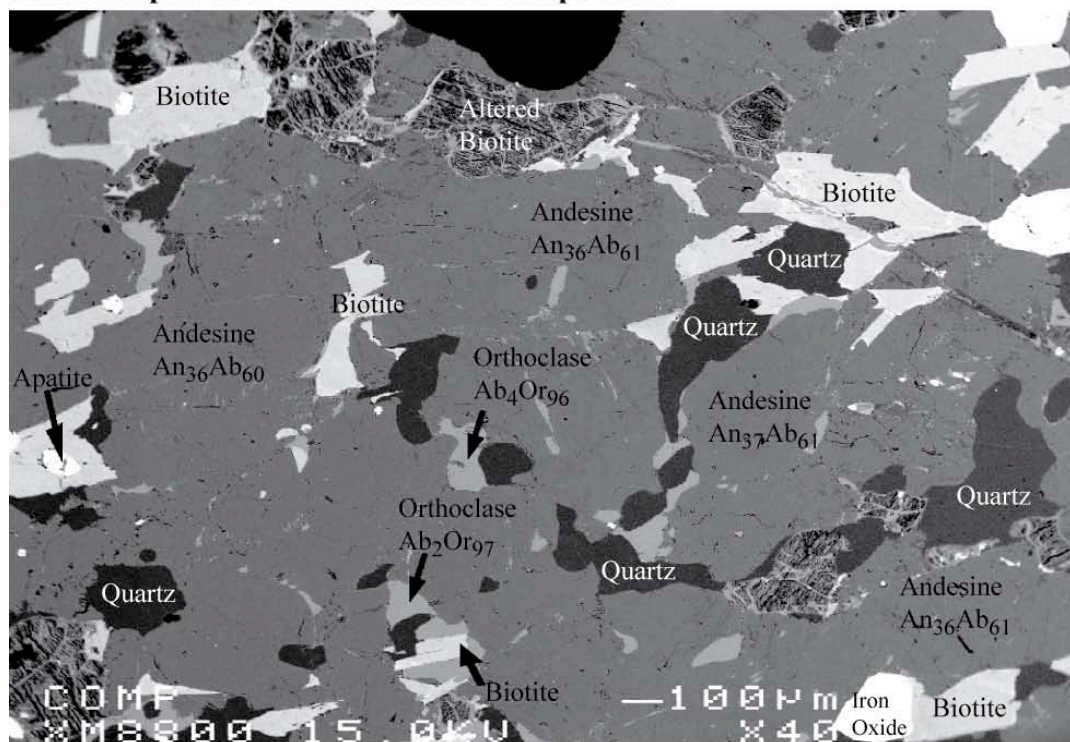
Rocks with intermediate chemical compositions have been collected on Lepage Island, Drillers Island and on the central islands (Figure 1.3). They represent ten samples out of the forty-five basement rocks samples I have been able to positively identify. In the core, they are the second most common rock type, usually appearing in the top 1/3 of the drill core. They generally can be distinguished from granitic rocks by the greater relative abundance of plagioclase, the presence of one or two pyroxenes, and a lower SiO₂ content and higher MgO content; compared to gabbros, they generally contain quartz, and their proportion of mafic minerals (pyroxenes, biotite and opaque oxides) varies between ~20% and ~5% (Figure 5.5 and Table 5.4).

These rocks are typically massive and medium to coarse grained. They generally are gray, with reddish hues on freshly broken surfaces. There is, however, a section of strongly altered tonalite to diorite in drill core 4-63 that has taken on a dark red color. Most of the samples are inequigranular: typically, a thin section contains a range of grain sizes going from 0.1 mm wide or less up to 6 or 7 mm across; the size distributions are not bimodal, that is, these rocks are not porphyritic; rather, grain size varies gradationally. However, at least one of the samples is clearly porphyritic.

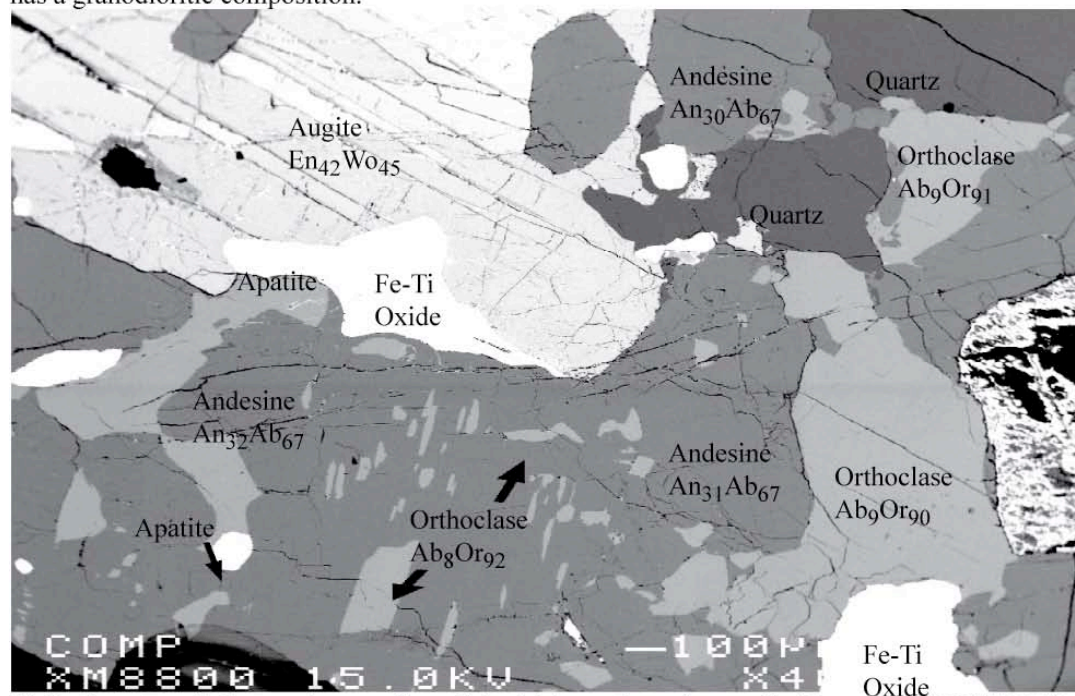
Plagioclase is dominant, usually making up ~50 to ~70% of these rocks. Quartz is the second most abundant mineral, generally representing ~20 to ~30% of the rock composition. The proportion of alkali feldspar is low, ranging from 0 to about 10%. Mafic minerals usually represent less than 10% of the rock: biotite content ranges from 1 to 3%; clinopyroxene is by far the most common pyroxene, its proportion varying between 2 and 5%; opaque oxides represent about 3 to 10% of the rock minerals. Orthopyroxene is present in at least one sample (DCW-77-3), where it represents less

Figures 5.5 A and B Two samples with a granodioritic composition. Sample 3-63-65 was collected from core 3-63 (see chapter 4), at a depth of 20 meters (65') below lake level. DCW-77-10 is a surface sample collected in the fractured basement of Marie-Claude Island.

Rock samples with an intermediate composition:



A) Back-scattered electron image of a polished thin-section of core sample 3-63-65, which has a granodioritic composition.



B) Back-scattered electron image of a polished thin-section of granodioritic sample DCW-77-10.

Table 5.4 Representative compositions of the minerals found in the granodioritic, enderbitic and tonalitic rocks of the West Clearwater Lake impact structure.

	3-63-882-65- Region 1- Kspar 1 (<i>Orthoclase</i>)	1-63-834-113- Region 1- Plagioclase 4 (<i>Andesine</i>)	DCW-77-3- Region 2- Kspar 2 (<i>Orthoclase</i>)	DCW-77-3- Region 4- Plagioclase 1 (<i>Andesine/ Labradorite</i>)
SiO ₂ wt. %	64.33	60.26	65.79	56.32
TiO ₂	0.02	0.03	0.121	0.03
Cr ₂ O ₃	0.01	0.00	0.00	0.00
Al ₂ O ₃	18.27	24.74	18.89	27.08
FeO _{total}	0.03	0.07	0.25	0.44
MnO	0.00	0.01	0.00	0.00
MgO	0.00	0.00	0.01	0.02
CaO	0.02	6.49	0.43	9.67
Na ₂ O	0.28	7.68	3.85	5.79
K ₂ O	16.78	0.39	10.76	0.40
P ₂ O ₅	0.00	0.00	0.00	0.00
Total	99.74	99.66	99.89	99.73

Number of cations on the basis of X (O)

	X = 8	X = 8	X = 8	X = 8
Si <i>apfu</i>	2.992	2.693	2.989	2.543
Ti	0.001	0.001	0.004	0.001
Cr	0.000	0.000	0.000	0.000
Al	1.001	1.303	1.001	1.441
Fe	0.001	0.003	0.010	0.017
Mn	0.000	0.000	0.000	0.000
Mg	0.000	0.000	0.001	0.001
Ca	0.001	0.311	0.021	0.468
Na	0.026	0.666	0.339	0.506
K	0.996	0.022	0.624	0.023
P	0.000	0.000	0.000	0.000
Total Cation	5.018	4.999	4.988	5.000
Or mol. %	97.39	2.22	63.41	2.28
Ab	2.50	66.65	34.47	50.81
An	0.12	31.13	2.12	46.91

Table 5.4 (continued) Representative compositions of the minerals found in the granodioritic, enderbitic and tonalitic rocks of the West Clearwater Lake impact structure.

	3-63-882-65- Region 1 - Biotite 3	DCW-77-3-Region 2-PX 6 (Mg-hornblende)	DCW-77-10- Region 3-CPX 1 (Augite)	DCW-77-3- Region1-Amphi 1 (Augite)
SiO ₂ wt. %	37.52	45.33	52.89	51.34
TiO ₂	5.05	1.60	0.21	0.52
Cr ₂ O ₃	0.00	0.04	0.02	0.00
Al ₂ O ₃	13.51	6.74	1.66	1.61
FeO _{total}	13.28	14.69	8.35	12.06
MnO	0.08	0.20	0.28	0.30
MgO	15.48	14.08	13.78	14.04
CaO	0.07	11.14	22.19	19.49
Na ₂ O	0.06	2.30	0.55	0.35
K ₂ O	10.42	1.19	0.00	0.01
P ₂ O ₅	0.00	0.00	0.00	0.00
Total	95.44	97.31	99.94	99.72

Number of cations on the basis of X (O)

	X = 22 ⁽¹⁾	X = 23 ⁽²⁾	X = 6	X = 6
Si <i>apfu</i>	5.595	6.797	1.969	1.940
Ti	0.566	0.181	0.006	0.015
Cr	0.000	0.005	0.001	0.000
Al	2.374	1.190	0.073	0.072
Fe	1.656	1.843	0.260	0.381
Mn	0.009	0.025	0.009	0.010
Mg	3.442	3.147	0.765	0.790
Ca	0.010	1.789	0.885	0.789
Na	0.016	0.669	0.040	0.026
K	1.982	0.228	0.000	0.000
P	0.000	0.000	0.000	0.000
Total Cation	15.651	15.873	4.008	4.023
En mol. %	---	---	40.03	40.32
Fs	---	---	13.61	19.44
Wo	---	---	46.36	40.24

⁽¹⁾ As neither H₂O nor F were determined by the analysis, the calculation was done on an anhydrous basis by replacing 4(OH, F)⁻ by two O²⁻.

⁽²⁾ As H₂O was not determined by the analysis, the calculation was done on an anhydrous basis by replacing 2(OH)⁻ by one O²⁻.

than 2% vol. of the mineral content. Microprobe analyses of this sample, however, only detected augite. This orthopyroxene-bearing sample might be a representative of the enderbitic rocks observed by Simard et al. (2004) in the vicinity of the impact structure.

Apatite is the most common accessory mineral, and some rare small crystals of zircon are also present. The most common secondary minerals are very fine-grained white micas (created by the alteration of plagioclase), chlorite and some rare amphibole (mostly the result of pyroxene breakdown). Also, some samples show rust-red hematite stains.

Most grains are allotriomorphic granular. The only generally euhedral minerals are biotite and apatite. Anhedral plagioclase varies in size from less than 0.1 mm across to, in a few samples, 5 or 6 mm wide. This mineral is typically altered, either looking cloudy, or converted to fine-grained white mica. Also, the characteristic polysynthetic twinning of plagioclase is poorly developed, or completely absent, particularly amongst the samples that seem to have been severely fractured by the impact. Patchy or wavy extinction is common. In at least one sample (DCW-77-10), alkali feldspar forms what I believe are blocky antiperthitic growths ranging in length from 50 μm up to 0.3 mm within coarse-grained plagioclase (Figure 5.4 B). The plagioclase in these rocks ranges in composition $\text{An}_{52-20}\text{Ab}_{68-56}\text{Or}_{5-1}$. However, most of this variation, particularly the compositions with an anorthite content greater than 40%, is found in sample DCW-77-3. All the other samples fall within the much narrower range $\text{An}_{37-30}\text{Ab}_{68-60}\text{Or}_{4-1}$ (andesine) (see Table 5.4 and Figure 5.6). Quartz usually forms clear homogeneous anhedral grains displaying wavy extinction. These grains are typically smaller than plagioclase and usually at the

Figure 5.6 Mineral compositions for feldspar in the granodiorites and tonalites at West Clearwater.

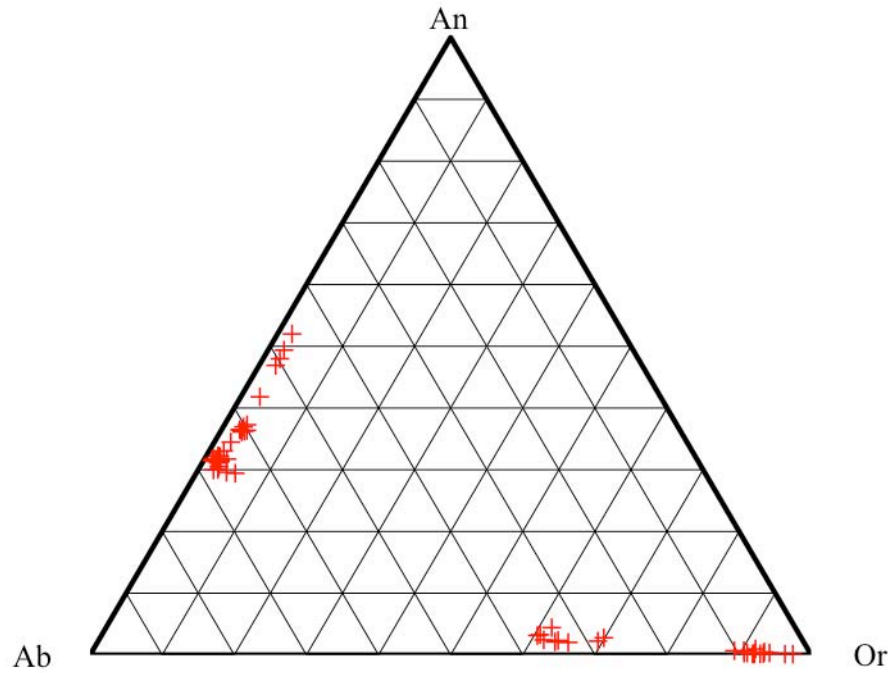
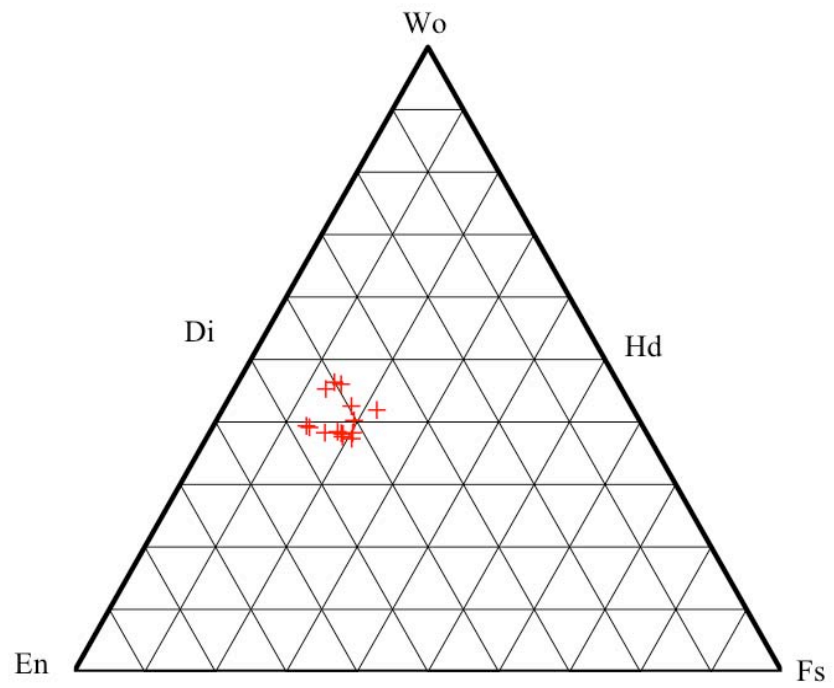


Figure 5.7 Mineral compositions for pyroxene in the tonalites and diorites at West Clearwater.



margin of the larger plagioclase grains (Figure 5.5 A); in one samples at least (DCW-77-3), they appear to be interstitial. Shock-metamorphic features such as planar deformation features (PDFs) are absent from the quartz in most of the samples, except for sample 1-63-281, which comes from the core drilled at the center of the impact structure.

Like quartz, anhedral alkali feldspar typically forms small irregular grains at the periphery of the larger grains of plagioclase; also, as mentioned above, in some cases alkali feldspar forms a blocky intergrowth within coarse-grained plagioclase. In most samples studied with the microprobe, the composition of this alkali feldspar (both the irregular alkali feldspar grains at the periphery of plagioclase and the blocky intergrowth within plagioclase) is close to that of a nearly pure orthoclase ($\text{An}_{1-0}\text{Ab}_{9-2}\text{Or}_{97-90}$) (see Table 5.4 and Figure 5.5 B). However, the alkali feldspars in sample DCW-77-3 contains more sodium ($\text{An}_{3-2}\text{Ab}_{36-27}\text{Or}_{70-61}$): many of these grains have a rim of what looks like crystalline regrowth, which suggests that their magmatic compositions may be the result of partial melting.

Where present, anhedral clinopyroxene (augite with the following range of compositions: $\text{En}_{47-36}\text{Fs}_{22-13}\text{Wo}_{46-37}$) is comparable in size to plagioclase, usually in the 1 to 2 mm range. It should be noted that the clinopyroxene in sample DCW-77-3 is poorer in Ca, with a greater variation in Ca content, than the clinopyroxene in the other dioritic and tonalitic samples (Wo_{42-37} for DCW-77-3 vs. Wo_{45-46} for the other samples) (see Table 5.4 and figure 5.7). Felsic minerals usually impinge on clinopyroxene margins, or are included in clinopyroxene, in a manner similar to a poorly developed subophitic texture (Figure 5.5 B).

The biotite in these rocks has a high TiO_2 content ($\sim 5\% \text{TiO}_2$), is relatively poor in Al ($\sim 14\%$), and has a high magnesium content ($\text{Mg/Fe} \sim 2$) (see Table 5.4). Lamellar

biotite, anhedral clinopyroxene, opaque oxides and apatite prisms usually are grouped together, forming small clumps. In these clumps, apatite is typically included in biotite, or is in contact with opaque oxides.

The opaque phases are typically anhedral, either resembling an assemblage of small globules, or small interstitial grains, both in 0.1 to 0.5 mm wide range. Back-scattered electron images of the opaque oxide grains in two of the samples show the typical oxy-exsolution microtextures of altered titaniferous magnetite. Both biotite and clinopyroxene are typically partially or even completely altered: the pyroxene is altered to blades of amphibole, and the biotite to chlorite.

5.5 Mafic Rocks

Surface samples with a gabbroic composition have been collected on Lepage Island, on the small islands at the center of West Clearwater Lake, where the central uplift of the impact structure projects above the lake surface, and on South Tad Island (Figure 1.3). With the exception of two diabasic layers in holes 3-63 and 5-63, all mafic rocks in the core extracted at West Clearwater Lake are restricted to hole 1-63, where they occupy two-thirds of the core length, from a depth of about 130 m to the end of the core, at 397 meters. As discussed earlier, drill core 1-63 crosses the central uplift region of the West Clearwater impact structure, where rocks from a depth of about 3 km below the pre-impact surface have been pushed up by the collapse of the crater and the accompanying rebound of the crater floor (see Section 3.3).

These rocks are dark gray, holocrystalline and generally fine to medium grained, the grain sizes varying from 0.5 to 1 mm across. Under the polarizing microscope, they appear roughly equigranular, and many of these samples show a well-developed

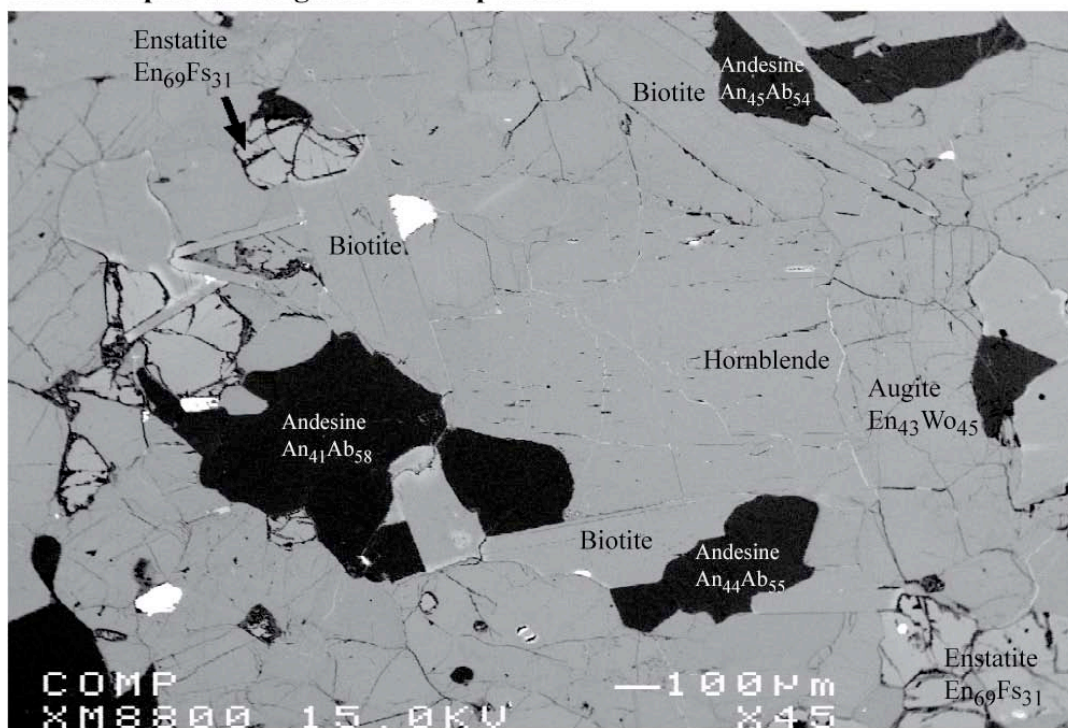
granoblastic texture, particularly those taken from the deepest part of drill core 1-63. However, I have observed some gabbro-norite hand-samples from drill core 1-63 that are composed of about 5% mafic phenocrysts 1 to 2 cm long, which gives them a “spotted” look.

The major mineral is usually plagioclase: in thin section, its proportion is quite variable, ranging from 20 to about 70%, that is, from leucocratic to melanocratic gabbro-norite. Pyroxene content is also very variable, from about 20% up to around 70% in the deepest sections of drill core 1-63. Dark red to dark brown biotite is common, usually representing 5 to 10% of the rock. Opaque phases are relatively scarce, usually making up 1 to 3% of the rock. Quartz and alkali feldspar are present together in only one of the samples (1-63-910), where they together represent less than 5% of the rock. Sample DCW-77-4 contains a small amount of alkali feldspar (less than 3%), but I have not observed quartz. Short-prismatic apatite is the most common accessory mineral. Secondary minerals include green amphibole, white mica, chlorite and, in at least one thin section, tiny grains of carbonate that are probably the result of alteration of a nearby clinopyroxene.

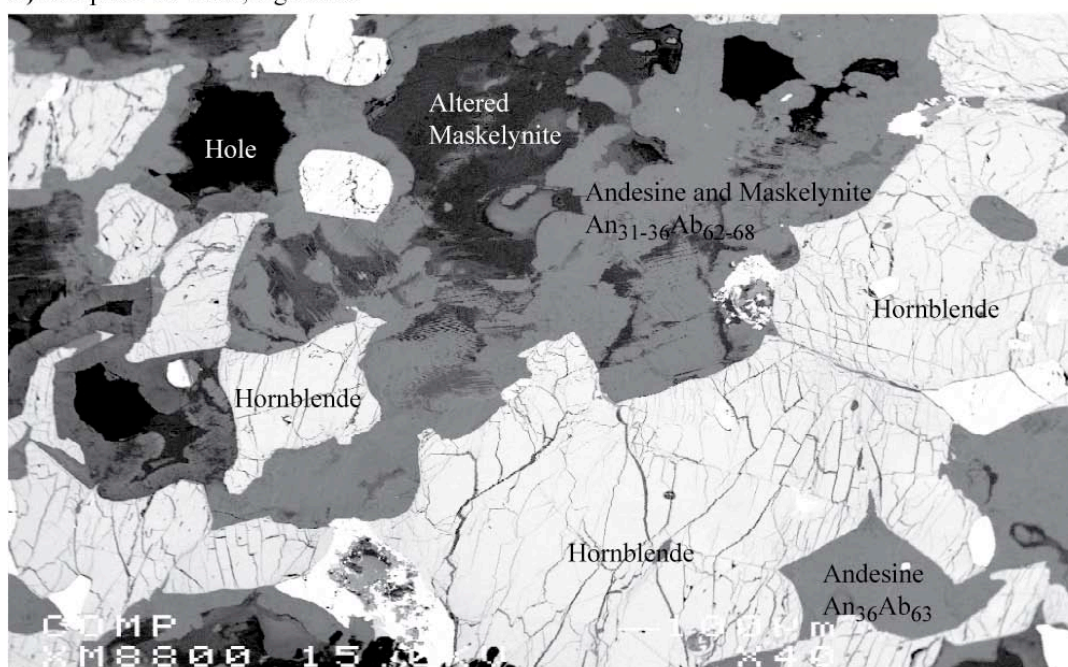
Plagioclase is typically anhedral to subhedral, roughly equant, with grain sizes ranging from 0.10 up to 2 mm. In the surface samples, plagioclase tends to display wavy extinction, and its polysynthetic twinning is poorly developed. Alteration to very fine-grained white mica is common. Surface sample DCW-77-47 (Figure 5.8 B), which was collected on one of the small islands near the center of the impact structure, contains abundant maskelynite (diaplectic glass with a plagioclase composition), which indicates that this rock was subjected to shock pressures above ~30 GPa (Stöffler, 1974; 1984)

Figures 5.8 A and B Back-scattered electron images of polished thin sections of rock samples with a gabbroic composition. Note the presence of maskelynite (diaplectic glass with a plagioclase composition) in sample DCW-77-47, which was collected in one of the small islands in the center of the West Clearwater Lake impact structure. Sample 1-63-1303 comes from a core drilled at the center of the impact structure. The sample was collected at a depth of about 400 meters (1303') below the lake surface.

Rock samples with a gabbroic composition:



A) Sample 1-63-1303, a gabbro.



B) Sample DCW-77-47, a shock metamorphosed gabbro.

This maskelynite is altered: the alteration is sand-colored in plane light, and very fine grained. In crossed polars, this alteration forms what appears to be a kind of spherulitic or axiolitic texture, similar to the devitrification textures observed in glass-bearing volcanic rocks. Microprobe analyses of this material gave compositions similar to that of the plagioclase in the thin section, but with low totals: I suspect that the devitrification of the maskelynite involves very fine-grained phases like calcite and, possibly, zeolites, which give the altered maskelynite its brownish tint in plane light and cause low analytical totals. This pattern of maskelynite alteration has been previously observed by Bunch et al. (1967), who mentioned that alteration of maskelynite to white carbonate and zeolite and brown devitrified glass is common in the gabbro of the central islands of West Clearwater Lake.

The composition of plagioclase is quite variable, over the range of $An_{60-32}Ab_{68-24}Or_{16-0}$ (andesine to labradorite). There is no obvious zoning. In fact, most of this variability is due to the plagioclase of the surface samples: compared to surface samples, the composition of the plagioclase in the drill-core samples is narrower, staying in the $An_{45-36}Ab_{62-53}Or_{2-1}$ range (see Table 5.5 and Figure 5.9). The compositional variability of the surface samples is probably related to partial melting of at least one sample (DCW-77-3) and the presence of altered maskelynite in rock samples from the islands in the central area of the impact structure (e.g. sample DCW-77-47, see Figure 5.8 B).

Pyroxene grains are typically subhedral, usually assembled in granular aggregates consisting of pale green clinopyroxene and pale pink orthopyroxene crystals jumbled together with biotite, short-prismatic apatite and opaque phases. The clinopyroxene is augite with a composition of $En_{43-40}Fs_{16-11}Wo_{47-44}$, whereas the orthopyroxene is enstatite, with a composition of $En_{70-65}Fs_{34-30}Wo_{2-1}$ (Figure 5.10).

Table 5.5 Representative compositions of the minerals found in the mafic rocks of the West Clearwater Lake Impact Structure.

	1-63-878-1303- Region 2-Opx 1 (<i>Enstatite</i>)	1-63-878-1303- Region 2-Cpx 2 (<i>Augite</i>)	1-63-878-1303- Region 2- Biotite 1	DCW-77-4-Region 1- Amphibole 1 (<i>Hornblende</i>)
SiO ₂ wt. %	52.88	51.89	37.54	43.31
TiO ₂	0.08	0.24	5.26	2.68
Cr ₂ O ₃	0.03	0.07	0.18	0.02
Al ₂ O ₃	1.21	6.83	13.79	8.75
FeO _{total}	20.05	0.16	10.49	10.40
MnO	0.42	0.16	0.03	0.17
MgO	25.27	15.02	17.88	16.37
CaO	0.45	22.48	0.01	11.48
Na ₂ O	0.00	0.50	0.09	2.60
K ₂ O	0.00	0.00	10.02	1.42
P ₂ O ₅	0.00	0.00	0.00	0.0
Total	100.38	99.28	95.30	97.30

	X = 6	X = 6	X = 22 O ⁽¹⁾	X = 23 O ⁽²⁾
Si <i>apfu</i>	1.943	1.937	5.523	6.428
Ti	0.002	0.007	0.581	0.299
Cr	0.001	0.002	0.021	0.002
Al	0.052	0.092	2.391	1.528
Fe	0.616	0.213	1.291	1.288
Mn	0.013	0.005	0.004	0.022
Mg	1.384	0.836	3.922	3.613
Ca	0.018	0.899	0.001	1.822
Na	0.000	0.036	0.027	0.746
K	0.000	0.000	1.881	0.268
P	0.000	0.000	0.000	0.000
Total Cation	4.029	4.027	15.643	16.015
En mol. %	68.59	42.90	---	---
Fs	30.53	10.94	---	---
Wo	0.87	46.15	---	---

⁽¹⁾ As neither H₂O, nor F were determined by the analysis, the calculation was done on an anhydrous basis by replacing 4(OH, F)⁻ by two O²⁻.

⁽²⁾ As H₂O was not determined, the calculation was done on an anhydrous basis by replacing 2(OH)⁻ by one O²⁻.

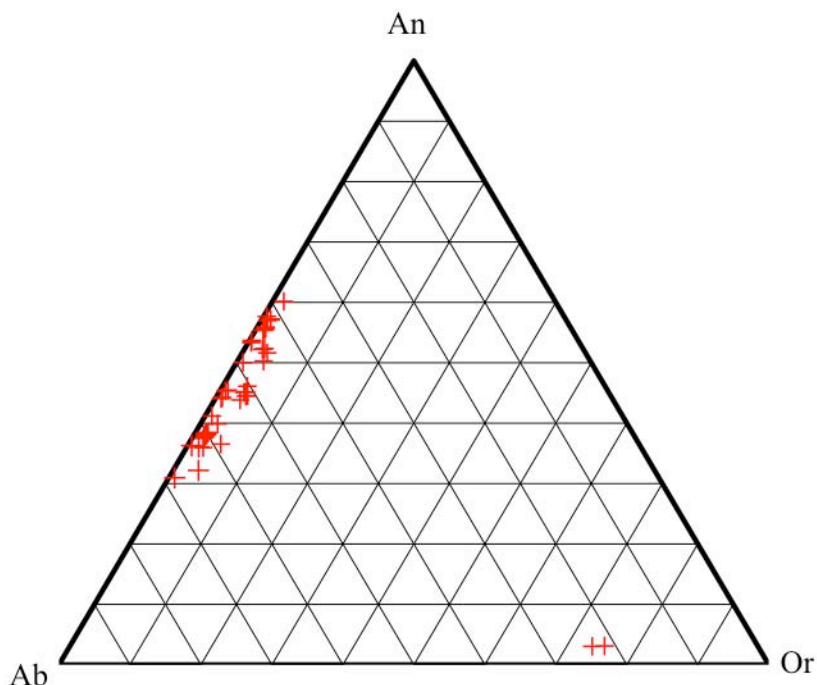
Table 5.5 (continued) – Representative compositions of the minerals found in the mafic rocks of the West Clearwater Lake Impact Structure.

	1-63-878-region 2-Feldspar 4 (<i>Andesine</i>)	1-63-852-593 - Region 2– Plagioclase 4 (<i>Andesine</i>)	DCW-77-4- Region 2-KSpar 2 (<i>Orthoclase</i>)
SiO ₂ wt. %	56.59	57.24	64.25
TiO ₂	0.00	0.04	0.075
Cr ₂ O ₃	0.02	0.00	0.03
Al ₂ O ₃	27.51	27.44	19.00
FeO _{total}	0.10	0.23	0.33
MnO	0.017	0.02	0.00
MgO	0.00	0.00	0.00
CaO	9.46	9.06	0.61
Na ₂ O	6.21	6.25	2.59
K ₂ O	0.14	0.14	12.44
NiO	0.00	0.00	0.00
Total	100.06	100.41	99.32

Number of cations on the basis of X (O)

	X = 8 O	X = 8 O	X = 8 O
Si <i>apfu</i>	2.541	2.557	2.961
Ti	0.000	0.001	0.003
Cr	0.001	0.000	0.001
Al	1.456	1.444	1.032
Fe	0.004	0.008	0.013
Mn	0.001	0.001	0.000
Mg	0.000	0.000	0.000
Ca	0.455	0.433	0.030
Na	0.541	0.541	0.232
K	0.008	0.008	0.731
Ni	0.000	0.000	0.000
Total Cation	5.006	4.994	5.002
Or mol. %	0.79	0.82	73.61
Ab	53.88	55.09	23.33
An	45.34	44.09	3.05

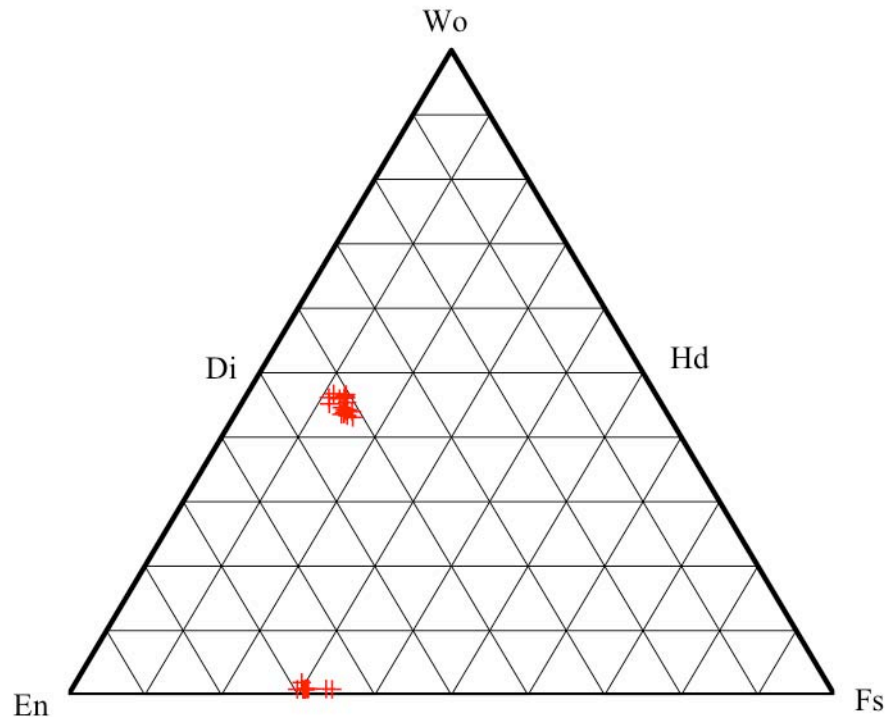
Figure 5.9 Mineral compositions for feldspar in the gabbros found at West Clearwater Lake



The biotite is subhedral to euhedral, usually forming strongly pleochroic dark reddish brown tabular crystals of variable size, 0.1 to 1 mm long. This biotite is slightly altered to chlorite, typically along grain margins. The biotite composition is low in Al (~14% to 15%), it contains a high proportion of TiO_2 (~2.6% to 5.2%), and it has a high magnesium content ($\text{Mg/Fe} \sim 2.5$ to 3, on a 22-anion basis) (Table 5.5).

Green amphibole is clearly pseudomorphic after clinopyroxene, typically only partially developed on clinopyroxene grains. Its composition is that of a Mg-rich hornblende (Table 5.5).

Figure 5.10 Mineral compositions for pyroxene in the gabbro at West Clearwater Lake.



As already stated, alkali feldspar is rare, occurring only in small quantities in samples 1-63-910 and DCW-77-4, where it is typically present either as small anhedral interstitial grains less than 0.1 mm across, or as small blocky inclusions in plagioclase. In sample 1-63-910, alkali feldspar is closely associated with quartz: grains share interstices with quartz, or they contain quartz inclusions. The interstitial alkali feldspar in sample DCW-77-4 is orthoclase ($An_3Ab_{23-22}Or_{75-74}$) (Table 5.5, Figure 5.9).

Like alkali feldspar, quartz occurs in sample 1-63-910 as an anhedral interstitial phase, or as an inclusion in plagioclase. Its grain size varies between 0.1 and 0.5 mm, the smaller grains usually being those included in plagioclase. In other gabbroic samples, I have observed some secondary quartz filling narrow cracks along with hematite and very fine-grained micas.

In the gabbro of drill hole 1-63 at least, the variations in whole-rock composition are mainly due to variations in the relative amounts of the minerals, not to changes in mineralogy. For instance, some of the gabbro samples in drill core 1-63 locally grade into cm- to dm-wide layers of very low plagioclase content. Also, as I mentioned in the description of drill core 1-63, this essentially gabbroic unit is interrupted by narrow (cm- to dm-wide) layers containing some quartz (as in the thin section taken from sample 1-63-910), giving these narrow layers a quartz gabbro mineralogy. However, all these samples, from the surface of the West Clearwater structure down to nearly 400 meters below lake level, alkali feldspar- and quartz-bearing samples included, roughly share the same general texture (i.e. nothing that could be clearly described as a cumulate texture was observed), the same narrow range of pyroxene composition, and a similar range of plagioclase compositions, which leads to the inference that the rock unit is a single body of uniform gabbro.

5.6 Diabase

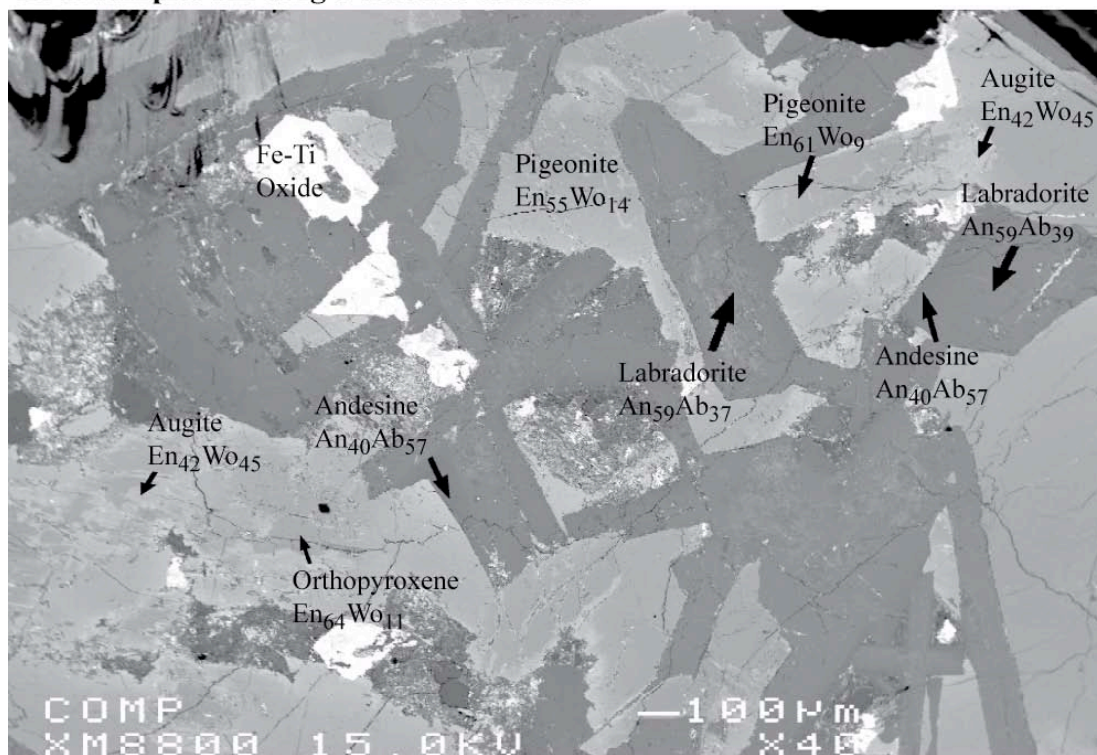
Diabase dykes have been observed in drill holes 3-63, 5-63 and a large fragment of diabasic rocks is embedded in the impact-related lithologies on the northern shore of Lepage Island, the northernmost island of the West Clearwater Lake ring of islands (Figure 1.3).

In drill core 3-63, a diabase layer appears at a depth of about 247 meters. The layer itself is about 9 meters thick. This diabase is dark gray to black, with a greenish hue, massive and fine-grained. The thin section was cut through a region where the rock was severely affected by the impact: it shows a texture similar to that of a breccia, with large lithic fragments surrounded by areas in which fine-grained angular to subangular

lithic fragments and individual mineral clasts are mixed with a dark cryptocrystalline material showing a fluidal texture. There are also abundant fluidal-textured opaque oxides and numerous thin anastomosing veins of pseudotachylite filled with dark aphanitic material. The lithic fragments are composed of plagioclase laths 0.3 to 1 mm long typically showing undulatory extinction, similar in size but less abundant euhedral clinopyroxene and finer-grained opaque oxide phases. Chlorite is plentiful, indicating strong alteration. The very strong alteration and the presence of abundant dark cryptocrystalline material make it difficult to ascertain the original proportion of minerals, but the rock seems originally to have contained at least 50% plagioclase (Figure 5.11).

Figure 5.11 Back-scattered electron images of a polished thin section of a rock sample of a diabase dyke of Proterozoic age. The dyke formed a large body within the fragmental breccia of the northern shore of Lepage island.

Rock samples showing a diabasic texture:



A) Diabase sample DCW-77-6.

Table 5.6 Representative compositions of the minerals found in the diabasic rocks of the West Clearwater Lake Impact Structure.

	DCW-77-6- R1-Plagioclase 6 (Core)	DCW-77-6-R1- Plagioclase 7 (Margin)	DCW-77-6-R1- Px 2 (Orthopyroxene)	DCW-77-6- R1-Px 6 (Augite)	DCW-77-6-R1- Pyroxene 4 (Augite)
SiO ₂ wt. %	52.89	57.52	52.45	52.27	50.23
TiO ₂	0.05	0.04	0.33	0.34	0.32
Cr ₂ O ₃	0.00	0.00	0.00	0.16	0.01
Al ₂ O ₃	28.64	25.76	1.15	1.96	1.54
FeO	0.75	0.71	19.34	7.12	16.71
MnO	0.00	0.02	0.463	0.19	0.50
MgO	0.156	0.04	21.98	17.85	9.44
CaO	12.23	8.26	4.60	19.47	20.87
Na ₂ O	4.47	6.41	0.07	0.22	0.52
K ₂ O	0.26	0.53	0.01	0.00	0.01
NiO	0.00	0.00	0.00	0.00	0.00
Total	99.45	99.29	100.38	99.57	100.14

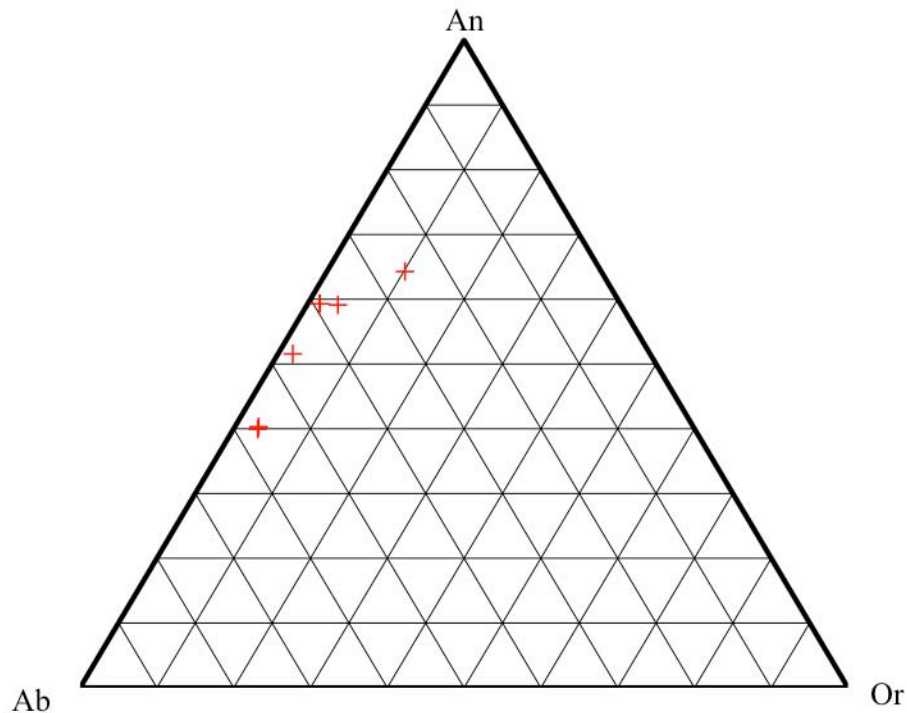
Number of cations on the basis of X (O)

	X = 8	X = 8	X = 6	X = 6	X = 6
Si <i>apfu</i>	2.418	2.604	1.946	1.930	1.944
Ti	0.002	0.001	0.009	0.009	0.009
Cr	0.000	0.000	0.000	0.005	0.000
Al	1.544	1.375	0.050	0.085	0.070
Fe	0.028	0.027	0.600	0.220	0.541
Mn	0.000	0.001	0.015	0.006	0.016
Mg	0.011	0.003	1.215	0.982	0.545
Ca	0.599	0.401	0.183	0.770	0.865
Na	0.396	0.562	0.005	0.016	0.039
K	0.015	0.031	0.000	0.000	0.000
Ni	0.000	0.000	0.000	0.000	0.000
Total Cation	5.014	5.004	4.023	4.024	4.031
Or mol. %	1.52	3.10	En 60.83	49.80	27.92
Ab	39.18	56.58	Fs 30.02	11.14	27.72
An	59.30	40.31	Wo 9.15	39.06	44.36

In drill core 5-63, diabase appears at a depth of 208 meters, and continues down to the end of the core, at a depth of about 220 meters. Therefore, its total thickness is unknown. This rock is similar to the diabase in drill hole 3-63: fine-grained (most grains are ~0.4 mm in size) and dark gray to black with a greenish hue.

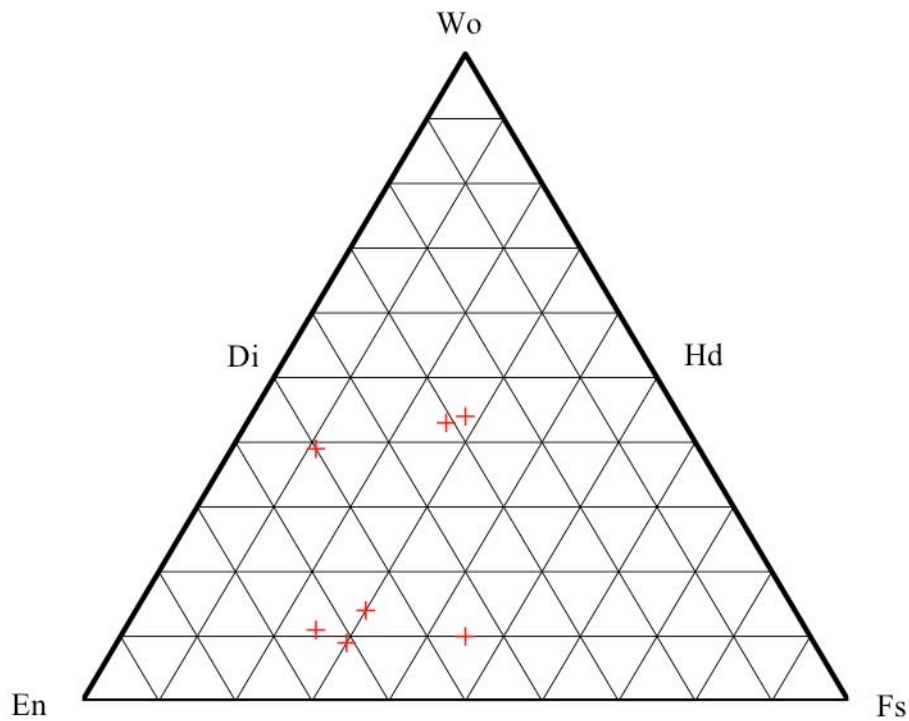
Under the microscope, this diabase is strongly altered: although it is still possible to recognize the original equigranular subophitic texture, plagioclase laths have been entirely converted to white mica, and the pyroxenes are either completely chloritized, or they have been transformed into green amphibole, which is usually, in turn, partially chloritized along its margins. Quartz occurs as small interstitial grains, either along narrow cracks, or as a product of plagioclase alteration.

Figure 5.12 Mineral compositions for feldspar in the diabase found at West Clearwater Lake



Opaque iron oxide is abundant and present either as subhedral to euhedral crystals, or as a fine coating disseminated throughout the rock. I estimate that the rock in this thin section is composed of about 70 to 75% euhedral altered plagioclase, 10 to 15% replaced pyroxene, 7 to 10% opaque oxides, and 3 to 5% quartz. Like the diabasic rocks described above, the diabase enclosed in the impact-related lithologies on the northern shore of Lepage Island also is altered, albeit not as severely. The rock is massive, dark gray to black, with a greenish hue, medium grained and equigranular.

Figure 5.13 Mineral compositions for pyroxene in the diabase at West Clearwater Lake.



It has a subophitic texture, with euhedral laths of plagioclase 1 to 2 mm long, and large subhedral grains of pyroxene about 2 mm wide. Smaller, finer-grained (~0.3 mm in size) euhedral to subhedral opaque oxide phases are quite common. Plagioclase cores are

commonly altered to a very fine-grained birefringent mineral, probably white mica. There are very fine-grained rusty, reddish deposits on the surface of pyroxene grains. I estimate that the thin section is composed of about 20 to 25% pyroxene, 40 to 50% plagioclase and 20 to 25% opaque phases (Figure 5.11). Microprobe analyses indicate that the plagioclase is zoned, from labradorite in the core ($\text{An}_{59-52}\text{Ab}_{47-39}\text{Or}_{2-1}$) to andesine at the margin ($\text{An}_{40}\text{Ab}_{57}\text{Or}_3$). The main pyroxene in the diabase must initially have been an orthopyroxene, but slow cooling of the rock produced abundant irregular patches of augite exsolution, a feature that, because of alteration, was not obvious from microscope observations. Augite compositions have a range of $\text{En}_{50-28}\text{Fs}_{28-11}\text{Wo}_{44-39}$, whereas the orthopyroxene compositions have a range of $\text{En}_{61-55}\text{Fs}_{30}\text{Wo}_{14-9}$, without any apparent regular zoning inside individual grains (Table 5.6 and Figure 5.13).

5.7 Comparison of the lithologies described in Simard et al. (2004) with those described in this study

Now that I have presented descriptions of the rocks beneath the West Clearwater Lake impact structure, it would be informative to compare my units to those described in Simard et al. (2004). As already mentioned, Simard et al. (2004) described geographically extensive units showing a large range of chemical compositions and mineral contents without providing any mineral compositions, or even photos, of the rocks. Furthermore, a large number of the rocks, particularly those collected at or near the surface of the impact structure, are severely fractured and pervasively altered. In addition, some of the data I present in Chapter 5, such as the volume % of the mineral in the rocks and the textures observed, are rough estimates and clearly preliminary. Therefore, with the information I have, it seems impossible to establish an unambiguous correspondence between the rocks I observed and the lithologies described by Simard et

al. (2004). Nevertheless, I will attempt to do so, and I will briefly mention the points of disagreement.

A comparison of Table 2.1 in Chapter 2 with Table 5.1 in Chapter 5 shows that the composition of the granitic rocks reported here agrees reasonably well with those of Simard et al. (2004) for granites and granodiorites of the Desbergères Suite: average compositions are close, and the ranges of compositions observed are similar. However, according to Simard et al. (2004), plagioclase is the dominant feldspar (30-65%) in the granites and granodiorites of the Desbergères Suite, with alkali feldspar representing 10-35%, which is almost the reverse of the proportions I have observed in the granites of the Clearwater Lake impact structure (I estimate 30-50% alkali feldspar and 10-25% plagioclase). Estimated quartz and biotite proportions agree (see Table 5.7).

According to the compositions provided by Simard et al. (2004) (see Figure 2.1 and Table 2.1), the SiO₂ content of the rocks I classified as granodiorites, enderbites and tonalites is lower than the range of SiO₂ content in the Loups Marins Complex granodiorites. Nonetheless, the whole-rock chemical composition of my rocks falls within the range of compositions of the enderbites and tonalites of the Loups Marins Complex. Simard et al. (2004) reported that the rocks of the Loup Marins Complex are mostly fine and medium grained, and only the porphyritic granodiorites are coarse grained. What I have interpreted as an inequigranular texture could be called a porphyritic texture by others but, as indicated by my whole-rock compositions, none of the “porphyritic” rocks seem to be granodioritic.

For the most part, the mineralogy of my granodiorites, enderbites and tonalites roughly agrees with that of the rocks of the Loups Marins Complex, with one exception: Simard et al. (2004) mapped a geographically extensive enderbitic unit with a

granoblastic texture containing 1 to 5% orthopyroxene (see the geological map of West Clearwater Lake region presented in chapter 2) in the vicinity of the Clearwater Lake impact structure, but I have not observed any granoblastic rock containing orthopyroxene. Sample DCW-77-3 may contain about 2% orthopyroxene, but this rock is very fractured and altered, which could possibly conceal the granoblastic texture. As confirmed by the microprobe analyses, I detected only augite.

The rocks of the Qullinaaraaluk Suite comprise gabbro, hornblendite and pyroxenite showing a large range of compositions. Simard et al. (2004) did not study this unit in detail. Both the whole-rock compositions and the mineralogy of the gabbros I have observed in the basement of the West Clearwater Lake impact structure roughly agree with the descriptions and compositions of the mafic rocks reported by Simard et al. (2004). This is not surprising, as these rocks are, for the most part, “generic” gabbros. However, Simard et al. (2004) noted the presence of cumulate textures in their ultramafic units, whereas I did not observe such textures in my high-Mg rocks. Also, coarse-grained (1 to 3 cm across) hornblende phenocrysts are common (5-15%) in some of the gabbroic units of the Qullinaaraaluk Suite, but they are absent in the gabbros in my area.

It should be noted, as already mentioned, that most of my gabbro samples come from drill core 1-63, which goes through the central uplift region of the West Clearwater impact structure, where rocks from a depth of about 3 km below the pre-impact surface have been pushed up by the collapse of the crater and the accompanying rebound of the crater floor (see Section 3.1.3). All the mafic intrusions studied by Simard et al. (2004) are surface samples. It is therefore unclear if my mafic units correspond to any of those briefly described by Simard et al. (2004)

Table 5.7 – Comparison between the main lithologies described by Simard et al. (2004) in the Clearwater Lakes region and the lithologies observed in the basement of the West Clearwater Lake impact structure.

Simard et al. (2004):

Units	Characteristics	Mineralogy	Remarks
<i>Desbergères Suite:</i> Granites and granodiorites	Pale pink to greyish pink, medium to coarse-grained, poorly developed foliation.	30-65% plagioclase, 20-30% quartz, 10-35% K-spar, 2-10% biotite, accessory minerals: zircon and hornblende.	Presence in some units of 15-35% porphyritic K-spar crystals 1 to 5 cm across. Pervasive feldspar alteration.
<i>Loups Marins Complex:</i> Enderbites, granodiorites and tonalites	Greenish or brownish tint, also pinkish (granodiorites), massive to weakly foliated, mostly fine to medium grained, granodiorites can be coarse-grained. Enderbites are granoblastic.	Enderbites: 55-80% plagioclase, 2-35% quartz, 1-15% biotite, 1-10% cpx, 1-5% opx, 1-3% anhedral magnetite. Granodiorites: similar to enderbites but with 10-25% K-spar phenocrysts and no opx.	In dioritic units: 10-25% K-spar phenocrysts 1 to 5 cm across. Pervasive feldspar alteration.
<i>Qullinarvaluk Suite:</i> Gabbro, gabbro-norite, hornblende, pyroxenite	Dark green to black, medium to coarse grained, phenocrysts give spotted appearance; ultramafic rocks show cumulate-like textures.	30-70% plagioclase, the rest is biotite, pyroxenes (opx+cpx) and up to 3% magnetite.	5-15% coarse-grained (1 to 3 cm across) hornblende phenocrysts giving rocks a spotted appearance, Gabbros are partly granoblastic

This study:

Units	Characteristics	Mineralogy	Remarks
Granitic rocks	Pinkish grey to reddish, medium-grained (~1 to 3 mm), hypidiomorphic, equigranular, usually massive but some slightly foliated.	30-50% subhedral to anhedral K-spar 20-30% anhedral quartz 10-25% subhedral to anhedral plagioclase <1-5% subhedral dark biotite Accessory minerals: apatite, zircon, altered magnetite and ilmenite, some green amphibole (up to 1%).	Pervasive feldspar alteration, micas are strongly chloritized.
Granodioritic, enderbite and tonalitic rocks	Grey with reddish hues on fresh surfaces, massive, generally medium to coarse grained, inequigranular, grain size varies gradationally (0.1 to 7 mm across).	50-70% anhedral plagioclase 20-30% anhedral quartz 0-10% anhedral K-spar 1-3% biotite, 2-5% cpx, 3-10% opaque oxides Accessory minerals: apatite	Blocky antiperthitic growths within coarse-grained plagioclase, micas and pyroxenes are typically altered to chlorite.
Mafic rocks with a gabbroic composition	Dark grey, holocrystalline, fine to medium grained (0.5 to 1 mm), equigranular, some with mafic phenocrysts.	20-70% anhedral to subhedral plagioclase 20-70% subhedral pyroxenes (cpx + opx) 5-10% subhedral to euhedral biotite 1-3% opaque oxides. Accessory minerals: euhedral apatite; some secondary green amphibole.	Some of these rocks show a well developed granoblastic texture.

Chapter 6: Fragmental Breccia, Infiltration Dykes and Glass Spheroids

As already mentioned in section 2.1.4 of Chapter 2, the impact-related rocks of Pennsylvanian age can be divided into three major successive impactite units, which are, in ascending order: *fragmental breccia* (also called allochthonous breccia by Grieve, 2006), *clast-rich melt* (also called impact-ignimbrite) and the *clast-poor melt* (also called impactite). A minor unit was briefly mentioned by Phinney et al. (1978) and clearly identified by Rondot et al. (1993) and Plante et al. (1990): this unit consists of narrow melt-filled dykes intruding the fragmental breccia and the crater basement, and it was therefore named by them *infiltration dykes*. The fragmental breccia and the infiltration dykes, the two lowermost units of the West Clearwater Lake impact structure, will be discussed in this chapter, whereas the clast-poor and clast-rich impact melt rocks are the subject of chapter 7. Chapter 6 will also cover a peculiar texture found in both the fragmental breccia and the infiltration dykes, the so-called “glass spheroids”, first described by Dence et al. (1974).

6.1 The impact-related lithologies of the West Clearwater Lake impact structure

The designations “fragmental breccia”, “clast-rich melt rock” and “clast-poor melt rock” are those used by Simonds *et al.* (1978) and Phinney *et al.* (1978), whereas impact-ignimbrite and impactite are used in Rondot *et al.* (1993). Although the terminology of Rondot *et al.* is more technical, I prefer to conform to that of Simonds *et al.* (1978) and Phinney *et al.* (1978), which I find clearer and more informative.

According to Phinney et al. (1978), the combined impact-related units reach a maximum thickness of about 116 m on Drillers island, in the eastern part of the impact structure. The entire sequence (fragmental breccia, clast-rich melt rock and clast-poor melt rock) mantles the fractured basement, following its relief.

Crater fillings consisting of basal units of clast-rich impact melt rock underlying relatively clast-poor impact melt units have been observed at other complex impact craters. Two well-studied Canadian examples are the Manicouagan impact structure in Quebec (Floran et al., 1978) and the Mistastin Lake impact structure in Labrador (Grieve, 1975; Marion and Sylvester, 2010). It has been proposed (Grieve, 2006) that this layering is created when the leading edge of the impact melt was driven down and out at high velocity into the expanding crater cavity, eroding and incorporating rock debris from the transient cavity floor and walls in the process. This process cools and slows the leading edge of the impact melt, and considerably increases its viscosity. The trailing impact melt, which has a lower clast content and a higher temperature (and consequently a lower viscosity), overrides the slower, clast-burdened leading edge of the impact melt, thus overlying it and infiltrating it here and there downward into the underlying fractured basement rock (Grieve, 2006). This, presumably, is the origin of the infiltration dykes described by Rondot et al. (1993) and Plante et al. (1990). After the whole system comes to rest, the higher temperature of the trailing clast-poor impact melt favours the assimilation of the clastic debris and reaction with the melt. Clastic debris that have been affected by shock metamorphism are particularly susceptible to reaction and assimilation by the impact melt (Grieve, 2006).

Several chemical analyses of all the impact melt units in the West Clearwater Lake impact structure were performed by Simonds et al. (1978) but, unfortunately, only a

table with an average impact melt composition and a AFM diagram are presented in their article. However, the reports of Bostock (1969), Hische (1995) and Dence et al. (1974) contain analytical data.

Table 6.1 presents average major-element compositions of the impact lithologies at West Clearwater obtained in previous studies, whereas Tables 6.2 and 6.3 show the average major- and trace-element composition, and the range of compositions, of impact lithologies at West Clearwater obtained in this study. Bulk chemical data were acquired using the facilities at the Trace Element Analysis Laboratories (TEAL), at the

Table 6.1 Average major-element composition of impact lithologies at West Clearwater obtained in previous studies. Sources: (1) Bostock (1969), (2) Simonds et al. (1978), (3) Hische (1995), (4) Dence et al. (1974).

Rock Unit	Clast-rich impact melt rock ⁽¹⁾	Clast-poor impact melt rock ⁽¹⁾	Average impact melt rock ⁽¹⁾	Average impact melt rock ⁽²⁾		Average impact melt rock ⁽³⁾	Matrix glass ⁽⁴⁾	
n	5	6	11	84		7		
				average	1 σ		Fresh	Altered
SiO ₂ (%)	59.6	60.4	60.0	59.09	2.64	62.2	57.90	46.14
TiO ₂	0.9	0.7	0.8	0.97	0.60	0.7	0.56	0.61
Al ₂ O ₃	16.2	15.9	16.1	16.15	1.56	15.7	15.33	15.28
Cr ₂ O ₃	---	---	---	0.15	0.8	---	---	---
Fe ₂ O ₃	3.7	4.1	3.9	---	---	5.2**	2.94	6.10
FeO	0.7	1.2	1.0	5.22*	1.49	---	2.31	<0.01
MnO	0.08	0.05	0.07	0.20	0.09	0.06	0.07	0.08
MgO	2.5	2.7	2.6	2.77	0.78	2.8	3.14	8.22
CaO	4.6	4.5	4.6	3.70	1.07	4.3	4.55	2.99
Na ₂ O	4.2	3.8	4.0	3.90	0.87	3.9	3.51	0.27
K ₂ O	3.2	3.6	3.4	4.08	0.79	3.4	3.56	0.58
P ₂ O ₅	---	---	---	0.29	0.08	---	0.27	0.29
H ₂ O	1.4	1.3	1.4	1.58	0.68	0.8	4.63 ⁺	11.00 ⁺
Total	97.1	98.3	97.9	98.10		99.0	100.03	99.39

* Total iron as FeO. ** Total iron as Fe₂O₃. ⁺ H₂O+

Department of Earth and Planetary Sciences, McGill University. Major oxide and trace-element concentration were measured using X-ray fluorescence (XRF) analysis conducted with a Philips PW2440 4kW X-ray fluorescence spectrometer system with a PW2540 VRC 168 sample autochanger. All the chemical data obtained with XRF are given in Appendices A and B., at the end of this thesis.

All of these units have essentially the same chemical composition, with a few subtle differences: compared to the other lithological units of the West Clearwater Lake impact structure, fragmental breccia samples have, on average, a higher MgO content (about 4% for the fragmental breccia versus 2.7-3% for the other units), a lower CaO content (about 3.5% for the fragmental breccia versus about 4.5% for the other units) and their volatile content (the material lost on ignition, which I assume is mostly H₂O) is greater (about 3.5% for the fragmental breccia versus about 1.5% for the other units). These differences are consistent with the greater degree of alteration of the fragmental breccia.

According to the analytical results presented here, there is no apparent enrichment in nickel, a siderophile trace element, in the impact melt rocks at West Clearwater. This finding confirms the findings of Palme et al. (1979), who detected a siderophile enrichment in the impact melt of the *East* Clearwater lake impact structure, but found no indications of a similar enrichment in the impact melt of the *West* Clearwater Lake structure. Nickel levels in my samples range from 22 to 63 ppm (see Table 6.3), whereas average Ni levels in the samples of impact melt rock from the East Clearwater Lake crater studied by Palme et al. (1979) are 663 ppm, with some samples as high as 1070 ppm.

Table 6.2 - Average major-element composition, and minimum-maximum range of compositions, of impact lithologies at West Clearwater obtained by the author.

Rock Unit	Clast-rich impact melt rock		Clast-poor impact melt rock		Average impact melt rock		Fragmental breccia matrix		Infiltration dykes	
n	14		32		46		13		5	
	aver.	max.-min.	aver.	max.-min.	aver.	max.-min.	aver.	max.-min.	aver.	max.-min.
SiO ₂ (%)	60.65	62.96-58.09	61.01	61.64-59.96	60.90	62.96-58.09	59.42	62.68-51.74	59.56	61.23-58.80
TiO ₂	0.77	1.09-0.61	0.77	0.85-0.66	0.77	1.09-0.61	0.72	1.25-0.54	0.80	0.90-0.72
Al ₂ O ₃	16.09	17.27-14.95	15.77	16.23-15.08	15.87	17.27-14.95	15.47	16.21-14.25	16.42	17.30-15.37
Cr ₂ O ₃	0.01	0.02-0.01	0.01	0.02-0.01	0.01	0.02-0.01	0.01	0.03-0.01	0.01	0.02-0.01
Fe ₂ O ₃	6.19**	7.87-5.09	6.16**	6.88-5.60	6.17**	7.87-5.09	6.65**	10.26-4.69	6.36**	7.00-5.64
FeO	---	---	---	---	---	---	---	---	---	---
MnO	0.06	0.10-0.03	0.06	0.15-0.04	0.06	0.15-0.03	0.08	0.17-0.03	0.07	0.09-0.06
MgO	2.79	4.20-2.28	2.73	3.12-2.33	2.75	4.20-2.28	4.06	9.03-2.21	3.03	4.04-2.22
CaO	4.22	6.61-3.02	4.56	5.03-3.82	4.46	6.61-3.02	3.49	4.64-1.97	4.53	5.12-3.65
Na ₂ O	3.84	4.30-3.49	3.73	3.92-3.60	3.76	4.30-3.49	3.43	4.03-2.46	3.98	4.13-3.64
K ₂ O	3.42	4.31-2.88	3.53	4.02-3.11	3.50	4.31-2.88	2.97	5.70-1.35	3.30	4.84-2.57
P ₂ O ₅	0.31	0.49-0.22	0.30	0.35-0.25	0.30	0.49-0.22	0.28	0.63-0.17	0.32	0.38-0.28
L.O.I.	1.69	2.78-1.03	1.49	2.12-0.89	1.55	2.78-0.89	3.48	6.43-1.26	1.84	2.84-0.99
Total	100.19	100.42-99.93	100.26	100.63-99.79	100.24	100.63-99.79	100.19	100.92-99.74	100.37	100.56-99.94

** Total iron as Fe₂O₃. L.O.I. – Loss On Ignition**Table 6.3** - Average abundances, and minimum-maximum ranges, of trace elements of impact lithologies at West Clearwater obtained by the author.

Rock Unit	Clast-rich impact melt rock		Clast-poor impact melt rock		Average impact melt rock		Fragmental breccia		Infiltration dykes	
n	21		32		53		6		5	
	aver.	max.-min.	aver.	max.-min.	aver.	max.-min.	aver.	min.-max.	aver.	max.-min.
Ba (ppm)	1199	1555-872	1186	1357-1105	1191	1555-872	844	1256-410	1181	1460-1081
Ce	73	160-28	74	102-38	74	160-28	54	83-27	93	152-68
Co	11	18-<d/l	11	18-<d/l	11	18-<d/l	22	37-16	17	30-10
Cu	33	73-20	33	78-14	33	78-14	59	123-72	30	38-19
Ni	32	63-22	32	41-26	32	63-22	42	65-27	39	39-27
Sc	2	12-<d/l	1	13-<d/l	1	13-<d/l	4	13-<d/l	3	13-<d/l
V	92	141-73	93	105-85	93	141-73	105	147-77	102	111-94
Zn	14	44-<d/l	17	63-4	16	63--<d/l	38	80-<d/l	30	43-10

Finally, I wish to express a caveat: for logistical reasons, I was unfortunately only able to visit the impact crater for about six consecutive hours in 2002, when I was preparing a master's thesis on the contact metamorphism of large Paleozoic clasts of limestone caught in the impact melt (Rosa, 2004). Therefore, nearly all field observations reported in the following sections are summaries of published articles on the West Clearwater Lake impact structure, augmented by the observations of Michael Dence (pers. commun.). There are a number of features described in these articles that I wish I could have seen for myself, but alas, I am entirely dependent on the interpretation of the field workers who described them, and I must rely on their judgement.

6.2 Fragmental breccia

The term “fragmental breccia” is used in Simonds et al. (1978) and Phinney et al. (1978), and other reports on the West Clearwater Lake impact structure. Because of this, I am conforming to its use. However, according to the terminology proposed by Stöffler and Grieve (2003), the term fragmental breccia should be abandoned and replaced by either allochthonous breccia or lithic breccia.

The fragmental breccia is an allochthonous breccia located immediately below the clast-rich melt unit and above the Precambrian basement rocks, usually forming a steep talus at the bottom of cliffs. This unit is typically less than 5 meters thick, but attains 20 to 30 meters in some places, and is absent in others (Grieve, 2006; Rondot et al., 1993; Simonds et al., 1978b). The fragmental breccia typically mantles the underlying fractured basement, the relief usually being greater than its thickness. Its absence in some places is attributed by Grieve (2006) to scouring by outflowing impact melt. Such

erosion of basal breccia by outwardly moving impact melt has also been proposed for other impact structures (Simonds and Kieffer, 1993).

The fragmental breccia is a friable reddish rock mostly composed (over 50%) of an assortment of clasts that include mineral and lithic fragments from the basement rocks, glass fragments containing numerous inclusions, devitrified glass, cryptocrystalline impact-melt rock and various breccias. In an article published in 1974, Dence et al. (1974) mentioned that some glass samples of the fragmental breccia contain tiny glass spheroids 10 to 500 μm across. They interpreted these glass spheroids as indications of “fluid immiscibility” that took place during the earliest stages of impact melt formation. I have also observed small glass globules that closely resemble Dence’s glass spheroids within confirmed samples of fragmental breccia, infiltrating impact melt (see section 6.2 on infiltration dykes) and within two samples that I believe are, for textural reasons, probably fragmental breccia, but for which I do not have an exact location (samples DCW-77-64 and DCW-77-65). These features are described in detail in section 6.3 of this chapter.

According to Phinney et al. (1978), 50% of the rock and mineral fragments in the fragmental breccia are coarser than 1 mm, between 20 and 40% have sizes that are in the 1 cm to 1 m range, and at least 1% of these fragments are larger than 1 m across (up to 10 m in some places). Details of the distribution in size of clasts are given in Phinney et al. (1978). On the whole, the breccia appears to be massive, but well-developed flow foliations are visible around some of the larger lithic fragments (Simonds *et al.* 1978).

The overlying clast-rich melt rock can be distinguished from the fragmental breccia by its greater coherency, the presence of prominent columnar joints, and by a smaller amount of large clasts [according to Simonds et al. (1978), less than 20% of the

clasts in the clast-rich rock are over 1 millimeter across]. Conversely, the fragmental breccia is distinguished from the underlying fractured basement rock by the presence of a rust-red clay-like matrix that composes less than 20% of the unit.

The contact between the fragmental breccia and the overlying clast-rich impact melt is described by Simonds et al. (1978) as being a sharp, chilled margin. The location of the lower contact of this unit with the underlying fractured basement is less obvious: in the field, the bottom of the fragmental breccia is usually covered by a talus (Simonds et al. 1978); also, core samples from depths that should correspond to the contact between basement rock and fragmental breccia are very fractured, with meter-long sections missing. The surviving core sections in hole 4-63 suggest that the contact is gradual, with an increase in clast abundance and a decrease in matrix with depth. Nevertheless, because of absent sections and the small diameter of the drill-core samples, it is difficult to ascertain if rock in the vicinity of the putative contact belongs to the fragmented basement, or if the core section was drilled through a clast still in the fragmental breccia.

I have obtained eight samples that I have classified as fragmental breccia. Two of these samples (DCW-77-64 and DCW-77-65) were cut into several pieces, which were analyzed separately. A suffix designation was added to these extra cuts: for instance, sample DCW-77-65-4 is the fourth cut of sample DCW-77-65. Tables 6.4 and 6.5 provide major- and trace-element compositions that are typical of this unit. Figure 6.1 shows graphs of compositional variation in samples of fragmental breccia matrix.

Six of these samples are indubitably from the fragmental breccia, whereas the exact location of two samples is not quite as well constrained. Four of these samples are from the upper sections of the core drilled in 1963-1964 (see Chapter 4) by M.R. Dence

Table 6.4 – Major-element compositions of selected samples of fragmental breccia from West Clearwater.

Rock Unit						Average impact melt rock	
Sample	LP-12	1-63-125	4-63-214	DCW-77-64	DCW-77-65-4	n = 46	
						aver.	max.-min.
SiO ₂ (%)	59.93	52.24	59.65	61.17	60.75	60.90	62.96-58.09
TiO ₂	0.64	1.25	0.54	0.87	0.58	0.77	1.09-0.61
Al ₂ O ₃	15.63	16.18	14.25	15.70	15.24	15.87	17.27-14.95
Cr ₂ O ₃	0.01	0.01	0.02	0.01	0.02	0.01	0.02-0.01
Fe ₂ O ₃	6.30*	9.97*	6.79*	6.66*	5.71*	6.17*	7.87-5.09
FeO	---	---	---	---	---	---	---
MnO	0.07	0.17	0.11	0.06	0.07	0.06	0.15-0.03
MgO	3.57	5.29	6.13	2.66	3.22	2.75	4.20-2.28
CaO	4.12	4.64	2.07	3.72	4.01	4.46	6.61-3.02
Na ₂ O	3.44	4.03	3.62	3.76	3.07	3.76	4.30-3.49
K ₂ O	2.46	1.90	2.08	3.86	2.00	3.50	4.31-2.88
P ₂ O ₅	0.27	0.63	0.17	0.34	0.22	0.30	0.49-0.22
L.O.I.	4.08	4.47	4.71	1.26	4.85	1.55	2.78-0.89
Total	100.63	100.92	100.22	100.20	99.85	100.24	100.63-99.79

* Total iron as Fe₂O₃. L.O.I. – Lost On Ignition**Table 6.5** – Trace-element abundances in chosen fragmental breccia samples from West Clearwater.

Rock Unit						Average impact melt rock	
Sample	LP-12	1-63-125	4-63-214	DCW-77-64	DCW-77-65-4	n = 53	
						aver.	max.-min.
Ba (ppm)	905	891	650	1153	961	1191	1555-872
Ce	70	83	27	89	41	74	160-28
Co	19	22	20	12	15	11	18-<d/l
Cu	37	72	54	26	31	33	78-14
Ni	43	40	45	24	39	32	63-22
Sc	<d/l	11	<d/l	<d/l	12	1	13-<d/l
V	96	147	86	102	80	93	141-73
Zn	3	78	60	<d/l	38	16	63-<d/l

at West Clearwater Lake (samples 1-63-125, 4-63-214, 4A-63-195 and 5-63-124). Two samples of fragmental breccia have been obtained by Langis Plante, of Université Laval. The two Plante samples are LP-24, which was collected on the northeastern shore of Lepage Island, a large island to the north of the West Clearwater Lake ring of islands, and LP-12, which comes from the southwestern shore of Drillers Island, the large island that occupies the eastern area of the ring of islands. As mentioned above, samples DCW-77-64 and DCW-77-65, which are surface samples collected by M.R. Dence in 1977, probably belong to the fragmental breccia: DCW-77-64 was collected on the southern shore of the third Tadpole Island (a group of four islands roughly to the northwest of the West Clearwater lake ring of islands, the island is third counting from the south); DCW-77-65 was collected on the southwestern shore of Drillers Island. Although I know their approximate location, their exact emplacements relative to the impact units are uncertain. Nevertheless, because of their textural similarity to other confirmed samples of fragmental breccia, I am assuming that these two samples are fragmental breccia as well.

I tried to collect as much matrix as possible when I prepared the samples for whole-rock chemical analysis. Similarly, when cutting these thin sections, I tried to maximize the amount of matrix present on the section. In spite of this, the first feature one notices is the large number of clasts of varying size, ranging from large lithic fragments several mm across down to clasts that are nearly invisible under the microscope. Naturally, in the thin sections, the percentage of clasts versus matrix is very variable, going from 95% or more in LP-24 down to 30-40% in 5-63-124; most thin sections, however, contain more matrix than clasts. Typically, the clasts are angular to subangular (see Figure 6.2 A), and they do not appear to have reacted with the enveloping matrix: reaction rims and The exception is sample 5-63-124, where lithic

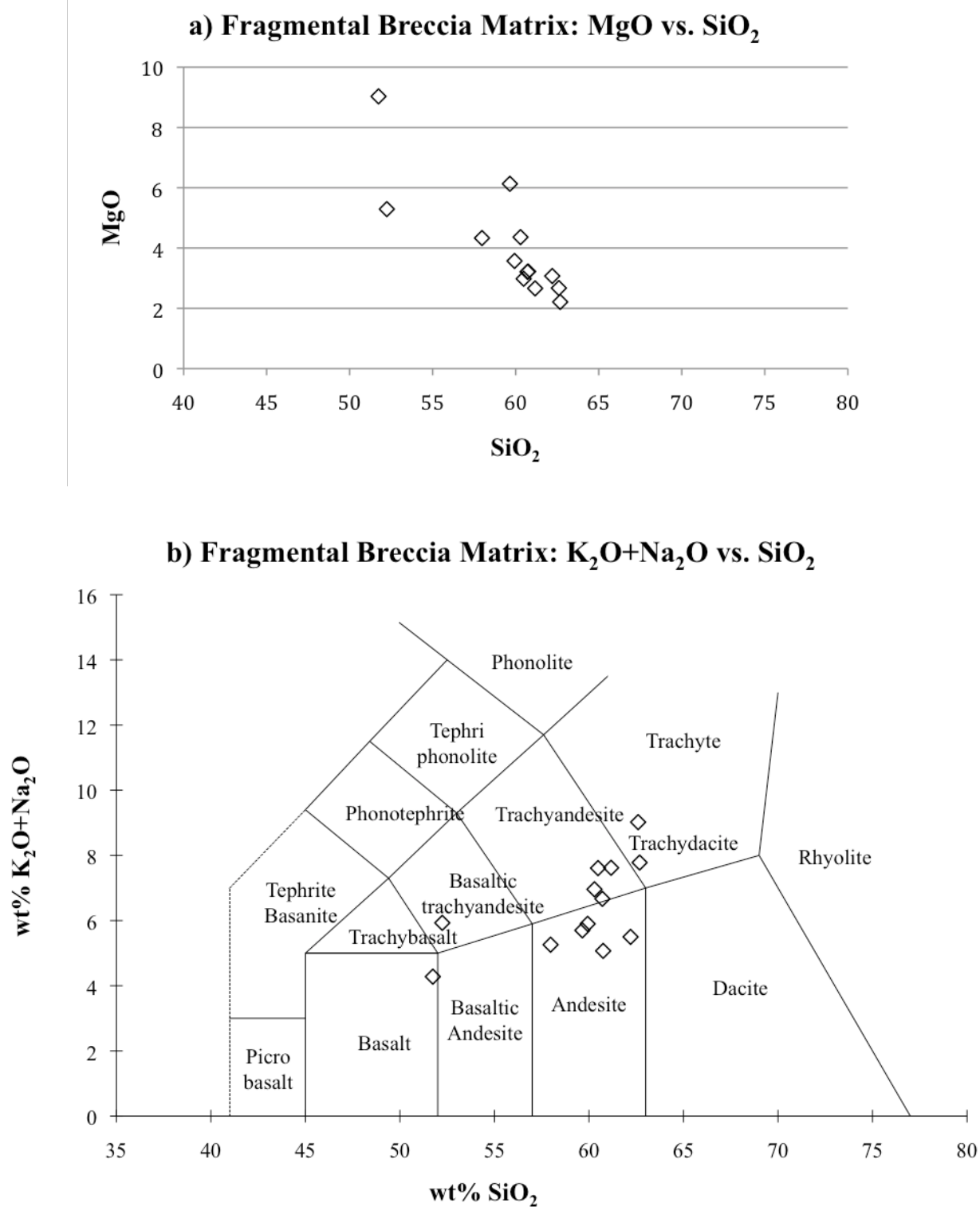


Figure 6.1 a and b Compositional variation in samples of fragmental breccia matrix from the West Clearwater Lake impact structure (n=13).

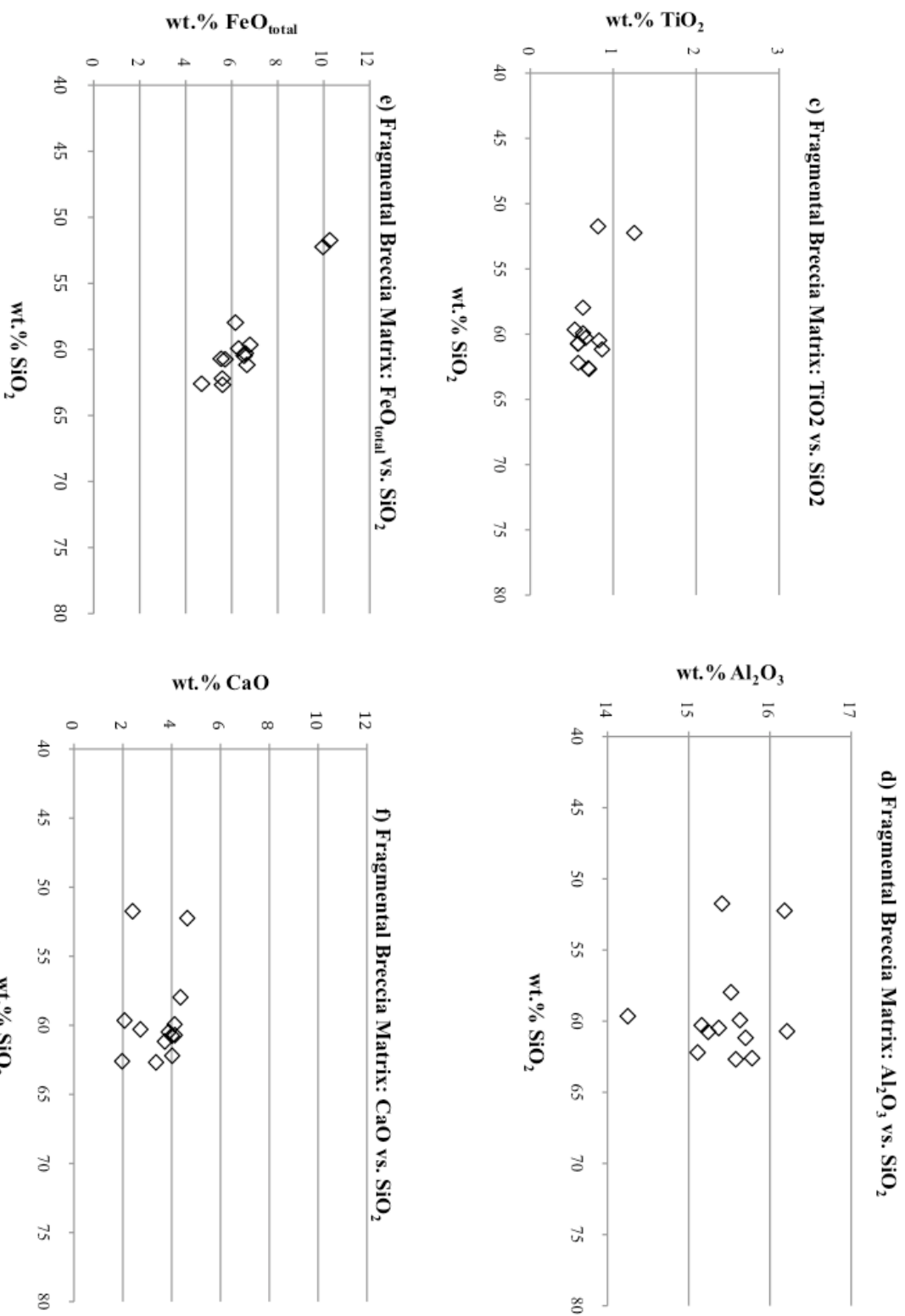


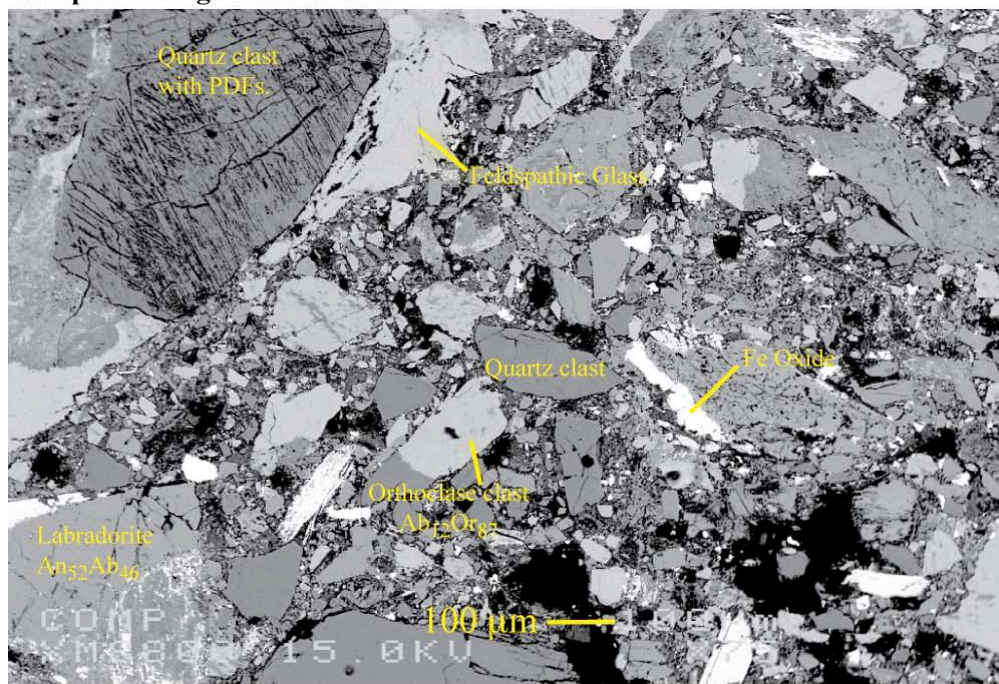
Figure 6.1 c to f – Compositional variation in samples of fragmental breccia matrix from the West Clearwater Lake impact structure (n=13).

fragments look partially melted and deformed. “Granitic” compositions predominate amongst the larger lithic fragments: they mostly consist of feldspars typically altered to white mica and quartz. Quartz in single-crystal fragments is the most common mineral in the clast population. Some of these quartz crystals display planar deformation features. Other common mineral fragments are plagioclase, alkali feldspar, biotite (which is common in sample LP-24, where it forms ~2% of the clasts) and opaque oxides. I have also observed fragments of pyroxene and at least one small clast in sample 4-63-214 that could be a carbonate.

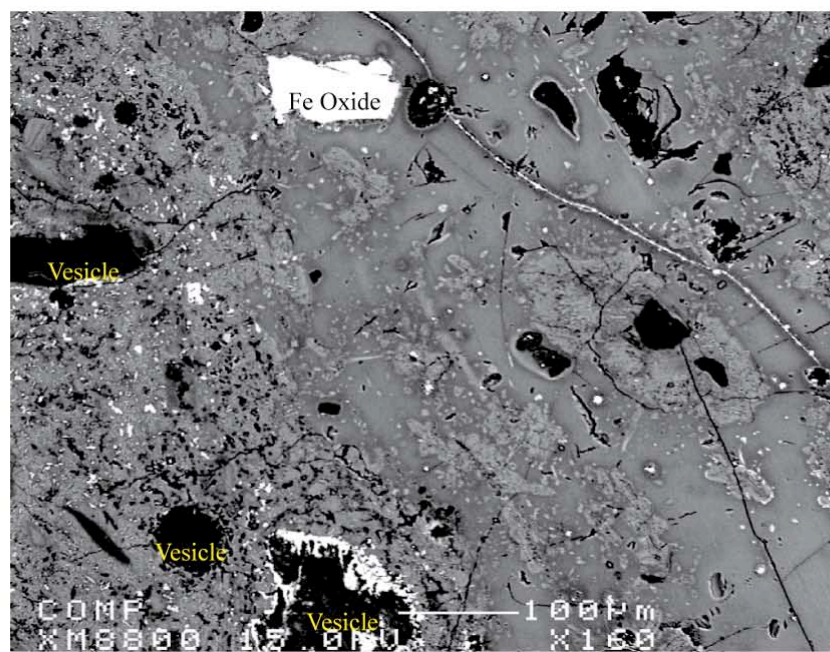
The matrix in samples 5-63-124 and 4-63-214 is stained dark brown to rust-red by hematite, and is nearly cryptocrystalline. At high magnification, the matrix of these samples appears patchy, with tiny very dark globular grains in a lighter grainy groundmass; these are probably tiny hematite grains embedded in partially altered glass. In sample 5-63-124, the matrix surrounding large clasts looks both darker and smoother, possibly finer-grained, whereas sample 4-63-214 has finer-grained areas (the largest is about 3 mm across) that are quite dark in plane light and contain fewer clasts. The matrix of sample 1-63-125 is composed of dark brown areas and lighter-coloured greenish areas. Some of the darker brown areas show fluidal textures, and they are either cryptocrystalline or glassy. In contrast, the greenish areas contain a great number of very fine-grained fragments. The matrix in these samples is mostly a mixture of very fine-grained mineral clasts and glass that has been partially or completely altered by hydrothermal activity. Sample LP-12, however, looks comparatively fresh: its matrix is composed of clear glassy material, some of it slightly coloured in red, but all of it isotropic, or nearly isotropic, under crossed polars. Similarly, the matrix of

Figure 6.2 A and B Two samples of fragmental breccia exemplifying the textures typical of this unit: image A is from an area of thin section LP-94 that is particularly rich in angular clasts. Note the near-absence of matrix glass melt, and the presence of numerous planar deformation features in a quartz clast at the upper left. In contrast, image B shows a section of glass matrix of thin section DCW-77-64-5 where clasts are nearly absent.

Samples of fragmental breccia:



A) Back-scattered electron image of a polished thin-section of sample LP-24.



B) Back-scattered electron image of a polished thin section of sample DCW-77-64-5.

sample 4A-63-195 is glassy, light-coloured, nearly transparent in plane light, and it contains numerous tiny opaque granules. Inclusions of mineral and rock fragments of a large range of sizes and at different stages of shock metamorphism in a fine-grained altered-looking matrix give an overall impression of heterogeneity and general disorder in these rocks. The glass matrix itself contains many small schlieren that display a range of indices of refraction and textures, melts consisting of fused quartz (i.e. lechatelierite), and some sections show very fine microlites of pyroxene and feldspar indicating incipient but arrested crystallization. Much of the glass is altered to rust-red, brownish and yellowish clays. Nevertheless, many samples show glass that is still relatively unaltered, fresh-looking and black (i.e. obsidian), which is, considering the Carboniferous age of these rocks, somewhat surprising!

According to Rondot et al. (1993), the fragmental breccia is criss-crossed by veins (in the centimeter to decimeter range) of a polymictic impact breccia called “mylolisthénite”, defined by them as a kind of mylonite formed by violent fracturing and moving of the impacted country-rock in several directions during the cratering event. It should be noted that the basement is also criss-crossed by numerous mm- to cm-wide pseudotachylite veins (dyke-like mylonite formed by frictional melting) showing a variety of colors, from very dark, nearly black to dark green to dark brownish red. According to Rondot et al. (1993), “mylolisthénite” veins can be distinguished from these veins of pseudotachylite by their lighter colour and the absence of a dark-coloured glassy groundmass. Also, pseudotachylite veins are present all through the cores, from near the surface to deep below the surface of the impact structure, whereas the “mylolisthénite” veins are supposedly only present in the fragmental breccia, that is, near the surface. I have not observed anything in the drill-core samples that unambiguously

conforms to their description of “mylolisthénite”. Because “mylolisthénite” is not a term commonly used by geologists working in impact structures, and because, according to Rondot et al. (1993), “mylolisthénite” veins have the same origin as impact pseudotachylite, I decided to ignore Rondot’s “mylolisthénite” and describe these kinds of features under the general name *impact-generated pseudotachylite*, that is, a dyke-like breccia formed by frictional melting in the basement of impact craters that may contain unshocked and shocked mineral and lithic clasts in a fine-grained aphanitic matrix (Stöffler and Grieve, 2003). Impact pseudotachylite is described in chapter 5, section 5.2 (the section on deformation and fracturing of target rocks).

6.3 Infiltration dykes

According to Rondot et al. (1993), Plante et al. (1990) and a brief mention in Phinney et al. (1978), the fragmental breccia and the Archean basement are cut by narrow dykes (cm to dm wide) of impact melt. It is clear from the brief descriptions offered by Phinney et al. (1978), Plante et al. (1993) and Rondot et al. (1993) that these dykes of impact melt infiltrated the fragmental breccia and the fractured Archean basement-rock from the units of overlying impact melt; see figure 2.3, which is based on Rondot et al. (1993). For reasons explained earlier, I contend that these dykes are examples of how the impact melt looked during the earliest phases of impact cratering, before the impact melt cooled and crystallized. I will therefore describe them in some detail.

Typically, infiltration dykes are brick-red or black, a few cm to dm wide and, compared to the matrix of the fragmental breccia, they contain relatively few small angular rock fragments. They can be distinguished from pseudotachylite veins by their irregular margins and numerous lateral veinlets infiltrating the wallrock. According to

field observations made by Rondot et al. (1993), they do not penetrate deeply into the country rock. I have not observed anything unequivocally resembling this description either in the surface samples obtained by M.R. Dence or in the West Clearwater Lake drill core I studied. However, in preparation for his thesis on the geophysical attributes of the Clearwater impact structure, Langis Plante, then of Université Laval, spent some time at the West Clearwater Lake impact structure, where he collected a number of samples of these dykes, which he called infiltration dykes. I obtained five of Plante's infiltration dyke samples (LP-21, LP-94, LP-122, LP-125 and LP-130), together with a brief description of the sample emplacements and a map giving their location. Sample LP-21 was collected on the southeastern shore of Marie-Claude Island (a small island on the southeastern area of the West Clearwater ring of islands), LP-94 was collected on the southwestern shore of Atkinson Island (the large island to the south of the ring of islands), LP-122 and LP-125 were collected on the northern shore of Lepage Island (the northernmost island of the ring of islands), and LP-130 was collected on the southeastern shore of the second Tadpole island (a group of four islands roughly in the northwest quadrant of the ring of islands, this island comes second counting from the south). All of these samples were collected near lake level and, with the exception of sample LP-130, all samples were collected on the "external" shores of the islands (maps with approximate locations of all samples are provided in Appendix C). Because the units dip approximately 5° toward the center of the impact structure, the lowermost units of the impact structure (the basement rocks and the fragmental breccia) are preferentially exposed in the island shores that face away from the center of the structure. Tables 6.6 and 6.7 provide major- and trace-element compositions that are typical of this unit. Figure 6.4 shows compositional variations of the infiltration dykes.

Table 6.6 – Major-element compositions of the infiltration dyke samples from West Clearwater obtained by the author.

Rock Unit						Average impact melt rock	
Sample	LP-21	LP-94	LP-122	LP-125	LP-130	n = 46	
						aver.	max.-min.
SiO ₂ (%)	58.93	58.80	61.23	59.38	58.47	60.90	62.96-58.09
TiO ₂	0.72	0.90	0.85	0.75	0.78	0.77	1.09-0.61
Al ₂ O ₃	17.26	17.30	15.84	15.37	16.32	15.87	17.27-14.95
Cr ₂ O ₃	0.01	0.01	0.01	0.02	0.01	0.01	0.02-0.01
Fe ₂ O ₃	6.42*	5.64*	6.42*	7.00*	6.33*	6.17*	7.87-5.09
FeO	---	---	---	---	---	---	---
MnO	0.07	0.06	0.09	0.08	0.08	0.06	0.15-0.03
MgO	2.80	2.22	2.83	4.04	3.26	2.75	4.20-2.28
CaO	4.98	3.65	4.60	5.12	4.32	4.46	6.61-3.02
Na ₂ O	4.09	4.12	3.91	3.64	4.13	3.76	4.30-3.49
K ₂ O	2.94	4.84	3.24	2.92	2.57	3.50	4.31-2.88
P ₂ O ₅	0.29	0.38	0.33	0.28	0.31	0.30	0.49-0.22
L.O.I.	1.77	1.85	0.99	1.74	2.84	1.55	2.78-0.89
Total	100.42	99.94	100.47	100.47	100.56	100.24	100.63-99.79

* Total iron as Fe₂O₃. L.O.I. – Loss On Ignition**Table 6.7** – Trace-element concentrations in the infiltration dyke samples from West Clearwater obtained by the author.

Rock Unit						Average impact melt rock	
Sample	LP-21	LP-94	LP-122	LP-125	LP-130	n = 53	
						aver.	max.-min.
Ba (ppm)	1120	1460	1097	1081	1147	1191	1555-872
Ce	77	152	82	68	86	74	160-28
Co	15	19	12	30	10	11	18-<d/l
Cu	32	36	38	23	19	33	78-14
Ni	39	26	27	78	27	32	63-22
Sc	<d/l	<d/l	<d/l	13	<d/l	1	13-<d/l
V	111	106	98	101	94	93	141-73
Zn	10	21	42	34	43	16	63-<d/l

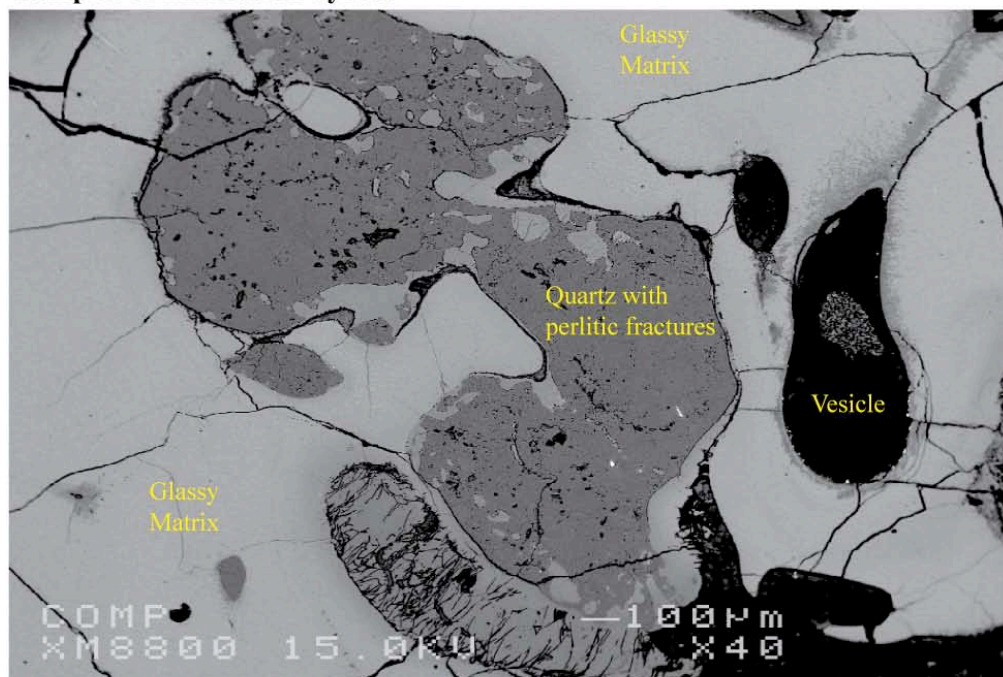
In thin section, the samples of impact melt dykes collected by Plante are nearly vitric: they are 70 to >90% relatively homogeneous glassy groundmass, 30 to <10% clasts and contain, in a couple of thin sections, roughly 5% vacuoles. The glassy groundmass is black, brick red or brown in plane light, usually criss-crossed by numerous thin cracks, and it generally becomes extinct with crossed polars. Clasts are typically angular to subangular, and their size is quite variable, ranging from ~4 mm to less than 0.1 mm across. The largest clasts are lithic fragments composed essentially of altered feldspars and quartz. The smaller clasts are typically single crystals of quartz, plagioclase and some rare pyroxene. Jumbles of very fine-grained microlites of plagioclase, Fe-oxides and pyroxene commonly surround clasts (Figure 6.16 A, p. 149). Clasts of polycrystalline quartz are common, and they usually display perlitic fractures. It has been suggested by Carstens (1975) that this kind of fracturing is created when quartz is shocked and heated to form cristobalite or lechatelierite (silica glass, i.e. amorphous SiO₂) and then is cooled quickly. The strain from shrinkage would cause the perlitic fracturing. Resorption textures, such as embayments, reaction rims and fine-grained dark-coloured reaction coronas rich in small augite crystals, which are present around nearly all the clasts in the clast-rich impact melt, are far less common around the clasts in the infiltration dykes. Quartz clasts with sharp boundaries and without visible reaction rims can be found right beside a well-embayed blob of silica or a partially digested quartz clast surrounded by a halo of tiny pyroxene and Fe-oxide crystals (figures 6.3 A and B). Nevertheless, it is clear that infiltration dyke glasses are *quenched melts*.

Viewed in plane light at high magnification, the groundmass of sample LP-21 appears to be very fine-grained, with minute black grains mixed in with clear amorphous

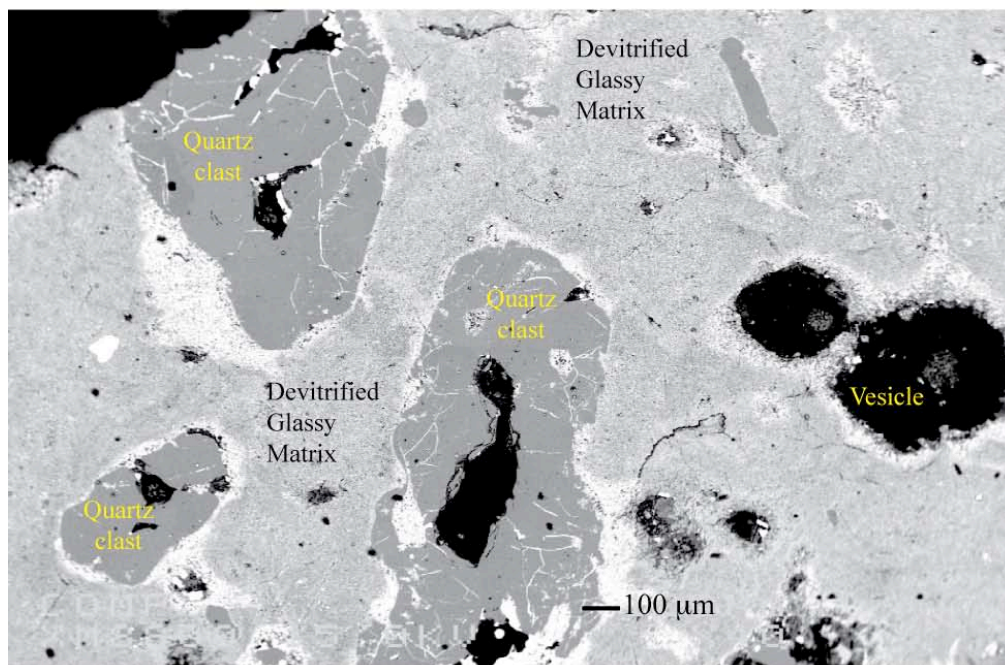
Figure 6.3 A and B Two samples of infiltration dykes. In image A one sees, embedded in a featureless glassy matrix, an embayed, resorbed quartz clast displaying perlitic

fractures. In image B, the quartz clasts appear less strongly resorbed, and they are surrounded by a halo of tiny Fe-oxide crystals. The glassy matrix appears grainy, partially recrystallized and probably altered.

Samples of infiltration dykes:



A) Back-scattered electron image of a polished thin section of sample LP-122.



B) Back-scattered electron image of a polished thin section of sample LP-94.

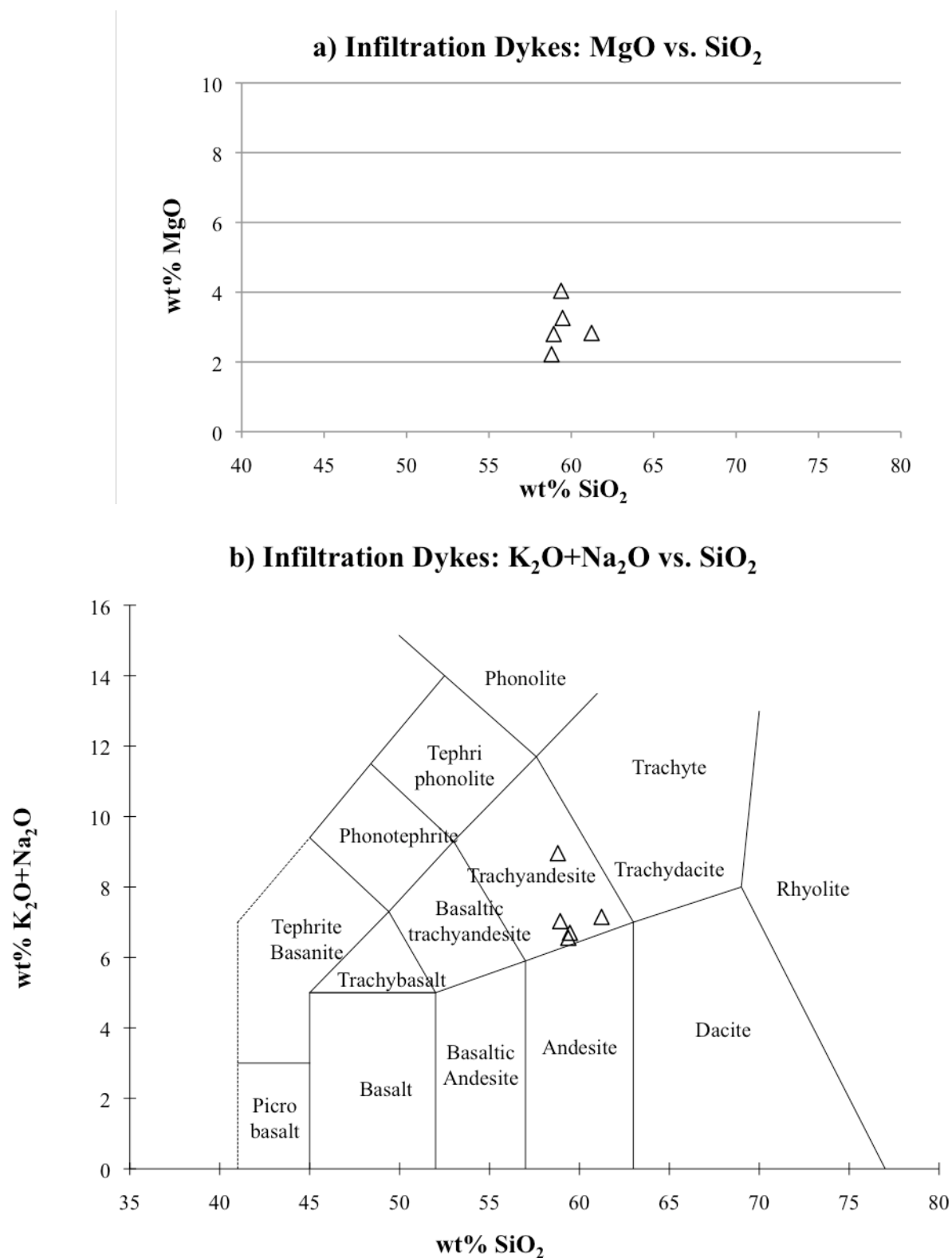


Figure 6.4 a and b Compositional variation in samples of infiltration dykes from the West Clearwater Lake impact structure (n=5).

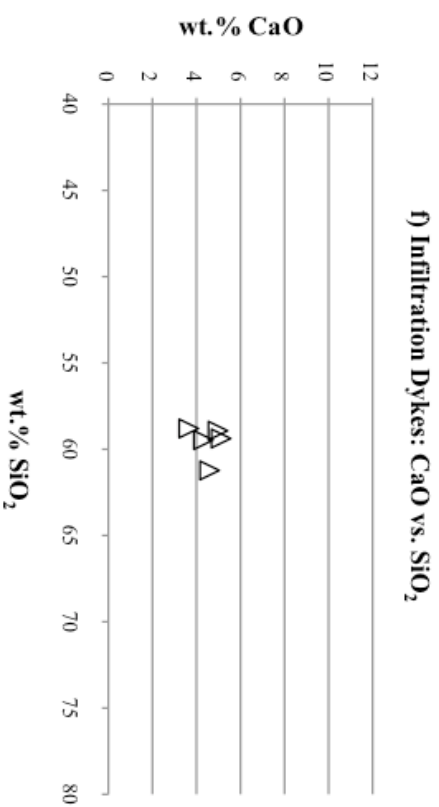
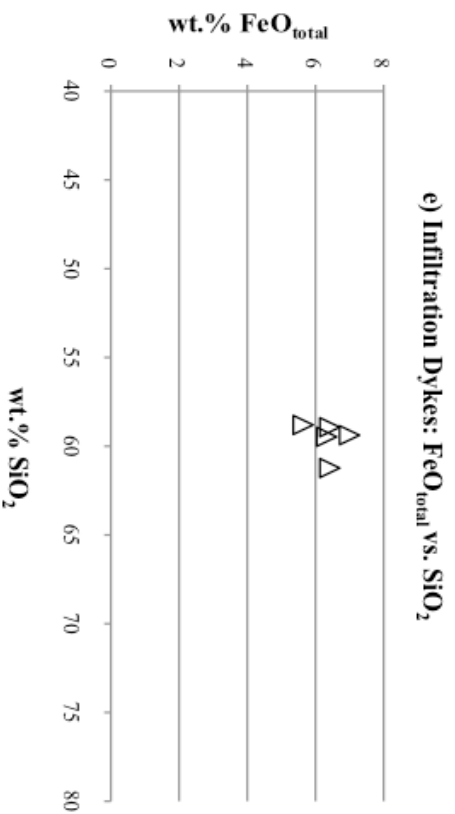
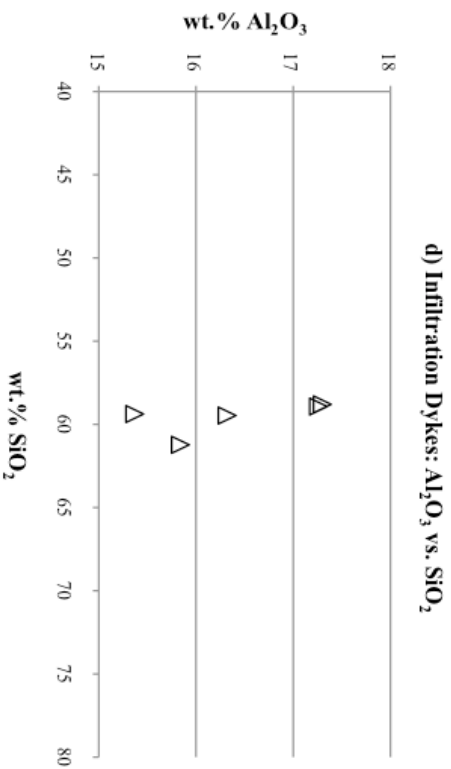
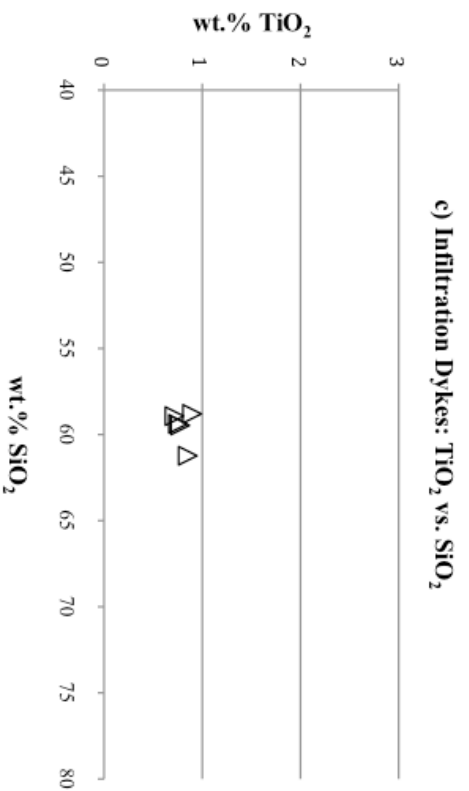


Figure 6.4 c to f Compositional variation in samples of infiltration dykes from the West Clearwater Lake impact structure (n=5).

material. Comparatively, the groundmasses of the other thin sections have an overall homogeneous aspect even at high magnification. However, these groundmasses are not featureless. For instance, in a couple of thin sections (LP-130, LP-122), groundmass colours gradually vary from light brown to dark brown, the dark brown areas usually forming rounded spots around clasts or near cracks, which leads me to believe that the variation in colour is related to alteration of the glass. Thin section LP-94 appears layered to the naked eye, and the layers are parallel to the narrow side of the thin section: the layering is probably due to a gradual increase in the number of small clasts from one side of the thin section to the other (Plante's notes indicate that this sample was obtained at a contact between the dyke and the enclosing rock). Thin sections LP-122 and LP-125 have regions roughly 1 mm across that contain tiny acicular or fibrous minerals arranged in nearly radial textures reminiscent of spherulites created by devitrification.

Samples LP-122 and LP-94 have abundant vesicles distributed throughout more or less randomly (around 5% in LP-94 up to 15-20% in LP-122). These vesicles are usually rounded, ranging in size from ~1 mm down to ~0.1 mm across or less. They are typically empty, but some have their interior walls coated with a clear glassy substance, and in LP-94 I found a few vesicles that appear to be filled with a clear material.

Most interestingly, thin sections LP-125 and LP-130 contain small globules resembling drops of liquid (the larger globules are 0.1 mm up to 0.5 mm across, but there are numerous smaller globules) filled with a material that appears clear in plane light, but becomes nearly extinct under crossed polars. These globules closely resemble the "glass spheroids" described by Dence et al. (1974) in "Indications of Fluid Immiscibility in Glass from West Clearwater Lake Impact Crater, Quebec, Canada". However, Dence et al. (1974) only observed these glass spheroids in drill core 4-63 and 4A-63, in bodies of

fresh-looking black glass found between 52 m and 54 m, that is, in the lower fragmental breccia (at about 60 meters, the core intersects porous pale pink medium-grained heavily altered rock with a probable granitic composition). I have found these glass spheroids in the samples of infiltration dyke collected by Plante and in two surface samples collected by M.R. Dence in 1977 (samples DCW-77-64 and DCW-77-65). The texture of the surface samples suggests that they are pieces of allochthonous breccia similar to parts of the fragmental breccia described above. These globules or glass spheroids are described in detail in the next section.

6.4 Glass Spheroids in glass of the West Clearwater Lake impact structure

The samples bearing glass spheroids (Dence's term) come from dykes of impact melt infiltrating fragmental breccia and fractured basement rock (samples LP-94, LP-125 and LP-130) and from fragmental breccia rock at the base of the impact structure (samples DCW-77-64 and DCW-77-65). Both these units are described in some detail in sections 6.1 (fragmental breccia) and 6.2 (infiltration dykes).

6.4.1 Petrography of the glass spheroids

The spheroids occur in both fresh-looking glass and in partially altered or recrystallized glass. They usually consist of a clear material that typically has a yellow, brown or green tint, but which can also be almost colorless. The vast majority of the smaller glass spheroids are roughly spherical in cross section, whereas the larger spheroids (>100 μm) tend to be elliptical. These shapes clearly suggest a resemblance to drops of liquid. I have also observed a number of glass bodies resembling stretched or

flattened spheroids that appear to have deformed in response to flow in the surrounding glass (Figures 6.16 A, p. 149, and 6.18 A, p. 151).

Glass spheroids form as much as 5% of the glass content in the thin sections studied and, generally speaking, they seem to be randomly distributed throughout the glass matrix, without any obvious clustering. Normally, the spheroids are clearly separated from each other but, in thin section DCW-77-64-5, I have observed what appear to be two spheroids in contact, possibly in the process of either coalescing or splitting apart (Figure 6.14 B). In thin sections DCW-77-65-4, DCW-77-64-1 and LP-125, the spheroids are associated with blobs and schlieren of what probably is lechatelierite, that is, silica glass created by high-pressure shock metamorphism of quartz (e.g. Figures 6.14 A, p. 147 and 6.15 A, p. 148).

The glass matrix in thin section LP-94 is rather porous, showing numerous empty elongate vesicles that in some cases seem to be aligned in a way that suggests a bead necklace (Figure 6.18 B, p.151). In areas of glass away from these bead necklace vesicles, there are also isolated spheroids that are of a size comparable to that of the glass spheroids in the other samples. A few of these vesicles are partially filled: I was able to analyze the material filling one of these rare filled vesicles; it has some similarities with that of the spheroids in other samples. It is therefore possible that sample LP-94 represents a rather altered example of a glass-spheroid-bearing infiltration dyke: the elongate bead necklace vesicles may have been formed (or enlarged) by dissolution by circulating fluids, with a few isolated partially filled glass spheroids surviving in areas away from these regions.

In order to determine the size distribution of these objects, I measured the sizes of 156 separate spheroids in back-scattered electron images of the regions of the thin

sections where the spheroids are abundant. This method was used instead of direct measurements with a polarizing microscope simply because the glass spheroids are far easier to distinguish from silica glass and clasts when viewed on back-scattered electron images. In the thin sections studied, the size of the glass spheroids ranges from 13 μm up to 1.46 mm across (taken as the diameter for the spherical bodies, or the length of the major axis for the elliptical bodies). A plot of frequency versus length of the major axis (Figure 6.5) shows a regular distribution with a maximum in the 40 to 59 μm category, and about half of the spheroids measured are smaller than 100 μm .

Most glass spheroids consist of a yellow or pale brown, almost clear, very fine-grained, homogeneous material. Some spheroids are filled with a dark brown material that becomes partially extinct when viewed under crossed polarizers; some of these dark brown spheroids become darker towards their center, which suggests some kind of compositional zoning. Both pale and dark spheroids contain a coarser mica-like mineral that is clearly birefringent. I have also observed a few spheroids that contain small grains of a crystalline material with a low first-order birefringence. This material generally forms small slivers or irregular grains in the spheroid walls, at the contact between the spheroid and the matrix glass. Microprobe analyses of this material revealed that it is essentially composed of silica: one such composition is given in Table 6.11 under analysis 33 (chemical composition will be discussed in section 6.4.2).

The largest spheroids are commonly cracked and partially empty, presumably owing to damage during thin section preparation. In most cases, the empty areas are

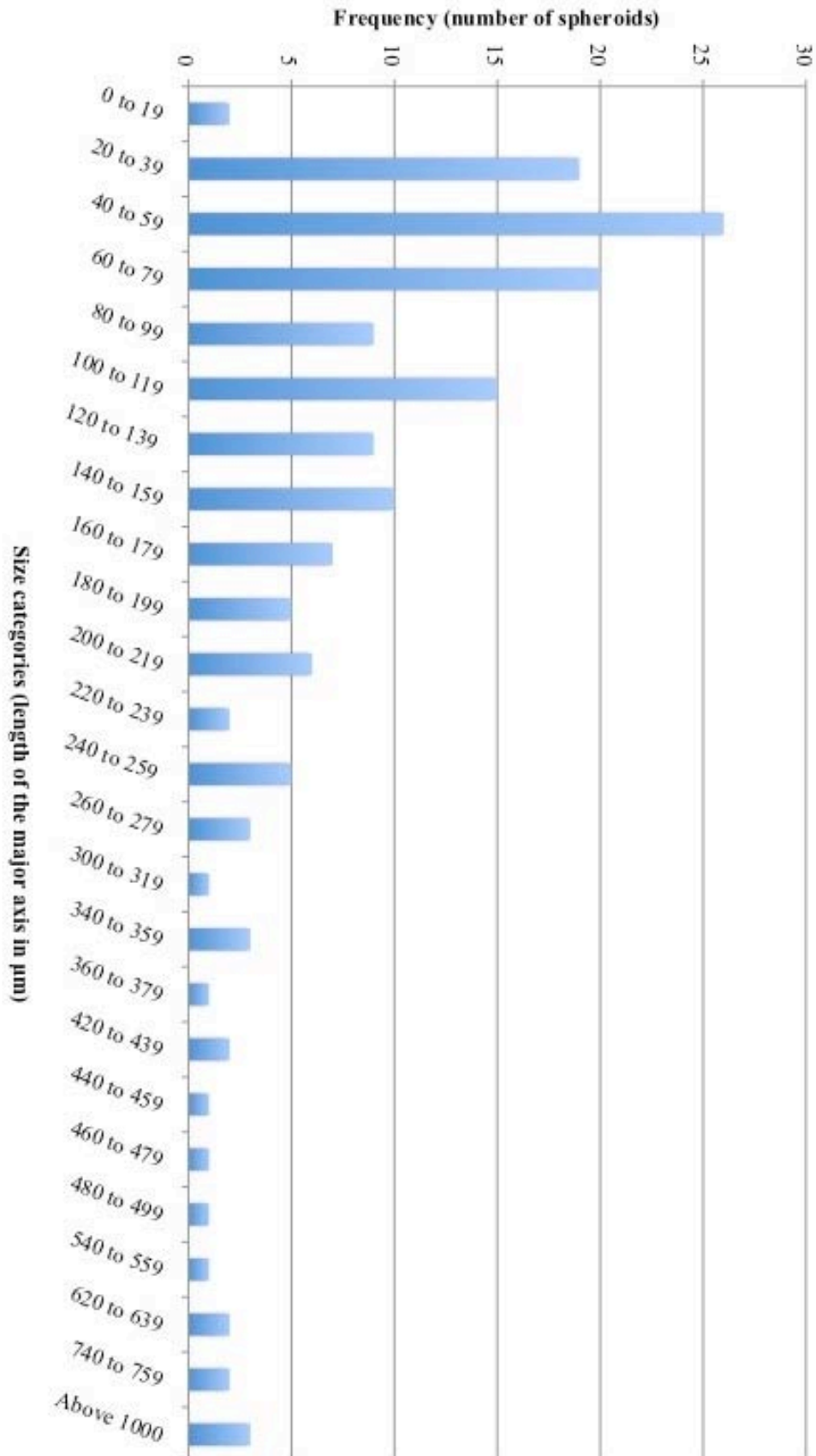


Figure 6.5 - Size distribution of the glass spheroids (n=156)

clearly delimited by sharp fracture planes but, in some cases, the cracked margins seem to be less distinct, and some kind of diffuse grainy material still partially fills the empty area. I have observed one large spheroid in thin section DCW-77-65-4 that has been cut by a vein of glassy material that shows a granular texture on back-scattered electron images: this material probably infiltrated the rock after the assemblage solidified, filling a crack that happened to cut through the glass spheroid (see Figure 6.15 B). A granular material similar to this vein filling partially occupies the interior of a glass spheroid in sample LP-125, but there are no infiltration cracks visible in this case. The composition of both these fillings are given under numbers 34 and 35 in Table 6.11. Except for their SiO₂ content (52 vs. 70 wt.%) and consequently their low totals (78% vs. 94%, respectively), these two compositions are quite similar. Their chemical compositions show a distinctively high Na₂O content (10 and 12 wt.%, respectively), which is significantly higher than the Na₂O contents of both the glass matrix and the glass spheroids.

It is clear that some spheroids were deformed by flow in the cooling melt, which demonstrates that the spheroids were initially filled with a material in a fluid state. Examples of strong deformation of spheroids are shown in Figures 6.16 A and 6.18 A, both obtained from back-scattered electron images of thin section LP-125.

6.4.2 Chemical composition of the glasses

The analysis of the glass spheroids and the adjacent glass matrix was done by wavelength-dispersion spectroscopy (WDS) with a JEOL 8900 electron microprobe using the ZAF correction method at McGill University. Both natural and synthetic standards were selected to minimize the correction factors. The accelerating voltage was 15 keV

for all analyses, and the beam current was 20 nA. Counting intervals were 20 seconds, and the beam diameter was kept mostly in the 10 to 15 μm range, with the occasional analysis done at 5 μm for small glass spheroids. The estimated precision is $\pm 1\%$ for major elements.

When analyzing the glass matrix, special care was taken to place the microprobe beam to avoid clasts and microlites. I employed the following procedure to choose areas for analysis: firstly, observation on an optical polarizing microscope was used to select a spot containing matrix glass, spheroids and a relatively small number of clasts; secondly, immediately before analysis, a back-scattered electron image of the area previously selected was taken. This image was then used to select the exact spot for analysis.

On a back-scattered electron (BSE) images, most mineral clasts and microlites are fairly obvious, as they are coarser-grained than the glass matrix, and they commonly have a different colour. For instance, microlites of minerals rich in Fe and Mg look like tiny bright spots; silica-rich clasts and melts appear as smooth dark gray regions. It is harder, however, to distinguish feldspar microlites and clasts from the glass matrix, and feldspar microlites from feldspar clasts: on BSE images, all of these phases have roughly the same colour, and tiny feldspar microlites and clasts can be embedded in the glass matrix, and their boundary is indistinct. Nevertheless, larger clasts and microlites are relatively easy to spot, as they tend to look smoother and to show regular cracks. I am fairly confident that I was able to avoid sampling clasts or microlites larger than about 10 μm in diameter. Microprobe analyses of both the matrix glass and the glass spheroids typically sum to low totals (see Table 6.8 and Table 6.10). To make sure that calibration with mineral standards was adequate, I compared my quantitative microprobe results (which require

Table 6.8 - Average compositions, and minimum and maximum range of compositions, of the glassy matrix in the samples that contain glass spheroids. Average composition of impact melt is presented for comparison.

Sample	DCW-77-64-5		DCW-77-65-4		LP-94		LP-125		LP-130		Average impact melt rock (XRF analyses)	
	7		12		6		29		26		46#	
Number of analyses	aver.	max.-min.	aver.	max.-min.	aver.	max.-min.	aver.	max.-min.	aver.	max.-min.	aver.	max.-min.
SiO ₂ (%)	58.99	59.82-57.95	58.61	62.04-53.01	55.96	57.77-54.70	58.87	66.14-40.30	59.42	62.61-40.20	60.90	62.96-58.09
TiO ₂	0.62	0.66-0.56	0.64	0.76-0.57	0.79	1.04-0.54	0.94	5.03-0.00	0.82	1.32-0.02	0.77	1.09-0.61
Al ₂ O ₃	16.01	16.48-15.82	16.45	18.76-14.91	18.17	19.69-16.26	16.37	18.83-3.38	16.27	24.36-10.53	15.87	17.27-14.95
Cr ₂ O ₃	0.01	0.00-0.04	0.01	0.04-0.00	0.00	0.02-0.00	0.01	0.04-0.00	0.01	0.04-0.00	0.01	0.02-0.01
FeO _{total}	4.56	5.10-3.40	4.81	7.08-3.68	3.93	6.12-1.74	4.68	7.40-0.12	5.47	6.64-0.52	6.17*	7.87-5.09
MnO	0.07	0.06-0.09	0.06	0.10-0.02	0.05	0.08-0.01	0.07	0.11-0.00	0.08	0.11-0.03	0.06	0.15-0.03
MgO	2.97	3.38-2.20	3.35	7.73-0.92	0.74	1.76-0.02	2.54	4.22-0.05	2.85	5.07-0.22	2.75	4.20-2.28
CaO	3.93	4.68-2.93	3.16	4.33-2.08	3.70	4.28-3.22	4.88	7.77-0.73	4.58	6.98-3.68	4.46	6.61-3.02
Na ₂ O	2.80	3.45-2.18	2.41	6.25-0.71	5.52	5.83-5.20	4.89	11.02-2.84	4.71	7.48-2.30	3.76	4.30-3.49
K ₂ O	3.75	4.44-2.53	2.54	4.29-1.23	5.39	6.21-4.65	3.67	9.50-0.78	2.53	4.43-0.51	3.50	4.31-2.88
H ₂ O	---	-----	---	-----	---	-----	---	-----	---	-----	1.55	2.78-0.89
Total	93.71	94.99-91.24	92.04	96.23-85.01	94.24	95.45-93.22	96.91	100.3-63.89	96.74	100.4-70.42	100.24	112.14-91.87

Table 6.9 - Individual analyses of the glassy matrix from the samples that contain glass spheroids.

Sample	DCW-77-64-5							LP-94							LP-130						
Analysis #	1	2	3	4	5	6	7*	8*	9	10	11	12	13	14	15	16	17				
SiO ₂ (%)	59.17	58.86	59.48	60.94	60.50	60.09	53.01	55.19	57.77	57.82	57.99	60.36	57.73	59.77	62.61	59.94	59.07				
TiO ₂	0.63	0.56	0.66	0.64	0.61	0.62	0.76	0.95	0.54	0.94	0.92	0.86	1.71	0.79	0.87	0.86	0.90				
Al ₂ O ₃	15.82	16.16	15.97	16.86	16.39	16.36	14.91	16.47	19.69	17.36	16.97	16.02	16.54	15.68	16.34	15.87	17.19				
Cr ₂ O ₃	0.00	0.04	0.02	0.00	0.01	0.00	0.04	0.02	0.00	0.01	0.01	0.01	0.00	0.00	0.02	0.00	0.00				
FeO _{total}	4.22	5.02	4.49	4.92	5.00	3.68	4.04	6.12	1.75	4.89	6.17	7.40	5.38	5.39	5.58	5.87	5.88				
MnO	0.07	0.08	0.07	0.08	0.10	0.06	0.06	0.07	0.03	0.07	0.09	0.07	0.07	0.08	0.07	0.09	0.06				
MgO	3.38	3.00	3.07	1.58	2.89	3.40	7.73	1.99	0.02	3.17	2.93	1.62	2.57	2.67	2.54	2.95	2.90				
CaO	4.49	2.93	3.63	2.75	3.31	4.33	2.72	4.28	3.41	5.29	5.93	3.95	5.37	4.25	4.28	4.40	4.58				
Na ₂ O	2.70	3.09	2.70	2.92	2.62	1.93	0.74	5.36	5.52	4.96	5.15	4.65	5.38	3.94	6.31	3.27	6.47				
K ₂ O	4.44	3.80	4.09	3.12	2.80	4.29	1.28	5.01	6.11	2.73	2.44	4.10	2.04	3.11	1.22	3.76	2.02				
Total	94.99	93.52	94.18	93.81	94.23	94.74	85.01	95.45	94.84	97.23	98.60	99.05	96.79	95.69	99.82	97.00	99.06				
Sample	DCW-77-64-5-9	DCW-77-64-5-10	DCW-77-64-5-15	DCW-77-65-4-1	DCW-77-65-4-5	DCW-77-65-4-9	DCW-77-65-4-15	LP-94-7	LP-94-8	LP-125-6	LP-125-13	LP-125-21	LP-125-24	LP-130-1	LP-130-5	LP-130-15	LP-130-25				

* Analyses of altered matrix glass.

calibration) with qualitative energy-dispersive spectra (EDS). This comparison showed that all non-volatile elements were detected in my quantitative analyses. However, because the Fe content was measured as FeO and, as indicated by the rust-red colouring of many of these samples, most Fe must be under the form of Fe^{3+} , not Fe^{2+} , it is likely that the wt.% of Fe present was underestimated. However, because the amount of FeO present in these samples is small (typically less than 5 wt.%), this underestimation must account for only a small proportion of the low totals. Also, some of the alkali content, particularly Na, measured by the microprobe may have been lost due to volatilization, but since alkali content is below 6 wt.% for the vast majority of my samples, this alone cannot account for the low totals. This therefore suggests that the low totals can be best explained by a high volatile content, probably mostly H_2O , of about 4 to 8 wt.% for the matrix glass and 10 to 18 wt.% for the glass spheroids. These values for volatile content are similar to those estimated by Dence et al. (1974), who attributed their low totals to a high H_2O content of the order of 4 wt.% for the matrix glass and 10 to 20 wt.% for the glass spheroids. This obviously suggests that the material now filling the “glass” spheroids is secondary, the result of either the alteration of the primary material, or the filling of an empty vesicle by a new substance.

On average, the microprobe-derived compositions of matrix glass have similar values to that of the average bulk composition of the impact melt (see Table 6.8). There are, however, a few differences among samples: for instance, microprobe analyses of the matrix glass of infiltration dyke samples typically show a slightly greater content of Na_2O and higher totals than the matrix glass analysis of the samples of fragmental breccia (about 5 wt.% vs. 2 wt.% for NaO_2 , and 97 wt.% vs. 92 wt.% for totals, respectively). Compared to the matrix glass of the other samples, analyses of sample LP-94 are

distinguished by a lower wt.% SiO_2 , a higher alkali content, a very low MgO wt.%. Compositions from LP-94 have totals that are, on average, similar to those of the fragmental breccia samples. I attribute these differences to alteration of the matrix glass, which explains the lower SiO_2 contents and the lower totals. The higher Na_2O and very low MgO contents of sample LP-94 are puzzling, as I would expect both these elements to increase in a sample that, compared to other infiltration dyke samples, appears to be more altered. The high Na_2O may be related to the presence in the altered samples of veins like the one described cutting a glass spheroid in thin section DCW-77-65-4, which may have enriched the matrix glass in sodium. Sample LP-94 was collected at the contact with fragmental breccia, a relatively porous zone of weakness that presumably may have served as a conduit for fluids: the rock may have been washed out of some of its more mobile elements, which may have caused Mg depletion, removed most glass spheroids and produced the bead necklace vesicle texture of figure 6.18 B.

Compared to the adjacent glass matrix, the glass spheroids contain a higher proportion of volatiles: as mentioned above, 4-8 wt.% for the matrix glass vs. 10-18 wt.% for the glass spheroids. Also, on average, the spheroids are poorer in SiO_2 (58-60 wt.% in the glass matrix vs. 48-53 wt.% in the spheroids) and Al_2O_3 (16-18 wt.% vs. 8-15 wt.%, respectively) and much richer in MgO (about 3 wt.% vs. 12-18 wt.%, respectively). The glass spheroids contain small amounts of alkali elements: $\text{Na}_2\text{O} + \text{K}_2\text{O}$ of the spheroids is generally close to 1 wt.%, whereas the alkali content of the matrix glass is in the 5 to 10 wt.% range (see Figures 6.9 and 6.13). In order to emphasize the mafic character of the glass spheroids, I calculated, according to the method of Winter (2001), CIPW norms of a variety of glass spheroid compositions (see Table 6.11). For most compositions, the dominant normative mineral is hypersthene; only for the most Al-rich

compositions does quartz replace hypersthene as the dominant normative mineral. Finally, the compositions of the glass spheroids typically show a greater variation in major-element content from thin section to thin section, and even within the same thin section, than the glass matrix analyses (see Table 6.9 and Table 6.11).

The SiO₂ content of all the glass spheroids is comparable, with the possible exception of LP-125, which has an average SiO₂ wt.% that is lower than that of the glass spheroids in other samples: about 50 wt.% SiO₂ for LP-125 versus about 52-53 wt.% for the other samples. The lowest SiO₂ wt.% (and highest wt.% Al₂O₃) in the glass spheroids of LP-125 invariably come from spots on glass spheroids that appear flaky and mica-like (see figure 6.14 B and associated analysis 31 in Table 6.11). Also, the compositions with the lowest SiO₂ values invariably correspond to the compositions with the lowest totals.

Table 6.10 - Average compositions, and minimum and maximum range of compositions, of the glass spheroids.

Sample	DCW-77-64-5		DCW-77-65-4		LP-125		LP-130	
Number of analysis	30		14		28		21	
	aver.	min.-max.	aver.	min.-max.	aver.	min.-max.	aver.	min.-max.
SiO ₂ (%)	52.66	47.28-54.97	52.40	47.06-54.77	49.82	39.31-53.44	53.41	49.92-57.79
TiO ₂	0.04	0.00-0.37	0.04	0.00-0.08	0.06	0.00-0.21	0.03	0.01-0.06
Al ₂ O ₃	13.76	12.25-24.35	15.22	12.87-26.12	8.13	8.40-10.5	12.84	11.84-17.60
Cr ₂ O ₃	0.01	0.00-0.05	0.01	0.00-0.03	0.01	0.00-0.04	0.00	0.00-0.02
FeO _{total}	3.08	0.34-4.61	2.51	0.25-3.98	2.36	0.18-3.81	2.98	0.46-3.94
MnO	0.04	0.01-0.06	0.04	0.03-0.05	0.03	0.02-0.07	0.03	0.00-0.06
MgO	12.60	8.88-14.59	12.14	8.52-13.53	17.62	3.96-20.56	15.44	6.23-17.05
CaO	2.47	1.27-2.69	2.29	1.09-2.65	1.08	0.73-5.59	1.26	1.13-1.49
Na ₂ O	0.08	0.03-0.13	0.04	0.01-0.07	0.76	0.26-11.92	0.35	0.26-0.40
K ₂ O	0.78	0.19-1.36	0.74	0.12-1.23	0.63	0.32-1.04	1.06	0.87-1.30
Total	85.52	77.35-89.17	85.44	83.31-88.06	84.47	65.86-86.14	87.39	80.78-90.89

Table 6.11 - Individual analyses of glass spheroids.

Analysis #	High MgO			Intermediate MgO					
	18	19	20	21	22	23	24	25	26
SiO ₂ (%)	51.95	49.34	51.29	53.58	54.73	54.97	53.66	54.92	53.20
TiO ₂	0.01	0.08	0.04	0.02	0.01	0.04	0.01	0.02	0.06
Al ₂ O ₃	7.67	7.79	8.35	12.39	13.44	13.45	12.57	17.60	14.89
Cr ₂ O ₃	0.01	0.00	0.02	0.00	0.00	0.00	0.00	0.01	0.01
FeO _{total}	1.67	3.81	2.29	2.60	3.22	3.33	4.61	0.75	3.98
MnO	0.02	0.06	0.03	0.03	0.02	0.05	0.04	0.04	0.05
MgO	20.56	20.04	18.48	17.05	16.92	13.18	12.69	12.53	12.26
CaO	0.74	1.12	0.76	1.13	1.24	2.49	2.58	1.40	2.34
Na ₂ O	0.39	0.35	0.36	0.34	0.30	0.10	0.10	0.40	0.05
K ₂ O	0.49	0.61	0.56	0.95	1.00	0.83	0.90	1.04	1.23
Total	83.51	83.19	82.18	88.09	90.89	88.44	87.17	88.70	88.06
CIPW normative minerals (wt.%)*	hy	hy	hy	hy	hy	hy	hy	hy	hy
	51.18	49.80	45.97	42.43	42.12	32.76	31.59	31.17	30.43
	q	q	q	q	q	q	q	q	q
	15.58	12.75	17.90	20.14	21.29	26.26	25.20	26.95	24.96
	cor	cor	cor	cor	cor	cor	cor	cor	cor
	5.15	4.52	5.77	8.75	8.75	7.86	6.74	13.27	9.22
	an	an	an	an	an	an	an	an	an
	3.67	5.56	3.77	5.61	6.15	12.35	12.80	6.95	11.61
	ab	ab	ab	ab	ab	ab	ab	ab	ab
	3.30	2.96	3.05	2.88	2.54	0.85	0.85	3.38	3.38
Sample	or	or	or	or	or	or	or	or	or
	2.90	3.60	3.31	5.61	9.61	4.90	5.32	6.15	7.27
	hem	hem	hem	hem	hem	hem	hem	hem	hem
	1.62	3.67	2.22	2.53	3.17	3.22	4.52		3.87
	LP-125	LP-125	LP-125	LP-130	LP-130	DCW-77-	DCW-77-	LP-130	DCW-77-
	image 3	image 3	image 2	image 3	image 1	64-5 - Maf	64-5-	image 3	65-4-
	maf.glass 6	maf.glass 2	maf.glass 3	maf.glass 2	maf.glass 2	blob 10	maf.blob	maf.glass 9	Region 1-
						fresh	26		Glass 12
									(blob)

* CIPW norm calculated according to the method of Winter (2001).

Table 6.11 continued - Individual analyses of glass spheroids.

	Low MgO		High Al ₂ O ₃					High SiO ₂	High Na ₂ O	
	27	28	29	30	31	32	33	34	35	
Analysis #	27	28	29	30	31	32	33	34	35	
SiO ₂ (%)	50.48	57.79	47.06	48.47	48.27	33.89	96.81	52.24	69.89	
TiO ₂	0.04	0.03	0.01	0.00	0.00	0.18	0.00	0.00	0.03	
Al ₂ O ₃	12.56	16.89	26.12	25.27	24.35	19.81	0.01	3.51	3.14	
Cr ₂ O ₃	0.00	0.00	0.00	0.00	0.04	0.02	0.00	0.00	0.03	
FeO _{total}	2.02	0.46	0.25	0.26	0.34	5.73	0.03	0.18	0.84	
MnO	0.02	0.05	0.05	0.05	0.04	0.05	0.00	0.02	0.02	
MgO	11.17	6.23	8.60	8.52	8.88	10.14	0.00	3.96	3.54	
CaO	2.31	1.49	1.09	1.20	1.27	1.30	0.00	5.59	5.67	
Na ₂ O	0.07	0.36	0.01	0.04	0.03	0.72	0.00	11.92	9.66	
K ₂ O	0.49	0.94	0.12	0.19	0.19	0.68	0.01	0.91	0.86	
Total	79.16	84.24	83.31	83.99	83.41	72.51	96.86	78.33	93.69	
CIPW normative minerals (wt.%)*	hy 27.76	hy 15.47	hy 21.40	hy 21.22	hy 22.08	hy 25.14				
	q 26.61	q 39.64	q 31.39	q 32.24	q 31.43	q 9.25				
	cor 7.71	cor 12.57	cor 23.99	cor 22.82	cor 21.79	cor 15.53				
	an 11.46	an 7.39	an 5.41	an 5.95	an 6.30	an 6.45				
	ab 3.38	ab 3.05		or 1.12	or 1.12	ab 6.09				
	or 2.90	or 5.55				or 4.02				
	hem 1.97					hem 5.62				
Sample	DCW-77-	LP-130	DCW-77-	DCW-77-	DCW-77-	LP-94-	DCW-	LP-125	DCW-77-	
	64-5 - maf	image 3	65-4-	65-4-	64-5 - Maf	Blob a	77-64-5	image 10	65-4-Region	
	blob 19 alt	maf:glass 5	Region 1-	Region 2-	Blob 22 alt	center	- Maf	Maf. glass	2-Glass	
			Glass 10	Glass (blob alt) 3			blob 11	1	(blob alt) 5	
							clear			

* CIPW norm calculated according to the method of Winter (2001).

This observation is the most evident in glass spheroids from LP-125, but it applies to all glass spheroid compositions in all samples: compositions with a low SiO_2 wt.% invariably correspond to flaky, mica-like spots and have low totals. High SiO_2 values are typically associated with high totals, but the correspondence is not as clear as the low SiO_2 - low total connection. Note that MgO and Al_2O_3 contents stay roughly the same with varying SiO_2 content (see Figures 6.10 and 6.11). Alteration of the spheroids involves a loss of SiO_2 and an increase in volatile content, which is to be expected. Generally speaking, glass spheroids in samples LP-125 and LP-130, which are samples of infiltration dykes, are richer in MgO and poorer in Al_2O_3 relative to the glass spheroids in samples DCW-77-64 and DCW-77-65, which are fragmental breccia samples. Glass spheroids in sample LP-125 generally have the highest MgO and the lowest Al_2O_3 contents. The glass spheroids from the fragmental breccia samples (DCW-77-64-5 and DCW-77-65-4) cluster together and share the lowest values of MgO and the highest Al_2O_3 contents, whereas the MgO content of the spheroids in LP-130 is intermediate between LP-125 and the fragmental breccia spheroids, and their Al_2O_3 content is similar to that of the fragmental breccia samples (see Figure 6.10 and Figure 6.11). A plot of MgO vs. Al_2O_3 clearly shows the grouping by samples described above (Figure 6.12). This plot also clearly shows that there is an inverse correlation between MgO content and Al_2O_3 content. The compositional variations of the spheroids do not match compositional variations in the matrix that surrounds them. In particular, the inverse correlation between MgO and Al_2O_3 content measured in the glass spheroids does not have an equivalent in the glass matrix compositions (compare Figure 6.8 to Figure 6.12). This inverse relation between MgO and Al_2O_3 suggests mixing between two different phases, one richer in MgO and poorer in Al_2O_3 , another richer in Al_2O_3 and

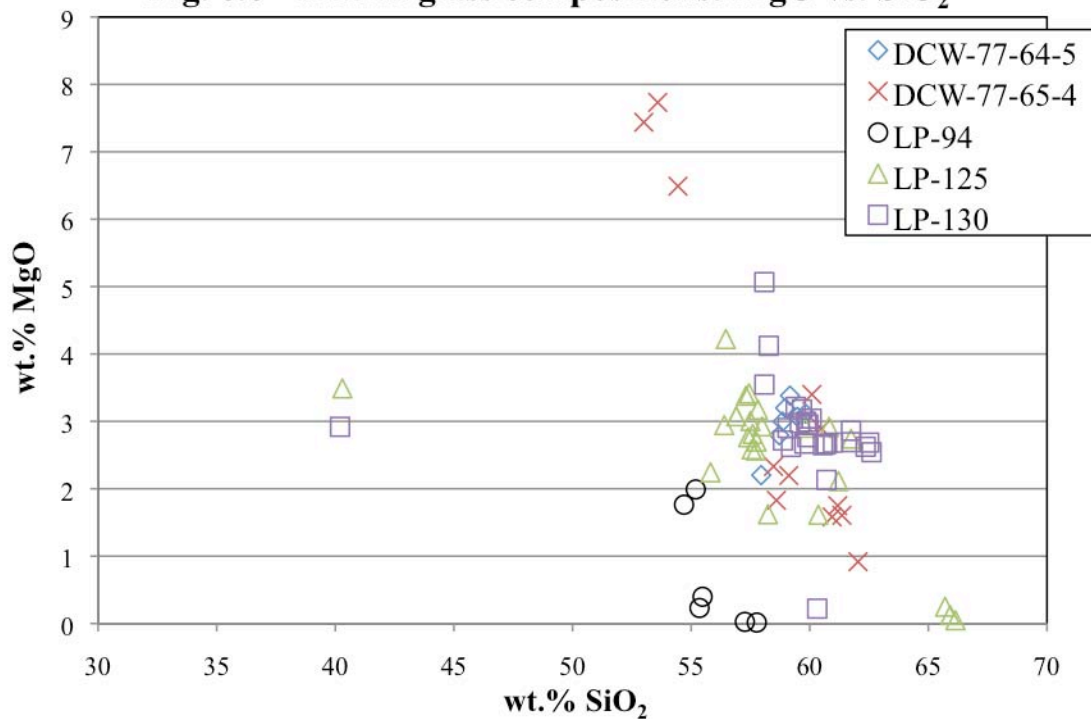
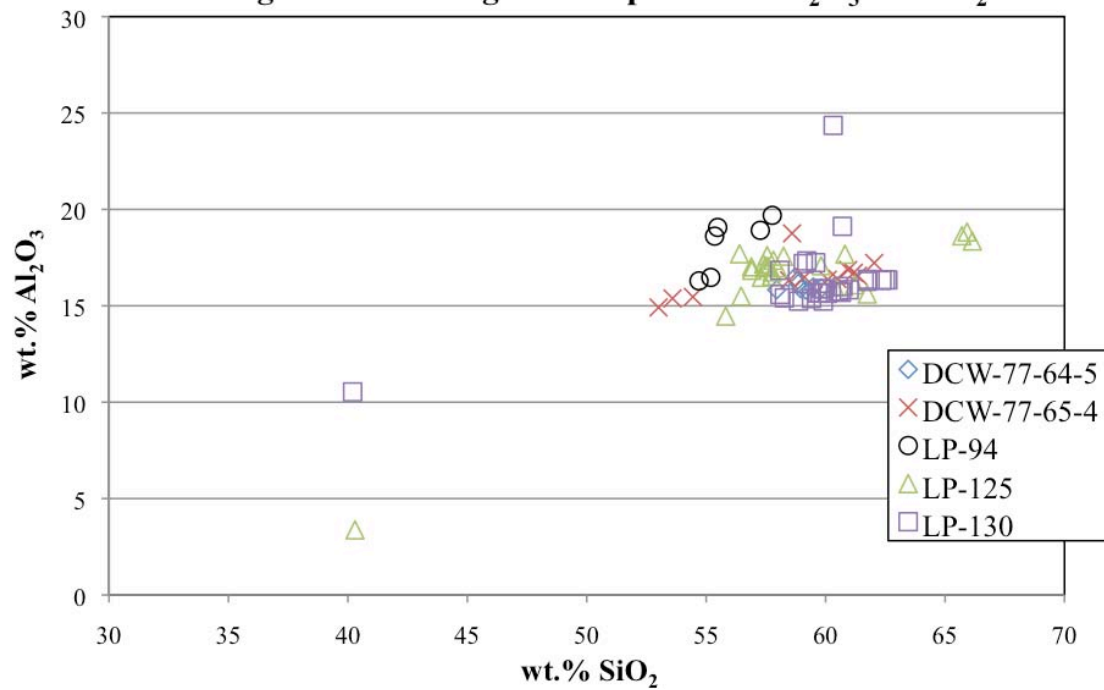
Fig. 6.6 - Matrix glass compositions: MgO vs. SiO₂**Fig. 6.7 - Matrix glass compositions: Al₂O₃ vs. SiO₂**

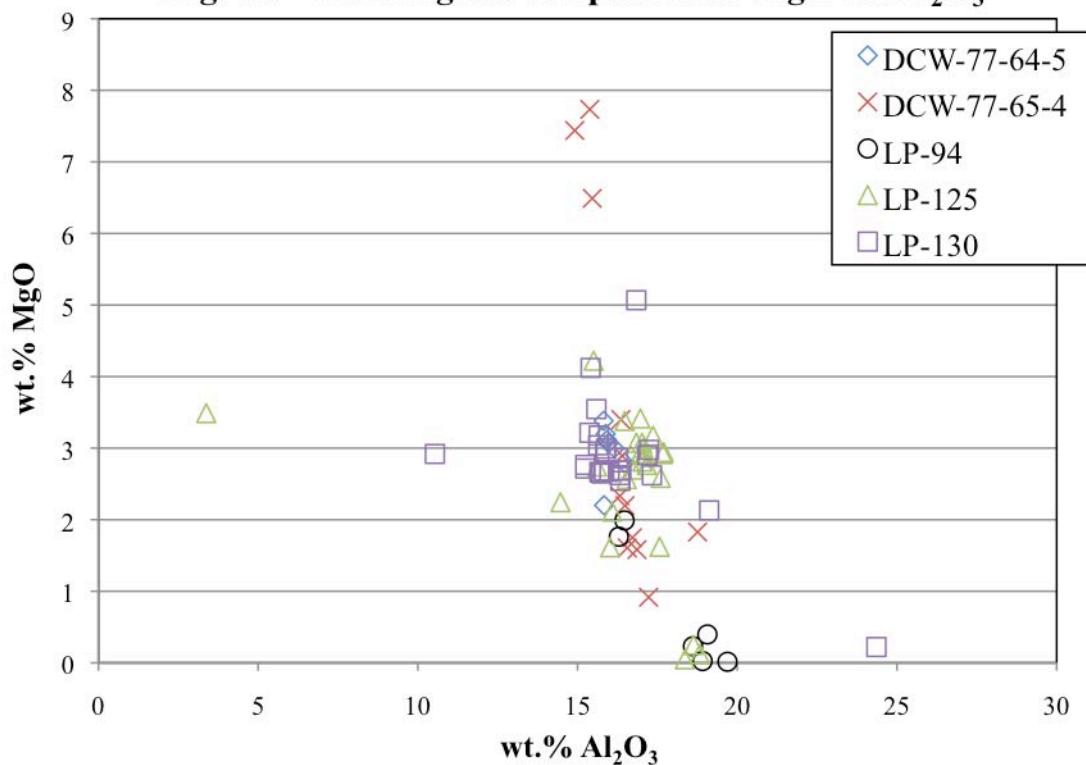
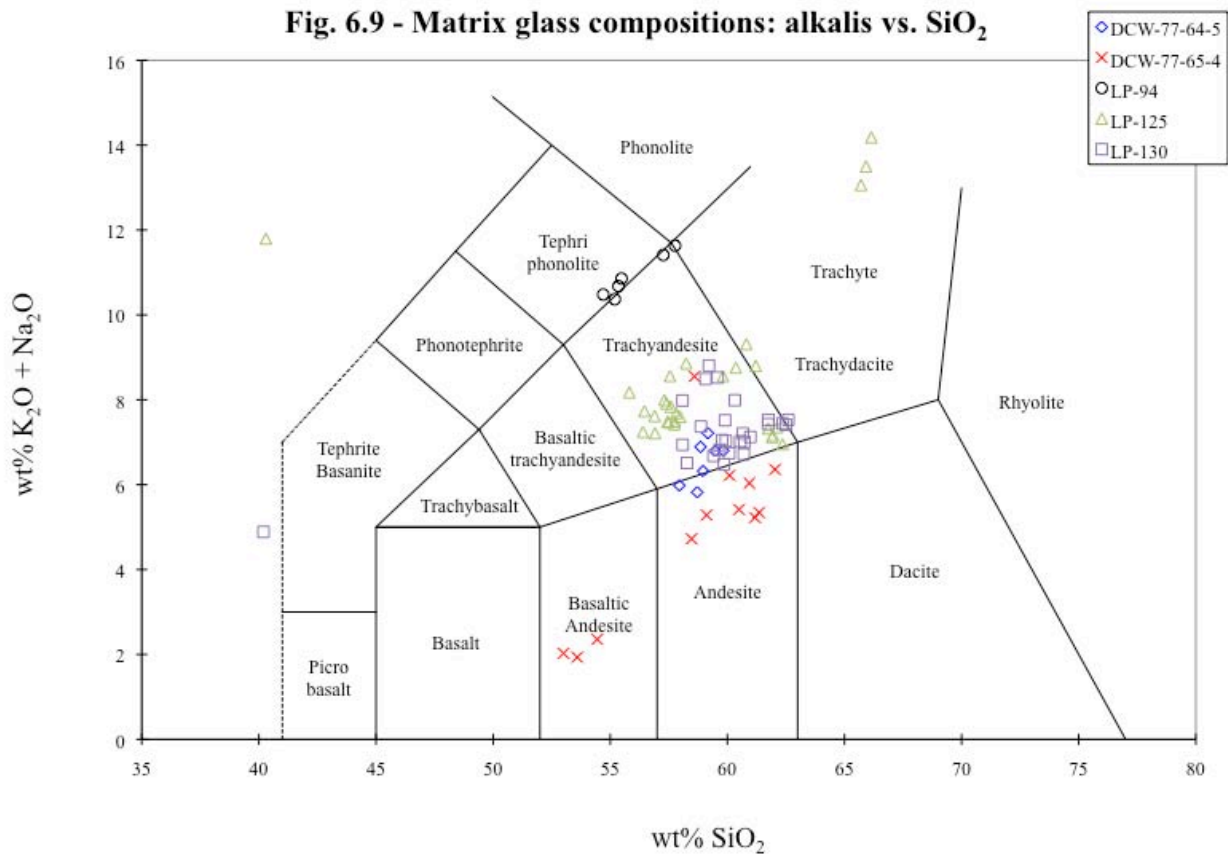
Fig. 6.8 - Matrix glass compositions: MgO vs. Al_2O_3 **Fig. 6.9 - Matrix glass compositions: alkalis vs. SiO_2** 

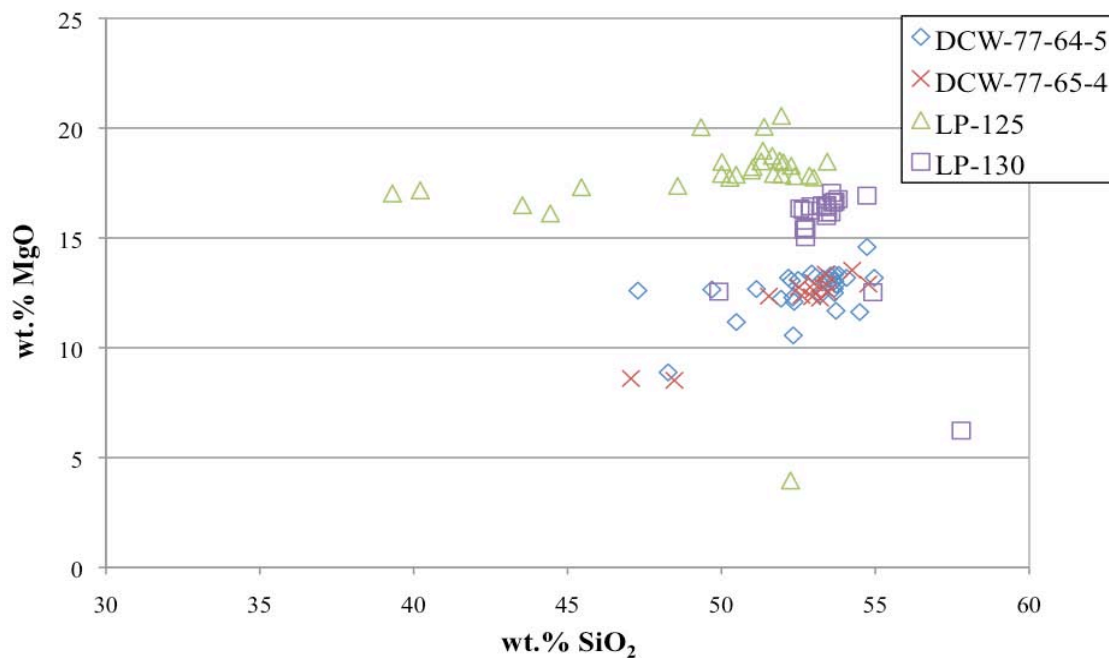
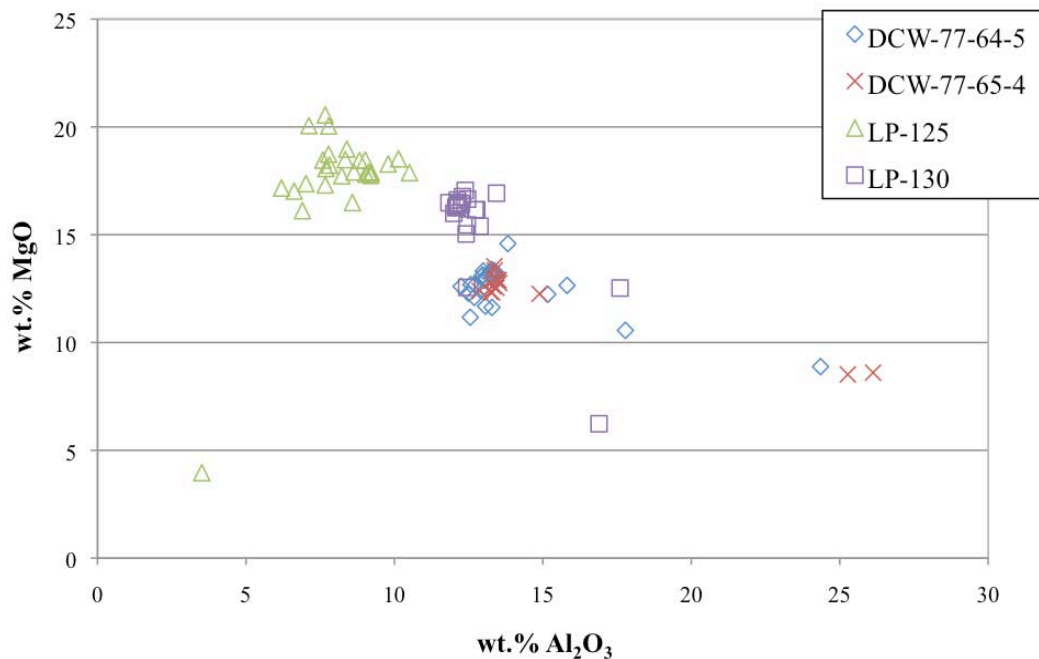
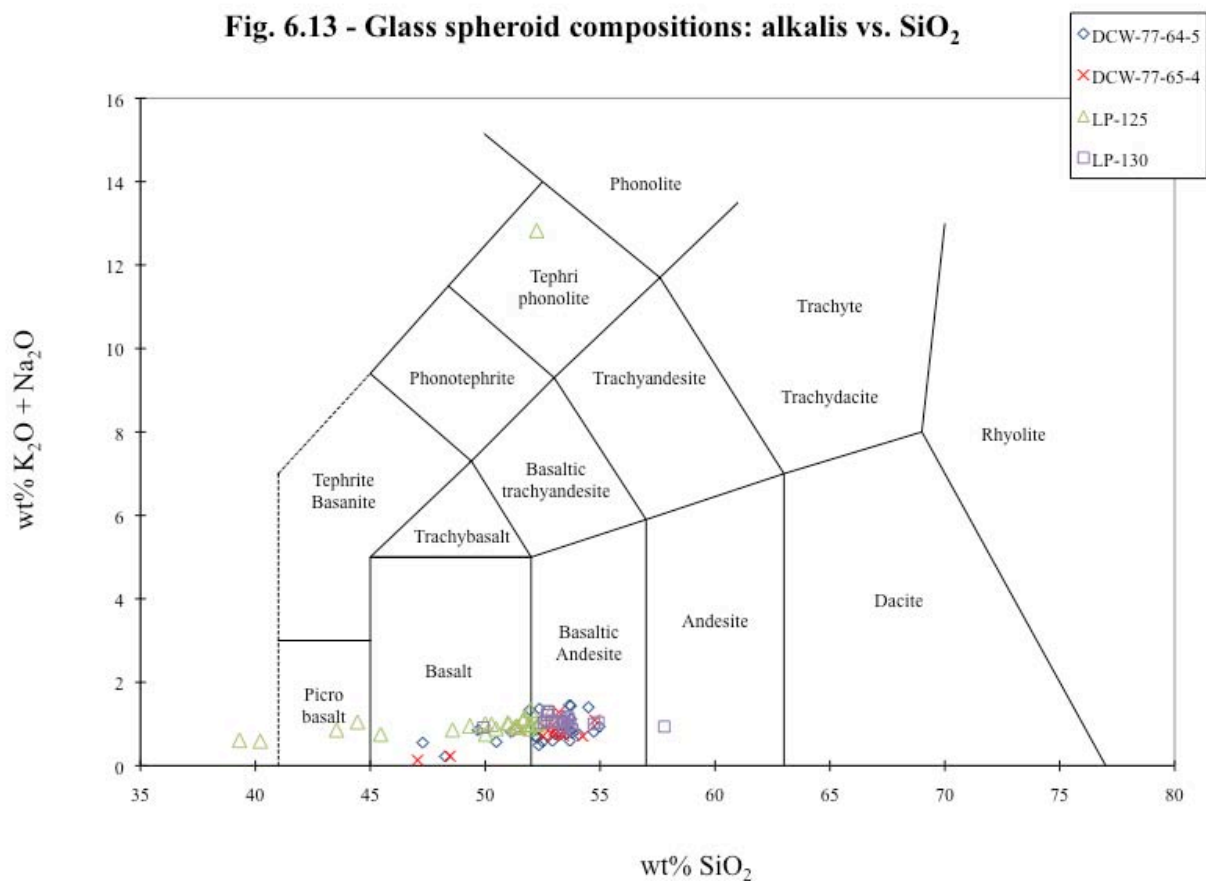
Fig. 6.10 - Glass spheroid compositions: MgO vs. SiO₂

Fig. 6.12 - Glass spheroid compositions: MgO vs. Al₂O₃**Fig. 6.13 - Glass spheroid compositions: alkalis vs. SiO₂**

poorer in MgO, one phase being created at the expense of the other. The more magnesian glass spheroids are found in infiltration dyke samples LP-125 and LP-130, whereas the more Al-rich glass spheroids are in the glass of the fragmental breccia. Fragmental breccia samples typically look quite altered: they are stained red to brown by hematite, and they are usually devitrified; fresh looking black glass is nearly absent. In contrast, infiltration dykes typically appear glassy and relatively well preserved. It is therefore possible that the higher Al content of the glass spheroids in the fragmental breccia is the result of a more advanced state of alteration.

In an article about hydrothermal systems in impact craters and the secondary alteration products created by hydrothermal activity, Naumov (2005) mentioned that Fe-Mg chlorites and saponite with high ^{IV}Al content are the predominant phyllosilicates within the autochthonous breccia (that is, the fragmental breccia). He also mentioned that impact glass is replaced by clay minerals such as montmorillonite and, in some cases, Al-Fe beidellite. Saponite (a trioctahedral smectite) also “occurs locally”, generally together with a dioctahedral smectite. Zeolites also are common, with calcium zeolites (e.g., laumontite, stilbite, chabazite) and analcime being common within impact breccias and Si- and alkali-rich zeolites predominating in the impact melt rock.

Naumov (2005) also observed that Fe-Mg-rich clay minerals are replaced by high-aluminum varieties “upward in a generalized vertical section through an impact rock sequence”. As the upper regions of impact rock sequences are initially hotter than the lower regions, one could propose that Fe-Mg-rich clay minerals are replaced with Al-rich varieties as alteration becomes more intense. Except for an excess of Al, glass spheroid compositions with high MgO (see Table 6.11) are similar to the composition of saponite, an Mg-rich and Al-poor trioctahedral smectite (Table 6.12). It is more difficult to

speculate about the mineralogy of other glass spheroid compositions: they do not show compositional similarities to the minerals listed by Naumov (2005). They are generally too silica-rich to be chlorites, they have too much MgO and not enough alkalis to be zeolites, and they seem to be too Mg-rich to be clays of the smectite group. Assuming that the original material filling the glass spheroids was a mafic glass (the reasons for this assumption will be discussed in chapter 9, section 9.2), I believe that it is reasonable to speculate that they are in fact a mixture of very fine-grained smectites, chlorites and zeolites: the hydrolysis of many mafic minerals usually produces clays that consist of chlorite - smectite mixed layers associated with very fine grained zeolite (Meunier, 2005). An X-ray diffraction study would be essential to make sense of the composition of the glass spheroids. Extracting individual glass spheroids without destroying or altering them, however, will in all probability be an arduous affair!

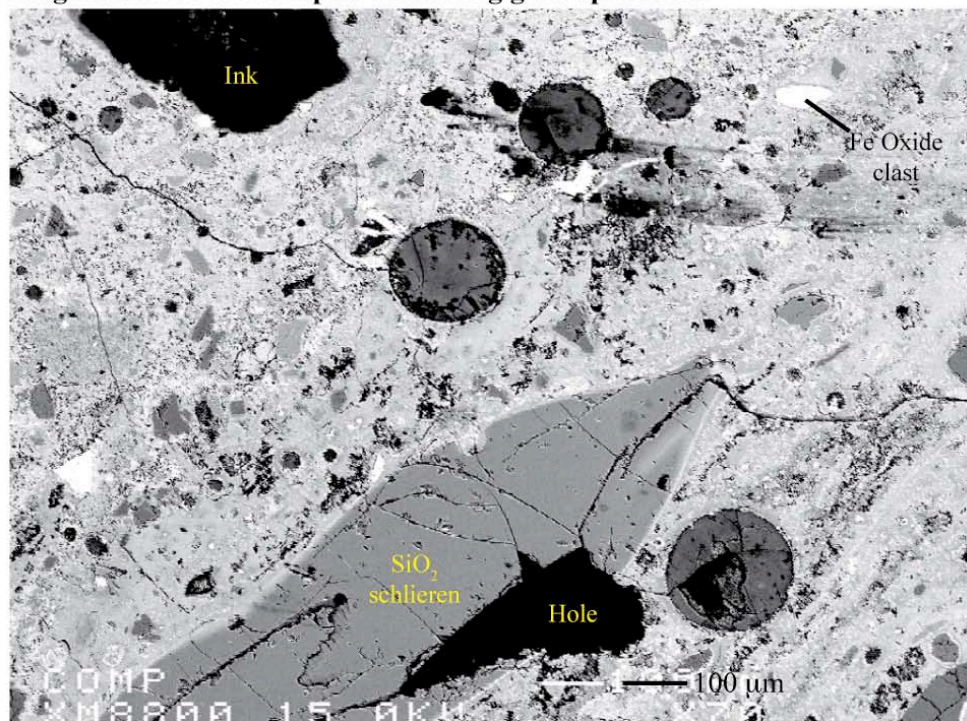
Table 6.12 Comparison of a high-MgO glass spheroid composition with Saponite.

Sample	LP-125 image 3-maf glass 6	Saponite (Deer et al., 1992)
SiO ₂ wt. %	51.95	50.25
TiO ₂	0.01	0.03
Cr ₂ O ₃	0.01	---
Al ₂ O ₃	7.67	4.44
FeO _{total}	1.67	0.50
MnO	0.02	0.02
MgO	20.56	23.81
CaO	0.74	1.70
Na ₂ O	0.39	0.76
K ₂ O	0.49	0.10
H ₂ O ⁺	---	7.25
H ₂ O ⁻	---	10.76
Total	83.51	99.69
Number of cations on the basis of X (O)		
	X = 22	X = 22
Si <i>apfu</i>	7.606	7.513
Al	0.394	0.487
Al	0.929	0.296
Ti	0.001	0.003
Fe ³⁺	0.092	0.056
Mn	0.002	0.003
Mg	4.487	5.306
Ca	0.117	0.272
Na	0.112	0.220
K	0.092	0.019
OH	4.000*	4.000
Total Cation	17.833	18.18

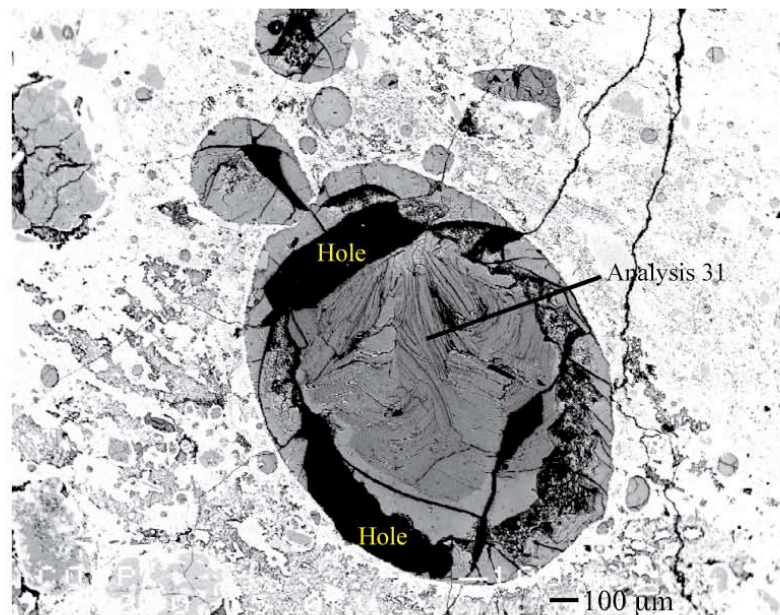
* Estimated assuming stoichiometry.

Figure 6.14 A and B Glass spheroids within samples of fragmental breccia. Image A shows four glass spheroids in a matrix composed of devitrified glass and small clasts. Note the schlieren of SiO_2 at the bottom of the image. Image B shows a “swarm” of glass spheroids. The largest spheroid appears either to be splitting apart or joining with a smaller spheroid. Note the flaky-looking material filling the center of the larger spheroid. Analysis numbers refer to the compositions listed in Table 6.11.

Fragmental breccia samples containing glass spheroids:



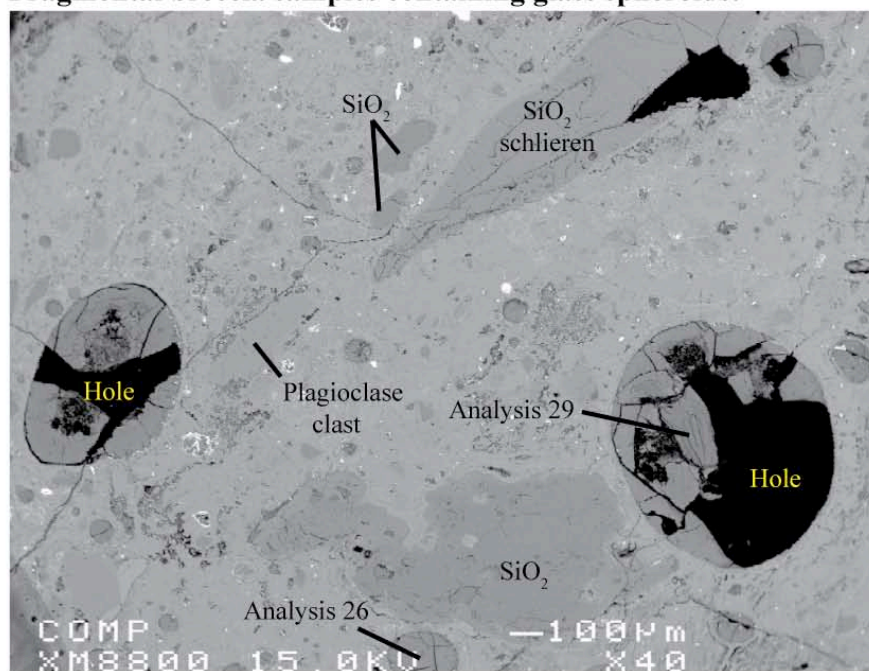
A - Back-scattered electron image of a polished thin-section of sample DCW-77-64-1.



B - Back-scattered electron image of a polished thin-section of sample DCW-77-64-5.

Figure 6.15 A and B Glass spheroids within samples of fragmental breccia. Image A shows the association between the glass spheroids and blobs and schlieren of SiO_2 . Image B shows a large glass spheroid cut by a crack filled with a material that clearly differs from that filling the glass spheroid. Please ignore the black rectangles. Analysis numbers refer to the compositions listed in Table 6.11.

Fragmental breccia samples containing glass spheroids:



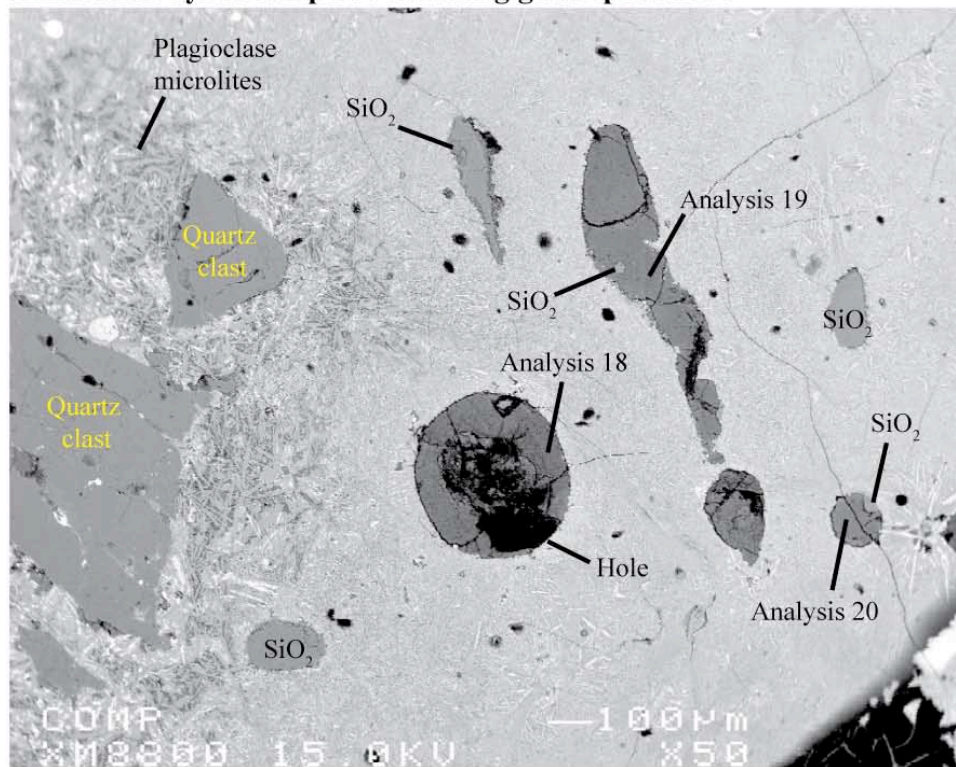
A - Back-scattered electron image of a polished thin-section of sample DCW-77-65-4.



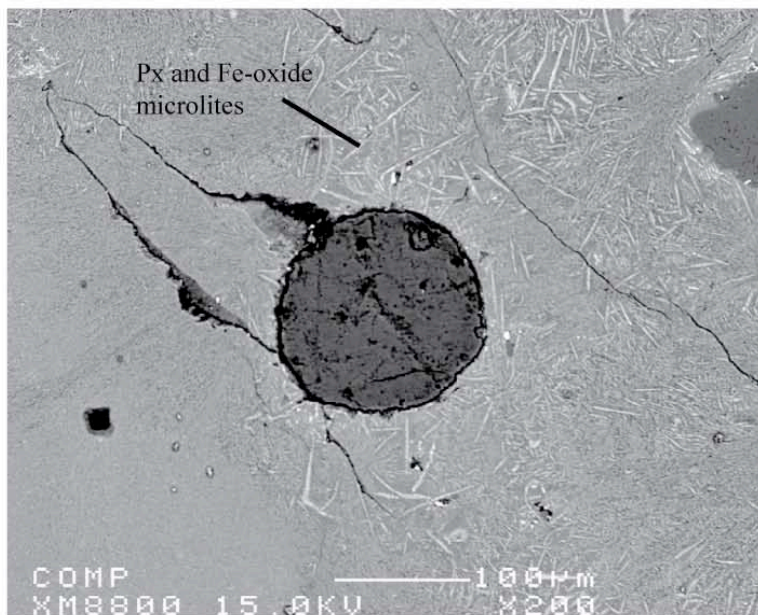
B - Back-scattered electron image of a polished thin-section of sample DCW-77-65-4.

Figure 6.16 A and B Glass spheroids within samples of infiltration dyke. Image A: glass spheroids near a deformed glass spheroid: all have the same composition. Note the abundant plagioclase microlites surrounding quartz clasts and the SiO_2 blob to the left of the deformed glass spheroid. Image B: isolated glass spheroid. Analysis numbers refer to the compositions listed in Table 6.11.

Infiltration dykes samples containing glass spheroids:



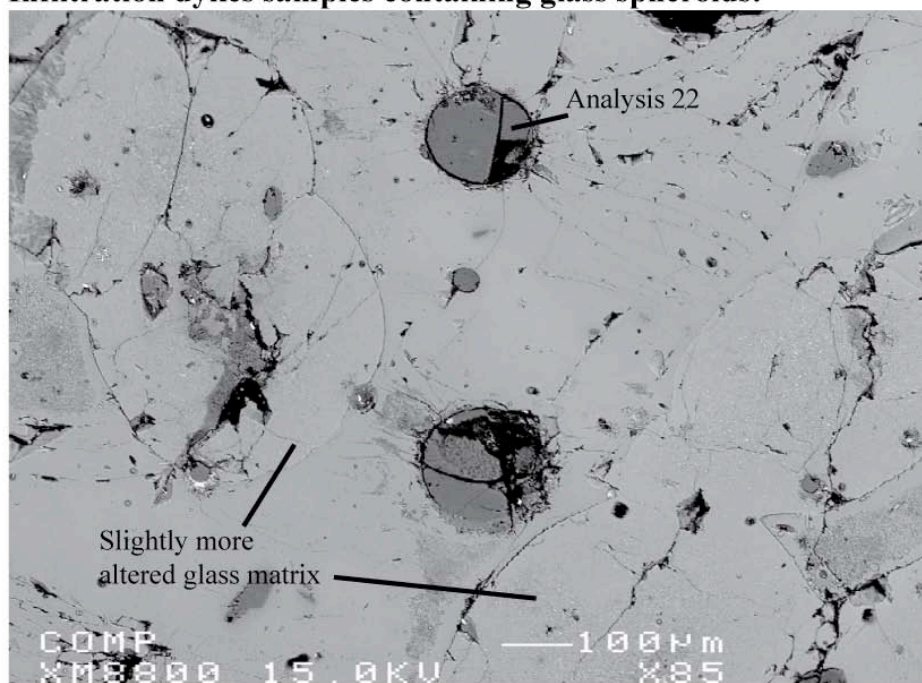
A - Back-scattered electron image of a polished thin-section of sample LP-125.



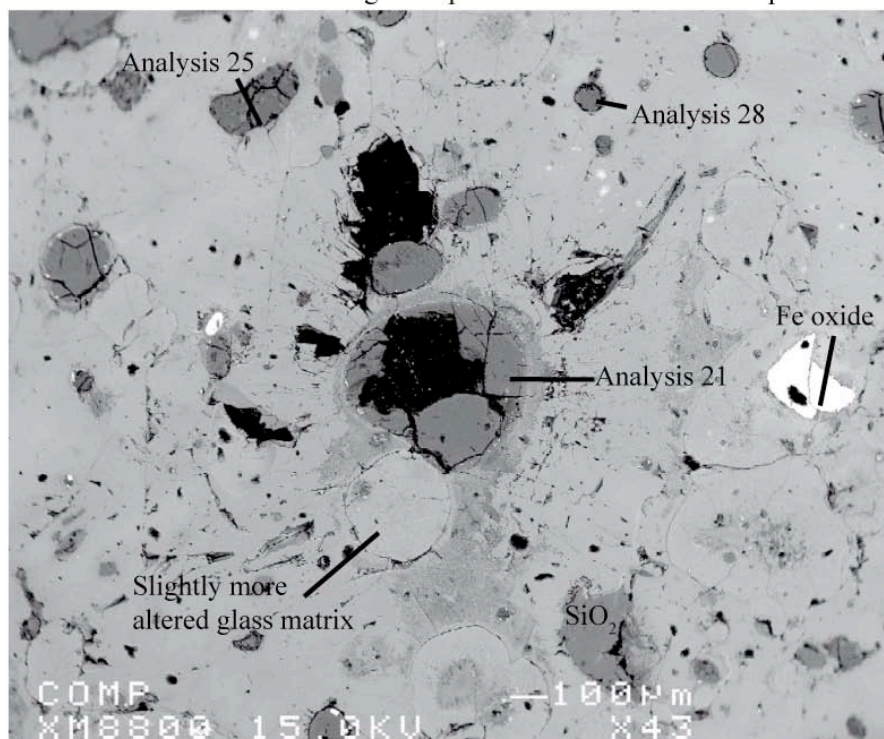
B - Back-scattered electron image of a polished thin-section of sample LP-125.

Figure 6.17 A and B Glass spheroids within samples of infiltration dyke. Images A and B: more examples of glass spheroids. Note the rounded domains of slightly more altered matrix glass. Analysis numbers refer to the compositions listed in Table 6.11.

Infiltration dykes samples containing glass spheroids:



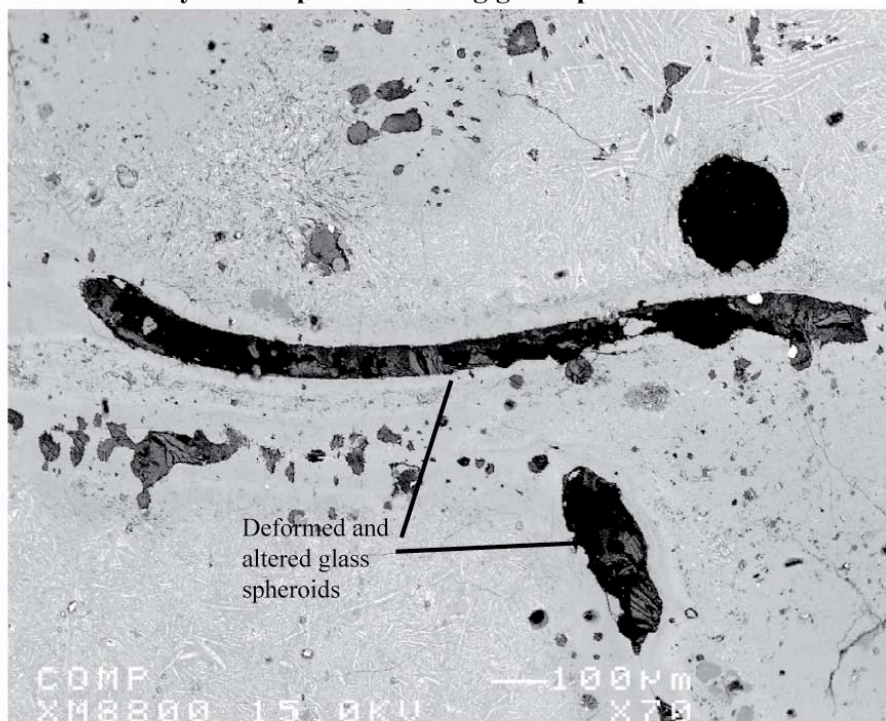
A - Back-scattered electron image of a polished thin-section of sample LP-130.



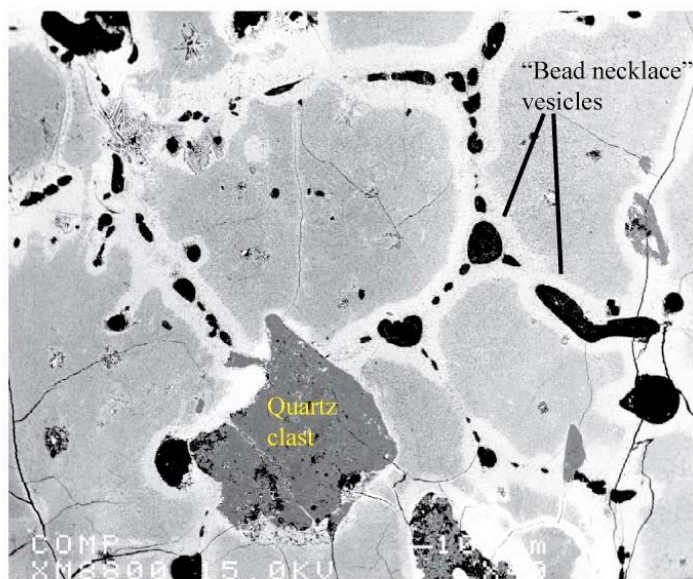
B - Back-scattered electron image of a polished thin-section of sample LP-130.

Figure 6.18 A and B Images of samples of infiltration dyke. In image A, one sees what I believe are two examples of stretched and flattened glass spheroids, almost emptied of their contents. Nearby, in the right corner, one sees what appears to be an empty glass spheroid. Image B shows “bead-necklace vesicles”, a series of vesicles of variable size that seem to follow cracks in the devitrified matrix. The elongate bead-necklace vesicles may have been formed (or enlarged) by dissolution by circulating fluids. The matrix near these vesicles is enriched in Fe, which gives, in BSE images, the usually gray matrix a white color.

Infiltration dykes samples containing glass spheroids:



A - Back-scattered electron image of deformed a polished thin-section of sample LP-125.



B - Back-scattered electron image of a polished thin-section of sample LP-94.

6.5 Summary of chapter 6

- The lowermost unit of impact related rock in the West Clearwater impact structure is the fragmental breccia, an allochthonous breccia that overlies the fractured basement, mostly composed of clastic debris with a composition similar to that of the impacted rocks mixed with glass fragments. There is a small amount of heavily altered matrix, containing abundant clays and stained red by hematite.
- The fragmental breccia is cut by dykes of impact melt that infiltrated the fragmental breccia (and the fractured Archean basement-rock) from the units of overlying impact melt. The infiltration dykes are mostly composed of quenched impact melt. They typically appear glassy, with only a few inclusions of target rock.
- Within the glass of the fragmental breccia and the infiltration dykes, there are roughly spherical droplet-like inclusions that correspond to the “glass spheroids” described in Dence et al. (1974). These “glass spheroids” are filled with clays. This finding obviously suggests that the material now filling the “glass” spheroids is secondary, the result of either the alteration of a primary material, or the filling of an empty vesicle by newly formed minerals.

Chapter 7:

Clast-rich impact melt rock and clast-poor impact melt rock

This chapter is divided in two major sections: a short section dedicated to the description of the textures, composition and mineralogy of the clast-rich impact melt, and a longer section dedicated to a detailed description of the clast-poor impact melt. The brevity of the first section is due to the difficulty in obtaining interesting mineralogical and chemical information from the very fine-grained matrix of the clast-rich impact melt. In contrast, the coarser-grained and relatively holocrystalline clast-poor melt yielded an abundance of data, which permitted a detailed study of the mineralogy of the individual phases found within the unit. Particular attention was given to the textures and compositions of the feldspars, the most abundant phases in the clast-poor melt: their attributes provide important clues regarding the petrogenesis of the clast-poor melt rock of the West Clearwater Lake impact structure. Some attention was also given to the titanium content of quartz, the last phase to crystallize from the impact melt, which, as it will be shown in the next chapter (chapter 8), can be used as a geothermometer.

7.1 Clast-rich impact melt rock

The clast-rich impact melt rock is red to purple and resembles a breccia. Like the unit below (the fragmental breccia), this unit covers the local relief like a blanket but, unlike the fragmental breccia, it has a relatively constant thickness of ~15 to ~18 meters. Compared to the fragmental breccia, the clast-rich melt is much more coherent, it contains fewer clasts (roughly 25% of the fragments are coarser than 1 mm), and its

matrix, unlike that in the fragmental breccia, has enough melted material to weld the clasts together.

As already mentioned, a quite sharp and easily visible chilled margin marks the lower limit of the clast-rich melt rock, that is, its contact with the fragmental breccia. The upper contact with the clast-poor impact melt has been defined by Phinney et al. (1978) as the location of a sudden decrease in clast content that persists into the clast-poor impact melt rock; subangular lithic clasts < 1 m across are more abundant near the basal contact, and the transition from clast-rich to clast-poor melt rock invariably takes place over a vertical distance of less than 3 m (Phinney et al. 1978).

According to Simonds et al. (1978), most of the clastic debris is concentrated at the base of the melt sheet: about 1% of these clasts are more than one meter across, and clasts in the 1 cm to 1 m range make up around 10% of the unit in the lowermost few meters, falling off to about 1% in areas more than 15 meters from the base. It is in this part of the clast-rich impact melt that the greatest abundance of impact-shocked material is found. In particular, Rondot et al. (1993) mentioned small masses of black glass with flow texture “resembling anthracite” (they were probably describing obsidian-like glass) and in some cases engulfing numerous granitic fragments.

I have characterized thirteen samples of clast-rich impact melt: ten of these samples were collected in 1977 by M.R. Dence (samples with the DCW prefix); the remaining three (LP-34, LP-45 and LP-95) were collected by Langis Plante of Laval University. Five samples were collected on Lepage Island, four samples come from Drillers Island, two samples are from Marie-Claire Island, two others were collected on Atkinson Island and one sample was obtained on the southernmost Tadpole Island (Appendix C). Tables 7.1 and 7.2 provide bulk-rock compositions (major and trace

elements) that are typical of this unit. Figure 7.4 shows their compositional variation relative to SiO_2 . Once again, as for the fragmental breccia, I attempted to analyze as much matrix as I possibly could. Nevertheless, because of the clast-rich nature of these rocks, it is inevitable that a certain amount of clasts were included in the material sampled.

Clasts usually compose ~40 to ~60% of most samples. Like in the fragmental breccia, clasts are lithic fragments and mineral debris of variable size derived from the basement rocks. Fragments of monocrystalline quartz are typically most abundant, but I have also observed polycrystalline quartz fragments, plagioclase and alkali feldspar, and in some cases, biotite, pyroxene and opaque iron oxides. Unlike most clasts in the underlying fragmental breccia, clasts in the clast-rich impact melt rock typically show various degrees of reaction with the matrix: I have observed in numerous cases reaction coronas made of tiny crystals of augite, alkali feldspar and quartz rimming quartz clasts, and partially resorbed plagioclase clasts displaying a sieve texture are common.

In most of the thin sections of clast-rich impact melt rock, the matrix is rust-red or dark brown, nearly extinct under crossed polars, and very fine grained (grain size $<10\ \mu\text{m}$ across). At high magnification, plagioclase laths and small blocky pyroxene crystals show an interstitial texture, with tiny grains of iron oxide and variable amounts of brown glass also present; in some thin sections, I have also observed blocky or acicular oxides and even interstitial quartz.

The matrix generally occupies 60-40% of the thin sections of clast-rich impact melt rock. In samples DCW-77-58 and LP-95-4, however, the matrix composes more than ~80% of the thin section, whereas in sample LP-45-3, ~90% of the thin section is

Table 7.1 - Major element compositions of chosen clast-rich impact melt rock samples from West Clearwater compared to average clast-rich melt rock and average impact melt rock, that is clast-rich plus clast-poor impact melt rock.

Rock Unit						Average clast-rich impact melt rock		Average impact melt rock	
Sample	DCW-77-13	DCW-77-55	DCW-77-58	LP-34	LP-45-3	n = 14		n = 46	
						aver.	max.-min.	aver.	max.-min.
SiO ₂ (%)	62.07	58.09	60.92	60.56	62.96	60.65	62.96-58.09	60.90	62.96-58.09
TiO ₂	0.65	1.09	0.79	0.89	0.88	0.77	1.09-0.61	0.77	1.09-0.61
Al ₂ O ₃	15.83	16.26	15.96	15.94	15.23	16.09	17.27-14.95	15.87	17.27-14.95
Cr ₂ O ₃	0.01	0.01	0.01	0.01	0.01	0.01	0.02-0.01	0.01	0.02-0.01
Fe ₂ O ₃	5.51*	7.87*	6.11*	6.93*	5.74*	6.19*	7.87-5.09	6.17*	7.87-5.09
FeO	---	---	---	---	---	---	---	---	---
MnO	0.05	0.10	0.07	0.06	0.04	0.06	0.10-0.03	0.06	0.15-0.03
MgO	2.66	3.13	3.08	2.39	2.28	2.79	4.20-2.28	2.75	4.20-2.28
CaO	4.18	4.56	4.54	4.11	3.02	4.22	6.61-3.02	4.46	6.61-3.02
Na ₂ O	3.71	3.83	3.90	3.95	3.66	3.84	4.30-3.49	3.76	4.30-3.49
K ₂ O	3.30	3.17	3.32	3.72	4.31	3.42	4.31-2.88	3.50	4.31-2.88
P ₂ O ₅	0.25	0.49	0.30	0.38	0.38	0.31	0.49-0.22	0.30	0.49-0.22
L.O.I.	1.75	1.42	1.03	1.40	1.26	1.69	2.78-1.03	1.55	2.78-0.89
Total	100.11	100.17	100.17	100.49	99.94	100.19	100.42-99.93	100.24	100.63-99.79

* Total iron as Fe₂O₃. L.O.I. – Lost On Ignition

Table 7.2 – Trace element compositions of chosen clast-rich impact melt rock samples from West Clearwater.

Rock Unit						Average clast-rich impact melt rock		Average impact melt rock	
Sample	DCW-77-13	DCW-77-55	DCW-77-58	LP-34	LP-45-3	n = 14		n = 46	
						aver.	max.-min.	aver.	max.-min.
Ba (ppm)	1164	1190	1162	1237	1465	1199	1555-872	1191	1555-872
Ce	61	114	74	109	160	73	160-28	74	160-28
Co	16	12	11	12	13	11	18-<d/l	11	18-<d/l
Cu	26	45	35	37	24	33	73-20	33	78-14
Ni	36	36	36	30	22	32	63-22	32	63-22
Sc	<d/l	<d/l	<d/l	<d/l	<d/l	2	12-<d/l	1	13-<d/l
V	83	129	98	84	91	92	141-73	93	141-73
Zn	17	14	<d/l	22	2	14	44-<d/l	16	63--<d/l

made up of clasts. In sample LP-95-4, most of the thin section is occupied by a matrix made of oxide microlites (tiny acicular or feathery crystals typically 0.2 or 0.3 mm across) and blocky or lath-like plagioclase microlites of comparable size. The thin section is composed of about 10% clasts, some of which appear partially melted, showing indistinct margins and resorption-induced embayments. At least one vesicle (~1 mm across) is visible: its interior wall is covered in a concentric layer which, at the contact with the matrix, is composed of a glassy sand-coloured material (possibly devitrified glass) that becomes dark brown inward, with laths arranged radially away from the contact. About 30% of the matrix of sample DCW-77-58 is very fine grained, nearly cryptocrystalline and of gray colour, with abundant small clasts (less than 0.1 mm across) of quartz and pyroxene and rounded vacuoles of varying sizes (the largest is ~5 mm across, but most are 0.5 mm across or less). About 60% of the matrix of this thin section is rust red and filled with abundant laths of acicular plagioclase about 3 mm long forming a pilotaxitic to hyalopilitic texture. This portion of the matrix contains very few clasts, and no vesicles.

Because of the small size of the microlites (usually less than 10 μm), it was generally challenging to obtain reliable compositions of the feldspar and the pyroxene using an electron microprobe in the matrix: many of the totals are low, and the SiO_2 contents in many cases are too high. However, I was able to obtain a few reliable feldspar compositions from microlites in sample DCW-77-58. Their composition is very variable ($\text{An}_{53-13}\text{Ab}_{57-44}\text{Or}_{38-4}$), and at least two compositions are almost in the miscibility gap in the ternary system An-Ab-Or (Figure 7.1). Phinney et al. (1978) had similar problems obtaining reliable compositions for the feldspars and pyroxenes in the matrix of the clast-rich melt rock. Nevertheless, they were able to estimate these compositions qualitatively using the energy-dispersive spectra (EDS) that they acquired with a scanning electron microscope. The range of compositions obtained by them is presented in Figure 7.2. Note that the six compositions I obtained with the electron microprobe fall within the range that they observed (see Figure 7.1). Also note that many of their compositions are situated in the miscibility gap in the three-component system Ab-Or-An. This may be the result of rapid cooling, which froze into place compositions that normally should not be stable.

Texturally, samples of clast-rich impact melt rock resemble fragmental breccia samples: they both have high clast contents and similar colours. However, resorption textures and reaction coronas, which are relatively rare in fragmental breccia samples, are generally much more commonly developed here (Figure 7.3). Also, fluidal textures, with alignment of rock and mineral fragments, although not absent in the thin sections of clast-rich impact melt rock, are far more abundant in the fragmental breccia. Finally, the matrix of the fragmental breccia is mostly composed of glass and tiny clasts, typically

Figure 7.1 - Composition of feldspar microlites from the matrix of the clast-rich impact melt rock

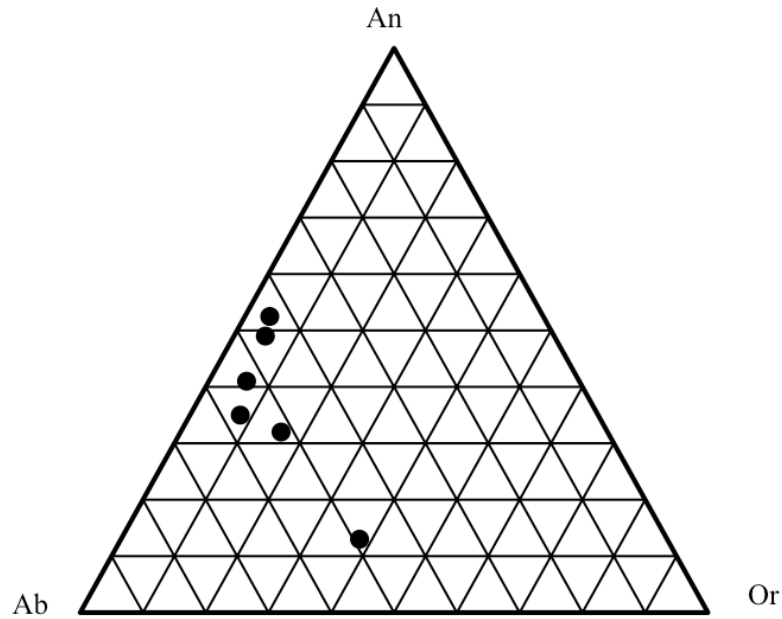


Figure 7.2 Range of feldspar compositions in the very fine-grained matrix of the clast-rich impact melt rock of the West Clearwater impact structure. Modified from Phinney et al. (1978).

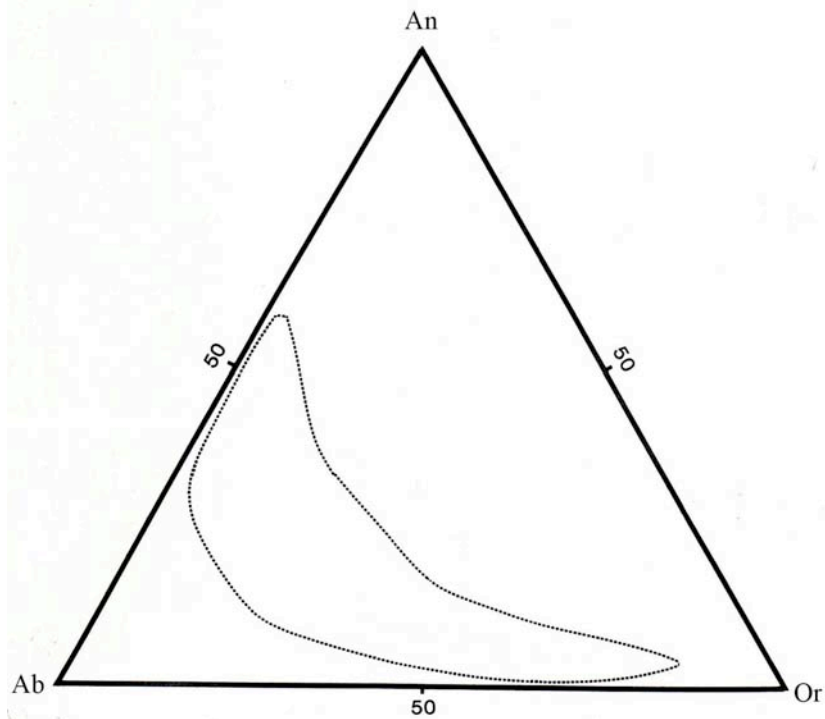
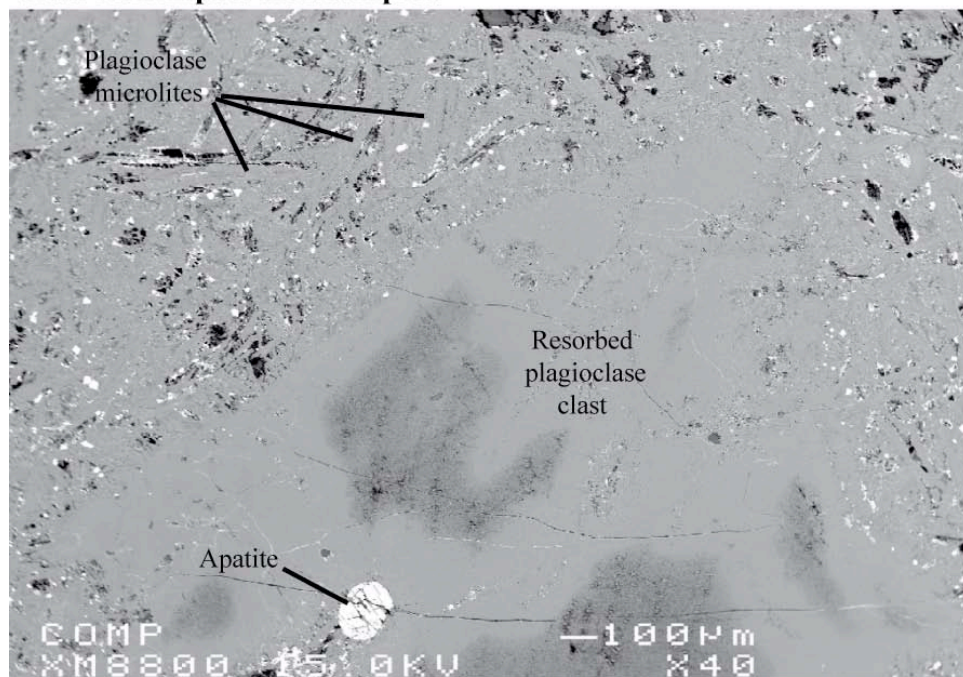
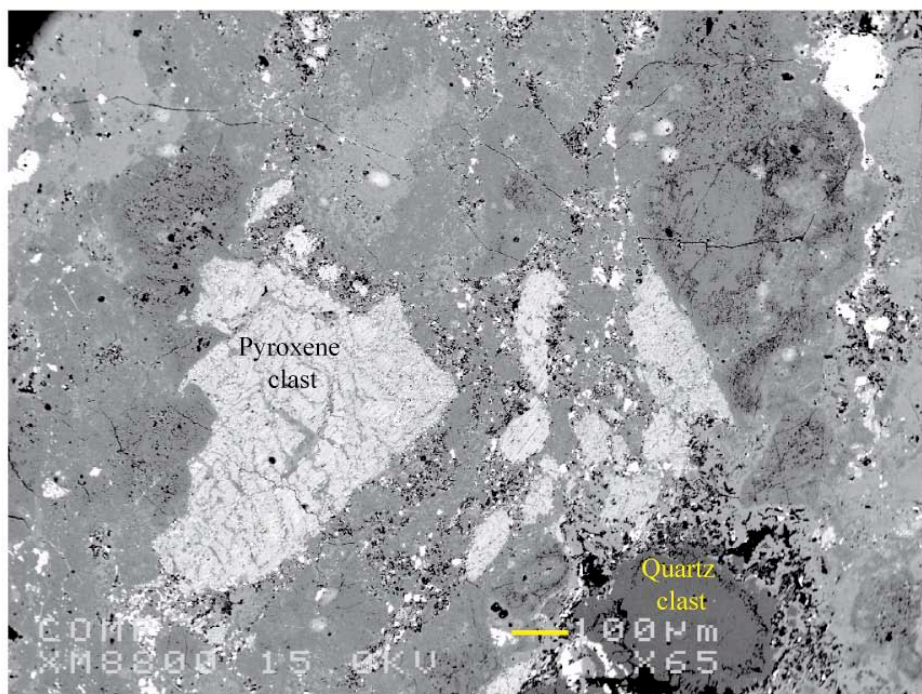


Figure 7.3 A and B Images of clast-rich impact melt rock. Image A: nearly completely resorbed plagioclase clast in a matrix of stubby plagioclase microlites and tiny, round Fe oxide crystals. Image B shows broken-up pyroxene clasts, feldspar clasts and, at the bottom, a subrounded quartz clast rimmed by a reaction corona. The matrix consists of devitrified glass, with a few microlites of plagioclase and Fe oxides.

Clast-rich impact melt samples:

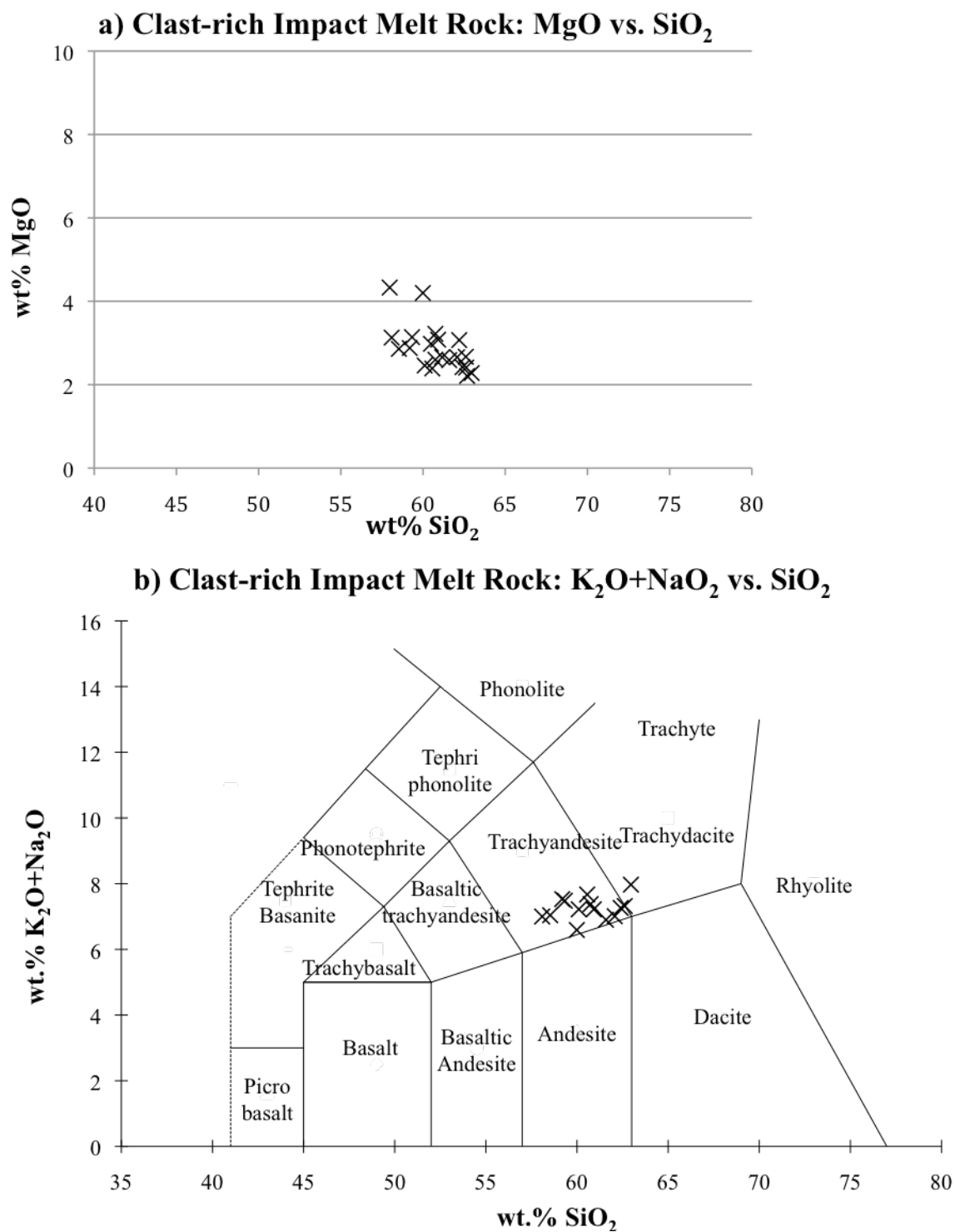


A - Back-scattered electron image of a polished thin-section of sample DCW-77-58.



B - Back-scattered electron image of a polished thin-section of sample LP-45-3.

Figure 7.4 a and b Compositional variation in samples of clast-rich impact melt rock from the West Clearwater Lake impact structure (n = 14).



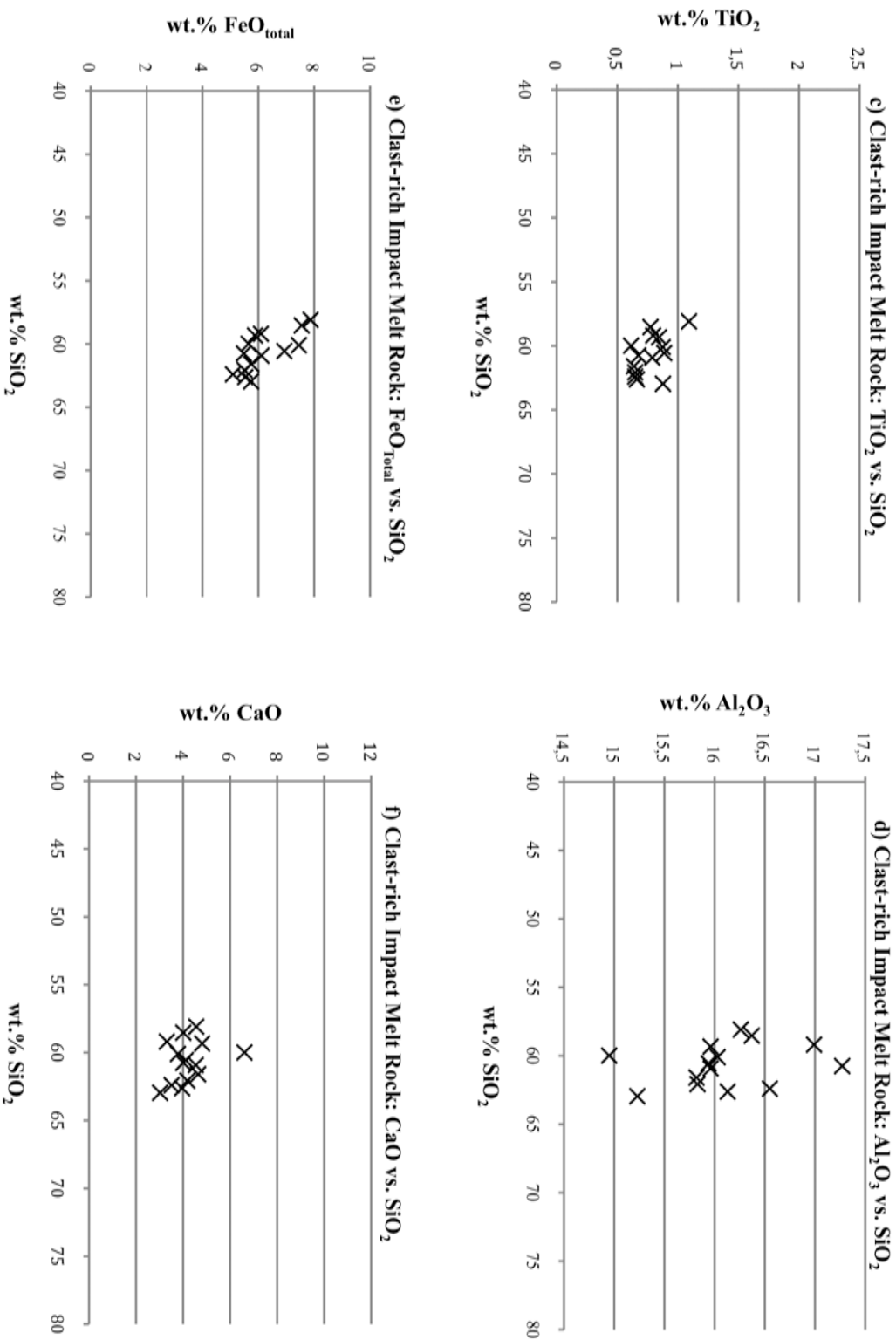


Figure 7.4 c to f – Compositional variation in samples of clast-rich impact melt rock from the West Clearwater Lake impact structure (n=14)

partially or totally altered to clay minerals, whereas the matrix of the clast-rich impact melt rock is composed of very fine-grained plagioclase and pyroxene showing an intergranular to intersertal texture and numerous patches of generally altered glass mixed in with small clasts.

I interpret the abundance of glass and the comparative scarcity of resorption features and reaction rims in the fragmental breccia as indications that it cooled rapidly, and was consequently unable to crystallize minerals or react with clasts. The matrix of the clast-rich impact melt rock, however, stayed hot for long enough to crystallize visibly, and it was able to react with the abundant clasts embedded in it. By its mineralogy and texture, the matrix of the crystallized clast-rich impact melt rock resembles a finer-grained version of the clast-poor impact melt rock, to be described in section 7.2.

7.2 Clast-poor impact melt rock

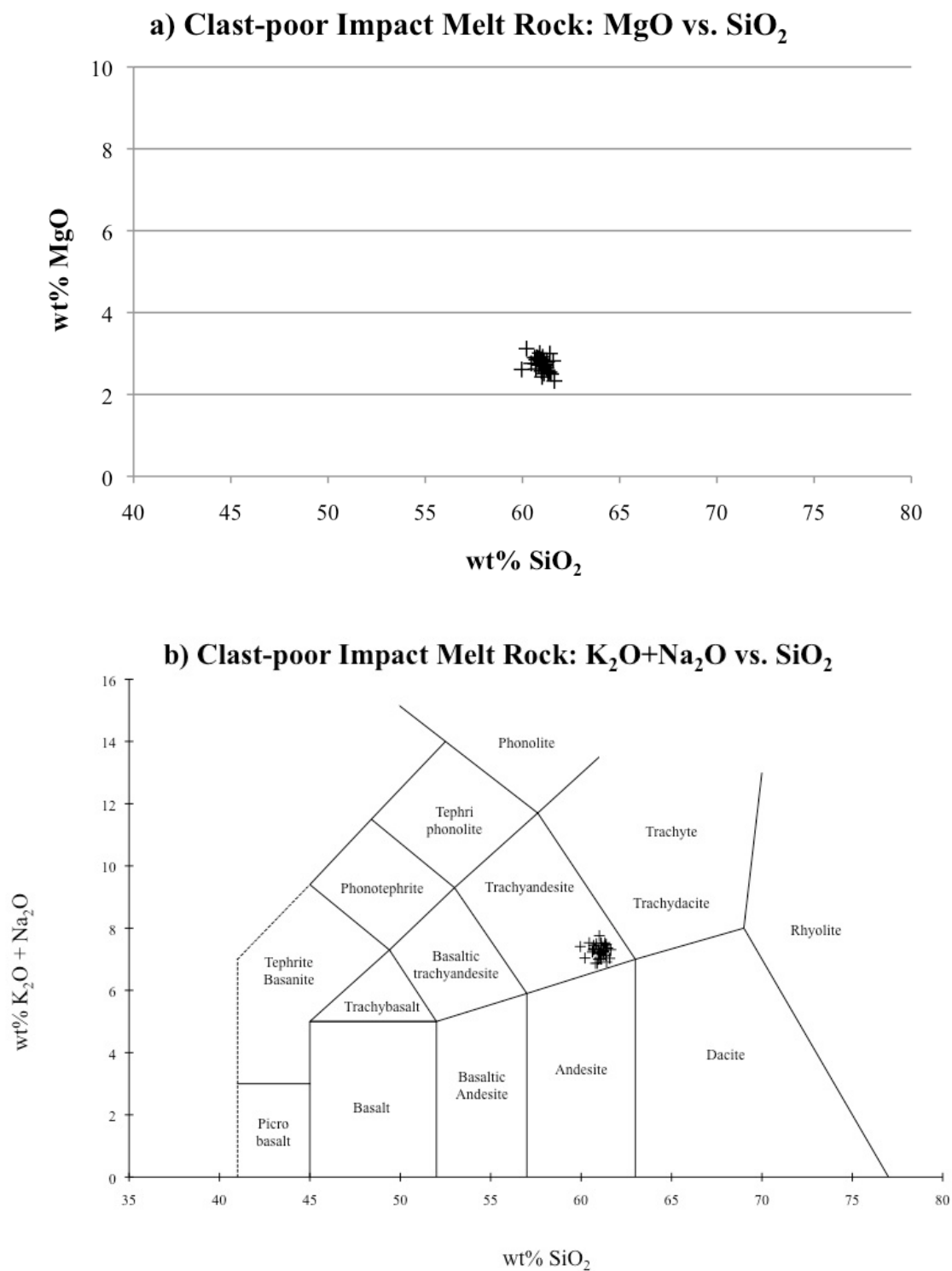
The clast-poor melt rock is a gray, light brown or reddish rock unit that contains less than 15% clasts larger than 1 mm across (Simonds et al., 1978b). The coarser grain-size, lower clast content and almost holocrystalline aspect of clast-poor impact melt rock readily distinguished it from the clast-rich impact melt rock. This unit has a maximum preserved thickness of about 85 m, and it occurs at all the highest points of the West Clearwater Lake ring of islands (Grieve, 2006; Rondot et al., 1993). Because clast content decreases and grain size of crystals in the rock increase upward to the eroded top, it is clear that a large amount of the clast-poor melt rock unit was lost to erosion: Phinney and Simonds (1977) assumed that the melt sheet was originally at least twice as thick as at present.

In the higher parts of this unit, the rocks are normally gray, but become sand colored where weathered, whereas only the rocks near the contact with the underlying

clast-rich melt sheet have been oxidized to either reddish or purple colours. Like the underlying impact-generated units of the West Clearwater impact structure, the clast-poor impact melt mantles the irregular relief of the fractured basement. The transition from clast-rich melt rock to clast-poor melt rock invariably takes place over a vertical distance of less than 3 meters (Phinney et al. 1978). The base of the sheet of clast-poor melt, where it abuts against the underlying clast-rich melt rock, is described as “locally displaying a knife-edge contact” by Simonds et al. (1978). This contact shows the 0.5° dip towards the center of the impact structure, similar to the contacts of the lower units.

My descriptions are based on thirty-two surface samples of clast-poor melt. Twenty-five of these samples were collected by M.R. Dence in 1977 (DCW prefix), six were collected by Langis Plante (LP prefix), and one has been obtained by me (sample DR-010). Samples of clast-poor melt were collected on all the major islands of the West Clearwater ring of islands: eight samples come from Atkinson Island, Drillers Island accounts for eleven samples, eleven samples come from Lepage Island, one sample was collected on the northernmost Tadpole Island and another sample came from the southernmost Tadpole Island. These samples cover the entire height of the present exposure of impact melt, from near the contact with the clast-rich melt to hilltops on Atkinson and Drillers islands (see the maps detailing the approximate location of the samples presented in Appendix C). Major and trace element compositions of the clast-poor impact melt rock are given in Tables 6.1, 6.2 and 6.3. Figure 7.5 shows the compositional variation relative to SiO₂ of these samples.

Figure 7.5 a and b Compositional variation in samples of clast-poor impact melt rock from the West Clearwater Lake impact structure (n = 32).



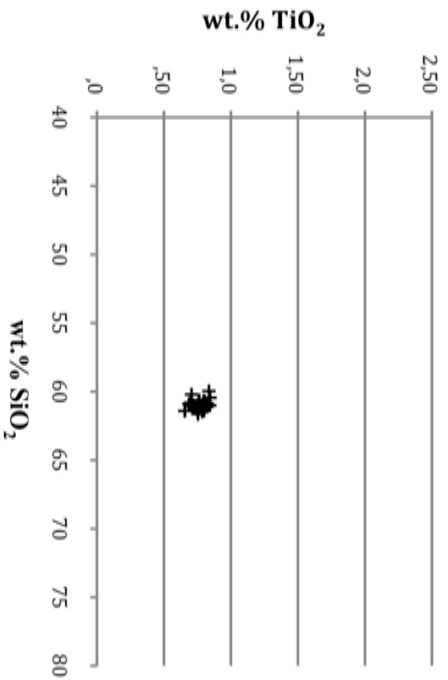
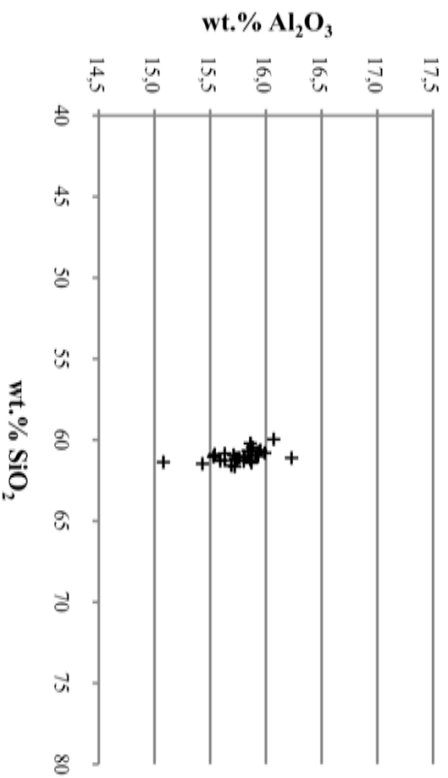
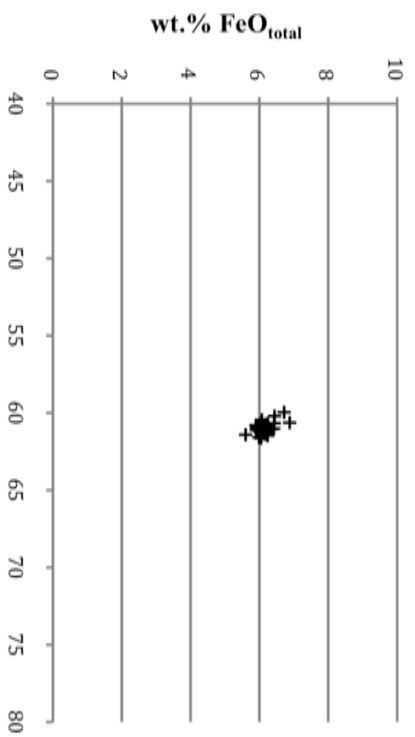
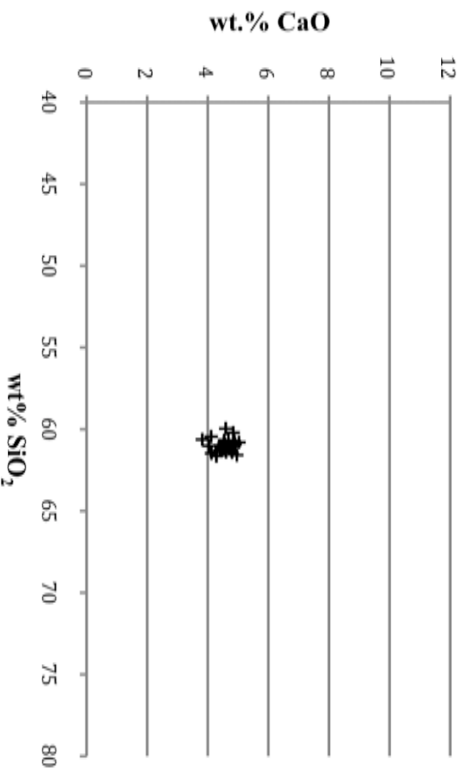
c) Clast-poor Impact Melt Rock: TiO_2 vs. SiO_2 d) Clast-poor Impact Melt Rock: Al_2O_3 vs. SiO_2 e) Clast-poor Impact Melt Rock: $\text{FeO}_{\text{Total}}$ vs. SiO_2 f) Clast-poor Impact Melt Rock: CaO vs. SiO_2 

Figure 7.5 c to f – Compositional variation in samples of clast-poor impact melt rock from the West Clearwater Lake impact structure ($n=32$).

At the base of the unit, the rock typically is fine-grained, with an obvious clast-matrix texture similar to that of the clast-rich impact melt. The proportion of clasts in the clast-poor impact melt is at its highest at the base of the unit, where it can reach about 35%. Almost all the clasts are composed of quartz and feldspar crystals (remnants of mafic minerals are rarely observed), and lithic fragments of mostly granitic composition are visible only in the bottom 15 meters of the unit. The fragments show an increasing degree of recrystallization or resorption as the distance from the bottom of the unit increases.

As the clast content decreases and the grain size increases upward, the unit gradually develops a coarser-grained, diabasic to subophitic texture (Figure 7.9, p. 173). The entirely crystalline matrix of the clast-poor melt rock is essentially composed of plagioclase, alkali feldspar, pyroxene, quartz and opaque iron-titanium oxides.

7.2.1 Feldspars

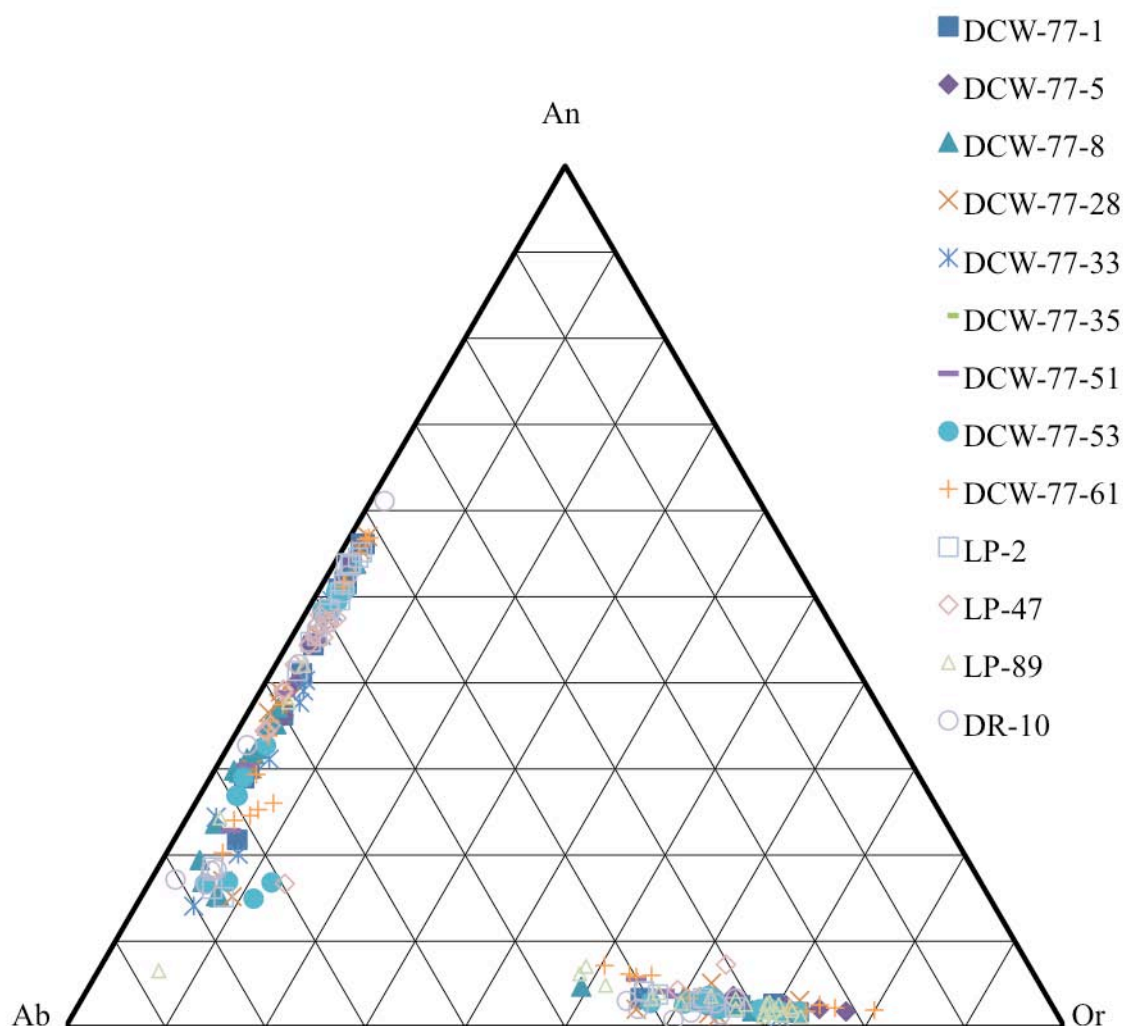
The clast-poor impact melt rock contains both plagioclase and alkali feldspar. The feldspar minerals in the clast-poor melt rock are closely associated in composite grains, with alkali feldspar typically mantling the plagioclase. Because of this texture, the two feldspars are generally difficult to differentiate; they will therefore be treated together.

Feldspars are, by far, the most common minerals in the clast-poor impact melt rock, typically forming ~70% or more of the matrix. The range of compositions of the plagioclase is quite wide, going from labradorite to oligoclase ($\text{An}_{61-7}\text{Ab}_{87-38}\text{Or}_{14-1}$); the range of alkali feldspar compositions is somewhat narrower: $\text{An}_{7-1}\text{Ab}_{46-21}\text{Or}_{80-48}$ (Figures 7.6). Because sanidine is characteristic of rocks that cooled quickly from an

Table 7.3 – Representative compositions of the feldspars found in the clast-poor impact melt rocks of the West Clearwater Lake Impact Structure.

Sample	DCW-77-28- R3-Kspar 1 (Sanidine rim)	DCW-77-61- R1-Feldspar 11 (Sanidine Rim)	DR-10-R2-8 (Transition zone plagioclase)	DCW-77-51- Region 4- Feldspar 5 (Melt plag.)	DCW-77-53- R1-Feldspar 7 (Melt plag.)	DCW-77-61- R3-Feldspar 8 (Relict plag. core)	DCW-77-33- R2-Feldspar 11 (Relict plag. core)	LP-47-Region 1- Plag 7 (Plagioclase lath)
SiO ₂ wt. %	65.56	65.43	64.00	56.69	55.49	61.60	60.17	56.50
TiO ₂	0.05	0.12	0.12	0.04	0.08	0.12	0.08	0.08
Cr ₂ O ₃	0.02	0.00	0.04	0.03	0.01	0.00	0.00	0.00
Al ₂ O ₃	18.80	18.54	22.03	26.47	27.04	23.03	23.97	26.40
FeO _{total}	0.22	0.19	0.42	0.74	0.80	0.42	0.48	0.67
MnO	0.02	0.00	0.00	0.00	0.02	0.01	0.00	0.01
MgO	0.00	0.00	0.00	0.04	0.05	0.02	0.03	0.20
CaO	0.42	0.38	3.44	9.22	9.95	5.23	6.41	9.41
Na ₂ O	4.66	2.86	8.88	5.93	5.36	7.35	7.28	5.92
K ₂ O	9.48	12.73	1.01	0.45	0.42	1.32	0.83	0.55
Total	99.24	100.25	99.93	99.60	99.21	99.08	99.24	99.76
Number of cations on the basis of X (O)								
	X = 8	X = 8	X = 8	X = 8	X = 8	X = 8	X = 8	X = 8
Si <i>apfu</i>	2.985	2.987	2.837	2.564	2.525	2.768	2.708	2.556
Ti	0.002	0.004	0.004	0.001	0.003	0.004	0.003	0.003
Cr	0.001	0.000	0.001	0.001	0.000	0.000	0.000	0.000
Al	1.009	0.997	1.151	1.411	1.450	1.220	1.271	1.407
Fe	0.008	0.007	0.016	0.028	0.030	0.016	0.018	0.025
Mn	0.001	0.000	0.000	0.000	0.001	0.000	0.000	0.000
Mg	0.000	0.000	0.000	0.003	0.003	0.001	0.002	0.014
Ca	0.021	0.019	0.163	0.447	0.485	0.252	0.309	0.456
Na	0.411	0.253	0.763	0.520	0.473	0.640	0.635	0.519
K	0.551	0.741	0.057	0.026	0.024	0.076	0.048	0.032
Ni	0.000	0.000	0.000	0.000	0.000	0.000	0.000	0.000
Total Cation	4.989	5.008	4.993	5.001	4.995	4.976	4.995	5.013
Or	56.1	73.1	5.8	2.6	2.5	7.8	4.8	3.2
Ab	41.8	25.0	77.6	52.4	48.1	66.2	64.0	51.6
An	2.1	1.8	16.6	45.0	49.4	26.0	31.2	45.3

Figure 7.6 Range of mineral compositions for all feldspars in the clast-poor impact melt unit of the West Clearwater Lake impact structure (N=227).



initial high temperature, I am assuming that the alkali feldspar present in the clast-poor impact melt rock is sanidine solid-solution.

Individual crystals of plagioclase either form finer-grained unzoned euhedral to subhedral laths, or zoned coarse-grained subhedral to anhedral grains. The finer-grained lath-like euhedral plagioclase crystals are typically ~0.1 to 0.3 mm across by ~0.3 to 0.5 mm in length, and they usually display polysynthetic twinning. Unlike the larger

plagioclase crystals described below, the finer-grained lath-like plagioclase either has a thin rim of sanidine, or no rim at all. Laths are typically calcium-rich, and their compositional range is $\sim\text{An}_{61-42}$ (Figure 7.12).

The larger, blocky or rounded subhedral plagioclase crystals are about 0.5 to 1 mm across, and they are commonly normally zoned. Many of these larger grains of plagioclase have a core with a relatively Na-rich composition ($\sim\text{An}_{55-17}$) that shows a sieve texture (Figure 7.9 B). Discontinuities in the usually poorly developed polysynthetic twinning at the irregular core boundary suggest that partial resorption has taken place. Others exhibit a vague, irregularly zoned core with a calcium-rich composition, which may either be a “ghost” of former Na-rich core, or sections cut through the Ca-rich rim surrounding a more sodic core (see paragraph below). These cores are typically surrounded by an optically distinct thin rim of untwinned plagioclase with a relatively narrow range of calcium-rich compositions (An_{61-44}) (Figures 7.8 and 7.9 B). Note that the compositional range of this plagioclase rim is quite similar to that of the plagioclase laths described above, which was $\sim\text{An}_{61-42}$. This has led me to believe that this rim is, in fact, plagioclase that, like the laths, crystallized from the melt (that is, “melt-derived plagioclase”), whereas the Na-rich cores must be relict plagioclase clasts, i.e., xenocrysts.

This calcium-rich rim is, in turn, surrounded by another rim that commonly forms either an irregular overgrowth or a comb-like assemblage of tiny plagioclase spines intergrown with sanidine oriented perpendicularly to the contact between the overgrowth and the calcic rim; Figure 7.9 B shows a particularly well-developed example of this comb texture. The composition of this rim is quite variable, but it is generally sodium-rich (An_{44-14}) (Figure 7.10, p.174).

Figure 7.7 - Range of compositions in confirmed relict xenocrysts in the clast-poor impact melt unit of the West Clearwater Lake impact structure (N=17).

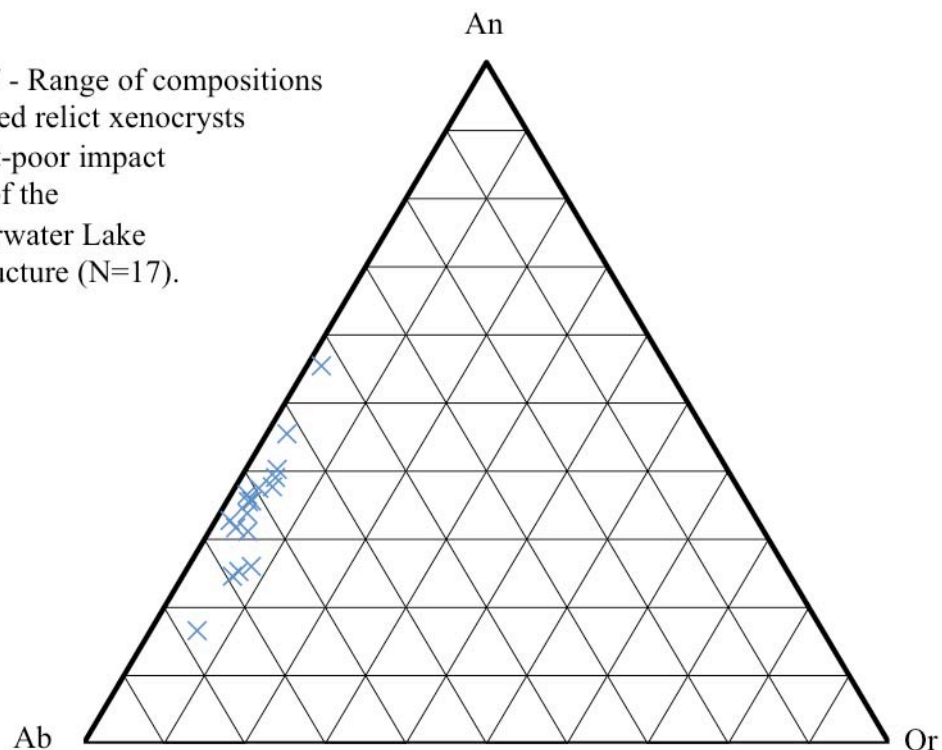
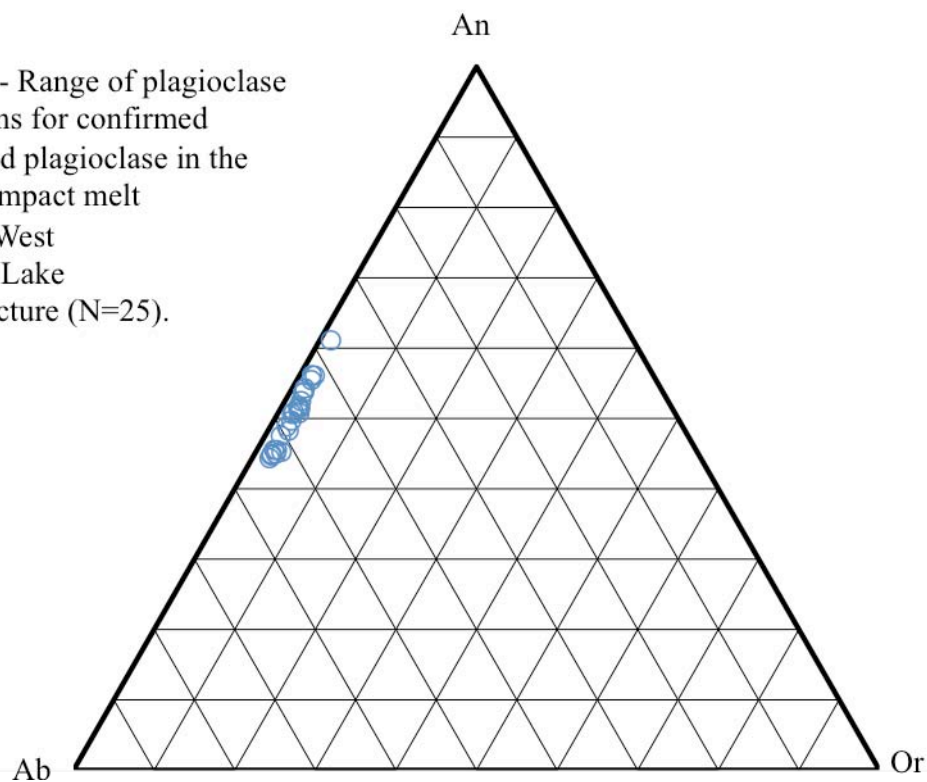


Figure 7.8 - Range of plagioclase compositions for confirmed melt-derived plagioclase in the clast-poor impact melt unit of the West Clearwater Lake impact structure (N=25).



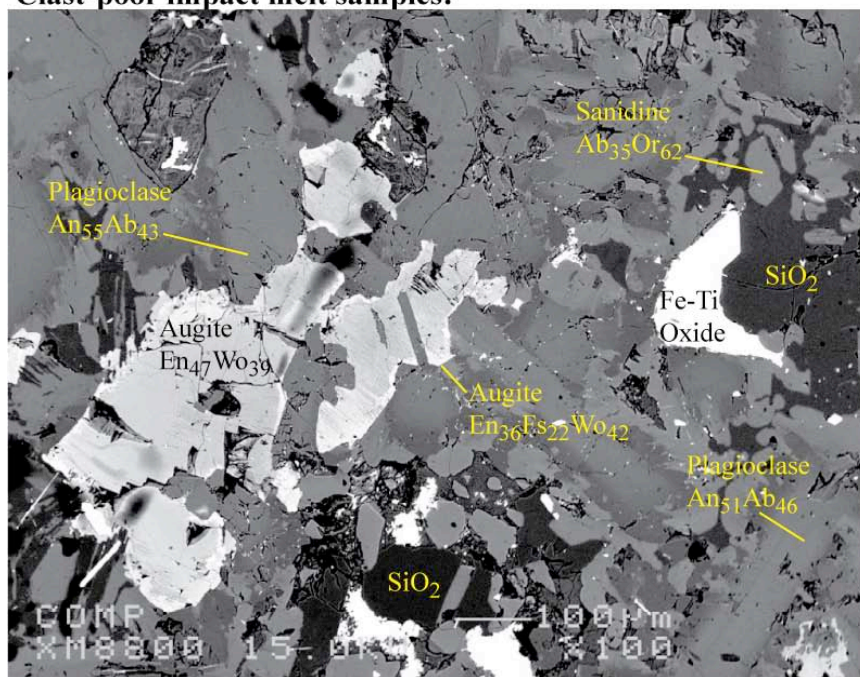
This comb-like overgrowth is intergrown and mantled by a thick rim of anhedral to subhedral sanidine that typically extends to patches of interstitial quartz, which must have been the last phase to crystallize from the melt. The comb texture at the contact between the sanidine rim and the external plagioclase rim closely resembles the plagioclase-sanidine intergrowths that were grown synthetically by Lofgren and Gooley (1977), who concluded that they were formed by simultaneous crystallization from the melt (see section 9.3 in chapter 9). I have called this region the “transition zone” between plagioclase and sanidine, and the plagioclase within it “transition-zone plagioclase”.

The sanidine rims range in composition from Or₅₀ to Or₇₇ (Figure 7.11). The wide compositional variation of this alkali feldspar may be due in part to the probe analysis: a number of the points I analyzed are near the sanidine-plagioclase boundary, and may represent average compositions of the feldspar intergrowths. Because of this close relation to the transition-zone plagioclase, the amount of sanidine is hard to estimate, but it typically must represent ~20% of the matrix.

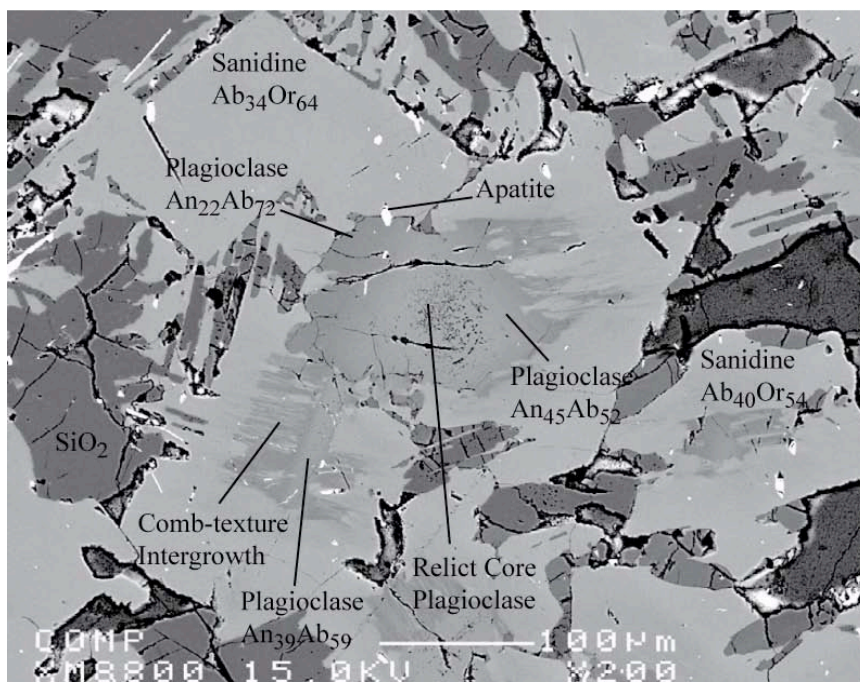
The relations between these different feldspar compositions are illustrated in Figures 7.13 to 7.16. These figures represent microprobe traverses across a variety of larger feldspar crystals displaying a number of core-rim arrangements. Both figures 7.13 and 7.14 show a partially resorbed central Ca-rich core surrounded by a rim of melt-derived plagioclase and melt-derived sanidine. The grain in figures 7.13 displays a relatively thick transition zone between the melt-derived plagioclase rim and the melt-derived sanidine. Figure 7.14 shows a poikilitic feldspar grain: resorption of the original clast may have created the sieve-like texture. The grain may have been infiltrated by

Figure 7.9 A and B Images of clast-poor impact melt rock. Image A: hypidiomorphic granular texture typical of the clast-poor impact melt rock. Augite and plagioclase occur in ophitic to subophitic intergrowth, sanidine mantles plagioclase and quartz is interstitial. The white mineral is a Fe-Ti oxide. Image B: plagioclase xenocryst mantled by newer plagioclase and then sanidine; a complex comb-texture intergrowth developed at the contact between the newer feldspars.

Clast-poor impact melt samples:



A - Back-scattered electron image of a polished thin-section of sample LP-2.



B - Back-scattered electron image of a polished thin-section of sample DCW-77-51.

Figure 7.10 - Range of compositions for confirmed transition- zone plagioclase margins in the clast-poor impact melt unit of the West Clearwater Lake impact structure (N=25).

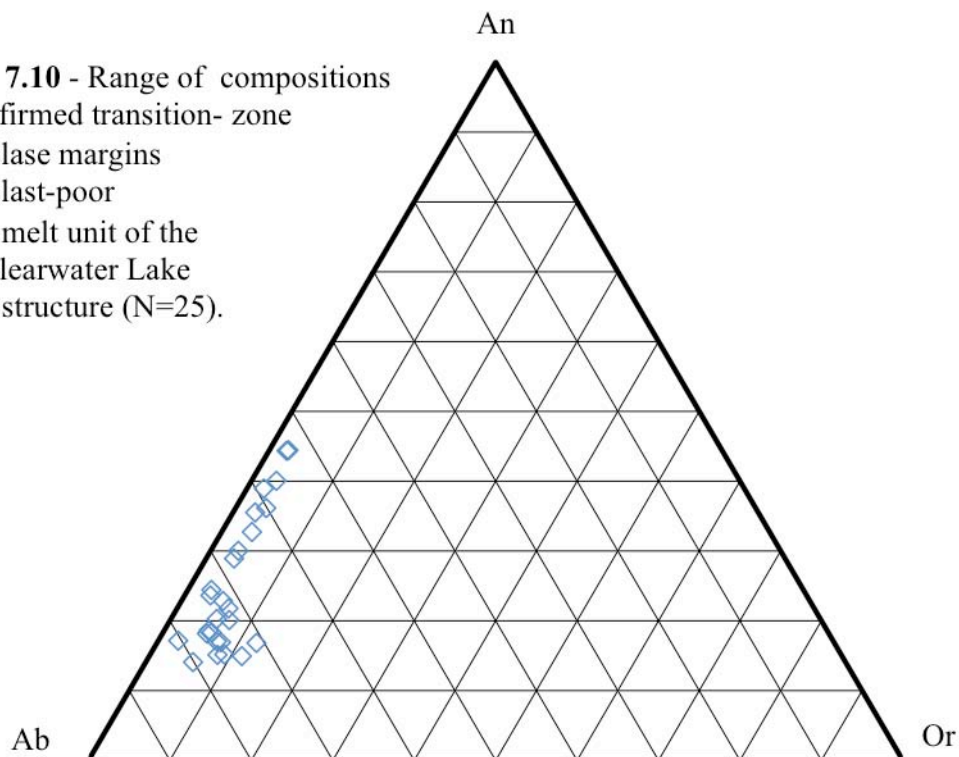


Figure 7.11 - Range of compositions for confirmed primary sanidine feldspar rims in the clast-poor impact melt unit of the West Clearwater Lake impact structure (N=40).

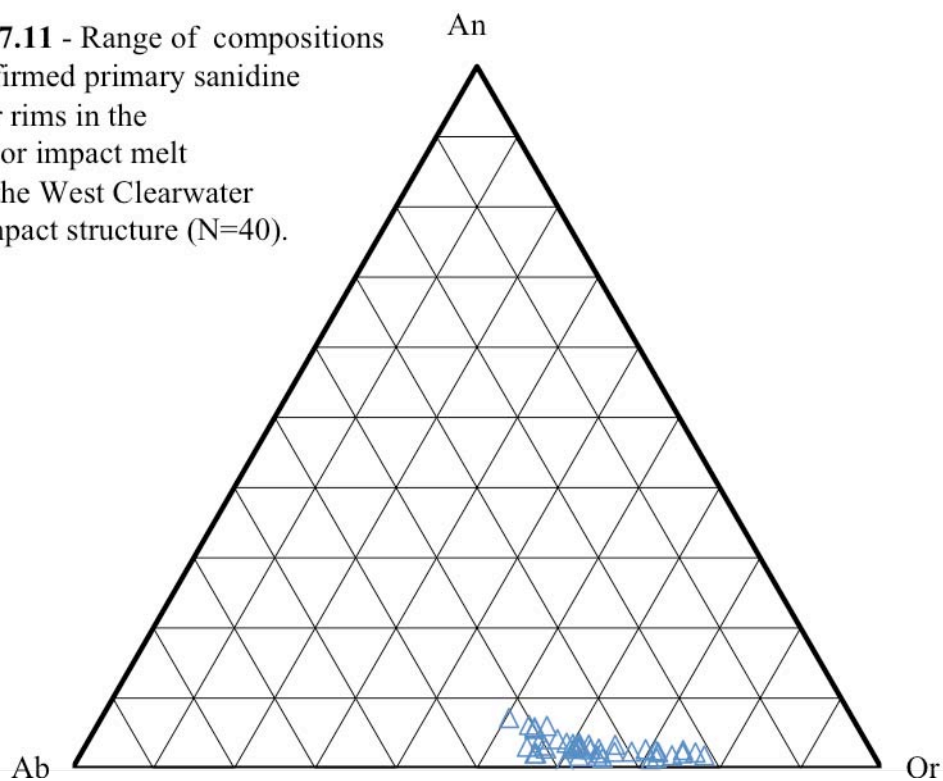
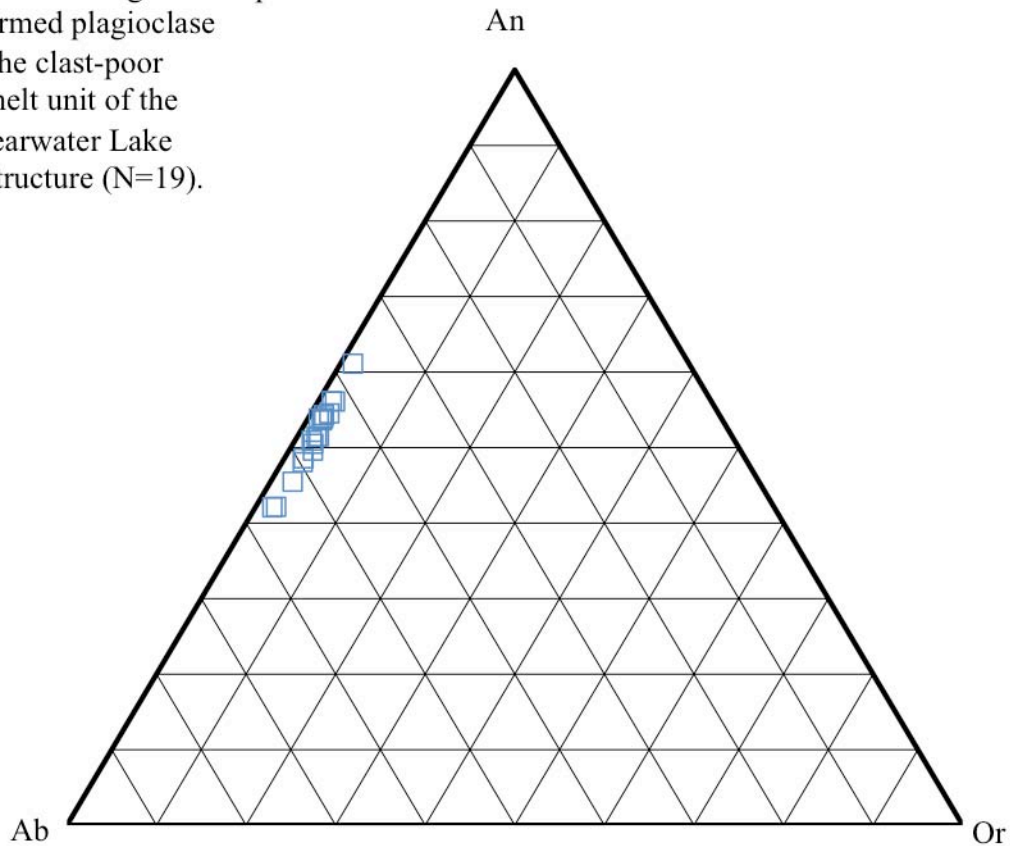


Figure 7.12 - Range of compositions for confirmed plagioclase laths in the clast-poor impact melt unit of the West Clearwater Lake impact structure (N=19).



melt, which then crystallized as melt-derived sanidine. Note that the transition zone between melt-derived plagioclase and melt-derived sanidine, which appears as a darker irregular overgrowth near the contact between the two feldspars, is relatively narrow and was not sampled. Figure 7.15 shows the comb-like intergrowth associated with the transition zone. The central compositions are not as Na-rich as those in the samples described above: the melt-derived plagioclase composition seems to dominate, with only a small central dip in Ca content. This grain could either be a “ghost” relict core, or a section cut through the periphery of a larger central core.

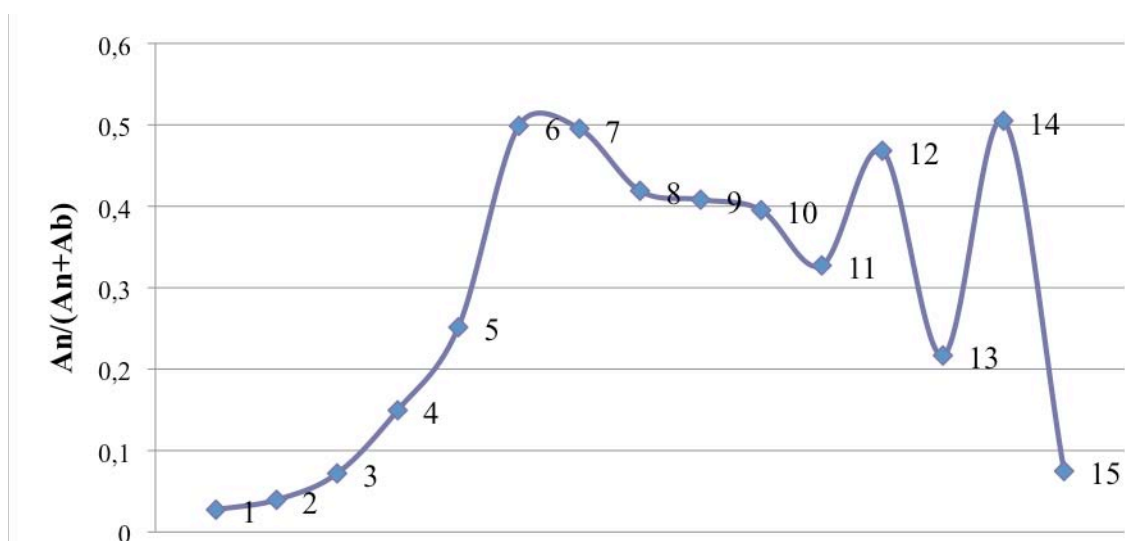
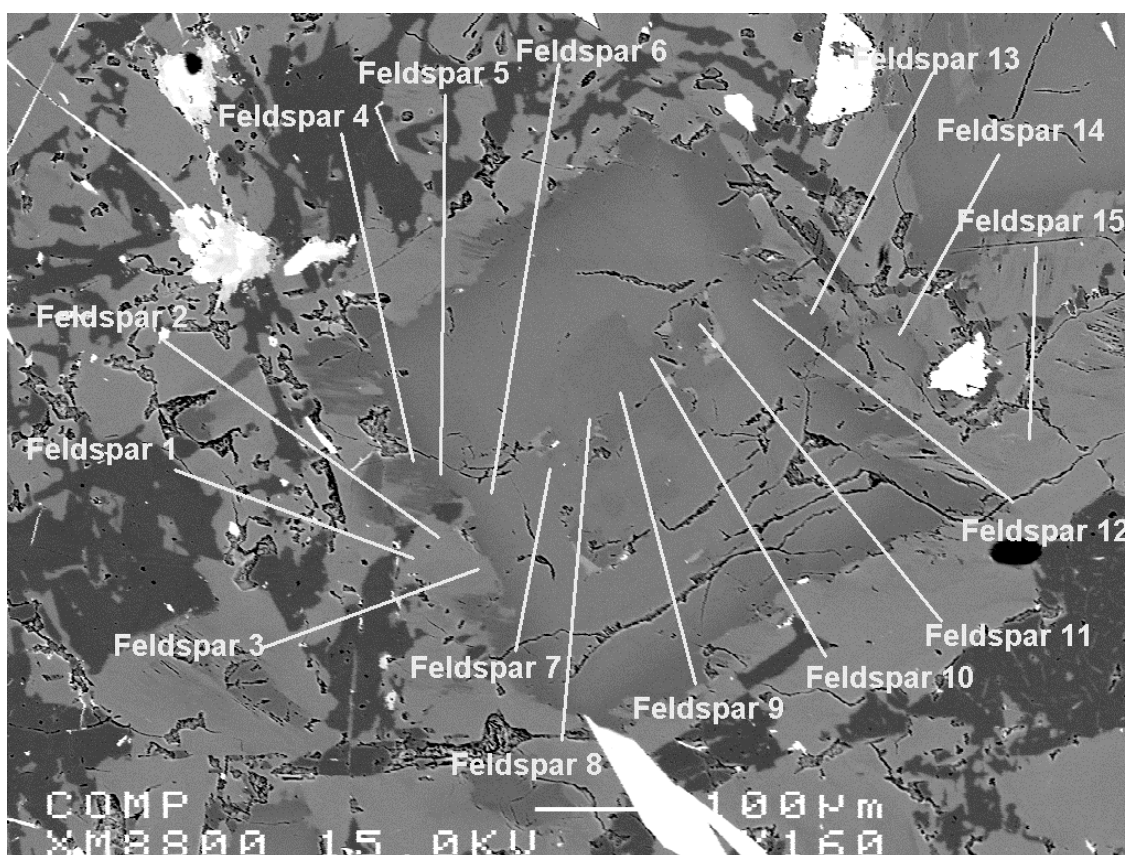


Figure 7.13 Variation in An/(An+Ab) content in microprobe traverses across a feldspar grain in sample DCW-77-33 of the clast-poor impact melt rock of the West Clearwater Lake impact structure. Points 1, 2 and 3 sample melt-derived sanidine, points 4 and 5 are in a transition zone between the melt-derived sanidine rim and the melt-derived plagioclase rim, points 6 and 7 sample melt-derived plagioclase, points 8 to 11 are relict plagioclase, points 12 and 14 are melt-derived plagioclase and points 13 and 15 are melt-derived sanidine. Interstitial dark gray minerals: quartz; white minerals: clinopyroxene, Fe-Ti oxides and, at the bottom of the image, apatite.

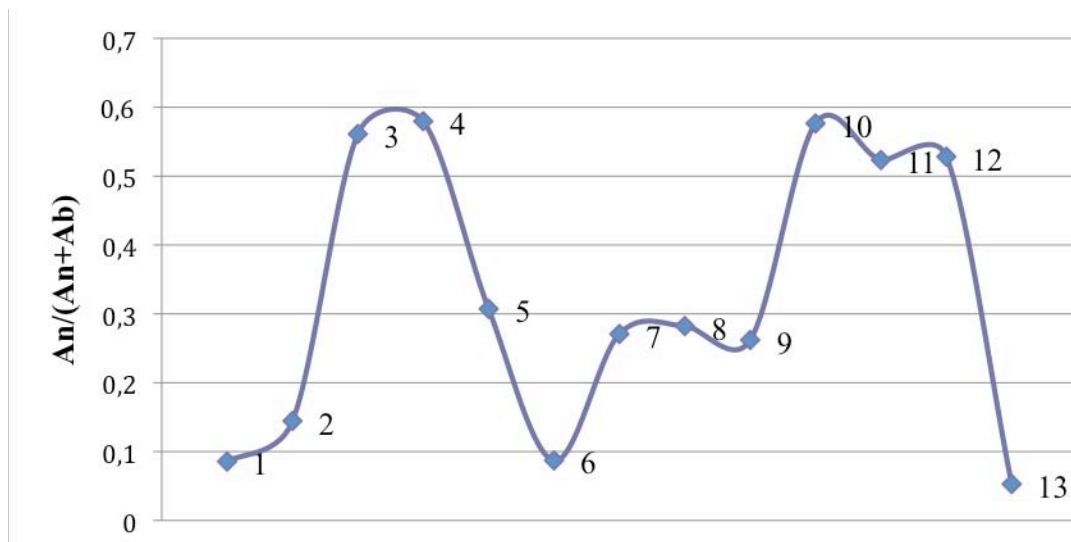
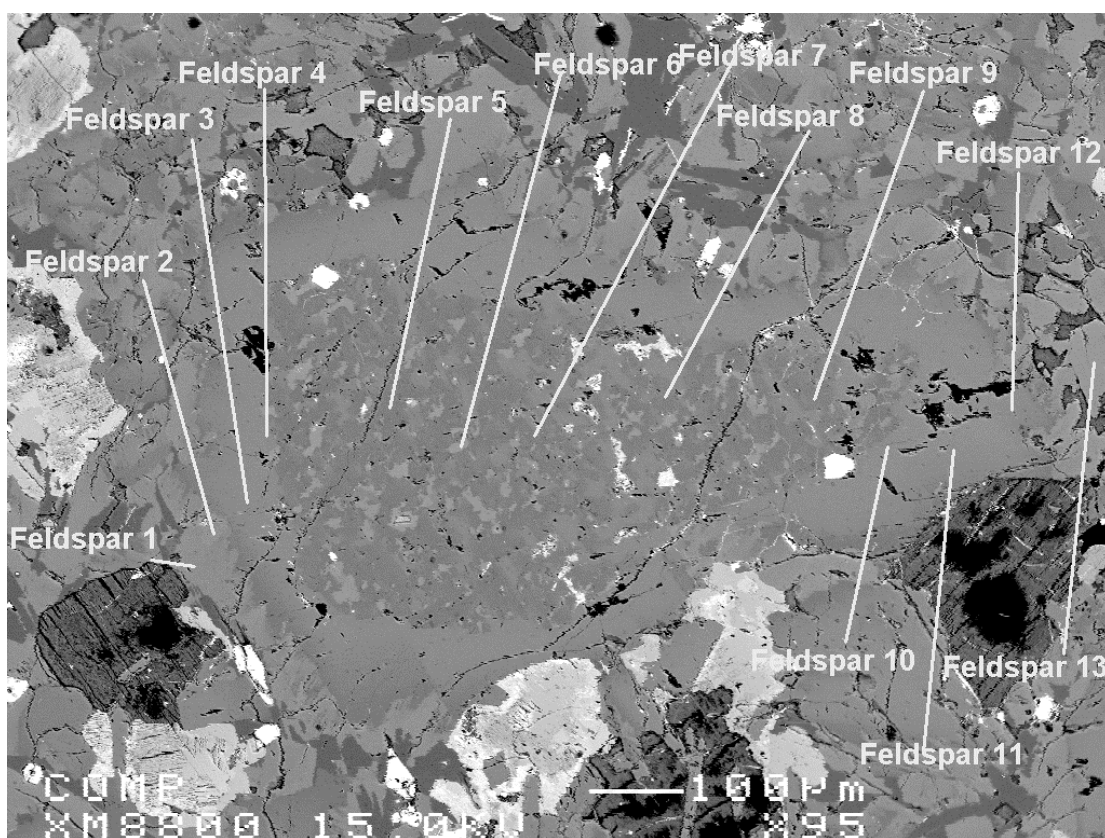


Figure 7.14 Variation in An/(An+Ab) content in microprobe traverses across a poikilitic feldspar grain in sample DCW-77-61 of the clast-poor impact melt rock of the West Clearwater Lake impact structure. Points 1 and 2 are melt-derived sanidine, points 3 and 4 are melt-derived plagioclase, points 5, 7, 8 and 9 are relict plagioclase, point 6 is probably melt-derived sanidine, points 10, 11 and 12 are melt-derived plagioclase and point 13 is melt-derived sanidine. Interstitial dark gray minerals: quartz; note the presence of clinopyroxene (whitish and light gray minerals) and altered clinopyroxene (flaky dark gray and black).

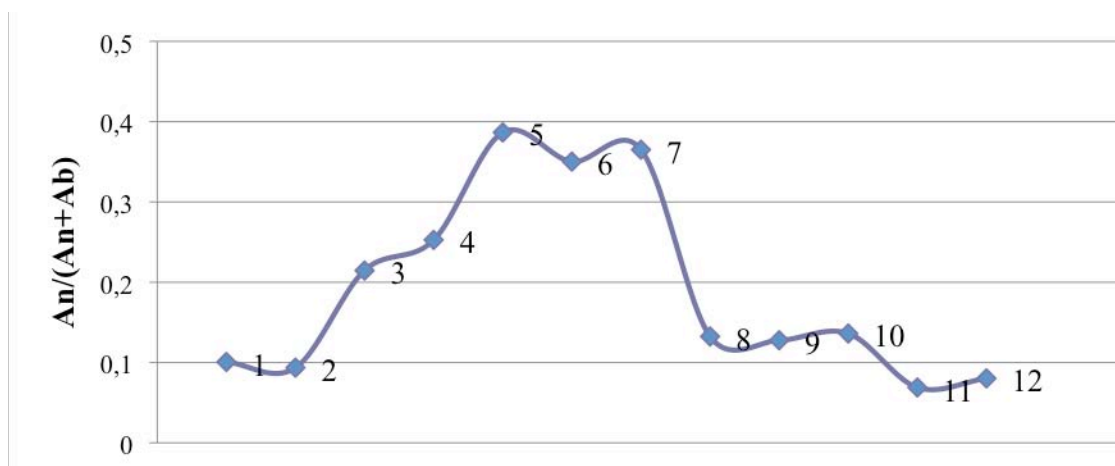
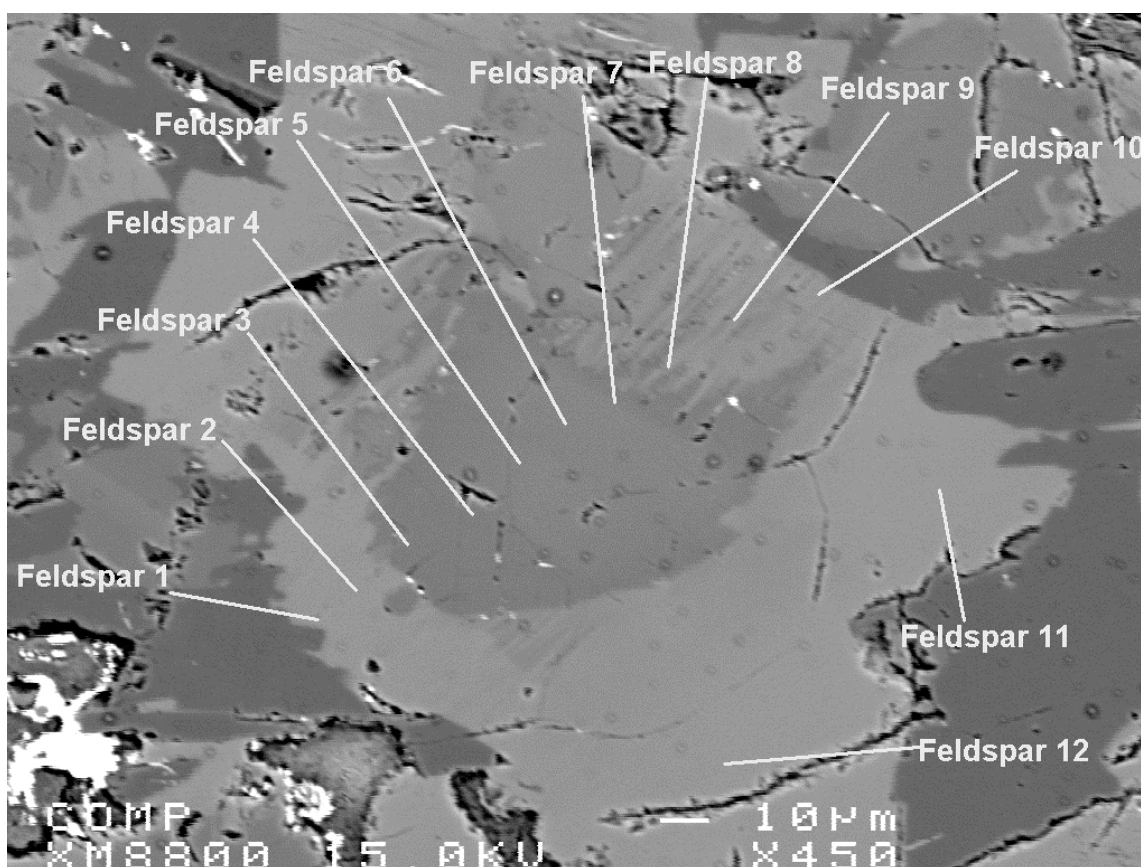


Figure 7.15 Variation in An/(An+Ab) content in microprobe traverses across a feldspar grain in sample DCW-77-61 of the clast-poor impact melt rock of the West Clearwater Lake impact structure. Points 1 and 2 are melt-derived sanidine, points 3 and 4 are in a transition zone between the melt-derived sanidine rim and the plagioclase core, points 5, 6 and 7 are probably a mixture of melt-derived plagioclase and what is left of the relict plagioclase core, points 8, 9 and 10 are in the comb-texture area, and they melt-derived sanidine mixed with some melt-derived plagioclase, points 11 and 12 are melt-derived sanidine. Interstitial dark gray minerals: quartz; white minerals: iron oxides.

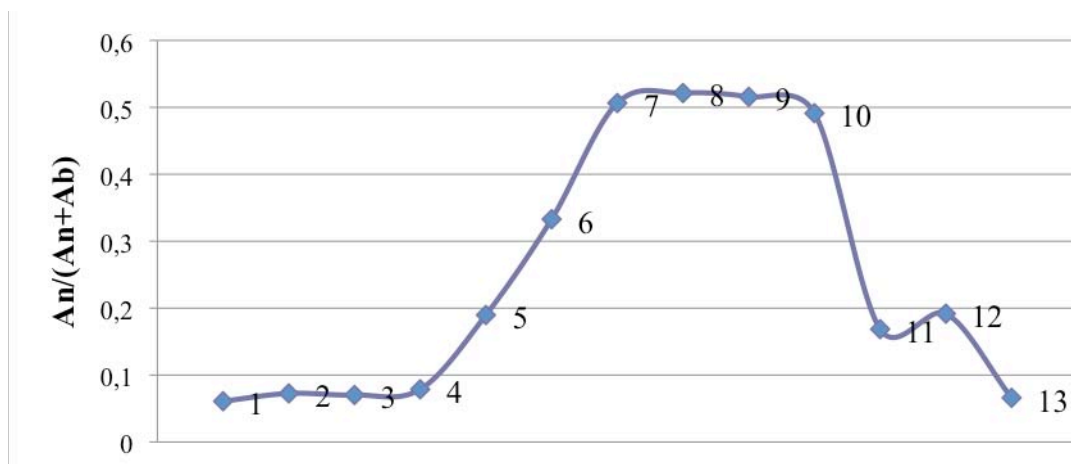
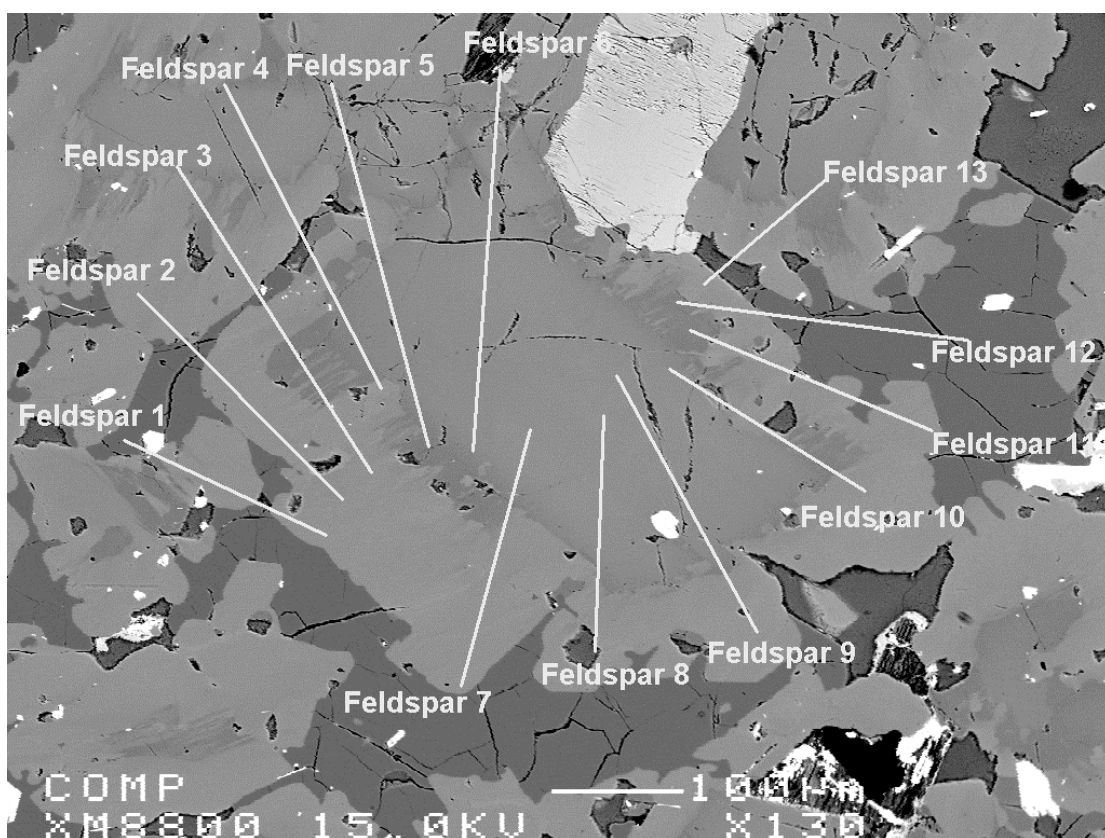


Figure 7.16 Variation in An/(An+Ab) content in microprobe traverses across a feldspar grain in sample DCW-77-53 of the clast-poor impact melt rock of the West Clearwater Lake impact structure. Points 1, 2, 3 and 4 are melt-derived sanidine, points 5 and 6 are in a transition zone between the melt-derived sanidine rim and the plagioclase core, points 7, 8, 9 and 10 are melt-derived plagioclase, points 11 and 12 are in a comb-textured transition zone between the core and the sanidine rim, and point 13 is melt-derived sanidine. Interstitial dark gray minerals: quartz; white minerals: Fe-Ti oxides; light gray at the top center: clinopyroxene.

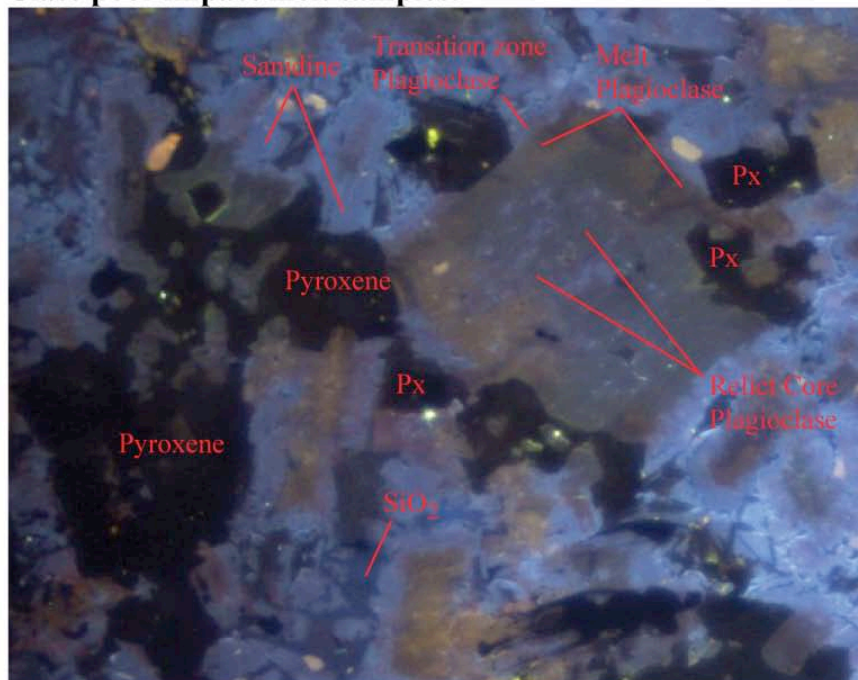
Figure 7.16 has the familiar melt-derived sanidine - transition zone - melt-derived plagioclase sequence, but seems to be missing a central Na-rich region. This may be because the grain is composed only of melt-derived feldspar, the relict clast being absent, or because this part of the grain represents a cut through a section of the periphery of a larger grain. It is also possible that the relict clast was originally present but has been entirely resorbed in the impact melt.

Because of problems with mineral identification, it is very difficult to estimate solely from microscope and microprobe observations how much of the matrix is composed of relict plagioclase clasts. In plane light, the boundaries between the melt-derived feldspars and the relict plagioclase are indiscernible, making the feldspars appear as large, uniform grains. Cathodoluminescence (CL) imaging could, in theory, provide a way to distinguish between neoformed plagioclase and relict plagioclase (see section 7.2.3 for details concerning the CL apparatus). Relict plagioclase clasts should have a trace-element content different from that of melt-derived plagioclase, and thus could display cathodoluminescence colors specific to them.

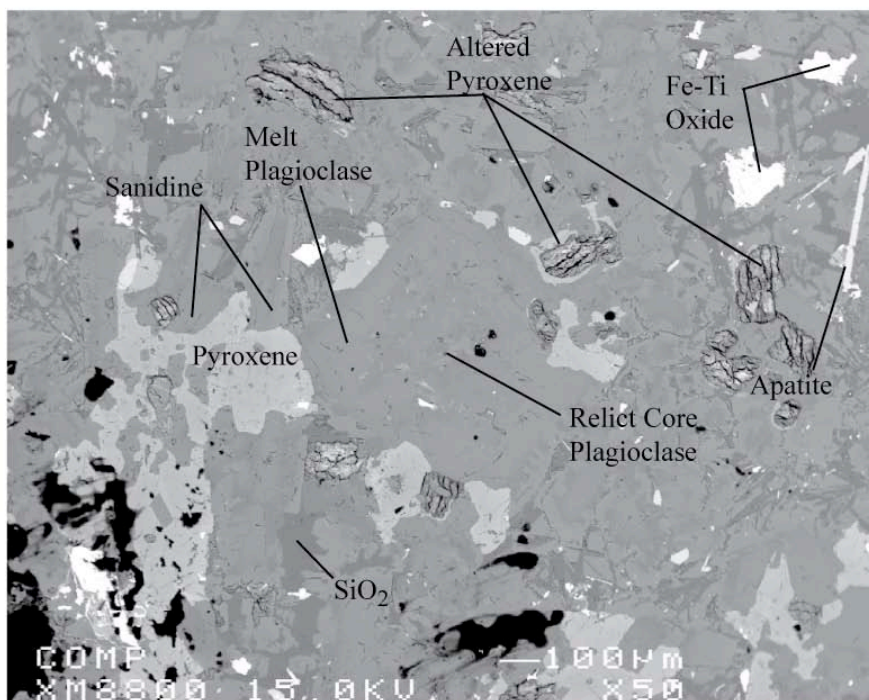
In CL images, mafic minerals appear black, quartz is dark blue to dark purple and sanidine appears bright blue. Plagioclase shows a variety of colors: transition zone plagioclase looks purplish, melt-derived plagioclase generally appears olive brown and relict plagioclase is dark green (see Figures 7.17 A and B). However, I have observed several plagioclase laths impinging on pyroxene margins (which implies that they are neoformed plagioclase) that display green colors. Melt-derived plagioclase must contain

Figure 7.17 A and B A cathodoluminescence (CL) image and a back-scattered electron image of the same area of a thin section of sample DCW-77-36. In CL images, transition-zone plagioclase looks purplish, melt-derived plagioclase generally appears olive brown and relict plagioclase is dark green. See text for more details.

Clast-poor impact melt samples:



A - Cathodoluminescence (CL) image of a section of a polished thin-section of sample DCW-77-36.



B - Back-scattered electron image of the region of sample DCW-77-36 shown in the CL image above.

a range of trace-element contents, causing some melt-derived plagioclase to luminesce in colors similar to that of relict plagioclase, perhaps because they are, in some way, “reworked” relict plagioclase. Therefore, it is impossible to state with complete certainty whether every plagioclase displaying a greenish color in CL is a relict clast. Nevertheless, I estimate, from optical microscope, microprobe and CL observations of the clast-poor impact melt rock, that relict plagioclase (“ghost” crystals included) must form ~5% to ~15% of the clast-poor impact melt rock, depending on the thin section (sections higher up the stratigraphic column likely contain less relict plagioclase). One must keep in mind that that this estimate is largely speculative: the feldspars grains are fine-grained and so closely associated within one another that any modal analysis by the count method would certainly be unreliable. Nevertheless, it is quite clear that relict plagioclase is relatively common and, more importantly, *it must have been much more common when the impact melt formed.*

Finally, feldspar grains also form, along with clouds of small pyroxene crystals, reaction rims or coronas surrounding clasts. Sanidine is generally the most abundant feldspar in these coronas, and its range of composition falls within the range of the rim sanidine described above. Plagioclase is relatively rare in these coronas, and I am not certain if it crystallized as part of the reaction rim, or if it represents neoformed plagioclase caught in the rim. In any case, the composition of the few grains I analyzed falls within the range of melt-derived plagioclase.

7.2.2 Pyroxenes

Pyroxene makes up 5 to 10% of the matrix. Commonly, pyroxenes form anhedral to subhedral crystals approximately 0.1 to 0.5 mm across in the coarser-grained rocks

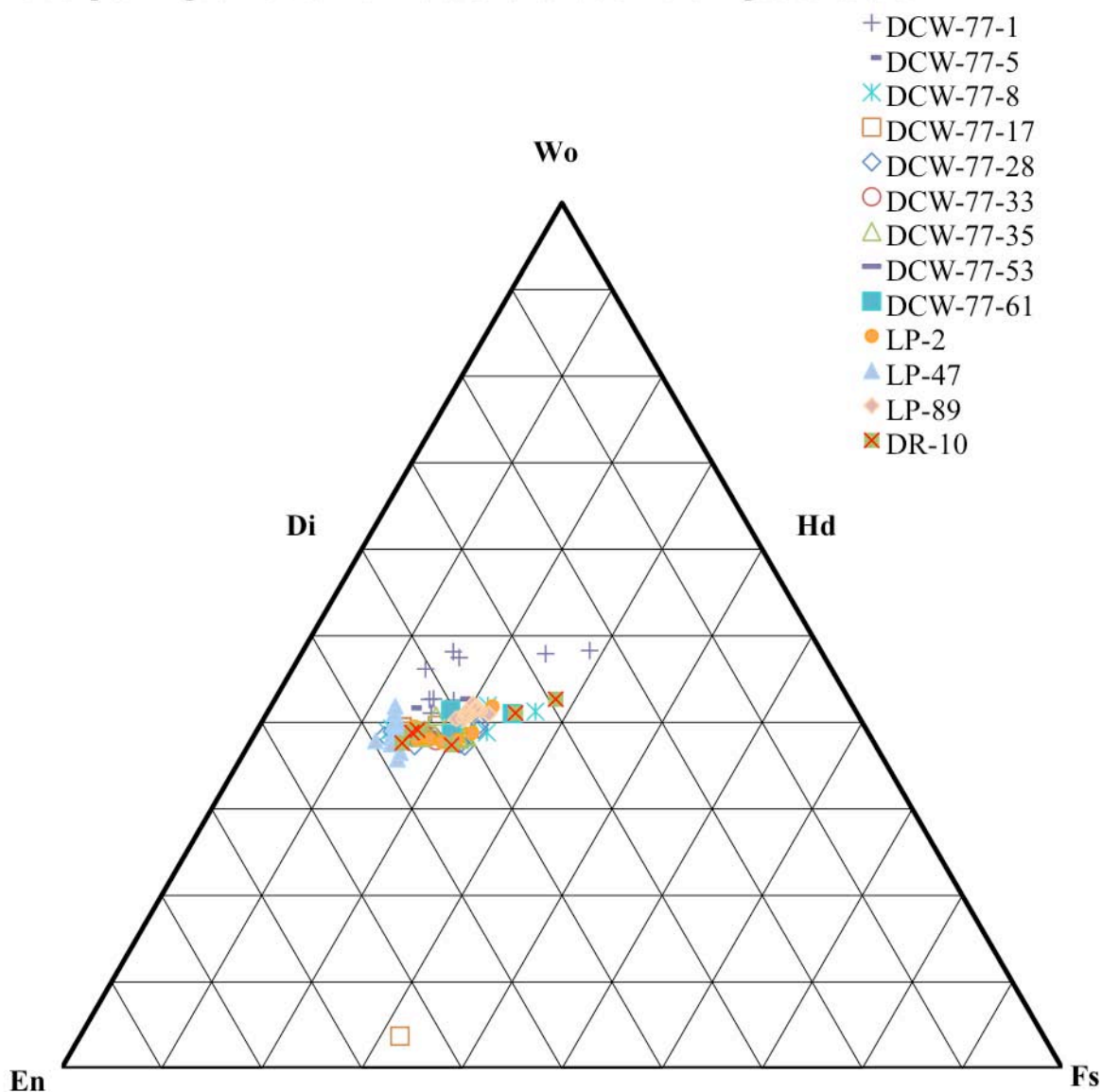
(like sample DR-10), and platy to acicular crystals ~0.1 mm long or less in the finer-grained samples of clast-poor impact melt rock (sample LP-47, for instance). This pyroxene typically shows extensive alteration: a thick orange-brown rim surrounds a relatively fresh core, presumably indicating post-crystallization oxidation. Alteration can also take the form of a complete or partial pseudomorphic replacement (see Figure 7.19 A) by a smectite clay, presumably montmorillonite. Plagioclase impinges on the margins of the pyroxene, producing what Simonds et al. (1978) described as “a somewhat ophitic texture” (Figure 7.9 A, p.173).

Pyroxene is also present as numerous stubby, granular crystals typically 0.01 to 0.05 mm across in reaction rims, or coronas, surrounding clasts. These coronas typically show successive rims of fine-grained pyroxene (on the inside) and quartz interspersed with feldspars (on the outside) surrounding target-rock fragments; these tend to be monomineralic quartz clasts, but can also be lithic fragments (figure 7.19 B). The formation of concentric rims has been interpreted to result from dissolution of SiO₂ faster than it can diffuse or become mixed with the surrounding melt. Enriching the melt in SiO₂ moves the local melt composition into a pyroxene liquidus field resulting in the crystallization of augite rims (Simonds et al., 1978a).

A calcium-rich pyroxene with an augitic composition (En₅₀₋₂₃Fs₂₉₋₁₂Wo₄₈₋₃₆) is, by far, the most common pyroxene (Figure 7.18). The larger pyroxene crystals are not conspicuously zoned: some crystals do show a slight increase in Ca toward the core (e.g., Wo₃₈ to Wo₄₀) whereas others show the reverse trend. However, the altered orange brown rim on the larger pyroxene grains, which appear brighter in back-scattered electron images, typically have a composition richer in Fe compared to unaltered areas (e.g., Fe₂₅ vs. Fe₁₅). The vast majority of augite compositions are crowded in the low-Ca, low-Fe

augite area, around Wo_{40} , in the upper left of the Pyroxene quadrilateral. The compositions with the highest calcium and iron contents (e.g., $En_{23}Fs_{29}Wo_{48}$) all come from a thick reaction corona surrounding a lithic fragment in sample DCW-77-1.

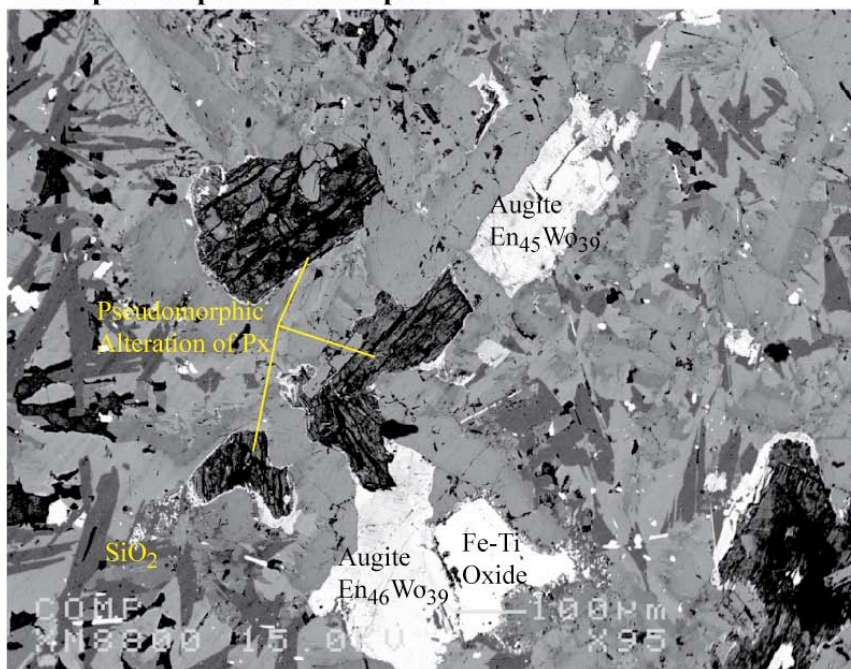
Figure 7.18 - Range of mineral compositions for the pyroxenes in the clast-poor impact melt unit of the West Clearwater Lake impact structure.



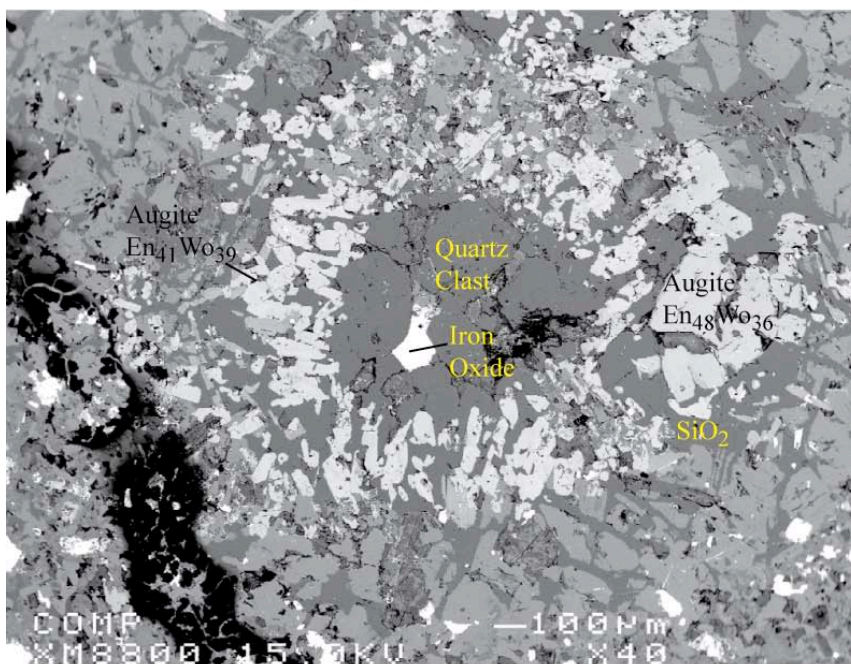
The pseudomorphic alterations typically have a low total, generally around 80% (and even down to 62%). Compared to the composition of the original clinopyroxene, the pseudomorphic alteration has lower silica content (e.g., 43 vs. 52 wt.%), higher Al_2O_3

Figure 7.19 A and B Images of clast-poor impact melt rock. Image A shows partially altered clinopyroxene in subophitic intergrowth with plagioclase. Image B: a quartz xenocryst reacted with the impact melt, creating a corona of stubby prismatic augite.

Clast-poor impact melt samples:



A - Back-scattered electron image of a polished thin-section of sample DR-10.



B - Back-scattered electron image of a polished thin-section of sample LP-89.

content (5.7 vs. 1.5 wt.%), higher FeO_{total} (14.8 vs. 9.9 wt.%) and significantly lower calcium (e.g. 2.0 vs. 19.2 wt% CaO). Assuming that the low total is due to the presence of H₂O, the pseudomorphic alteration of clinopyroxene has a composition similar to that of certain clays (possibly a mix of several smectite-group minerals).

Table 7.4 Representative compositions of the pyroxenes found in the clast-poor impact melt rocks of the West Clearwater Lake Impact Structure.

Sample	LP-47-Region 1-Cpx 2 (small acicular crystal)	LP-2-R2-a (center of large crystal)	DR-10-R2- 13 (margin alteration)	DCW-77-1- R1-Rim-PX3 (in reaction corona)	DCW-77- 17-PX5 (Ca-poor)	DR-10-R5b-6 (pseudo- morphic alteration)
SiO ₂ wt. %	49.96	51.83	51.50	48.92	53.26	43.31
TiO ₂	0.96	0.42	0.50	0.44	0.19	0.03
Cr ₂ O ₃	0.09	0.12	0.00	0.02	0.05	0.12
Al ₂ O ₃	4.32	1.59	0.58	1.87	0.52	5.68
FeO _{total}	9.71	9.29	15.16	17.34	20.65	14.79
MnO	0.23	0.25	0.42	0.17	0.37	0.18
MgO	16.85	16.52	11.68	7.84	23.33	16.56
CaO	17.26	19.03	19.58	22.84	1.89	1.96
Na ₂ O	0.31	0.24	0.28	0.27	0.04	0.65
K ₂ O	0.00	0.00	0.00	0.01	0.02	0.99
NiO	0.00	0.02	0.02	0.00	0.00	0.00
Total	99.69	99.28	99.70	99.71	100.32	84.26

Number of cations on the basis of X (O)

	X = 6	X = 6	X = 6	X = 6	X = 6	X = 22*
Si <i>apfu</i>	1.858	1.938	1.975	1.920	1.970	7.295
Ti	0.027	0.012	0.015	0.013	0.005	0.004
Cr	0.003	0.003	0.000	0.001	0.001	0.016
Al	0.189	0.070	0.026	0.086	0.022	1.128
Fe	0.302	0.290	0.486	0.569	0.639	0.937
Mn	0.007	0.008	0.014	0.006	0.012	0.026
Mg	0.934	0.921	0.668	0.459	1.286	4.158
Ca	0.688	0.763	0.804	0.960	0.075	0.354
Na	0.022	0.018	0.020	0.021	0.003	0.212
K	0.000	0.000	0.000	0.000	0.001	0.213
Ni	0.000	0.001	0.001	0.000	0.000	0.000
Total Cation	4.030	4.022	4.008	4.034	4.015	14.342
Wo	35.75	46.7	41.1	48.3	3.8	---
Fs	15.70	14.7	24.8	28.6	31.9	---
En	48.55	46.7	34.1	23.1	64.3	---

* Anhydrous calculation.

Calcium-poor pyroxene is present, but it is very rare: none of my petrographic descriptions revealed unambiguous signs of it, but the general extensive alteration of the pyroxenes would have made visual identification difficult. Nevertheless, in the 108 microprobe analyses of the pyroxenes in 13 separate thin sections that were sampled during the course of this study, orthopyroxene was only detected once, in thin section DCW-77-17 (see composition DCW-77-17-PX5 in table 7.4). This lone orthopyroxene, a single isolated grain, has a composition like that of enstatite ($\text{En}_{64}\text{Fs}_{32}\text{Wo}_4$). Because of the extensive alteration of the pyroxenes and the rarity of the Ca-poor pyroxenes, it is unclear what the relation between Ca-rich pyroxenes and Ca-poor pyroxenes is. Phinney et al. (1978) reported intergrowths of Ca-rich and Ca-poor pyroxenes that could be exsolution lamellae, but I have not seen anything resembling this. In the opinion of Hische (1995), orthopyroxene was the second most common mineral in the clast-poor impact melt rock matrix, and he proposed that orthopyroxene has been transformed to clinopyroxene or clay minerals. Although I have seen clear evidence of clinopyroxene alteration to clay, compositions or textures that could be interpreted as orthopyroxene altering to clinopyroxene are not present. This apparent rarity of orthopyroxene is puzzling: a CIPW norm of the average composition of the impact melt indicates orthopyroxene to be the dominant pyroxene, even if all Fe is calculated as Fe_2O_3 . Either the orthopyroxene did not crystallize for some reason, or it was nearly completely altered to clinopyroxene in a manner that I haven't recognized. It is also possible that my sampling somehow missed it.

7.2.3 Quartz and its titanium content


Xenomorphic quartz represents about 10% of the matrix. It occurs interstitially, typically forming interconnected dendritic patches with margins defined by neighboring subhedral to euhedral sanidine. It indubitably was the last phase to crystallize from the melt. It commonly contains acicular inclusions of apatite, small euhedral crystals of alkali feldspar and small euhedral crystals of Fe-Ti oxide.

The clast-poor impact melt rock contains 0.77 wt.% TiO_2 , and 10-15% of its matrix is composed of Fe-Ti oxides. Because this assemblage must have, by its very nature, crystallized at very high temperature, I established the concentration of titanium in quartz, in the hope of using the Ti-in-quartz geothermometer first developed by Wark and Watson (2006) to determine the temperature of crystallization of quartz in the clast-poor impact melt. As the quartz is interstitial, this would also be the temperature of the solidus. This Ti-in-quartz geothermometer is relatively easy to apply, as it typically requires analysis of only one phase. Additionally, the thermal history of the quartz can usually be studied by cathodoluminescence (CL) imaging, because CL intensity in many quartz crystals is a function of Ti content (Müller et al., 2003; Watt et al., 1997), which in turn depends on the temperature of crystallization of the quartz. It should therefore be possible to ascertain if post-crystallization hydrothermal activity affected the quartz.

For this investigation, I chose samples according to their approximate stratigraphic position (Table 7.5), in order to obtain, if possible, temperature information covering the entire extant thickness of the clast-poor melt rock. Samples from other units were not considered simply because their grain size is too small, and because I wanted to avoid accidentally analyzing clasts of relict quartz.

Because the sample locations provided by Dence's field notes are not very precise, the stratigraphical positions given in table 7.5 below are, for the most part, based on my interpretation. I am only certain of the position of samples DCW-77-18 and DCW-77-36, as Dence specifically indicated in his notes that they were respectively from the bottom and the top of the clast-poor impact melt sheet. The positions of the other samples are estimated from the descriptions and distances written in Dence's notebook, and from the grain size of the samples, as crystal size tends to increase with stratigraphic height.

Table 7.5 Samples chosen for cathodoluminescence (CL) imaging and Ti-in-quartz analysis, with their approximate relative stratigraphic location.

Sample	Approximate location	
DCW-77-18	Drillers Island, basal exposure of buff gray impact melt, <i>near the bottom the of the clast-poor impact melt rock unit.</i>	
DCW-77-49	Central Lepage Island, same traverse as DCW-77-50 and DCW-77-52, this particular sample was "on a bench on the hill" near sample DCW-77-50, <i>about 1/4 to 1/3 up the stratigraphic thickness of the clast-poor impact melt.</i>	
DCW-77-50	Central Lepage Island, same traverse as DCW-77-49 and DCW-77-52, this particular sample was "on a bench on the hill", near sample DCW-77-49, <i>about 1/4 to 1/3 up the stratigraphical thickness of the clast-poor impact melt.</i>	
DCW-77-7	Drillers Island, hilltop west of south end of large central lake, probably, <i>about halfway up the clast-poor melts sheet.</i>	
DCW-77-30	Drillers island, SE point of the island; small outcrop of gray melt on the side of hill, <i>about halfway up the clast-poor melts sheet.</i>	
DCW-77-52	Central Lepage Island, same traverse as DCW-77-49 and DCW-77-50, about 30 to 35 m higher than DCW-77-49 and DCW-77-50, <i>about 2/3 up the stratigraphic thickness of the clast-poor impact melt.</i>	
DCW-77-34	Atkinson Island, SW corner, abundant outcrops of impact melt on N, E and S shores of small lake, <i>near the top of the extant impact melt sheet.</i>	
DCW-77-36	Highest point of SW corner of Atkinson Island; sample from outcrop at top of cliff, <i>highest point of the extant impact melt sheet.</i>	Top of unit

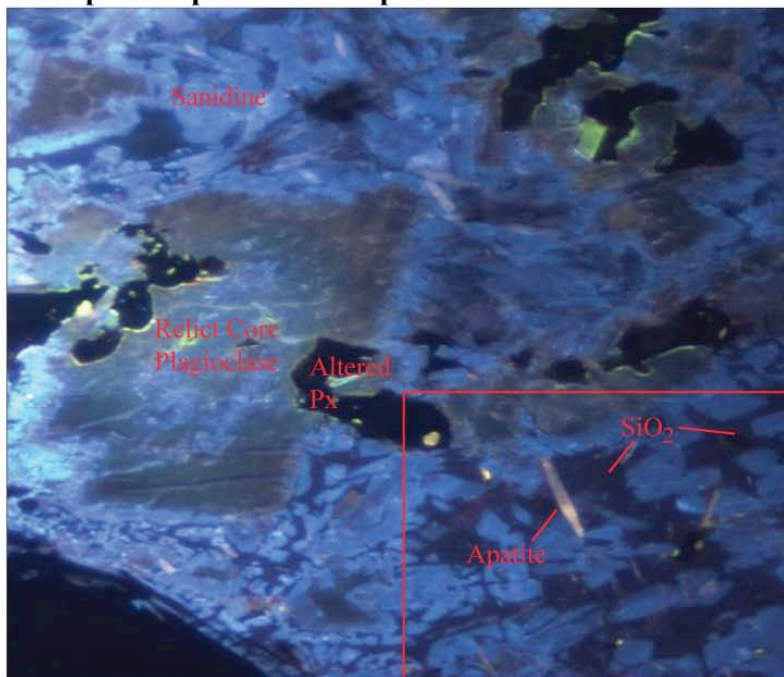
CL imaging of the samples was done using a Reliotron III Cathodoluminescence Instrument, a desktop apparatus consisting of a small vacuum chamber equipped with an electron gun. The chamber is mounted on a petrographic microscope. Samples are placed within the chamber, which has a base window for transmitted light microscopy allowing it to be fitted in place of the normal microscope stage. Both X and Y external controls are used to position the specimen. Vacuum is produced and maintained by a vacuum pump attached to the chamber. Both the pump and the electron gun are controlled from an electronic console, which lets the operator regulate the electron gun and the level of vacuum in the chamber. The petrographic microscope was fitted with a small camera attached to an Apple desktop computer, allowing the operator to take pictures of the luminescent sample. My samples were kept under a vacuum chamber pressure of about 60 to 70 mtorr, and an operating voltage of -8.0 kV.

The CL images of quartz in the clast-poor impact melt rock showed that it generally has a fairly uniform CL pattern, of a dark purple color, without any apparent zoning (figure 7.20 A). However, in some areas, particularly in the vicinity of Fe-Ti oxides, quartz may display a brighter reddish hue, probably indicating a higher concentration of impurities. Also, in some CL images, there are areas where the normal purple hue of the quartz becomes bluish and progressively darker, eventually becoming entirely black, which I assumed is due to a local progressive decrease in Ti content, the area affected becoming too poor in Ti to luminesce.

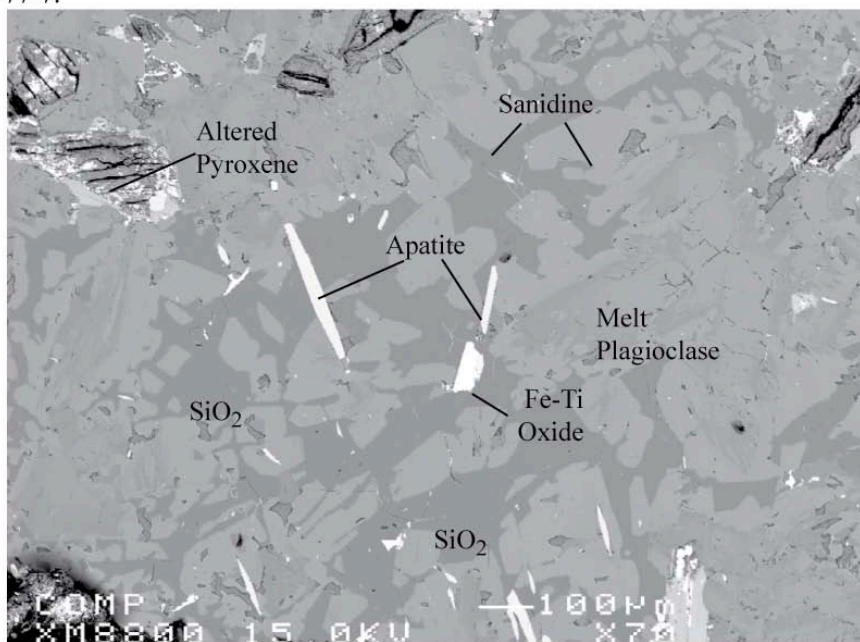
The Ti content in quartz was determined by electron microprobe microanalysis (EMPA). The analyses were performed with a JEOL 8900 electron microprobe operated

Figure 7.20 A and B A cathodoluminescence (CL) image and a back-scattered electron (BSE) image of a thin section of sample DCW-77-7 show what the interstitial quartz looks like in both CL and BSE imaging. The boxed area in image A is shown as a BSE image in image B. Quartz appears purplish in CL images and dark gray in BSE images. In CL images, sanidine is blue, plagioclase several shades of brown and dark green. Mafic minerals are black. Note the presence of apatite needles (in white).

Clast-poor impact melt samples:



A - Cathodoluminescence (CL) image of a section of a polished thin-section of sample DCW-77-7.



B - Back-scattered electron image of the region of sample DCW-77-7 shown in the CL image above.

by Shi Lang, at McGill University. The analyses were performed at an accelerating voltage of 15 kV and a beam current of 1×10^{-7} A, with count times of 500 seconds for each analysis. The data regression was performed by applying the ZAF correction method. This yielded detection limits for Ti on the order of 34 ppm. Care was taken to select areas for analysis that were far from Fe-Ti oxides; I expected the Ti concentrations in the reddish region near the oxides to be greater than that of normal quartz. I also avoided areas that appeared black in CL images. Nevertheless, I specifically selected a number of points in the reddish region surrounding the oxides and in the black non-luminescent regions, in order to compare their Ti contents with normal Ti-in-quartz concentrations. The exact placement of each point analysis was marked on a back-scattered electron image of the area being studied, which could then be compared with the CL images taken before going to the microprobe.

Table 7.6 Representative levels of titanium in the quartz found in the clast-poor impact melt rocks of the West Clearwater Lake Impact Structure. Designations such as DCW-77-7-R1-Qtz 5 indicate that the composition was obtained from the 5th microprobe analysis of quartz in region 1 of a thin section of sample DCW-77-7.

	DCW-77-7- R1-Qtz 5	DCW-77-34- R3-Qtz 2	DCW-77-18- R3-Qtz 2	DCW-77-36- R4 b-Qtz 2	DCW-77-49- R1-Qtz 4
SiO₂ wt. %	99.93	99.40	97.04	99.23	99.19
TiO₂ wt. %	0.06	0.05	0.243	0.155	0.01
Total	99.99	99.45	97.28	99.39	99.20
TiO₂ ppm	330	324	1457	929	78

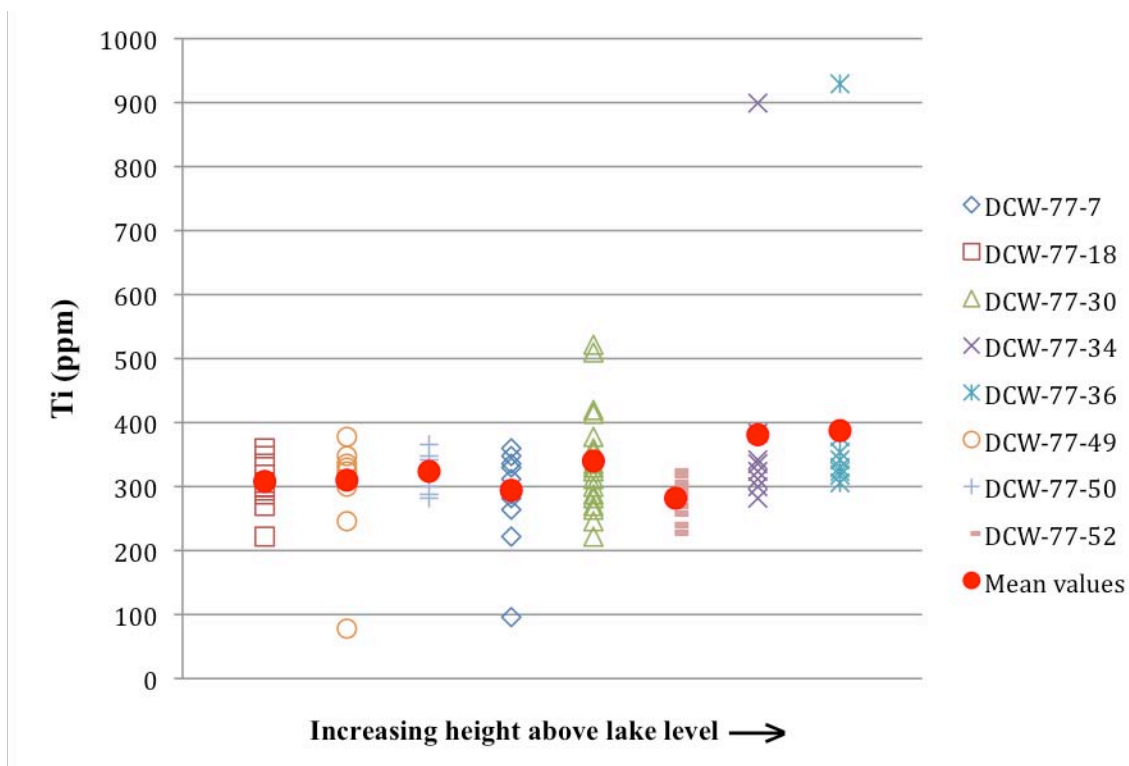


Figure 7.21 Variations in Ti content in quartz according to sample and estimated relative stratigraphic position of samples above lake level. This plot includes all values.

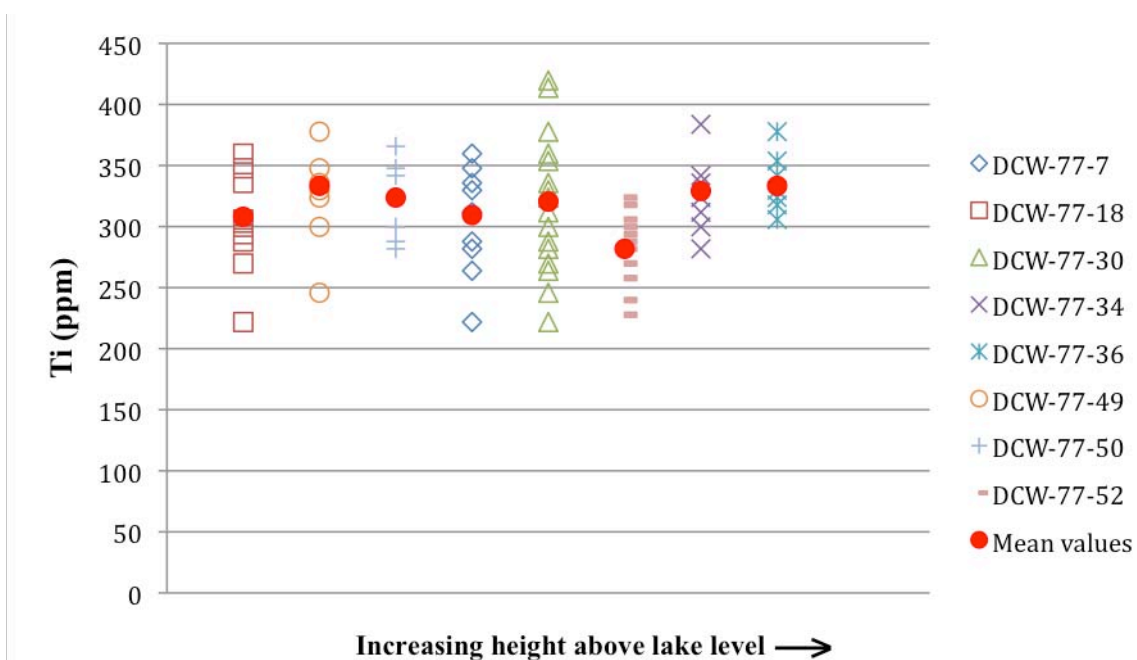


Figure 7.22 Variations in Ti content in quartz according to sample and estimated relative stratigraphic position of samples above lake level. This plot excludes very high and very low values.

Sample	DCW-77-7		DCW-77-18		DCW-77-30	
	All	Abnormal removed	All	Abnormal removed	All	Abnormal removed
N	14	13	13	13	20	18
Ti (ppm)						
Mean values	294	309	308	---	340	320
σ	68.17	38.82	37.72	---	78.82	53.90

Sample	DCW-77-34		DCW-77-36		DCW-77-49	
	All	Abnormal removed	All	Abnormal removed	All	Abnormal removed
N	11	10	11	10	11	10
Ti (ppm)						
Mean values	381	329	387	333	310	333
σ	173.88	27.61	180.77	21.00	85.29	38.67

Sample	DCW-77-50		DCW-77-52	
	All	Abnormal removed	All	Abnormal removed
N	8	8	16	16
Ti (ppm)				
Mean values	324	---	282	---
σ	30.74	---	26.72	---

Table 7.7 Ti contents in the quartz in selected samples from the clast-poor melt impact rock of the West Clearwater Lake impact structure. Under **All** are calculations which include all values; under **Abnormal removed** are calculations made without extreme values, that is values that are either very high or very low. N : number of point analysis; σ : standard deviation.

Analyses DCW-77-7-R1-Qtz 5 and DCW-77-34-R3-Qtz 2 in table 7.6 provide examples of typical concentrations of Ti in the quartz of the clast-poor melt rock. Analyses DCW-77-18-R3-Qtz 2 and DCW-77-36-R4b-Qtz 2 yielded the two highest values for Ti measured in the quartz of the clast-poor melt rock, whereas analysis DCW-77-49-R1-Qtz 4 is one of the lowest values. There are a number of analyses that yielded lower values,

but they correspond to datasets with very low totals. The lowest value was obtained close to a poorly developed pyroxene reaction rim with residual quartz clast at its center, and it is possible that the anomalous composition is the result of contamination by a clast of partially melted quartz. The high values are associated with areas where, on the CL images, the quartz luminesces in a brighter red color instead of the usual purplish hue, which clearly shows that the red color is associated with higher titanium content. A detailed explanation of the calculation employed to estimate temperatures from the content in Ti present in the interstitial quartz will be presented in chapter 8. Quartz was the last phase to crystallize. Therefore, estimating its temperature of crystallization provides a direct measure of the temperature of the solidus of the clast-poor melt rock.

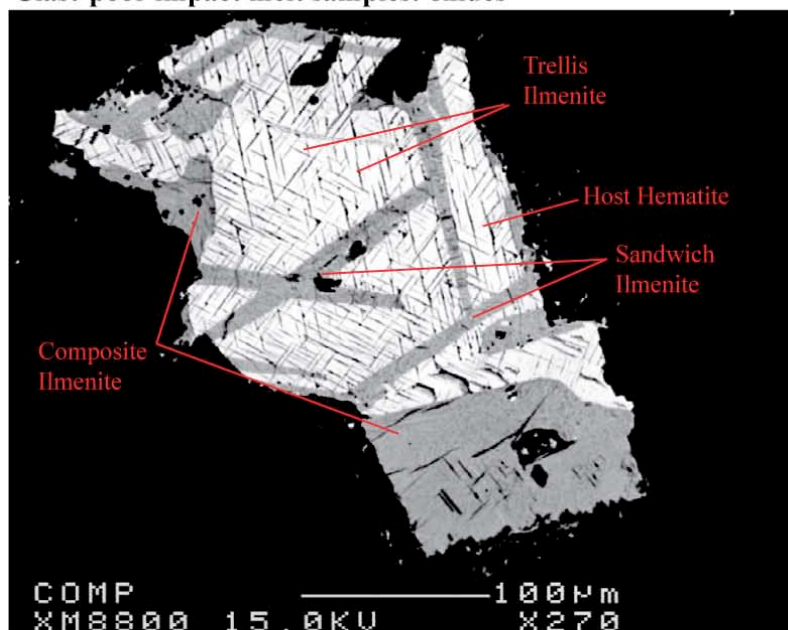
7.2.4 Iron-Titanium Oxides

Opaque minerals form 10 to 15% of the matrix. The grains are typically rust-colored, anhedral to subhedral and generally ~200 to 300 μm across. Inclusions of plagioclase have been observed, but they are uncommon. This assemblage, which originally must have consisted of titaniferous magnetite, has undergone complex subsolidus oxidation processes that have caused the exsolution of ilmenite and rutile, and replaced the magnetite by hematite.

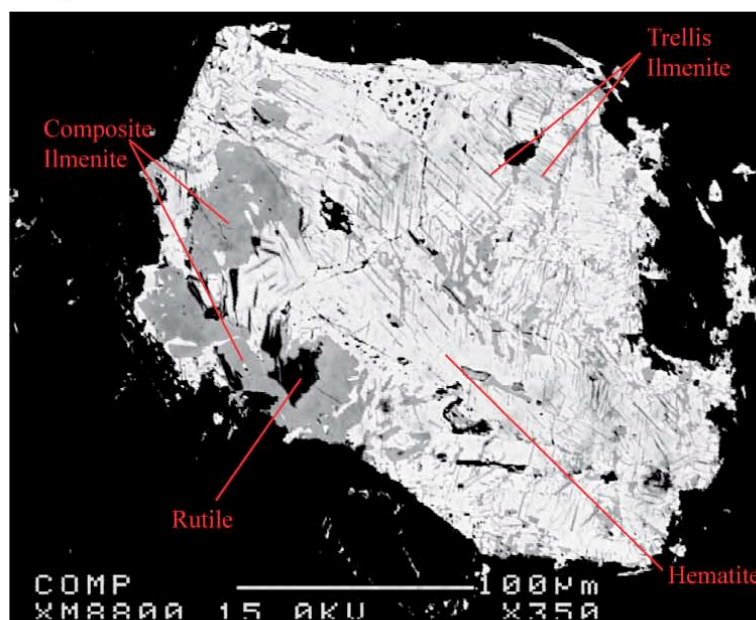
The most common hematite-ilmenite assemblage involves a hematite host containing anhedral to subhedral lamellae of ilmenite. The ilmenite plates tend to be, but are not in every case, found along host crystal margins, and they may contain small irregular domains of rutile, which seem to have formed at the expense of the ilmenite (figure 7.23 B). The contact of these ilmenite regions with the hematite is usually quite

Figure 7.23 A and B Images of Fe-Ti oxides found within the clast-poor melt. In image A, several dark gray thick sandwich laths of ilmenite cut the grain. The brighter areas are hematite, which is cut by lamellae of trellis ilmenite. Note the lens-like shape of the ilm lamellae and the constricted diffusion contacts with other ilm lamellae. Domains of composite ilmenite occupy the bottom and left margins of the grain. Image B shows a grain of titaniferous magnetite that underwent more intense oxidation. The ilmenite domains have developed irregular margins; rutile has been exsolved within the composite ilmenite.

Clast-poor impact melt samples: oxides



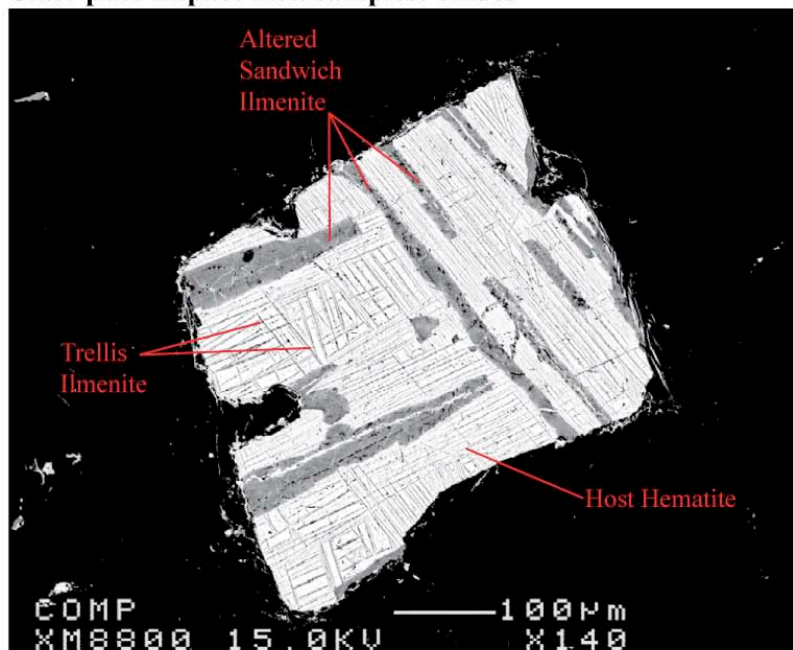
A - Back-scattered electron image of an oxide grain in a polished thin-section of sample DCW-77-35.



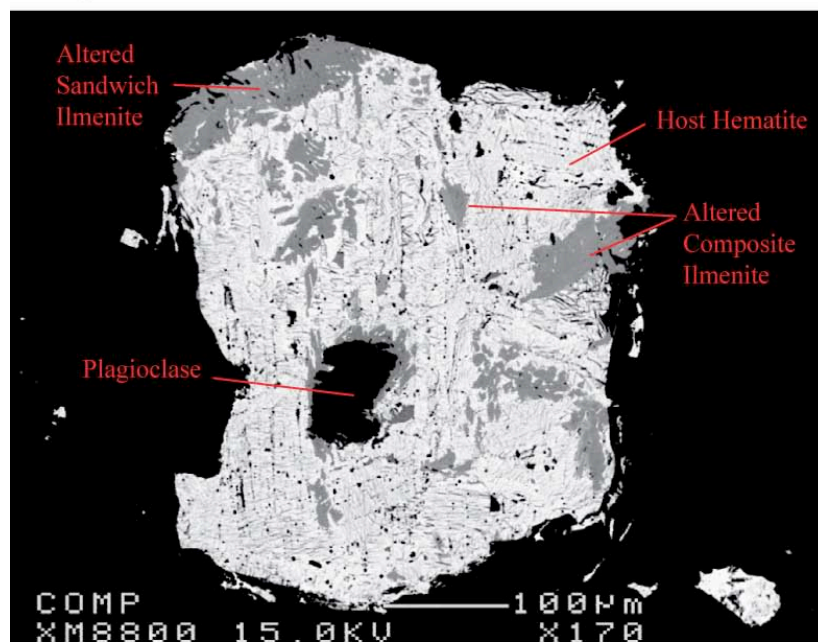
B - Back-scattered electron image of an oxide grain in a polished thin-section of sample DCW-77-28.

Figure 7.24 A and B Images of Fe-Ti oxides found within the clast-poor melt. In image A, the grain is cut by several sandwich ilmenite laths with irregular margins that have a crude $\{111\}$ spinel orientation. The grain also shows second and tertiary trellis ilmenite sets along $\{111\}$ spinel planes. Image B shows a grain that underwent a stronger oxidation. Composite ilmenite domains with irregular margins and roughly following spinel planes are still visible, but the array of trellis ilmenite has been disrupted.

Clast-poor impact melt samples: oxides



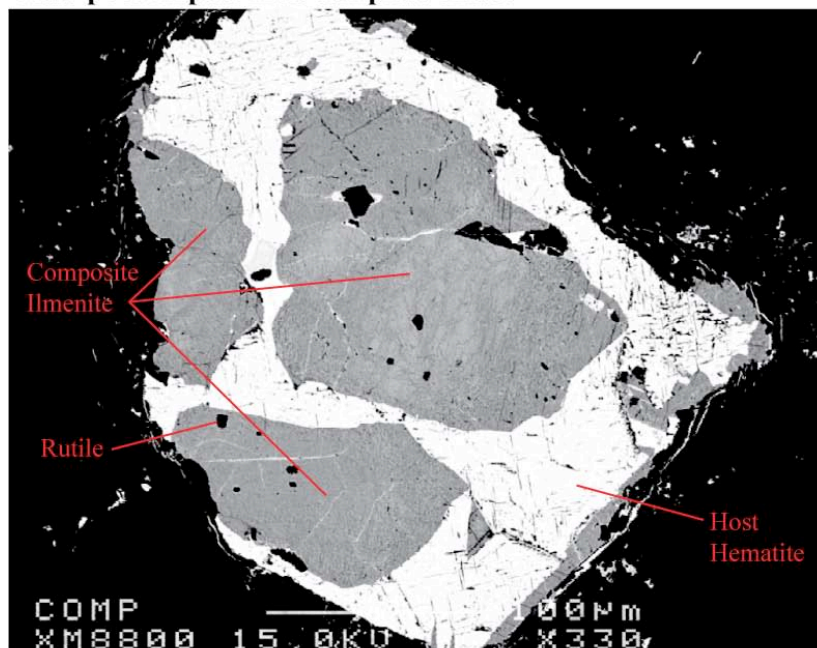
A - Back-scattered electron image of an oxide grain in a polished thin-section of sample DCW-77-8.



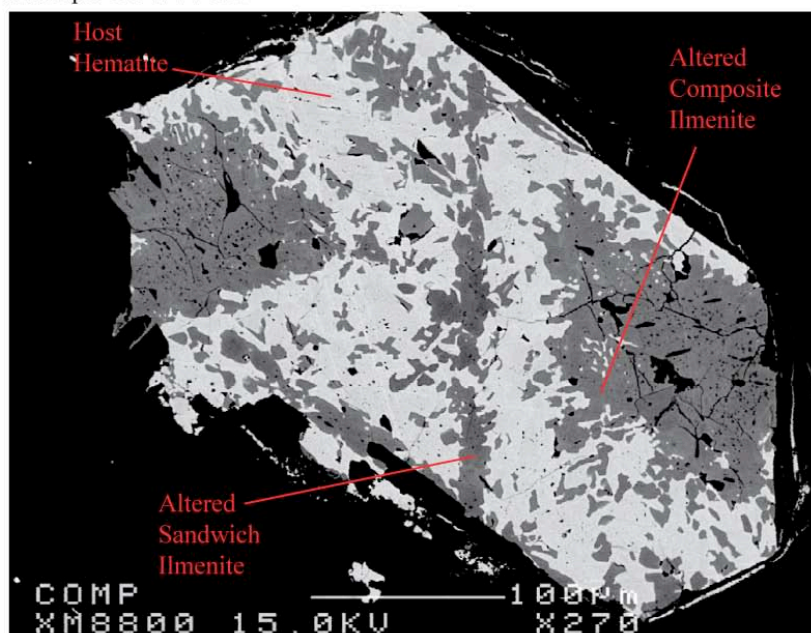
B - Back-scattered electron image of an oxide grain in a polished thin-section of sample DCW-77-35.

Figure 7.25 A and B Images of Fe-Ti oxides found within the clast-poor melt. In image A, composite ilmenite domains have atypical rounded contacts with the hematite host: the contacts do not follow in any way the {111} orientation of exsolved ilmenite; the composition of these ilmenite domains totals near 100%, which is unusual. This “composite” ilmenite may be a candidate for included primary ilmenite. Image B shows a strongly oxidized grain of titanomagnetite. Note the “serrations” developed at the oxy-exsolution interface between ilmenite and hematite.

Clast-poor impact melt samples: oxides



A - Back-scattered electron image of an oxide grain in a polished thin-section of sample DCW-77-51.



B - Back-scattered electron image of an oxide grain in a polished thin-section of sample DR-10.

irregular, serrated, although straight or rounded contacts have also been observed. These ilmenite regions correspond to a type of oxidation-induced intergrowth called “composite type” by Haggerty (1991). Another common arrangement shows several types of ilmenite lamellae cross-cutting the hematite host. Lamellae can either form thick laths that occur in small numbers (the “sandwich type” lamellae of Haggerty, 1991) or as numerous thin lamellae that commonly follow the {111} planes of the original magnetite host. This intergrowth of thin lamellae is similar in appearance to the well-known Widmanstätten texture found in iron meteorites, and is called “trellis type” growth by Haggerty (1991) (Figure 7.23 A and 7.24 A).

Well-developed “trellis type” lamellae typically have two main textural orientations that follow {111} spinel planes. Apparent thicknesses of the thin “trellis type” lamellae are fairly uniform and range from sub- μm to $\sim 1\text{-}2\ \mu\text{m}$. The distance between lamellae is highly variable and depends on the grain. “Trellis” lamellae margins are typically sharp, with an outline that is not parallel: the lamellae typically taper at the extremities, ending at the intersection with other lamellae, giving many individual “trellis” lamellae a lens-like outline. Lamellae terminations that abut crystal margins and “sandwich type” lamellae, however, do not taper but end abruptly.

“Sandwich type” lamellae (or laths) typically have a {111} spinel orientation and, unlike the “trellis type” lamellae, rarely show tapered ends: they terminate abruptly, usually at crystal boundary or against an intersecting “sandwich” lath. The majority of the “sandwich” lamellae I have observed are less than $10\ \mu\text{m}$ wide, but there is a large variation in thickness: the thicker “sandwich” lamellae can be nearly $60\ \mu\text{m}$ wide, whereas the thinner are $\sim 3\text{-}5\ \mu\text{m}$ across. These laths commonly coexist with “trellis type” lamellae, commonly sharing the same orientation, but they clearly predate them:

the thinner and more abundant “trellis” lamellae do not cut them. Instead, “trellis” lamellae end abruptly at the contact with the “sandwich” laths (Figures 7.23 A and 7.24 A).

Although most of these ilmenite textures are indubitably the result of the “oxidation-exsolution” documented in the classic paper by Buddington and Lindsley (1964), that is, they were exsolved at the expense of the titaniferous magnetite host, it is also possible that some “composite” and “sandwich” types of ilmenite domains are primary grains that have been included into the magnetite during crystal growth. The hematite-ilmenite grain shown in Figure 7.25 A, for instance, has a number of “composite” ilmenite regions that do not resemble the “composite” ilmenite commonly found in these Fe-Ti oxide grains. For example, 1) the “composite” ilmenite regions in figure 7.25 A occupy most of the center of the grain, 2) they have atypical rounded contacts with the hematite host that do not follow in any way the {111} orientation of exsolved ilmenite, 3) their Ti-rich composition totals near 100%, closer to the ideal composition of ilmenite than most of the other ilmenite compositions, suggesting that it is much less altered than the ilmenite found in the other Fe-Ti oxide grains. This “composite” ilmenite may be a candidate for included primary ilmenite, but it should be noted that I have not observed a single grain composed entirely of ilmenite.

Examples of representative compositions of the Fe-Ti oxides of the clast-poor impact melt rock are given in Table 7.8. Only two analyses, both obtained in the composite ilmenite of the grain shown in Figure 7.25 A, yielded totals close to 100%. Nearly all the compositions I have obtained by microprobe analysis have totals in the 89 to 95% range. Analyses of the hematite host invariably produce the lowest totals, with

Table 7.8 Representative compositions of the iron-titanium oxides found in the clast-poor impact melt rocks of the West Clearwater Lake impact structure.

Sample	DCW-77-8- Region 1 - FeTi Ox 3 (Ilmenite sandwich lath)	DCW-77-28- R1-Ti Ox (Fe-rich rutile inclusion)	DCW-77-35- Region 1-Fe Ti Ox 3 (Hematite host)	DCW-77-51- Region 3-Fe Ti Ox 2 (Composite ilmenite)	DR-10-Region 1-Fe Ti Ox 7 (Altered Fe-rich composite ilmenite)
SiO ₂ wt. %	0.00	0.03	0.02	0.00	0.09
TiO ₂	53.49	86.61	0.16	50.29	37.97
Cr ₂ O ₃	0.05	0.10	0.14	0.01	0.06
Al ₂ O ₃	0.21	0.14	0.49	0.08	1.01
FeO _{total}	41.16	8.30	92.06*	46.27	52.56
MnO	0.36	0.09	0.04	1.62	0.26
MgO	0.48	0.11	0.02	1.09	1.60
CaO	0.00	0.03	0.00	0.03	0.00
Na ₂ O	0.02	0.02	0.00	0.02	0.10
K ₂ O	0.01	0.05	0.00	0.00	0.00
NiO	0.00	0.00	0.00	0.00	0.02
Total	95.78	95.45	92.92	99.40	93.68

Number of cations on the basis of X (O)

	X = 3	X = 2	X = 3	X = 3	X = 3
Si <i>apfu</i>	0.000	0.000	0.000	0.000	0.003
Ti	1.037	0.944	0.003	0.965	0.810
Cr	0.001	0.001	0.003	0.000	0.001
Al	0.006	0.002	0.017	0.002	0.034
Fe	0.888	0.101	1.974	0.988	1.246
Mn	0.020	0.001	0.001	0.035	0.006
Mg	0.008	0.002	0.001	0.041	0.067
Ca	0.000	0.000	0.000	0.001	0.000
Na	0.001	0.000	0.000	0.001	0.005
K	0.000	0.000	0.000	0.000	0.001
Ni	0.000	0.000	0.000	0.000	0.000
Total Cation	1.960	1.054	1.999	2.034	2.173

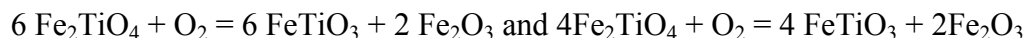
* Total Fe calculated as Fe₂O₃.

Fe₂O₃ typically composing ~85% of the sampled point and various amounts of Al₂O₃, TiO₂ and MgO combining together to form ~5% of the composition. Ilmenite compositions typically yield totals in the 93 to 95% range. It is likely that these low totals result from the presence of a significant amount of H₂O, which must have been introduced into the minerals at a late stage. My investigation of the metamorphism of a large carbonate xenolith by contact with the impact melt, which has generated minerals of

the low-pressure, high-temperature sanidine facies such as periclase (hydrated to brucite), merwinite and spurrite, suggests that significant amounts of H₂O were circulating in the impact melt when temperatures were on the order of 600 to 700°C (Rosa, 2005; Rosa and Martin, 2010).

As already mentioned, the ilmenite that is closest to the ideal composition is found in the rounded regions shown in Figure 7.25 A. I have also obtained two analyses of “sandwich” ilmenite that are close to ideal ilmenite (i.e. they contain more Ti than Fe) but with totals in the 95% range. These Ti-rich compositions are unusual: in most cases, the ilmenite analyzed contains more iron than titanium. I believe this to be a result of stronger oxidation, which has produced a range of compositions usually showing a decrease in the amount of Ti relative to the Fe component, producing an iron-rich ilmenite composition. In some Fe-rich ilmenite, this increased oxidation is accompanied by the presence of significant amounts of elements such as Mg and Al, and the exsolution of irregular patches of iron-rich rutile (see Figure 7.23 B).

In summary, most Fe-Ti grains must have, at the time of crystallization, been composed of homogeneous titaniferous magnetite. It is possible that a few ilmenite grains also crystallized, some being included in the growing magnetite. With decreasing temperature and changing fugacity of oxygen, the magnetite host “exsolved” ilmenite lamellae parallel to {111}. The number of lamellae “exsolved” increased with increasing oxidation of the titaniferous magnetite host (here represented by Fe₂TiO₄, i.e., ulvöspinel) into ilmenite (FeTiO₃) and hematite (Fe₃O₂) according to the following reactions:



As ilmenite “exsolved”, the titaniferous magnetite must have been able to accommodate the increase in hematite in solid solution but, with increasing oxidation, the titaniferous

magnetite was entirely transformed into hematite; with increasing oxidation, the initially homogeneous “exsolved” ilmenite in turn exsolved rutile, forming Fe-rich ilmenite + Fe-rich rutile.

7.2.5 Apatite

Apatite is common, usually present in the form of acicular crystals of variable length and accounting for about 1% of the clast-poor impact melt matrix. Apatite needles are typically found included in the interstitial quartz and in the sanidine margins (see figure 7.20 B). Some needles that are as long as 300 μm , but they are generally in the 20 to 50 μm . Most apatite needles are found completely embedded in quartz, but some are entirely in sanidine. In several cases, the longest apatite needles are partially embedded into both sanidine and quartz. I have not observed apatite included in plagioclase, which indicates that apatite crystallized late, before quartz and after plagioclase.

7.2.6 Fine-grained aggregates of quartz and feldspars

In addition to the complex coronas surrounding clasts and the composite plagioclase relict clasts, thin sections of clast-poor impact melt rock also contain numerous patches of a material that is much finer-grained than the matrix and commonly formed of numerous tiny crystals of quartz and feldspar. The margins of these patches are usually rounded and sharp, unaffected by nearby matrix minerals. I have interpreted these patches, which generally compose ~1% of most thin sections, as rock fragments that have been disintegrated by quick heating in the impact melt and recrystallized to fine-grained aggregates of felsic minerals.

7.3 Summary of chapter 7

- An increase in matrix grain-size accompanied by a decrease in clast abundance and glass content of the matrix with increasing height allows the division of the impact melt rock into two units: 1) a lower unit, the clast-rich impact melt rock, dominated by clastic debris showing varying degrees of reaction with a very fine-grained matrix, now strongly altered and stained by hematite, and 2) a fine- to medium-grained hypidiomorphic clast-poor upper unit with a subophitic to ophitic texture of plagioclase and clinopyroxene.

- The so-called “clast-poor” melt rock contains a larger amount of clasts than previously recognized. In addition to containing 15% clasts (or less, the clast content decreases upward) that are easily recognizable in hand samples (larger than 1 mm in size), the clast-poor rock also contains less obvious but very abundant plagioclase xenocrysts. Plagioclase xenocrysts must form ~5% to ~15% of the clast-poor impact melt rock, depending on the thin section (sections higher up the stratigraphic column likely contain less relict plagioclase). It is quite clear that relict plagioclase is relatively common and, more importantly, because many of these xenocrysts have been resorbed into the impact melt, *it must have been much more common when the impact melt formed.*

- New plagioclase nucleated around plagioclase xenocrysts. This melt-derived plagioclase was, in turn, mantled by alkali feldspar (sanidine solid-solution), creating a distinctively zoned overgrowth. A complex comb-texture intergrowth developed at the interface between the melt-derived plagioclase and the mantling alkali feldspar.

- Augite is the dominant mafic mineral. The clinopyroxene and plagioclase form an ophitic to subophitic texture, indicating that clinopyroxene formed after plagioclase. Sanidine is rarely found impinging against pyroxene margins, indicating that it formed after plagioclase and pyroxene. Apatite needles are found within sanidine and quartz.

- Quartz was the last phase to crystallize in the clast-poor impact melt. In order to estimate its crystallization temperature, the Ti content of quartz was measured: quartz typically contains about 300 to 330 ppm Ti.

- Fe-Ti oxides must have been, with plagioclase, one of the first phases to crystallize in the clast-poor impact melt. These oxides must originally have consisted of titaniferous magnetite. In back-scattered electron images, the oxides display the textures typical of complex subsolidus oxidation processes involving the exsolution of ilmenite and rutile, and the replacement of magnetite by hematite. It is possible that some Fe-Ti oxide xenocrysts have been included in the clast-poor impact melt rock, but their recognition is made difficult by their small size and their advanced state of oxidation.

Chapter 8:

Titanium-in-Quartz Thermometry

Despite its widespread occurrence in the Earth's crust, quartz has rarely been the target of a geochemical study. Therefore, although certain trace elements can fit in the structure (Müller et al., 2003; Rusk et al., 2006), few investigators have attempted to quantify trace-element solubility in quartz in order to provide information regarding the conditions of crystallization of the rocks (Thomas and Lanzirotti, 2010). This has recently begun to change, in great part simply because it has become increasingly easier to establish trace-element concentrations using electron-microprobe and laser-ablation instruments.

A number of experiments were conducted between 600 and 1000°C and at a constant pressure of 10 kbar by Wark and Watson (2006) to calibrate the temperature dependence of the solubility of titanium in quartz. The results of this experimental study are the basis of a titanium-in-quartz (TitaniQ) thermometer. Wark and Watson singled out titanium because concentrations of Ti in quartz found in most igneous and metamorphic rocks are relatively high, up to several hundred ppm. Also, because both Si and Ti are tetravalent, Ti can substitute for Si without having to be charge-balanced by coupled substitution with another element. Finally, the activity of Ti in many systems is fixed by the presence of a nearly pure TiO_2 phase, which is typically rutile; if there are inclusions of rutile in the Ti-bearing quartz, one can assume that the activity of TiO_2 in the system equals 1.

Because this assemblage, by its very nature, must have crystallized at a very high temperature, and because the concentration of titanium in the quartz of the rock is above the limits of detection, I set out to determine the temperature of crystallization of quartz

in the clast-poor impact melt. Because the quartz is interstitial, this would also be the temperature of the solidus. However, the absence of rutile inclusions in the quartz in the West Clearwater impact melt sheet causes a number of complications, which will be fully discussed in section 8.2.

8.1 Calculating the temperatures

According to Wark and Watson (2006), the equation used to calculate temperatures from the content of titanium in quartz is:

$$(1) \quad \log(X_{Ti}^{qtz}) = (5.69 \pm 0.02) - \frac{(3765 \pm 24)}{T(K)}$$

where Ti concentrations in quartz are in ppm by weight and temperature is in degrees Kelvin (the temperature in degrees Celsius can be calculated by simply rearranging the above equation). In practical terms, in rutile-undersaturated rocks, the equation becomes:

$$(2) \quad T(^{\circ}C) = \frac{-3765}{\log\left(\frac{X_{Ti}^{quartz}}{a_{TiO_2}}\right) - 5.69} - 273$$

where T is temperature in degrees Celsius, X_{Ti}^{quartz} is the amount of TiO₂ in quartz in ppm, and a_{TiO_2} is the activity of TiO₂ in the system.

As already mentioned, the TitaniQ thermometer was originally calibrated at 10 kbar. Only a few experiments were done to evaluate the effects of pressure on the solubility of Ti in quartz: the results initially suggested that the Ti-in-quartz thermometer is relatively insensitive to pressure. Furthermore, when the TitaniQ thermometer was first applied to geological systems at a range of different pressures, it produced temperatures considered consistent with other thermometric methods (Wark et al., 2007;

Wark and Watson, 2006; Wiebe et al., 2007). However, it soon became apparent that the TitaniQ thermometer, calibrated at 10 kbar, produced temperatures that were incompatible with phase equilibria and other constraints on crystallization temperatures at pressures other than the calibration pressure (Ghiorso and Evans, 2008; Ghiorso and Evans, 2008; Ostapenko et al., 2007).

To account for the pressure dependence of Ti-in-quartz solubility, Thomas et al. (2010) proposed the following expression, which was calibrated in experiments with pressures between 5 and 20 kbar:

$$(3) \quad RT \ln X_{\text{TiO}_2}^{\text{quartz}} = -(60952 \pm 3122) + (1.520 \pm 0.04)T(K) - (1741 \pm 63)P(\text{kbar}) + RT \ln a_{\text{TiO}_2}$$

where R is the gas constant ($R=8.31447$ J/mol K), T is temperature in Kelvin, P is the pressure in kbar, $X_{\text{TiO}_2}^{\text{quartz}}$ is the mole fraction of TiO_2 in quartz and a_{TiO_2} is the activity of TiO_2 in the system. This equation simplifies to:

$$(4) \quad T(^{\circ}\text{C}) = \frac{-60952 - 1741P(\text{kbar})}{R \ln\left(\frac{X_{\text{TiO}_2}^{\text{quartz}}}{a_{\text{TiO}_2}}\right) - 1.520} - 273$$

The equation to convert Ti (ppm) to mole fraction TiO_2 in quartz ($X_{\text{TiO}_2}^{\text{quartz}}$) is:

$$(5) \quad X_{\text{TiO}_2}^{\text{quartz}} = \frac{\frac{\text{Ti}(\text{ppm})}{1 \times 10^4 \times 0.599 \times 79.87}}{\frac{\text{Ti}(\text{ppm})}{1 \times 10^4 \times 0.599 \times 79.87} + \left[\left(100 - \frac{\text{Ti}(\text{ppm})}{1 \times 10^4 \times 0.599 \times 79.87} \right) \times \frac{1}{60.09} \right]}$$

Three values are needed in order to estimate temperature with these equations: the amount of TiO₂ in quartz in ppm, the activity of TiO₂ in the system, and the pressure in the system. The concentration of titanium in quartz is given in section 7.2.3. As already mentioned, no rutile was observed included in the quartz of the clast-poor impact melt rock: the limitations imposed by the absence of rutile will be discussed in section 8.2.

In the particular context of the West Clearwater Lake impact structure, the maximum pressure on the quartz in the clast-poor melt rock can only be estimated approximately. However, I can safely assume that the maximum pressure will be much lower than that for which Wark and Watson (2006) and Thomas et al. (2010) calibrated their thermometers. This assumption is based on a simple calculation of lithostatic pressure, which is given by:

$$(6) \quad P_{\text{litho}} = \rho gh$$

where ρ is the approximate density of the rocks (2500 kg/m³; Plante *et al.* 1990); g is the gravitational constant (i.e., 9.8 m/s²) and h is the postulated maximum thickness of impact melt. The thickest preserved outcrop of impact melt is ~130 meters. The grain size of the matrix feldspars in the melt rock progressively increases with height in the exposures of melt rock (Phinney et al., 1978), suggesting that the melt sheet was originally much thicker than what remains of it today. It is therefore not unreasonable to assume that the melt sheet was at least twice as thick as present (Phinney and Simonds 1977), giving a pre-erosional estimate of ~260 m. This must be considered to be associated with an uncertainty of at least a factor of two. Calculations of the maximum lithostatic pressure on the crystallizing interstitial quartz show that it cannot have exceeded ~65 bars, as the amount of solidified impact melt removed by erosion probably

did not exceed a thickness of about 130 meters. To account for uncertainties, I will consider that the maximum pressure was 100 bars, that is, I will use a pressure of 0.1 kbar in my calculations.

8.2 Limitations imposed by the absence of rutile

The Ti-in-quartz thermometer described above were calibrated in experiments that used quartz equilibrated with rutile, a pure TiO_2 phase. If rutile and quartz crystallized contemporaneously (e.g., quartz shows rutile inclusions), saturation in Ti is assumed and $a_{\text{TiO}_2} = 1$, but if rutile is absent, $0 < a_{\text{TiO}_2} < 1$ applies. This, however, does not restrict the use of these thermometers to rutile-bearing rocks. As equations (2) and (3) show, these thermometers can be applied even in the absence of rutile if the activity of TiO_2 is known. Also, as can be seen by inspecting equations 2 and 3, assuming $a_{\text{TiO}_2} = 1$ for a system without rutile will *at least provide a minimum temperature of equilibration*.

Felsic igneous rocks typically do not have rutile as a stable phase and consequently have a_{TiO_2} values below one. However, as is the case in the West Clearwater impact melt sheet, most quartz-bearing magmas have at least one phase in which Ti is a stoichiometric component, such as ilmenite or titanite. It is therefore possible to estimate TiO_2 activity directly from equilibria among coexisting equilibrium phases, although this may require knowledge of the temperature of crystallization and an absence of alteration by subsolidus activity. Also, if the Ti content of quartz is known, and if temperature can be estimated by using another geothermometer (Fe-Ti oxide thermometry, for example), it is possible to use equations (1) and (3) to solve for a_{TiO_2} . Using these methods, it has been established that, for silicic igneous assemblages,

activities of 0.5 or higher seem to be the norm. For instance, the TiO_2 activity of the rhyolitic Bishop tuff system is assumed to have been buffered at about $a_{\text{TiO}_2} = 0.53$ by the presence of Fe-Ti oxides during its crystallization (Reid et al., 2011; Thomas and Lanzirotti, 2010).

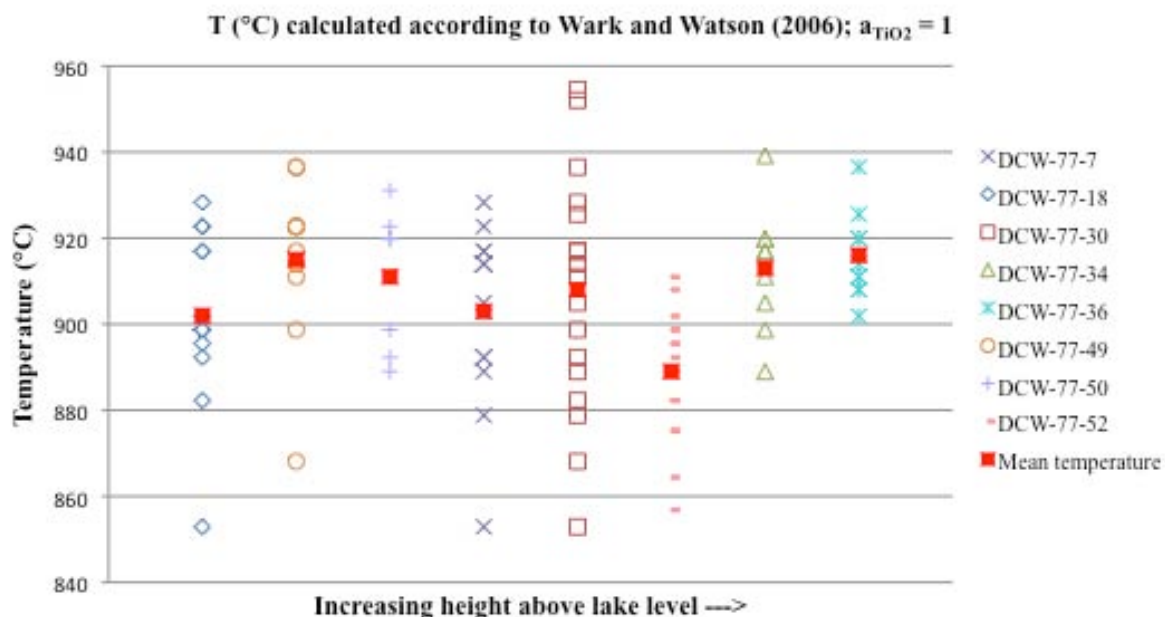
Solving for a_{TiO_2} using equations (2) and (3) is complicated by difficulties in determining the temperature of crystallization of the phases present in the West Clearwater impact melt sheet. The alteration of the Fe-Ti assemblages, where the oxidation of the originally homogeneous titaniferous magnetite has produced complex “oxy-exsolution” textures (see section 7.2.4), renders Fe-Ti oxide thermometry impracticable. The near-absence of orthopyroxene makes two-pyroxene thermometry impossible.

8.3 Results

As mentioned in chapter 7 (section 7.2.3), the Ti content in quartz was determined by electron-microprobe analysis (EMPA). Mean Ti values per sample vary from 282 ppm up to 333 ppm. Detection limits for Ti are on the order of 34 ppm. I will estimate the temperature of crystallization of quartz using the Ti-in-quartz contents presented in chapter 7, and both the equations of Wark and Watson (equation 2) and Thomas et al. (equation 4): equation 2 will be used because it has become the standard equation employed in most Ti-in-quartz studies published since 2006; equation 4 will be used because it takes the effects of pressure into account. I will, however, use both these equations with reservations: as already mentioned, the equation of Wark and Watson (2006) was calibrated at a pressure much above the pressure estimated for the West Clearwater impact melt sheet. It is therefore likely that the temperatures calculated with

the Wark and Watson (2006) formulation will be much too high for this system. The

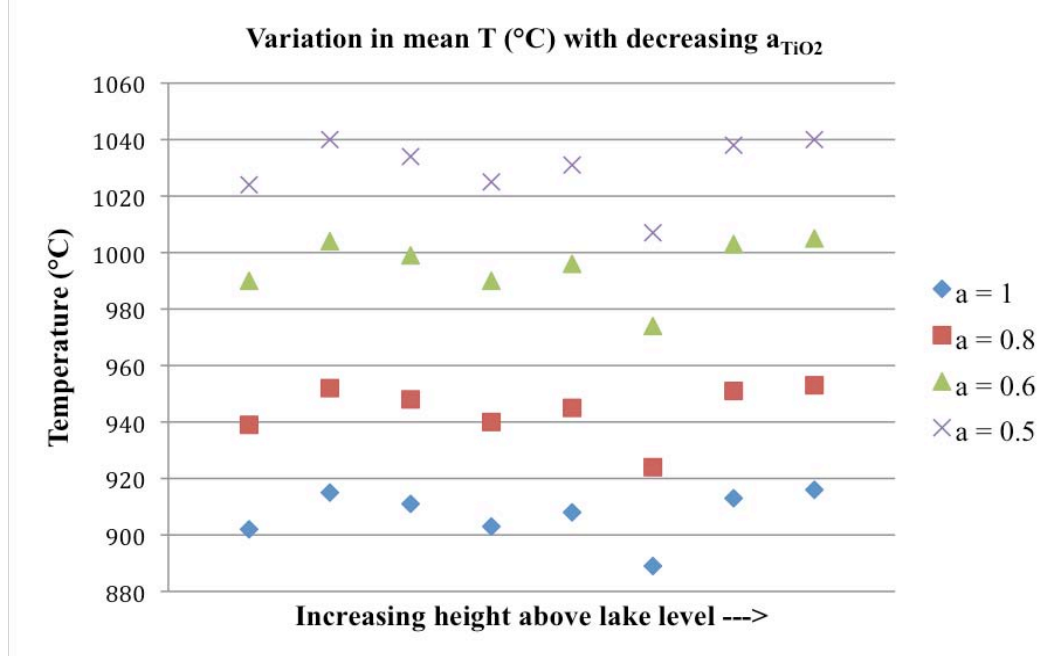
Figure 8.1 Temperature estimated with the Ti content of quartz from the clast-poor impact melt rock of the West Clearwater impact structure. The temperatures are given according to sample and relative to stratigraphic position of samples above lake level. Each mark represents a temperature obtained from a single point-analysis. The temperature ($^{\circ}\text{C}$) was calculated using the equation of Wark and Watson (2006), with an activity of TiO_2 in quartz equal to one.



equation of Thomas et al. (2010) was estimated for pressures between 5 and 20 kbar, still much higher than the 0.1 kbar of maximum pressure I estimated for the West Clearwater impact melt sheet. But Thomas et al. (2010) at least took into account the pressure dependency of the solubility of Ti-in-quartz, whereas Wark and Watson (2006) did not: the equation of Wark and Watson probably does not apply to my system, but the equation of Thomas et al. (2010) provides, at least, the possibility of an extrapolation. The temperatures obtained with the equation of Wark and Watson (2006) are given in Figures 8.1 and 8.2; average temperatures per sample are given in Table 8.3. The temperatures obtained with Thomas et al. (2010) are given in Figures 8.3 and 8.4; in Table 8.4, I provide average temperatures per sample.

If the activities of Ti in quartz in this system are within the values of the activities estimated for silicic igneous systems (that is, about $a_{\text{TiO}_2} = 0.5$ or slightly higher), quartz would have crystallized at temperatures slightly above 1000°C according to the equation of Wark and Watson (2006), and at temperatures of about 730°C according to the equation of Thomas et al. (2010). The high temperatures of crystallization obtained with

Figure 8.2 Temperature estimated with the Ti content of quartz from the clast-poor impact melt rock of the West Clearwater impact structure. The temperatures are given according to sample and relative to stratigraphic position of samples above the lake level. Each mark represents the mean temperature for the sample. T (°C) was calculated using the equation of Wark and Watson (2006) employing a number of activities for TiO_2 in quartz.



Wark and Watson (2006) are in the ballpark of the temperatures I initially expected for this system, whereas the temperatures obtained with Thomas et al. (2010) seem much too low. Therefore, before making any kind of pronouncement concerning the temperature at which quartz crystallized, it is necessary to find some way of independently confirming the temperatures obtained with Thomas et al. (2010) and estimating the correct value of the activity of TiO_2 in quartz.

Table 8.1 Average temperatures per sample and their variation with decreasing a_{TiO_2} estimated with the equation of Wark and Thompson (2006). **DCW-77-7**: sample designation; N : number of point analysis; σ : standard deviation.

	N	$a_{\text{TiO}_2} = 1$	$a_{\text{TiO}_2} = 0.8$	$a_{\text{TiO}_2} = 0.6$	$a_{\text{TiO}_2} = 0.5$
DCW-77-7 Average T(°C) σ	13	903 21.03	940 22.35	990 24.24	1025 25.57
DCW-77-18 Average T(°C) σ	13	902 20.34	939 21.62	990 23.45	1024 24.74
DCW-77-30 Average T(°C) σ	18	908 27.40	945 29.15	996 31.65	1031 33.41
DCW-77-34 Average T(°C) σ	10	913 13.63	951 14.50	1003 15.76	1038 16.64
DCW-77-36 Average T(°C) σ	10	916 10.11	953 10.76	1005 11.69	1040 12.35
DCW-77-49 Average T(°C) σ	10	915 19.96	952 21.23	1004 23.05	1040 24.32
DCW-77-50 Average T(°C) σ	8	911 15.49	948 16.48	999 17.90	1034 18.89
DCW-77-52 Average T(°C) σ	16	889 15.05	924 15.99	974 17.34	1007 18.28

Note that bringing the pressure down to atmospheric values (0.001 kbar instead of 0.1 kbar) decreases the temperature by 3°C, whereas multiplying the pressure by a factor of two (0.2 kbar instead of 0.1 kbar) increases the temperature by 2°C. In other words, the uncertainties regarding the exact pressure of crystallization of the quartz do not significantly affect the temperature calculated with the equation provided by Thomas et al. (2010). Also, if I fix the pressure in the equation of Thomas et al. (2010) (equation 3) at 10 kbar, I obtain temperatures that are similar to those calculated with the equation of Wark and Watson (2006) (equation 1).

Figure 8.3 Temperature estimated with the Ti content of quartz from the clast-poor impact melt rock of the West Clearwater impact structure. The temperatures are given for each sample and relative to its stratigraphic position above lake level. Each mark represents a temperature obtained from a single point analysis. T ($^{\circ}\text{C}$) calculated using the equation of Thomas et al. (2010) with activity of TiO_2 in quartz equal to one.

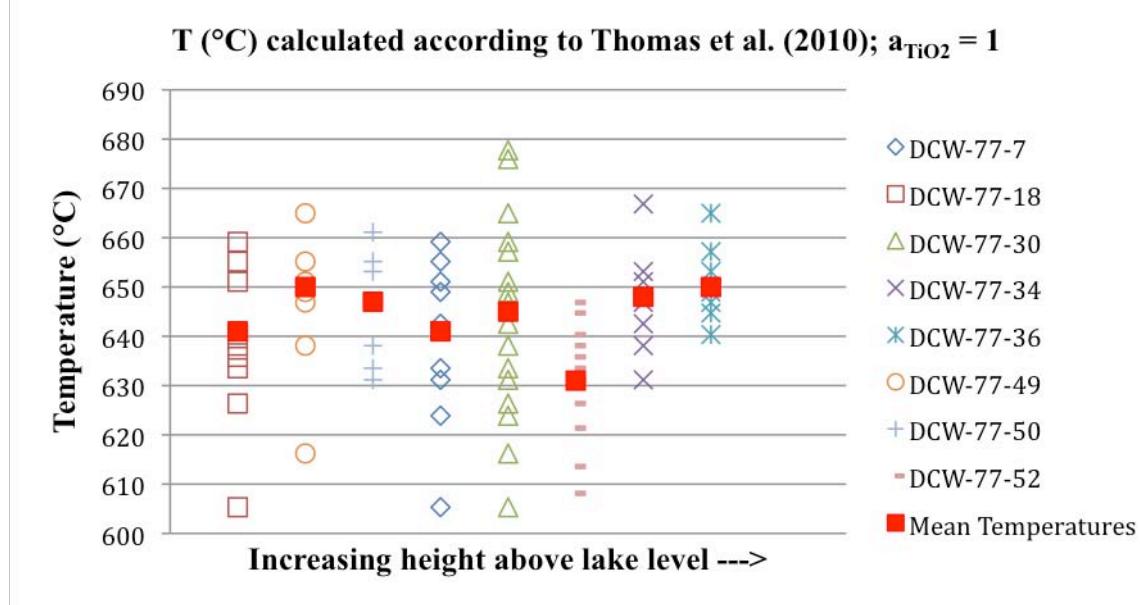


Figure 8.4 Temperature estimated with the Ti content of quartz from the clast-poor impact melt rock of the West Clearwater impact structure. The temperatures are given for each sample and relative to its stratigraphic position above lake level. Each mark represents the mean temperature for the sample. T ($^{\circ}\text{C}$) calculated using the equation of Thomas et al. (2010) employing various of activities for TiO_2 in quartz.

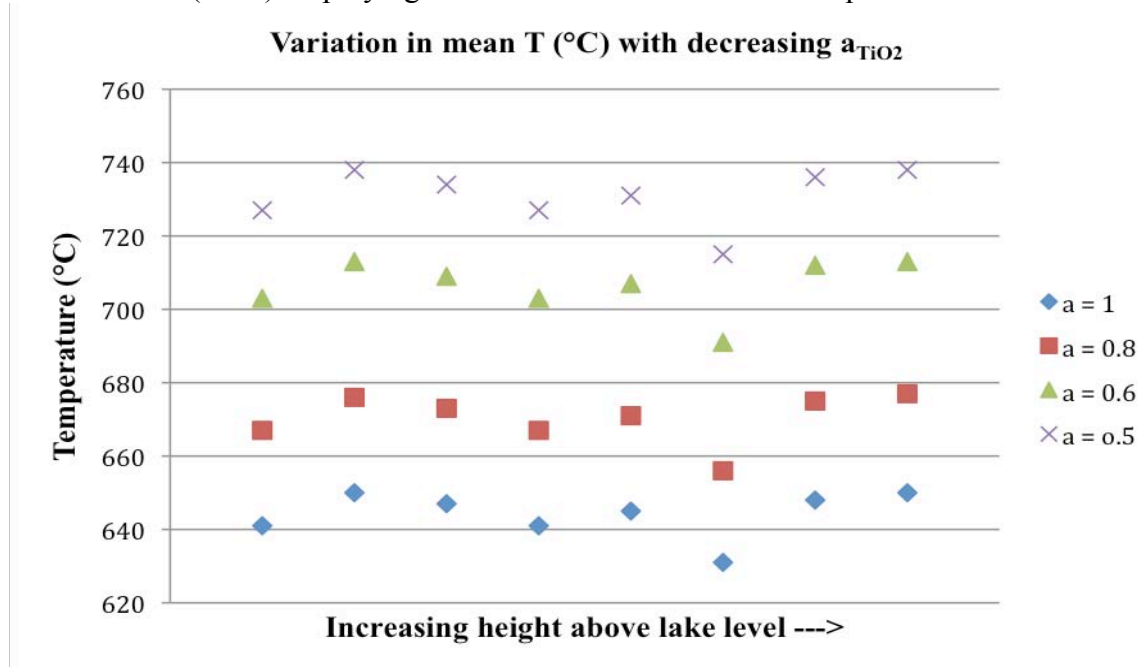


Table 8.2 Average temperatures per sample and their variation with decreasing a_{TiO_2} estimated with the equation of Thomas et al. (2010). **DCW-77-7**: sample designation; N : number of point analysis; σ : standard deviation.

	N	$a_{\text{TiO}_2} = 1$	$a_{\text{TiO}_2} = 0.8$	$a_{\text{TiO}_2} = 0.6$	$a_{\text{TiO}_2} = 0.5$
DCW-77-7 Average T(°C) σ	13	641 15.01	667 15.87	703 17.09	727 17.94
DCW-77-18 Average T(°C) σ	13	641 14.51	667 15.35	703 16.53	727 17.36
DCW-77-30 Average T(°C) σ	18	645 19.52	671 20.65	707 22.26	731 23.38
DCW-77-34 Average T(°C) σ	10	648 9.70	675 10.26	712 11.07	736 11.63
DCW-77-36 Average T(°C) σ	10	650 7.18	677 7.61	713 8.21	738 8.62
DCW-77-49 Average T(°C) σ	10	650 14.22	676 15.05	713 16.22	738 17.03
DCW-77-50 Average T(°C) σ	8	647 11.03	673 11.67	709 12.58	734 13.22
DCW-77-52 Average T(°C) σ	16	631 10.76	656 11.37	691 12.24	715 12.85

8.4 Two-feldspar thermometry

Because of the uncertainties surrounding the value of the activity of TiO_2 in the quartz of the clast-poor impact melt rock in the West Clearwater lake impact structure, it is desirable to estimate the temperature of crystallization of other phases in the clast-poor melt rock. This would allow me, by solving the equations of Wark and Watson (2006) and Thomas et al. (2010) (equations 1 and 3 above) for a_{TiO_2} , to obtain an approximation of the activity of TiO_2 in quartz (see the section on the limitations imposed by the

absence of rutile, section 8.2). However, the near absence of orthopyroxene makes two-pyroxene thermometry impossible, and the strong oxidation of the Fe-Ti oxides makes ilmenite-magnetite thermometry futile. Thus, other than Ti-in-quartz, the only phases I can employ to obtain a temperature are the feldspars.

To employ two-feldspar geothermometry, one must assume that the minerals being analyzed represent equilibrium assemblages, and that their compositions also represent an equilibrium distribution of the components. Particular care must be taken if minerals are chemically zoned, as it is the case in the feldspars of the West Clearwater impact structure: comparing the plagioclase core of one feldspar grain to the sanidine rim of another will invariably lead to erroneous results, as the two compositions were never in equilibrium with each other.

According to the interpretation to be given in section 9.3 of chapter 9, which explains the formation of the comb-texture intergrowths described in chapter 7 (see Figure 7.9 B), the only feldspar compositions that formed at (or near) equilibrium are probably those of the feldspar intergrowths: as explained in Petersen and Lofgren (1986), these intergrowths are the result of cotectic crystallization. However, analyzing these intergrowths with a microprobe beam is tricky: they are quite narrow, in cases narrower than the microprobe beam, and their margins can be indistinct. Because of this, I was forced to rely instead on point analyses taken near the sanidine-plagioclase margin of feldspar grains that did not form intergrowths. These will not be at equilibrium but, hopefully, the first sanidine will have started deposition shortly after the last plagioclase, and the temperature difference between the two will not be too great.

Because the conditions of formation of the feldspars in the clast-poor impact melt rock have certain similarities with those in volcanic systems (possibly moderate

undercooling, relatively rapid crystallization), I decided to employ the two-feldspar thermometers given in Putirka (2008b), who reviewed thermometers and barometers for volcanic systems. In the section dedicated to two-feldspar thermometers, Putirka (2008b) gave the following equations:

$$(7) \quad \frac{10^4}{T(^{\circ}\text{C})} = 9.8 - 0.098P(\text{kbar}) - 2.46 \ln \left[\frac{X_{Ab}^{afs}}{X_{Ab}^{plag}} \right] - 14.2(X_{Si}^{afs}) + 423(X_{Ca}^{afs}) - 2.42(X_{An}^{afs}) - 11.4(X_{An}^{plag} X_{Ab}^{pl})$$

$$(8) \quad T(^{\circ}\text{C}) = \frac{-442 - 3.72P(\text{kbar})}{-0.11 + 0.11 \ln \left[\frac{X_{Ab}^{afs}}{X_{Ab}^{plag}} \right] - 3.27(X_{An}^{afs}) + 0.098 \ln(X_{An}^{afs}) + 0.52(X_{An}^{plag} X_{Ab}^{pl})}$$

where T is the temperature in $^{\circ}\text{C}$, P is the pressure in kbar, and terms such as X_{Si}^{afs} are the cation fraction of the element or component (in this case Si) in the mineral (in this case alkali feldspar). Equation (7) was calibrated from results of 30 of 41 experimental studies [references to the sources of the data are listed in Putirka (2008b); Elkins and Grove (1990) is one of the sources], and this equation recovers T for the calibration data to $\pm 23^{\circ}\text{C}$, and $\pm 44^{\circ}\text{C}$ for the test data. Equation (8) represents a global calibration from all 41 experimental observations and recovers T to $\pm 30^{\circ}\text{C}$.

Most conveniently, to facilitate the usage of these thermometers, Putirka made available for download a Microsoft Excel worksheet that uses both the equations above, and a third equation which is a correction to equations (7) and (8) that was determined by global regression analysis of 42 experiments (Putirka, 2008a). This Excel worksheet also provides a test for equilibrium that uses the models of Elkins and Grove (1990) to

compare the activities calculated for alkali feldspar and plagioclase. As pointed out by Elkins and Grove (1990), at equilibrium, one must have:

$$\begin{aligned} a_{Ab}^{plag} &= a_{Ab}^{afs} \\ a_{An}^{plag} &= a_{An}^{afs} \\ a_{Or}^{plag} &= a_{Or}^{afs} \end{aligned}$$

Therefore, by subtracting the activities of plagioclase from the activities of alkali feldspar, it is possible to calculate $\Delta a_{\text{feldspar}}$ i.e., Δa_{An} , Δa_{Ab} and Δa_{Or} . These should nominally be zero for a system at equilibrium. In the real world, however, equilibrium is rarely attained: for instance, in the case of the experiments of Elkins and Grove (1990), Δa_{An} ranges from -0.57 to 0.33, Δa_{Ab} from -0.07 to 0.31 and Δa_{Or} from -0.09 to 0.32. Finally, Putirka (2008a) warned that experimental tests are required to determine whether this measure of equilibrium is effective at reducing error for T calculated using experimental data. Nevertheless, considering the problems with my two-feldspar system alluded to above, the inclusion of this test of equilibrium should be useful in determining which temperature estimates might be reliable.

8.4.1 Results

Table 8.5 presents a detailed presentation of the two-feldspar thermometry calculations, whereas Figures 8.5 to 8.7 give a general overview of the results. Finally, Table 8.6 gives the average temperatures obtained with the two-feldspar thermometers as formulated by Putirka (2008a, 2008b).

In order to calculate average temperatures (Table 8.6), I have somewhat arbitrarily divided the temperatures obtained with the equations of Putirka (2008a) in three groups: the first group includes all two-feldspar temperatures, the second group

Table 8.3 Two-feldspar temperatures determined using Putirka (2008a). The columns under the Feldspar Pairs heading give the designations of the point analyses used for the calculations. The compositions of the feldspars employed are given in appendix D. The columns beneath Two-Feldspar Temperatures give the results of the thermometry calculations. The columns under the Test For Equilibrium heading use the models of Elkins and Grove (1990) to compare the activities calculated for alkali and plagioclase feldspar: these should nominally be equal to zero.

# Fspar Pairs	Feldspar Pairs		Two-Feldspars Temperatures (°C)			Test For Equilibrium: a(plag)-a(kspar)		
	Plagioclase	Alkali Feldspar	Eqn (7)	Eqn (8)	Global regression	$\Delta a(\text{An})$	$\Delta a(\text{Ab})$	$\Delta a(\text{Or})$
1	DCW-77-5-R4- Plag 4	DCW-77-5-R4-Kspar 2	1019	886	875	-0.41	0.16	-0.31
2	DCW-77-8-R1-Plag 1	DCW-77-8-R1-Kspar 2	931	850	811	-0.52	0.07	-0.31
3	DCW-77-28-R3-Plag 3	DCW-77-28-R3-Kspar 1	937	804	796	-0.17	0.05	-0.12
4	DCW-77-33-R2- Feldspar 4	DCW-77-33-R2- Feldspar 2	799	700	690	-1.05	0.14	-0.16
5	DCW-77-33-R2-Fspar 4	DCW-77-33-R2-Fspar 3	876	786	771	-0.90	0.12	-0.23
6	DCW-77-33-R2-Feldspar13	DCW-77-33-R2-Feldspar 3	927	826	806	-0.48	0.06	-0.09
7	DCW-77-51-R4-Feldspar 3	DCW-77-51-R4-Feldspar 2	905	825	788	-1.03	0.09	-0.15
8	DCW-77-53-R1-Feldspar 5	DCW-77-53-R1-Feldspar 4	882	791	777	-0.98	0.10	-0.10
9	DCW-77-53-R1-Feldspar12	DCW-77-53-R1-Feldspar 13	913	808	807	-0.37	0.04	0.01
10	DCW-77-61-R3-Feldspar 3	DCW-77-61-R3-Feldspar 2	954	919	866	-0.63	0.06	-0.13
11	DCW-77-61-R1-Feldspar 3	DCW-77-61-R1-Feldspar 8	813	779	734	-1.86	0.10	-0.09
12	DR-10-R2-5	DR-10-R2-1	874	762	749	-0.43	0.09	-0.16
13	DR-10-R2-6	DR-10-R2-1	864	754	739	-0.60	0.13	-0.43
14	DR-10-R2-6	DR-10-R2-4	845	732	720	0.01	0.06	-0.38
15	LP-2-R1-j	LP-2-R1-l	882	792	777	-1.24	0.13	-0.20
16	LP-2-R1-f	LP-2-R1-h	867	786	776	-1.11	0.11	-0.11

combines two-feldspar temperatures with $\Delta a_{\text{feldspar}}$ values smaller than $|0.6|$, and the third group only takes into account temperatures with associated $\Delta a_{\text{feldspar}}$ smaller than $|0.4|$.

Because quartz was the last phase to crystallize from the melt, to make physical sense, the temperatures of crystallization determined with the two-feldspar need to be slightly higher than the temperatures calculated for the crystallization of quartz. From this inference, it is apparent that the most of the temperatures estimated with Wark and Watson (2006) are much too high to fit with the temperatures calculated with the two-feldspar thermometers of Putirka (2008a, 2008b). However, the results obtained with Thomas et al. (2010) seem to be in good agreement with those obtained with the two-feldspar thermometer.

Table 8.4 Average two-feldspar temperatures determined using the software of Putirka (2008a). The temperatures of the first row were calculated using all values obtained, irrespective of the results of the tests for equilibrium. The second row excludes values with $\Delta a_{\text{feldspar}}$ larger than $|0.6|$, the third row excludes all values with $\Delta a_{\text{feldspar}}$ larger than $|0.4|$. N : number of feldspar pairs; σ : standard deviation; $|x|$: absolute value of x.

	Equation (7)	Equation (8)	Global regression
All values N=16 Average T(°C) σ	893 54.54	800 54.53	780 48.77
Near equilibrium + near disequilibrium N=9 Average T(°C) σ	898 47.72	781 42.77	774 47.37
Near equilibrium only N=3 Average T(°C) σ	918 52.81	816 62.04	797 53.41

Figure 8.5 Two-feldspar temperatures determined using equation (7); calculations made with the software of Putirka (2008a). Error bars: $\pm 44^\circ\text{C}$. The numbers in the Feldspar pairs axis refer to the Feldspar Pairs # column in Table 8.5.

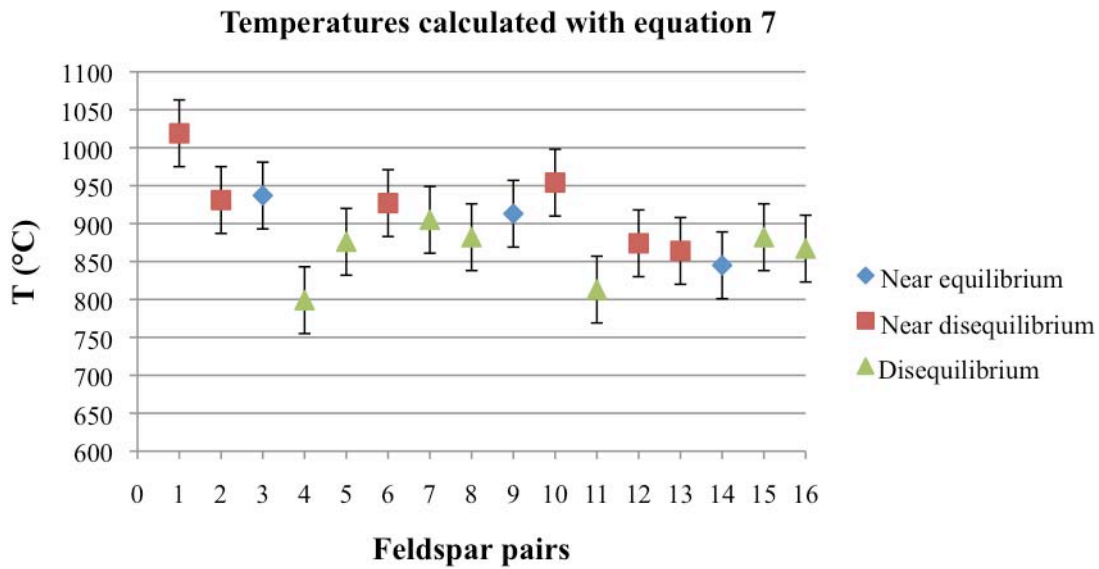


Figure 8.6 Two-feldspar temperatures determined using equation (8); calculations made with the software of Putirka (2008a). Error bars: $\pm 30^\circ\text{C}$. The numbers in the Feldspar pairs axis refer to the Feldspar Pairs # column in Table 8.5.

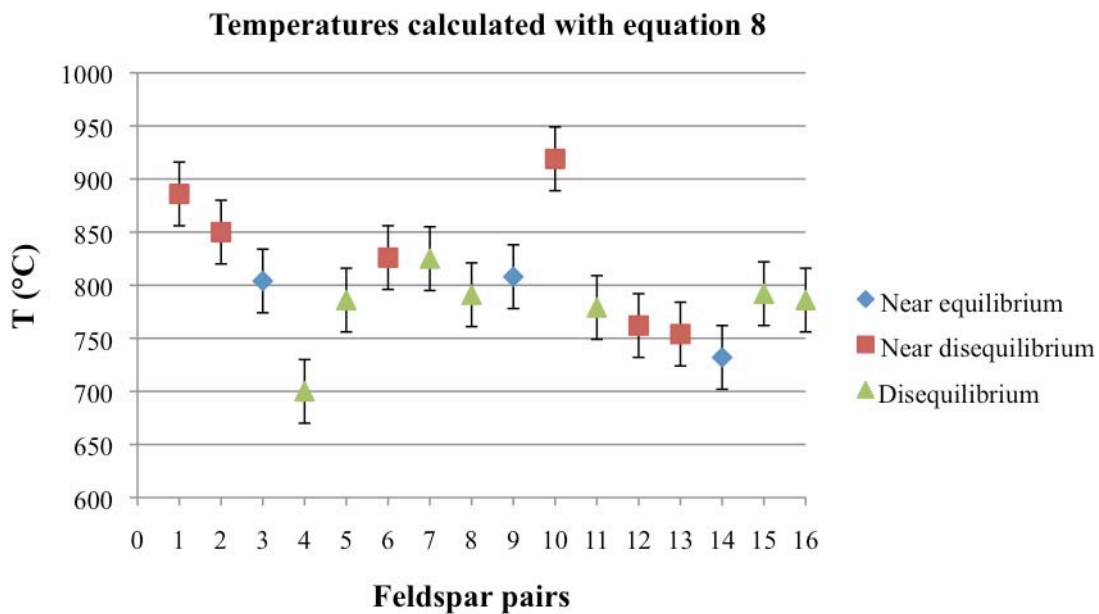
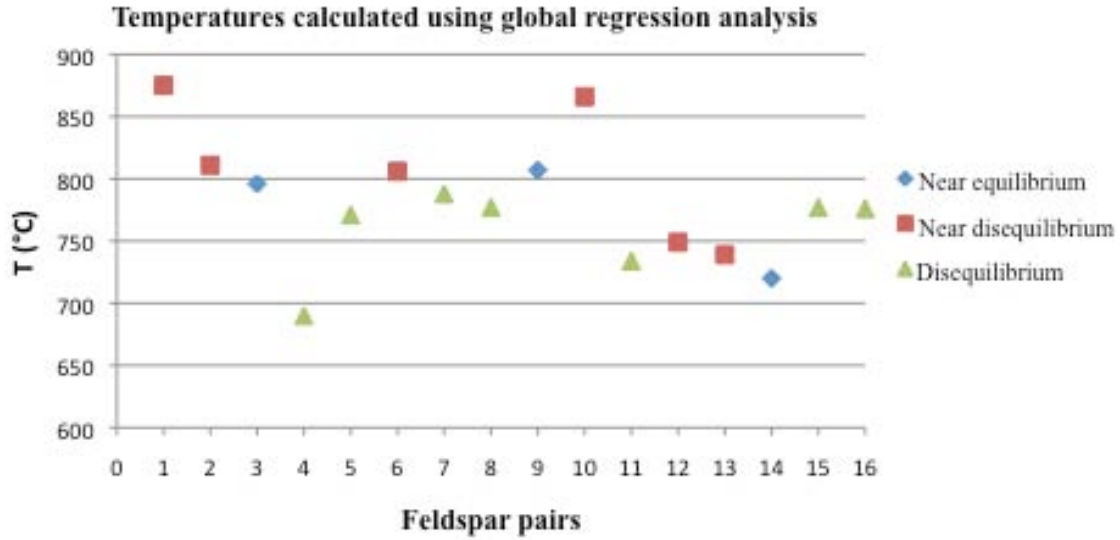


Figure 8.7 Two-feldspar temperatures determined using global regression analysis; calculations made with the software of Putirka (2008a). The numbers in the Feldspar pairs axis refer to the Feldspar Pairs # column in Table 8.5.



8.4.2 Estimating a_{TiO_2} from two-feldspar temperatures

Solving the equation of Wark and Watson (2006) for a_{TiO_2} , I obtain:

$$(9) \quad \text{Log}(a_{\text{TiO}_2}) = \text{Log}(X_{\text{Ti}}^{\text{qtz}}) + \frac{3765}{(T(^{\circ}\text{C}) + 273)} - 5.69$$

where T is temperature in degrees Celsius, $X_{\text{Ti}}^{\text{quartz}}$ is the amount of TiO_2 in quartz in ppm, and a_{TiO_2} is the activity of TiO_2 in the system. Solving the equation of Thomas et al. (2010) for a_{TiO_2} , I obtain:

$$(10) \quad \text{Ln}(a_{\text{TiO}_2}) = \frac{RT(K)\text{Ln}(X_{\text{Ti}}^{\text{qtz}}) + 60952 - 1.520T(K) + 1741P(\text{kbar})}{RT(K)}$$

where R is the gas constant ($R=8.31447$ J/mol K), T is temperature in Kelvin, P is the pressure in kbar, $X_{\text{TiO}_2}^{\text{quartz}}$ is the mole fraction of TiO_2 in quartz, and a_{TiO_2} is the activity of TiO_2 in the system.

As the feldspars did crystallize *before* quartz, therefore at a higher temperature than quartz, obtaining a_{TiO_2} from two-feldspar temperatures will not give the exact value of the activity of Ti in quartz. It will, however, *provide a minimum value for a_{TiO_2}* (recall that there is an inverse relation between temperature and activity). The real a_{TiO_2} values will have to be larger than the a_{TiO_2} values obtained from the two-feldspar thermometer temperatures.

Entering the average temperatures obtained with two-feldspar thermometry (see table 8.6) and the amount of Ti in quartz measured previously (see section 7.2.3) into equation (9) only yielded a_{TiO_2} values smaller than unity if I employed the two-feldspar temperatures obtained with equation (7) and Ti contents in quartz below about 300 ppm. Entering two-feldspar temperatures obtained with equation (8) or the temperatures obtained with the global regression method yielded impossible a_{TiO_2} values (the activities were greater than unity). Assuming that my two-feldspar temperatures are correct, this clearly shows that equation (9), the equation of Wark and Watson (2006), is not appropriate for my system.

Entering two-feldspar temperatures into equation (10), the equation of Thomas et al. (2010), however, does yield realistic values for the activity of TiO_2 in quartz.

Table 8.5 Minimum values for the activities of TiO_2 in quartz estimated from two-feldspar temperatures obtained using equation (7), (8) and global regression. The Ti contents in ppm in the sample column are the average values for the sample; the first temperature under the Equation (7), (8) and global regression columns is the average temperature calculated using feldspar pairs near equilibrium; the second temperature is the average temperature obtained by combining feldspar pairs near equilibrium and pairs near disequilibrium (see Table 8.6 above).

Sample	Estimated minimum values for the activities of TiO_2 in quartz					
	Equation (7)		Equation (8)		Global regression	
	T=898°C	T=918°C	T=781°C	T=816°C	T=774°C	T=816°C
DCW-77-7 Ti = 309 ppm	0.21	0.19	0.42	0.33	0.43	0.33
DCW-77-18 Ti = 308 ppm	0.21	0.19	0.41	0.33	0.43	0.33
DCW-77-30 Ti = 320 ppm	0.21	0.19	0.43	0.34	0.45	0.34
DCW-77-34 Ti = 329 ppm	0.22	0.20	0.44	0.35	0.46	0.35
DCW-77-36 Ti = 333 ppm	0.22	0.20	0.45	0.36	0.47	0.36
DCW-77-49 Ti = 333 ppm	0.22	0.20	0.45	0.36	0.47	0.36
DCW-77-50 Ti = 324 ppm	0.22	0.20	0.44	0.35	0.46	0.35
DCW-77-52 Ti = 282 ppm	0.19	0.17	0.38	0.30	0.40	0.30

As mentioned in section 8.2, for silicic igneous assemblages, activities of 0.5 or higher seem to be the norm: for example, the titanium activity of the rhyolitic Bishop tuff system is assumed to have been buffered at about $a_{\text{TiO}_2} = 0.53$ by the presence of Fe-Ti oxides during crystallization (Reid et al., 2011; Thomas and Lanzirrotti, 2010). Assuming that quartz solidified at temperatures no more than 50 to 100°C below the temperatures at which feldspar crystallized, the temperatures obtained with equation (7) give minimum a_{TiO_2} values that are much too low for a felsic igneous assemblage: a decrease of 100°C produces a_{TiO_2} values that are still far from the 0.5 estimated for felsic igneous systems,

that is, entering $T=798^{\circ}\text{C}$ into equation (7) instead of $T=898^{\circ}\text{C}$ makes the value of a_{TiO_2} jump from 0.22 to 0.39. For equation (8) and the global regression equation, a decrease of only 30°C is enough to put most of the values of a_{TiO_2} above 0.5.

From all this, I can conclude that the activity of Ti in quartz was in the vicinity of 0.5 to 0.6, which implies that quartz, the last phase to have crystallized in the clast-poor impact melt rock, solidified at temperatures of 700 to 730°C .

This results came as a surprise: I had initially assumed, because the melt created by the impact would necessarily have been superheated and consequently dry, that the temperatures of the solidus of the system would have been unusually high, above 1000°C . For instance, Onorato et al. (1978) assumed that the impact melt was dry and estimated that the temperature of the end of crystallization in the Manicouagan impact melt sheet, which has an average composition only slightly more mafic than that of the impact melt sheet at West Clearwater Lake, was about 1027°C .

A solidus temperature of 700 to 730°C , 300°C lower than what I expected, puts the system within the temperatures of crystallization of normal siliceous igneous intrusions that are rich in H_2O . I believe that the simplest way to explain the low temperature of crystallization of the West Clearwater clast-poor melt rock is to introduce H_2O into the system, a matter that will be more fully developed in the following chapter.

8.6 Summary of chapter 8

- Two-feldspar thermometry calculations suggest that the last plagioclase and the first alkali feldspar crystallized at temperatures of about 781 to 816°C ($\pm 44^{\circ}\text{C}$).

- Quartz was the last phase to crystallize in the clast-poor impact melt rock of the West Clearwater impact structure. This mineral crystallized at temperatures of 700 to 730°C, with an activity of Ti in quartz between 0.5 and 0.6.

Chapter 9: Discussion and Conclusions

In this, the final chapter of my thesis, all the descriptions given earlier will be integrated into a narrative about the impact melt of the West Clearwater Lake structure, how it formed and crystallized. I will start by proposing a mixing model for the formation of the impact melt; I will present a hypothesis on the origin of the glass spheroids documented in chapter 6. These sections will then be followed by an explanation of the origin of the most conspicuous texture involving the main minerals that crystallized from the impact melt. The petrological implications of the geothermometric data presented in chapter will then be discussed. I will close with a few final thoughts on the subject of impact melts and a Summary and Conclusions section.

9.1 Mixing model

To estimate the proportions of each target rock contributing to the impact melt, I use a mixing model employing an approach of least-squares approximations as used by Bryan et al. (1969) and Wright and Doherty (1970). These calculations were done using the mathematical software MATLAB (The MathWorks Inc.), where the common inverse least-squares function $x = \text{inv}(A' * A) * A' * b$ was converted to a MATLAB function with $x \geq 0$ as $[x, \lambda] = \text{lsqnonneg}(A, b)$ to avoid a negative proportion. Here, A is the matrix grouping the average target-rock compositions, b is the average composition of the impact melt, and x is the proportion of target rock modeled by the least-squares mixing approximation.

Table 9.1 presents results of the least-squares mixing model for the major-element composition of the average impact-melt-derived rock and the main lithological units found in the West Clearwater Lake impact structure, as determined in this study (see Table 6.2). The model is based on the average compositions of the four principal basement rocks types identified in chapter 5: granitic rocks, granodioritic, enderbitic and tonalitic rocks, mafic and ultramafic rocks and diabase. The compositions of these rocks are given in Table 5.1.

As shown in Table 9.1, to obtain the average melt-rock composition, one needs to mix about 62% granodioritic, enderbitic and tonalitic rocks, 31% granitic rocks and 6% mafic and ultramafic rocks. The proportions were about the same for the relatively homogeneous clast-poor melt (60%, 32%, and 7%, respectively) and the slightly less homogeneous clast-poor impact melt rock (67%, 28%, 4%). Both the fragmental breccia (50%, 33%, 15%) and the infiltration dykes (75%, 20%, 4%) deviate considerably from this. This difference is probably explained by the higher amount of MgO present in my samples of infiltration dykes and fragmental breccia. Totals of the calculated proportions of the target rocks are close to 100% (97.93-99.45%).

According to the models, diabase is an inconsequential component, unnecessary to obtain the average compositions of the units of impact melt. Also, the total proportions are not improved by including Ordovician limestone in the mixture. Minor amounts of both of these units are presently found within the impact melt, but they are unnecessary to the mixing models. Nevertheless, I cannot rule out the presence of a small proportion (probably less than 5%) of limestone and diabase mixed in the impact melt. The rock compositions obtained with the mixing model are obtained by

Table 9.1 Least-squares modeling of sources to account for melt-rock compositions at West Clearwater Lake.

Units of impact melt rock	Average impact melt rock	Clast-poor impact melt rock	Clast-rich impact melt rock	Fragmental breccia matrix	Infiltration dykes
n	46	32	14	13	5
SiO ₂ wt. %	60.90	61.01	60.65	59.42	59.56
TiO ₂	0.77	0.77	0.77	0.72	0.80
Al ₂ O ₃	15.87	15.77	16.09	15.47	16.42
FeO _{total}	6.17	6.16	6.19	6.65	6.36
MnO	0.06	0.06	0.06	0.08	0.07
MgO	2.75	2.73	2.79	4.06	3.03
CaO	4.46	4.56	4.22	3.49	4.53
Na ₂ O	3.76	3.73	3.84	3.43	3.98
K ₂ O	3.50	3.53	3.42	2.97	3.30
P ₂ O ₅	0.30	0.30	0.31	0.28	0.32
Target-rock proportions (%)					
Granitic rocks	30.84	32.03	28.21	32.51	20.28
Granodioritic, Enderbitic and tonalitic rocks	62.22	60.17	66.87	50.07	75.01
Mafic and ultramafic rocks	6.32	7.25	4.16	15.17	3.93
Diabase	0.00	0.00	0.00	0.18	0.00
Total	99.38	99.45	99.24	97.93	99.22
Mixing model melt rock compositions					
SiO ₂ wt. %	60.94	61.05	60.70	59.48	59.63
TiO ₂	0.79	0.78	0.81	0.76	0.86
Al ₂ O ₃	15.80	15.73	15.94	15.11	16.18
FeO _{total}	6.20	6.19	6.23	6.38	6.60
MnO	0.08	0.08	0.08	0.08	0.08
MgO	2.62	2.68	2.51	3.24	2.64
CaO	4.48	4.49	4.45	4.78	4.69
Na ₂ O	3.86	3.84	3.90	3.64	3.95
K ₂ O	2.88	2.88	2.88	2.72	2.79
P ₂ O ₅	0.34	0.33	0.35	0.32	0.38
Residuals (observed - calculated)					
SiO ₂ wt. %	-0.04	-0.04	-0.05	-0.06	-0.07
TiO ₂	-0.02	-0.01	-0.04	-0.04	-0.06
Al ₂ O ₃	0.08	0.04	0.15	0.36	0.24
FeO _{total}	-0.03	-0.03	-0.04	0.26	-0.24
MnO	-0.02	-0.02	-0.02	-0.00	-0.01
MgO	0.12	0.05	0.28	0.81	0.39
CaO	-0.02	0.07	-0.23	-1.29	-0.16
Na ₂ O	-0.10	-0.11	-0.06	-0.21	0.03
K ₂ O	0.62	0.65	0.54	0.25	0.51
P ₂ O ₅	-0.04	-0.03	-0.40	-0.04	-0.06

multiplying the matrix with the target-rock compositions in the proportions calculated with least-squares modeling. To compare these calculated compositions to the observed compositions, I calculated the residuals, which are the observed compositions minus the calculated compositions. The fit is generally quite good, below $|0.10|$ wt.%, except for K_2O in all samples, and MgO and CaO in the infiltration dykes and fragmental breccia samples.

The proportions of target rock obtained in my mixing model do not agree with the proportions observed in the core sunk in basement rocks (see chapter 4), where granitic compositions dominate all others. However, they do fit with the surface geology described in Simard et al. (2004): according to them, the most common rock types revealed by mapping in the vicinity of the West Clearwater impact structure belong to the Loups Marins Complex, which consists of enderbites, diorites and tonalites; the second most common rock types are the granites and granodiorites of the Desbergères Suite.

Least-squares modeling of the West Clearwater Lake impact melt rock was done previously by Grieve (1978) and Hische (1995). Because the classification of their target rocks differs from mine, our results are not directly comparable, but there are some similarities between our models: like my own calculations, their model forms impact melt by mixing a larger proportion of intermediate rock (their granulite, 54 wt% SiO_2) with a smaller proportion of felsic rock (their quartz monzonite, 72 wt% SiO_2). Like my own results, their mixing models do not require the presence of limestone. Whereas my mixing calculations indicate the presence of 4 to 15% mafic and ultramafic rock (depending on the impact melt unit: Table 9.1), their results do not require any mafic target rocks. I have based the classification of the units that mixed to form the impact melt on the general regional geology described in Simard et al. (2004), which is the latest

regional study of the West Clearwater Lake area. The regional geology was very poorly known when Grieve (1978) and Hische (1995) calculated their mixing models. Because of this, I consider my mixing model to be more accurate than theirs.

9.2 On the origin of the glass spheroids

As described in chapter 6, within the glass of the fragmental breccia and the infiltration dykes, there are roughly spherical droplet-like inclusions that have been named “glass spheroids” by Dence et al. (1974). These “glass spheroids” now consist largely of clay minerals. As Dence et al. (1974) pointed out, there are two possibilities for the formation of the glass spheroids: either the glass spheroids developed as normal vesicles created by exsolution of a gas phase later filled by clay minerals, that is, the filling of the glass spheroids occurred after solidification of the glass matrix, or the materials presently filling the glass spheroids are the altered remains of the primary material.

I will argue for the second hypothesis by making the following observations: first, the drop-like shapes of the spheroids are most probably the result of the action of interfacial tension between the matrix melt and the glass spheroids. Both Dence et al. (1974) and I have observed examples of glass spheroids in the process of either coalescing or rupturing, possibly breaking apart, which are interpreted as indications of complete filling at the time these disruptions took place, when both the matrix glass and the spheroids were in the molten state.

Secondly, present-day spheroids typically are completely filled with what I believe are clays (see section 6.4.2), and there is no indication of shrinkage on cooling. The fillings vary widely in composition (see Table 6.11), even where the spheroids are in

close association. Neither Dence et al. (1974) nor I have observed cracks or veins, either in the vicinity of the glass spheroids or elsewhere in the samples of glass, filled with material with a composition similar to that of the substances filling the glass spheroids. I have, however, observed a few examples of secondary material infiltrating cracks in the glass matrix and even *cutting across* the glass spheroids themselves. For instance, one large spheroid in thin section DCW-77-65-4 has been cut by a vein of material that shows a granular texture on back-scattered electron images. But this material has a composition rich in Na_2O (see analysis 35 in table 6.11) that is distinctly different from that of the glass spheroid material. This material must have been injected into the cracks when all the glass solidified. Lastly, vesicles in some cases are present in the glass matrix (see, for instance, figure 6.2). Most are empty, but some can be partially filled by a material with a composition very rich in volatiles (totals tend to be very low, 10 to 30 wt.% and most of it Al_2O_3), which is, once again, distinctly different from that of the material filling the glass spheroids. These points argue against the formation of the “glass spheroids” by a late filling of vesicles with a secondary material.

As explained in chapter 6, I do not know what the original composition of the glass in the spheroids was. The presence of a smectitic clay must reflect a glass that was originally relatively mafic. The rocks melted during the impact event contain variable amounts of pyroxene, amphibole, biotite and iron oxides, in some cases altered to secondary minerals. In particular, a least-squares mixing model of the composition of the fragmental breccia suggest that this unit contains about 15% amphibole- and biotite-bearing mafic and ultramafic rock (Table 9.1). It is therefore possible that some of the volatile component in the glass spheroids is primary. But it is more likely that the present volatile-rich composition of the material filling the glass spheroids is the result of a later

deuteric alteration of a dry glass. As mentioned in section 7.2.2, pseudomorphic replacement of clinopyroxene by clays is common in the massive, well-crystallized clast-poor melt (see Figures 7.17 B and 7.19 A). Table 9.2 compares the compositions of the clay assemblage formed by the alteration of the clinopyroxene and the high-Mg material found within a glass spheroid of sample LP-125.

Table 9.2 Composition of the clays formed by the alteration of clinopyroxene vs. the composition of the material presently filling some of the glass spheroids.

Sample	DR-10-R5b-6 <i>(pseudomorphic alteration of clinopyroxene)</i>	LP-125-image3-mafic glass 6 <i>(High MgO material filling glass spheroid)</i>
SiO ₂ wt. %	43.31	51.95
TiO ₂	0.03	0.01
Cr ₂ O ₃	0.12	0.01
Al ₂ O ₃	5.68	7.67
FeO _{total}	14.79	1.67
MnO	0.18	0.02
MgO	16.56	20.56
CaO	1.96	0.74
Na ₂ O	0.65	0.39
K ₂ O	0.99	0.49
Total	84.26	83.51

If pseudomorphic alteration of pyroxene is common within the relatively unaltered and impermeable clast-poor impact melt rock, then it must have been even easier to transform a mafic glass to clay within the friable, heterogeneous and permeable fragmental breccia and in the partially devitrified glass of the infiltration dykes, both of which are typically heavily altered to clay minerals and stained by hematite.

Dence et al. (1974) also favoured the hypothesis that the materials filling the glass spheroids are the altered remains of the primary glassy material, and some of their observations concur with mine. But, writing in 1974, at a time when fluid immiscibility was a popular topic, Dence et al. conjectured that “the melt, with its content of about 1% of volatiles, unmixed at high temperatures into two immiscible fluids, one almost dry (the

matrix), the other containing as much as 20% H₂O (the glass spheroids)”. In other words, the high volatile content of the glass spheroids was interpreted to make them immiscible in the drier matrix glass.

The occurrence of micrometric to millimetric globular heterogeneities in igneous rocks has been frequently explained by invoking liquid immiscibility. For instance, the formation of small-scale carbonatite globules surrounded by silicate glass observed in natural samples has been attributed to immiscibility between silicate and carbonate melts, e.g., Kjarsgaard and Peterson (1991), Bailey et al. (2005; 2006). I do not know, however, if immiscibility between volatile-rich silicate melts and volatile-poor silicate melts has ever been observed in nature, or if it is even possible.

The existence of such textures is not necessarily related to immiscibility. For instance, similar textures have been observed both in natural samples and in laboratory experiments that involved silicate-silicate magmatic pairs that have been proven to be mutually miscible (Schreiber et al., 1999; Valentini and Moore, 2009; Yoder Jr., 1973; Zimanowski et al., 2004). In an impact-related context, Zieg and Marsh (2005) proposed that the development of a viscous emulsion between two miscible magmas might explain the formation of the Sudbury Igneous Complex.

Valentini and Moore (2009) pointed out that the possibility that miscible liquids can develop a transient surface tension and mimic the behaviour of immiscible liquids was first suggested by Korteweg (1901). The ideas of Korteweg were applied to magmas by Mungall (1994), who presented results of experiments in which smooth menisci formed at the interface between two miscible magmas. Mungall suggested that their formation was related to the action of “Korteweg stresses” generated by compositional gradients at the interface between the two miscible liquids. Morra and Yuen (2008)

suggested that Korteweg stress may play an important role in processes involving sharp compositional gradients and occurring at different scales, from subduction and plume rise to crystal lattice deformation.

The experiments of Zimanowski et al. (2004) are of particular interest to the understanding of the formation of the glass spheroids of the West Clearwater impact melt: these authors produced globules with a morphology similar to those observed in the West Clearwater impact melt rock. In their experiments, a basaltic melt was introduced in the lower third of the cylindrical crucible of a modified high-temperature rotational viscometer. After cooling to room temperatures, a granulate with a rhyolitic composition was filled in over the solidified basalt and the crucible was heated to the final temperature (1327°C). As basaltic melt is denser than the rhyolitic melt, a stable stratification was obtained. A small, metallic cylindrical rotating body was then introduced into the rhyolitic melt, at the center and parallel to the sides of the crucible and perpendicularly to the rhyolite-basalt interface. This rotating body was used to generate shear stress within the crucible for a set time-period. After each experiment, the melts were quenched, and the glass was cut into thin sections.

Preliminary experiments in which basaltic and rhyolitic melts were stratified without induced shear produced a well-defined simple and stable interface between both melts. However, experiments in which moderate shear stress was applied for two hours produced, at the interface between the melts, small globules of basaltic melt about 1.1 mm in average diameter. In experiments run at a low shear-rate, Zimanowski et al. produced domains of basaltic melt 4 mm in diameter on average; at high shear-rate, they produced basaltic globules 0.9 mm across. The formation of these globules started at the interface; these moved downward into the basaltic melt by filling void spaces between

the globules with rhyolitic melt. Running this experiment for eight hours increased the distance between globules and, although the average globule diameter stayed the same, the larger globules were increasingly fragmented by hydrodynamic separation, whereas the smaller globules got dissolved into the host melt. In addition, the rhyolitic matrix melt evolved to an andesitic composition, indicating that the melts were progressively mixing and diluting. Scaling their experiments to natural systems, the authors estimated that, for systems involving mixtures of basaltic and rhyolitic compositions, time spans for equilibration should be in the range of days.

Summarizing, I attribute the origin of the glass spheroids to the formation, during the opening of the crater, of a superheated melt that incorporated bits and pieces of the target rock. The extremely short times involved prevented the complete homogenization of the mixture. Shortly after impact, the melt was composed of matrix melt, the homogenized product of the melt produced by the highest shock pressures, with blobs of pure molten silica derived from quartz, and mafic glass spheroids that were probably derived from phases such as pyroxenes, biotites, amphiboles and iron oxides present in the target rocks. The preservation of this mixture, and therefore the preservation of the glass spheroids, was possible because the heterogeneous melt was injected into, or mixed with, the cooler brecciated rocks of the basement, which rapidly chilled the melt within the breccias and dykes lining the crater floor. Much later, the vigorous circulation of aqueous fluids associated with hydrothermal activity preferentially altered the mafic glasses within the glass spheroids to clay minerals. Generally, whatever the reactions involved, the chemical compositions of altered and unaltered rocks are similar, except for H₂O contents (Meunier, 2005).

Similar glassy spheroids have also been observed in glasses of the Zhammanshin structure, an impact crater with a diameter of 14 km in Kazakhstan that is estimated to be ~1 Ma old (Fel'dman and Sazonova, 1993; Grieve, 2006). More recently, Osinski et al. (2004) reported that suevitic glass of the Ries structure, a ~24 km-diameter impact crater in southern Germany, contains numerous clay-rich globules similar to the ones I have observed in the glass of the West Clearwater Lake impact structure. These and other features have led Osinski et al. to suggest that the glassy groundmass of the Ries impact structure represents a mixture of several types of impact-generated melts which may have possibly originated as some form of impact melt flow(s) that emanated from different regions of the evolving crater. However, unlike the glassy spheroids of the West Clearwater Lake and Zhammanshin impact structures, the heterogeneities in the Ries glass are found outside the crater, within material that was ejected during the impact. Some of Ries globules could be tektites trapped into the outflowing melt, whereas the globules at West Clearwater Lake and, I believe, at Zhammanshin also, clearly formed in the impact melt.

9.3 Plagioclase-sanidine intergrowths (comb texture)

The complex zoning of feldspars observed in the clast-poor melt rock and described in section 7.2.1 of chapter 7 has also been observed in the melt sheets of other impact structures. Therriault et al. (2002) reported on complex patterns of twinning and zoning, including Na-rich plagioclase cores interpreted as being xenocrystic within the lower (“norite”) and middle units (“quartz gabbro” and transition zone) of the Sudbury Igneous Complex. Heterogeneous plagioclase crystals with reverse zoning and a complex pattern of twinning have also been observed in impact-melt rocks from the Manicouagan impact

structure, northern Quebec (Floran et al., 1978) and in impact melt rocks from the Morokweng impact structure, South Africa (Reimold et al., 1999).

In particular, the comb-texture intergrowths described in section 7.2.1 and shown in Figure 7.9B, where plagioclase is found to be intergrown with sanidine, have also been observed in the upper unit of the melt sheet at the Manicouagan impact crater (Floran et al., 1978). The same authors also described a sodic rim occurring as an irregular overgrowth or as tiny “spines” oriented perpendicularly to the plagioclase core. This sodic plagioclase is intergrown with and then mantled by sanidine.

Interestingly, similar plagioclase-sanidine intergrowths have been produced in experiments by Lofgren and Gooley (1977) and Petersen and Lofgren (1986). In this section, I will briefly describe the experiments in which they synthesized these plagioclase-sanidine comb textures in order to better interpret the petrological implications.

In the experiments described of Petersen and Lofgren (1986), ternary feldspar starting materials with a variety of compositions (e.g., $\text{An}_{20}\text{Ab}_{60}\text{Or}_{20}$, $\text{An}_{37}\text{Ab}_{45}\text{Or}_{18}$, $\text{An}_{11}\text{Ab}_{45}\text{Or}_{44}$) were prepared by the gel method. Approximately 70 mg of gel was combined with 4-10 wt.% H_2O , sealed in a platinum capsule and run in an internally heated pressure vessel. A uniform liquid was first produced by heating the charges to the point of melting during 6 to 24 hours. The temperature was then decreased either at a linear cooling rate of 2°C/h or in 50°C steps, with the temperature being maintained at each step for two or three days. This slow rate of cooling was chosen in order to avoid growing highly branching skeletal crystals. Initially, the pressure was about 6 kbar, but it decreased during cooling to as low as 3 kbar for runs quenched at 400°C (the volume of

the pressure vessel was constant). The presence of vapor bubbles indicates that most runs were H₂O-saturated when the experiments were terminated.

Plagioclase is first observed at about 875°C in most runs. These crystals typically form branching needles or skeletal prismatic grains. Individual crystal shapes change continuously during progressive solidification, as the cores of initially highly skeletal crystals become filled. Plagioclase crystals in most solidification runs typically have a normally zoned core with a composite rim made of a lamellar intergrowth. Petersen and Lofgren (1986) described a particularly distinctive and common type of intergrowth structure that greatly resembles the comb texture observed both in the Manicouagan impact-melt rock and the impact melt sheet at the West Clearwater impact structure: this intergrowth is fine-grained and lamellar, comprising parallel lamellae of albite and sanidine 1-10 µm wide oriented roughly perpendicularly to the crystal-liquid interface. Nearly all crystals have a plagioclase core and a sanidine overgrowth, with a composite lamellar rim in between.

In most of these experiments, the initial feldspar (the crystal core) is An-rich, typically labradoritic (e.g., An₇₅). In the experiments cooled down to 740°C, the crystal-melt system has fractionated so that the rim of the plagioclase is andesine (e.g., An₄₅); experiments cooled to 700°C formed an oligoclase rim (e.g., An₃₀). In other words, as the melt cools, it produces zoned plagioclase crystals in which the rim has an increasingly sodic composition. By about 700°C, most experiments started forming a “composite margin” on the oligoclase rim, that is, the plagioclase margin became mantled by an intergrowth formed by the simultaneous crystallization of sanidine and plagioclase. These intergrowths are typically thicker than the inner plagioclase layers, indicating that they have substantially faster growth-rates than the sodic margins on which they grow.

This is most clearly seen in step-cooled experiments, where the temperature was dropped 50°C for constant time-intervals of two days: each temperature drop created a new growth-zone whose width is related to the relative growth-rate for each time interval. In their experiment F-8, which was done with a starting composition of $An_{11}Ab_{45}Or_{44}$, and step-cooled by 50°C, plagioclase with a composition of about An_{30} formed simultaneously with alkali feldspar with a composition of Or_{70} when the system was at 750°C. At 700°C, the plagioclase was $\sim An_{23-25}$, and the alkali feldspar, $\sim Or_{67}$; at 650°C, plagioclase with a composition of about An_{18-20} formed simultaneously with alkali feldspar with a composition of Or_{58-62} .

Petersen and Lofgren (1986) attributed the formation of the intergrowth zone and the increased growth-rate to closed-system fractionation, which they believe ultimately causes the liquid to reach the conditions necessary for cotectic crystallization. During normal growth, under the conditions reflected in the lower growth-rate of the core plagioclase and its rim, a planar solid-liquid interface forms that reflects the isotherms along the solidification front. The rate of growth in this case is controlled only by the rate of attachment of constituent atoms to the interface and removal of expelled solute by diffusion. In contrast, during eutectic or cotectic growth, this growth rate is minimized because neighboring phases consume complementary solute and thus mutually favor their growth by two-way diffusion. This reduces the boundary-layer width and permits a very high growth-rate because the rate-controlling range of diffusion is reduced to the order of the interlamellar spacing. Therefore, cotectic crystallization causes a dramatic change in growth conditions that leads to an intergrowth zone much wider than the previous monophasic zones (Petersen and Lofgren, 1986).

The feldspar textures and compositions produced in the experiments of Lofgren and Gooley (1977) and Petersen and Lofgren (1986) conform closely to the feldspar textures and compositions observed in the clast-poor impact melt rock of the West Clearwater impact structure. In the feldspars of the clast-poor melt, initial crystallization of plagioclase, typically occurring around plagioclase clasts, first produced a Ca-rich plagioclase (which I called melt-derived plagioclase, An_{61-44}) that depleted the melt in Ca. In the clast-poor melt rock, the depletion in Ca would also be favored by the simultaneous crystallization of augite along with plagioclase. As temperatures dropped and Ca depletion continued, a plagioclase rim with an increasingly sodic composition was deposited, forming the transition zone plagioclase (An_{44-14}), until the corresponding enrichment in K of the melt eventually favored the production of the sanidine-plagioclase intergrowth and then of an external sanidine rim. The alkali feldspar that crystallized near the last plagioclase has a composition of about Or_{56-60} .

Note that the compositions of the feldspars in the clast-poor melt of the West Clearwater impact structure closely follow the compositions obtained experimentally by Lofgren and Gooley (1977) and Petersen and Lofgren (1986). Also, like in these experiments, the thickness of the region containing the intergrowths in the clast-poor melt is typically larger than that of the inner plagioclase and the outer sanidine layers. I was unable to analyze the compositions of the intergrowths but, if they formed under conditions similar to those described by Petersen and Lofgren (1986), their compositions must be similar to those of the last plagioclase and the first alkali feldspar.

Lofgren and Gooley (1977) stated that their experiments cannot set lower limits on the cooling rates at which the intergrowths could develop. Nevertheless, it is clear from the experiments that the intergrowths are the result of relatively rapid cooling rates

in a closed system, involving moderate to low supercooling, the kind of cooling rates that would be expected in a relatively thick and immobile sheet of clast-laden impact melt.

9.4 On the presence of H₂O during the crystallization of the West Clearwater impact melt sheet

There is independent evidence for the presence of significant amounts of H₂O late in the crystallization sequence at West Clearwater. In the impact melt sheet of the West Clearwater impact structure, blocks of limestone are found embedded in the impact melt. These blocks represent recrystallized remnants of a cover of Middle Ordovician limestone, now completely eroded in the area. The metamorphism at the contact between the impact melt and the limestone has produced a metamorphic assemblage of unusually high-grade marbles. The episode of contact metamorphism was extremely brief, as it involved the incorporation of blocks in a sheet of likely superheated silicate magma generated by the meteor impact. The margins of the fossiliferous dolomite-bearing limestone recrystallized to granoblastic calcite + periclase marble when the blocks were incorporated in the sheet of impact-generated melt. The silica content of the marble led to the formation, through decarbonation reactions, of a sanidinite-facies assemblage of unusual nesosilicates such as spurrite, merwinite, and monticellite (Rosa, 2005; Rosa and Martin, 2010), the latter item reproduced as Appendix E. The presence of these minerals indicates that temperatures of at least 820°C were reached in some parts of the carbonate enclaves during the prograde stage of metamorphism.

The assemblage periclase + calcite quickly reverts to dolomite if it is kept at about 700°C in a CO₂-rich environment (Graf & Goldsmith 1955). Furthermore, if sufficient CO₂ is present, wollastonite starts to form at the expense of spurrite according to reaction

$\text{Spurrite} + 2 \text{CO}_2 \rightarrow 2 \text{Wollastonite} + 3 \text{Calcite}$ (a carbonation reaction) once temperatures drop below about 650°C (Tuttle & Harker 1957). Also, in an H₂O-CO₂ fluid mixture, merwinite is stable at low P_{fluid} (e.g., 0.5–1.0 kbar) and $X(\text{CO}_2)$ [e.g., $0.02 < X(\text{CO}_2) < 0.1$] and high T (e.g., above 700°C) (Zhou & Hsu 1992). Therefore, the preservation of merwinite indicates that the metasomatic fluid present in the Clearwater Lake carbonates had, in all likelihood, a value of $X(\text{CO}_2)$ less than 0.1 when temperatures in the enclave had dropped to about 700°C. In other words, CO₂ became scarce early in the retrograde metamorphic phase. The preservation of merwinite, spurrite and periclase shows that retrograde reactions were not possible owing to loss of a CO₂-rich gas phase, possibly flushed out of the enclaves by the appearance of a significant amount of H₂O when temperatures in the carbonate enclaves decreased to about 700°C. This is supported by the formation of the hydrous minerals brucite and portlandite during the retrograde stage of metamorphism, reflecting CO₂-poor, H₂O-dominant conditions in the temperature range $700 \leq T \leq 400^\circ\text{C}$ (Rosa, 2005; Rosa and Martin, 2010).

The presence of significant amounts of H₂O during the crystallization of an impact melt sheet has been proposed for other impact structures. For instance, Theriault et al. (2002) reported the occurrence of primary hydrous minerals (hornblende and biotite) in the impact melt of the Sudbury Igneous Complex (S.I.C.), and they attributed the deuteritic alteration and abundant micrographic and granophyric intergrowths in the rocks of the S.I.C. to rapid crystallization triggered by “exsolution of a hydrous volatile phase”. Simonds et al. (1978a) observed, in the impact melt rock of the Manicouagan structure, anomalously coarse alkali feldspar plus quartz with small amounts of apatite and smectite, centimeter-thick quartz veins and pervasive deuteritic alteration of the mafic

silicates, which they attributed to the formation throughout the structure of an aqueous phase late in the crystallization of the impact melt.

Where did this H₂O come from? As far as I know, there is no mechanism known to introduce H₂O into a system after the melt had formed. Therefore, it is likely that H₂O was introduced early in the system by the partial or complete assimilation, dehydration and degassing of minerals in the clasts of target rock incorporated into the impact melt as the crater formed. Most of the basement consisted of altered granulite- and amphibolite-facies rocks, which are relatively dry. The XRF analyses of core samples of the basement rocks (see appendix A) give loss on ignition values as high as 7 wt.%, but it is probable that most of this volatile material was introduced into the basement by strong hydrothermal activity after the impact event, when the impact melt had settled and cooled: the poorly consolidated fragmental breccias and the fractured basement would provide a permeable conduit for the expected influx from the hydrostatic head developed between the bottom of the excavated crater and the groundwater level in the surrounding rocks (Phinney et al. 1978).

Nevertheless, the granitic, granodioritic and enderbitic rocks of the basement contain both biotite and amphibole, and, according to Simard et al. (2004), they show the effects of alteration that produced hydrous phases such as muscovite, talc and serpentine. The initial amount of H₂O in the melt must have been relatively low: to a first approximation, the crystallizing assemblage was anhydrous. At the low confining pressures in the impact melt, the amount of H₂O that can be dissolved in the magma is very small. Therefore, as anhydrous phases such as feldspars and pyroxene crystallized, the H₂O in the melt must have increased to the point of H₂O saturation. It is thus possible

that the melt was unsaturated at the liquidus but had achieved H₂O saturation at the solidus.

9.5 Estimating liquidus and solidus temperatures of the clast-poor impact melt sheet with MELTS

MELTS is a software package designed to facilitate thermodynamic modeling of phase equilibria in magmatic systems. It provides the ability to compute equilibrium phase relations for igneous systems over the temperature range 500-2000°C and the pressure range 0-2 GPa. The thermodynamic model for the liquid phase included in the MELTS package was fitted largely from low-pressure experimental phase-equilibria. Independent sets of thermodynamic data and models were used for mineral phases. MELTS is intended for modeling magmatic phase relations at low pressure (<2 GPa). It is better calibrated in mafic systems and should work especially well for basalts and alkalic mafic magmas. Therefore, the creators of the software do not recommend using MELTS to simulate the evolution of intermediate to silica-rich calc-alkaline systems (Asimow and Ghiorso, 1998; Ghiorso et al., 2011; Ghiorso, 1995). Thus, MELTS is far from being the ideal method to model the crystallization of a quartz-saturated impact melt. However, I am using MELTS only to evaluate the effects of the presence of H₂O upon the temperatures of the liquidus and solidus of my relatively silicic system, that is, I want to test whether the addition of a small amount of H₂O to the average composition of the impact melt sheet rocks is enough to depress the solidus to the vicinity of the temperatures that I calculated using the Ti-in-quartz and the two-feldspar thermometers. This is not intended to be a rigorous treatment of this subject.

The average composition of the impact melt (see Tables 6.1 and 6.2) was entered into the MELTS program. The pressure was set at 100 bars. The fugacity of O₂ was kept

at QFM conditions. This may not be appropriate for this system: because the impact melt was turbulently mixed with the atmosphere during the opening of the crater, f_{O_2} values were probably greater. However, MELTS would have to be used with values of O_2 fugacity that do not follow a particular buffer. It is possible that the program was not designed to accommodate such values. Also, I do not know the initial ratio of FeO to Fe_2O_3 , as only FeO_{total} is known. To compensate, I entered a variety of possible values into the system, keeping FeO_{total} equal to the value in Tables 6.1 and 6.2, i.e. ~6 wt.%. However, according to Bostock (1969) and Hische (1995), most of the country rocks have a FeO/ Fe_2O_3 of about 1.4.

Running MELTS under these conditions, for a dry assemblage with FeO/ Fe_2O_3 = 1.4, I obtain a liquidus temperature of 1206°C. Varying FeO/ Fe_2O_3 from 0.09 to 11 caused the liquidus temperature to decrease from 1251°C to 1133°C. MELTS calculates that the solidus for this dry impact melt is ~880°C.

Setting FeO/ Fe_2O_3 = 1.4 and adding 1.5% H_2O to the system, which is the average amount of H_2O contained in the impact melt rocks, brings the liquidus down to 1035°C. MELTS calculates that under these conditions, the solidus of the system is at about 800°C.

This small amount of H_2O is enough, according to MELTS, to bring the solidus of the system within 100°C of the temperatures of crystallization of quartz (the last phase to crystallize in the clast-poor melt) estimated with the Ti-in-quartz thermometer.

Finally, note that it is very likely that a certain amount of supercooling was involved (MELTS only computes equilibrium phase-relations). Also, because of the massive crystallization of anhydrous phases such as feldspars and pyroxenes, H_2O was more plentiful late in the crystallization of the impact melt. These two factors should

suffice to explain reasonably the difference between the solidus estimated by MELTS and the temperatures of crystallization of quartz determined with the geothermometers... if it is assumed, of course, that the solidus temperature calculated by MELTS is trustworthy.

9.5.1 Addendum: Estimating liquidus and solidus temperatures of the clast-poor impact melt sheet with Rhyolite-MELTS

In the period between the initial version and the final version of this thesis, the authors of MELTS introduced a new version of their program called Rhyolite-MELTS. This new version is identical to MELTS, but the enthalpies of formation of both quartz and endmember KAlSi_3O_8 in feldspar solid solution have been adjusted in order to better model phase relations in hydrous silicic systems.

Running Rhyolite-MELTS under the same conditions as those described in section 9.5 above gave essentially the same general results. It should be noted that MELTS can be accessed on-line via an applet interface, whereas Rhyolite-MELTS is only provided as a downloadable program. All the calculations provided in section 9.5 above were made with the web applet version of MELTS. In my experience, the applet configuration is far more stable than the downloadable program: I had considerable difficulty running the downloadable program to temperatures close to the hypothetical solidus of my system. Most of the time, the program would crash after a few iterations.

9.6 Final thoughts regarding impact cratering and the differentiation of impact melts

As mentioned in the introduction to this thesis, impact melts differ from “normal” volcanic and plutonic melts in at least two fundamental aspects: their very variable content of clasts, caused by admixing fractured country-rock during crater excavation,

and the wide range of initial temperatures, going from the melting to the boiling point of rock. In spite of this apparent initial heterogeneity, it has been generally observed that, at the hand sample scale at least, known sheets of coherent impact melt at terrestrial impact structures are relatively homogeneous in major-element composition (Grieve, 2006). In the case of the impact melt of the West Clearwater Lake impact structure, Tables 6.1, 6.2 and 6.3, and Figures 7.4 and 7.5 attest to this overall homogeneity.

There is, however, one very prominent exception to this rule: the impact-related Sudbury Igneous Complex (S.I.C.) is strongly differentiated into two major petrographic units. The ~60- x 27-km elliptical S.I.C. is the deformed and eroded remnant of a 1.8 Ga impact crater which originally must have been ~200 km wide (Grieve, 2006). At Sudbury, the units attributed to the impact are, *roughly speaking*, compositionally bimodal, consisting of a silica-poor layer (the so-called “mafic norite” ~56% SiO₂) overlain by a silica-rich layer (“granophyre” ~70% SiO₂), separated by a thin transition zone of Fe-enriched intermediate composition (“quartz gabbro” ~62% SiO₂) (Zieg and Marsh, 2005). Geophysical studies of the Sudbury Igneous Complex have estimated that the overall thickness of the S.I.C. is about 4.5 km beneath the center of the Sudbury basin (Milkereit et al., 1994).

Several models have been proposed to explain the formation of the Sudbury Igneous Complex, some involving a strictly impact-related genesis, others proposing that the S.I.C. is the result of a combination of impact melts and impact-triggered crustal melts. The present consensus, however, points toward a strictly impact-related genesis (see section 3.6 of chapter 3). I will briefly describe two of the most recent impact-only models, those of Therriault et al. (2002) and Zieg and Marsh (2005), as these models

exemplify clearly the different views on how impact-melted target rocks are chemically reorganized.

Zieg and Marsh (2005) postulated that at Sudbury, flash melting of the impact-formed breccias produced an initially heterogeneous magma that reflected the nature of the local crust. In the words of the authors, “blobs, globs, and dollops of different compositions formed a confused magmatic emulsion due to slight density and viscosity differences” (Marsh, 2006). This “impact emulsion” of mafic and felsic liquids then separated into the two massive layers of different composition, the silica-rich layer on top and the denser, more mafic layer on the bottom. The two layers then separately underwent vigorous convection that further homogenized their chemical composition. Finally, solidification fronts migrated inward from the top and bottom, meeting at the transition zone. The final result was the formation of two essentially uniform layers of rock. Implicit in this model is the idea that the impact event is not responsible for the observed organization of the impact melt, i.e., that differentiation (or homogenization) took place after the impact event, as a consequence of processes that do not directly involve cratering. To Zieg and Marsh, the differentiation of an impact melt sheet is an accident: impacts that occur in compositionally uniform terranes will produce homogeneous melt sheets; impacts that occur in heterogeneous targets will produce heterogeneous melt sheets.

Therriault et al. (2002), on the other hand, assumed that an initially superheated impact melt moved into the growing crater, mixed turbulently while incorporating a certain volume of inclusions. Once thermal equilibrium between the melt and the inclusions was reached, cooling of the now-homogeneous melt slowed down, allowing it to differentiate through crystal fractionation and gravitational settling. In this model, the

impact melt is assumed to have been initially homogeneous, that is, the chemical uniformity of the initial melt is produced during the impact event, throughout the excavation and collapse of the transient cavity, a process that is considered to take no more than a few minutes. To explain the peculiarities of the S.I.C., Therriault et al. (2002) argued that, in order to differentiate, magma bodies must be at least a few hundred meters thick and of the appropriate composition: therefore, the geochemical homogeneity and lack of differentiation at terrestrial impact craters, they believe, are due to the fact that the sheets of impact melt produced were not thick enough (less than 600 m thick), probably too siliceous and too viscous, and crystallized too quickly, for differentiation to occur.

Whereas the ideas of Therriault et al. (2002) follow the orthodox line regarding the origin of the S.I.C., the hypothesis of Zieg and Marsh (2005) was proposed in the context of a broader hypothesis, in which Marsh advanced that phenocryst-free magmas should not be able to differentiate in crustal magma chambers because all evolved interstitial liquid is locked in solidification fronts, producing compositionally uniform intrusions. Instead of explaining layering and differentiation of plutonic intrusions by appealing to fractional crystallization in a slowly cooling magma, Zieg and Marsh attributed the formation of layered, differentiated intrusions to the emplacement of successive pulses of magma with phenocrysts of different mineral and chemical compositions (Latypov, 2009; Marsh, 2006). Marsh has used the Sudbury igneous complex (S.I.C.) as an example of what happens when magma is instantly formed without phenocrysts. In his words, the S.I.C. is the “ultimate magmatic experiment”: in the S.I.C., “there is no sign of layering and very little sign of differentiation. Thus, instantaneous injection of crystal-free magma does not form exotically layered, well-

differentiated intrusions.” The Sudbury testimony is clear: “no phenocrysts, no layering” (Marsh, 2006). This unconventional view has been summarily described by the phrase “no phenocrysts, no post-emplacement differentiation” (Latypov, 2009).

I do not subscribe to Marsh’s general hypothesis regarding magmatic systems. I believe that, in what concerns normal magmatic systems, the “no phenocrysts, no post-emplacement differentiation” idea, with its requirement that layering must be caused by successive pulses of phenocryst-laden magma, is unnecessarily complicated. Furthermore, phenocrysts have to form elsewhere, presumably as a result of crystal fractionation, before they are transported in individual pulses and deposited to form a differentiated magma chamber. If phenocrysts form elsewhere before transport and deposition, why can’t they form inside the magma chamber and then be deposited? The reader interested in a more detailed treatment of this subject should consult Latypov (2009), who criticised, in rather scathing terms, Marsh’s general hypothesis.

However, I do think that the part of the hypothesis specifically concerned with the origin of the differentiation observed in the Sudbury Igneous Complex (the “impact emulsion” idea) does have some merit. The mechanism by which the S.I.C. melt crystallised is not well understood: *in situ* fractionation models (like the one presented by Theriault et al., 2002) cannot explain the bimodal character of the Sudbury igneous complex. For instance, Lightfoot et al. (1997) wrote that the observed volume of silica-rich granophyre is difficult to explain by simple *in situ* fractionation involving a single body of magma. Ariskin et al. (1999) attempted to model the crystallization of the S.I.C. by the fractional crystallization of a melt with an original granodioritic composition: they could reproduce the observed volume of norite and quartz gabbro, but their model could only generate a small cap of granophyre, much less than the volume of granophyre

observed at Sudbury. This inability to obtain the observed volume-ratio of granophyres to norites by differentiation has also been noted by Masaitis (1993), Warren et al. (1996) and Chai and Eckstrand (1993; 1994), among many others.

In light of this, I believe it is essential to explore ideas (such as the “impact emulsion” hypothesis) that move away from conventional fractionation scenarios. Unfortunately, the association of the “impact emulsion” idea, which only concerns impact cratering, with the more general and unorthodox “no phenocrysts, no post-emplacement differentiation” hypothesis may have, I’m afraid, caused a number of workers to reject out-of-hand the “impact emulsion” idea for Sudbury: Latypov (2009), for instance, treated the Sudbury igneous complex as a normal layered intrusion, irrespective of the fact that the S.I.C. was generated in manner quite different from typical plutonic rocks.

The melts found in the fragmental breccia and the infiltration dykes of the West Clearwater impact structure must represent early heterogeneous batches of liquid created by an imperfect mixing of varying amounts of shock-melted rocks of different compositions. If the small “glass spheroids” found in the infiltration dykes and the fragmental breccia described in chapter 6 are the altered remains of globules of mafic glass, then it is possible that impact cratering can, in the early stages of impact melt formation at least, generate something akin to the “impact emulsion” of Zieg and Marsh. As I already pointed out, the model of Marsh and Zieg (2005) for the Sudbury Igneous Complex requires the formation of an “emulsion” of miscible melts which then separated into the two massive layers of different composition, the silica-rich layer on top and the denser more mafic layer on the bottom. As shown by the experiments of Zimanowski et al. (2004), globular heterogeneities formed by mixing two miscible melts tend to

dissipate with time, eventually producing a homogeneous melt, if the system is subjected to shear stresses. Therefore, for the model of Zieg and Marsh to work, vigorous convection must start only *after* the separation of the impact melt into two layers, which then individually undergo the vigorous convection (i.e., shear stresses) necessary to homogenize their chemical composition.

It is not at all clear what, in the model of Zieg and Marsh, prevents convection from starting *before* the formation of the two separate layers, therefore inevitably homogenizing the whole system. Furthermore, assuming that separation did take place and was followed by the formation of two superposed convection cells, I do not understand what would keep the two layers isolated from each other. Are the density differences of the melts involved large enough to keep the layers stably in their particular portions of the Sudbury Igneous Complex? It will be important, if possible, to create numerical models in order to test the viscous emulsion idea of Zieg and Marsh.

One aspect that is not usually considered in the hypotheses that seek to explain the singularities of the Sudbury Igneous Complex is the presence of clasts in the impact melt. The mass of material melted or vaporized is determined in the early high-pressure phase of shock-wave expansion. Since this mass is related to the kinetic energy of the impact, that is, it depends on the size and the impact velocity of the meteorite, the mass of material melted by the impact is independent of either material strength or gravity. The final size of large craters, however, is determined by gravity, that is, the volume of target rock set in motion and ultimately displaced and ejected during the formation of the transient crater relative to the amount of kinetic energy apportioned into the target rocks decreases with event size (Grieve, 2006). Because of this, when normalized to projectile size and velocity, larger craters are less efficiently excavated than smaller craters.

Because the cratering efficiency decreases with increasing size of crater, the mass of melt and vapor makes up a progressively larger proportion of the total mass displaced as crater size increases (Figure 9.2, p.257). Obviously, not all the displaced material stays within the crater: some is expelled as ejecta. But this must represent only a small fraction of the displaced material; most of the rock fractured by impact will stay in the crater and mix with the impact melt, or be deposited on top of the melt as fallback breccia.

The proportion of melt thus increases with increasing crater diameter, whereas the proportion of clastic debris decreases with increasing crater diameter (Grieve, 2006). In other words, larger craters will contain more melt and less clastic debris than smaller craters: a Sudbury-sized crater will necessarily have considerably fewer inclusions of clastic debris than a 30-km-wide crater like West Clearwater Lake; simple craters (that is, bowl-shaped craters lacking a central peak that occur up to diameters of about 4 km on Earth) will contain an interior breccia lens mostly consisting of target rocks mixed in with shocked (and in some cases melted) materials.

Melosh (1989) gave a simplified general formula for the ratio of the mass of rock melted relative to the mass displaced from the crater:

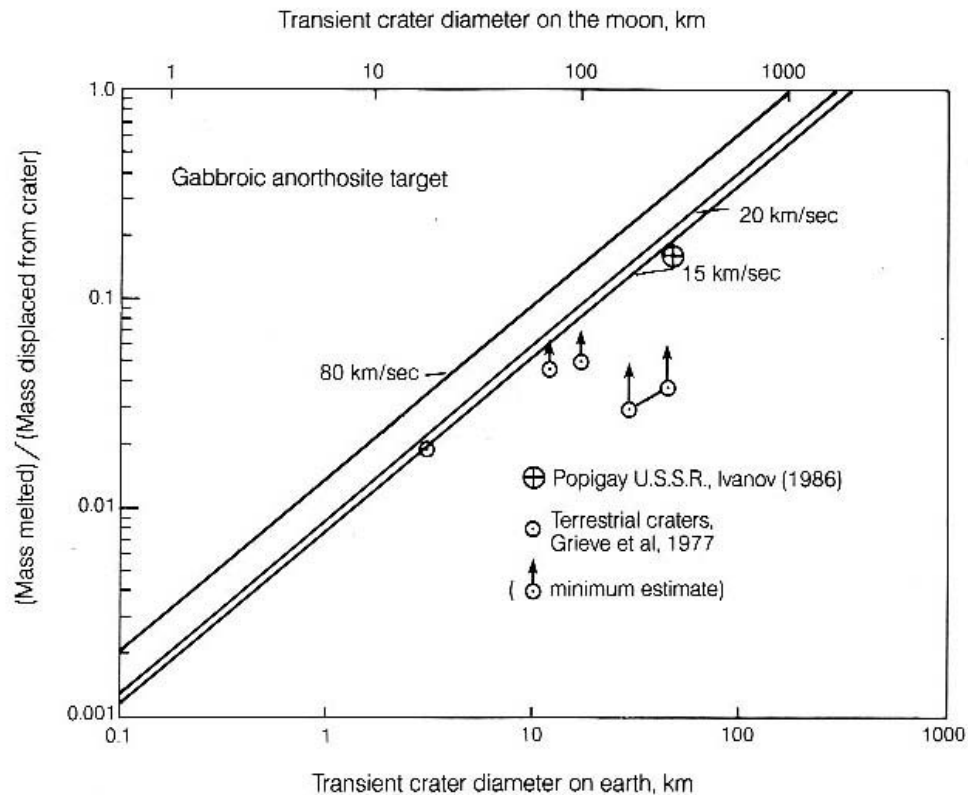
$$(1) \quad \frac{\text{Mass Melted}}{\text{Mass Displaced}} \approx 1.6 \times 10^{-7} (g D_{at})^{0.83} v_i^{0.33}$$

where g is the gravitational constant, D_{at} is the diameter of the transient crater in meters, and v_i is the velocity of impact of the meteorite. This equation applies only to a target made of gabbroic anorthosite, but we can assume that any silicate rock will probably behave in a way similar to that of gabbroic anorthosite.

The ratio between the mass of target material melted and the mass displaced from the crater is plotted in Figure 9.1 as a function of crater diameter for

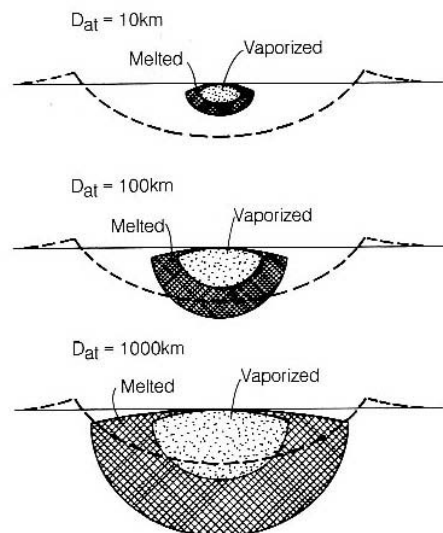
several impact velocities on the Earth and Moon. This figure shows that only a part of the material melted by impact is superheated and, because the clast content of most craters is quite high, this superheated melt should quickly attain thermal equilibrium with its clast content, which implies rapid intervals of cooling (e.g., Onorato et al., 1978). For the West Cleawater impact structure, which has a diameter of 32 km, and assuming that the target rock was entirely composed of gabbroic anorthosite, the ratio of Mass Melted to Mass Displaced is about 0.14 for an impact velocity of 15 km/s, 0.15 for an impact velocity of 20 km/s and 0.24 for an impact velocity of 80 km/s. Note that the ratio of the mass melted to the mass displaced in a Sudbury-sized impact (diameter ~200 km)

Figure 9.1 The ratio between the mass melted in an impact into gabbroic anorthosite and the mass displaced from a crater is plotted against crater diameter on the Earth (lower horizontal scale) and the Moon (upper horizontal scale). The mass of melt increases with crater size and impact velocity (adapted from Melosh 1989).



is a factor of about 4.5 higher than that for a structure in the 30 km range. The melt sheet produced by a Sudbury-sized impact thus will start out having considerably less inclusions of clastic debris than an impact melt sheet produced in a crater 30 km wide like at West Clearwater Lake. Furthermore, the melt sheet of a Sudbury-sized crater will tend to stay at a high temperature for longer: not only is heat loss to a large extent controlled by the amount of colder clasts included in the melt sheet (Onorato et al., 1978), but the larger mass of melted material insures a slower rate of cooling. A Sudbury-sized melt sheet should start out having less clastic debris, and its capacity to absorb and assimilate this debris should be greater than that of a smaller size of crater like at West Clearwater Lake. This is probably the main reason why a relatively complex composition of impact melt was able to differentiate in the Sudbury Igneous Complex.

Figure 9.2 As crater diameter increases the volume of melt and vaporized material may eventually approach the volume of the crater itself. Although melt and vapor may be only a minor component of the ejecta of small craters, extremely large craters may form almost entirely in a melt pool. This figure is constructed for impacts at 35 km/s on Earth (adapted from Melosh 1989).



Craters such as the West Clearwater Lake impact structure, with their high clast contents and relatively minor amounts of impact melt, probably cool and solidify too rapidly to be able to differentiate. In smaller craters, most of the events that determine the composition of the impact melt must take place during the formation of the transient crater, when the superheated melt created by the impact turbulently mixes with the fragmented target rock.

In my view, however, the role of target-rock debris should not be ignored in studies of large craters. For a crater the size of Sudbury (diameter ~200 km), the ratio of Mass Melted to Mass Displaced is of about 0.64 for an impact velocity of 15 km/s, 0.70 for an impact velocity of 20 km/s, and 1.11 for an impact velocity of 80 km/s. At Sudbury, therefore, the impact melt must initially have contained a significant amount of clasts, as attested by the observations of Therriault et al. (2002) who, as mentioned in section 9.3, reported the occurrence, in the Sudbury Complex, of plagioclase xenocrysts with complex patterns of twinning and zoning similar to those I observed in the “clast-poor” impact rock of the West Clearwater Lake impact structure. The preservation of plagioclase as a clast indicates that the impact melt, after mixing with the target rocks, equilibrated to temperatures below the liquidus and within the range of plagioclase crystallization.

As far as I know, none of the models that seek to explain the origin of the differentiation observed in the Sudbury Igneous Complex have taken into account the presence of a significant amount of monomineralic clastic debris such as resorbed plagioclase cores within the impact melt of the Sudbury structure. Instead of the “magmatic emulsion” of Zieg and Marsh (2005), the impact melt at Sudbury may have been a mixture of melt and a variety of clasts of different composition, that then separated

into layers according to their density. Many of these clasts may have been monomineralic, and they may have served as seeds for crystallization, in a manner similar to what was described for the plagioclase of the West Clearwater impact melt.

I am not, at present, sufficiently familiar with the intricacies of the geology of the Sudbury Igneous Structure to propose a more developed model. However, it seems to me that it is of the utmost importance to consider the role of clastic debris to understand the composition of impact melts, including the impact melt of the S.I.C.

9.7 Topics for future research

- The scarcity of orthopyroxene in the impact melt is puzzling. As mentioned in chapter 7, low-Ca pyroxene is the main normative mafic mineral. In the Manicouagan impact melt, which has a composition only slightly more mafic than that of the West Clearwater impact melt, orthopyroxene is abundant in most impact melt units. But, in the impact melt of the West Clearwater structure, orthopyroxene is nearly absent. I've only detected it once.

Both Hische (1995) and Phinney et al. (1978) commented on the scarcity of orthopyroxene. Phinney et al. (1978) reported intergrowths of Ca-rich and Ca-poor pyroxenes that could be exsolution lamellae, but I have not seen anything resembling this. In the opinion of Hische (1995), orthopyroxene was the second most common mineral in the clast-poor impact melt rock matrix, and he proposed that orthopyroxene has been transformed to clinopyroxene or clay minerals.

Although I have seen clear evidence of clinopyroxene alteration to clay, compositions or textures that could be interpreted as orthopyroxene altering to clinopyroxene are not present, nor is this considered a likely possibility. Either the

orthopyroxene did not crystallize for some reason, or it was nearly completely replaced by clinopyroxene in a manner that I have not recognized. It is also possible that my sampling somehow missed it.

Floran et al. (1978) reported that the spherulitic rocks of the lower impact melt unit of the Manicouagan impact structure, unlike the other units of melt, does not contain orthopyroxene. They explained the absence of low-Ca pyroxene in the spherulitic rocks as “indicative of the importance of clast-controlled thermal gradients”. Supercooling may have favored the formation of metastable pyroxene compositions within the solvus gap and of pigeonite. Such metastable compositions may have preferentially broken down upon oxidation.

Has this absence been observed elsewhere, in volcanic rocks or other impact melts? I believe that it will be interesting to further investigate this subject.

- The exact nature of the material in the “glass spheroids” described in chapter 6 remains conjectural. I have assumed that this material consists of a mixture of clay minerals, the result of the alteration of a mafic glass. Ascertaining the types of clay minerals present would probably help confirm this assumption. An X-ray diffraction study will be essential to make sense of the composition of the glass spheroids.

- Finally, I believe it is of the utmost importance to study the role of clastic debris in the solidification of impact melts. “The thermal history of the Manicouagan impact melt sheet, Quebec, by Onorato, Uhlmann and Simonds”, a study that dates from 1978, is the only article I know that has provided a numerical model of the interaction between superheated melt and clastic debris. New numerical models should be produced using

the powerful computing tools available today.

9.8 Summary and conclusions

- Two hundred and eighty seven million years ago (± 26 Ma), in what is now Northern Quebec, a meteorite of unknown composition impacted a relatively dry target rock composed of metamorphosed granites, granodiorites, enderbites, tonalites and gabbros overlain by a thin veneer of Ordovician limestone.

- Initially, the melt was a superheated silicate liquid produced by the almost instantaneous total melting of a relatively small volume of country rock near the point of impact. As the transient crater opened, the melt expanded downward and radially outward at velocities of several kilometers per second. Motions of the melt were initially extremely turbulent. The superheated liquid mixed turbulently with relatively cold inclusions nearer the periphery of the expanding crater cavity.

- At the hand-sample scale, the impact melt is chemically homogeneous and has a bulk composition similar to that of a trachyandesitic volcanic rock. The average composition of the West Clearwater Lake impact melt can be modeled by mixing the average chemical compositions of three types of lithologies present in the vicinity of the impact structure: 1) granitic rocks; 2) granodioritic, enderbitic and tonalitic rocks, 3) mafic and ultramafic rocks, according to the following proportions: 1) 31%, 2) 62% and 3) 6%.

- Blocks ranging up to tens of meters and down to less than 0.1 mm were incorporated, with the bulk of the material in the submillimeter range. This process produced a relatively homogeneous matrix melt containing molten silica derived from quartz-bearing rocks, molten mafic spheroids which would later form the glass spheroids of chapter 6, and a large amount of partially resorbed clasts with a variety of compositions. The entire mixing stage probably occurred over a time span of only a few minutes at most. The turbulent mixing of the superheated liquid with colder material resulted in rapid thermal equilibration of the melt. After collapse of the transient crater, the structure stabilized, and the bulk of the clast-laden melt pooled within the crater, where it underwent solidification.

- Although the clast-poor impact melt has a low abundance of recognizable clasts (~15% or less, the clast content decreases upward into the unit), the initial clast content before the onset of crystallization must have been much higher. This conclusion is supported by the widespread occurrence in the clast-poor impact melt rock of plagioclase grains with an irregular partially resorbed relict core. Plagioclase xenocrysts must form ~5% to ~15% of the clast-poor impact melt rock, depending on the thin section (sections higher up the stratigraphical column likely contain less relict plagioclase). The preferential preservation of plagioclase as a clast implies that the melt equilibrated to temperatures below the liquidus and within the range of plagioclase crystallization.

- New plagioclase nucleated around plagioclase xenocrysts. This melt-derived plagioclase was, in turn, mantled by alkali feldspar (sanidine solid-solution), creating a distinctively zoned overgrowth. A complex comb-texture intergrowth developed at the interface

between the melt-derived plagioclase and the mantling alkali feldspar.

- Augite is the dominant mafic mineral. Clinopyroxene and plagioclase form an ophitic to subophitic texture, indicating that clinopyroxene formed after plagioclase. Sanidine is rarely found impinging against pyroxene margins, indicating that it formed after plagioclase and pyroxene.

- Zoning of early-formed plagioclase and growth of augite led to Ca depletion and K enrichment in the melt. Continued fractionation led to coprecipitation of sanidine + quartz + apatite.

- Two-feldspar thermometry calculations suggest that the last plagioclase and the first alkali feldspar crystallized at temperatures of about 781 to 816°C ($\pm 44^\circ\text{C}$).

- Quartz was the last phase to crystallize in the clast-poor impact melt rock of the West Clearwater impact structure. This mineral crystallized at temperatures of 700 to 730°C, with an activity of Ti in quartz between 0.5 and 0.6. To my knowledge, this study is the first to use geothermometry to estimate the temperature of solidification of a melt sheet created by a meteoritic impact.

- The initial amount of H₂O in the melt must have been relatively low. To a first approximation, the crystallizing assemblage was anhydrous. At the low confining pressures in the impact melt, the amount of H₂O that can be dissolved in the magma is very small. As anhydrous phases such as feldspars and pyroxene crystallized, the H₂O in

the melt must have increased to the point of H₂O saturation. It is thus possible that the melt was highly undersaturated at the liquidus but had achieved H₂O saturation at the solidus.

- Fe-Ti oxides must have been one of the first phases to crystallize in the impact melt, along with plagioclase. Late-stage enrichment of the melt in H₂O led to the abundant production of an orthomagmatic fluid, which caused efficient oxidation of titaniferous magnetite and widespread alteration of clinopyroxene.

- An active hydrothermal system must have been in place shortly after the impact melt solidified. Hydrothermal fluids probably penetrated the impact melt through the poorly consolidated fragmental breccias and the fractured basement, which provided a permeable conduit for the expected influx from the hydrostatic head developed between the bottom of the excavated crater and the groundwater level in the surrounding rocks. The circulation of hydrothermal fluids altered much of the impact-generated glasses, shock-disordered clasts and mafic minerals crystallized from the impact melt to a variety of secondary minerals stable at low temperatures.

Acknowledgements

The assistance of Dr. R.A.F. Grieve (at the Geological Survey of Canada), Dr. M.R. Dence, Dr. John Spray (at the University of New Brunswick) and Karen Shea (at the Planetary and Space Science Center of the University of New Brunswick) is gratefully acknowledged. Thin sections were cut at the petrographic facilities of the University of New Brunswick. All the electron microprobe, geochemical and X-ray powder-diffraction analyses were performed at the Earth & Planetary Sciences Department of McGill University with the assistance of Shi Lang (electron microprobe technician) and Glenna Keating (manager of the geochemistry laboratories).

I also wish to acknowledge the assistance of my supervisor, Dr. Robert R. Martin, whose editorial skills and attention to detail greatly contributed to the improvement of this thesis. Finally, I wish to acknowledge my wife, Renée Landry, without whom the completion of this thesis would not have been possible.

References

- Ariskin, A.A., Deutsch, A. and Ostermann, M., 1999. Sudbury Igneous Complex: simulating phase equilibria and in situ differentiation for two proposed parental magmas. *Geological Society of America Special Paper*, Paper 339: 373-387.
- Artemieva, N.A., 2007. Possible reasons of shock melt deficiency in the Bosumtwi drill cores. *Meteoritics and Planetary Science*, 42: 883-894.
- Asimow, P.D. and Ghiorso, M.S., 1998. Algorithmic modifications extending MELTS to calculate subsolidus phase relations. *American Mineralogist*, 83: 1127-1131.
- Bailey, K., Garson, M., Kearns, S. and Velasco, A.P., 2005. Carbonate volcanism in Calatrava, central Spain: a report on the initial findings. *Mineral. Mag.*, 69: 907-915.
- Bailey, K., Kearns, S., Mergoïl, J., Mergoïl, D.J. and Paterson, B., 2006. Extensive dolomitic volcanism through the Limagne Basin, central France: a new form of carbonatite activity. *Mineral. Mag.*, 70: 231-236.
- Beals, C.S., Innes, M.J.S. and Rottenberg, J.A., 1960. The search for fossil meteorite craters. *Contrib. Dominion Observatory* 4(4): 1-3.
- Bostock, H.H., 1969. The Clearwater Complex, New Quebec. *Geological Survey of Canada*, 178: 63 pages.
- Bryan, W.B., Finger, L.W. and Chayes, F., 1969. Estimating proportions in petrographic mixing equations by least-squares approximations. *Science*, 163: 926-927.
- Buchan, K.L., Mortensen, J.K., Card, K.D. and Percival, J.A., 1998. Paleomagnetism and U-Pb geochronology of diabase dyke swarms of Minto block, Superior Province, Quebec, Canada. *Canadian Journal of Earth Sciences*, 35: 1054-1069.
- Buddington, A.F. and Lindsley, D.H., 1964. Iron-titanium oxide minerals and synthetic equivalents. *Journal of Petrology*, 5: 310-357.
- Bunch, T.E., 1968. Some characteristics of selected minerals from craters. In *Shock Metamorphism of Natural Materials* (B. M. French and N. M. Short, eds.) Mono, Baltimore: 413-432.
- Bunch, T.E., Cohen, A.J. and Dence, M.R., 1967. Natural terrestrial maskelynite. *American Mineralogist*, 52: 244-253.
- Card, K.D. and Ciesielski, A., 1986. Subdivision of the Superior Province of the Canadian Shield. *Geoscience Canada*, 13: 5-13.
- Carstens, H., 1975. Thermal history of impact melt rocks in the Fennoscandian Shield. *Contrib. Mineral. Petrol.*, 50: 145-155.

- Chai, G. and Eckstrand, O.R., 1993. Origin of the Sudbury Igneous Complex, Ontario - differentiate of two separate magmas. Geological Survey of Canada Paper, 93-1E: 219-230.
- Chai, G. and Eckstrand, O.R., 1994. Rare-earth element characteristics and origin of the Sudbury Igneous Complex, Ontario, Canada. Chemical Geology, 113: 221-244.
- Ciesielski, A. and Plante, L., 1990. Archean granulites in the Lac à l'Eau Claire area, north Bienville Subprovince, Superior Province, Quebec. Geological Survey of Canada, Current Research, Part C, Paper 90-1C: 59-67.
- Coffin, M.F. and Eldholm, O., 2001. Large Igneous Provinces: progenitors of some ophiolites? In Mantle Plumes: their identification through time (Ernst, R.E. and Buchan, K.L., eds.) Geological Society of America, Special Paper 352: 59-70.
- Cohen, A.S., Burnham, O.M., Hawkesworth, C.J. and Lightfoot, P.C., 2000. Pre-emplacement Re-Os ages for ultramafic inclusions in the sublayer of the Sudbury Igneous Complex, Ontario. Chemical Geology, 165: 37-46.
- Currie, K.L., 1971. Origin of igneous rocks associated with shock metamorphism as suggested by geochemical investigations of Canadian craters. J. Geophys. Res., 76: 5575-5585.
- Deer, W.A., Howie, R.A. and Zussman, J., 1992. An introduction to the rock-forming minerals (2nd edition). Longman Scientific & Technical, New York, 696 pp.
- Dence, M.R., 1964. A comparative structural and petrographic study of probable Canadian meteorite craters. Meteoritics, 2: 249-269.
- Dence, M.R., 1981. Meteorite breakup. Nature, 289: 346-347.
- Dence, M.R., Innes, M.J.S. and Beals, C.S., 1965. On the probable meteorite origin of the Clearwater Lakes, Quebec. J. Roy. Astron. Soc. Can., 59: 13-22.
- Dence, M.R., von Engelhardt, W., Plant, A.G. and Walter, L.S., 1974. Indications of fluid immiscibility in glass from West Clearwater Lake impact crater, Quebec, Canada. Contrib. Mineral. Petrol., 46: 81-97.
- Dickin, A.P., Nguyen, T. and Crocket, J.H., 1999. Isotopic evidence for a single impact melting origin of the Sudbury Igneous Complex. In Large Meteorite Impacts and Planetary Evolution II (Dressler, B.O. and Sharpton, V.L., eds.), The Geological Society of America, Special Paper 339: 361-371.
- Elkins, L.T. and Grove, T.L., 1990. Ternary feldspar experiments and thermodynamic models. American Mineralogist, 75: 544-559.
- Faggart, B.E., Basu, A.R. and Tatsumoto, M., 1985. Origin of the Sudbury complex by meteoritic impact: neodymium isotopic evidence. Science, 230: 436-439.

- Fel'dman, V.I. and Sazonova, L.V., 1993. Conditions of impact melt formation and solidification in the Zhamanshin astrobleme. *Petrology*, 1: 523-538.
- Fleischer, R.L., Viertl, J.R.M. and Price, P.B., 1969. Age of the Manicouagan and Clearwater Lakes craters. *Geochim. Cosmochim. Acta*, 33: 523-527.
- Floran, R.J. et al., 1978. Manicouagan impact melt, Quebec, 1, Stratigraphy, petrology and chemistry. *Journal of Geophysical Research*, 83: 2737-2759.
- Fowler, C.M.R., 1990. *The Solid Earth*. Cambridge University Press, New York.
- Ghiorso, M.S. and Evans, B.W., 2008. Thermodynamics of rhombohedral oxide solid solutions and a revision of the Fe-Ti two-oxide geothermometer and oxygen barometer. *Am. J. Sci.*(308): 957-1039, page 1020.
- Ghiorso, M.S., Sack, R.O. and Asimow, P.D., 2011. The MELTS web page at: <http://melts.ofm-research.org/index.html#Sixth>.
- Ghiorso, M.S., Sack, R. O., 1995. Chemical mass transfer in magmatic Processes. IV. A revised and internally consistent thermodynamic model for the interpolation and extrapolation of liquid-solid equilibria in magmatic systems at elevated temperatures and pressures *Contrib. Mineral. Petrol.*, 119: 197-212.
- Ghisoro, M.S. and Evans, B.W., 2008. Thermodynamics of rhombohedral oxide solid solutions and a revision of the Fe-Ti two-oxide geothermometer and oxygen barometer. *Am. J. Sci.*(308): 957-1039, page 1020.
- Glickson, A.Y., 1999. Oceanic mega-impacts and crustal evolution. *Geology*, 27: 387-390.
- Gosselin, C., Roy, P. and David, J., 2002. *Géologie de la région du lac Bienville (33P)*. Ministère des Ressources Naturelles du Québec, RG 2002-11: 38 pages.
- Gosselin, C. and Simard, M., 2000. *Géologie de la région du lac Gayot (SNRC 23M)*. Ministère des Ressources Naturelles du Québec, RG 99-06: 29 pages.
- Gosselin, C., Simard, M. and David, J., 2001. *Géologie de la région des lacs des Loups Marins (34A)*. Ministère des Ressources Naturelles du Québec, RG 2001-10: 42 pages.
- Graup, G., 1999. Carbonate-silica liquid immiscibility upon impact melting: Ries Crater, Germany. *Meteoritics and Planetary Science*, 34: 425-438.
- Grieve, R.A.F., 1975. Petrology and chemistry of the impact melt at Mistastin Lake crater, Labrador. *Geological Society of America Bulletin*, 86: 1617-1629.
- Grieve, R.A.F., 1978. Meteoritic component and impact melt composition at the Lac à l'Eau Claire, Quebec. *Geochim. Cosmochim. Acta* 42: 429-431.

- Grieve, R.A.F., 2006. Impact Structures in Canada. GEOText 5, Geological Association of Canada: 210 pages.
- Grieve, R.A.F. and Cintala, M.J., 1992. An analysis of different impact melt-crater scaling and implications for the terrestrial impact record. *Meteoritics*, 27: 526-538.
- Grieve, R.A.F., Dence, M.R. and Robertson, P.B., 1976. The generation and distribution of impact melts: implications for cratering processes (abstract). In *Papers Presented to the symposium on Planetary Cratering Mechanics*, The Lunar Science Institute, Houston.: pp. 40-42.
- Grieve, R.A.F., Palme, H. and Plant, A.G., 1980. Siderophile-rich particles in the melt rocks at E. Clearwater impact structure, Quebec: their characteristics and relationships to the impacting body. *Contrib. Mineral. Petrol.*, 75: 187-198.
- Grieve, R.A.F. and Pilkington, M., 1996. The signature of terrestrial impacts. *AGSO Journal of Australian Geology & Geophysics*, 16: 399-420.
- Haggerty, S.E., 1991. Oxide textures - A mini-atlas. In D.H. Lindsley, Ed., *Oxide Minerals: Petrologic and Magnetic Significance*, *Reviews in Mineralogy*, Mineralogical Society of America, 25: 129-137.
- Hische, R., 1995. *Geologie des Clearwater Impakstruktur / Quebec*. Ph. D. thesis, Westfälischen Wilhelms Universität, Münster, Germany: 145 pages.
- Ivanov, B.A., 2001. Mars/Moon cratering rate ratio estimates. *Chronology and Evolution of Mars*, Space Science Series of ISSI (Kallenbach, R. Geiss, J. and Hartmann, W.K., eds.) Dordrech-Boston-London, Kluwer Academic Press, 12: 87-104.
- Ivanov, B.A. and Melosh, H.J., 2003. Impacts do not initiate volcanic eruptions: Eruptions close to the crater. *Geology*, 31: 869-872.
- Jones, A.P., Claeys, P. and Heuschkel, S., 2000. Impact melting of carbonates from the Chicxulub crater, (Gilmour, I., Koeberl, C., eds.). *Impacts and the Early Earth*, *Lecture Notes in Earth Sciences*, Springer-Verlag, Berlin, 91: 343-361.
- Jones, A.P., Price, G.D., Price, N.J., DeCarli, P.S. and Clegg, R.A., 2002. Impact induced melting and the development of large igneous provinces. *Earth and Planetary Science Letters*, 202: 551-561.
- Kenkmann, T., Jahn, A., Scherler, D. and Ivanov, B.A., 2005. Structure and formation of a central uplift: a case study at the Upheaval Dome impact crater, Utah. In *Large Meteorite Impacts III* (Kenkmann, T., Hörz, F. and Deutsch, A., eds.) The Geological Society of America, Special Paper 384: 85 - 115.
- Kieffer, S.W. and Simonds, C.H., 1980. The role of volatiles and lithology in the impact cratering process. *Reviews of Geophysics and Space Physics*, 18: 143-181.

- Kjarsgaard, B. and Peterson, T., 1991. Nephelinite-carbonatite liquid immiscibility at Shombole volcano, East-Africa: petrographic and experimental evidence *Mineralogy and Petrology* 43: 293-314.
- Korteweg, D.J., 1901. Sur la forme que prennent les équations du mouvement des fluides si l'on tient compte des formes capillaires causées par des variations de densité considérables mais continues et sur la théorie de la capillarité dans l'hypothèse d'une variation continue de la densité. *Arch. Neerl. Sci. Exactes Nat. Ser. II*, 6: 1-24.
- Krank, S.H. and Sinclair, G.W., 1963. Clearwater Lake, New Quebec. Geological Survey of Canada, Bulletin 100.
- Latypov, R., 2009. Testing the validity of the petrological hypothesis "no phenocrysts, no post-emplacement differentiation". *Journal of Petrology*, 50(6): 1047-1069.
- Lightfoot, P.C., Keays, R.R., Morrison, G.G., Bite, A. and Farrel, K.P., 1997. Geochemical relationships in the Sudbury Igneous Complex: origin of the main mass and offset dikes. *Economic Geology*, 92: 289-307.
- Lofgren, G.E. and Gooley, R., 1977. Simultaneous crystallization of feldspar intergrowths from the melt. *American Mineralogist*, 62: 217-228.
- Marion, C.L. and Sylvester, P.J., 2010. Composition and heterogeneity of anorthositic impact melt at Mistastin Lake crater, Labrador. *Planet. Space. Sci.* , 58(4): 552-573.
- Marsh, B.D., 2006. Dynamics of magma systems. *Elements*, 2: 287-292.
- Masaitis, V.L., 1993. Origin of the Sudbury structure from the points of new petrographic, mineralogical and geochemical data. *Transactions of the all-Russian mineralogical society (in Russian)*, 122: 1-7.
- McDonald, I., 2002. Clearwater East impact structure: a re-interpretation of the projectile type using new platinum-group element data from meteorites. *Meteoritics & Planetary Science*, 37: 459-464.
- McIntyre, D.B., 1968. Impact metamorphism at Clearwater Lake, Quebec. In *Shock Metamorphism of Natural Materials* (B. M. French and N. M. Short, eds.) Mono, Baltimore: 363-366.
- Melosh, H.J., 1989. *Impact Cratering: A Geological Process*. Oxford Monographs on Geology and Geophysics, Oxford University Press, No. 11: 245 Pages.
- Melosh, H.J. and Ivanov, B.A., 1999. Impact crater collapse. *Annual Review of Earth and Planetary Science*, 27: 385-415.
- Meunier, A., 2005. *Clays*. Springer, Berlin, Heidelberg, New York.

- Milkereit, B., Green, A., Wu, J., White, D. and Adam, E., 1994. Integrated seismic and borehole geophysical study of the Sudbury Igneous Complex. *Geophysical Research Letters*, 21(10): 931-934.
- Morgan, J.W., Walker, R.J., Horan, M.F., Beary, E.S. and Naldrett, A.J., 2002. ^{190}Pt - ^{186}Os and ^{187}Re - ^{187}Os systematics of the Sudbury Igneous Complex, Ontario. *Geochim. Cosmochim. Acta*, 66: 273-290.
- Morra, G. and Yuen, D.A., 2008. Role of Korteweg stresses in geodynamics. *Geophysical Research Letters*, 35: L07304.
- Mortensen, J.K. and Ciesielski, A., 1987. U-Pb zircon and sphene geochronology of Archean plutonic and orthogneissic rocks of the James Bay region and Bienville Domain, Quebec. In *Radiogenic Age and Isotopic Studies*, Geological Survey of Canada, Report I, Paper 87-2: 129-134.
- Müller, A., Wiedenbeck, M., M. Van Den Kerkhof, A., Kronz, A. and Simon, K., 2003. Trace elements in quartz - a combined electron microprobe, secondary ion mass spectrometry, laser-ablation ICP-MS, and cathodoluminescence study. *European Journal of Mineralogy*, 15: 747-763.
- Mungall, J.E., 1994. Interfacial tension in miscible two-fluid systems with linear viscoelastic rheology. *Phys. Rev. Lett.*, 73: 288-291.
- Naumov, M.V., 2005. Principal features of impact-generated hydrothermal circulation systems: mineralogical and geochemical evidence. *Geofluids*, 5: 165-184.
- Neukum, G., Ivanov, B.A. and Hartmann, W.K., 2001. Cratering record in the inner solar system in relation to the lunar reference system. *Chronology and Evolution of Mars*, Space Science Series of ISSI (Kallenbach, R. Geiss, J. and Hartmann, eds.) W.K. Dordrech-Boston-London, Kluwer Academic Press, 12: 55-86.
- Onorato, P.I.K., Uhlmann, D.R. and Simonds, C.H., 1978. The thermal history of the Manicouagan impact melt sheet, Quebec. *Journal of Geophysical Research*, 83: 2789-2798.
- Osinski, G.R. and Spray, J.G., 2001. Impact-generated carbonate melts: evidence from the Haughton structure, Canada. *Earth and Planetary Science Letters*, 194: 17-29.
- Osinski, G.R., Spray, J.G. and Grieve, R.A.F., 2004. The nature of the groundmass of surficial suevite from the Ries impact structure, Germany and constraints on its origin. *Meteoritics & Planetary Science*, 39: 1655-1683.
- Osinski, G.R., Spray, J.G. and Grieve, R.A.F., 2008. Impact melting in sedimentary target rocks: an assessment. *The sedimentary record of meteorite impacts* (Evans, K., Horton, W., King, D., Morrow, J., Warne, J., eds.). Geological Society of America, Special Paper 437.

- Ostapenko, G.T., Tarashchan, A.N. and Mitsyuk, B.M., 2007. Rutile-quartz geothermobarometer. *Geochem. Int.*, 45: 506-508.
- Palme, H., Göbel, E. and Grieve, R.A.F., 1979. The distribution of volatile and siderophile elements in the impact melt of East Clearwater (Quebec). *Proc. 10th Lunar Planet. Sci. Conf.* : 2465-2492.
- Palme, H., Janssen, M.J., Takahashi, H., Anders, E. and Hertogen, J., 1978. Meteoritic material at five large impact craters. *Geochim. Cosmochim. Acta*, 42: 313-323.
- Parent, M., Leclair, A., David, J., Sharma, K. and Lacoste, P., 2002. Géologie de la région du lac Vernon (SNRC 34J). Ministère des Ressources Naturelles du Québec, RG 2001-11: 40 pages.
- Percival, J.A., Mortensen, J.K., Stern, R.A., Card, K.D. and Bégin, N.J., 1992. Giant granulite terranes of northwestern Superior Province; the Ashuanipi Complex and Minto Block. *Canadian Journal of Earth Sciences*, 29: 2287-2308.
- Petersen, J.S. and Lofgren, G.E., 1986. Lamellar and patchy intergrowths in feldspars: experimental crystallization of eutectic silicates. *American Mineralogist*, 71: 343-355.
- Phinney, W.C. and Simonds, C.H., 1977. Dynamical implications of the petrology and distribution of impact melt rocks. In *Impact and Explosion Cratering* (Roddy D.J, Pepin R.O. and Merrill R.B., eds.). Pergamon Press, N.Y.: 771-790.
- Phinney, W.C., Simonds, C.H., Cochran, A. and McGee, P., 1978. West Clearwater, Quebec, impact structure, Part II: Petrology *Proc. 9th Lunar Planet. Sci. Conf.*: 2659-2693.
- Pierazzo, E. and Melosh, H.J., 2000. Melt production in oblique impacts. *Icarus*, 145: 252-261.
- Pierazzo, E., Vickery, A.M. and Melosh, H.J., 1997. A reevaluation of impact melt production. *Icarus*, 127: 408-423.
- Plante, L., 1986. Modélisation géophysique des cratères météoritiques du Lac à l'Eau Claire, Nouveau-Québec. Thèse de maîtrise, Université Laval, Québec: 171 pages.
- Plante, L., Seguin, M.-K. and Rondot, J., 1990. Étude gravimétrique des astroblèmes du Lac à l'Eau Claire, Nouveau-Québec. *Geoexploration*(26): 303-323.
- Putirka, K., 2008a. Microsoft Excel calculator available for download at www.minsocam.org/MSA/RIM/RiM69_Ch03_two-feldspar_T.xls.
- Putirka, K., 2008b. Thermometers and barometers for volcanic systems. In *Minerals, Inclusions and Volcanic Processes* (Putirka, K., Tepley, F., eds.). *Reviews in Mineralogy and Geochemistry*, Mineralogical Soc. Am., 69: 61-120.

- Reid, M.R., Vazquez, J.A. and Schmitt, A.K., 2011. Zircon-scale insights into the history of a supervolcano, Bishop Tuff, Long Valley, California, with implications for the Ti-in-zircon geothermometer. *Contrib. Mineral. Petrol.*, 161: 393-311.
- Reimold, W.U., Grieve, R.A.F. and Palme, H., 1981. Rb-Sr dating of the impact melt from East Clearwater, Quebec. *Contrib. Mineral. Petrol.*(76): 73-76.
- Reimold, W.U., Koeberl, C., Brandstätter, F., Kruger, F.J., Armstrong, R.A. and Bootsman, C., 1999. Morokweng impact structure, South Africa: geologic, petrologic, and isotopic results, and implications for the size of the structure. *Geological Society of America, Special Paper 339*: 61-90.
- Robertson, P.B., Dence, M.R. and Vos, M.A., 1968. Deformation in rock-forming minerals from Canadian craters. In *Shock Metamorphism of Natural Materials* (B. M. French and N. M. Short, eds.) *Mono*, Baltimore: 433-452.
- Ronca, L.B., 1966. Meteoritic impact and volcanism. *Icarus*, 5: 515-520.
- Rondot, J., 1995. Les Impacts Météoritiques à l'exemple de ceux du Québec. *Publications MNH Inc. Beauport (Québec)*: 157 pages.
- Rondot, J., Plante, L. and Séguin, M.-K., 1993. Géologie postarchéenne de la partie centrale du Lac à l'Eau Claire ouest (Nouveau-Québec). *Gouvernement du Québec, Direction Générale de l'Exploration Géologique et Minérale, ET92-06, carte no. 2157*.
- Rosa, D.F., 2005. Marble Enclaves in the Melt Sheet at the West Clearwater Lake Impact Crater, northern Quebec. M.Sc. thesis, McGill University, Montreal, Quebec, Canada. : 136 pages.
- Rosa, D.F. and Martin, R.F., 2010. A spurrite-, merwinite- and srebrodolskite-bearing skarn assemblage, West Clearwater impact crater, Northern Quebec. *Canadian Mineralogist*, 48: 1519-1532.
- Rusk, B.G., Reed, M.H., Dilles, J.H. and Kent, A.R., 2006. Intensity of quartz cathodoluminescence and trace-element content in quartz from the porphyry copper deposit at Butte, Montana. *Am. Mineral*, 91: 1300-1312.
- Sanford, B.V., 1987. Paleozoic geology of the Hudson Bay Platform. In *Sedimentary basins and basin-forming mechanisms* (C. Beaumont and A. J. Tankard, eds.) *Canadian Society of Petroleum Geologists, Memoir 12*: 483-505.
- Sanford, B.V. and Grant, A.C., 1990. New findings relating to the stratigraphy and structure of the Hudson Platform. In *Current Research, part D. Geological Survey of Canada, Paper 90-1D*: 17-30.
- Schreiber, U., Anders, D. and Koppen, J., 1999. Mixing and chemical interdiffusion of trachytic and latitic magma in a subvolcanic complex of the Tertiary Westerwald (Germany). *Lithos*, 46: 695-714.

- Scott, R.G., Pilkington, M. and Tanczyk, E.I., 1995. Magnetic rock properties of the Clearwater Lake impact craters, Quebec: formation of magnetic lows. Geological Association of Canada - Mineralogical Association of Canada., Program and abstracts 20: A-95.
- Simard, M., Gosselin, C., David, J., 2001. Géologie de la région de Maricourt (SNRC 24D). Ministère des Ressources Naturelles du Québec, RG 2000-07: 50 pages.
- Simard, M., Parent, M., Thériault, R., David, J., Lacoste, J. and Sharma, K., 2004. Géologie de la région du lac à l'Eau Claire (34B et 34C). Ministère des Ressources Naturelles du Québec, RG 2003-8: 46 pages.
- Simonds, C.H., Floran, R.J., McGee, P., Phinney, W.C. and Warner, J.L., 1978a. Petrogenesis of melt rocks, Manicouagan impact structure, Quebec. Journal of Geophysical Research, 83: 2773-2788.
- Simonds, C.H. and Kieffer, S.W., 1993. Impact and volcanism: a momentum scaling law for erosion. Journal of Geophysical Research, 98: 14321-14337.
- Simonds, C.H., Phinney, W.C., McGee, P. and Cochran, A., 1978b. West Clearwater, Quebec, impact Structure, Part I: Field Geology, Structure and Bulk Chemistry. Proc. 9th Lunar Planet. Sci. Conf. : 2633-2658.
- Stöffler, D., 1974. Deformation and transformation of rock-forming minerals by natural and experimental shock processes. I. Behaviour of minerals under shock compression. Fortschritte der Mineralogie, 51: 259-289.
- Stöffler, D., 1984. Glasses formed by hypervelocity impact. Journal of Non-Crystalline Solids, 67: 465-502.
- Stöffler, D. and Grieve, R.A.F., 2003. A proposal on behalf of the IUGS Subcommittee on the Systematics of Metamorphic Rocks. Web version of 30.04.2003.
- Storzer, D. and Wagner, G.A., 1977. Fission track dating of meteorite impacts. Meteoritics, 12: 368-369.
- Therriault, A.M., Fowler, A.D. and Grieve, R.A.F., 2002. The Sudbury Igneous Complex: a differentiated impact melt sheet. Economic Geology, 97: 1521-1540.
- Thomas, J.B., Watson, E. B., Spear, F. S., Shemella, P. T., Nayak, S. K. and Lanzirotti, A., 2010. TitaniQ under pressure: the effect of pressure and temperature on the solubility of Ti in quartz. Contrib. Mineral. Petrol., 160: 743-759.
- Treppmann, C.A. and Spray, J.G., 2006. Shock-induced crystal-plastic deformation and post-shock annealing of quartz. European Journal of Mineralogy, 18(2): 161-173.
- Valentini, L. and Moore, K.R., 2009. Numerical modeling of the development of small-scale magmatic emulsions by Korteweg stress driven flow. Journal of Volcanology and Geothermal Research, 179: 87-95.

- Wanless, R.K., Stevens, R.D., Lachance, G.R. and Rimsaite, J.Y.H., 1964. Age determinations and geologic studies (part 1). Isotopic ages, report 5. . Geological Survey of Canada Paper, 64: 17.
- Wark, D.A., Hildreth, W., Spear, F.S., Cherniak, D.J. and Watson, E.B., 2007. Pre-eruption recharge of the Bishop magma system. *Geology*, 35: 235-238.
- Wark, D.A. and Watson, E.B., 2006. TitaniQ: a titanium-in-quartz geothermometer. *Contrib. Mineral. Petrol.*, 152: 743-754.
- Warren, P.H., Claeys, P. and Cedillo-Pardo, E., 1996. Mega-impact melt petrology (Chicxulub, Sudbury and the Moon): effects of scale and other factors on potential for fractional crystallization and development of cumulates. In *The Cretaceous-Tertiary event and other catastrophes in Earth history* (Ryder, G., Fastovsky, D. and Gartner, S., eds.), Geological Society of America Special Paper 307: 105-124.
- Watt, G.R., Wright, P., Galloway, S. and McClean, C., 1997. Cathodoluminescence and trace element zoning in quartz phenocrysts and xenocrysts. *Geochim. Cosmochim. Acta*, 61(20): 4337-4338.
- Wiebe, R.A., Wark, D.A. and Hawkins, D.P., 2007. Insights from quartz cathodoluminescence zoning into crystallization of the Vinalhaven granite, coastal Maine. *Contrib. Mineral. Petrol.*, 154: 439-453.
- Winter, J.D., 2001. An introduction to igneous and metamorphic petrology, Appendix. Prentice-Hall: 636-643.
- Wright, T.L. and Doherty, P.C., 1970. A linear-programming and least-squares computer method for solving petrologic mixing problems. *Geological Society of America Bulletin*, 81: 1995-2008.
- Wünnemann, K., Collins, G.S. and Osinski, G.R., 2008. Numerical modelling of impact melt production in porous rocks. *Earth and Planetary Science Letters*, 269: 530-539.
- Yoder Jr., H.S., 1973. Contemporaneous basaltic and rhyolitic magmas. *American Mineralogist*, 58: 153-171.
- Zieg, M.J. and Marsh, B.D., 2005. The Sudbury Igneous Complex: viscous emulsion differentiation of a superheated impact melt sheet. *Geological Society of America Bulletin*, 117(no. 11/12): 1427-1450.
- Zimanowski, B., Büttner, R. and Koopmann, A., 2004. Experiments on magma mixing. *Geophysical Research Letters*, 31: L09612.

Appendix A

Chemical compositions of rock samples obtained
from the core drilled at the West Clearwater impact
structure

Table A.1 - Compositions of fragmental breccia obtained from the core drilled at the West Clearwater Lake Impact structure.

Sample	4-63-214	5-63-124	1-63-125	4A-63-195
SiO₂ (wt.%)	59.65	60.71	52.24	51.74
TiO₂	0.54	0.58	1.25	0.82
Al₂O₃	14.25	16.21	16.18	15.41
Fe₂O₃	6.79	5.54	9.97	10.26
MnO	0.11	0.05	0.17	0.17
MgO	6.13	3.21	5.29	9.03
CaO	2.07	4.13	4.64	2.40
Na₂O	3.62	3.78	4.03	2.93
K₂O	2.08	2.89	1.90	1.35
P₂O₅	0.17	0.23	0.63	0.23
Ba (ppm)	650	1256	891	410
Ce	27	58	83	27
Co	20	16	22	37
Cr	318	214	238	572
Cu	54	42	72	123
Ni	45	31	40	65
Sc	<d/l	<d/l	11	13
V	86	77	147	136
Zn	60	5	78	80
LOI (wt.%)	4.71	2.89	4.47	6.43
Total (wt.%)	100.22	100.37	100.92	100.88

LOI : loss on ignition

Table A.2 - Compositions similar to granites and granodiorites obtained from the core drilled at the West Clearwater Lake Impact structure.

Sample	3-63-977	3-63-1217	4-63-322	5-63-174	5-63-514
SiO₂ (wt.%)	69.65	73.79	73.00	71.23	68.31
TiO₂	0.30	0.20	0.07	0.14	0.65
Al₂O₃	14.37	13.96	12.27	15.35	13.80
Fe₂O₃	3.40	1.85	2.18	2.29	4.69
MnO	0.06	0.03	0.03	0.05	0.05
MgO	1.54	0.38	0.52	0.97	1.44
CaO	1.78	1.96	2.03	3.06	1.70
Na₂O	3.55	3.74	2.25	4.37	3.33
K₂O	3.68	3.82	5.96	1.32	4.56
P₂O₅	0.09	0.07	0.03	0.05	0.22
Ba (ppm)	951	948	3172	355	1742
Ce	<d/l	<d/l	<d/l	<d/l	122
Co	<d/l	<d/l	<d/l	<d/l	<d/l
Cr	186	60	124	56	92
Cu	22	7	10	33	15
Ni	24	11	22	14	12
Sc	<d/l	<d/l	<d/l	<d/l	<d/l
V	20	15	19	<d/l	55
Zn	2	<d/l	<d/l	<d/l	<d/l
LOI (wt.%)	1.22	0.26	1.57	1.19	1.36
Total (wt.%)	99.75	100.16	100.23	100.06	100.31

LOI : loss on ignition

Table A.3 - Compositions similar to those of enderbites, diorites and tonalites obtained from the core drilled at the West Clearwater Lake Impact structure.

Sample	1-63-113	1-63-281	3-63-65	4-63-290
SiO₂ (wt.%)	50.45	56.00	63.28	58.91
TiO₂	1.77	0.61	0.65	1.45
Al₂O₃	16.31	19.47	16.79	15.94
Fe₂O₃	10.78	6.49	6.13	7.98
MnO	0.13	0.12	0.04	0.22
MgO	4.01	3.19	2.25	2.28
CaO	6.85	5.24	4.88	5.06
Na₂O	4.62	5.26	3.97	4.03
K₂O	1.23	1.37	1.38	1.62
P₂O₅	0.89	0.24	0.21	0.74
Ba (ppm)	835	553	528	853
Ce	126	33	35	95
Co	22	<d/l	<d/l	<d/l
Cr	152	162	224	194
Cu	28	23	35	27
Ni	33	28	32	32
Sc	<d/l	<d/l	<d/l	<d/l
V	165	89	104	126
Zn	46	54	14	29
LOI (wt.%)	3.68	2.55	0.84	1.55
Total (wt.%)	100.85	100.62	100.51	99.91

LOI : loss on ignition

Table A.4 - Compositions of mafic and ultramafic rocks obtained from the core drilled at the West Clearwater Lake Impact structure.

Sample	1-63-434	1-63-593	1-63-910	1-63-1163	1-63-1303	3-63-832	3-63-944	4-63-358
SiO₂ (wt.%)	51.89	47.16	49.70	49.65	50.37	48.35	41.75	45.68
TiO₂	1.25	0.86	0.77	0.50	0.63	0.87	0.45	3.40
Al₂O₃	12.76	12.93	7.10	11.96	7.17	15.53	9.83	15.04
Fe₂O₃	10.74	10.25	10.57	8.70	11.48	11.09	14.45	15.43
MnO	0.20	0.29	0.17	0.16	0.19	0.17	0.15	0.11
MgO	8.32	11.17	14.11	11.43	15.21	8.38	18.01	4.05
CaO	8.98	10.37	14.85	13.43	12.81	8.11	5.30	8.51
Na₂O	3.53	2.22	1.27	2.05	1.28	3.02	0.44	3.75
K₂O	0.74	2.07	0.91	0.99	0.84	0.62	2.42	0,83
P₂O₅	0.55	0.30	0.38	0.15	0.12	0.08	0.04	2.29
Ba (ppm)	447	679	374	337	315	151	299	262
Ce	52	75	37	32	17	<d/l	29	340
Co	39	46	54	41	63	36	120	35
Cr	802	1404	2788	1866	2046	662	11454	270
Cu	118	32	149	122	230	274	129	83
Ni	164	190	277	198	329	116	1958	66
Sc	24	23	54	35	46	24	25	15
V	193	168	211	148	177	200	162	286
Zn	1720	256	33	33	43	20	209	44
LOI (wt.%)	1.73	3.13	0.82	1.28	0.65	4.77	6.95	1.76
Total (wt.%)	101.00	100.96	100.90	100.49	100.98	101.09	100.65	100,97

LOI : loss on ignition

Table A.5 – Various compositions obtained from the core drilled at the West Clearwater Lake Impact structure that do not clearly correspond to one of the major units found in the vicinity of the impact structure.

Sample	3-63-325	4-63-306	5-63-293	5-63-298	5-63-493	5-63-696
Description	Altered granite	Altered impact breccia?	Altered impact breccia?	Altered impact breccia?	Altered impact breccia?	Diabase
SiO₂ (wt.%)	60.42	54.29	49.22	50.63	51.58	51.44
TiO₂	0.73	0.74	1.73	1.60	0.76	2.35
Al₂O₃	18.35	12.01	17.98	15.87	8.43	12.50
Fe₂O₃	4.70	7.89	10.60	10.88	13.44	15.59
MnO	0.05	0.17	0.08	0.19	0.22	0.17
MgO	1.73	6.04	6.11	5.93	12.33	4.60
CaO	4.16	8.59	3.61	4.89	8.68	5.81
Na₂O	3.99	1.90	5.57	3.90	2.13	3.46
K₂O	4.60	4.77	1.09	0.86	0.09	1.43
P₂O₅	0.27	0.93	1.13	0.75	0.32	0.40
Ba (ppm)	1670	3133	295	290	<d/l	551
Ce	42	208	93	100	55	34
Co	10	22	18	26	22	34
Cr	190	414	364	214	3486	142
Cu	81	14	30	37	8	55
Ni	32	70	73	62	332	39
Sc	<d/l	39	14	12	33	20
V	99	102	225	190	116	291
Zn	<d/l	70	58	89	219	71
LOI (wt.%)	1.25	2.06	3.65	4.90	2.82	2.66
Total (wt.%)	100.46	99.78	100.87	100.49	101.05	100.53

LOI : loss on ignition

Appendix B

Chemical compositions of rock samples obtained
from the surface of the inner ring of islands at the
West Clearwater impact structure

Table B.1.1 - Compositions of fragmental breccia groundmass obtained from the surface of the inner ring of islands at the West Clearwater Lake Impact structure.

Sample	LP-12	LP-24	DCW-77-64	DCW-77-64-3	DCW-77-64-4
SiO₂ (wt.%)	59.93	60.29	61.17	62.60	60.48
TiO₂	0.64	0.67	0.87	0.70	0.83
Al₂O₃	15.63	15.16	15.70	15.78	15.37
Fe₂O₃	6.30	6.59	6.66	4.69	6.54
MnO	0.07	0.06	0.06	0.03	0.07
MgO	3.57	4.36	2.66	2.67	2.98
CaO	4.12	2.72	3.72	1.97	3.88
Na₂O	3.44	3.73	3.76	3.32	3.71
K₂O	2.46	3.23	3.86	5.70	3.90
P₂O₅	0.27	0.27	0.34	0.26	0.33
Ba (ppm)	905	949	1153	1555	1104
Ce	70	59	89	29	89
Co	19	16	12	10	14
Cr	298	138	148	162	166
Cu	37	28	26	21	31
Ni	43	27	24	22	29
Sc	<d/l	<d/l	<d/l	<d/l	10
V	96	89	102	78	100
Zn	3	<d/l	<d/l	44	5
LOI (wt.%)	4.08	2.85	1.26	1.84	1.60
Total (wt.%)	100.63	100.05	100.20	99.74	99.83

LOI : loss on ignition

Table B.1.2 - Compositions of fragmental breccia groundmass obtained from the surface of the inner ring of islands at the West Clearwater Lake Impact structure.

Sample	DCW-77-64-5	DCW-77-65-1A	DCW-77-65-1B
SiO₂ (wt.%)	62.68	57.97	62.20
TiO₂	0.71	0.64	0.58
Al₂O₃	15.58	15.52	15.11
Fe₂O₃	5.60	6.16	5.59
MnO	0.04	0.08	0.07
MgO	2.21	4.33	3.07
CaO	3.36	4.36	4.02
Na₂O	3.64	3.14	2.46
K₂O	4.14	2.12	3.04
P₂O₅	0.27	0.20	0.23
Ba (ppm)	1523	872	1058
Ce	90	32	35
Co	10	18	13
Cr	154	466	332
Cu	20	73	21
Ni	27	63	38
Sc	<d/l	12	<d/l
V	83	98	82
Zn	<d/l	34	42
LOI (wt.%)	1.33	5.14	3.74
Total (wt.%)	99.74	99.80	100.26

LOI : loss on ignition

Table B.2.1 - Compositions of infiltration dykes obtained from the surface of the inner ring of islands at the West Clearwater Lake Impact structure.

Sample	LP-21	LP-94	LP-122	LP-125	LP-130	LP-133
SiO₂ (wt.%)	58.93	58.80	61.23	59.38	59.47	59.38
TiO₂	0.72	0.90	0.85	0.75	0.78	0.88
Al₂O₃	17.26	17.30	15.84	15.37	16.32	16.16
Fe₂O₃	6.42	5.64	6.42	7.00	6.33	6.72
MnO	0.07	0.06	0.09	0.08	0.08	0.05
MgO	2.80	2.22	2.83	4.04	3.26	3.21
CaO	4.98	3.65	4.60	5.12	4.32	4.91
Na₂O	4.09	4.12	3.91	3.64	4.13	3.69
K₂O	2.94	4.84	3.24	2.92	2.57	3.35
P₂O₅	0.29	0.38	0.33	0.28	0.31	0.40
Ba (ppm)	1120	1460	1097	1081	1147	1270
Ce	77	152	82	68	86	73
Co	15	19	12	30	10	12
Cr	244	170	144	330	174	216
Cu	32	36	38	23	19	23
Ni	39	26	27	78	27	34
Sc	<d/l	<d/l	<d/l	13	<d/l	<d/l
V	111	106	98	101	94	116
Zn	10	21	42	34	43	16
LOI (wt.%)	1.77	1.85	0.99	1.74	2.84	1.50
Total (wt.%)	100.42	99.94	100.47	100.47	100.56	100.41

LOI : loss on ignition

Table B.3.1 - Compositions of clast-rich impact melt rock obtained from the surface of the inner ring of islands at the West Clearwater Lake Impact structure.

Sample	DCW-77-9	DCW-77-11F	DCW-77-13	DCW-77-22	DCW-77-55
SiO₂ (wt.%)	62.62	58.53	62.07	61.59	58.09
TiO₂	0.66	0.77	0.65	0.64	1.09
Al₂O₃	16.13	16.37	15.83	15.82	16.26
Fe₂O₃	5.53	7.55	5.51	5.75	7.87
MnO	0.09	0.04	0.05	0.08	0.10
MgO	2.41	2.86	2.66	2.59	3.13
CaO	3.96	4.01	4.18	4.64	4.56
Na₂O	3.84	3.70	3.71	4.02	3.83
K₂O	3.48	3.34	3.30	2.88	3.17
P₂O₅	0.24	0.31	0.25	0.23	0.49
Ba (ppm)	1195	1251	1164	1209	1190
Ce	73	85	61	59	114
Co	13	16	16	16	12
Cr	200	248	230	260	228
Cu	50	31	26	40	45
Ni	33	31	36	37	36
Sc	<d/l	<d/l	<d/l	<d/l	<d/l
V	85	88	83	84	129
Zn	<d/l	13	17	8	14
LOI (wt.%)	1.22	2.77	1.75	1.42	1.42
Total (wt.%)	100.34	100.42	100.11	99.82	100.17

LOI : loss on ignition

Table B.3.2 - Compositions of clast-rich impact melt rock obtained from the surface of the inner ring of islands at the West Clearwater Lake Impact structure.

Sample	DCW-77-58	DCW-77-59	DCW-77-62	DCW-77-66	DCW-77-67
SiO₂ (wt.%)	60.92	59.99	59.19	62.40	60.75
TiO₂	0.79	0.61	0.80	0.65	0.67
Al₂O₃	15.96	14.95	16.99	16.55	17.27
Fe₂O₃	6.11	5.65	6.09	5.09	5.48
MnO	0.07	0.08	0.03	0.06	0.05
MgO	3.08	4.20	2.88	2.42	2.60
CaO	4.54	6.61	3.31	3.51	4.01
Na₂O	3.90	3.70	3.79	3.91	4.30
K₂O	3.32	2.89	3.74	3.35	3.08
P₂O₅	0.30	0.22	0.32	0.23	0.26
Ba (ppm)	1162	1033	1286	1247	1088
Ce	74	42	80	28	76
Co	11	12	11	11	<d/l
Cr	190	202	160	220	220
Cu	35	21	36	21	31
Ni	36	34	24	31	32
Sc	<d/l	<d/l	<d/l	<d/l	<d/l
V	98	80	92	79	73
Zn	<d/l	29	17	<d/l	<d/l
LOI (wt.%)	1.03	1.19	2.78	2.14	1.72
Total (wt.%)	100.17	100.23	100.08	100.46	100.33

LOI : loss on ignition

Table B.3.3 - Compositions of clast-rich impact melt rock obtained from the surface of the inner ring of islands at the West Clearwater Lake Impact structure.

Sample	LP-34	LP-45	LP-45-3
SiO₂ (wt.%)	60.56	60.10	62.96
TiO₂	0.89	0.88	0.88
Al₂O₃	15.94	16.03	15.23
Fe₂O₃	6.93	7.45	5.74
MnO	0.06	0.07	0.04
MgO	2.39	2.46	2.28
CaO	4.11	3.78	3.02
Na₂O	3.95	3.93	3.66
K₂O	3.72	3.29	4.31
P₂O₅	0.38	0.33	0.38
Ba (ppm)	1237	1050	1465
Ce	109	72	160
Co	12	<d/l	13
Cr	182	210	142
Cu	37	31	24
Ni	30	32	22
Sc	<d/l	10	<d/l
V	84	103	91
Zn	22	<d/l	2
LOI (wt.%)	1.40	1.68	1.26
Total (wt.%)	100.49	100.14	99.94

LOI : loss on ignition

VIII

Table B.4.1 - Compositions of clast-poor impact melt rock obtained from the surface of the inner ring of islands at the West Clearwater Lake Impact structure.

Sample	DCW-77-1	DCW-77-5	DCW-77-7	DCW-77-8	DCW-77-15	DCW-77-16
SiO₂ (wt. %)	60.93	61.22	61.26	60.96	60.89	61.47
TiO₂	0.79	0.776	0.739	0.717	0.686	0.786
Al₂O₃	15.71	15.86	15.63	15.91	15.54	15.43
Fe₂O₃	6.26	6.17	6.03	5.96	6.08	6.24
MnO	0.15	0.06	0.05	0.05	0.06	0.07
MgO	2.81	2.71	2.80	2.86	3.01	2.50
CaO	4.88	4.70	4.49	4.90	4.56	4.12
Na₂O	3.67	3.73	3.74	3.72	3.68	3.69
K₂O	3.63	3.41	3.55	3.28	3.19	3.67
P₂O₅	0.30	0.29	0.29	0.28	0.26	0.27
Ba (ppm)	1134	1105	1159	1142	1117	1192
Ce	86	64	74	61	66	57
Co	11	<d/l	<d/l	<d/l	15	13
Cr	150	154	192	282	300	160
Cu	35	33	35	25	23	28
Ni	31	29	32	38	41	26
Sc	<d/l	<d/l	<d/l	<d/l	<d/l	<d/l
V	95	105	92	89	87	99
Zn	17	6	16	18	24	15
LOI (wt. %)	0.95	1.34	1.38	1.48	2.12	1.47
Total (wt. %)	100.22	100.41	100.11	100.26	100.22	99.87

LOI : loss on ignition

Table B.4.2 - Compositions of clast-poor impact melt rock obtained from the surface of the inner ring of islands at the West Clearwater Lake Impact structure.

Sample	DCW-77-17	DCW-77-18	DCW-77-28	DCW-77-29	DCW-77-30	DCW-77-31
SiO₂ (wt. %)	60.80	61.10	61.37	61.64	61.12	60.84
TiO₂	0.70	0.72	0.75	0.75	0.75	0.82
Al₂O₃	15.99	15.76	15.08	15.72	15.74	15.63
Fe₂O₃	5.90	5.91	6.14	6.05	5.96	6.14
MnO	0.05	0.05	0.05	0.04	0.05	0.05
MgO	2.89	2.68	2.55	2.33	2.81	2.72
CaO	5.03	4.61	4.28	4.28	4.70	4.53
Na₂O	3.66	3.71	3.62	3.80	3.77	3.64
K₂O	3.21	3.30	3.49	3.51	3.39	3.86
P₂O₅	0.27	0.27	0.28	0.34	0.29	0.34
Ba (ppm)	1114	1155	1166	1186	1161	1244
Ce	55	71	63	53	75	81
Co	10	17	14	<d/l	14	11
Cr	214	210	208	168	172	188
Cu	24	22	14	25	30	23
Ni	34	34	36	27	29	30
Sc	<d/l	<d/l	<d/l	<d/l	<d/l	<d/l
V	88	92	93	86	89	98
Zn	24	13	17	13	22	30
LOI (wt.%)	1.68	1.86	2.03	1.49	1.51	1.60
Total (wt. %)	100.33	100.12	99.79	100.10	100.24	100.33

LOI : loss on ignition

Table B.4.3 - Compositions of clast-poor impact melt rock obtained from the surface of the inner ring of islands at the West Clearwater Lake Impact structure.

Sample	DCW-77-32	DCW-77-33	DCW-77-34	DCW-77-35	DCW-77-36	DCW-77-37-4
SiO₂ (wt. %)	60.67	60.21	61.23	61.29	61.13	60.69
TiO₂	0.80	0.71	0.79	0.79	0.81	0.80
Al₂O₃	15.84	15.86	15.59	15.59	15.73	15.87
Fe₂O₃	6.43	6.44	6.15	6.21	6.00	6.05
MnO	0.05	0.06	0.05	0.06	0.05	0.05
MgO	2.75	3.12	2.65	2.59	2.75	2.62
CaO	4.54	4.84	4.54	4.40	4.54	4.68
Na₂O	3.69	3.77	3.68	3.76	3.71	3.78
K₂O	3.61	3.27	3.56	3.67	3.71	3.67
P₂O₅	0.33	0.28	0.31	0.32	0.33	0.33
Ba (ppm)	1225	1145	1204	1221	1215	1244
Ce	91	52	73	98	85	88
Co	17	12	12	18	10	12
Cr	150	250	148	186	182	196
Cu	21	34	29	78	23	41
Ni	28	39	29	33	28	35
Sc	12	<d/l	<d/l	<d/l	10	<d/l
V	85	85	91	92	94	96
Zn	17	19	17	12	26	42
LOI	1.77	1.83	1.80	1.61	1.53	1.61
Total	100.63	100.54	100.51	100.45	100.44	100.31

LOI : loss on ignition

Table B.4.4 - Compositions of clast-poor impact melt rock obtained from the surface of the inner ring of islands at the West Clearwater Lake Impact structure.

Sample	DCW-77-49	DCW-77-50	DCW-77-51	DCW-77-52	DCW-77-53	DCW-77-54
SiO₂ (wt. %)	61.01	61.39	61.11	61.32	60.71	60.74
TiO₂	0.84	0.80	0.82	0.80	0.76	0.76
Al₂O₃	15.93	15.87	16.23	15.80	15.87	15.93
Fe₂O₃	6.42	6.22	6.19	6.24	6.24	6.18
MnO	0.05	0.07	0.08	0.07	0.06	0.08
MgO	2.43	2.55	2.51	2.53	2.85	2.91
CaO	4.04	4.60	4.44	4.45	4.85	4.88
Na₂O	3.74	3.80	3.72	3.79	3.77	3.78
K₂O	4.02	3.68	3.81	3.74	3.57	3.54
P₂O₅	0.32	0.32	0.32	0.32	0.30	0.30
Ba (ppm)	1357	1218	1275	1202	1166	1151
Ce	87	99	90	90	82	88
Co	13	16	<d/l	18	<d/l	17
Cr	178	198	168	192	212	168
Cu	36	35	29	25	33	67
Ni	31	32	27	33	33	29
Sc	<d/l	13	<d/l	<d/l	<d/l	<d/l
V	100	90	94	101	85	99
Zn	6	10	15	29	9	12
LOI (wt. %)	1.24	0.97	0.98	1.05	0.89	0.97
Total (wt. %)	100.22	100.43	100.38	100.26	100.02	100.22

LOI : loss on ignition

Table B.4.5 - Compositions of clast-poor impact melt rock obtained from the surface of the inner ring of islands at the West Clearwater Lake Impact structure.

Sample	DCW-77-61	DR-010	LP-2	LP-23	LP-23-B
SiO₂ (wt. %)	60.45	60.98	61.05	61.41	60.63
TiO₂	0.85	0.75	0.71	0.66	0.76
Al₂O₃	15.88	15.80	15.81	15.87	15.95
Fe₂O₃	6.07	5.92	6.06	5.60	6.88
MnO	0.06	0.06	0.05	0.06	0.05
MgO	2.76	2.57	2.81	3.00	2.90
CaO	4.11	4.41	4.81	4.80	3.82
Na₂O	3.69	3.76	3.73	3.80	3.92
K₂O	3.84	3.47	3.33	3.11	3.31
P₂O₅	0.34	0.29	0.28	0.25	0.26
Ba (ppm)	1292	1190	1137	1121	1131
Ce	102	78	72	38	51
Co	16	12	11	14	14
Cr	176	168	178	230	160
Cu	38	30	25	59	29
Ni	30	30	29	37	26
Sc	<d/l	<d/l	<d/l	<d/l	<d/l
V	102	95	92	86	94
Zn	63	8	17	10	7
LOI (wt. %)	1.65	1.80	1.61	1.81	1.73
Total (wt. %)	99.87	99.96	100.39	100.51	100.36

LOI : loss on ignition

Table B.4.6 - Compositions of clast-poor impact melt rock obtained from the surface of the inner ring of islands at the West Clearwater Lake Impact structure.

Sample	LP-23-D	LP-47	LP-89	LP-95-4
SiO₂ (wt. %)	61.58	61.04	59.96	59.33
TiO₂	0.75	0.79	0.84	0.84
Al₂O₃	15.69	15.53	16.07	15.96
Fe₂O₃	5.99	6.36	6.72	5.88
MnO	0.11	0.06	0.06	0.05
MgO	2.82	2.92	2.61	3.14
CaO	4.96	4.54	4.59	4.81
Na₂O	3.66	3.74	3.60	3.49
K₂O	3.37	3.46	3.81	3.99
P₂O₅	0.28	0.29	0.35	0.37
Ba (ppm)	1132	1122	1317	1367
Ce	64	55	88	89
Co	11	11	13	<d/l
Cr	162	178	160	148
Cu	24	37	36	45
Ni	30	37	30	25
Sc	<d/l	<d/l	<d/l	<d/l
V	95	93	92	141
Zn	4	7	10	14
LOI (wt. %)	0.96	1.30	1.55	1.89
Total (wt. %)	100.32	100.17	100.32	99.93

LOI : loss on ignition

Table B.5.1 - Compositions similar to those of granites and granodiorites obtained from the surface of the inner ring of islands at the West Clearwater Lake Impact structure.

Sample	DCW-77-11	DCW-77-12	DCW-77-14	DCW-77-20	DCW-77-21	DCW-77-27
SiO₂ (wt. %)	71.29	70.38	65.58	71.41	73.75	72.36
TiO₂	0.24	0.43	0.62	0.13	0.05	0.28
Al₂O₃	14.72	14.89	16.25	15.15	14.20	13.67
Fe₂O₃	1.83	3.13	5.51	1.64	1.04	2.38
MnO	0.030	0.033	0.046	0.013	0.009	0.013
MgO	0.76	0.86	0.69	0.43	0.10	0.59
CaO	2.01	2.01	3.44	2.09	0.97	1.64
Na₂O	3.16	4.24	3.46	4.04	3.90	3.39
K₂O	4.86	3.10	3.36	3.98	5.24	4.21
P₂O₅	0.08	0.11	0.20	0.06	0.03	0.07
Ba (ppm)	2065	699	1284	1003	803	1211
Ce	<d/l	31	<d/l	<d/l	<d/l	<d/l
Co	<d/l	<d/l	13	<d/l	<d/l	<d/l
Cr	72	68	74	96	48	54
Cu	24	37	23	8	6	5
Ni	22	8	11	16	7	10
Sc	<d/l	<d/l	<d/l	<d/l	<d/l	<d/l
V	27	32	88	<d/l	<d/l	18
Zn	<d/l	<d/l	4	<d/l	<d/l	<d/l
LOI (wt. %)	0.62	0.61	1.02	0.82	0.35	1.04
Total (wt. %)	99.82	99.87	100.32	99.88	99.73	99.77

LOI : loss on ignition

Table B.5.2 - Compositions similar to those of granites and granodiorites obtained from the surface of the inner ring of islands at the West Clearwater Lake Impact structure.

Sample	DCW-77-42	DCW-77-46-2	DCW-77-60	DCW-77-63-2	DCW-77-63-3
SiO₂ (wt. %)	68.63	76.34	68.41	73.38	72.64
TiO₂	0.44	0.03	0.47	0.15	0.25
Al₂O₃	14.30	12.53	15.49	13.50	14.07
Fe₂O₃	2.73	1.49	3.81	1.57	2.63
MnO	0.14	0.07	0.05	0.02	0.02
MgO	1.42	1.00	1.39	0.89	1.10
CaO	1.65	1.85	2.94	0.70	2.40
Na₂O	2.85	3.97	4.41	3.18	4.74
K₂O	5.59	1.11	2.18	5.19	1.11
P₂O₅	0.08	0.02	0.16	0.02	0.02
Ba (ppm)	1699	254	897	1239	135
Ce	18	<d/l	24	<d/l	<d/l
Co	16	<d/l	<d/l	<d/l	<d/l
Cr	132	110	118	60	190
Cu	334	56	6	16	19
Ni	86	28	13	7	21
Sc	<d/l	<d/l	<d/l	<d/l	<d/l
V	35	<d/l	44	<d/l	18
Zn	<d/l	<d/l	10	<d/l	<d/l
LOI (wt. %)	2.01	1.48	0.85	1.10	0.82
Total (wt. %)	100.07	99.93	100.26	99.83	99.83

LOI : loss on ignition

Table B.5.3 - Compositions similar to those of granites and granodiorites obtained from the surface of the inner ring of islands at the West Clearwater Lake Impact structure.

Sample	DR-006	DR-011
SiO₂ (wt. %)	68.28	76.42
TiO₂	0.66	0.12
Al₂O₃	14.55	12.00
Fe₂O₃	4.12	1.35
MnO	0.02	0.04
MgO	0.86	0.66
CaO	2.27	0.71
Na₂O	3.45	2.68
K₂O	4.32	5.11
P₂O₅	0.27	0.02
Ba (ppm)	1536	983
Ce	141	<d/l
Co	<d/l	<d/l
Cr	86	40
Cu	14	59
Ni	8	10
Sc	<d/l	<d/l
V	43	10
Zn	<d/l	<d/l
LOI (wt. %)	1.33	0.91
Total (wt. %)	100.30	100.12

LOI : loss on ignition

Table B.6.1 - Compositions similar to those of enderbites, diorites and tonalites obtained from the surface of the inner ring of islands at the West Clearwater Lake Impact structure.

Sample	DCW-77-2A	DCW-77-2B	DCW-77-3	DCW-77-10	DCW-77-19	DCW-77-43
SiO₂ (wt. %)	58.06	61.09	58.08	62.32	53.51	55.01
TiO₂	1.07	0.82	1.00	0.68	1.05	1.11
Al₂O₃	16.23	15.50	16.68	16.94	18.66	18.20
Fe₂O₃	7.80	6.19	7.61	5.04	8.95	7.79
MnO	0.06	0.05	0.06	0.06	0.08	0.08
MgO	3.01	2.54	2.87	2.18	2.39	2.55
CaO	5.34	4.57	5.19	4.70	5.16	4.98
Na₂O	3.81	3.70	3.95	4.23	4.45	3.70
K₂O	2.94	3.76	2.93	2.88	3.61	4.60
P₂O₅	0.26	0.33	0.40	0.21	0.83	0.46
Ba (ppm)	892	1261	972	1365	1726	3710
Ce	56	94	82	41	144	63
Co	17	12	17	<d/l	19	13
Cr	138	144	200	248	82	112
Cu	47	27	30	29	467	83
Ni	32	26	38	44	24	27
Sc	10	<d/l	<d/l	<d/l	<d/l	<d/l
V	146	95	128	81	161	139
Zn	28	30	32	<d/l	<d/l	12
LOI (wt. %)	1.55	1.58	1.64	0.98	1.43	1.83
Total (wt. %)	100.25	100.29	100.54	100.40	100.38	100.72

LOI : loss on ignition

Table B.7.1 - Compositions of mafic and ultramafic rocks obtained from the surface of the inner ring of islands at the West Clearwater Lake Impact structure.

Sample	DCW-77-4	DCW-77-39	DCW-77-39-2	DCW-77-40
SiO₂ (wt. %)	47.45	48.86	49.23	48.46
TiO₂	1.64	0.43	0.42	0.58
Al₂O₃	17.87	12.87	11.92	8.25
Fe₂O₃	12.91	10.38	10.41	11.68
MnO	0.14	0.17	0.18	0.18
MgO	4.66	11.92	12.48	15.09
CaO	9.15	10.70	11.18	11.73
Na₂O	3.90	1.58	1.66	1.53
K₂O	1.24	0.46	0.44	0.70
P₂O₅	0.56	0.09	0.09	0.13
Ba (ppm)	472	193	240	289
Ce	82	<d/l	<d/l	<d/l
Co	35	58	62	74
Cr	256	926	1050	1560
Cu	36	235	228	290
Ni	51	201	251	313
Sc	17	31	29	51
V	236	133	142	171
Zn	83	41	23	12
LOI (wt. %)	1.14	3.13	2.70	2.27
Total (wt. %)	100.78	100.73	100.87	100.80

LOI : loss on ignition

Table B.7.2 - Compositions of mafic and ultramafic rocks obtained from the surface of the inner ring of islands at the West Clearwater Lake Impact structure.

Sample	DCW-77-41	DCW-77-45-1	DCW-77-47
SiO₂ (wt. %)	48.28	48.35	47.06
TiO₂	0.46	1.39	1.81
Al₂O₃	12.56	17.46	17.42
Fe₂O₃	10.32	12.39	12.40
MnO	0.18	0.13	0.15
MgO	11.98	4.92	5.18
CaO	10.28	7.39	8.19
Na₂O	2.05	3.92	4.98
K₂O	0.51	1.96	0.97
P₂O₅	0.12	0.57	0.60
Ba (ppm)	262	985	322
Ce	<d/l	100	84
Co	58	33	34
Cr	940	148	246
Cu	206	94	97
Ni	224	41	56
Sc	35	27	28
V	136	214	234
Zn	48	77	60
LOI (wt. %)	3.19	2.25	1.87
Total (wt.%)	100.07	100.89	100.73

LOI : loss on ignition

Table B.8.1 – Various compositions obtained from the surface of the inner ring of islands at the West Clearwater Lake Impact structure that do not clearly correspond to one of the major units found in the vicinity of the impact structure.

Sample	DCW-77-6	DCW-77-38	DCW-77-45-2	DCW-77-48	DCW-77-56
Description	Diabase	Altered tonalite/ diorite?	Altered gabbro?	Altered granite?	Altered granite?
SiO₂ (wt. %)	49.47	57.89	52.25	66.07	66.51
TiO₂	1.08	0.94	1.40	0.55	0.52
Al₂O₃	15.08	17.11	18.41	13.36	16.41
Fe₂O₃	12.83	6.40	9.43	5.40	4.00
MnO	0.18	0.11	0.12	0.07	0.04
MgO	7.62	2.46	3.88	2.27	1.55
CaO	10.19	3.80	5.90	1.62	3.91
Na₂O	2.38	5.28	4.41	2.04	4.71
K₂O	0.76	1.32	1.82	5.51	1.60
P₂O₅	0.12	0.20	0.52	0.43	0.28
Ba (ppm)	282	388	621	735	612
Ce	<d/l	72	68	47	44
Co	40	17	20	12	<d/l
Cr	368	56	126	106	174
Cu	40	60	124	48	8
Ni	69	48	35	18	27
Sc	33	<d/l	<d/l	<d/l	<d/l
V	242	60	158	69	38
Zn	35	45	52	10	<d/l
LOI (wt. %)	1.19	4.54	2.41	2.29	0.66
Total (wt. %)	100.99	100.12	100.67	99.72	100.28

LOI : loss on ignition

Table B.8.2 – Various compositions obtained from the surface of the inner ring of islands at the West Clearwater Lake Impact structure that do not clearly correspond to one of the major units found in the vicinity of the impact structure.

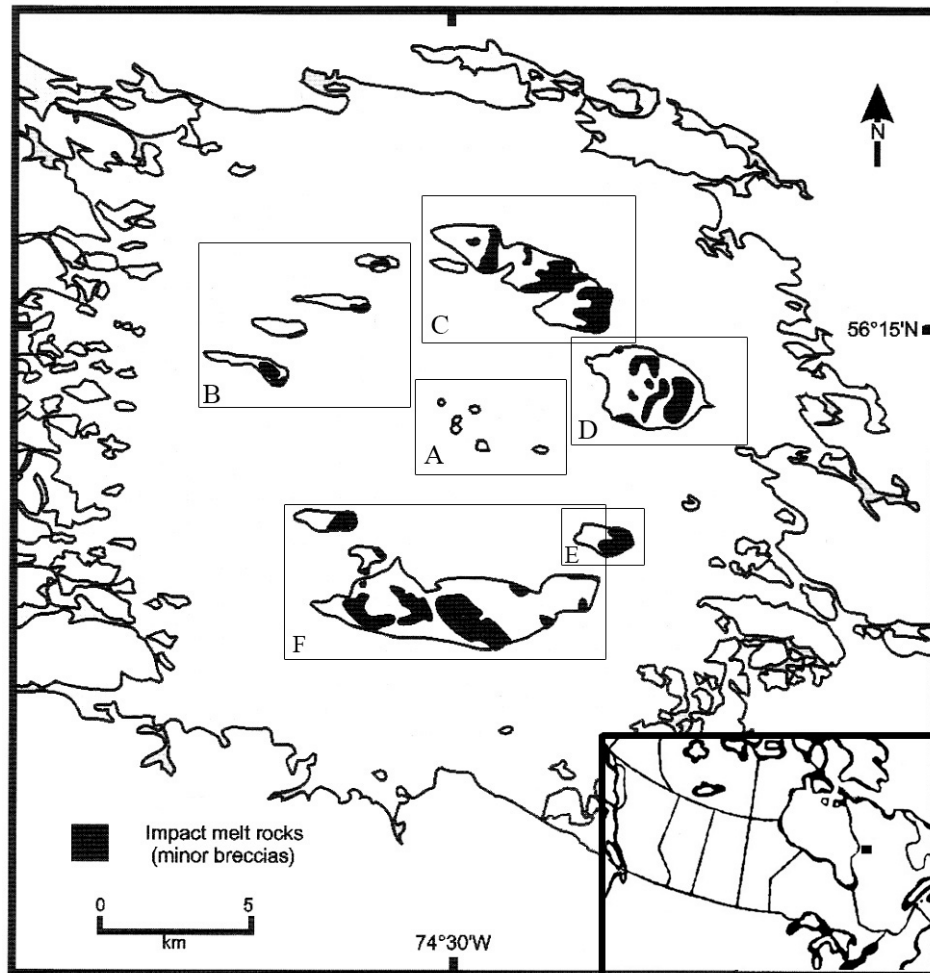
Sample	DCW-77-57	DCW-77-57-1	DCW-77-63-1
Description	Altered granite?	Altered tonalite/ diorite?	Diabase?
SiO₂ (wt. %)	60.17	56.27	45.06
TiO₂	0.98	1.07	0.89
Al₂O₃	15.77	17.05	14.78
Fe₂O₃	6.49	7.65	15.01
MnO	0.08	0.09	0.13
MgO	2.97	3.86	9.22
CaO	2.62	2.65	8.22
Na₂O	4.04	4.25	2.36
K₂O	4.61	4.31	1.48
P₂O₅	0.49	0.47	0.09
Ba (ppm)	1562	1346	344
Ce	81	86	28
Co	13	11	49
Cr	192	202	230
Cu	20	26	64
Ni	25	25	66
Sc	<d/l	<d/l	30
V	91	107	292
Zn	30	34	106
LOI (wt. %)	1.77	2.49	3.44
Total (wt. %)	100.18	100.33	100.80

LOI : loss on ignition

Appendix C

Approximate locations of surface samples

Maps detailing the location of samples at the West Clearwater Lake impact structure



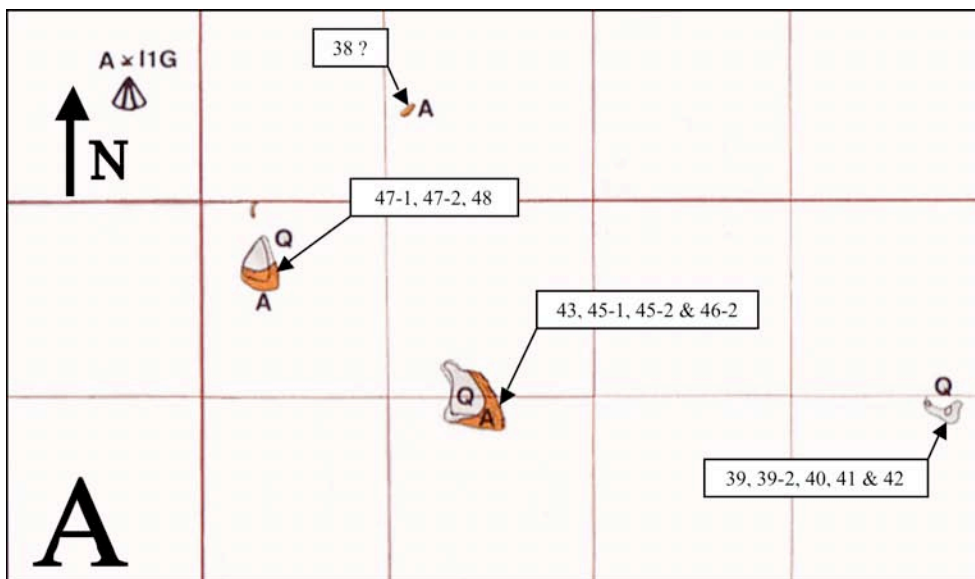
Map of West Clearwater Lake adapted from Grieve (2006).

Legend to
the maps
of sample
locations

- | | |
|--|--------------------|
| | Quaternary Rubble |
| | Clast Poor Melt |
| | Clast Rich Melt |
| | Impact Melt Dikes |
| | Fragmental Breccia |
| | Limestone Enclaves |
| | Diabase Dike |
| | Archean Basement |
| | Shatter Cones |
| | Pegmatite |
| | Cross-section |

III

A - Central Island sample locations



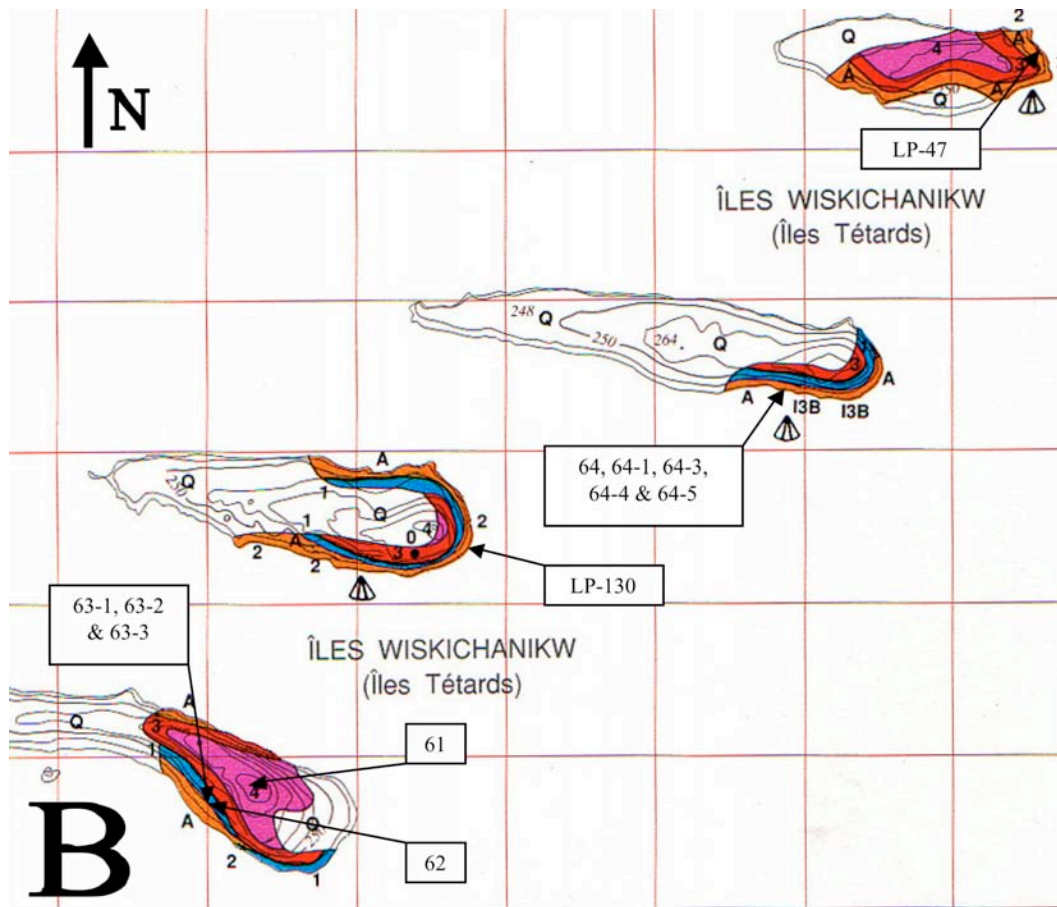
Map adapted from Rondot et al. (1993). One square is 1000 m by 1000 m.

Sample	Rock type according to Dence	Approximate Location
DCW-77-38	Country rock, altered granite?	NE Central Island, that is, one of the small central islands.
DCW-77-39	Country rock, melanocratic gabbro, according to Dence, maskelynite bearing gabbro with breccia dyke and some pegmatite.	E Central Island - NE end of the island; According to Dence, gabbro from NE end of the island.
DCW-77-39-2	Country rock, melanocratic gabbro	E Central Island - NE end of the island; according to Dence, taken in maskelynite bearing gabbro with breccia dyke and some pegmatite.
DCW-77-40	Country rock, melanocratic gabbro	E Central Island - SE end of the island according to Dence, taken in maskelynite bearing gabbro with breccia dyke and some pegmatite.
DCW-77-41	Country rock, melanocratic gabbro	E Central Island - NE end of the island; Breccia Dyke from NE end of the island, according to Dence, taken in maskelynite bearing gabbro with breccia dyke and some pegmatite.

IV

DCW-77-42	Granitic Rock, Dence says mesocratic granitic gneiss, shatter cone bearing pegmatite.	E Central Island - NE end of the island; according to Dence, maskelynite bearing gabbro with breccia dyke and some pegmatite.
DCW-77-43	Basement rock with an intermediate composition, Dence says mesocratic granodioritic gneiss, shocked gneiss	SW central Island - according to Dence, taken near oxidized gabbro outcrop with pegmatite mixed with gneiss cut by oxidized pseudotachylite dykes.
DCW-77-45-1	Gabbro, Dence says mesocratic gneiss, coarse-grained, according to Dence, shocked gneiss mixed with pegmatite	SW central Island - according to Dence, oxidized gabbro outcrop with pegmatite mixed with gneiss cut by oxidized pseudotachylite dykes.
DCW-77-45-2	Altered gabbro? Dence says mesocratic gneiss, coarse-grained, shocked gneiss mixed with pegmatite	SW central Island - according to Dence, oxidized gabbro outcrop with pegmatite mixed with gneiss cut by oxidized pseudotachylite dykes.
DCW-77-46-2	Granitic rock, according to Dence, it's pegmatite	SW central Island - according to Dence, oxidized gabbro outcrop with pegmatite mixed with gneiss cut by oxidized pseudotachylite dykes.
DCW-77-47-1	Gabbro, according to Dence, shocked gabbro	NW Central Island - according to Dence, shocked gabbro outcrop cut by pegmatite and mixed gneiss
DCW-77-47-2	Gabbro, according to Dence, shocked gabbro	NW Central Island - according to Dence, shocked gabbro outcrop cut by pegmatite and mixed gneiss
DCW-77-48	Altered granite? According to Dence, shocked gabbro	NW Central Island - according to Dence, shocked gabbro outcrop cut by pegmatite and mixed gneiss

B – Tadpole Islands sample locations



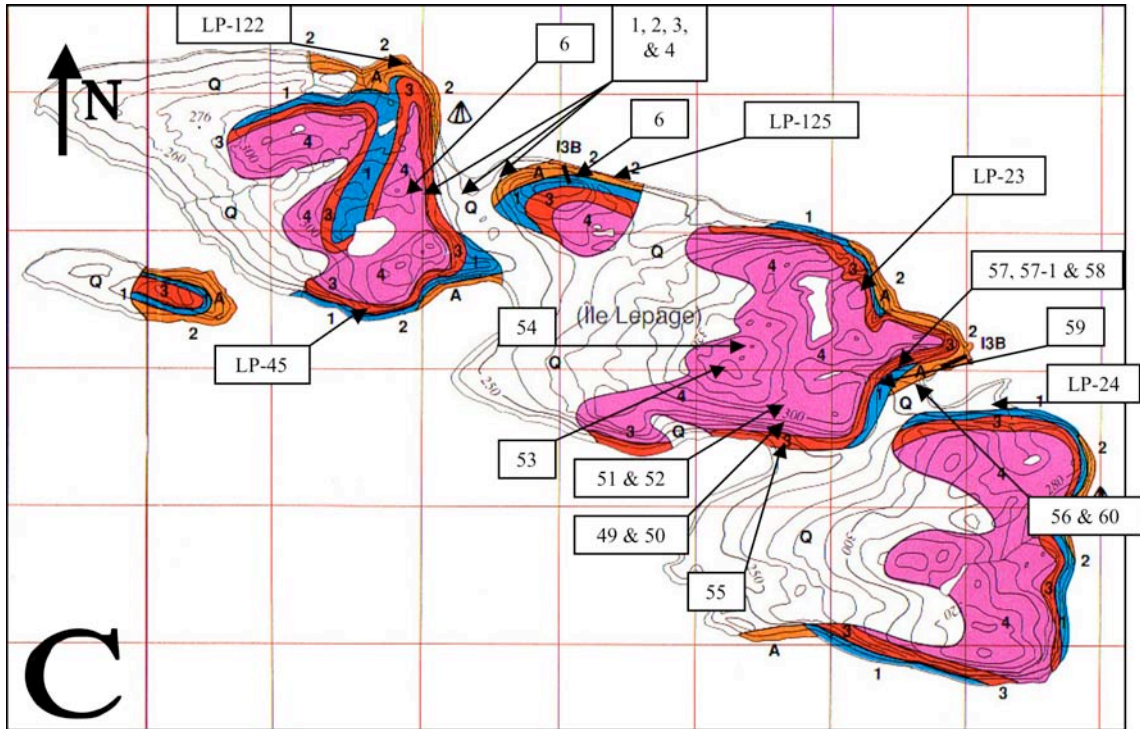
Map adapted from Rondot et al. (1993). One square is 1000 m by 1000 m.

Samples	Rock Type	Approximate Location
DCW-77-61	Clast-poor impact melt rock	South Tad Island, taken at the highest point on South Tad Island.
DCW-77-62	Clast-rich impact melt rock. Dence says melt rock, 35% inclusions, contact of breccia with melt	South Tad Island, not clear exactly from where, but probably along the South shore - contact of basement breccia with melt.
DCW-77-63-1	Severely altered diabase?	South Tad Island, not clear exactly from where, but probably along the South shore, looking E across basement to melt cliffs
DCW-77-63-2	Granitic rock, mesocratic granite, coarse-grained	South Tad Island, not clear exactly from where, but probably along the South shore, looking E across basement to melt cliffs

VI

DCW-77-63-3	Granitic Rock, leucocratic granitic gneiss	South Tad Island, not clear exactly from where, but probably along the South shore, looking E across basement to melt cliffs
DCW-77-64	Melt Rock, 45% inclusions: taken from the mega-breccia veins?	3rd Tad Island (North central Tad island), south cliff face; taken from mega-breccia with vein-like bodies of rust-red impact melt (see photo in Bostock)
DCW-77-64-1	Melt Rock, 45% inclusions: taken from the mega-breccia veins?	3rd Tad Island (North central Tad island), south cliff face; taken from mega-breccia with vein-like bodies of rust-red impact melt (see photo in Bostock)
DCW-77-64-3	Melt Rock, 50% inclusions: taken from the mega-breccia veins?	3rd Tad Island (North central Tad island), south cliff face; taken from mega-breccia with vein-like bodies of rust-red impact melt (see photo in Bostock)
DCW-77-64-4	Melt Rock, 45% inclusions: taken from the mega-breccia veins?	3rd Tad Island (North central Tad island), south cliff face; taken from mega-breccia with vein-like bodies of rust-red impact melt (see photo in Bostock)
DCW-77-64-5	Melt Rock, 20% inclusions: taken from the mega-breccia veins?	3rd Tad Island (North central Tad island), south cliff face; taken from mega-breccia with vein-like bodies of rust-red impact melt (see photo in Bostock)
LP-47	Clast-poor impact melt rock	L. Plante sample. Eastern shore of the northern-most Tadpole island, at lake level.
LP-130	Infiltration dyke	L. Plante sample. Eastern shore of the second southern Tadpole island, at lake level.

C – Lepage Island sample locations



Map adapted from Rondot et al. (1993). One square is 1000 m by 1000 m.

Samples	Rock Types	Approximate Locations
DCW-77-1	Clast-poor impact melt rock. Dence says probably rust-red fine-grained clast-poor impact melt rock.	North Island, landing at NW bay; traverse W to top of hill near large oval lake; Dence mentions a large mass of Diabase 50 m uphill, which doesn't appear in the MRN map; sample taken near top of the hill.
DCW-77-2	Probably a clast of rock with an intermediate composition, tonalitic or enderbitic.	North Island, landing at NW bay; traverse W to top of hill near large oval lake; Dence mentions a large mass of Diabase 50 m uphill, which doesn't appear in the MRN map; sample taken near top of the hill.
DCW-77-3	Probably a clast of rock with an intermediate composition, tonalitic or enderbitic.	North Island, landing at NW bay; traverse W to top of hill near large oval lake; Dence mentions a large mass of Diabase 50 m uphill which doesn't appear in the MRN map; sample taken near top of the hill.

VIII

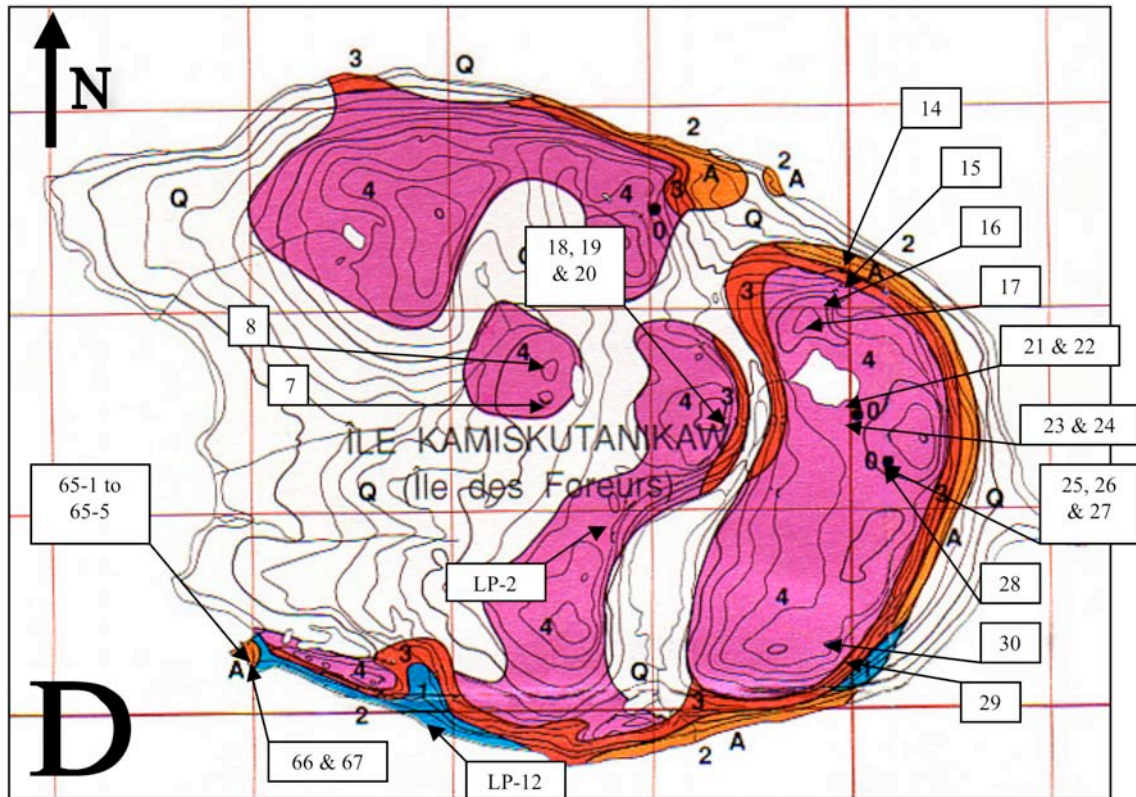
DCW-77-4	Mafic or ultramafic country rock, described by Dence as a coarse-grained ultramafic.	North Island, landing at NW bay; traverse W to top of hill near large oval lake; Dence mentions a large mass of Diabase 50 m uphill which doesn't appear in the MRN map; sample taken near top of the hill.
DCW-77-5	Clast-poor impact melt rock. Rust-red clast poor impact melt, taken near the transition from clast-poor to clast-rich impact melt.	North Island, landing at NW bay; traverse W to top of hill near large oval lake; Dence mentions a large mass of Diabase 50 m uphill which doesn't appear in the MRN map; sample taken near top of the hill; cliff on north side of hill.
DCW-77-6	Altered diabase	North Island, landing at NW bay; traverse W to top of hill near large oval lake; Dence mentions a large mass of Diabase 50 m uphill which doesn't appear in the MRN map; sample probably taken near, or at, the large outcrop of uniform fractured and altered diabase.
DCW-77-49	Clast-poor impact melt rock: Dence says "transition from unit 5 to 6, clasts to 1 m across, fine grained mottled red matrix."	Central North Island, I'm uncertain about the exact location, Dence says "land at SE Bay, traverse up hill to W"... Must be the southernmost bay on the south shore of Lepage Island. This particular sample was "on a bench on the hill"...
DCW-77-50	Rust-red clast-poor impact melt rock	Central North Island, I'm uncertain about the exact location, Dence says "land at SE Bay, traverse up hill to W"... Must be the southernmost bay on the south shore of Lepage Island. This particular sample was "on a bench on the hill"...
DCW-77-51	Clast-poor impact melt rock, according to Dence, mainly red-mottled variety, some clasts up to 6 cm across, about 10% clasts	Central North Island (see above), 25 to 30 m higher uphill from DCW-77-49 and DCW-77-50
DCW-77-52	Rust-red clast-poor impact melt rock, massive outcrops.	Central North Island (see above), about 5 m higher than DCW-77-51.

IX

DCW-77-53	Rust-red clast-poor impact melt rock, massive outcrops.	Central North island (see above), from the highest point on the hill, 5 m higher than DCW-77-52? Or DCW-77-50?
DCW-77-54	Clast-poor impact melt rock.	Central North Island (see above), according to Dence, massive outcrop top of the hill to N.
DCW-77-55	Clast-rich impact melt rock. Dence says Impact melt rock, hematized, 10% inclusions	Central North Island (see above), 10 m below the emplacement of samples DCW-77-49 and DCW-77-50.
DCW-77-56	Altered granite? Dence calls it strongly fractured basement granite	North Island, traverse to north shore, starting on beach to the W of Horseshoe bay (that must be the horseshoe shaped bay on the North shore of central North Island); small outcrop about 15 m above water; strongly fractured granite
DCW-77-57	Altered granite? Dence says clasts up to 5 m across enclosed in red impact-melt, close spaced jointing radiates from clasts in all directions.	North Island, traverse to north shore, starting on beach to the W of Horseshoe bay (see above); Dence says base of 10 m cliff near top of hill about 40 m above water
DCW-77-57-1	Altered tonalite or diorite? Leucocratic gneiss, coarse-grained	North Island, traverse to north shore, starting on beach to the W of Horseshoe bay (see above); Dence says base of 10 m cliff near top of hill about 40 m above water

DCW-77-58	Clast-rich impact melt rock. Dence says impact melt rock, 50% inclusions	North Island, traverse to north shore, starting on beach to the W of Horseshoe bay (see above); Dence says it's at the base of 10 m cliff near top of hill, about 40 m above water
DCW-77-59	Clast-rich impact melt rock. Dence says melt rock, vesicular, 20% inclusions, fine grained melt sample, with 50% large (larger than 1 m) clasts, some shattercones.	North Island, traverse to north shore, starting on beach to the W of Horseshoe bay (see above); Dence says it's from a cliff with waterfall near the beach, therefore near water level.
DCW-77-60	Granitic rock, Dence says it's a sample of fractured granitic gneiss.	North Island, traverse to north shore, starting on beach to the W of Horseshoe bay (see above); at the beach, near water line.
LP-23	Clast-poor impact melt rock.	L. Plante sample. Northeastern shore of Drillers island, at lake level.
LP-24	Fragmental breccia	L. Plante sample: northeastern shore of Drillers island, at lake level.
LP-45	Clast-rich impact melt rock	L. Plante sample: southwestern shore of Drillers island, at lake level.
LP-122	Infiltration dyke	L. Plante sample. Northwestern shore of Lepage island, at lake level.
LP-125	Infiltration dyke	L. Plante sample. North shore of Lepage island, at lake level.

D – Drillers Island sample locations



Map adapted from Rondot et al. (1993). One square is 1000 m by 1000 m.

Sample Number	Rock Type	Approximate Location
DCW-77-7	Rust-red clast-poor impact melt rock	Drillers Island, hilltop west of south end of large central lake.
DCW-77-8	Rust-red clast-poor impact melt rock	Drillers Island, overlooking NW shore of large central lake; similar outcrop to DCW-77-7
DCW-77-9	Clast-rich impact melt rock. Dence says Rust-red impact melt rock, 30% inclusions	Drillers island, unknown location
DCW-77-14	Granitic rock, according to Dence, mesocratic granitic gneiss; gneissic basement	Drillers island, traverse in Eastern Drillers island, to the ridge overlooking eastern Cleawater Lake; gneissic basement, probably taken somewhere near the shore; I think they may have been walking South from Drillers island NE shore.

XII

DCW-77-15	Clast-poor impact melt rock - according to Dence, broad outcrop of grey impact melt with abundant cm-size clasts	Drillers island, traverse in Eastern Drillers island, to the ridge overlooking eastern Clearwater Lake; 25 to 50m E of the emplacement of DCW-77-14 and slightly up-hill.
DCW-77-16	Rust-red clast-poor impact melt rock	Drillers island, traverse in Eastern Drillers island, to the ridge overlooking eastern Clearwater lake; taken higher up-hill?
DCW-77-17	Clast-poor impact melt rock. According to Dence's notes, this should be grey clast poor impact-melt.	Drillers island, hilltop outcrops overlooking north end of large lake on the Eastern part of the island.
DCW-77-18	Probably rust-red impact melt.	Drillers Island, near the small valley west of the large lake, traverse E to limestone on next ridge; melt through 30 to 40 m drop towards small lake in valley; basal exposure of buff grey impact melt - massive outcrops.
DCW-77-19	Altered basement rock with an intermediate composition.	Drillers Island, across the small valley west of the large lake, traverse E to limestone on next ridge; Dence says it's apparently altered basement; irregular bodies of melt in contact with basement, no apparent chill.
DCW-77-20	Granitic rock, Dence says it's apparently altered basement	Drillers Island, across the small valley west of the large lake, traverse E to limestone on next ridge; irregular bodies of melt in contact with basement, no apparent chill.
DCW-77-21	Granitic rock, Dence calls this a "gneiss"	Drillers island, small exposure of "gneiss" almost surrounded by melt about 50 m from small limestone outcrop nearer to the SE shore of the large lake.
DCW-77-22	Clast-rich impact melt rock. Dence says Impact melt Rock, 20% Breccia	Drillers island, melt in the vicinity of the small limestone outcrop nearer to SE shore of large lake (5 m E of small limestone outcrop?).
DCW-77-23	According to Dence's notes: metamorphosed limestone	Drillers island, small limestone outcrop nearer to the SE shore of the large lake.
DCW-77-24	According to Dence's notes: metamorphosed limestone	Drillers island, small limestone outcrop nearer to SE shore of the large lake.

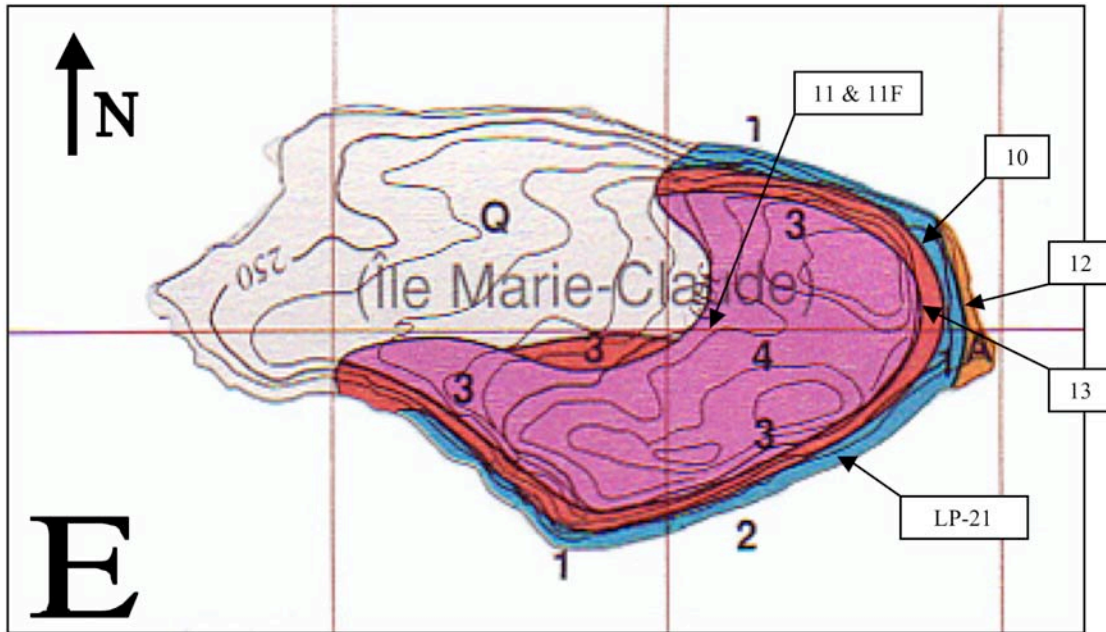
XIII

DCW-77-25	According to Dence's notes: metamorphosed limestone	Drillers island, main limestone mass in eastern part of the island.
DCW-77-26	According to Dence's notes: metamorphosed limestone	Drillers island, main limestone mass in eastern part of the island.
DCW-77-27	Granitic rock, Dence calls this a "gneiss"	Drillers island, adjacent to north part of the main limestone outcrop; this could be, in fact, the grey limestone on the north of the limestone outcrop.
DCW-77-28	Fine-grained rust-red clast-poor impact melt rock	Drillers island, taken from blocky melt east of the main limestone outcrop.
DCW-77-29	Rust-red clast-poor impact melt	Drillers Island, at its SE point.
DCW-77-30	Clast-poor impact melt rock. Dence says it's grey impact melt.	Drillers island, SE point of the island; small outcrop of grey melt on the side of hill.
DCW-77-65-1	Fragmental breccia. Dence says: melt rock, 50% inclusions.	Drillers Island, traverse to breccia-melt exposures on SW point of Drillers Island
DCW-77-65-2	Fragmental breccia. Dence says melt Rock, 50% inclusions.	Drillers Island, traverse to breccia-melt exposures on SW point of Drillers Island
DCW-77-65-3	Fragmental breccia. Dence says melt Rock, 50% inclusions.	Drillers Island, traverse to breccia-melt exposures on SW point of Drillers Island
DCW-77-65-4	Fragmental breccia. Dence says melt Rock, 50% inclusions.	Drillers Island, traverse to breccia-melt exposures on SW point of Drillers Island
DCW-77-65-5	Fragmental breccia. Dence says melt Rock, 40% inclusions.	Drillers Island, traverse to breccia-melt exposures on SW point of Drillers Island
DCW-77-66	Clast-rich impact melt rock. Dence says breccia, monomict; taken at breccia-melt contact.	Drillers Island, traverse to breccia-melt exposures on SW point of Drillers Island; contact of melt and breccia
DCW-77-67	Clast-rich impact melt rock. Dence says rust-red impact melt rock, 20% inclusions; flow banding in melt	Traverse to breccia-melt exposures on SW point of Drillers Island
LP-2	Clast-poor impact melt rock	L. Plante sample. Hills at the center of Drillers island.

XIV

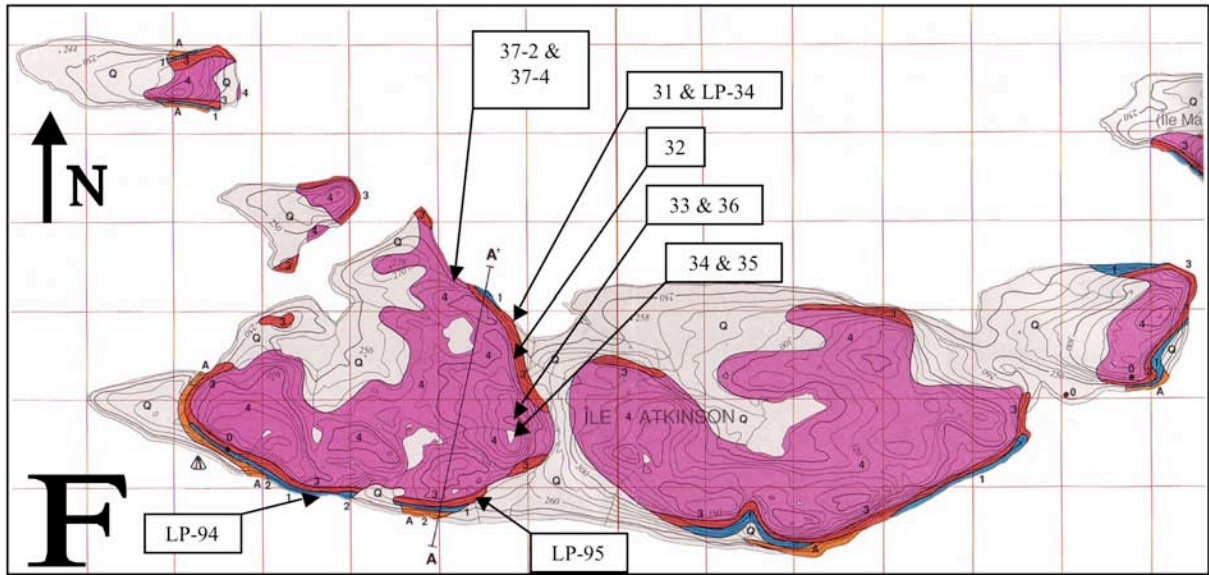
LP-12	Fragmental breccia	L. Plante sample: southwestern shore of Drillers island, at lake level.
DR-06	Granitic rock, partially melt	D. Rosa sample. Eastern plateau of Drillers island.
DR-10	Grey clast-poor impact melt rock.	D. Rosa sample. Eastern plateau of Drillers island.
DR-11	Granitic rock	D. Rosa sample. Eastern shore of Drillers island.

E – Marie-Claude Island sample locations



Map adapted from Rondot et al. (1993). One square is 1000 m by 1000 m.

Sample	Rock Type	Approximate Location
DCW-77-10	Country rock with an intermediate composition, Dence says granodiorite (hematized), fractured basement	SE Island (probably île Marie-Claire), taken on the slope on the NE shore of the island.
DCW-77-11	Granitic rock, Dence calls it a leucocratic granitic gneiss	SE island (probably île Marie-Claire), talus slope about 250 m W of the E shore of the island, at the contact between melt and friable breccia.
DCW-77-11F	Clast-rich impact melt rock. Dence says 30% inclusions; small sample of contact between melt and friable breccia, oriented sample.	SE island (probably île Marie-Claire), talus slope about 250 m W of the NE corner of the island, at the contact between melt and friable breccia.
DCW-77-12	Granitic rock, according to Dence, pale pink granitic basement	SE Island (probably île Marie-Claire), waterline exposure on E shore.
DCW-77-13	Clast-rich impact melt rock. Dence says Grey melt rock, 30% inclusions, oriented sample.	SE Island (probably île Marie-Claire), E shore, up small talus to small cliff of mainly grey clast poor melt (?)
LP-21	Infiltration dyke	L. Plante sample. Southeastern shore of Marie-Claude island, at lake level.

F – Atkinson Island sample locations

Map adapted from Rondot et al. (1993). One square is 1000 m by 1000 m.

Samples	Rock Types	Approximate Locations
DCW-77-31	Grey clast-poor impact melt rock	South Island (aka Atkinson Island), SW corner of the island, pebble beach beside cliff of grey clast-poor melt, probably on the north shore of South island.
DCW-77-32	Grey clast-poor impact melt rock	South Island (aka Atkinson Island), SW corner of the island, approximately half-way along ridge leading S, outcrops of grey clast poor impact melt generally at 50 to 100 m intervals.
DCW-77-33	Grey clast-poor impact melt rock	South Island (aka Atkinson Island), SW corner, highest point of SW corner of South Island.
DCW-77-34	Grey clast-poor impact melt rock; contains rounded to irregular small white clasts, 5-10%, up to 8 cm long.	South Island (aka Atkinson Island), SW corner, abundant outcrops of impact melt on N, E and S shores of small lake.
DCW-77-35	Grey clast-poor impact melt rock	South Island (aka Atkinson Island), SW corner, abundant outcrops of impact melt on N, E and S shores of small lake; about 100 m SW of small lake mentioned above.
DCW-77-36	Grey clast poor impact melt rock	South Island (aka Atkinson Island), SW corner, highest point of SW corner of South Island; sample from outcrop at top of cliff.

XVII

DCW-77-37-2	Grey clast-poor impact melt rock. Dence says it was mapped as clast-rich impact-melt, but it's probably lower clast-poor impact melt.	South Island (aka Atkinson Island), SW corner, back to beach on the north shore of the SW corner of the island (probably on the bay in that area), then boating along shore to the NNW; waterline exposure.
DCW-77-37-4	Grey clast-poor impact melt rock	South Island (aka Atkinson Island), SW corner, back to beach on the north shore of the SW corner of the island (probably on the bay in that area), then boating along shore to the NNW; waterline exposure; there might be a photo of the outcrop.
LP-34	Clast-rich impact melt rock	L. Plante sample. Northwestern shore of Atkinson island, at lake level.
LP-94	Infiltration dyke	L. Plante sample. Southwestern shore of Atkinson island, at lake level.
LP-95	Clast-poor impact melt rock	L. Plante sample. Southwestern shore of Atkinson island.

Appendix D

Electron microprobe compositions

Sample rock types	Starting page
Granitic	1
Granodioritic, enderbritic and tonalitic	4
Mafic and ultramafic	8
Fragmental breccia	13
Infiltration dykes	18
Clast-rich impact melt	24
Clast-poor impact melt	28
Diabase	40
Altered impact breccia	41

Microprobe compositions

Page 1

Granitic Rocks

Sample 5-63-939-174	SiO ₂	TiO ₂	Cr ₂ O ₃	Al ₂ O ₃	FeO _{total}	MnO	MgO	CaO	Na ₂ O	K ₂ O	P ₂ O ₅	Total
5-63-939-Region 1- PLAG 1	56,31	0,002	0,002	23,81	3,08	0,073	2,66	0,619	5,89	3,80	0,007	96,25
5-63-939-Region 1- QTZ	98,31	0,017	0,000	0,009	0,033	0,000	0,004	0,000	0,000	0,003	0,000	98,37
5-63-939-Region 1- Vein material	54,21	0,000	0,000	17,37	0,949	0,029	3,74	1,06	6,90	0,664	0,000	84,92
Sample DCW-77-11	SiO ₂	TiO ₂	Cr ₂ O ₃	Al ₂ O ₃	FeO _{total}	MnO	MgO	CaO	Na ₂ O	K ₂ O	P ₂ O ₅	Total
DCW-77-11-Region 1-Kspar 1	64,63	0,021	0,000	18,39	0,066	0,024	0,004	0,098	1,46	14,37	0,000	99,06
DCW-77-11-Region 1-Kspar 2	64,54	0,053	0,009	18,43	0,049	0,000	0,000	0,049	1,27	14,80	0,000	99,20
DCW-77-11-Region 1-Kspar 3	64,88	0,029	0,025	18,57	0,009	0,000	0,000	0,166	1,68	14,23	0,000	99,59
DCW-77-11-Region 1-Kspar 4	64,57	0,034	0,000	18,59	0,022	0,000	0,004	0,095	1,57	14,37	0,000	99,26
DCW-77-11-Region 1-Plag 1	61,04	0,000	0,000	24,22	0,068	0,010	0,000	6,07	8,02	0,190	0,000	99,62
DCW-77-11-Region 1-Plag 2	60,65	0,016	0,000	24,37	0,076	0,019	0,000	6,06	8,15	0,086	0,000	99,42
DCW-77-11-Region 1-Plag 3	60,80	0,019	0,000	24,51	0,053	0,009	0,006	6,25	7,87	0,140	0,000	99,64
DCW-77-11-Region 1-Fe Ox 1	0,174	0,124	0,304	0,406	88,29	0,047	0,173	0,021	0,000	0,000	0,000	89,54
DCW-77-11-Region 1-Biotite 1	36,19	4,45	0,003	15,09	10,67	0,073	16,22	0,534	0,100	6,76	0,000	90,09
DCW-77-11-Region 1-Fe Ox 2	0,187	0,114	0,199	0,553	86,95	0,117	0,285	0,024	0,000	0,000	0,000	88,43
DCW-77-11-Region 1-Plag 4	60,66	0,022	0,000	24,52	0,097	0,000	0,000	6,23	7,87	0,153	0,000	99,56
DCW-77-11-Region 1-Plag 5	60,98	0,030	0,016	24,14	0,057	0,000	0,034	5,89	8,02	0,193	0,000	99,35
DCW-77-11-Region 1-Plag 6	61,25	0,000	0,000	24,48	0,071	0,001	0,000	6,03	8,13	0,121	0,000	100,08
DCW-77-11-Region 2- Apatite 1	0,191	0,000	0,000	0,007	0,200	0,090	0,043	54,42	0,112	0,015	40,89	95,97
DCW-77-11-Region 2- Fe Ti Ox 1	0,956	55,71	0,096	0,643	36,07	0,642	1,29	0,199	0,006	0,024	0,000	95,63
DCW-77-11-Region 2- Fe Ti Ox 2	1,21	57,57	0,196	0,626	33,05	0,526	0,620	0,225	0,033	0,015	0,000	94,08
DCW-77-11-Region 2- Kspar 1	64,71	0,011	0,000	18,47	0,018	0,000	0,004	0,070	1,40	14,68	0,000	99,36
DCW-77-11-Region 2- Kspar 2	64,70	0,020	0,000	18,42	0,038	0,013	0,000	0,048	1,05	15,06	0,000	99,35
DCW-77-11-Region 2- Kspar 3	64,72	0,038	0,000	18,36	0,001	0,012	0,000	0,059	0,901	15,37	0,000	99,47
DCW-77-11-Region 2- Kspar 4	64,76	0,033	0,000	18,09	0,007	0,000	0,006	0,047	1,09	15,30	0,000	99,33
DCW-77-11-Region 2- Kspar 5	64,99	0,035	0,000	18,67	0,018	0,000	0,003	0,133	1,57	14,27	0,000	99,68
DCW-77-11-Region 2- Kspar 6	64,73	0,049	0,000	18,40	0,033	0,007	0,000	0,022	0,938	15,47	0,000	99,65
DCW-77-11-Region 2- Plag 1	61,49	0,044	0,000	24,24	0,064	0,017	0,001	5,84	8,05	0,216	0,000	99,95
DCW-77-11-Region 2- Plag 2	61,51	0,022	0,000	24,71	0,094	0,000	0,000	5,99	7,99	0,211	0,000	100,53
DCW-77-11-Region 2- Plag 3	61,34	0,033	0,000	24,29	0,074	0,000	0,000	5,91	8,05	0,211	0,000	99,92
DCW-77-11-Region 2- Plag 4	61,38	0,021	0,000	24,33	0,189	0,001	0,084	5,95	8,06	0,174	0,000	100,19
DCW-77-11-Region 2- Plag 5	61,51	0,004	0,000	24,46	0,109	0,004	0,003	6,04	8,12	0,163	0,000	100,41
DCW-77-11-Region 2- Plag 6	61,41	0,021	0,004	24,27	0,076	0,017	0,011	5,88	8,00	0,286	0,000	99,97

Microprobe compositions

Page 2

Sample DCW-77-20	SiO ₂	TiO ₂	Cr ₂ O ₃	Al ₂ O ₃	FeO _{total}	MnO	MgO	CaO	Na ₂ O	K ₂ O	Total
DCW-77-20-R1-Biotite 1	41,09	2,29	0,000	11,71	9,78	0,080	20,83	0,093	0,518	9,17	95,57
DCW-77-20-R1-KSpar 1	64,86	0,069	0,034	19,50	0,218	0,000	0,008	1,16	5,29	8,20	99,34
DCW-77-20-R1-KSpar 2	65,45	0,053	0,005	18,51	0,130	0,019	0,000	0,286	3,10	12,23	99,78
DCW-77-20-R1-KSpar 3	74,01	0,189	0,000	13,19	0,263	0,000	0,027	0,262	2,26	8,15	98,34
DCW-77-20-R1-KSpar 4	75,94	0,017	0,000	12,20	0,115	0,000	0,007	0,204	1,95	7,90	98,34
DCW-77-20-R1-Plag 1	61,23	0,035	0,000	23,50	0,302	0,000	0,000	5,53	7,79	0,945	99,33
DCW-77-20-R1-Plag 2	61,71	0,012	0,000	23,52	0,288	0,000	0,001	5,65	8,01	0,595	99,79
DCW-77-20-R1-KSpar 5	77,06	0,044	0,000	11,76	0,065	0,015	0,012	0,376	2,00	7,00	98,33
DCW-77-20-R1-Plag 4	61,49	0,020	0,001	23,48	0,273	0,002	0,000	5,53	7,86	0,731	99,39
DCW-77-20-R1-Kspar 5	76,39	0,070	0,000	12,31	0,118	0,023	0,000	0,211	1,82	8,06	99,00
DCW-77-20-R1-Kspar 6	75,49	0,154	0,000	12,39	0,220	0,000	0,000	0,236	1,95	7,90	98,33
DCW-77-20-R2-Fe Ti Oxide	0,06	8,95	0,070	3,18	79,78	0,268	0,415	0,000	0,008	0,015	92,74
Sample DCW-77-27	SiO ₂	TiO ₂	Cr ₂ O ₃	Al ₂ O ₃	FeO _{total}	MnO	MgO	CaO	Na ₂ O	K ₂ O	Total
DCW-77-27 region 1 - Kspar 1	65,91	0,025	0,000	18,59	0,075	0,014	0,000	0,430	3,73	11,15	99,93
DCW-77-27 region 1 - Kspar 2	75,84	0,037	0,001	12,67	0,191	0,000	0,002	0,479	2,06	7,89	99,18
DCW-77-27 region 1 - Kspar 3	65,79	0,025	0,000	18,67	0,031	0,001	0,000	0,480	3,89	10,86	99,74
DCW-77-27 region 1 - Kspar 4	65,51	0,037	0,000	18,74	0,050	0,004	0,000	0,476	3,97	10,75	99,54
DCW-77-27 region 1 - Plag 1	61,86	0,019	0,001	23,34	0,073	0,014	0,006	5,22	7,80	1,01	99,34
DCW-77-27 region 1 - Plag 2	61,86	0,001	0,000	23,31	0,111	0,012	0,000	5,03	7,85	0,984	99,16
DCW-77-27 region 1 - K-spar 5	77,07	0,048	0,008	11,68	0,117	0,000	0,003	0,28	1,81	7,64	98,66
DCW-77-27 region 2 - K-spar 1	65,41	0,008	0,000	18,70	0,090	0,010	0,001	0,473	3,78	11,13	99,60
DCW-77-27 region 2 - K-spar 2	65,84	0,034	0,010	18,69	0,073	0,017	0,000	0,597	4,01	10,70	99,96
DCW-77-27 region 2 - K-spar 3	65,41	0,074	0,000	18,76	0,136	0,001	0,002	0,539	3,31	12,04	100,27
DCW-77-27 region 2 - plag 1	61,52	0,038	0,012	23,41	0,127	0,010	0,000	5,40	7,92	0,811	99,24
DCW-77-27 region 2 - plag 2	61,93	0,000	0,000	23,77	0,548	0,000	0,013	5,66	7,65	0,957	100,53
DCW-77-27 region 2 - Biotite 1	40,87	0,211	0,012	11,53	10,32	0,032	20,60	0,01	0,400	10,28	94,26
DCW-77-27 region 2 - Kspar 3	75,62	0,127	0,000	12,72	0,198	0,006	0,001	0,210	1,74	9,25	99,88
DCW-77-27 region 2 - Kspar 4	65,44	0,049	0,000	18,62	0,106	0,002	0,005	0,349	3,41	11,86	99,83
DCW-77-27 region 2 - plag 3	61,75	0,032	0,000	23,50	0,181	0,000	0,009	5,38	8,05	0,695	99,60
DCW-77-27 region 2 - Kspar 5	77,29	0,111	0,000	11,15	1,11	0,031	0,063	0,386	2,23	6,58	98,95

Microprobe compositions

Page 3

Sample DR-06	SiO ₂	TiO ₂	Cr ₂ O ₃	Al ₂ O ₃	FeO _{total}	MnO	MgO	CaO	Na ₂ O	K ₂ O	Total
DR-06-R2-a-Plag 1	62,646	0,000	0,000	23,499	0,054	0,000	0,018	5,381	7,254	1,336	100,188
DR-06-R2-b (lighter)-Kspar 1	65,986	0,034	0,000	18,568	0,031	0,001	0,000	0,368	2,518	13,321	100,827
DR-06-R3-a (dark)-Plag 1	62,846	0,000	0,009	23,633	0,120	0,000	0,017	5,605	7,216	1,390	100,836
DR-06-R3-b (light)-Kspar 2	65,767	0,015	0,017	18,657	0,053	0,000	0,002	0,384	3,323	11,841	100,059
DR-06-R4-a-Kspar 1	66,181	0,037	0,000	18,830	0,040	0,002	0,001	0,442	3,387	12,056	100,976
DR-06-R4-b-Kspar 2	66,216	0,000	0,000	18,592	0,025	0,000	0,004	0,498	3,609	11,454	100,398
DR-06-R4-c-Plag 1	62,711	0,001	0,000	23,598	0,114	0,000	0,000	5,468	7,772	0,892	100,556
DR-06-R4-d-Plag 2	63,078	0,010	0,000	23,653	0,068	0,000	0,011	5,335	7,698	0,735	100,588
DR-06-R4-e-Plag 3	62,580	0,003	0,016	23,520	0,081	0,000	0,000	5,414	7,570	1,154	100,338

Microprobe compositions

Page 4

Granodioritic, enderbitic and tonalitic rocks

Sample 1-63-113	SiO ₂	TiO ₂	Cr ₂ O ₃	Al ₂ O ₃	FeO _{total}	MnO	MgO	CaO	Na ₂ O	K ₂ O	Total
1-63-113 vein material 1	30,84	0,572	0,000	8,54	7,90	0,102	10,15	3,36	0,231	0,101	61,78
1-63-113 vein material 2	35,58	0,101	0,000	14,17	16,32	0,450	18,17	1,56	0,06	0,000	86,41
1-63-113 region 1 plag 1	60,17	0,000	0,000	24,65	0,095	0,003	0,000	6,55	7,71	0,326	99,50
1-63-113 region 1 plag 2	59,68	0,000	0,000	25,01	0,090	0,002	0,000	7,16	7,25	0,398	99,59
1-63-113 region 1 plag 3	60,05	0,006	0,000	24,63	0,071	0,024	0,000	6,54	7,58	0,375	99,26
1-63-113 region 1 - plag 4	60,26	0,025	0,000	24,74	0,073	0,007	0,000	6,49	7,68	0,389	99,66
1-63-113 region 1 - plag 5	60,28	0,026	0,000	24,74	0,053	0,000	0,000	6,68	7,57	0,341	99,68
1-63-113 region 1 - biotite 1	38,23	4,64	0,000	13,60	11,57	0,056	16,69	0,001	0,080	10,18	95,05
1-63-113 region 1 - biotite 2	38,10	4,58	0,000	13,85	11,10	0,041	17,11	0,035	0,137	10,33	95,28
1-63-113 region 1 - biotite 3	38,28	4,70	0,000	13,49	11,49	0,058	16,77	0,039	0,147	10,12	95,09
1-63-113 region 1 - Biotite 4	38,17	4,42	0,023	13,62	11,25	0,066	16,86	0,000	0,083	10,38	94,88
1-63-113 region 1 - Biotite 5	38,45	4,47	0,004	13,55	10,97	0,066	17,05	0,019	0,183	10,23	94,97
1-63-113 region 1 - Biotite 6	38,31	4,68	0,000	13,65	11,11	0,067	16,97	0,035	0,088	10,35	95,26
1-63-113 region 1 - Biotite 7	38,32	4,67	0,000	13,67	11,59	0,038	16,48	0,019	0,147	10,31	95,25
1-63-113 region 2 - plag 1	59,92	0,014	0,000	24,81	0,102	0,012	0,009	6,63	7,51	0,280	99,29
1-63-113 region 2 - plag 2	60,03	0,015	0,000	25,00	0,128	0,000	0,005	6,87	7,46	0,353	99,86
1-63-113 region 2 - plag 3	60,61	0,028	0,000	24,57	0,080	0,000	0,000	6,54	7,60	0,326	99,77
1-63-113 region 2 - plag 4	60,39	0,000	0,000	24,91	0,078	0,019	0,000	6,56	7,74	0,303	100,00
1-63-113 region 2 - plag 5	60,27	0,001	0,000	24,69	0,045	0,000	0,000	6,541	7,60	0,342	99,49
1-63-113 region 2 - Fe Ti Ox 1	0,013	12,26	0,094	0,025	78,27	0,473	0,014	0,047	0,000	0,000	91,19
1-63-113 region 2 - Fe Ti Ox 2	0,000	55,44	0,009	0,019	41,89	0,029	0,000	0,006	0,026	0,000	97,42
1-63-113 region 2 - Biotite 1	38,22	4,63	0,022	13,82	11,40	0,050	16,81	0,024	0,153	10,47	95,60
1-63-113 region 2 - Biotite 2	38,23	4,74	0,000	13,72	11,24	0,037	17,00	0,026	0,149	10,34	95,47
1-63-113 region 2 - Biotite 3	36,81	4,46	0,000	13,85	18,27	0,104	11,94	0,101	0,146	9,38	95,05
1-63-113 region 2 - Biotite 4	38,41	4,52	0,005	13,92	11,11	0,061	17,15	0,017	0,137	10,24	95,57
1-63-113 region 2 - Biotite 5	38,33	4,32	0,007	13,97	10,15	0,062	17,78	0,036	0,141	10,49	95,28
1-63-113 region 2 - Apatite	0,279	0,005	0,000	0,003	0,075	0,017	0,032	54,91	0,070	0,000	97,99
1-63-113 region 2 - biotite 6	y	4,53	0,000	13,72	11,09	0,035	17,33	0,007	0,162	10,41	95,45
1-63-113 region 2 - biotite 7	38,12	4,62	0,000	13,74	11,45	0,046	16,78	0,008	0,114	10,39	95,27

Microprobe compositions

Page 5

Sample 3-63-882-65	SiO ₂	TiO ₂	Cr ₂ O ₃	Al ₂ O ₃	FeO _{total}	MnO	MgO	CaO	Na ₂ O	K ₂ O	P ₂ O ₅	Total
3-63-882 region 1 - Fe Oxide	0,000	0,00	0,107	0,123	92,12	0,020	0,000	0,000	0,000	0,000	0,000	92,38
3-63-882 region 1 - Fe Oxide 1	0,005	0,017	0,116	0,181	91,87	0,000	0,002	0,000	0,000	0,000	0,000	92,19
3-63-882 region 1 - Apatite	0,357	0,000	0,000	0,000	0,250	0,096	0,018	54,42	0,098	0,040	42,340	97,62
3-63-882 region 1 - Biotite 1	37,64	5,92	0,015	13,74	12,47	0,121	15,26	0,015	0,076	10,34	0,000	95,60
3-63-882 region 1 - Biotite 2	37,54	5,92	0,008	13,79	12,43	0,160	15,12	0,032	0,049	10,40	0,000	95,44
3-63-882 region 1 - Kspar 1	64,33	0,016	0,011	18,27	0,031	0,000	0,000	0,024	0,283	16,78	0,000	99,74
3-63-882 region 1 - biotite 3	37,52	5,05	0,000	13,51	13,28	0,075	15,48	0,065	0,055	10,42	0,000	95,44
3-63-882 region 1 - biotite 4	37,63	4,43	0,000	13,63	12,85	0,118	16,27	0,078	0,079	10,10	0,000	95,19
3-63-882 region 1 - Kspar 2	63,90	0,037	0,000	18,37	0,041	0,002	0,00	0,028	0,410	16,80	0,000	99,59
3-63-882 region 1 - Biotite 5	37,92	4,92	0,000	13,35	12,47	0,125	15,85	0,032	0,067	10,50	0,000	95,24
3-63-882 region 1 - Biotite 6	38,17	4,73	0,008	13,43	12,67	0,060	15,61	0,017	0,049	10,29	0,000	95,02
3-63-882 region 1 - Plag 1	58,81	0,021	0,002	25,47	0,066	0,003	0,000	7,64	6,89	0,486	0,000	99,39
3-63-882 region 1 - Plag 2	58,84	0,014	0,000	25,60	0,118	0,009	0,000	7,57	6,99	0,436	0,000	99,58
3-63-882 region 1 - Plag 3	58,77	0,001	0,000	25,51	0,088	0,000	0,005	7,56	7,00	0,439	0,000	99,37
3-63-882 region 1 - Plag 4	59,35	0,033	0,000	25,36	0,090	0,003	0,000	7,47	6,95	0,511	0,000	99,77
3-63-882 region 1 - Plag 5	59,05	0,000	0,010	25,51	0,083	0,035	0,000	7,50	6,84	0,615	0,000	99,64
Sample DCW-77-3	SiO ₂	TiO ₂	Cr ₂ O ₃	Al ₂ O ₃	FeO _{total}	MnO	MgO	CaO	Na ₂ O	K ₂ O	Total	
DCW-77-3-R1-Ti Fe Ox 1	0,000	50,81	0,000	0,145	42,85	0,561	1,36	0,012	0,013	0,002	95,75	
DCW-77-3-R1-Ti Fe Ox 2	0,055	26,50	0,225	1,21	67,11	0,412	0,993	0,000	0,047	0,002	96,56	
DCW-77-3-R1-PX 1	51,34	0,522	0,000	1,61	12,06	0,298	14,04	19,49	0,354	0,008	99,72	
DCW-77-3-R1-Plag 1	64,93	0,205	0,000	18,87	0,516	0,003	0,029	0,90	3,79	10,53	99,76	
DCW-77-3-R1-PX 2	51,50	0,713	0,000	1,78	12,59	0,280	14,46	17,83	0,371	0,004	99,52	
DCW-77-3-R1- PX 3 altered	50,34	0,638	0,045	1,57	11,15	0,269	15,15	17,72	0,327	0,019	97,22	
DCW-77-3-R1-PX 4	51,17	0,709	0,021	1,67	11,66	0,234	15,14	18,67	0,278	0,000	99,55	
DCW-77-3-R1-PX 5	51,05	0,763	0,004	1,67	12,58	0,281	14,45	18,56	0,307	0,003	99,66	
DCW-77-3-R1-PX 6	51,08	0,743	0,000	1,76	11,29	0,243	15,30	18,79	0,306	0,000	99,51	
DCW-77-3-R1-PX 7	50,99	0,698	0,016	1,50	13,12	0,326	13,75	18,76	0,339	0,001	99,50	
DCW-77-3-R1-Plag 2	56,02	0,054	0,000	27,15	0,647	0,047	0,026	9,55	5,47	0,390	99,35	
DCW-77-3-R1-Plag 3	64,66	0,085	0,000	18,85	0,250	0,018	0,002	0,452	3,17	11,74	99,23	
DCW-77-3-R1-Plag 4	60,71	0,074	0,000	23,96	0,386	0,000	0,012	6,10	7,47	0,943	99,65	
DCW-77-3-R1-Kspar 1	63,03	0,131	0,008	19,29	0,333	0,000	0,000	1,39	5,58	6,97	96,72	
DCW-77-3-R1-Kspar 2	63,13	0,091	0,000	18,70	0,293	0,019	0,010	0,602	3,91	9,94	96,69	
DCW-77-3-R1-Plag 6	45,70	0,080	0,000	19,69	0,272	0,000	0,043	4,66	6,37	0,328	77,15	
DCW-77-3-R2-Fe Ti Ox 1	0,001	3,01	0,051	0,434	87,13	0,197	0,307	0,008	0,000	0,008	91,14	

Microprobe compositions

Page 6

Sample DCW-77-3	SiO ₂	TiO ₂	Cr ₂ O ₃	Al ₂ O ₃	FeO _{total}	MnO	MgO	CaO	Na ₂ O	K ₂ O	Total	
DCW-77-3-R2-Kspar 1	65,62	0,041	0,004	18,87	0,198	0,002	0,000	0,497	4,05	10,57	99,85	
DCW-77-3-R2-Kspar 2	65,79	0,121	0,000	18,69	0,251	0,000	0,011	0,428	3,85	10,76	99,89	
DCW-77-3-R2-Kspar 3	65,08	0,055	0,000	19,05	0,205	0,000	0,002	0,408	3,64	11,03	99,46	
DCW-77-3-R2-Kspar 4	65,24	0,149	0,023	18,97	0,232	0,015	0,008	0,675	4,08	10,49	99,88	
DCW-77-3-R2-Kspar 5	65,27	0,062	0,021	18,92	0,225	0,000	0,000	0,475	3,81	10,89	99,67	
DCW-77-3-R2-Plag 1	59,90	0,080	0,000	24,39	0,489	0,000	0,030	6,56	7,45	0,544	99,44	
DCW-77-3-R2-Plag 2	59,18	0,138	0,000	24,66	0,706	0,000	0,216	7,72	6,82	0,543	99,98	
DCW-77-3-R2-Plag 3	65,25	0,117	0,000	18,72	0,321	0,000	0,000	0,643	4,11	10,37	99,52	
DCW-77-3-R2-Plag 4	58,92	0,090	0,000	25,10	0,662	0,000	0,033	7,51	6,92	0,566	99,81	
DCW-77-3-R2-Plag 5	57,67	0,085	0,000	25,74	0,746	0,021	0,032	8,66	6,36	0,459	99,76	
DCW-77-3-R2-Plag 6	54,77	0,045	0,000	27,84	0,499	0,000	0,033	10,72	5,24	0,348	99,49	
DCW-77-3-R2-PX 1	51,67	0,485	0,064	1,56	10,29	0,276	16,07	18,84	0,293	0,006	99,54	
DCW-77-3-R2-PX 2	51,20	0,689	0,012	1,60	11,88	0,240	15,10	18,64	0,331	0,017	99,70	
DCW-77-3-R2-PX 3	51,91	0,350	0,039	1,41	8,72	0,240	16,86	19,47	0,250	0,000	99,24	
DCW-77-3-R2-PX 4	51,78	0,434	0,073	1,70	8,35	0,207	16,90	19,51	0,303	0,000	99,25	
DCW-77-3-R2-PX 5	51,58	0,288	0,023	0,674	13,51	0,355	12,60	20,26	0,272	0,023	99,58	
DCW-77-3-R2-PX 6	45,33	1,60	0,038	6,74	14,69	0,197	14,08	11,14	2,30	1,19	97,31	
DCW-77-3-R3-Plag 1	61,01	0,097	0,008	23,78	0,556	0,005	0,038	6,10	7,55	0,714	99,87	
DCW-77-3-R3-Plag 2	55,83	0,078	0,000	27,31	0,522	0,000	0,036	10,20	5,53	0,383	99,89	
DCW-77-3-R3-Plag 2 alteration	64,58	0,110	0,000	18,52	0,294	0,008	0,007	0,570	3,10	12,02	99,21	
DCW-77-3-R4-PX 1	51,30	0,718	0,000	1,53	12,40	0,261	15,01	18,40	0,341	0,004	99,96	
DCW-77-3-R4-Plag 1	56,32	0,029	0,000	27,08	0,438	0,000	0,020	9,67	5,79	0,395	99,73	
DCW-77-3-R4-Px 2	51,03	0,668	0,025	1,45	11,97	0,248	15,21	18,43	0,304	0,000	99,34	
Sample DCW-77-10	SiO ₂	TiO ₂	Cr ₂ O ₃	Al ₂ O ₃	FeO _{total}	MnO	MgO	CaO	Na ₂ O	K ₂ O	P ₂ O ₅	Total
DCW-77-10 Region 1 - Plag 1	60,38	0,032	0,022	24,35	0,126	0,000	0,000	6,39	7,74	0,452	0,000	99,48
DCW-77-10 Region 1 - Plag 2	60,98	0,000	0,000	24,41	0,136	0,012	0,019	6,28	7,77	0,477	0,000	100,08
DCW-77-10 Region 1 - Plag 3	60,25	0,003	0,000	24,52	0,336	0,000	0,011	6,52	7,58	0,412	0,000	99,63
DCW-77-10 Region 1 - Kspar 1	64,73	0,006	0,000	18,28	0,049	0,011	0,006	0,069	0,642	16,34	0,000	100,12
DCW-77-10 Region 1 - Kspar 2	64,24	0,037	0,000	18,30	0,031	0,001	0,003	0,101	0,722	16,36	0,000	99,79
DCW-77-10 Region 1 - Kspar 3	63,95	0,085	0,002	18,50	0,008	0,003	0,011	0,204	0,839	16,18	0,000	99,79
DCW-77-10 Region 1 - Kspar 4	64,15	0,033	0,006	18,29	0,045	0,000	0,000	0,033	0,905	15,90	0,000	99,36
DCW-77-10 Region 1 - Kspar 5	63,86	0,044	0,000	18,42	0,028	0,000	0,007	0,037	0,810	16,30	0,000	99,51

Microprobe compositions

Page 7

Sample DCW-77-10	SiO ₂	TiO ₂	Cr ₂ O ₃	Al ₂ O ₃	FeO _{total}	MnO	MgO	CaO	Na ₂ O	K ₂ O	P ₂ O ₅	Total
DCW-77-10 Region 1 - Kspar 6	64,30	0,011	0,000	18,33	0,019	0,000	0,000	0,033	0,931	16,14	0,000	99,77
DCW-77-10 Region 3 - Kspar 1	64,10	0,063	0,000	18,44	0,037	0,000	0,008	0,145	1,03	15,71	0,000	99,53
DCW-77-10 Region 3 - Kspar 2	64,37	0,000	0,008	18,49	0,029	0,000	0,000	0,140	1,18	15,47	0,000	99,68
DCW-77-10 Region 3 - Kspar 3	64,12	0,050	0,000	18,31	0,042	0,011	0,000	0,045	0,754	16,38	0,000	99,72
DCW-77-10 Region 3 - Kspar 4	64,39	0,037	0,000	18,39	0,032	0,000	0,000	0,059	1,04	15,65	0,000	99,60
DCW-77-10 Region 3 - Kspar 5	64,57	0,000	0,000	18,41	0,039	0,014	0,000	0,056	0,888	16,03	0,000	100,00
DCW-77-10 Region 3 - Kspar 6	64,37	0,015	0,000	18,61	0,059	0,006	0,000	0,064	1,01	15,98	0,000	100,12
DCW-77-10 Region 3 - Plag 2	60,91	0,003	0,000	24,42	0,132	0,007	0,006	6,19	7,75	0,368	0,000	99,79
DCW-77-10 Region 3 - Plag 3	60,11	0,004	0,000	24,58	0,130	0,015	0,012	6,58	7,78	0,228	0,000	99,44
DCW-77-10 Region 3 - Plag 4	60,29	0,025	0,000	24,59	0,094	0,013	0,000	6,54	7,71	0,196	0,000	99,46
DCW-77-10 Region 3 - Plag 5	60,64	0,019	0,023	24,56	0,139	0,009	0,002	6,28	7,62	0,453	0,000	99,75
DCW-77-10 Region 3 - CPX 1	52,89	0,211	0,024	1,66	8,35	0,280	13,78	22,19	0,552	0,000	0,000	99,94
DCW-77-10 Region 3 - CPX 2	48,45	0,179	0,000	1,57	7,08	0,312	12,83	19,35	0,548	0,000	0,000	90,32
DCW-77-10 Region 3 - CPX 3	52,86	0,161	0,027	1,72	8,92	0,324	13,35	21,79	0,590	0,000	0,000	99,73
DCW-77-10 Region 3 - Fe Ti Ox	0,028	51,22	0,051	0,061	42,60	0,519	1,86	0,000	0,000	0,000	0,000	96,34
DCW-77-10 Region 3 - Fe Ti Ox	0,058	15,17	0,254	0,261	73,55	0,186	0,473	0,001	0,028	0,000	0,000	89,98
DCW-77-10 Region 2 - Biotite	37,43	5,28	0,014	14,03	13,89	0,036	15,07	0,013	0,152	10,35	0,000	96,28
DCW-77-10 Region 2 - Kspar	64,06	0,030	0,001	18,45	0,074	0,010	0,000	0,028	0,910	16,21	0,000	99,78
DCW-77-10 Region 2 - Plag	60,09	0,014	0,000	24,52	0,096	0,000	0,010	6,48	7,59	0,418	0,000	99,22
DCW-77-10 Region 2 - Fe Oxide	0,036	0,046	0,376	0,251	87,44	0,000	0,013	0,017	0,000	0,000	0,000	88,18
DCW-77-10 Region 3 - Apatite	0,469	0,000	0,000	0,008	0,129	0,014	0,025	55,05	0,045	0,008	42,412	98,16
DCW-77-10 Region 3 - Plag 1	60,53	0,011	0,000	24,62	0,100	0,000	0,000	6,63	7,72	0,209	0,000	99,81

Microprobe compositions

Page 8

Mafic and ultramafic rocks

Sample 1-63-852-593	SiO ₂	TiO ₂	Cr ₂ O ₃	Al ₂ O ₃	FeO _{total}	MnO	MgO	CaO	Na ₂ O	K ₂ O	P ₂ O ₅	Total
1-63-852-region 1-Plag 1	58,51	0,000	0,006	25,70	0,113	0,000	0,000	7,58	7,19	0,415	0,000	99,51
1-63-852-region 1-Plag 2	58,68	0,000	0,012	26,07	0,047	0,000	0,000	7,93	6,97	0,294	0,000	100,01
1-63-852-region 1-Plag 3	58,42	0,035	0,019	26,18	0,197	0,015	0,021	7,99	6,89	0,324	0,000	100,09
1-63-852-region 1-Plag 4	58,74	0,017	0,000	26,22	0,157	0,010	0,009	7,88	6,84	0,257	0,000	100,13
1-63-852-region 1-Plag 5	58,79	0,013	0,000	26,05	0,134	0,005	0,004	7,73	6,94	0,275	0,000	99,94
1-63-852-region 1-Plag 6	58,44	0,008	0,000	25,91	0,103	0,005	0,000	7,83	6,96	0,300	0,000	99,55
1-63-852-region 1-Plag 7	58,59	0,000	0,000	26,25	0,187	0,000	0,003	7,85	6,89	0,285	0,000	100,05
1-63-852-region 1-Apatite 1	0,19	0,000	0,000	0,000	0,115	0,024	0,000	55,17	0,043	0,004	41,41	96,95
1-63-852-region 1-Biotite 1	37,07	2,66	0,120	14,78	12,00	0,035	17,65	0,031	0,047	9,68	0,000	94,08
1-63-852-region 1-Biotite 2	37,05	2,66	0,062	14,80	11,83	0,031	17,71	0,054	0,088	9,80	0,000	94,09
1-63-852-region 1-Biotite 3	36,99	2,86	0,142	14,70	12,16	0,054	17,28	0,041	0,072	9,79	0,000	94,08
1-63-852-region 1-Biotite 4	37,05	2,83	0,089	14,56	11,85	0,047	17,20	0,076	0,142	9,62	0,000	93,47
1-63-852-region 1-Px 1	51,11	0,129	0,078	2,32	7,92	0,227	14,02	22,26	0,679	0,003	0,000	98,75
1-63-852-region 1-Px 2	51,33	0,102	0,048	2,32	8,02	0,227	14,09	22,12	0,662	0,000	0,000	98,92
1-63-852-region 1-Px 3	51,51	0,127	0,054	2,28	7,98	0,263	14,12	22,13	0,647	0,000	0,000	99,11
1-63-852-region 1-Px 4	50,85	0,103	0,090	2,28	7,99	0,252	13,98	22,42	0,680	0,000	0,000	98,64
1-63-852-region 1-Px 5	52,13	0,024	0,028	0,979	21,89	0,654	23,52	0,451	0,004	0,007	0,000	99,69
1-63-852-region 1-Px 6	52,45	0,019	0,027	1,04	21,43	0,592	23,87	0,477	0,006	0,000	0,000	99,90
1-63-852-region 1-Px 7	51,44	0,046	0,032	2,01	8,23	0,283	14,48	21,37	0,586	0,000	0,000	98,48
1-63-852-region 1-Biotite 5	37,18	2,93	0,111	14,63	12,03	0,029	17,62	0,048	0,174	9,787	0,000	94,54
1-63-852-region 1-Biotite 6	36,86	2,79	0,114	14,82	12,10	0,035	17,44	0,029	0,064	9,91	0,000	94,16
1-63-852-region 1-Px 8	51,24	0,095	0,072	2,39	8,07	0,202	14,00	22,12	0,709	0,015	0,000	98,90
1-63-852-region 2 - Plag 1	58,64	0,002	0,000	26,08	0,110	0,002	0,007	7,89	6,90	0,251	0,000	99,88
1-63-852-region 2 - Plag 2	58,60	0,005	0,000	26,03	0,075	0,000	0,006	7,89	6,89	0,307	0,000	99,79
1-63-852-region 2 - Plag 3	58,53	0,000	0,005	26,22	0,254	0,014	0,000	7,85	6,84	0,304	0,000	100,02

Microprobe compositions

Page 9

Sample 1-63-852-593	SiO ₂	TiO ₂	Cr ₂ O ₃	Al ₂ O ₃	FeO _{total}	MnO	MgO	CaO	Na ₂ O	K ₂ O	P ₂ O ₅	Total
1-63-852-region 2 - Px 1	50,89	0,104	0,051	2,45	8,41	0,223	14,11	21,77	0,61	0,022	0,000	98,65
1-63-852-region 2 - Px 2	51,31	0,086	0,037	2,56	8,79	0,273	14,23	21,15	0,65	0,000	0,000	99,08
1-63-852-region 2 - Px 3	51,29	0,120	0,068	2,57	8,021	0,286	13,95	21,98	0,65	0,001	0,000	98,94
1-63-852-region 2 - Plag 4	57,24	0,037	0,000	27,44	0,227	0,015	0,000	9,06	6,25	0,141	0,000	100,41
1-63-852-region 2 - Plag 5	58,14	0,000	0,000	26,27	0,080	0,000	0,004	7,97	6,87	0,273	0,000	99,61
1-63-852-region 2 - Vein (glassy) 1	32,86	0,941	0,042	17,01	15,12	1,37	18,23	1,32	0,022	0,027	0,000	86,94
1-63-852-region 2 - Vein (glassy) 2	32,25	0,723	0,071	16,46	15,45	2,00	17,77	1,62	0,022	0,032	0,000	86,40
1-63-852-region 2 - Vein (glassy) 3	31,61	0,956	0,028	16,31	16,38	2,10	18,11	0,918	0,030	0,032	0,000	86,47
1-63-852-region 2 - Vein (glassy) 4	37,75	0,311	0,008	15,97	16,03	1,27	14,84	2,61	0,068	0,031	0,000	88,89
1-63-852-region 2 - Vein (glassy) 5	34,97	0,808	0,104	16,05	15,79	1,77	16,48	1,96	0,047	0,028	0,000	88,00
1-63-852-region 2 - Vein (glassy) 6	39,15	1,30	0,072	11,92	14,90	0,864	13,78	10,42	0,194	0,022	0,000	92,62
1-63-852-region 2 - Vein (glassy) 7	38,57	1,02	0,422	12,00	15,55	0,734	14,76	8,85	0,186	0,048	0,000	92,14
1-63-852-region 2 - Vein (glassy) 8	35,83	3,90	0,077	11,82	14,09	1,02	14,35	7,91	0,089	0,019	0,000	89,10
Sample 1-63-878-1303	SiO ₂	TiO ₂	Cr ₂ O ₃	Al ₂ O ₃	FeO _{total}	MnO	MgO	CaO	Na ₂ O	K ₂ O	Total	
1-63-878-region 2-plag 1	58,36	0,020	0,003	26,15	0,086	0,024	0,000	8,50	6,59	0,167	99,91	
1-63-878-region 2-plag 2	56,63	0,009	0,035	27,30	0,121	0,000	0,006	9,39	6,10	0,188	99,77	
1-63-878-region 2-plag 3	56,76	0,006	0,000	27,18	0,079	0,006	0,000	9,17	6,28	0,154	99,64	
1-63-878-region 2-plag 4	56,59	0,000	0,022	27,51	0,102	0,017	0,000	9,46	6,21	0,138	100,06	
1-63-878-region 2-biotite 1	37,54	5,26	0,179	13,79	10,49	0,032	17,88	0,009	0,095	10,02	95,30	
1-63-878-region 2-opx 1	52,88	0,079	0,034	1,21	20,05	0,420	25,27	0,446	0,000	0,002	100,38	
1-63-878-region 2-Biotite 2	37,67	5,17	0,216	13,76	10,66	0,042	17,87	0,005	0,080	9,95	95,42	
1-63-878-region 2-cpx 1	52,18	0,206	0,087	1,92	7,26	0,169	15,38	22,29	0,415	0,000	99,92	
1-63-878-region 2-cpx 2	51,89	0,239	0,073	2,09	6,83	0,158	15,02	22,48	0,495	0,000	99,28	
1-63-878-region 2-amphibole 3	43,46	2,23	0,233	10,73	10,65	0,080	14,69	11,84	1,63	1,46	97,00	
Sample DCW-77-4	SiO ₂	TiO ₂	Cr ₂ O ₃	Al ₂ O ₃	FeO _{total}	MnO	MgO	CaO	Na ₂ O	K ₂ O	Total	
DCW-77-4-R1-Fe Ti Ox 1	1,04	13,76	0,139	1,57	73,07	0,719	0,339	0,431	0,000	0,000	91,06	
DCW-77-4-R1-Fe Ti Ox 2	1,39	14,77	0,106	0,896	72,36	0,464	0,183	0,488	0,002	0,001	90,67	
DCW-77-4-R1-PX 1	50,32	0,97	0,000	2,91	9,34	0,259	14,26	21,29	0,449	0,000	99,80	
DCW-77-4-R1-PX 2	42,95	3,15	0,014	9,29	10,15	0,116	16,17	11,52	2,64	1,31	97,31	
DCW-77-4-R1-PX 3	43,12	3,00	0,006	9,20	9,99	0,148	16,47	11,52	2,59	1,36	97,40	

Microprobe compositions

Page 10

Sample DCW-77-4	SiO ₂	TiO ₂	Cr ₂ O ₃	Al ₂ O ₃	FeO _{total}	MnO	MgO	CaO	Na ₂ O	K ₂ O	Total
DCW-77-4-R1-Amphi 1	43,41	2,68	0,015	8,75	10,40	0,174	16,37	11,48	2,60	1,42	97,30
DCW-77-4-R1-Amphi 2	42,15	2,79	0,017	9,02	8,66	0,114	16,26	10,79	2,67	1,19	93,67
DCW-77-4-R1-plag 1	55,14	0,096	0,005	27,83	0,565	0,000	0,050	10,75	5,16	0,615	100,20
DCW-77-4-R1-plag 2	57,10	0,047	0,000	26,60	0,582	0,011	0,044	9,11	6,03	0,629	100,16
DCW-77-4-R1-plag 3	56,29	0,082	0,015	26,81	0,599	0,012	0,044	9,52	5,94	0,668	99,98
DCW-77-4-R1-Fe Ti Ox 3	1,45	13,75	0,010	1,33	72,25	0,927	0,503	0,208	0,007	0,012	90,44
DCW-77-4-R1-Plag 4	54,63	0,079	0,001	27,94	0,651	0,002	0,032	10,99	5,26	0,451	100,03
DCW-77-4-R1-altered Px 4?	0,258	0,000	0,007	0,000	0,191	0,040	0,133	52,03	0,113	0,003	52,78
DCW-77-4-R1-Aletred Px 5?	0,134	0,000	0,000	0,031	0,147	0,006	0,094	47,04	0,104	0,000	47,55
DCW-77-4-R1-cpx 1	50,79	0,963	0,005	2,38	8,87	0,231	14,44	21,27	0,499	0,005	99,45
DCW-77-4-R1-cpx 2	51,20	0,894	0,000	2,21	9,15	0,274	14,62	21,03	0,523	0,000	99,89
DCW-77-4-R1-cpx 3	51,03	0,854	0,000	2,14	8,81	0,234	14,69	21,11	0,487	0,000	99,35
DCW-77-4-R1-cpx 4	50,90	0,905	0,024	2,37	8,79	0,202	14,71	21,35	0,536	0,000	99,79
DCW-77-4-R1-cpx 5	50,88	0,968	0,000	2,42	8,64	0,230	14,87	21,16	0,518	0,002	99,69
DCW-77-4-R1-Plag 5	56,83	0,078	0,013	26,20	0,606	0,000	0,051	9,26	5,88	0,750	99,67
DCW-77-4-R1-Plag 6	55,09	0,070	0,000	27,52	0,522	0,000	0,042	10,30	5,21	0,632	99,38
DCW-77-4-R1-Plag 7	56,21	0,080	0,012	26,82	0,530	0,016	0,041	9,55	5,76	0,605	99,62
DCW-77-4-R1-Plag 8	56,35	0,072	0,000	26,56	0,557	0,011	0,033	9,23	5,90	0,714	99,43
DCW-77-4-R2-Fe Ti Ox 1	0,169	13,75	0,194	2,20	72,82	0,166	0,693	0,316	0,012	0,001	90,31
DCW-77-4-R2-Fe Ti Ox 2	1,54	14,40	0,095	0,737	72,12	1,500	0,250	0,637	0,009	0,001	91,29
DCW-77-4-R2-Plag 1	54,45	0,083	0,000	27,88	0,512	0,021	0,038	10,89	5,16	0,487	99,51
DCW-77-4-R2-Plag 2	56,43	0,079	0,000	26,80	0,536	0,000	0,030	9,25	5,83	0,608	99,56
DCW-77-4-R2-Plag 3	55,97	0,058	0,000	23,73	0,961	0,012	0,029	7,14	6,36	0,745	95,01
DCW-77-4-R2-Plag 4	61,35	0,039	0,000	23,16	0,316	0,008	0,014	5,10	6,86	2,90	99,75
DCW-77-4-R2-KSpar 1	64,24	0,115	0,000	18,80	0,287	0,000	0,000	0,623	2,39	12,65	99,10
DCW-77-4-R2-KSpar 2	64,25	0,075	0,028	19,00	0,326	0,000	0,000	0,614	2,59	12,44	99,32
DCW-77-4-R2-Biotite 1	40,18	4,45	0,000	11,88	8,06	0,060	20,65	0,046	0,869	9,12	95,32
DCW-77-4-R2-Biotite 2	40,21	4,26	0,016	12,03	7,73	0,074	20,99	0,033	0,796	9,32	95,46
DCW-77-4-R2-PX 1	52,14	0,259	0,013	0,769	22,27	0,685	22,60	1,52	0,023	0,001	100,28
DCW-77-4-R2-PX 2	50,30	1,06	0,004	2,97	8,74	0,184	14,64	21,60	0,454	0,002	99,96
DCW-77-4-R2-PX 3	51,08	0,845	0,053	2,15	9,67	0,298	14,38	20,85	0,476	0,007	99,82

Microprobe compositions

Page 11

Sample DCW-77-39	SiO ₂	TiO ₂	Cr ₂ O ₃	Al ₂ O ₃	FeO _{total}	MnO	MgO	CaO	Na ₂ O	K ₂ O	P ₂ O ₅	Total
DCW-77-39-region 1- Plag 1	53,60	0,012	0,013	29,09	0,099	0,024	0,000	11,43	4,88	0,219	0,000	99,36
DCW-77-39-region 1- Plag 2	53,94	0,011	0,000	28,97	0,092	0,000	0,000	11,29	4,87	0,216	0,000	99,39
DCW-77-39-region 1- Plag 3	47,15	0,000	0,000	26,57	0,017	0,004	0,061	13,48	0,470	0,422	0,000	88,16
DCW-77-39-region 1- Plag 4	47,83	0,000	0,000	23,87	0,087	0,044	0,048	11,91	0,355	0,329	0,000	84,47
DCW-77-39-region 1- Plag 5	53,96	0,014	0,000	29,32	0,119	0,006	0,010	11,51	4,71	0,149	0,000	99,80
DCW-77-39-region 1- Plag 6	48,24	0,036	0,016	24,64	0,054	0,000	0,017	11,83	0,794	0,287	0,000	85,91
DCW-77-39-region 1- Plag 7	53,96	0,001	0,000	28,76	0,156	0,010	0,014	10,75	5,15	0,071	0,000	98,88
DCW-77-39-region 1- Plag 8	54,11	0,000	0,000	29,15	0,102	0,000	0,000	11,30	4,91	0,185	0,000	99,76
DCW-77-39-region 1- Plag 9	47,31	0,000	0,000	23,85	0,126	0,053	0,108	12,04	0,336	0,436	0,000	84,26
DCW-77-39-region 1- Plag 10	52,55	0,014	0,028	27,24	0,044	0,004	0,016	9,73	5,27	0,149	0,000	95,04
DCW-77-39-region 1- Plag 11	48,01	0,019	0,000	23,87	0,031	0,013	0,018	11,83	0,420	0,351	0,000	84,56
DCW-77-39-region 1- Plag 12	53,86	0,024	0,005	29,06	0,117	0,000	0,000	11,37	4,83	0,198	0,000	99,46
DCW-77-39-region 1- Px 1	50,72	0,379	0,043	2,90	7,62	0,149	14,31	22,00	0,525	0,007	0,000	98,64
DCW-77-39-region 1- Px 2	52,20	0,067	0,040	1,50	19,97	0,436	24,83	0,459	0,015	0,008	0,000	99,53
DCW-77-39-region 1- Px 3	50,96	0,275	0,053	2,40	7,02	0,180	14,68	22,72	0,478	0,013	0,000	98,77
DCW-77-39-region 1- Plag 13	50,53	0,014	0,000	26,61	0,233	0,000	0,012	1,06	13,03	0,014	0,000	91,51
DCW-77-39-region 1- Biotite 1	36,37	5,25	0,225	14,37	11,48	0,031	16,27	0,029	0,138	9,59	0,000	93,75
DCW-77-39-region 1- Biotite 2	36,61	5,14	0,192	14,63	11,36	0,033	16,42	0,092	0,290	9,12	0,000	93,88
DCW-77-39-region 1- Biotite 3	36,23	5,19	0,198	14,42	11,43	0,029	16,54	0,024	0,130	9,67	0,000	93,85
DCW-77-39-region 1- Px 4	42,39	2,54	0,206	11,59	11,34	0,082	13,63	11,927	1,77	1,38	0,000	96,86
DCW-77-39-region 1- Px 5	52,69	0,036	0,060	1,07	19,18	0,362	25,47	0,456	0,011	0,000	0,000	99,33
DCW-77-39-region 3- Plag 1	53,95	0,020	0,017	28,99	0,114	0,000	0,011	11,64	4,69	0,219	0,000	99,65
DCW-77-39-region 3- Plag 2	53,38	0,014	0,016	29,45	0,121	0,000	0,019	11,75	4,72	0,206	0,000	99,67
DCW-77-39-region 3- Plag 3	54,44	0,031	0,014	29,05	0,124	0,000	0,000	10,91	5,16	0,054	0,000	99,78
DCW-77-39-region 3- Plag 4	47,14	0,037	0,023	24,68	0,635	0,036	0,720	11,26	0,375	0,337	0,000	85,24
DCW-77-39-region 3- Plag 5	57,73	0,051	0,025	26,31	0,051	0,016	0,000	7,98	6,38	0,407	0,000	98,95
DCW-77-39-region 3- Plag 6	47,92	0,000	0,031	24,57	0,019	0,023	0,041	12,01	0,508	0,325	0,000	85,45
DCW-77-39-region 3- Plag 7	47,57	0,002	0,010	23,96	0,081	0,020	0,127	11,84	0,281	0,309	0,000	84,19
DCW-77-39-region 3- Plag 8	45,97	0,000	0,000	23,61	1,06	0,064	1,42	10,49	0,303	0,330	0,000	83,25

Microprobe compositions

Page 12

Sample DCW-77-39	SiO ₂	TiO ₂	Cr ₂ O ₃	Al ₂ O ₃	FeO _{total}	MnO	MgO	CaO	Na ₂ O	K ₂ O	P ₂ O ₅	Total
DCW-77-39-region 3- Plag 9	45,88	0,000	0,000	24,10	0,514	0,044	0,763	10,98	0,245	0,332	0,000	82,85
DCW-77-39-region 3- Plag 10	53,08	0,000	0,000	29,47	0,128	0,015	0,015	11,69	4,69	0,075	0,000	99,16
DCW-77-39-region 3- Plag 11	54,07	0,000	0,039	29,06	0,138	0,000	0,001	11,27	3,96	0,252	0,000	98,79
DCW-77-39-region 3- Px 1	52,11	0,100	0,031	1,49	19,94	0,431	24,72	0,487	0,000	0,005	0,000	99,32
DCW-77-39-region 3- Px 2	52,10	0,095	0,020	1,49	19,65	0,403	24,77	0,518	0,004	0,000	0,000	99,04
DCW-77-39-region 3- Px 3	52,07	0,117	0,051	1,48	19,67	0,397	24,94	0,427	0,025	0,005	0,000	99,17
DCW-77-39-region 3- Px 4	52,24	0,040	0,065	1,48	19,06	0,407	24,85	0,989	0,018	0,014	0,000	99,15
DCW-77-39-region 3- Px 4	52,46	0,065	0,000	1,51	19,60	0,432	25,08	0,442	0,000	0,000	0,000	99,59
Sample DCW-77-47	SiO ₂	TiO ₂	Cr ₂ O ₃	Al ₂ O ₃	FeO _{total}	MnO	MgO	CaO	Na ₂ O	K ₂ O	P ₂ O ₅	Total
DCW-77-47-2-Region 1-Apatite 1	0,296	0,000	0,000	0,003	0,171	0,098	0,011	53,39	0,117	0,000	40,14	94,23
DCW-77-47-2-Region 1-Alt. PX 1	41,69	1,90	0,011	10,85	15,72	0,217	11,64	11,59	1,43	1,98	0,000	97,02
DCW-77-47-2-Region 1-Alt. PX 2	41,39	2,07	0,010	10,91	15,54	0,228	11,65	11,38	1,72	1,89	0,000	96,80
DCW-77-47-2-Region 1- Alt. PX 3	41,44	2,22	0,013	10,90	15,48	0,207	11,64	11,35	1,59	2,02	0,000	96,86
DCW-77-47-2-Region 1- Alt. PX 4	41,91	2,09	0,008	10,83	15,19	0,177	11,82	11,63	1,56	1,96	0,000	97,18
DCW-77-47-2-Region 1- Alt. PX 5	0,187	0,000	0,000	0,002	0,089	0,098	0,02	51,88	0,084	0,000	0,000	52,36
DCW-77-47-2-Region 1- Alt. PX 6	42,03	1,90	0,000	10,82	14,79	0,200	11,90	11,59	1,37	1,97	0,000	96,57
DCW-77-47-2-Region 1- Alt. PX 7	41,78	1,71	0,017	11,06	14,82	0,204	12,03	11,47	1,44	1,94	0,000	96,46
DCW-77-47-2-Region 1- Alt. PX 8	42,18	2,12	0,021	10,70	14,67	0,226	11,84	11,34	1,54	1,85	0,000	96,48
DCW-77-47-2-Region 1- Alt. PX 9	41,80	2,092	0,000	10,89	15,03	0,184	11,65	11,48	1,46	1,95	0,000	96,54
DCW-77-47-2-Region 1- Pyrite ?	0,196	0,000	0,000	0,126	55,80	0,003	0,018	0,015	0,014	0,000	0,000	56,18
DCW-77-47-2-Region 1- Plag 1	59,69	0,000	0,004	25,11	0,084	0,000	0,015	6,66	7,35	0,620	0,000	99,53
DCW-77-47-2-Region 1- Alt. Plag 2	57,68	0,015	0,003	25,48	0,043	0,013	0,017	7,59	6,69	0,134	0,000	97,66
DCW-77-47-2-Region 1- Plag 3	60,00	0,015	0,007	25,32	0,066	0,009	0,003	6,23	7,59	0,140	0,000	99,38
DCW-77-47-2-Region 1- Plag 4	59,02	0,000	0,003	25,67	0,099	0,010	0,000	7,47	7,12	0,287	0,000	99,68
DCW-77-47-2-Region 1- Plag 5	58,78	0,032	0,000	25,62	0,089	0,007	0,000	7,54	7,25	0,097	0,000	99,42
DCW-77-47-2-Region 1- Alt. Plag 6	56,05	0,008	0,015	24,17	0,011	0,017	0,015	2,01	8,12	0,059	0,000	90,47
DCW-77-47-2-Region 1- Alt. Plag 7	55,69	0,049	0,000	24,27	0,005	0,001	0,000	1,28	8,97	0,062	0,000	90,32
DCW-77-47-2-Region 1- Alt. Plag 8	58,84	0,000	0,000	23,82	0,043	0,002	0,000	1,57	8,45	0,132	0,010	92,86
DCW-77-47-2-Region 1- Alt. Plag 9	48,05	0,016	0,020	21,84	0,014	0,000	0,021	2,91	7,58	0,081	0,000	80,54

Microprobe compositions

Page 13

Fragmental Breccia

Sample DCW-77-64-5 Glass spheroids	SiO ₂	TiO ₂	Cr ₂ O ₃	Al ₂ O ₃	FeO _{total}	MnO	MgO	CaO	Na ₂ O	K ₂ O	Total
DCW-77-64-5 - Maf blob 1	49,69	0,077	0,046	15,82	3,34	0,048	12,65	2,27	0,075	0,774	84,78
DCW-77-64-5 - Maf blob 2	52,36	0,045	0,000	12,69	4,35	0,049	12,09	2,51	0,099	1,27	85,45
DCW-77-64-5 - Maf blob 3 fresh	53,67	0,042	0,000	13,35	2,98	0,039	13,34	2,45	0,032	0,797	86,70
DCW-77-64-5 - Maf blob 3 Alt	52,18	0,039	0,018	13,19	2,92	0,031	13,19	2,63	0,085	0,620	84,90
DCW-77-64-5 - Maf blob 6	53,67	0,029	0,005	13,09	4,03	0,040	12,50	2,57	0,093	1,36	87,39
DCW-77-64-5 - Maf blob 7	53,47	0,011	0,000	13,35	3,38	0,011	13,14	2,64	0,078	0,830	86,91
DCW-77-64-5 - Maf blob 8	53,72	0,040	0,000	13,07	4,51	0,040	11,68	2,55	0,094	1,34	87,04
DCW-77-64-5 - Maf blob (small) 9	54,49	0,035	0,001	13,29	4,34	0,032	11,63	2,66	0,101	1,30	87,87
DCW-77-64-5 - Maf blob 10 fresh	54,97	0,04	0,00	13,45	3,33	0,05	13,18	2,49	0,10	0,83	88,44
DCW-77-64-5 - Maf blob 10 alt	54,73	0,049	0,017	13,82	2,90	0,044	14,59	2,22	0,130	0,680	89,17
DCW-77-64-5 - Maf blob 11 dark area	52,27	0,018	0,001	12,94	2,56	0,017	13,05	2,57	0,082	0,581	84,10
DCW-77-64-5 - Maf blob 12	53,06	0,000	0,000	13,19	2,76	0,040	13,22	2,54	0,075	0,676	85,57
DCW-77-64-5 - Maf blob 15	52,49	0,005	0,000	13,28	2,35	0,025	13,09	2,51	0,042	0,532	84,32
DCW-77-64-5 - Maf blob 16 fresh	53,68	0,047	0,011	13,45	2,33	0,018	13,04	2,44	0,086	0,510	85,61
DCW-77-64-5 - Maf blob 16 alt	47,28	0,011	0,000	12,25	2,12	0,037	12,60	2,50	0,068	0,484	77,35
DCW-77-64-5 - Maf blob 17	54,07	0,013	0,000	13,46	2,72	0,035	13,18	2,63	0,058	0,696	86,86
DCW-77-64-5 - maf blob 19 fresh	53,55	0,077	0,000	13,38	2,26	0,020	13,29	2,47	0,121	0,634	85,81
DCW-77-64-5 - maf blob 19 alt	50,48	0,04	0,00	12,56	2,02	0,02	11,17	2,31	0,07	0,49	79,16
DCW-77-64-5 - maf blob 20	52,93	0,008	0,004	13,28	2,60	0,017	13,38	2,69	0,054	0,540	85,49
DCW-77-64-5 - maf blob 21	51,94	0,047	0,000	15,17	4,31	0,050	12,23	2,36	0,085	1,25	87,44
DCW-77-64-5 - Maf Blob 22 alt	48,27	0,00	0,04	24,35	0,34	0,04	8,88	1,27	0,03	0,19	83,41
DCW-77-64-5 - Maf Blob 22 clear	52,33	0,025	0,018	17,78	1,12	0,037	10,56	2,18	0,032	0,459	84,54
DCW-77-64-5 - Maf Blob 23	53,47	0,060	0,000	13,02	2,89	0,031	12,97	2,57	0,088	0,834	85,93
DCW-77-64-5 - Maf Blob 24	53,73	0,048	0,014	13,04	3,41	0,042	12,88	2,57	0,079	1,04	86,86
DCW-77-64-5 - Maf Blob 25	53,22	0,368	0,007	12,90	3,49	0,053	12,42	2,60	0,065	0,755	85,89
DCW-77-64-5 - maf blob 25	52,32	0,040	0,000	12,49	4,27	0,060	12,29	2,57	0,095	0,851	84,99

Microprobe compositions

Page 14

Sample DCW-77-64-5 Glass spheroids	SiO ₂	TiO ₂	Cr ₂ O ₃	Al ₂ O ₃	FeO _{total}	MnO	MgO	CaO	Na ₂ O	K ₂ O	Total	
DCW-77-64-5 - maf blob 26	53,661	0,01	0,00	12,574	4,61	0,04	12,69	2,58	0,10	0,90	87,17	
DCW-77-64-5 - maf blob 27	51,136	0,009	0,000	12,723	3,74	0,027	12,67	2,56	0,059	0,746	83,67	
DCW-77-64-5 - maf blob 28	53,303	0,015	0,003	12,979	3,32	0,033	13,14	2,55	0,085	0,669	86,10	
DCW-77-64-5 - maf blob 29	53,811	0,017	0,000	12,992	3,17	0,034	13,32	2,53	0,094	0,703	86,66	
Sample DCW-77-64-5 Silica rich glass	SiO ₂	TiO ₂	Cr ₂ O ₃	Al ₂ O ₃	FeO _{total}	MnO	MgO	CaO	Na ₂ O	K ₂ O	Total	
DCW-77-64-5 - Maf blob 11 clear area	96,81	0,00	0,000	0,01	0,03	0,00	0,00	0,00	0,00	0,01	96,86	
Sample DCW-77-64-5 Matrix glass	SiO ₂	TiO ₂	Cr ₂ O ₃	Al ₂ O ₃	FeO _{total}	MnO	MgO	CaO	Na ₂ O	K ₂ O	Total	
DCW-77-64-5 - Si glass 1	59,8	0,622	0,028	15,92	3,40	0,087	3,12	4,68	2,42	4,38	94,47	
DCW-77-64-5 - Si Glass 3	58,0	0,631	0,000	15,83	5,10	0,059	2,20	3,48	3,45	2,53	91,24	
DCW-77-64-5 - Si Glass 6	59,0	0,622	0,000	15,88	4,80	0,059	3,20	4,24	2,18	4,15	94,09	
DCW-77-64-5 - Si Glass 7	58,7	0,640	0,017	16,48	4,90	0,088	2,79	4,03	2,98	2,84	93,48	
DCW-77-64-5 - Si Glass 9	59,17	0,63	0,00	15,82	4,22	0,07	3,38	4,49	2,78	4,44	94,99	
DCW-77-64-5 - Si Glass 10	58,86	0,56	0,04	16,16	5,02	0,08	3,00	2,93	3,09	3,80	93,52	
DCW-77-64-5 - Si Glass 15	59,48	0,66	0,02	15,97	4,49	0,07	3,07	3,63	2,70	4,09	94,18	
Sample DCW-77-65-4	SiO ₂	TiO ₂	Cr ₂ O ₃	Al ₂ O ₃	FeO _{total}	MnO	MgO	CaO	Na ₂ O	K ₂ O	P ₂ O ₅	Total
DCW-77-65-4-Region 1-Plag 1	59,90	0,02	0,026	25,36	0,099	0,005	0,000	7,10	7,51	0,189	0,000	100,21
DCW-77-65-4-Region 1-Glass 1	60,94	0,642	0,000	16,86	4,92	0,075	1,58	2,75	2,92	3,12	0,000	93,81
DCW-77-65-4-Region 1-Glass 2	61,18	0,624	0,028	16,72	4,68	0,058	1,75	2,97	2,69	2,53	0,000	93,24
DCW-77-65-4-Region 1-Plag 3	65,08	0,063	0,005	18,65	0,112	0,000	0,006	0,470	2,69	12,22	0,000	99,29
DCW-77-65-4-Region 1-Glass 3	62,04	0,567	0,000	17,23	4,22	0,049	0,917	2,08	3,02	3,34	0,000	93,46
DCW-77-65-4-Region 1-Glass 4	61,36	0,617	0,028	16,56	5,11	0,054	1,61	2,84	2,76	2,58	0,000	93,50
DCW-77-65-4-Region 1-Glass 5	60,50	0,608	0,014	16,39	5,00	0,097	2,89	3,31	2,62	2,80	0,000	94,23
DCW-77-65-4-Region 1-Glass 6	53,40	0,023	0,011	13,38	2,50	0,031	13,35	2,47	0,019	0,695	0,000	85,87
DCW-77-65-4-Region 1-Glass 7	54,25	0,036	0,025	13,37	2,40	0,047	13,53	2,45	0,045	0,662	0,000	86,80
DCW-77-65-4-Region 1-Glass 8	53,40	0,076	0,018	13,51	2,81	0,036	12,89	2,56	0,060	1,00	0,000	86,36
DCW-77-65-4-Region 1-Glass 9	52,99	0,049	0,000	13,32	2,50	0,033	12,62	2,55	0,061	0,768	0,000	84,88
DCW-77-65-4-Region 1-Glass 10	47,06	0,005	0,000	26,12	0,245	0,052	8,60	1,09	0,010	0,123	0,000	83,31
DCW-77-65-4-Region 1-Glass 11	52,60	0,032	0,023	12,87	3,22	0,036	12,38	2,49	0,064	0,844	0,000	84,57
DCW-77-65-4-Region 1-Glass 12	53,20	0,055	0,005	14,89	3,98	0,054	12,26	2,34	0,052	1,23	0,000	88,06
DCW-77-65-4-Region 2-Glass 1	54,77	0,026	0,012	13,48	2,75	0,028	12,90	2,32	0,026	1,07	0,000	87,38

Microprobe compositions

Page 15

Sample DCW-77-65-4	SiO ₂	TiO ₂	Cr ₂ O ₃	Al ₂ O ₃	FeO _{total}	MnO	MgO	CaO	Na ₂ O	K ₂ O	P ₂ O ₅	Total
DCW-77-65-4-Region 2-Glass 2	53,02	0,051	0,022	13,38	2,40	0,033	12,95	2,31	0,029	0,695	0,000	84,87
DCW-77-65-4-Region 2-Glass 3	48,47	0,002	0,000	25,27	0,259	0,048	8,52	1,20	0,037	0,193	0,000	83,99
DCW-77-65-4-Region 2-Glass 4	58,37	0,035	0,000	1,20	0,610	0,028	3,65	5,32	7,68	0,856	0,000	77,75
DCW-77-65-4-Region 2-Glass 5	69,89	0,034	0,026	3,14	0,837	0,023	3,54	5,67	9,657	0,864	0,000	93,69
DCW-77-65-4-Region 2-Glass 6	51,54	0,033	0,028	13,23	3,17	0,054	12,35	2,58	0,046	0,805	0,000	83,85
DCW-77-65-4-Region 2-Glass 7	52,95	0,044	0,000	13,30	3,38	0,029	12,32	2,57	0,073	0,895	0,000	85,55
DCW-77-65-4-Region 2-Glass 8	53,47	0,011	0,011	13,44	2,78	0,028	12,54	2,52	0,048	0,770	0,000	85,61
DCW-77-65-4-Region 2-Plag 1	59,69	0,000	0,000	25,47	0,159	0,000	0,003	7,39	7,16	0,416	0,000	100,29
DCW-77-65-4-Region 2-Plag 2	59,56	0,000	0,000	24,55	0,552	0,017	0,096	7,01	6,62	0,714	0,000	99,11
DCW-77-65-4-Region 2-Glass 9	60,09	0,615	0,000	16,36	3,68	0,055	3,40	4,33	1,93	4,29	0,000	94,74
Sample DCW-77-65-4	SiO ₂	TiO ₂	Cr ₂ O ₃	Al ₂ O ₃	FeO _{total}	MnO	MgO	CaO	Na ₂ O	K ₂ O	P ₂ O ₅	Total
DCW-77-65-4-Region 2-Glass 10	58,60	0,630	0,000	18,76	4,30	0,024	1,83	3,54	6,25	2,30	0,000	96,23
DCW-77-65-4-Region 2-Glass 11	59,12	0,626	0,000	16,48	4,93	0,044	2,20	3,89	2,14	3,15	0,000	92,57
DCW-77-65-4-Region 2-Glass 12	52,52	0,069	0,003	13,53	2,79	0,042	12,76	2,65	0,055	0,660	0,000	85,08
DCW-77-65-4-Region 2-Glass 13	58,47	0,726	0,000	16,32	7,08	0,057	2,33	3,52	2,25	2,48	0,000	93,23
DCW-77-65-4-Region 2-Glass 14	54,45	0,692	0,000	15,46	3,94	0,058	6,49	2,97	0,921	1,43	0,000	86,41
DCW-77-65-4-Region 2-Glass 15	53,01	0,763	0,043	14,91	4,04	0,061	7,44	2,72	0,742	1,28	0,000	85,01
DCW-77-65-4-Region 2-Glass 16	53,59	0,578	0,025	15,38	5,82	0,044	7,73	2,97	0,707	1,23	0,000	88,08
DCW-77-65-4-Region 2-Plag 3	60,21	0,006	0,000	24,13	0,132	0,020	0,039	6,17	7,64	0,386	0,000	98,73
DCW-77-65-4 Glass spheroids	SiO ₂	TiO ₂	Cr ₂ O ₃	Al ₂ O ₃	FeO _{total}	MnO	MgO	CaO	Na ₂ O	K ₂ O	Total	
DCW-77-65-4-Reg 1-Glass 6 (blob)	53,40	0,023	0,011	13,38	2,50	0,031	13,35	2,47	0,019	0,695	85,87	
DCW-77-65-4-Reg 1-Glass 7 (blob)	54,25	0,036	0,025	13,37	2,40	0,047	13,53	2,45	0,045	0,662	86,80	
DCW-77-65-4-Reg 1-Glass 8 (blob)	53,40	0,076	0,018	13,51	2,81	0,036	12,89	2,56	0,060	1,00	86,36	
DCW-77-65-4-Reg 1-Glass 9 (blob)	52,99	0,049	0,000	13,32	2,50	0,033	12,62	2,55	0,061	0,768	84,88	
DCW-77-65-4-Reg 1-Glass 10 (blob alt)	47,06	0,01	0,00	26,12	0,25	0,05	8,60	1,09	0,01	0,12	83,31	
DCW-77-65-4-Reg 1-Glass 11 (blob)	52,60	0,032	0,023	12,87	3,22	0,036	12,38	2,49	0,064	0,844	84,57	
DCW-77-65-4-Reg 1-Glass 12 (blob)	53,20	0,06	0,01	14,89	3,98	0,05	12,26	2,34	0,05	1,23	88,06	
DCW-77-65-4-Reg 2-Glass (blob) 1	54,77	0,026	0,012	13,48	2,75	0,028	12,90	2,32	0,026	1,07	87,38	
DCW-77-65-4-Reg 2-Glass (blob margin)	53,02	0,051	0,022	13,38	2,40	0,033	12,95	2,31	0,029	0,695	84,87	
DCW-77-65-4-Reg 2-Glass (blob alt) 3	48,47	0,00	0,00	25,27	0,26	0,05	8,52	1,20	0,04	0,19	83,99	

Microprobe compositions

Page 16

DCW-77-65-4 Glass spheroids	SiO ₂	TiO ₂	Cr ₂ O ₃	Al ₂ O ₃	FeO _{total}	MnO	MgO	CaO	Na ₂ O	K ₂ O	Total	
DCW-77-65-4-Reg 2-Glass (blob) 6	51,54	0,033	0,028	13,23	3,17	0,054	12,35	2,58	0,046	0,805	83,85	
DCW-77-65-4-Reg 2-Glass (blob) 7	52,95	0,044	0,000	13,30	3,38	0,029	12,32	2,57	0,073	0,895	85,55	
DCW-77-65-4-Reg 2-Glass (prob. blob) 8	53,47	0,011	0,011	13,44	2,78	0,028	12,54	2,52	0,048	0,770	85,61	
DCW-77-65-4-Reg 2-Glass (blob) 12	52,52	0,069	0,003	13,53	2,79	0,042	12,76	2,65	0,055	0,660	85,08	
DCW-77-65-4 Glass matrix	SiO ₂	TiO ₂	Cr ₂ O ₃	Al ₂ O ₃	FeO _{total}	MnO	MgO	CaO	Na ₂ O	K ₂ O	Total	
DCW-77-65-4-Region 1-Glass (matrix) 1	60,94	0,64	0,000	16,86	4,92	0,08	1,58	2,75	2,92	3,12	93,81	
DCW-77-65-4-Region 1-Glass (matrix) 2	61,18	0,62	0,028	16,72	4,68	0,06	1,75	2,97	2,69	2,53	93,24	
DCW-77-65-4-Region 1-Glass 3 (Matrix)	62,04	0,57	0,000	17,23	4,22	0,05	0,917	2,08	3,02	3,34	93,46	
DCW-77-65-4-Region 1-Glass 4 (matrix)	61,36	0,62	0,028	16,56	5,11	0,05	1,61	2,84	2,76	2,58	93,50	
DCW-77-65-4-Region 1-Glass 5 (matrix)	60,50	0,61	0,014	16,39	5,00	0,10	2,89	3,31	2,62	2,80	94,23	
DCW-77-65-4-Region 2-Glass (matrix) 9	60,09	0,62	0,000	16,36	3,68	0,06	3,40	4,33	1,93	4,29	94,74	
DCW-77-65-4-Reg 2-Glass (matrix) 10	58,60	0,63	0,000	18,76	4,30	0,02	1,83	3,54	6,25	2,30	96,23	
DCW-77-65-4 Glass matrix	SiO ₂	TiO ₂	Cr ₂ O ₃	Al ₂ O ₃	FeO _{total}	MnO	MgO	CaO	Na ₂ O	K ₂ O	Total	
DCW-77-65-4-Reg 2-Glass (matrix) 11	59,12	0,63	0,000	16,48	4,93	0,04	2,20	3,89	2,14	3,15	92,57	
DCW-77-65-4-Reg 2-Glass (matrix) 13	58,47	0,73	0,000	16,32	7,08	0,06	2,33	3,52	2,25	2,48	93,23	
DCW-77-65-4-R 2-Glass (alt matrix) 14	54,45	0,69	0,000	15,46	3,94	0,06	6,49	2,97	0,921	1,43	86,41	
DCW-77-65-4-R 2-Glass (alt matrix) 15	53,01	0,76	0,043	14,91	4,04	0,06	7,44	2,72	0,742	1,28	85,01	
DCW-77-65-4-R 2-Glass (alt matrix) 16	53,59	0,58	0,025	15,38	5,82	0,04	7,73	2,97	0,707	1,23	88,08	
DCW-77-65-4 cracks thru spheroids	SiO ₂	TiO ₂	Cr ₂ O ₃	Al ₂ O ₃	FeO _{total}	MnO	MgO	CaO	Na ₂ O	K ₂ O	Total	
DCW-77-65-4-R 2-Glass (crack mat) 4	58,37	0,035	0,000	1,20	0,610	0,028	3,65	5,32	7,68	0,856	77,75	
DCW-77-65-4-R 2-Glass (crack mat) 5	69,89	0,03	0,03	3,14	0,84	0,02	3,54	5,67	9,66	0,86	93,69	
Sample LP-12	SiO ₂	TiO ₂	Cr ₂ O ₃	Al ₂ O ₃	FeO _{total}	MnO	MgO	CaO	Na ₂ O	K ₂ O	NiO	Total
LP-12-R6 (Clast 1)	53.878	0.000	0.015	29.019	0.207	0.000	0.019	11.161	5.033	0.105	0.043	99.480
LP-12-R6 (Clast 2)	34.155	0.063	0.000	11.524	22.991	0.095	19.410	0.813	0.318	3.341	0.006	92.716
LP-12-R7-1-Plag clast	63,624	0,012	0,000	23,328	0,120	0,016	0,013	5,864	6,960	0,930	0,000	100,867
Sample LP-24	SiO ₂	TiO ₂	Cr ₂ O ₃	Al ₂ O ₃	FeO _{total}	MnO	MgO	CaO	Na ₂ O	K ₂ O	NiO	Total
LP-24-R1-1-Feldspar clast	64,876	0,000	0,022	21,368	0,161	0,000	0,391	1,454	8,936	2,693	0,000	99,901
LP-24-R1-2-Feldspar clast	66,432	0,008	0,000	20,758	0,074	0,016	0,019	1,119	10,194	1,142	0,000	99,762
LP-24-R1-Feldspar clast	64,966	0,039	0,000	18,484	0,119	0,006	0,063	0,166	1,286	14,695	0,000	99,824
LP-24-R1-4-Feldspar clast	64,133	0,046	0,000	18,543	0,023	0,012	0,002	0,079	1,247	15,239	0,000	99,324
LP-24-R1-5-Feldspar clast	64,672	0,050	0,000	18,611	0,119	0,099	0,044	0,388	1,337	14,509	0,000	99,829
LP-24-R1-6-Feldspar clast	66,567	0,019	0,011	20,851	0,135	0,004	0,034	1,746	9,729	1,053	0,000	100,149

Microprobe compositions

Page 17

Sample LP-24	SiO ₂	TiO ₂	Cr ₂ O ₃	Al ₂ O ₃	FeO _{total}	MnO	MgO	CaO	Na ₂ O	K ₂ O	NiO	Total
LP-24-R1-7-Feldspar clast	65,897	0,000	0,000	18,455	0,018	0,026	0,009	0,227	1,987	14,219	0,000	100,838
LP-24-R1-8-Feldspar clast	68,463	0,004	0,033	20,180	0,034	0,000	0,014	0,986	10,804	0,353	0,000	100,871
LP-24-R3-1-Feldspar clast	65,296	0,056	0,018	18,478	0,012	0,000	0,000	0,099	1,391	15,247	0,000	100,597
LP-24-R3-2-Qtz	100,405	0,023	0,057	0,175	0,063	0,002	0,020	0,034	0,015	0,000	0,000	100,794
LP-24-R3-3-Feldspar clast	65,647	0,034	0,000	18,527	0,038	0,024	0,001	0,127	1,530	14,833	0,000	100,761
LP-24-R3-4-Feldspar clast	64,523	0,021	0,000	18,344	0,045	0,036	0,014	0,116	0,983	15,407	0,000	99,489
LP-24-R3-5-Feldspar clast	60,243	0,035	0,010	25,118	0,103	0,007	0,004	7,110	7,011	0,480	0,000	100,121
LP-24-R1-9-Maf. Clast	38,070	4,931	0,017	13,256	13,190	0,069	16,255	0,023	0,195	10,310	0,055	96,371
LP-24-R1-10-Maf. Clast	38,589	4,642	0,075	13,986	10,698	0,046	17,737	0,004	0,086	10,452	0,000	96,315

Infiltration Dykes

Sample LP-94	SiO ₂	TiO ₂	Cr ₂ O ₃	Al ₂ O ₃	FeO _{total}	MnO	MgO	CaO	Na ₂ O	K ₂ O	Total
LP-94-C1-1-Qtz clast	97,651	0,032	0,000	0,869	0,021	0,000	0,013	0,283	0,071	0,046	98,986
LP-94-C1-2-Qtz clast	100,484	0,027	0,001	0,023	0,018	0,000	0,000	0,016	0,000	0,000	100,569
LP-94 Glass Spheroids	SiO ₂	TiO ₂	Cr ₂ O ₃	Al ₂ O ₃	FeO _{total}	MnO	MgO	CaO	Na ₂ O	K ₂ O	Total
LP-94-Region 1 - Maf blob 1	1,48	0,14	0,00	4,28	1,64	0,03	0,05	0,61	0,00	0,20	8,43
LP-94-Region 1 - Maf blob 2	0,55	0,10	0,01	4,89	0,72	0,04	0,01	0,42	0,00	0,06	6,79
LP-94- matrix b - Maf blob 1	0,08	0,07	0,01	0,40	2,60	0,03	0,01	0,12	0,01	0,09	3,42
LP-94- matrix b - Maf blob 2	4,54	0,14	0,00	26,86	0,94	0,04	0,91	0,74	0,39	0,22	34,78
LP-94- matrix b - Maf blob 3	8,99	0,13	0,00	24,28	1,22	0,02	0,80	1,41	1,01	0,35	38,20
LP-94- Blob a center	33,89	0,18	0,02	19,81	5,73	0,05	10,14	1,30	0,72	0,68	72,51
LP-94 Matrix glass	SiO ₂	TiO ₂	Cr ₂ O ₃	Al ₂ O ₃	FeO _{total}	MnO	MgO	CaO	Na ₂ O	K ₂ O	Total
LP-94-R3-Matrix glass	62,047	0,030	0,028	23,261	0,164	0,007	0,017	5,577	7,672	0,730	99,533
LP-94-Region 1 - Matrix glass 1	54,70	0,87	0,00	16,29	6,09	0,083	1,76	4,12	5,83	4,65	94,39
LP-94-Region 1 - Matrix glass 2	55,35	0,71	0,00	18,61	4,64	0,053	0,23	3,70	5,68	5,00	93,98
LP-94-Region 1 - Matrix glass 3	55,48	1,04	0,00	19,07	3,22	0,020	0,40	3,49	5,51	5,35	93,57
LP-94- matrix b - Matrix glass 5	57,27	0,64	0,00	18,91	1,74	0,012	0,03	3,22	5,20	6,21	93,22
LP-94- matrix b - Matrix glass 7	55,19	0,95	0,02	16,47	6,12	0,068	1,99	4,28	5,36	5,01	95,45
LP-94- matrix b - Matrix glass 8	57,77	0,54	0,00	19,69	1,75	0,034	0,02	3,41	5,52	6,11	94,84
LP-94 Glass Spheroids	SiO ₂	TiO ₂	Cr ₂ O ₃	Al ₂ O ₃	FeO _{total}	MnO	MgO	CaO	Na ₂ O	K ₂ O	Total
LP-94-Region 1 - Alt Maf blob 1	1,48	0,14	0,00	4,28	1,64	0,03	0,05	0,61	0,00	0,20	8,43
LP-94-Region 1 - Alt Maf blob 2	0,55	0,10	0,01	4,89	0,72	0,04	0,01	0,42	0,00	0,06	6,79
LP-94- matrix b - Alt Maf blob 1	0,08	0,07	0,01	0,40	2,60	0,03	0,01	0,12	0,01	0,09	3,42
LP-94- matrix b - Alt Maf blob 2	4,54	0,14	0,00	26,86	0,94	0,04	0,91	0,74	0,39	0,22	34,78
LP-94- matrix b - Alt Maf blob 3	8,99	0,13	0,00	24,28	1,22	0,02	0,80	1,41	1,01	0,35	38,20
Sample LP-122	SiO ₂	TiO ₂	Cr ₂ O ₃	Al ₂ O ₃	FeO _{total}	MnO	MgO	CaO	Na ₂ O	K ₂ O	Total
LP-122-R1-Matrix glass 1	63,266	0,268	0,000	18,292	3,382	0,063	1,340	5,333	3,381	2,912	98,237
LP-122-R1-Matrix glass 2	57,733	0,029	0,000	25,468	0,642	0,011	0,216	9,378	4,245	1,429	99,151
LP-122-R1-Matrix glass 3	62,050	0,774	0,000	16,399	5,243	0,078	2,554	5,465	4,819	2,217	99,599
LP-122-R3-Matrix glass 1	64,035	0,770	0,023	15,503	4,622	0,091	2,168	4,149	4,118	3,710	99,189

Microprobe compositions

Page 19

Sample LP-122	SiO ₂	TiO ₂	Cr ₂ O ₃	Al ₂ O ₃	FeO _{total}	MnO	MgO	CaO	Na ₂ O	K ₂ O	NiO	Total
LP-122-R3-Matrix glass 2	66.656	0.542	0.000	14.257	4.351	0.081	2.072	3.737	3.844	3.684	0,000	99.224
LP-122-R3-Matrix glass 3	65.367	0.813	0.058	14.912	4.868	0.091	2.139	3.864	3.939	3.475	0,000	99.526
LP-122-R3-Matrix glass 4	62.408	0.849	0.000	15.743	5.613	0.070	2.523	4.548	4.051	3.393	0,000	99.198
LP-122-R3-Matrix glass 5	71.551	0.514	0.011	14.783	2.057	0.000	0.857	1.636	2.598	3.978	0,000	97.985
LP-122-R3-Matrix glass 6	68.588	0.928	0.011	11.876	4.314	0.077	1.966	2.846	2.020	3.438	0,000	96.064
LP-122-R3-9-Alt. Maf. Clast ?	43,454	0,057	0,026	10,281	1,652	0,182	5,918	1,714	0,026	0,423	0,012	63,745
Sample LP-125	SiO ₂	TiO ₂	Cr ₂ O ₃	Al ₂ O ₃	FeO _{total}	MnO	MgO	CaO	Na ₂ O	K ₂ O	Total	
LP-125 - Region 1 - maf glass 1	51,33	0,041	0,000	8,03	2,64	0,021	18,79	0,719	0,314	0,546	82,43	
LP-125 - Region 1 - maf glass 2	51,54	0,053	0,031	8,06	2,77	0,030	18,95	0,773	0,319	0,641	83,16	
LP-125 - Region 1 - maf glass 3	49,95	0,036	0,000	7,20	1,71	0,049	19,61	0,762	0,307	0,457	80,07	
LP-125 - Region 1 - Matrix Melt 1	56,75	0,836	0,034	17,57	5,69	0,085	2,88	5,89	4,89	2,69	97,31	
LP-125 - Region 1 - Marix Melt 2	57,20	0,742	0,004	17,22	5,25	0,083	2,78	5,19	4,39	3,41	96,27	
LP-125 - Region 1 - Cpx clast 1	51,97	0,247	0,000	2,09	8,69	0,268	14,16	22,38	0,419	0,025	100,24	
LP-125 - Region 1 - Cpx clast 2	52,29	0,170	0,000	1,70	8,41	0,285	14,37	22,43	0,434	0,023	100,11	
LP-125 - Region 1 - Plag clast 1	57,48	0,400	0,001	21,78	1,63	0,025	1,80	6,81	5,43	1,75	97,10	
LP-125 - Region 1 - Fe Ox	0,32	0,666	0,229	0,952	85,63	0,100	0,878	0,095	0,016	0,020	88,91	
LP-125 - Region 1 - Plag clast 2	56,02	0,087	0,006	26,67	0,918	0,020	0,192	9,85	5,32	0,625	99,70	
LP-125 Matrix glass	SiO ₂	TiO ₂	Cr ₂ O ₃	Al ₂ O ₃	FeO _{total}	MnO	MgO	CaO	Na ₂ O	K ₂ O	Total	
LP-125 image 2 felsic glass 1 (mineral?)	61,95	0,85	15,84	0,00	5,82	0,08	2,81	5,23	5,15	2,02	99,73	
LP-125 image 2 felsic glass 2	62,35	0,85	16,10	0,00	5,32	0,06	2,81	5,81	5,35	1,60	100,26	
LP-125 image 2 felsic glass 3	62,13	0,80	16,09	0,00	5,45	0,05	2,66	5,52	4,75	2,60	100,05	
LP-125 image 2 felsic glass 4	61,91	0,88	16,01	0,00	5,60	0,08	2,58	5,34	5,00	2,12	99,52	
LP-125 image 2 felsic glass 6	57,55	0,89	17,61	0,00	5,40	0,09	2,58	5,44	4,38	4,18	98,12	
LP-125 image 3 fels. glass 1	57,82	0,94	17,36	0,01	4,89	0,07	3,17	5,29	4,96	2,73	97,23	
LP-125 image 3 fels. glass 2+microlites	57,31	0,84	16,48	0,03	5,94	0,09	3,38	5,66	3,74	4,26	97,71	
LP-125 image 3 fels. glass 3+microlites	57,59	0,95	17,03	0,00	5,82	0,09	2,81	5,65	4,61	3,23	97,79	
LP-125 image 3 fels. glass 4	56,40	0,93	17,70	0,00	6,24	0,06	2,95	6,19	5,29	1,96	97,69	
LP-125 image 3 fels. glass 5	59,81	0,98	17,08	0,03	4,17	0,07	2,91	4,50	4,55	4,01	98,09	
LP-125 image 6 fels. glass 1	60,81	0,93	17,67	0,00	2,47	0,03	2,92	4,24	4,06	5,25	98,38	
LP-125 image 6 fels. glass 2	56,91	0,94	16,84	0,03	6,54	0,10	3,08	5,99	4,94	2,28	97,64	
LP-125 image 6 fels. glass 3	57,99	0,92	16,97	0,01	6,17	0,09	2,93	5,93	5,15	2,44	98,60	

Microprobe compositions

Page 20

LP-125 Matrix glass	SiO ₂	TiO ₂	Cr ₂ O ₃	Al ₂ O ₃	FeO _{total}	MnO	MgO	CaO	Na ₂ O	K ₂ O	Total
LP-125 image 6 fels. glass 4+microlites	58,24	0,86	17,57	0,00	4,34	0,04	1,62	4,95	4,33	4,53	96,49
LP-125 image 6 fels. glass 5+microlites	57,40	0,83	17,17	0,00	5,77	0,10	2,77	5,59	4,65	3,27	97,54
LP-125 image 6 fels. glass 6+microlite	56,46	0,91	15,50	0,02	5,78	0,10	4,22	7,77	2,84	4,90	98,51
LP-125 image 6 fels. glass 7 out image	57,50	0,99	17,05	0,04	6,32	0,10	3,01	6,05	5,26	2,21	98,53
LP-125 image 8 Fels. Glass 1	55,82	5,03	14,47	0,00	2,98	0,03	2,24	2,83	3,84	4,34	91,58
LP-125 image 8 Fels. Glass 2	66,14	0,00	18,36	0,00	0,13	0,00	0,05	0,73	4,69	9,50	99,59
LP-125 image 8 Fels. Glass 3+microlites	61,21	0,85	16,09	0,00	4,21	0,06	2,11	4,32	4,70	4,10	97,66
LP-125 image 8 Fels. Glass 4+microlites	60,36	0,86	16,02	0,01	7,40	0,07	1,62	3,95	4,65	4,10	99,05
LP-125 image 8 Fels. Glass 5	65,92	0,00	18,83	0,00	0,27	0,00	0,13	1,28	5,24	8,26	99,92
LP-125 image 8 Fels. Glass 6	65,70	0,02	18,63	0,03	0,45	0,02	0,25	1,44	4,66	8,40	99,61
LP-125 image 9 Fels. Glass 1(6)	57,73	1,71	16,54	0,00	5,38	0,07	2,57	5,37	5,38	2,04	96,79
LP-125 image 9 Fels. Glass 2	61,74	0,82	15,61	0,01	5,62	0,10	2,74	5,13	5,00	2,32	99,09
LP-125 image 9 Fels. Glass 3+microlites	57,76	0,91	16,76	0,03	5,93	0,11	2,70	5,48	4,77	2,73	97,16
LP-125 image 10 Fels. glass 1 (alt.)	40,30	0,03	3,38	0,00	0,12	0,03	3,49	4,75	11,02	0,78	63,89
LP-125 image 10 Fels. glass 2+microlite	56,90	0,87	17,02	0,02	5,79	0,05	3,08	5,38	4,06	3,56	96,72
LP-125 image 10 Fels. glass 3	57,45	0,90	16,97	0,00	5,46	0,08	3,42	5,80	4,65	2,83	97,54
LP-125 Glass Spheroids	SiO ₂	TiO ₂	Cr ₂ O ₃	Al ₂ O ₃	FeO _{total}	MnO	MgO	CaO	Na ₂ O	K ₂ O	Total
LP-125 image 2 mafic glass 1	51,35	0,016	8,40	0,000	2,25	0,027	18,97	0,776	0,379	0,558	82,72
LP-125 image 2 mafic glass 2	50,48	0,062	10,5	0,002	1,84	0,045	17,88	0,926	0,323	0,566	82,63
LP-125 image 2 mafic glass 3	51,29	0,04	8,35	0,02	2,29	0,03	18,48	0,76	0,36	0,56	82,18
LP-125 image 2 mafic glass 4	51,89	0,034	10,1	0,001	2,34	0,026	18,52	0,906	0,354	0,616	84,83
LP-125 image 2 mafic glass 5	50,00	0,081	9,13	0,000	2,37	0,033	17,91	0,990	0,339	0,669	81,53
LP-125 image 3 maf. glass 1	51,03	0,032	7,81	0,014	2,48	0,024	18,23	0,796	0,373	0,638	81,42
LP-125 image 3 maf. glass 2	49,34	0,08	7,79	0,00	3,81	0,06	20,04	1,12	0,35	0,61	83,19
LP-125 image 3 maf. glass 3	51,65	0,09	7,78	0,00	3,40	0,05	18,74	0,98	0,37	0,71	83,76
LP-125 image 3 maf. glass 4 outside ima	44,44	0,129	6,90	0,000	3,12	0,022	16,12	1,14	0,468	0,579	72,91
LP-125 image 3 maf. glass 5 outside ima	48,58	0,045	7,02	0,000	2,87	0,031	17,37	0,964	0,287	0,573	77,73
LP-125 image 3 maf. glass 6	51,95	0,01	7,67	0,01	1,67	0,02	20,56	0,74	0,39	0,49	83,51
LP-125 image 3 maf. glass 7	51,39	0,053	7,12	0,000	1,90	0,036	20,06	0,754	0,441	0,511	82,27
LP-125 image 3 maf. glass 8	50,02	0,006	7,59	0,000	1,56	0,057	18,46	0,923	0,328	0,424	79,36
LP-125 image 3 maf. glass 9 Out of imaj	50,97	0,043	7,69	0,000	2,80	0,032	18,07	0,815	0,364	0,660	81,45
LP-125 image 6 maf. glass 1	52,38	0,051	9,04	0,000	2,45	0,031	17,81	0,852	0,332	0,707	83,64

Microprobe compositions

Page 21

LP-125 Glass Spheroids	SiO ₂	TiO ₂	Cr ₂ O ₃	Al ₂ O ₃	FeO _{total}	MnO	MgO	CaO	Na ₂ O	K ₂ O	Total
LP-125 image 6 maf. glass 2	50,27	0,074	8,23	0,000	2,45	0,041	17,7	0,916	0,337	0,652	80,71
LP-125 image 6 maf. glass 3	51,69	0,213	8,63	0,028	3,34	0,016	17,9	1,09	0,324	0,823	84,07
LP-125 image 6 maf. glass 4	51,96	0,067	9,22	0,000	3,16	0,068	17,9	1,08	0,287	1,04	84,76
LP-125 image 6 maf. glass 5	52,86	0,069	9,19	0,035	3,17	0,044	17,8	1,05	0,260	1,02	85,54
LP-125 image 6 maf. glass 6	52,01	0,191	8,82	0,000	2,53	0,031	18,4	0,872	0,360	0,627	83,89
LP-125 image 8 maf. glass 1	45,45	0,000	7,67	0,016	1,89	0,029	17,3	0,966	0,314	0,437	74,08
LP-125 image 8 maf. glass 2	40,21	0,000	6,20	0,000	1,41	0,026	17,2	0,732	0,268	0,321	66,33
LP-125 image 8 maf. glass 3	39,31	0,000	6,62	0,008	1,48	0,015	17,0	0,796	0,263	0,345	65,86
LP-125 image 8 Maf. Glass 6	43,53	0,011	8,59	0,015	1,35	0,042	16,5	0,936	0,327	0,529	71,82
LP-125 image 9 Maf. Glass 1	53,00	0,045	9,21	0,000	2,78	0,018	17,8	0,927	0,374	0,703	84,81
LP-125 image 9 Maf. Glass 2	53,44	0,080	9,02	0,000	3,03	0,024	18,5	0,937	0,381	0,766	86,14
LP-125 image 10 Maf. glass 1	52,24	0,00	3,51	0,00	0,18	0,02	3,96	5,59	11,92	0,91	78,33
LP-125 image 10 Maf. glass 2	52,27	0,074	9,79	0,007	2,11	0,034	18,3	0,925	0,341	0,646	84,47
LP-130 Glass Spheroids	SiO ₂	TiO ₂	Cr ₂ O ₃	Al ₂ O ₃	FeO _{total}	MnO	MgO	CaO	Na ₂ O	K ₂ O	Total
LP-130 image 1 maf. glass 1	53,44	0,023	12,7	0,000	3,15	0,016	16,2	1,27	0,382	1,05	88,20
LP-130 image 1 maf. glass 2	54,73	0,01	13,44	0,00	3,22	0,02	16,92	1,24	0,30	1,00	90,89
LP-130 image 1 maf. glass 3	53,56	0,055	12,8	0,000	3,23	0,022	16,2	1,30	0,372	1,19	88,66
LP-130 image 1 maf. glass 4	49,92	0,026	12,4	0,014	3,19	0,023	12,6	1,44	0,273	0,916	80,78
LP-130 image 1 Maf. glass 5	52,69	0,042	12,9	0,000	3,68	0,016	15,4	1,18	0,352	1,21	87,45
LP-130 image 2 Maf. Glass 1	52,88	0,022	12,1	0,017	3,38	0,045	16,3	1,29	0,357	1,04	87,39
LP-130 image 2 Maf. Glass 2	53,41	0,011	12,0	0,000	3,50	0,000	16,0	1,33	0,391	1,03	87,66
LP-130 image 2 Maf. Glass 3	52,74	0,011	12,5	0,000	3,94	0,034	15,5	1,24	0,336	1,30	87,50
LP-130 image 2 Maf. Glass 4	52,55	0,022	12,1	0,014	3,37	0,044	16,3	1,19	0,403	1,04	87,06
LP-130 image 2 Maf. Glass 5	53,42	0,029	12,2	0,016	3,23	0,019	16,5	1,29	0,370	1,07	88,09
LP-130 image 2 Maf. Glass 6 Out image	52,73	0,044	12,4	0,000	3,92	0,032	15,0	1,15	0,309	1,30	86,94
LP-130 image 3 maf. glass 1	53,39	0,045	12,1	0,003	2,61	0,040	16,4	1,18	0,327	0,898	87,04
LP-130 image 3 maf. glass 2	53,58	0,02	12,39	0,00	2,60	0,03	17,05	1,13	0,34	0,95	88,09
LP-130 image 3 maf. glass 3	53,79	0,058	12,3	0,000	2,66	0,030	16,8	1,17	0,333	0,868	87,97
LP-130 image 3 maf. glass 4	53,69	0,027	12,5	0,000	2,97	0,035	16,7	1,27	0,342	0,998	88,44
LP-130 image 3 maf. glass 5	57,79	0,03	16,89	0,00	0,46	0,05	6,23	1,49	0,36	0,94	84,24

Microprobe compositions

Page 22

LP-130 Glass Spheroids	SiO ₂	TiO ₂	Cr ₂ O ₃	Al ₂ O ₃	FeO _{total}	MnO	MgO	CaO	Na ₂ O	K ₂ O	Total
LP-130 image 3 maf. glass 6	53,27	0,040	11,8	0,000	3,16	0,020	16,5	1,22	0,366	1,07	87,47
LP-130 image 3 maf. glass 7 out image	52,66	0,051	12,1	0,002	3,34	0,045	16,3	1,24	0,353	1,08	87,10
LP-130 image 3 maf. glass 8	52,90	0,041	12,3	0,000	3,17	0,008	16,4	1,19	0,361	1,06	87,43
LP-130 image 3 maf. glass 9	54,92	0,02	17,60	0,01	0,75	0,04	12,53	1,40	0,40	1,04	88,70
LP-130 image 3 maf. glass 10 out image	53,63	0,040	12,1	0,012	3,04	0,058	16,6	1,28	0,257	1,13	88,18
LP-130 Matrix Glass	SiO ₂	TiO ₂	Cr ₂ O ₃	Al ₂ O ₃	FeO _{total}	MnO	MgO	CaO	Na ₂ O	K ₂ O	Total
LP-130 image 1 fels. glass 1	59,77	0,79	15,68	0,00	5,39	0,08	2,67	4,25	3,94	3,11	95,68
LP-130 image 1 fels. glass 2	60,56	0,77	15,75	0,00	5,45	0,11	2,65	4,31	3,91	3,11	96,60
LP-130 image 1 fels. glass 3	59,41	0,91	15,37	0,03	6,27	0,11	3,22	4,74	3,19	3,49	96,75
LP-130 image 1 fels. glass 4	61,75	0,81	16,37	0,00	5,70	0,05	2,69	4,54	6,20	1,33	99,45
LP-130 image 1 fels. glass 5	62,61	0,87	16,34	0,02	5,58	0,07	2,54	4,28	6,31	1,22	99,82
LP-130 image 1 fels. glass 6	62,36	0,78	16,31	0,00	5,53	0,07	2,62	4,32	5,94	1,50	99,43
LP-130 image 1 fels. glass 7	58,08	0,63	16,84	0,03	4,86	0,10	5,07	3,82	6,39	1,60	97,41
LP-130 image 1 fels. glass 8	61,74	0,90	16,27	0,00	5,96	0,07	2,86	4,72	5,74	1,69	99,94
LP-130 image 1 fels. glass 9	62,51	0,83	16,35	0,04	5,55	0,10	2,69	4,40	6,18	1,23	99,86
LP-130 image 1 fels. glass 10	40,20	0,79	10,53	0,00	6,33	0,07	2,92	4,69	2,30	2,59	70,42
LP-130 image 1 fels. glass 11	60,98	0,77	15,83	0,00	5,42	0,07	2,68	3,84	3,87	3,25	96,71
LP-130 image 1 fels. glass 12	58,27	0,82	15,41	0,00	5,83	0,08	4,12	3,68	3,11	3,40	94,73
LP-130 image 1 fels. glass 13	60,66	0,82	15,70	0,00	5,56	0,08	2,66	4,43	3,40	3,82	97,11
LP-130 image 2 Fels. glass 1	59,85	1,09	15,89	0,00	6,21	0,08	2,99	4,44	3,46	3,02	97,04
LP-130 image 2 Fels. glass 2	59,94	0,86	15,87	0,00	5,87	0,09	2,95	4,40	3,27	3,76	97,00
LP-130 image2Fels.glass3	58,87	0,77	15,24	0,01	5,54	0,06	2,72	5,20	6,29	1,08	95,78
LP-130 image 2 Fels. glass 4	60,73	0,78	16,00	0,00	5,31	0,10	2,67	4,34	3,94	3,07	96,93
LP-130 image 2 Fels. glass 5	60,08	0,81	15,65	0,00	5,67	0,10	3,04	4,38	3,74	3,01	96,47
LP-130 image 3 Fels. Glass 1	59,21	0,93	17,33	0,00	5,72	0,08	2,62	4,18	6,28	2,53	98,87
LP-130 image 3 Fels. Glass 2	59,67	1,00	15,66	0,00	5,83	0,07	3,18	4,52	3,57	3,25	96,76
LP-130 image 3 Fels. Glass 3	59,90	0,82	15,24	0,00	5,53	0,07	2,77	4,35	3,33	4,19	96,21
LP-130 image 3 Fels. Glass 4	59,58	0,89	17,24	0,00	5,83	0,07	2,98	4,78	6,40	2,12	99,90
LP-130 image 3 Fels. Glass 5	60,32	0,02	24,36	0,01	0,52	0,03	0,22	6,98	7,48	0,51	100,44
LP-130 image 3 Fels. Glass 6	58,09	1,32	15,59	0,00	6,64	0,11	3,55	4,89	2,51	4,43	97,12
LP-130 image 3 Fels. Glass 7	59,07	0,90	17,19	0,00	5,88	0,06	2,90	4,58	6,47	2,02	99,06
LP-130 image 3 Fels. Glass 8	60,70	0,61	19,12	0,00	4,26	0,04	2,13	6,10	5,30	1,42	99,67

Microprobe compositions

Page 23

Sample LP-133	SiO ₂	TiO ₂	Cr ₂ O ₃	Al ₂ O ₃	FeO _{total}	MnO	MgO	CaO	Na ₂ O	K ₂ O	Total	
LP-133-R2-glass	59.916	0.041	0.000	25.240	0.617	0.010	0.022	7.734	6.767	0.426	100.773	
LP-133-R5-glass	59.450	0.046	0.000	25.252	0.566	0.013	0.037	7.967	6.373	0.516	100.220	
LP-133-R5-glass1	73.188	0.126	0.015	14.494	0.051	0.000	0.000	0.231	1.727	11.326	101.158	
LP-133-R5-glass2	79.379	0.382	0.000	11.200	0.078	0.014	0.023	0.252	1.603	7.970	100.901	
LP-133-R5-glass3	78.269	0.263	0.000	11.782	0.111	0.000	0.001	0.228	1.412	8.623	100.689	
LP-133-R1-e-Fspar clast	66,137	0,070	0,000	18,266	0,251	0,000	0,000	0,216	2,271	13,670	100,881	
LP-133-R1-f-Fspar clast	65,223	0,142	0,023	19,360	0,341	0,005	0,003	1,220	4,134	10,052	100,503	
LP-133-R1-g-fspar clast	65,130	0,133	0,000	19,066	0,323	0,000	0,004	0,914	3,479	11,013	100,062	
LP-133-R1-h-Feldspar	65,209	0,157	0,000	19,244	0,403	0,000	0,001	1,117	3,519	11,218	100,868	
LP-133-R2-g-Feldspar	63,246	0,006	0,000	23,133	0,309	0,000	0,000	5,109	7,957	0,931	100,691	
LP-133-R2-h-Feldspar	64,839	0,047	0,003	18,899	0,357	0,000	0,017	0,524	2,120	13,722	100,528	
LP-133-R2-I-Feldspar	55,824	0,087	0,000	27,650	0,994	0,005	0,040	10,691	5,232	0,280	100,803	
Sample LP-133	SiO ₂	TiO ₂	Cr ₂ O ₃	Al ₂ O ₃	FeO _{total}	MnO	MgO	CaO	Na ₂ O	K ₂ O	NiO	Total
LP-133-R1-a-Altered Px?	46,237	1,892	0,005	6,470	13,467	0,209	14,850	11,125	2,257	1,188	0,000	97,700
LP-133-R1-b-Altered Px?	52,572	0,359	0,020	0,357	10,782	0,271	15,580	19,182	0,287	0,070	0,000	99,480
LP-133-R1-c-Altered Px?	46,771	1,434	0,008	6,041	13,128	0,198	15,545	11,143	2,222	1,168	0,000	97,658
LP-133-R1-Altered Px?	47,171	1,144	0,022	5,733	12,759	0,191	15,778	11,088	2,131	1,084	0,023	97,124
LP-133-R2-a-Altered Px?	53,187	0,000	0,001	1,987	7,485	0,050	20,674	0,244	0,122	0,163	0,025	83,938
LP-133-R2-a (?)	59,897	0,005	0,000	1,723	7,096	0,037	26,577	0,143	0,088	0,101	0,034	95,701
LP-133-R2-b-Altered Px?	57,270	0,000	0,031	2,802	6,433	0,028	26,003	0,175	0,104	0,109	0,018	92,973
LP-133-R2-c-Altered Px?	58,960	0,027	0,000	1,471	6,998	0,092	25,977	0,130	0,121	0,104	0,001	93,881
LP-133-R2-d-Altered Px?	55,376	0,021	0,042	1,847	7,106	0,037	23,919	0,164	0,086	0,094	0,000	88,692
LP-133-R2-e-Altered Px?	56,858	0,001	0,000	1,570	6,719	0,037	25,387	0,121	0,092	0,079	0,000	90,864
LP-133-R2-f-CPX	51,999	0,231	0,066	1,815	9,392	0,268	13,982	21,981	0,508	0,000	0,000	100,242
LP-133-R2-j-Altered Px?	40,015	3,496	0,020	11,557	11,039	0,037	18,870	0,045	0,304	10,393	0,010	95,786
LP-133-R2-i-CPX	52,960	0,303	0,042	0,389	10,943	0,303	15,804	18,891	0,293	0,007	0,022	99,957

Microprobe compositions

Page 24

Clast-rich impact melt rock

Sample DCW-77-58	SiO ₂	TiO ₂	Cr ₂ O ₃	Al ₂ O ₃	FeO _{total}	MnO	MgO	CaO	Na ₂ O	K ₂ O	Total
DCW-77-58-R1-1-plag	59,637	0,184	0,000	23,071	1,445	0,016	0,319	6,854	6,198	1,399	99,123
DCW-77-58-R1-2-plag	58,435	0,108	0,000	24,576	1,042	0,027	0,230	8,182	5,938	1,023	99,561
DCW-77-58-R1-3-plag ?	65,061	0,610	0,008	18,826	1,735	0,009	0,454	5,218	4,759	2,184	98,864
DCW-77-58-R1-4-plag	55,611	0,061	0,000	27,116	0,743	0,000	0,133	10,669	4,907	0,599	99,839
DCW-77-58-R1-5-plag ?	66,845	0,815	0,042	17,539	1,441	0,031	0,124	2,336	4,714	5,631	99,518
DCW-77-58-R1-6-plag	57,678	0,223	0,010	25,511	1,145	0,002	0,175	9,357	4,867	0,816	99,784
DCW-77-58-R3-5-Kspar ?	68,396	0,010	0,000	18,541	0,446	0,002	0,214	1,936	3,488	4,536	97,569
DCW-77-58-R3-6-kspar ?	74,328	0,824	0,017	10,455	3,471	0,050	1,487	1,915	1,957	2,817	97,321
DCW-77-58-R3-7-kspar ?	74,423	0,796	0,002	9,222	3,532	0,056	2,117	2,128	1,600	2,580	96,456
DCW-77-58-R3-8-Alt kspar ?	75,131	0,741	0,024	8,036	3,810	0,059	2,192	2,276	1,378	2,250	95,897
DCW-77-58-R3-9	43,454	0,057	0,026	10,281	1,652	0,182	5,918	1,714	0,026	0,423	63,745
Sample LP-34	SiO ₂	TiO ₂	Cr ₂ O ₃	Al ₂ O ₃	FeO _{total}	MnO	MgO	CaO	Na ₂ O	K ₂ O	Total
LP-34-R6-1	66,300	0,016	0,000	18,830	0,133	0,000	0,000	0,579	3,890	10,655	100,403
LP-34-R6-2	66,275	0,000	0,024	18,824	0,099	0,000	0,000	0,548	3,380	11,469	100,619
LP-34-R6-3	65,353	0,025	0,019	18,749	0,163	0,000	0,000	0,494	3,643	11,187	99,633
LP-34-R2-glass1	65,217	0,024	0,016	18,388	0,147	0,000	0,005	0,399	2,646	12,950	99,792
LP-34-R2-glass2	61,474	0,032	0,014	23,838	0,127	0,029	0,011	5,941	6,643	2,090	100,199
LP-34-R2-glass3	66,926	0,125	0,000	20,405	0,584	0,017	0,136	5,713	5,779	0,585	100,270
LP-34-R5-glass1	65,316	0,101	0,000	19,786	0,685	0,001	0,272	4,170	5,223	4,116	99,670
LP-34-R6-glass1	65,286	0,066	0,009	18,707	0,328	0,000	0,011	1,174	3,194	10,721	99,496
Sample LP-45	SiO ₂	TiO ₂	Cr ₂ O ₃	Al ₂ O ₃	FeO _{total}	MnO	MgO	CaO	Na ₂ O	K ₂ O	Total
Lp-45-3-R3-glass?	64,484	0,079	0,015	18,767	0,394	0,000	0,018	0,867	2,965	11,632	99,221
Lp-45-3-R3-glass?-1	64,619	0,091	0,048	18,461	0,346	0,001	0,020	0,602	2,735	12,574	99,497
Lp-45-3-R3-glass?-2	61,688	0,060	0,000	23,612	0,299	0,000	0,019	5,432	7,627	1,111	99,848
Lp-45-3-R3-glass?-3	61,493	0,030	0,000	23,670	0,144	0,000	0,000	5,474	7,425	1,276	99,512
Lp-45-3-R3-glass?-4	65,246	0,054	0,012	18,711	0,321	0,000	0,007	0,631	3,055	12,247	100,284
LP-45-3-R5-1	65,728	0,011	0,000	19,328	0,065	0,009	0,000	0,595	3,857	10,990	100,583
LP-45-3-R5-2	66,141	0,023	0,000	18,790	0,233	0,000	0,000	0,352	3,475	11,846	100,860
LP-45-3-R5-3	65,822	0,042	0,000	18,784	0,073	0,004	0,009	0,274	3,389	11,951	100,348

Microprobe compositions

Page 25

Sample LP-45	SiO ₂	TiO ₂	Cr ₂ O ₃	Al ₂ O ₃	FeO _{total}	MnO	MgO	CaO	Na ₂ O	K ₂ O	Total
LP-45-3-R5-4	65,691	0,052	0,019	18,705	0,082	0,005	0,000	0,237	3,323	12,096	100,210
LP-45-3-R5-5	65,425	0,043	0,000	18,672	0,110	0,000	0,074	0,402	3,168	11,929	99,823
LP-45-3-R3-6	61,821	0,013	0,000	23,576	0,168	0,007	0,008	5,605	7,021	1,891	100,110
LP-45-3-R3-7	62,725	0,035	0,000	23,515	0,340	0,026	0,010	5,415	7,615	1,197	100,878
LP-45-3-R3-8	63,218	0,000	0,000	22,980	0,174	0,013	0,036	4,724	7,704	1,622	100,471
LP-45-3-R3-9	63,443	0,010	0,006	22,758	0,244	0,034	0,012	4,748	7,657	1,760	100,672
LP-45-R3-1	38,587	4,332	0,027	13,014	9,827	0,080	19,814	0,031	0,242	10,311	96,265
LP-45-R3-2	40,025	4,316	0,000	12,667	8,528	0,110	20,268	0,077	0,285	10,329	96,605
LP-45-R3-3	38,790	3,858	0,029	12,940	9,704	0,072	20,102	0,062	0,292	10,162	96,011
LP-45-R3-4	37,907	3,939	0,045	12,633	11,368	0,087	19,433	0,031	0,341	9,897	95,681

Clast-poor impact melt rock

Sample DCW-77-1	SiO ₂	TiO ₂	Cr ₂ O ₃	Al ₂ O ₃	FeO _{total}	MnO	MgO	CaO	Na ₂ O	K ₂ O	Total
DCW-77-1-R1-xenol-Fe Ox 1	0,04	1,87	0,05	0,29	88,19	0,06	0,19	0,02	0,01	0,01	90,73
DCW-77-1-R2-Fe Ox	0,01	22,83	0,01	0,48	65,67	1,07	3,74	0,00	0,04	0,00	93,84
DCW-77-1-R2-Fe Ti Ox	0,06	28,54	0,00	0,05	57,36	0,36	7,16	0,08	0,00	0,02	93,63
DCW-77-1-R4-Fe Ox	0,81	6,86	0,00	2,81	80,93	0,34	0,16	0,10	0,04	0,03	92,06
DCW-77-1-R4-Fe Ti Ox	0,04	11,44	0,00	0,55	77,80	0,37	1,92	0,01	0,03	0,01	92,16
Sample DCW-77-8	SiO ₂	TiO ₂	Cr ₂ O ₃	Al ₂ O ₃	FeO _{total}	MnO	MgO	CaO	Na ₂ O	K ₂ O	Total
DCW-77-8-R1-Fe Ti Ox	0,013	36,05	0,068	0,258	57,61	0,008	0,028	0,007	0,000	0,005	94,05
DCW-77-8-R1-Fe Ti Ox 2	0,076	8,52	0,045	0,282	80,86	0,080	0,008	0,031	0,024	0,009	89,94
DCW-77-8-R1-Fe Ti Ox 3	0,000	53,49	0,049	0,205	41,16	0,363	0,478	0,000	0,021	0,008	95,78
DCW-77-8-R1-KSpar 1	65,24	0,108	0,000	18,91	0,261	0,000	0,000	0,701	4,07	10,21	99,50
DCW-77-8-R1-KSpar 2	65,24	0,113	0,023	19,27	0,286	0,003	0,000	0,961	5,17	8,41	99,47
DCW-77-8-R1-Plag 1	62,91	0,084	0,031	22,57	0,495	0,000	0,011	4,91	8,40	0,552	99,97
DCW-77-8-R1-Plag 2	60,63	0,082	0,000	23,74	0,560	0,007	0,000	6,57	7,48	0,528	99,59
DCW-77-8-R1-Plag 3	59,12	0,055	0,000	24,80	0,636	0,000	0,026	7,32	6,97	0,525	99,44
DCW-77-8-R1-Plag 4	60,58	0,100	0,000	23,71	0,550	0,000	0,018	6,27	7,92	0,345	99,49
DCW-77-8-R1-Fe Ox in Px	6,58	0,019	0,011	0,577	76,48	0,166	0,225	0,875	0,038	0,022	84,99
DCW-77-8-R1-Px 1	46,76	1,24	0,000	5,985	14,60	0,243	14,35	10,96	2,38	1,03	97,54
DCW-77-8-R1-Px 2	51,33	0,566	0,000	0,882	14,29	0,311	13,23	18,77	0,335	0,006	99,71
DCW-77-8-R1-Px 3	50,98	0,214	0,000	0,686	16,49	0,436	11,08	19,86	0,309	0,009	100,05
DCW-77-8-R2-Fe Ti Ox	0,00	51,49	0,013	0,148	43,59	0,194	0,165	0,000	0,012	0,012	95,62
DCW-77-8-R2-Fe Ox	0,19	7,16	0,063	1,68	79,24	0,061	0,281	0,000	0,027	0,000	88,70
DCW-77-8-R2-Px 1	52,01	0,471	0,074	1,54	9,28	0,235	16,61	19,20	0,246	0,000	99,67
DCW-77-8-R2-Px 2	52,19	0,401	0,214	1,60	8,49	0,221	16,82	19,41	0,257	0,000	99,60
DCW-77-8-R2-Px 3	52,38	0,483	0,194	1,82	8,46	0,197	16,69	19,21	0,262	0,006	99,70
DCW-77-8-R3-Fe Ti Ox in QTZ	18,35	44,30	0,028	0,054	39,74	0,801	0,490	0,028	0,000	0,027	103,82
DCW-77-8-R3-Px 1	52,32	0,452	0,101	1,55	9,40	0,241	16,78	18,82	0,260	0,000	99,93
DCW-77-8-R3-Px 2	51,32	0,542	0,049	1,54	11,46	0,277	15,04	18,52	0,309	0,002	99,04
DCW-77-8-R5-Plag 1	58,94	0,088	0,000	24,83	0,607	0,010	0,020	7,71	6,90	0,479	99,58

Microprobe compositions

Page 27

Sample DCW-77-8	SiO ₂	TiO ₂	Cr ₂ O ₃	Al ₂ O ₃	FeO _{total}	MnO	MgO	CaO	Na ₂ O	K ₂ O	Total
DCW-77-8-R5-Plag 2	63,53	0,088	0,000	21,99	0,457	0,000	0,024	4,02	8,79	0,649	99,54
DCW-77-8-R5-Plag 3	60,50	0,099	0,000	23,88	0,582	0,010	0,032	6,50	7,62	0,449	99,67
DCW-77-8-R5-Plag 4	59,46	0,036	0,000	24,72	0,626	0,000	0,028	7,19	7,05	0,457	99,57
DCW-77-8-R5-Plag 5	64,35	0,106	0,000	21,31	0,411	0,000	0,003	3,16	8,85	1,30	99,48
DCW-77-8-R5-Plag 6	60,59	0,068	0,002	23,74	0,577	0,003	0,034	6,34	7,65	0,480	99,49
DCW-77-8-R5-Plag 7	61,14	0,057	0,000	23,70	0,570	0,000	0,016	6,18	7,83	0,455	99,96
DCW-77-8-R5-Plag 8	59,32	0,069	0,000	24,46	0,633	0,000	0,039	7,24	6,97	0,604	99,32
DCW-77-8-R5-Plag 9	60,38	0,124	0,000	23,92	0,614	0,025	0,035	6,72	7,42	0,534	99,77
DCW-77-8-R5-Plag 10	63,99	0,010	0,000	21,88	0,488	0,000	0,005	3,48	8,86	0,910	99,63
DCW-77-8-R5-Plag 11	64,55	0,086	0,012	21,14	0,429	0,000	0,000	3,13	8,79	1,36	99,50
DCW-77-8-R5-KSpar 1	65,32	0,113	0,000	18,60	0,222	0,000	0,000	0,498	3,60	11,31	99,67
DCW-77-8-R5-KSpar 2	65,27	0,061	0,000	18,53	0,204	0,000	0,000	0,383	3,41	11,58	99,45
DCW-77-8-R5-KSpar 3	65,28	0,106	0,002	18,46	0,194	0,005	0,003	0,404	3,43	11,68	99,56
DCW-77-8-R5-KSpar 4	65,43	0,127	0,009	18,35	0,203	0,000	0,000	0,352	3,10	12,32	99,90
DCW-77-8-R5-Plag 12	54,77	0,088	0,000	27,74	0,682	0,001	0,048	11,03	4,98	0,373	99,71
DCW-77-8-R5-Px 1	51,94	0,260	0,027	0,679	13,36	0,351	12,62	20,22	0,302	0,008	99,78
DCW-77-8-R5-Px 2	51,75	0,470	0,083	1,55	10,33	0,236	15,95	18,82	0,282	0,000	99,46
DCW-77-8-R5-Px 3	52,33	0,345	0,201	1,44	8,38	0,231	17,09	19,28	0,254	0,008	99,56
DCW-77-8-R5-Px 4	46,38	1,75	0,000	5,92	14,24	0,230	14,47	10,96	2,38	1,07	97,40
DCW-77-8-R5-Px 5	46,00	1,53	0,000	5,90	15,56	0,225	13,79	10,76	2,42	0,968	97,16
DCW-77-8-R5-Fe Ox square xtal	0,02	12,35	0,099	0,778	80,10	0,210	0,190	0,000	0,000	0,000	93,75
DCW-77-8-R5-KSpar 5	65,50	0,131	0,000	18,47	0,237	0,005	0,004	0,635	4,13	10,49	99,60
DCW-77-8-R5-KSpar 6	58,99	0,054	0,000	24,73	0,674	0,000	0,030	7,28	7,05	0,474	99,29
Sample DCW-77-17	SiO ₂	TiO ₂	Cr ₂ O ₃	Al ₂ O ₃	FeO _{total}	MnO	MgO	CaO	Na ₂ O	K ₂ O	Total
DCW-77-17-PX1	51,82	0,48	0,13	1,70	9,00	0,20	16,37	19,41	0,26	0,03	99,39
DCW-77-17-PX2	52,04	0,48	0,10	1,56	9,68	0,20	16,05	19,07	0,29	0,00	99,46
DCW-77-17-PX3	51,82	0,45	0,04	1,74	9,01	0,20	16,34	19,45	0,27	0,00	99,32
DCW-77-17-PX4	51,71	0,48	0,06	1,92	10,98	0,23	14,81	19,17	0,26	0,03	99,65
DCW-77-17-PX5	53,26	0,19	0,05	0,52	20,65	0,37	23,33	1,89	0,04	0,02	100,32
DCW-77-17-PX6	51,48	0,49	0,11	1,52	10,01	0,28	16,05	19,00	0,28	0,02	99,24

Microprobe compositions

Page 28

Sample DCW-77-28	SiO ₂	TiO ₂	Cr ₂ O ₃	Al ₂ O ₃	FeO _{total}	MnO	MgO	CaO	Na ₂ O	K ₂ O	Total
DCW-77-28-R1-Fe Ox	0,247	6,82	0,172	0,758	81,13	0,357	1,20	0,007	0,014	0,000	90,71
DCW-77-28-R1-Fe Ti Ox	0,039	39,07	0,113	1,47	50,26	0,116	2,16	0,034	0,014	0,000	93,27
DCW-77-28-R1-Ti Ox	0,031	86,61	0,095	0,135	8,30	0,086	0,109	0,028	0,017	0,046	95,45
DCW-77-28-R1-PX 1	52,33	0,480	0,046	1,46	10,03	0,237	16,21	18,80	0,287	0,004	99,89
DCW-77-28-R1-PX 2	51,73	0,566	0,000	0,862	13,52	0,343	13,29	19,16	0,318	0,022	99,81
DCW-77-28-R1-PX 3	52,60	0,413	0,077	1,47	8,67	0,241	16,99	19,36	0,280	0,005	100,10
DCW-77-28-R1-PX 4	52,43	0,508	0,029	1,49	9,92	0,229	16,14	19,16	0,281	0,000	100,19
DCW-77-28-R1-PX 5	51,67	0,600	0,005	1,39	12,37	0,312	14,98	18,63	0,300	0,016	100,29
DCW-77-28-R1-PX 6	47,67	1,25	0,020	5,93	12,45	0,185	15,50	11,18	2,16	1,07	97,41
DCW-77-28-R1-Plag 1	58,69	0,081	0,000	24,81	0,706	0,012	0,066	8,03	6,68	0,609	99,67
DCW-77-28-R1-KSpar 1	64,85	0,137	0,000	18,56	0,366	0,011	0,000	0,636	2,82	12,33	99,70
DCW-77-28-R1-KSpar 2	64,70	0,115	0,000	19,11	0,409	0,004	0,000	1,04	3,67	10,57	99,62
DCW-77-28-R1-KSpar 3	65,22	0,057	0,002	19,02	0,264	0,018	0,010	0,726	3,98	10,35	99,63
DCW-77-28-R1-Plag 2	56,04	0,076	0,011	26,92	0,779	0,015	0,039	9,91	5,54	0,341	99,68
DCW-77-28-R1-Plag 3	56,81	0,059	0,000	26,54	0,924	0,032	0,046	9,75	5,66	0,345	100,17
DCW-77-28-R2-Plag 1	54,59	0,043	0,000	28,13	0,514	0,000	0,027	11,49	4,89	0,310	100,00
DCW-77-28-R2-Plag 2	58,91	0,074	0,000	25,16	0,648	0,009	0,019	7,71	6,77	0,439	99,74
DCW-77-28-R2-Plag 3	64,40	0,073	0,000	21,50	0,354	0,005	0,030	3,16	8,72	1,59	99,83
DCW-77-28-R2-Fe Ox 1	0,192	5,31	0,002	0,288	82,70	0,354	0,482	0,015	0,012	0,036	89,39
DCW-77-28-R2-Fe Ox 2	0,009	3,28	0,008	0,534	85,79	0,326	0,448	0,000	0,023	0,000	90,42
DCW-77-28-R2-KSpar 1	66,01	0,048	0,000	18,38	0,269	0,000	0,000	0,326	3,91	10,86	99,80
DCW-77-28-R2-KSpar 2	65,61	0,081	0,000	18,67	0,296	0,017	0,000	0,622	4,03	10,47	99,79
DCW-77-28-R2-Plag 4	58,44	0,042	0,000	25,46	0,638	0,004	0,034	7,97	6,67	0,354	99,61
DCW-77-28-R2-Plag 5	56,96	0,043	0,000	26,31	0,807	0,000	0,034	9,23	5,83	0,423	99,63
DCW-77-28-R2-Px 1	51,64	0,572	0,000	1,29	13,16	0,347	14,50	18,29	0,315	0,016	100,13
DCW-77-28-R2-Px 2	51,24	0,584	0,005	1,53	13,53	0,317	14,40	18,17	0,339	0,006	100,13
DCW-77-28-R2-Px 3	52,49	0,398	0,062	1,54	9,24	0,235	16,79	18,99	0,245	0,000	99,98
DCW-77-28-R2-Px 4	52,77	0,307	0,126	1,53	8,31	0,238	17,30	19,11	0,281	0,013	99,98
DCW-77-28-R3-Fe Ti Ox 1	0,211	35,35	0,000	0,161	7,30	0,031	0,075	7,30	0,000	0,000	50,42
DCW-77-28-R3-Fe Ti Ox 2	0,015	12,17	0,338	1,02	78,37	0,195	0,082	0,026	0,033	0,000	92,24
DCW-77-28-R3-Fe Ti Ox 3	0,003	45,64	0,024	2,30	45,77	0,275	0,624	0,000	0,000	0,009	94,64
DCW-77-28-R3-Fe Ti Ox 4	0,072	10,57	0,098	0,797	79,03	0,165	0,173	0,017	0,018	0,000	90,94

Microprobe compositions

Page 29

Sample DCW-77-28	SiO ₂	TiO ₂	Cr ₂ O ₃	Al ₂ O ₃	FeO _{total}	MnO	MgO	CaO	Na ₂ O	K ₂ O	Total
DCW-77-28-R3-Px 1	50,80	0,612	0,000	1,79	12,98	0,280	12,95	18,52	0,739	0,008	98,68
DCW-77-28-R3-Px 2	51,82	0,457	0,011	1,50	10,50	0,263	16,32	18,38	0,269	0,015	99,54
DCW-77-28-R3-Plag 1	58,82	0,064	0,000	25,07	0,650	0,000	0,019	7,52	6,98	0,350	99,48
DCW-77-28-R3-Plag 2	60,44	0,095	0,000	23,91	0,574	0,000	0,019	6,21	7,59	0,639	99,47
DCW-77-28-R3-Plag 3	63,74	0,084	0,000	21,64	0,421	0,000	0,018	3,56	8,73	1,27	99,47
DCW-77-28-R3-KSpar 1	65,56	0,053	0,019	18,80	0,220	0,024	0,000	0,421	4,66	9,48	99,24
DCW-77-28-R3-KSpar 2	65,66	0,068	0,001	18,53	0,266	0,002	0,003	0,267	3,87	11,17	99,83
DCW-77-28-R4-Fe Ti Ox	0,180	5,26	0,010	1,03	82,27	0,227	0,255	0,026	0,006	0,046	89,31
DCW-77-28-R4-Fe Ti Ox 1	5,57	45,77	0,009	0,067	47,59	0,752	0,060	0,016	0,000	0,014	99,86
DCW-77-28-R4-Fe Ti Ox 2	4,54	44,88	0,032	0,109	48,15	0,567	0,190	0,008	0,000	0,000	98,47
DCW-77-28-R4-Fe Ti Ox 3	0,31	44,08	0,002	0,156	46,71	0,217	0,156	0,030	0,003	0,008	91,67
DCW-77-28-R5-Plag 1	54,01	0,041	0,000	28,56	0,610	0,000	0,032	11,52	4,61	0,298	99,67
DCW-77-28-R5-Plag 2	55,22	0,056	0,010	27,33	0,681	0,000	0,023	10,54	5,13	0,325	99,31
DCW-77-28-R5-Px 1	51,51	0,605	0,005	0,992	13,60	0,361	13,38	18,85	0,376	0,004	99,68
DCW-77-28-R5-Px 2	51,49	0,604	0,000	1,36	12,50	0,286	14,60	18,18	0,339	0,000	99,36
DCW-77-28-R5-Px 3	27,60	0,253	0,009	0,958	8,70	0,210	12,32	13,35	0,285	0,025	63,70
Sample DCW-77-33	SiO ₂	TiO ₂	Cr ₂ O ₃	Al ₂ O ₃	FeO _{total}	MnO	MgO	CaO	Na ₂ O	K ₂ O	Total
DCW-77-33-R2-Feldspar 1	72,24	0,10	0,00	14,22	0,26	0,01	0,01	0,13	2,60	9,34	98,91
DCW-77-33-R2-Feldspar 2	65,37	0,15	0,00	17,76	0,46	0,02	0,25	0,23	3,10	11,94	99,26
DCW-77-33-R2-Feldspar 3	64,73	0,11	0,00	18,83	0,27	0,00	0,00	0,64	4,58	9,85	99,01
DCW-77-33-R2-Feldspar 4	64,18	0,10	0,01	21,50	0,40	0,00	0,03	2,93	9,22	1,02	99,39
DCW-77-33-R2-Feldspar 5	62,03	0,08	0,00	23,10	0,43	0,03	0,03	5,05	8,31	0,50	99,55
DCW-77-33-R2-Feldspar 6	55,83	0,08	0,00	27,16	0,59	0,00	0,04	9,88	5,49	0,34	99,42
DCW-77-33-R2-Feldspar 7	55,68	0,07	0,00	27,04	0,50	0,01	0,03	10,04	5,65	0,45	99,46
DCW-77-33-R2-Feldspar 8	58,11	0,07	0,01	25,47	0,56	0,00	0,04	8,19	6,28	0,67	99,39
DCW-77-33-R2-Feldspar 9	58,19	0,10	0,03	25,24	0,56	0,00	0,04	7,89	6,32	0,73	99,09
DCW-77-33-R2-Feldspar 10	58,95	0,09	0,00	25,08	0,62	0,01	0,04	7,64	6,46	0,78	99,68
DCW-77-33-R2-Feldspar 11	60,17	0,08	0,00	23,97	0,48	0,00	0,03	6,41	7,28	0,83	99,24
DCW-77-33-R2-Feldspar 12	56,51	0,06	0,03	26,72	0,61	0,00	0,03	9,37	5,88	0,49	99,70
DCW-77-33-R2-Feldspar 13	62,61	0,09	0,00	22,21	0,46	0,00	0,02	4,19	8,37	1,27	99,21
DCW-77-33-R2-Feldspar 14	55,36	0,07	0,00	27,11	0,78	0,00	0,06	10,17	5,51	0,33	99,39
DCW-77-33-R2-Feldspar 15	64,85	0,08	0,00	18,66	0,61	0,03	0,16	0,67	4,58	9,85	99,48

Microprobe compositions

Page 30

Sample DCW-77-33	SiO ₂	TiO ₂	Cr ₂ O ₃	Al ₂ O ₃	FeO _{total}	MnO	MgO	CaO	Na ₂ O	K ₂ O	Total
DCW-77-33-PX1	51,41	0,53	0,11	1,60	10,34	0,22	15,89	19,18	0,29	0,03	99,59
DCW-77-33-PX2	51,16	0,58	0,05	1,59	11,62	0,27	15,43	18,63	0,32	0,02	99,65
DCW-77-33-PX3	51,25	0,50	0,05	1,59	10,64	0,29	15,75	18,84	0,28	0,02	99,20
DCW-77-33-PX4	51,42	0,56	0,08	1,62	11,16	0,27	15,47	18,87	0,31	0,03	99,78
DCW-77-33-PX5	51,16	0,52	0,08	1,61	10,89	0,25	15,60	18,78	0,30	0,03	99,22
DCW-77-33-PX6	52,07	0,44	0,21	1,66	9,23	0,21	16,68	19,19	0,29	0,02	99,99
Sample DCW-77-35	SiO ₂	TiO ₂	Cr ₂ O ₃	Al ₂ O ₃	FeO _{total}	MnO	MgO	CaO	Na ₂ O	K ₂ O	Total
DCW-77-35-Region 2-Fe Ti Ox 1	0,163	38,24	0,034	1,13	51,76	0,323	1,95	0,020	0,040	0,007	93,67
DCW-77-35-Region 2-Fe Ti Ox 2	0,124	3,05	0,030	0,957	84,45	0,325	1,19	0,000	0,050	0,022	90,20
DCW-77-35-Region 2-Fe Ti Ox 3	0,018	2,73	0,028	0,683	85,33	0,330	1,10	0,000	0,020	0,000	90,24
DCW-77-35-Region 2-Fe Ti Ox 4	0,011	36,99	0,049	0,977	53,84	0,236	1,38	0,013	0,007	0,002	93,50
DCW-77-35-Region 2-CPX 1 margi	50,85	0,595	0,000	1,20	12,93	0,320	14,45	18,56	0,365	0,006	99,28
DCW-77-35-Region 2-CPX 1 core	51,58	0,495	0,023	1,61	10,49	0,249	15,54	19,16	0,322	0,002	99,48
DCW-77-35-Region 2-CPX 2 margi	51,34	0,612	0,000	1,08	13,26	0,356	14,08	18,60	0,355	0,013	99,69
DCW-77-35-Region 2-CPX 2 core	50,81	0,496	0,073	1,68	11,28	0,265	15,27	18,91	0,306	0,000	99,09
DCW-77-35-Region 2-CPX 3	50,93	0,543	0,021	1,65	10,82	0,296	15,78	19,00	0,303	0,000	99,34
DCW-77-35-Region 2-CPX 4 margi	51,85	0,524	0,060	1,75	10,33	0,234	14,36	19,27	0,851	0,006	99,24
DCW-77-35-Region 2-CPX 4 core	51,47	0,543	0,026	1,67	10,51	0,253	15,84	19,04	0,330	0,006	99,69
DCW-77-35-Region 3-feldspar 1	64,86	0,157	0,000	18,68	0,986	0,001	0,000	0,535	4,09	10,27	99,57
DCW-77-35-Region 3-Fe Ti Ox 1	0,002	41,26	0,035	1,66	48,45	0,343	1,77	0,027	0,045	0,022	93,61
DCW-77-35-Region 3-Fe Ti Ox 2	0,040	6,94	0,037	0,790	82,98	0,281	0,555	0,000	0,033	0,000	91,65
DCW-77-35-Region 3-Fe Ti Ox 3	0,006	43,16	0,036	1,24	47,00	0,305	2,00	0,048	0,016	0,029	93,84
DCW-77-35-Region 3-Fe Ti Ox 4	0,084	7,28	0,065	0,753	81,44	0,258	0,509	0,023	0,122	0,000	90,54
DCW-77-35-Region 3-CPX 1 margi	51,69	0,558	0,000	1,09	12,92	0,364	14,42	18,60	0,347	0,004	99,99
DCW-77-35-Region 3-CPX 1 core	51,20	0,604	0,047	1,61	12,18	0,309	13,76	18,83	0,849	0,006	99,40
DCW-77-35-Region 1-CPX 1 margi	51,47	0,611	0,000	1,05	13,20	0,334	14,28	18,75	0,325	0,000	100,01
DCW-77-35-Region 1-CPX 1 core	51,33	0,517	0,076	1,58	10,65	0,304	15,97	18,93	0,292	0,000	99,65
DCW-77-35-Region 1-CPX 2 margi	51,17	0,552	0,026	1,63	12,62	0,329	13,30	18,78	1,03	0,000	99,43
DCW-77-35-Region 1-CPX 2 core	51,47	0,521	0,102	1,79	11,58	0,281	13,60	18,84	1,26	0,000	99,45
DCW-77-35-Region 1-Fe Ti Ox 1	0,000	44,97	0,000	0,185	50,60	0,736	0,325	0,004	0,000	0,006	96,83
DCW-77-35-Region 1-Fe Ti Ox 2	0,043	42,02	0,058	0,186	52,94	0,845	0,211	0,001	0,000	0,001	96,31

Microprobe compositions

Page 31

Sample DCW-77-35	SiO ₂	TiO ₂	Cr ₂ O ₃	Al ₂ O ₃	FeO _{total}	MnO	MgO	CaO	Na ₂ O	K ₂ O	Total
DCW-77-35-Region 1-Fe Ti Ox 3	0,017	0,156	0,140	0,493	92,06	0,035	0,020	0,000	0,000	0,000	92,92
DCW-77-35-Region 1-Fe Ti Ox 4	0,425	2,05	0,146	0,452	86,32	0,030	0,057	0,062	0,008	0,000	89,55
DCW-77-35-Region 1-Fe Ti Ox 5	0,114	1,23	0,098	0,421	90,10	0,051	0,041	0,005	0,000	0,006	92,07
DCW-77-35-Region 4-Fe Ti Ox 1	0,005	42,81	0,056	0,285	52,47	0,801	0,307	0,000	0,000	0,000	96,73
DCW-77-35-Region 4-Fe Ti Ox 2	0,844	0,972	0,075	0,533	86,69	0,027	0,143	0,076	0,000	0,018	89,38
DCW-77-35-Region 4-Fe Ti Ox 3	0,444	0,786	0,102	0,806	87,42	0,017	0,064	0,059	0,047	0,003	89,75
Sample DCW-77-51	SiO ₂	TiO ₂	Cr ₂ O ₃	Al ₂ O ₃	FeO _{total}	MnO	MgO	CaO	Na ₂ O	K ₂ O	Total
DCW-77-51-Region 1-Fe Ti Ox 1	0,174	37,59	0,036	0,407	53,35	0,303	1,74	0,022	0,009	0,000	93,62
DCW-77-51-Region 1-Fe Ti Ox 2	0,026	3,14	0,031	0,761	84,54	0,391	1,09	0,043	0,056	0,034	90,11
DCW-77-51-Region 1-Fe Ti Ox 3	0,000	3,51	0,036	0,804	84,33	0,339	1,10	0,000	0,029	0,010	90,16
DCW-77-51-Region 1-Fe Ti Ox 4	0,000	37,83	0,000	0,508	52,27	0,349	1,80	0,024	0,005	0,007	92,79
DCW-77-51-Region 2-Fe Ti Ox 1	0,051	3,92	0,019	0,803	84,19	0,416	1,35	0,014	0,000	0,000	90,76
DCW-77-51-Region 2-Fe Ti Ox 2	0,010	38,82	0,026	0,458	51,77	0,299	2,05	0,019	0,014	0,000	93,46
DCW-77-51-Region 2-Fe Ti Ox 3	0,028	37,72	0,000	0,420	53,03	0,247	1,93	0,005	0,000	0,000	93,38
DCW-77-51-Region 2-Fe Ti Ox 4	0,216	2,83	0,095	1,03	84,49	0,423	1,14	0,087	0,092	0,002	90,41
DCW-77-51-Region 2-Fe Ti Ox 5	0,265	5,93	0,000	0,788	83,43	0,138	0,293	0,000	0,000	0,008	90,86
DCW-77-51-Region 2-Fe Ti Ox 6	0,028	0,284	0,021	5,40	84,17	0,116	0,436	0,031	0,023	0,012	90,53
DCW-77-51-Region 3-Fe Ti Ox 1	0,385	0,870	0,088	1,01	86,56	0,079	0,048	0,055	0,000	0,000	89,09
DCW-77-51-Region 3-Fe Ti Ox 2	0,000	50,29	0,009	0,076	46,27	1,62	1,09	0,025	0,019	0,000	99,40
DCW-77-51-Region 3-Fe Ti Ox 3	0,015	52,26	0,001	0,105	43,77	0,876	0,589	0,023	0,000	0,000	97,64
DCW-77-51-Region 3-Fe Ti Ox 4	0,616	1,61	0,098	0,943	85,59	0,075	0,031	0,047	0,005	0,007	89,02
DCW-77-51-Region 3-Fe Ti Ox 5	0,158	49,27	0,000	0,099	45,59	1,91	0,932	0,011	0,015	0,027	98,00
DCW-77-51-Region 3-Fe Ti Ox 6	0,582	1,37	0,104	1,07	86,06	0,095	0,085	0,040	0,035	0,001	89,44
DCW-77-51-Region 3-Fe Ti Ox 7	0,552	1,33	0,091	1,01	86,00	0,085	0,071	0,062	0,045	0,000	89,25
DCW-77-51-Region 3-Fe Ti Ox 8	0,087	45,17	0,036	0,185	49,43	1,41	0,596	0,007	0,000	0,003	96,91
DCW-77-51-Region 4-Feldspar 1	65,22	0,059	0,000	18,77	0,190	0,000	0,026	0,354	3,86	10,96	99,43
DCW-77-51-Region 4-Feldspar 2	65,00	0,100	0,027	19,11	0,244	0,000	0,000	0,853	4,30	9,97	99,61
DCW-77-51-Region 4-Feldspar 3	62,35	0,082	0,000	23,14	0,371	0,024	0,019	4,80	8,38	0,902	100,06
DCW-77-51-Region 4-Feldspar 4	56,84	0,081	0,010	26,74	0,604	0,000	0,017	9,26	6,03	0,367	99,95
DCW-77-51-Region 4-Feldspar 5	56,69	0,038	0,027	26,47	0,738	0,000	0,040	9,22	5,93	0,449	99,60
DCW-77-51-Region 4-Feldspar 6	58,16	0,040	0,000	25,46	0,578	0,001	0,024	8,03	6,71	0,449	99,45

Microprobe compositions

Page 32

Sample DCW-77-51	SiO ₂	TiO ₂	Cr ₂ O ₃	Al ₂ O ₃	FeO _{total}	MnO	MgO	CaO	Na ₂ O	K ₂ O	Total
DCW-77-51-Region 4-Feldspar 7	65,22	0,081	0,000	18,96	0,243	0,006	0,000	0,742	4,18	10,15	99,58
DCW-77-51-Region 4-Feldspar 8	65,35	0,050	0,000	18,56	0,187	0,022	0,059	0,481	3,32	11,54	99,58
DCW-77-51-Region 4-Feldspar 9	60,18	0,079	0,000	24,37	0,429	0,017	0,027	6,31	7,64	0,52	99,57
DCW-77-51-Region 4-Feldspar 10	64,73	0,094	0,003	19,33	0,267	0,001	0,000	1,18	4,66	9,60	99,86
Sample DCW-77-53	SiO ₂	TiO ₂	Cr ₂ O ₃	Al ₂ O ₃	FeO _{total}	MnO	MgO	CaO	Na ₂ O	K ₂ O	Total
DCW-77-53-R1-Feldspar 1	65,11	0,08	0,00	18,35	0,20	0,00	0,01	0,45	3,83	11,12	99,15
DCW-77-53-R1-Feldspar 2	65,27	0,08	0,00	18,79	0,20	0,01	0,00	0,56	3,99	10,96	99,87
DCW-77-53-R1-Feldspar 3	64,85	0,05	0,00	18,74	0,24	0,00	0,00	0,57	4,19	10,51	99,14
DCW-77-53-R1-Feldspar 4	64,95	0,10	0,01	18,95	0,25	0,00	0,00	0,64	4,13	10,59	99,62
DCW-77-53-R1-Feldspar 5	63,41	0,10	0,00	21,70	0,47	0,00	0,00	3,48	8,54	1,35	99,04
DCW-77-53-R1-Feldspar 6	59,94	0,08	0,01	24,51	0,57	0,00	0,04	6,72	7,21	0,64	99,71
DCW-77-53-R1-Feldspar 7	55,49	0,08	0,01	27,04	0,80	0,02	0,05	9,95	5,36	0,42	99,21
DCW-77-53-R1-Feldspar 8	55,08	0,08	0,01	27,38	0,59	0,01	0,04	10,31	5,23	0,45	99,19
DCW-77-53-R1-Feldspar 9	55,11	0,05	0,00	27,81	0,50	0,01	0,01	10,36	5,38	0,31	99,51
DCW-77-53-R1-Feldspar 10	55,74	0,05	0,03	27,14	0,67	0,01	0,04	9,75	5,58	0,26	99,28
DCW-77-53-R1-Feldspar 11	63,72	0,10	0,00	21,64	0,37	0,00	0,01	3,09	8,42	1,97	99,32
DCW-77-53-R1-Feldspar 12	63,04	0,06	0,00	21,80	0,43	0,00	0,04	3,45	8,04	2,10	98,96
DCW-77-53-R1-Feldspar 13	65,12	0,12	0,00	19,13	0,26	0,00	0,00	0,59	4,59	9,94	99,73
DCW-77-53-R3-Feldspar 1	64,95	0,06	0,02	18,60	0,19	0,00	0,00	0,39	3,14	12,21	99,57
DCW-77-53-R3-Feldspar 2	65,32	0,11	0,00	18,51	0,21	0,00	0,00	0,44	3,81	11,14	99,54
DCW-77-53-R3-Feldspar 3	65,27	0,08	0,03	18,30	0,28	0,01	0,06	0,37	2,92	12,56	99,88
DCW-77-53-R3-Feldspar 4	65,76	0,08	0,00	19,12	0,27	0,00	0,02	0,76	3,88	10,90	100,78
DCW-77-53-R3-Feldspar 5	64,62	0,08	0,00	21,55	0,54	0,01	0,18	3,38	8,70	0,96	100,01
DCW-77-53-R3-Feldspar 6	61,48	0,09	0,00	23,41	0,51	0,00	0,03	5,50	7,83	0,65	99,50
DCW-77-53-R3-Feldspar 7	61,25	0,10	0,00	23,91	0,53	0,00	0,02	5,91	7,62	0,57	99,91
DCW-77-53-R3-Feldspar 8	62,06	0,06	0,01	23,33	0,51	0,00	0,02	5,52	7,87	0,63	100,02
DCW-77-53-R3-Feldspar 9	61,64	0,09	0,01	23,54	0,52	0,00	0,03	5,72	7,81	0,59	99,93
DCW-77-53-R3-Feldspar 10	65,07	0,12	0,00	18,87	0,30	0,00	0,00	0,67	3,81	10,98	99,82
DCW-77-53-R3-Feldspar 11	65,30	0,12	0,00	18,68	0,24	0,00	0,00	0,44	3,39	11,96	100,13
DCW-77-53-R3-Feldspar 12	65,29	0,08	0,00	18,58	0,19	0,00	0,01	0,44	3,23	11,97	99,79

Microprobe compositions

Page 33

Sample DCW-77-61	SiO₂	TiO₂	Cr₂O₃	Al₂O₃	FeO_{total}	MnO	MgO	CaO	Na₂O	K₂O	Total
DCW-77-61-R1-Feldspar 1	64,69	0,11	0,00	18,69	0,24	0,00	0,00	0,53	2,63	12,75	99,64
DCW-77-61-R1-Feldspar 2	65,27	0,06	0,01	18,61	0,21	0,00	0,01	0,46	2,48	13,09	100,20
DCW-77-61-R1-Feldspar 3	63,11	0,06	0,03	22,07	0,42	0,00	0,02	4,18	8,46	0,97	99,33
DCW-77-61-R1-Feldspar 4	62,69	0,05	0,00	22,78	0,47	0,00	0,15	4,87	7,97	0,83	99,80
DCW-77-61-R1-Feldspar 5	59,15	0,09	0,00	25,02	0,63	0,01	0,02	7,54	6,61	0,51	99,57
DCW-77-61-R1-Feldspar 6	60,04	0,06	0,00	24,62	0,54	0,00	0,03	6,94	7,11	0,58	99,92
DCW-77-61-R1-Feldspar 7	59,72	0,07	0,00	24,68	0,57	0,02	0,02	7,27	6,99	0,47	99,80
DCW-77-61-R1-Feldspar 8	65,24	0,07	0,00	19,37	0,25	0,00	0,04	1,27	4,59	9,19	100,03
DCW-77-61-R1-Feldspar 9	65,54	0,06	0,00	19,41	0,27	0,00	0,00	1,21	4,58	9,44	100,51
DCW-77-61-R1-Feldspar 10	65,44	0,06	0,00	19,31	0,26	0,00	0,02	1,25	4,38	9,67	100,39
DCW-77-61-R1-Feldspar 11	65,43	0,12	0,00	18,54	0,19	0,00	0,00	0,38	2,86	12,73	100,25
DCW-77-61-R1-Feldspar 12	64,87	0,06	0,00	18,44	0,19	0,02	0,00	0,47	3,01	12,29	99,34
DCW-77-61-R3-Feldspar 1	65,25	0,07	0,00	18,71	0,31	0,01	0,01	0,70	4,13	10,60	99,79
DCW-77-61-R3-Feldspar 2	64,73	0,10	0,00	19,31	0,31	0,00	0,00	1,45	4,74	8,54	99,17
DCW-77-61-R3-Feldspar 3	54,46	0,05	0,00	28,03	0,48	0,01	0,02	11,05	4,78	0,32	99,19
DCW-77-61-R3-Feldspar 4	54,04	0,04	0,00	28,38	0,54	0,00	0,03	11,47	4,59	0,33	99,44
DCW-77-61-R3-Feldspar 5	61,33	0,08	0,01	23,47	0,50	0,00	0,03	5,99	7,47	0,76	99,63
DCW-77-61-R3-Feldspar 6	64,49	0,06	0,00	18,60	0,24	0,00	0,00	0,41	2,35	13,04	99,19
DCW-77-61-R3-Feldspar 7	61,96	0,05	0,01	22,94	0,48	0,02	0,02	5,15	7,67	1,14	99,44
DCW-77-61-R3-Feldspar 8	61,60	0,12	0,00	23,03	0,42	0,01	0,02	5,23	7,35	1,32	99,08
DCW-77-61-R3-Feldspar 9	62,26	0,07	0,00	22,85	0,53	0,01	0,03	4,96	7,72	1,05	99,48
DCW-77-61-R3-Feldspar 10	53,53	0,05	0,02	28,43	0,72	0,00	0,04	11,50	4,67	0,29	99,23
DCW-77-61-R3-Feldspar 11	54,54	0,03	0,00	27,72	0,50	0,03	0,04	10,38	5,22	0,38	98,84
DCW-77-61-R3-Feldspar 12	54,94	0,04	0,00	27,85	0,55	0,00	0,02	10,42	5,14	0,35	99,30
DCW-77-61-R3-Feldspar 13	65,51	0,06	0,00	18,59	0,20	0,00	0,00	0,31	3,05	12,23	99,94
DCW-77-61-PX1	50,55	0,68	0,00	1,97	12,32	0,25	14,70	18,95	0,38	0,03	99,82
DCW-77-61-PX2	44,93	2,07	0,00	6,85	13,59	0,23	14,68	11,26	2,20	1,38	97,18
DCW-77-61-PX3	51,64	0,65	0,02	1,70	11,09	0,28	13,83	19,71	0,69	0,04	99,64
DCW-77-61-PX4	50,82	0,23	0,00	0,70	15,16	0,45	11,95	19,79	0,33	0,02	99,45
DCW-77-61-PX5	45,86	1,38	0,00	6,33	14,80	0,23	14,27	11,09	2,33	1,20	97,49
DCW-77-61-PX6	46,06	1,36	0,02	6,39	13,74	0,20	14,68	11,16	2,28	1,28	97,16
DCW-77-53-PX1	51,48	0,54	0,04	1,64	10,68	0,26	15,56	18,88	0,31	0,03	99,41

Microprobe compositions

Page 34

Sample DCW-77-61	SiO ₂	TiO ₂	Cr ₂ O ₃	Al ₂ O ₃	FeO _{total}	MnO	MgO	CaO	Na ₂ O	K ₂ O	Total	
DCW-77-53-PX2	51,29	0,56	0,07	1,66	10,24	0,26	16,06	18,86	0,28	0,02	99,30	
DCW-77-53-PX3	51,82	0,51	0,08	1,59	10,70	0,25	15,73	18,95	0,31	0,03	99,96	
DCW-77-53-PX4	51,77	0,48	0,05	1,65	9,81	0,28	16,46	18,88	0,28	0,03	99,69	
DCW-77-53-PX5	51,67	0,44	0,00	1,56	10,08	0,19	16,10	18,94	0,27	0,03	99,29	
DCW-77-53-PX6	51,66	0,43	0,03	1,54	9,36	0,25	16,51	19,20	0,27	0,02	99,27	
Sample LP-2 Feldspars	SiO ₂	TiO ₂	Cr ₂ O ₃	Al ₂ O ₃	FeO _{total}	MnO	MgO	CaO	Na ₂ O	K ₂ O	NiO	Total
LP-2-R2-c	57,09	0,08	0,04	26,40	0,68	0,00	0,03	9,11	5,76	0,41	0,00	99,60
LP-2-R2-d	56,34	0,05	0,00	27,04	0,70	0,01	0,03	10,07	5,36	0,45	0,00	100,06
LP-2-R2-e	56,94	0,06	0,00	26,63	0,90	0,00	0,05	9,81	5,60	0,39	0,00	100,38
LP-2-R2-f	56,38	0,08	0,02	26,69	0,88	0,00	0,04	9,84	5,52	0,36	0,00	99,81
LP-2-R2-g	54,96	0,06	0,05	28,08	0,70	0,02	0,05	10,97	5,06	0,20	0,00	100,15
LP-2-R2-h	65,41	0,08	0,00	21,44	0,38	0,00	0,00	3,31	8,78	1,15	0,00	100,54
LP-2-R2-I	66,17	0,18	0,00	18,54	0,24	0,02	0,00	0,50	3,71	11,64	0,00	100,99
LP-2-R3-e	57,65	0,08	0,02	26,47	0,60	0,02	0,01	9,17	6,02	0,37	0,00	100,40
LP-2-R3-f	56,28	0,06	0,01	27,47	0,76	0,00	0,04	10,43	5,39	0,39	0,00	100,83
LP-2-R3-g	55,40	0,06	0,00	27,60	0,85	0,02	0,04	10,89	5,02	0,28	0,00	100,16
LP-2-R3-h	65,69	0,08	0,00	18,72	0,24	0,00	0,00	0,62	4,05	10,89	0,00	100,31
LP-2-R3-I	55,56	0,05	0,00	27,48	0,66	0,00	0,05	10,54	5,25	0,37	0,00	99,96
LP-2-R3-j	54,63	0,04	0,00	28,26	0,45	0,00	0,02	11,26	4,82	0,36	0,00	99,83
LP-2-R1-e	58,64	0,07	0,00	25,68	0,63	0,03	0,03	8,48	6,36	0,43	0,00	100,35
LP-2-R1-f	65,07	0,10	0,02	21,12	0,42	0,00	0,01	3,08	8,63	1,42	0,00	99,86
LP-2-R1-h	66,07	0,06	0,01	19,00	0,29	0,00	0,01	0,79	4,46	10,04	0,00	100,72
LP-2-R1-I	55,02	0,02	0,04	27,67	0,82	0,01	0,04	11,02	4,85	0,34	0,00	99,83
LP-2-R1-j	64,23	0,06	0,01	21,86	0,41	0,00	0,02	3,77	8,53	0,93	0,00	99,82
LP-2-R1-l	65,84	0,04	0,01	18,74	0,28	0,01	0,01	0,70	3,95	10,80	0,00	100,38
LP-2-R1-m	56,94	0,10	0,00	26,20	0,86	0,01	0,06	9,51	5,64	0,42	0,00	99,74
LP-2-R1-n	65,98	0,09	0,00	18,94	0,28	0,00	0,00	0,86	4,61	9,77	0,00	100,52
LP-2-R1-o	55,26	0,06	0,00	27,77	0,65	0,00	0,02	10,79	4,92	0,28	0,00	99,76

Microprobe compositions

Page 35

Sample LP-2 Pyroxenes	SiO ₂	TiO ₂	Cr ₂ O ₃	Al ₂ O ₃	FeO _{total}	MnO	MgO	CaO	Na ₂ O	K ₂ O	NiO	Total
Lp-2-R2-Alt Px?	51,51	0,40	0,04	1,60	9,62	0,23	16,12	18,92	0,29	0,00	0,00	98,74
LP-2-R2-a Alt Px ?	50,78	0,58	0,04	1,59	11,89	0,26	15,00	18,27	0,32	0,01	0,00	98,74
LP-2-R2-b	51,34	0,62	0,02	1,32	12,79	0,33	14,45	18,41	0,32	0,00	0,01	99,60
LP-2-R3-a	51,83	0,42	0,12	1,59	9,26	0,25	16,52	19,03	0,24	0,00	0,02	99,28
LP-2-R3-b	52,04	0,40	0,08	1,57	9,21	0,22	16,46	19,07	0,23	0,00	0,03	99,30
LP-2-R3-c	51,73	0,41	0,15	1,71	9,68	0,21	15,70	19,21	0,32	0,01	0,01	99,13
LP-2-R3-d	51,34	0,56	0,01	0,69	13,65	0,36	12,45	20,13	0,32	0,01	0,03	99,56
LP-2-R3-l Alt Px ?	42,24	0,05	0,04	5,97	16,10	0,16	15,97	1,64	0,27	0,22	0,03	82,68
LP-2-R1-a	51,69	0,49	0,09	1,53	10,46	0,25	16,17	18,86	0,31	0,00	0,00	99,85
LP-2-R1-b Unknown CaCo3?	0,18	0,00	0,00	0,00	0,37	0,09	0,05	52,63	0,16	0,02	0,02	53,51
LP-2-R1-c Alt Px ?	50,86	0,59	0,04	1,22	13,18	0,32	13,55	18,46	0,37	0,00	0,00	98,59
LP-2-R1-d	51,49	0,51	0,06	1,56	11,00	0,23	15,42	18,50	0,28	0,00	0,03	99,08

Sample LP-47	SiO ₂	TiO ₂	Cr ₂ O ₃	Al ₂ O ₃	FeO _{total}	MnO	MgO	CaO	Na ₂ O	K ₂ O	Total
LP-47 - Region 1 - Plag 1	56,50	0,084	0,007	26,40	0,672	0,010	0,203	9,41	5,92	0,553	99,76
LP-47 - Region 1 - Plag 2	56,56	0,090	0,014	26,14	0,972	0,009	0,159	9,10	6,06	0,371	99,47
LP-47 - Region 1 - Plag 3	58,60	0,090	0,000	24,64	0,891	0,000	0,083	7,22	7,05	0,522	99,10
LP-47 - Region 1 - Plag 4	55,69	0,049	0,001	26,51	0,898	0,000	0,158	9,66	5,79	0,279	99,05
LP-47 - Region 1 - Plag 5	58,16	0,118	0,004	24,86	1,04	0,006	0,196	6,91	6,97	0,456	98,72
LP-47 - Region 1 - Plag 6	57,97	0,096	0,000	25,43	0,833	0,000	0,126	8,14	6,72	0,387	99,70
LP-47 - Region 1 - Plag 7	56,22	0,054	0,003	26,72	0,853	0,000	0,174	9,90	5,78	0,265	99,97
LP-47 - Region 1 - Kspar 1	68,85	0,563	0,000	14,73	2,13	0,036	0,039	1,21	2,78	8,71	99,03
LP-47 - Region 1 - Kspar 2	63,76	0,146	0,000	21,24	0,736	0,006	0,672	3,35	7,74	2,30	99,94
LP-47 - Region 1 - Kspar 3	66,34	0,393	0,000	17,31	0,970	0,070	0,056	0,806	3,76	9,22	98,92
LP-47 - Region 1 - cpx 1	50,49	0,762	0,074	3,67	7,66	0,129	15,83	20,17	0,280	0,000	99,06
LP-47 - Region 1 - cpx 2	49,96	0,964	0,092	4,32	9,71	0,226	16,85	17,26	0,309	0,000	99,69
LP-47 - Region 1 - cpx 3	50,42	0,738	0,062	3,66	8,49	0,160	16,53	18,47	0,296	0,015	98,84
LP-47 - Region 1 - cpx 4	50,51	0,769	0,120	3,80	7,96	0,177	16,16	19,99	0,266	0,027	99,77
LP-47 - Region 1 - cpx 5	50,91	0,680	0,206	3,50	7,59	0,151	16,98	18,01	0,332	0,017	98,37
LP-47-R1-glass1	68.268	0.255	0.018	16.991	1.080	0.043	0.500	0.493	3.322	10.302	101.272
LP-47-R1-glass2	70.864	0.307	0.000	16.005	0.762	0.026	0.033	0.512	3.412	9.267	101.188
LP-47-R1-glass3	74.340	0.459	0.072	13.253	1.399	0.025	0.239	0.512	2.714	7.892	100.905
LP-47-R7-glass1	71.708	0.048	0.000	16.747	0.242	0.002	0.000	2.960	3.692	4.954	100.353

Microprobe compositions

Page 36

Sample LP-47 Feldspars	SiO ₂	TiO ₂	Cr ₂ O ₃	Al ₂ O ₃	FeO _{total}	MnO	MgO	CaO	Na ₂ O	K ₂ O	Total	
LP-47-R1-7	60,116	0,077	0,000	24,663	0,909	0,000	0,070	6,894	6,945	0,502	100,176	
LP-47-R1-8	58,891	0,055	0,012	25,388	0,769	0,000	0,107	7,964	6,659	0,408	100,253	
LP-47-R1-9	57,424	0,038	0,000	26,564	0,740	0,000	0,163	9,611	5,684	0,504	100,728	
LP-47-R1-10	57,105	0,068	0,031	26,369	0,744	0,014	0,177	9,698	5,543	0,582	100,331	
LP-47-R1-11	57,245	0,056	0,000	26,112	0,938	0,000	0,128	9,479	5,726	0,323	100,007	
LP-47-R1-12	57,491	0,075	0,000	26,056	0,884	0,032	0,185	9,280	5,897	0,362	100,262	
LP-47-R1-13	58,435	0,119	0,002	25,767	1,014	0,021	0,063	8,693	6,394	0,328	100,836	
Sample LP-47 Pyroxenes	SiO ₂	TiO ₂	Cr ₂ O ₃	Al ₂ O ₃	FeO _{total}	MnO	MgO	CaO	Na ₂ O	K ₂ O	NiO	Total
LP-47-R1-1	49,849	1,100	0,188	4,925	8,716	0,166	16,185	18,614	0,286	0,010	0,023	100,062
LP-47-R1-2	50,166	0,768	0,085	4,397	9,615	0,220	16,550	17,568	0,278	0,015	0,023	99,685
LP-47-R1-3	50,430	0,859	0,009	4,200	8,837	0,212	16,302	18,672	0,278	0,005	0,017	99,821
LP-47-R1-4	50,606	0,851	0,032	3,729	8,170	0,192	16,255	19,114	0,306	0,018	0,010	99,283
LP-47-R1-5	50,124	0,924	0,126	4,357	8,761	0,230	16,718	18,055	0,283	0,014	0,026	99,618
LP-47-R1-6	50,638	0,730	0,020	3,890	8,549	0,225	16,097	19,241	0,295	0,022	0,018	99,725
Sample LP-89 Feldspars	SiO ₂	TiO ₂	Cr ₂ O ₃	Al ₂ O ₃	FeO _{total}	MnO	MgO	CaO	Na ₂ O	K ₂ O	Total	
LP-89-R2-10	65,853	0,103	0,000	19,013	0,258	0,000	0,008	0,684	3,573	11,360	100,852	
LP-89-R2-11	65,700	0,099	0,003	18,775	0,259	0,003	0,000	0,607	3,238	12,085	100,769	
LP-89-R2-12	65,710	0,085	0,013	18,633	0,243	0,002	0,001	0,415	3,035	12,588	100,725	
LP-89-R2-13	66,115	0,072	0,000	18,745	0,272	0,000	0,000	0,550	3,475	11,521	100,750	
LP-89-R3-1	65,459	0,076	0,006	18,644	0,241	0,004	0,004	0,495	3,041	12,521	100,491	
LP-89-R3-2	65,907	0,075	0,000	18,480	0,216	0,000	0,000	0,258	2,967	12,751	100,654	
LP-89-R3-3	66,572	0,061	0,033	18,450	0,198	0,000	0,000	0,367	3,359	12,069	101,109	
Sample LP-89 Pyroxenes	SiO ₂	TiO ₂	Cr ₂ O ₃	Al ₂ O ₃	FeO _{total}	MnO	MgO	CaO	Na ₂ O	K ₂ O	NiO	Total
LP-89-R2-1	51,528	0,244	0,000	0,729	13,129	0,340	13,015	19,996	0,279	0,000	0,013	99,273
LP-89-R2-2	46,530	1,563	0,023	6,353	12,475	0,139	15,598	10,912	2,188	1,140	0,015	96,936
LP-89-R2-3	52,016	0,236	0,029	0,661	12,927	0,267	13,330	20,510	0,245	0,000	0,054	100,275
LP-89-R2-4	51,576	0,488	0,023	0,889	12,405	0,292	13,698	19,768	0,317	0,000	0,009	99,465
LP-89-R2-5	51,814	0,168	0,049	0,672	13,861	0,321	12,895	19,964	0,260	0,000	0,000	100,004
LP-89-R2-6 Unknown	40,772	3,561	0,029	11,745	8,230	0,033	19,646	0,021	0,479	10,152	0,032	94,700

Microprobe compositions

Page 37

Sample LP-89	SiO₂	TiO₂	Cr₂O₃	Al₂O₃	FeO_{total}	MnO	MgO	CaO	Na₂O	K₂O	Total
Lp-89-Region 1 - cpx 1	46,24	1,53	0,000	6,53	12,80	0,190	14,97	11,19	2,202	1,13	96,78
Lp-89-Region 1 - cpx 2	46,29	0,517	0,000	0,940	19,59	0,246	12,22	17,76	0,393	0,000	97,97
Lp-89-Region 1 - cpx 3	46,29	1,68	0,004	6,45	12,64	0,171	15,60	11,13	2,29	1,11	97,35
Lp-89-Region 1 - Kspar 1	64,90	0,121	0,000	19,30	0,286	0,000	0,006	1,25	5,05	8,17	99,08
Lp-89-Region 1 - Kspar 2	61,97	0,110	0,016	23,04	0,418	0,009	0,019	5,06	8,32	0,578	99,53
Lp-89-Region 1 - Kspar 3	64,87	0,122	0,000	18,90	0,422	0,000	0,016	0,817	4,32	9,76	99,23
Lp-89-Region 1 - Kspar 4	65,19	0,130	0,000	19,14	0,343	0,000	0,098	0,990	4,88	8,80	99,56
Lp-89-Region 1 - Kspar 5	65,23	0,086	0,024	18,61	0,230	0,000	0,006	0,528	3,03	11,81	99,55
Lp-89-Region 1 - Kspar 6	64,81	0,094	0,010	19,00	0,365	0,000	0,013	0,714	3,67	10,42	99,11
Lp-89-Region 1 - Kspar 7	64,32	0,102	0,000	19,45	0,283	0,019	0,000	1,43	4,94	8,22	98,76
Lp-89-Region 1 - Kspar 8 (out of pic)	65,44	0,067	0,019	18,53	0,175	0,023	0,002	0,566	4,14	10,25	99,21
Lp-89-Region 1 - Fe ox 1	0,107	0,120	0,092	0,479	89,67	0,933	1,59	0,006	0,030	0,007	93,03
Lp-89-Region 1 - Fe ox 2	0,004	52,08	0,058	0,147	40,88	0,578	2,04	0,046	0,000	0,000	95,84
Lp-89-Region 1 - Altered biotite 1	46,54	0,061	0,005	7,28	8,75	0,083	20,16	1,20	0,297	0,407	84,78
Lp-89-Region 1 - Altered biotite 2	47,55	0,026	0,013	7,13	8,80	0,099	19,99	1,03	0,269	0,312	85,21
Lp-89-Region 2 - kspar 1	64,94	0,066	0,000	18,62	0,265	0,000	0,000	0,288	3,07	12,03	99,28
Lp-89-Region 2 - kspar 2	65,47	0,060	0,014	18,34	0,202	0,021	0,020	0,261	3,28	11,70	99,36
Lp-89-Region 2 - kspar 3	64,69	0,080	0,000	18,65	0,226	0,000	0,001	0,551	3,15	11,57	98,91
Lp-89-Region 2 - kspar 4	65,24	0,030	0,000	18,80	0,242	0,007	0,000	0,407	3,07	11,66	99,45
Lp-89-Region 2 - kspar 5	65,30	0,053	0,000	18,83	0,203	0,008	0,000	0,440	3,57	11,26	99,66
Lp-89-Region 2 - kspar 6	64,67	0,069	0,000	18,69	0,151	0,000	0,010	0,341	3,16	11,67	98,75
Lp-89-Region 2 - cpx 1	51,69	0,275	0,027	0,743	12,75	0,327	13,10	19,92	0,301	0,001	99,12
Lp-89-Region 2 - cpx 2	51,59	0,512	0,023	0,868	12,44	0,294	13,81	19,57	0,312	0,000	99,41
Lp-89-Region 2 - cpx 3	46,74	1,18	0,026	6,299	12,70	0,178	15,84	11,05	2,18	1,07	97,26
Lp-89-Region 2 - Fe ox 1 (bright area)	0,081	2,39	0,273	0,300	84,86	0,184	0,830	0,031	0,078	0,027	89,06
Lp-89-Region 2 - Kspar 7	58,47	0,097	0,000	25,11	0,600	0,001	0,037	7,88	6,77	0,608	99,58
Lp-89-Region 2 - Kspar 8	57,21	0,073	0,020	26,26	0,506	0,002	0,038	8,67	6,29	0,487	99,55
Lp-89-Region 2 - Fe Ti ox 1	0,081	41,21	0,000	0,028	50,32	0,537	2,86	0,009	0,000	0,000	95,04
Lp-89-Region 3 - cpx 1	46,06	1,68	0,036	6,65	14,06	0,164	14,70	10,92	2,15	1,08	97,49
Lp-89-Region 3 - cpx 2	45,75	1,62	0,000	6,56	14,02	0,214	14,77	11,16	2,15	1,13	97,37
Lp-89-Region 3 - cpx 3	51,75	0,283	0,018	0,656	12,74	0,298	13,57	19,91	0,297	0,000	99,51
Lp-89-Region 3 - biotite 1	40,23	3,79	0,000	11,89	8,74	0,046	19,54	0,026	0,479	9,558	94,30

Microprobe compositions

Page 38

Sample LP-89	SiO ₂	TiO ₂	Cr ₂ O ₃	Al ₂ O ₃	FeO _{total}	MnO	MgO	CaO	Na ₂ O	K ₂ O	Total	
Lp-89-Region 3 - Fe Ox 1	4,29	0,000	0,005	0,089	83,69	0,149	0,077	0,119	0,062	0,016	88,49	
Lp-89-Region 3 - Kspar 1	65,83	0,021	0,000	18,79	0,196	0,027	0,010	0,542	3,99	0,421	89,83	
Lp-89-Region 3 - Kspar 2	65,22	0,084	0,000	18,96	0,262	0,007	0,003	0,664	4,42	9,625	99,24	
Lp-89-Region 3 - Kspar 3	64,76	0,140	0,000	18,84	0,255	0,011	0,000	0,753	3,78	10,38	98,91	
Sample DR-10	SiO ₂	TiO ₂	Cr ₂ O ₃	Al ₂ O ₃	FeO _{total}	MnO	MgO	CaO	Na ₂ O	K ₂ O	Total	
DR-10-Region 1-Fe Ti Ox 2	0,156	2,31	0,012	0,374	86,14	0,431	0,598	0,030	0,029	0,010	90,09	
DR-10-Region 1-Fe Ti Ox 3	0,000	36,34	0,000	0,220	55,89	0,377	1,03	0,000	0,006	0,000	93,86	
DR-10-Region 1-Fe Ti Ox 4	0,000	36,79	0,000	0,102	55,40	0,396	1,21	0,000	0,015	0,000	93,91	
DR-10-Region 1-Fe Ti Ox 5	0,012	36,82	0,000	0,125	54,84	0,395	1,07	0,023	0,014	0,033	93,32	
DR-10-Region 1-Fe Ti Ox 6	0,110	36,05	0,033	0,535	54,94	0,264	0,899	0,020	0,018	0,004	92,88	
DR-10-Region 1-Fe Ti Ox 7	0,090	37,97	0,063	1,01	52,56	0,261	1,60	0,000	0,100	0,020	93,68	
DR-10-Region 1-Fe Ti Ox 8	0,000	2,22	0,030	0,592	86,82	0,201	0,538	0,000	0,000	0,000	90,40	
DR-10-Region 1-Fe Ti Ox 9	0,033	2,17	0,043	0,666	86,15	0,257	0,500	0,012	0,022	0,010	89,86	
DR-10-Region 1-Fe Ti Ox 10	0,023	36,68	0,034	1,28	53,38	0,266	1,70	0,000	0,026	0,000	93,39	
DR-10-Region 1-Fe Ti Ox 11	0,051	40,22	0,032	0,165	52,11	0,438	1,69	0,034	0,040	0,012	94,79	
DR-10-Region 1-Fe Ti Ox 12	0,009	35,06	0,008	0,833	55,57	0,345	1,00	0,076	0,013	0,000	92,92	
DR-10-Region 1-Fe Ti Ox 13	0,000	2,32	0,009	0,790	84,79	0,405	0,712	0,001	0,041	0,021	89,09	
DR-10-Region 1-Fe Ti Ox 14	0,019	2,61	0,021	0,702	85,03	0,443	0,829	0,012	0,031	0,002	89,70	
DR-10-Region 1-Fe Ti Ox 15	0,608	35,07	0,023	0,139	54,68	0,644	0,581	0,102	0,146	0,136	92,13	
DR-10-R5-glass?-1	65.710	0.057	0.034	18.285	0.203	0.000	0.003	0.289	2.478	13.411	100.470	
DR-10-R5-glass?-2	58.037	0.078	0.000	25.139	0.724	0.014	0.034	8.038	6.412	0.508	98.984	
DR-10-R5-glass?-3	65.393	0.026	0.000	18.444	0.262	0.000	0.000	0.383	2.363	13.476	100.347	
DR-10-R5-glass?-4	65.010	0.030	0.000	18.317	0.232	0.010	0.000	0.492	2.317	13.437	99.845	
Sample DR-10 Pyroxenes	SiO ₂	TiO ₂	Cr ₂ O ₃	Al ₂ O ₃	FeO _{total}	MnO	MgO	CaO	Na ₂ O	K ₂ O	NiO	Total
DR-10-R5b-1	52,001	0,560	0,037	1,588	10,145	0,211	15,929	19,333	0,297	0,000	0,012	100,113
DR-10-R5b-2	52,105	0,458	0,000	1,543	9,873	0,242	16,185	19,180	0,286	0,008	0,042	99,922
DR-10-R5b-3 Alt Px ?	51,232	0,479	0,091	1,641	9,081	0,237	15,482	20,206	0,284	0,000	0,026	98,759
DR-10-R5b-4 Alt Px ?	47,212	1,271	0,045	5,695	14,771	0,254	14,385	10,879	0,949	1,087	0,000	96,548
DR-10-R5b-5 Alt Px?	47,897	1,116	0,016	6,024	12,432	0,259	16,066	10,797	1,155	1,151	0,006	96,919
DR-10-R5b-6 Alt Px ?	43,310	0,027	0,118	5,678	14,786	0,179	16,558	1,960	0,651	0,988	0,000	84,255

Microprobe compositions

Page 39

Sample DR-10 Feldspars	SiO ₂	TiO ₂	Cr ₂ O ₃	Al ₂ O ₃	FeO _{total}	MnO	MgO	CaO	Na ₂ O	K ₂ O	Total
DR-10-R5b-10	65,162	0,095	0,000	18,828	0,245	0,002	0,004	0,696	3,573	11,367	99,972
DR-10-R5b-11	57,974	0,074	0,000	26,050	0,717	0,016	0,042	8,526	6,209	0,388	99,996
DR-10-R5b-12	56,933	0,052	0,029	26,565	0,791	0,007	0,039	9,454	5,830	0,345	100,045
DR-10-R5b-13	64,366	0,062	0,000	21,682	0,424	0,000	0,008	3,672	8,375	1,000	99,589
DR-10-R5b-14	54,992	0,057	0,036	27,951	0,488	0,009	0,025	10,688	5,124	0,340	99,710
DR-10-R5b-15	53,701	0,076	0,000	28,708	0,972	0,011	0,060	12,146	4,120	0,230	100,024
DR-10-R2-1	65,268	0,059	0,001	18,831	0,178	0,000	0,014	0,310	3,871	11,297	99,829
DR-10-R2-2	59,531	0,087	0,011	24,040	0,725	0,000	0,195	6,619	7,308	0,305	98,821
DR-10-R2-3	65,020	0,079	0,000	18,912	0,294	0,018	0,000	0,591	3,897	11,243	100,054
DR-10-R2-4	66,105	0,058	0,036	18,859	0,194	0,001	0,000	0,185	4,479	10,614	100,531
DR-10-R2-5	64,333	0,061	0,000	22,224	0,431	0,013	0,013	3,814	8,859	0,963	100,711
DR-10-R2-6	64,562	0,083	0,009	22,233	0,376	0,000	0,009	3,585	9,287	0,428	100,572
DR-10-R2-7	65,319	0,110	0,000	19,129	0,211	0,000	0,001	0,637	4,856	9,537	99,800
DR-10-R2-8	64,000	0,116	0,040	22,031	0,423	0,000	0,000	3,437	8,880	1,007	99,934
DR-10-R2-9	65,866	0,095	0,000	18,809	0,255	0,002	0,005	0,362	4,228	10,855	100,477
DR-10-R2-10	65,846	0,118	0,000	19,024	0,215	0,016	0,003	0,448	4,813	9,884	100,367

Diabase

Sample DR-6	SiO ₂	TiO ₂	Cr ₂ O ₃	Al ₂ O ₃	FeO _{total}	MnO	MgO	CaO	Na ₂ O	K ₂ O	Total
DCW-77-6-R1-Plag 1	47,58	0,024	0,012	29,89	4,32	0,087	0,511	11,81	2,59	1,57	98,39
DCW-77-6-R1-Plag 2	57,69	0,047	0,012	25,71	0,611	0,025	0,053	8,20	6,45	0,544	99,34
DCW-77-6-R1-Plag 3	50,88	0,025	0,017	28,27	3,62	0,033	0,390	11,88	4,09	0,677	99,87
DCW-77-6-R1-Plag 4	52,96	0,060	0,000	28,88	1,04	0,000	0,121	12,04	4,39	0,273	99,76
DCW-77-6-R1-Plag 5	54,67	0,079	0,000	27,28	0,758	0,000	0,074	10,68	5,33	0,334	99,20
DCW-77-6-R1-Plag 6	52,89	0,053	0,000	28,64	0,745	0,000	0,156	12,23	4,47	0,263	99,45
DCW-77-6-R1-Plag 7	57,52	0,041	0,000	25,76	0,706	0,021	0,040	8,26	6,41	0,534	99,29
DCW-77-6-R1-Px 1	51,39	0,466	0,005	1,57	19,15	0,447	19,44	7,10	0,146	0,000	99,70
DCW-77-6-R1-Px 2	52,45	0,327	0,000	1,15	19,34	0,463	21,98	4,60	0,072	0,006	100,38
DCW-77-6-R1-Px 3	50,57	0,365	0,000	0,776	27,74	0,609	15,50	4,92	0,049	0,002	100,53
DCW-77-6-R1-Px 4	50,23	0,315	0,008	1,54	16,71	0,496	9,44	20,87	0,522	0,009	100,14
DCW-77-6-R1-Px 5	52,10	0,242	0,295	1,94	6,93	0,196	17,93	19,68	0,192	0,010	99,52
DCW-77-6-R1-Px 6	52,27	0,341	0,159	1,96	7,12	0,193	17,85	19,47	0,221	0,000	99,57
DCW-77-6-R1-Px 7	50,12	0,284	0,000	1,80	15,85	0,497	10,52	20,23	0,458	0,063	99,83
DCW-77-6-R1-Px 8	52,83	0,209	0,030	1,02	16,13	0,374	23,39	5,66	0,090	0,004	99,73
DCW-77-6-R1-Fe Ti Ox 1	0,318	50,31	0,037	0,441	43,16	0,303	1,34	0,114	0,000	0,000	96,02

Microprobe compositions

Page 41

Altered impact breccia

Sample 4-63-931-306	SiO ₂	TiO ₂	Cr ₂ O ₃	Al ₂ O ₃	FeO _{total}	MnO	MgO	CaO	Na ₂ O	K ₂ O	NiO	Total
4-63-931-306-Reg1-PX1	51,82	0,169	0,110	1,87	8,85	0,378	13,58	22,28	0,585	0,002	0,000	99,65
4-63-931-306-Reg1-PX2	52,03	0,209	0,081	1,74	9,25	0,308	14,01	21,73	0,562	0,002	0,000	99,93
4-63-931-306-Reg1-Biot 1	38,23	4,66	0,100	13,56	11,87	0,086	17,31	0,007	0,072	10,03	0,000	95,92
4-63-931-306-Reg1-Fe Ox 1	0,080	0,071	1,32	0,286	89,12	0,050	0,094	0,056	0,000	0,044	0,000	91,12
4-63-931-306-Reg1-Plag 1	59,67	0,006	0,012	25,46	0,116	0,004	0,000	7,14	7,33	0,271	0,000	100,02
4-63-931-306-Reg1-Plag 2	59,41	0,000	0,000	25,61	0,080	0,000	0,000	7,34	7,27	0,263	0,000	99,97
4-63-931-306-Reg1-Plag 3	59,25	0,027	0,000	25,34	0,130	0,006	0,010	7,10	7,30	0,278	0,000	99,45
4-63-931-306-Reg1-Kspar 1	65,13	0,000	0,000	18,26	0,102	0,000	0,012	0,000	0,551	15,97	0,001	100,03
4-63-931-306-Reg1-Plag Plag 4	59,35	0,000	0,000	25,46	0,049	0,009	0,010	7,14	7,44	0,179	0,000	99,64
4-63-931-306-Reg1-Plag 5	59,26	0,017	0,004	25,53	0,087	0,000	0,017	7,03	7,26	0,228	0,000	99,42
4-63-931-306-Reg1-Apatite 1	1,04	0,000	0,000	0,253	0,095	0,045	0,018	54,11	0,076	0,002	40,38	96,03
4-63-931-306-Reg1-Apatite 2	0,664	0,000	0,000	0,139	0,092	0,042	0,027	54,74	0,120	0,000	40,44	96,27
4-63-931-306-Reg1-Fe Ox 2	0,239	0,032	1,14	0,155	87,88	0,000	0,061	0,082	0,000	0,008	0,000	89,59
4-63-931-306-Reg1-PX 3	51,65	0,191	0,045	1,89	8,81	0,332	13,68	22,25	0,561	0,012	0,000	99,42
4-63-931-306-Reg1-PX 4	52,02	0,169	0,088	1,60	8,80	0,337	13,86	22,16	0,589	0,011	0,000	99,65
4-63-931-306-Reg1-PX 5	51,49	0,272	0,062	2,01	10,19	0,368	13,83	21,03	0,589	0,009	0,000	99,85
4-63-931-306-Reg1-Biot 2	38,23	4,74	0,105	13,51	12,00	0,091	17,05	0,01	0,045	10,09	0,000	95,86
4-63-931-306-Reg1-Biot 3	38,32	4,39	0,125	13,35	12,15	0,075	17,07	0,00	0,082	10,07	0,000	95,64
4-63-931-306-Reg1-PX 6	52,07	0,136	0,087	1,65	8,78	0,338	13,94	22,00	0,528	0,000	0,000	99,52
4-63-931-306-Reg1-PX 8	51,83	0,205	0,061	1,96	8,79	0,355	13,57	22,46	0,622	0,000	0,000	99,86
4-63-931-306-Reg1-PX 8	51,82	0,208	0,126	1,84	9,33	0,370	13,73	21,73	0,608	0,008	0,000	99,77
4-63-931-306-Reg1-Plag 5	59,60	0,009	0,019	25,22	0,091	0,013	0,009	7,16	7,30	0,230	0,000	99,65
4-63-931-306-Reg1-Kspar 2	64,73	0,017	0,000	18,39	0,072	0,030	0,006	0,102	0,557	15,90	0,000	99,80
4-63-931-306-Reg1-Plag 6	59,32	0,000	0,000	25,56	0,223	0,012	0,072	7,37	7,28	0,199	0,000	100,04
4-63-931-306-Reg2-Apatite 1	0,382	0,000	0,000	0,008	0,145	0,052	0,015	54,59	0,091	0,014	40,74	96,04
4-63-931-306-Reg2-Apatite 2	0,882	0,000	0,000	0,165	0,122	0,045	0,068	53,78	0,114	0,000	39,74	94,91
4-63-931-306-Reg2-Apatite 3	0,445	0,000	0,000	0,011	0,128	0,049	0,033	54,76	0,022	0,009	40,64	96,10

Microprobe compositions

Page 42

Sample 4-63-931-306	SiO ₂	TiO ₂	Cr ₂ O ₃	Al ₂ O ₃	FeO _{total}	MnO	MgO	CaO	Na ₂ O	K ₂ O	NiO	Total
4-63-931-306-Reg2-Fe Oxide 1	5,76	0,002	0,000	0,496	79,61	0,337	0,148	0,728	0,011	0,010	0,000	87,11
4-63-931-306-Reg2-Biotite 1	37,81	4,65	0,098	13,50	12,86	0,096	16,14	0,025	0,079	9,90	0,000	95,15
4-63-931-306-Reg2-Biotite 2	37,64	4,53	0,090	13,32	12,39	0,082	16,48	0,028	0,086	9,94	0,000	94,57
4-63-931-306-Reg2-Biotite 3	38,06	4,71	0,091	13,36	12,45	0,090	16,41	0,006	0,082	9,94	0,000	95,20
4-63-931-306-Reg2-Biotite 4	37,84	4,67	0,054	13,32	12,59	0,041	16,34	0,061	0,087	9,85	0,000	94,84
4-63-931-306-Reg2-Biotite 5	37,48	4,82	0,025	13,41	12,75	0,058	16,35	0,028	0,093	9,97	0,000	94,98
4-63-931-306-Reg2-Plag 1	59,00	0,006	0,000	25,20	0,110	0,000	0,003	7,03	7,54	0,318	0,000	99,20
4-63-931-306-Reg2-Plag 2	59,87	0,000	0,016	25,02	0,108	0,000	0,002	6,88	7,42	0,383	0,000	99,71
4-63-931-306-Reg2-Plag 3	59,60	0,022	0,004	25,45	0,087	0,000	0,009	7,02	7,50	0,347	0,000	100,03
4-63-931-306-Reg2-Plag 4	58,85	0,018	0,005	25,84	0,204	0,010	0,013	7,43	7,29	0,249	0,000	99,90
4-63-931-306-Reg2-Plag 5	59,44	0,013	0,000	25,10	0,092	0,003	0,000	6,93	7,46	0,277	0,006	99,33
4-63-931-306-Reg2-Plag 6	59,20	0,003	0,006	25,17	0,154	0,000	0,001	7,14	7,38	0,255	0,000	99,31
4-63-931-306-Reg3-kspar 1	64,44	0,040	0,000	18,48	0,033	0,007	0,000	0,122	1,28	15,14	0,016	99,56
4-63-931-306-Reg3-kspar 2	64,63	0,063	0,000	18,46	0,051	0,000	0,000	0,071	1,15	15,13	0,006	99,56
4-63-931-306-Reg3-kspar 3	64,96	0,041	0,000	18,35	0,045	0,000	0,000	0,063	1,03	15,13	0,010	99,63
4-63-931-306-Reg3-kspar 4	68,41	0,000	0,010	19,21	0,002	0,018	0,000	0,130	11,56	0,214	0,003	99,56
4-63-931-306-Reg3-kspar 5	64,61	0,048	0,000	18,49	0,105	0,021	0,000	0,036	0,533	15,86	0,022	99,72
4-63-931-306-Reg3-biotite 1	38,34	3,90	0,000	13,56	11,37	0,102	17,99	0,029	0,088	9,87	0,000	95,24
4-63-931-306-Reg3-biotite 2	38,28	3,544	0,000	13,46	11,52	0,103	17,97	0,031	0,172	9,91	0,000	94,99
4-63-931-306-Reg3-apatite 1	0,733	0,012	0,000	0,051	0,121	0,064	0,149	53,13	0,043	0,000	39,64	93,95
4-63-931-306-Reg3-apatite 2	0,478	0,000	0,000	0,000	0,110	0,044	0,008	54,10	0,112	0,001	40,41	95,26
4-63-931-306-Reg3-Fe oxide 1	0,045	0,022	0,151	0,025	89,28	0,015	0,021	0,02	0,031	0,000	0,000	89,61
4-63-931-306-Reg3-Plag 1	59,76	0,012	0,025	25,19	0,063	0,009	0,013	6,87	7,62	0,130	0,000	99,70
4-63-931-306-Reg3-Plag 2	59,32	0,020	0,000	25,33	0,125	0,003	0,000	7,11	7,58	0,143	0,000	99,63
4-63-931-306-Reg3-Plag 3	58,85	0,000	0,001	25,53	0,119	0,000	0,012	7,39	7,41	0,116	0,000	99,44
4-63-931-306-Reg3-biotite 3	39,32	2,63	0,000	12,23	12,16	0,119	18,22	0,035	0,079	9,66	0,000	94,45
4-63-931-306-Reg3-Px 1	53,20	0,185	0,000	2,75	7,40	0,352	19,16	12,68	0,354	0,189	0,000	96,27
4-63-931-306-Reg4- Fe Ti Oxide	0,009	49,07	0,000	0,039	40,78	4,852	0,054	0,000	0,017	0,000	0,000	94,81
4-63-931-306-Reg4- Fe oxide 1	0,010	0,025	0,143	0,100	82,63	0,000	0,011	0,016	0,000	0,000	0,000	82,94

Microprobe compositions

Page 43

Sample 4-63-931-306	SiO ₂	TiO ₂	Cr ₂ O ₃	Al ₂ O ₃	FeO _{total}	MnO	MgO	CaO	Na ₂ O	K ₂ O	NiO	Total
4-63-931-306-Reg4- Fe oxide 2	0,092	49,38	0,000	0,070	39,66	4,428	0,059	0,019	0,030	0,001	0,000	93,73
4-63-931-306-Reg4- Fe oxide 3	0,499	0,039	0,160	0,076	88,00	0,033	0,000	0,085	0,000	0,010	0,000	88,90
4-63-931-306-Reg4- Apatite 1	0,410	0,000	0,000	0,000	0,070	0,051	0,008	54,41	0,085	0,013	40,28	95,33
4-63-931-306-Reg4- Px 1	51,38	0,222	0,000	2,02	10,19	0,369	13,59	20,79	0,559	0,012	0,000	99,13
4-63-931-306-Reg4- Px 2	51,47	0,245	0,019	2,16	9,48	0,354	13,52	21,86	0,610	0,000	0,000	99,71
4-63-931-306-Reg4- Px 3	49,45	0,257	0,037	2,03	8,36	0,338	13,01	20,40	0,622	0,000	0,000	94,51
4-63-931-306-Reg4- Px 4	51,51	0,248	0,015	2,24	10,28	0,358	13,48	21,30	0,624	0,000	0,000	100,05
4-63-931-306-Reg4- Px 5	51,41	0,276	0,034	2,21	10,11	0,313	13,27	21,29	0,665	0,000	0,000	99,57
Sample 4A-63-936-195	SiO ₂	TiO ₂	Cr ₂ O ₃	Al ₂ O ₃	FeO _{total}	MnO	MgO	CaO	Na ₂ O	K ₂ O	Total	
4A-63-936 - region 1 - kspar 1	64,55	0,023	0,000	18,28	0,049	0,000	0,010	0,060	0,859	15,32	99,15	
4A-63-936 - region 1 - kspar 2	66,45	0,000	0,000	19,86	0,372	0,010	0,174	0,143	10,77	0,833	98,61	
4A-63-936 - region 1 - plag 1	68,69	0,017	0,003	19,53	0,041	0,000	0,000	0,049	11,99	0,032	100,35	
4A-63-936 - region 1 - plag 2	99,59	0,052	0,000	0,008	0,046	0,000	0,000	0,003	0,000	0,009	99,71	
4A-63-936 - region 1 - kspar 3	64,11	0,000	0,000	18,25	0,081	0,000	0,000	0,009	0,397	16,02	98,87	

Altered diorite/tonalite ?

Sample DCW-77-38	SiO ₂	TiO ₂	Cr ₂ O ₃	Al ₂ O ₃	FeO _{total}	MnO	MgO	CaO	Na ₂ O	K ₂ O	Total
DCW-77-38-R1-PX1	52,00	0,095	0,000	0,861	22,60	0,910	22,34	0,770	0,025	0,002	99,60
DCW-77-38-R1-PX2	52,21	0,097	0,020	0,847	22,93	0,884	22,42	0,639	0,022	0,000	100,06
DCW-77-38-R1-PX3	52,51	0,088	0,012	0,523	22,70	0,883	22,55	0,607	0,000	0,000	99,87
DCW-77-38-R1-PX4	51,90	0,074	0,020	1,22	8,53	0,358	14,33	22,01	0,590	0,010	99,06
DCW-77-38-R1-PX5	52,26	0,086	0,005	0,738	22,50	0,924	22,82	0,570	0,028	0,000	99,92
DCW-77-38-R1-Fe Ox 1	0,065	0,016	0,000	0,285	88,67	0,041	0,003	0,008	0,025	0,000	89,11
DCW-77-38-R1-Fe Ox 2	0,025	0,023	0,063	0,256	89,27	0,011	0,000	0,025	0,014	0,007	89,69
DCW-77-38-R1-Plag 1	61,77	0,006	0,000	24,30	0,213	0,005	0,000	5,80	8,31	0,234	100,64
DCW-77-38-R1-Plag 2	60,36	0,000	0,000	20,84	0,215	0,010	0,000	0,012	12,22	0,082	93,75
DCW-77-38-R1-Plag 3	65,84	0,000	0,000	21,32	0,102	0,000	0,020	2,50	9,623	0,920	100,32
DCW-77-38-R1-Plag 4	61,59	0,022	0,000	20,35	0,013	0,025	0,000	0,313	9,944	0,060	92,31
DCW-77-38-R1-Plag 5	99,50	0,026	0,000	0,397	0,123	0,011	0,001	0,022	0,172	0,007	100,26
DCW-77-38-R1-Plag 6	100,24	0,007	0,010	0,032	0,026	0,000	0,004	0,037	0,005	0,000	100,36
DCW-77-38-R1-Plag 7	99,55	0,031	0,000	0,034	0,013	0,000	0,000	0,026	0,018	0,000	99,67
DCW-77-38-R1-Plag 8	62,91	0,036	0,000	19,80	0,035	0,023	0,000	0,334	8,98	0,073	92,19
DCW-77-38-R1-Plag 9	61,90	0,018	0,005	23,02	0,123	0,000	0,000	5,102	6,32	1,74	98,23
DCW-77-38-R1-Plag 10	61,54	0,000	0,000	23,11	0,109	0,000	0,000	5,149	6,46	1,76	98,13
DCW-77-38-R1-Plag 11	67,98	0,061	0,000	19,38	0,023	0,000	0,000	0,291	11,32	0,242	99,30
DCW-77-38-R1-Plag 12	61,48	0,011	0,000	22,98	0,081	0,000	0,003	5,35	6,38	1,64	97,91
DCW-77-38-R2-Plag 1	98,88	0,061	0,006	0,39	0,104	0,021	0,000	0,041	0,170	0,019	99,69
DCW-77-38-R2-Plag 2	61,57	0,006	0,011	23,01	0,122	0,000	0,000	4,99	6,54	1,70	97,95
DCW-77-38-R2-Plag 3	99,02	0,008	0,000	0,214	0,104	0,000	0,008	0,021	0,068	0,000	99,44
DCW-77-38-R2-Plag 4	61,45	0,014	0,000	23,05	0,105	0,000	0,006	5,13	6,40	1,78	97,92
DCW-77-38-R2-Plag 5	97,35	0,010	0,000	1,03	0,073	0,006	0,006	0,149	0,462	0,016	99,10
DCW-77-38-R2-Plag 6	61,43	0,016	0,037	23,18	0,087	0,015	0,000	4,82	6,52	1,80	97,91
DCW-77-38-R2-Plag 7	60,45	0,000	0,000	22,96	0,072	0,001	0,000	5,13	6,29	1,86	96,76
DCW-77-38-R2-Biot 1	37,24	4,84	0,026	14,49	12,92	0,005	15,92	0,016	0,130	9,84	95,42
DCW-77-38-R2-Biot 2	38,04	4,67	0,034	15,63	12,07	0,010	16,22	0,068	1,25	7,26	95,24
DCW-77-38-R2-Biot 3	36,91	4,80	0,020	14,67	13,04	0,015	15,94	0,002	0,146	9,91	95,45
DCW-77-38-R2-Px 1	51,94	0,086	0,000	0,821	22,39	1,02	22,47	0,587	0,013	0,020	99,34
DCW-77-38-R2-Px 2	52,00	0,105	0,019	0,835	22,55	1,02	22,60	0,676	0,026	0,012	99,84

A SPURRITE-, MERWINITE- AND SREBRODOLSKITE-BEARING SKARN ASSEMBLAGE, WEST CLEARWATER LAKE IMPACT CRATER, NORTHERN QUEBEC

DANIEL F. ROSA[§] AND ROBERT F. MARTIN

*Department of Earth and Planetary Sciences, McGill University, 3450 University Street,
 Montreal, Quebec H3A 2A7, Canada*

ABSTRACT

The meteorite impact that created the 32-km-wide Late Carboniferous West Clearwater structure, situated about 125 km east of the Hudson Bay arc, northern Quebec, formed a sheet of impact melt now exposed on a central ring of islands. We describe the textures and mineralogy of two xenoliths of partially metamorphosed limestone. These blocks represent recrystallized remnants of a cover of Middle Ordovician limestone, now completely eroded in the area. The fossiliferous dolomite-bearing limestone recrystallized to granoblastic calcite + periclase marble when the blocs landed in the sheet of impact-generated melt. The silica content of the marble led to the formation of a sanidinite-facies assemblage of unusual nesosilicates such as spurrite, merwinite, and monticellite. Aluminian srebrodolskite, $\text{Ca}_2(\text{Fe}^{3+}, \text{Al})_2\text{O}_5$, is found in material with a composition similar to “Portland cement clinker”. Phase equilibrium and stratigraphic data constrain the minimum peak conditions of metamorphism at $T > 815^\circ\text{C}$, $P < 100$ bar and $X(\text{CO}_2) > 0.1$. Retrograde mineral assemblages indicate that $X(\text{CO}_2)$ dropped to less than 0.1 shortly after the peak of metamorphism. Portlandite and brucite formed during the late hydration of the assemblage upon cooling.

Keywords: skarn assemblage, sanidine facies, spurrite, merwinite, srebrodolskite, retrograde effects, West Clearwater Lake impact, Quebec.

SOMMAIRE

L'impact météoritique qui a créé au Carbonifère supérieur la structure du lac à l'Eau Claire, cratère ouest, d'un diamètre de 32 km, située à environ 125 km à l'est de l'arc de la Baie d'Hudson, a causé la fusion de la croûte archéenne; les roches résultantes affleurent sur un anneau d'îles près du centre de la structure. Nous décrivons les textures et la minéralogie de deux fragments de calcaire partiellement recristallisé. Ces blocs seraient des fragments d'une couche de calcaire d'âge Ordovicien moyen, maintenant complètement érodée. Les blocs de calcaire fossilifère ont recristallisé en marbre granoblastique à calcite + périclase. La présence de quartz dans le calcaire a rendu possible la production de nésosilicates inhabituels appartenant au faciès sanidinite, comme la spurrite, la merwinite, et la monticellite. Nous y avons trouvé de la srébrodolskite alumineuse, $\text{Ca}_2(\text{Fe}^{3+}, \text{Al})_2\text{O}_5$, encastée dans un matériau ayant une composition semblable à celle des scories de ciment de Portland. L'étude des équilibres de phases, ainsi que des considérations stratigraphiques, indiquent un paroxysme métamorphique à $T > 815^\circ\text{C}$, $P < 100$ bars et $X(\text{CO}_2) > 0.1$. Les assemblages rétrogrades indiquent une phase fluide ayant $X(\text{CO}_2)$ inférieure à 0.1 tôt dans la période rétrograde. La portlandite et la brucite sont des phases rétrogrades formées lors de l'hydratation des enclaves pendant le refroidissement de l'assemblage.

Mots-clés: assemblage de skarn, faciès sanidinite, spurrite, merwinite, srébrodolskite, effets de rétrogression, structure d'impact du lac à L'Eau Claire (cratère ouest), Québec.

[§] E-mail address: daniel.rosa@mail.mcgill.ca

INTRODUCTION

Impact craters are the result of the hypervelocity impact of a comet or an asteroid with a planetary surface. Impact cratering is now recognized as a ubiquitous geological phenomenon that affects all the bodies of the solar system with a solid surface. The central area of the West Clearwater Lake, in northern Quebec, is one of the rare locations at the surface of the Earth where it is possible to observe and study the products of such an impact event. Impact melting occurs during the initial stages of impact crater formation, when the target rocks suddenly decompress after the passage of the shock wave through the target area. At the West Clearwater impact structure, blocks of limestone are found embedded in the impact melt. The metamorphism at the contact between the impact-generated melt and the limestone has produced a metamorphic assemblage of unusually high-grade marbles. The episode of contact metamorphism was extremely brief, as it involved the incorporation of blocks in a sheet of likely superheated silicate magma generated by the meteor impact. This locality constitutes one of only 30 or so known occurrences worldwide of rocks subjected to the sanidinite facies of contact metamorphism (Wiechmann 1995, Rosa 2004). Of the short list of occurrences of such high-grade skarn assemblages, this seems to be the first example of metamorphism of limestone by an impact-generated magma. Our purpose here is to describe the occurrence, characterize the unusual assemblages of minerals, and discuss the possible physical conditions of metamorphism.

THE GEOLOGICAL CONTEXT

The West Clearwater Lake structure is a complex impact structure located at 56°14'N, 74°30'W, in northern Quebec, about 125 km east of the Hudson Bay arc (Fig. 1). The structure forms the western half of a double circular lake known as Lac à l'Eau Claire, the partially eroded and flooded remains of two craters caused by the almost simultaneous impact of two asteroids, or of one fragmented asteroid (Dence *et al.* 1965, Phinney *et al.* 1978, Simonds *et al.* 1978, Grieve 1978, 2006, Reimold *et al.* 1981). In the western crater, 32 km in diameter, exposures of the impact melt overlying breccia and the shocked and fractured basement are prominent on a ring of islands about 12 km in diameter and at a few small islands near the center of the lake (Fig. 1). The smaller eastern crater, 22 km in diameter, is entirely flooded.

The target rocks are largely of Archean age. Simard *et al.* (2004) roughly divided these units into three major lithologies: 1) granites and granodiorites of the Desbergères Suite, 2) enderbites, diorites and tonalites of the Loups Marins Complex, and 3) mafic and ultramafic rocks of the Qullinaaraaluk suite. Simard *et al.* (2004) reported ages of 2714 ± 12 Ma and 2711

± 4 Ma for rocks of the Desbergères Suite in the area, whereas dating of the Lacs des Loups Marins diorites has yielded ages of 2694 ± 3 Ma (Gosselin *et al.* 2001). The mineral assemblages developed in these lithologies are consistent with metamorphism in the amphibolite to the granulite facies (Ciesielski & Plante 1990, Simard *et al.* 2004). The regional structural fabric is roughly oriented NNW–SSW, and its general orientation is delineated by strong positive aeromagnetic anomalies (Card & Ciesielski 1986, Percival *et al.* 1992). Several subvertical dykes of diabase of Proterozoic age have also been observed in the area (Plante 1986).

Blocks of grey fossiliferous dolomitic limestone float are regionally distributed and represent remnants of a veneer of Paleozoic rocks formerly covering the cratonic rocks. These blocks have been attributed an Edenian or Maysvillian age (Kranck & Sinclair 1963), and they are probably correlatives of the second member of the Portage Chute Formation of the Bad Cache Rapids Group. The type section is situated on the south side of Bad Cache Rapids on the Churchill River in northern Manitoba. Sanford *et al.* (1968) described these rocks as light grey microcrystalline dolomites and bioclastic limestones commonly exhibiting nodular bedding. Bostock (1969) was the first to map xenoliths of marble in the unusual “volcanic” (*sic*) rocks exposed on islands in West Clearwater Lake, and to notice the presence in them of spurrite, ideally $\text{Ca}_5(\text{SiO}_4)_2(\text{CO}_3)$. The unusual blocks of marble, locally still fossiliferous, represent partially to totally recrystallized middle Ordovician limestone embedded in the impact melt.

THE WEST CLEARWATER IMPACT STRUCTURE

Three major units of crater-fill deposits are exposed on the ring of islands in the western crater. In ascending order, they are: 1) a red friable impact-melt-bearing fragmental breccia between 0 and 20 m thick, 2) a red, massive and well-jointed clast-rich melt about 18 meters thick, commonly composed of a mixture of partially melted clasts of a variety of sizes in a very fine-grained groundmass of strongly altered glass, tiny partially melted fragments and rapidly crystallized melt, and 3) a massive, poorly jointed clast-poor melt, red at the base and greyish at the top, at least 85 m thick, that shows a fine-grained ophitic to subophitic texture (Simonds *et al.* 1978, Phinney *et al.* 1978, Rondot *et al.* 1993). Blocks up to 100 m across do occur in the impact-related units, but most of the visible population of clasts is centimetric to metric in scale. The clasts are most abundant in the fragmental breccia and the bottom of the clast-rich melt; they become rare above these two impact melt units. The clasts generally are pieces of the Archean target rock, but at least seven of the larger clasts observed at West Clearwater Lake are remnants of the Middle Ordovician limestone cover mentioned above (Rondot *et al.* 1993).

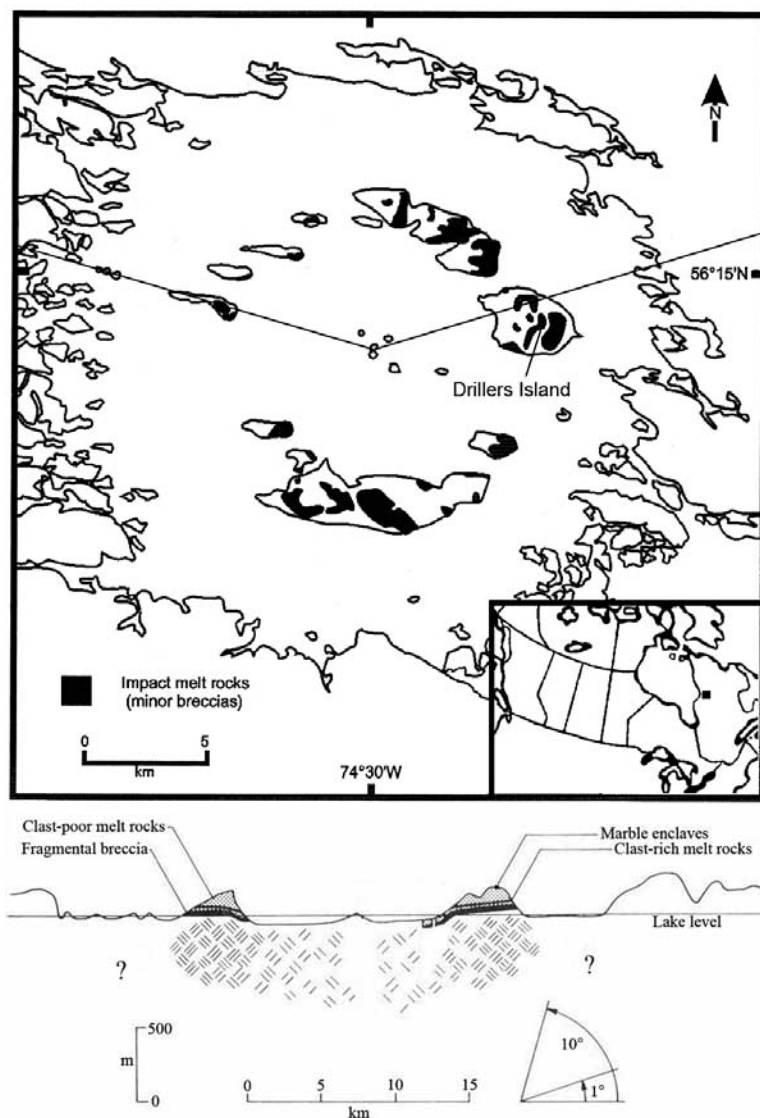


FIG. 1. Location map showing the West Clearwater Lake impact structure, and Drillers Island. Also shown is a generalized and vertically exaggerated cross-section of the West Clearwater structure (adapted from Simonds *et al.* 1978).

A quite sharp and easily visible chilled margin forms the contact between the fragmental breccia and the clast-rich melt; the transition from clast-rich melt rock to clast-poor melt rock above is even sharper (described as a knife-edge contact by Simonds *et al.* 1978). According to these authors, the contacts between these units all consistently dip at about 0.5° toward the center of the structure. The major-element composition of hand samples of the impact-generated melt rock is similar to the average composition of the country rocks

in the area of the impact structure. According to Rondot *et al.* (1993), the maximum thickness of impact melt exposed in the islands at the western crater is approximately 135 meters, from the fragmented target-rock up to the topmost melt unit. The preserved volume of the impact melt rocks is estimated by Grieve *et al.* (1977) and Simonds *et al.* (1978) to be about 24 km^3 .

The first estimates of age of impact were obtained by K–Ar whole-rock analysis of the impact melt from the western crater's ring of islands. These estimates

yielded Upper Pennsylvanian ages of 300 ± 24 Ma and 285 ± 23 Ma (Wanless *et al.* 1964, Bostock 1969). Later work on the eastern crater produced an age of 287 ± 26 Ma using the Rb–Sr method (Reimold *et al.* 1981). These ages are in agreement with fission-track annealing studies of glassy samples of melt from both craters (Fleischer *et al.* 1969, Storzer & Wagner 1977).

THE XENOLITHS SAMPLED

The main xenolith that was investigated, an approximately rectangular body of carbonate measuring 15×100 meters, is located in the northeastern uplands of Kamiskutanikaw Island (unofficially, Drillers Island; Fig. 1). Samples DR–01 to DR–05 and samples DR–07 and DR–08 were collected from this xenolith at a variety of locations. The southern part of the xenolith barely rises above the surrounding Quaternary rubble and impact melt, and white carbonate pebbles cover most of its surface, with a few white to bluish white blocks exposed. The northern part of the xenolith, however, lies a few meters above the surrounding impact melt, and it essentially consists of a less strongly metamorphosed grey limestone crossed by vein-like zones of metamorphosed white carbonate. Because most of the xenolith is covered by a talus of grey and white carbonate pebbles, ascertaining the location of the contacts between the main xenolith and the impact melt, and between the various domains of the main xenolith, would require extensive digging. The location of the hand samples relative to the contacts is, therefore, not well constrained (Fig. 2). Nevertheless, the distribution of the two colors

of carbonate suggests that the main xenolith consists of a relatively unmetamorphosed center of grey carbonate surrounded by an irregular shell of metamorphosed white carbonate (*i.e.*, marble).

The ninth sample, DR–09, was taken from the center of a much smaller and strongly altered xenolith of carbonate measuring about 5×5 m located approximately 200 m north of the much larger main xenolith.

MINERALOGY OF THE XENOLITHS

Hand samples from the main xenolith (Fig. 2) are composed of fine- to medium-grained, massive, bluish grey, white or grey granoblastic carbonate. Sample DR–09, recovered from the small xenolith, is very fine grained, almost aphanitic, and it displays centimetric veins of a very fine-grained dark grey material surrounding brownish grey areas of apparently less strongly altered minerals. With the exception of sample DR–09, all samples are composed, on average, of about 90–95% fine- to medium-grained calcite. The principal minerals encountered in the eight samples of marble are listed in Table 1. The methods of analysis used to characterize the main phases are described in an Appendix.

The *calcite* crystals generally adjoin each other at triple-point junctions and contain abundant tiny inclusions of a fluid phase, generally 1 to 3 μm across. Thin sections from two of the less strongly metamorphosed grey samples (DR–03 and DR–04) contain fossil fragments. An electron-microprobe analysis of the calcite reveals a high-purity phase, with little or no substitution of Mg, Fe or Sr for Ca (Table 2).

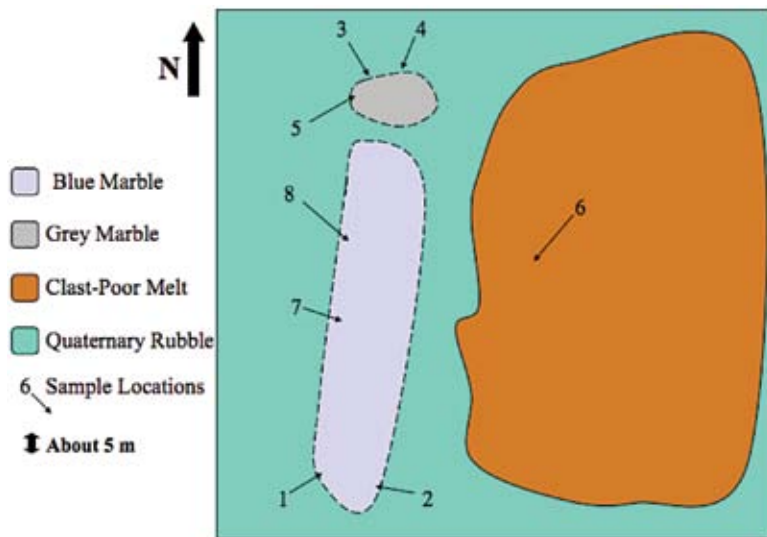


FIG. 2. Schematic map of the main enclave of marble, showing the approximate location of the samples.

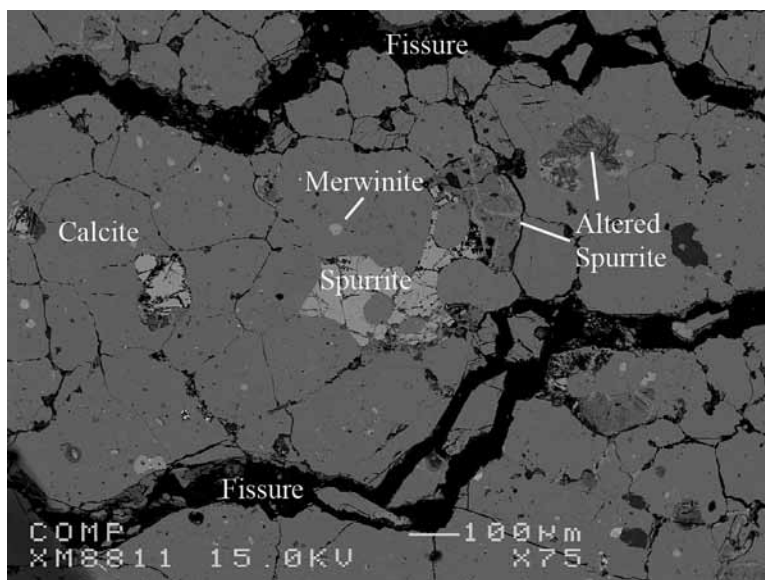


FIG. 3. Back-scattered electron (BSE) image of sample DR-02. Porphyroblasts of spurrite show signs of incipient alteration. Note the granoblastic texture of the calcite grains.

TABLE 1. DOMINANT MINERALS IN SAMPLES OF MARBLE FROM KAMISKUTANIKAW ISLAND*, WEST CLEARWATER LAKE, QUEBEC

DR-01	calcite + merwinite ± lizardite
DR-02	calcite + brucite + spurrite + merwinite ± perovskite ± monticellite
DR-03	calcite + spurrite ± pyrite ± spinel ± perovskite
DR-04	calcite + spurrite ± perovskite
DR-05	calcite + spurrite + brucite ± pyrite ± periclase
DR-07	calcite + spurrite + brucite + merwinite
DR-08	calcite + spurrite + brucite + merwinite
DR-09	calcite + portlandite + brucite ± periclase ± spurrite ± srebrodolskite

* unofficially, Drillers Island.

TABLE 2. REPRESENTATIVE COMPOSITIONS OF MINERALS FOUND IN MARBLE ENCLAVES, WEST CLEARWATER LAKE CRATER

	Cal	Brc	Spu	Mer	Srb	Per	Spl	Mtc
SiO ₂ wt. %	0.00	0.86	26.57	36.53	0.11	0.00	0.02	38.18
TiO ₂	0.00	0.00	0.07	0.03	0.94	0.00	0.20	0.04
Al ₂ O ₃	0.00	1.70	0.05	0.03	12.92	0.07	69.72	0.02
FeO _{total}	0.00	2.84	0.01	0.25	36.18	3.22	1.25	1.46
MgO	0.00	63.37	0.05	12.18	0.46	96.65	27.85	24.15
MnO	0.01					0.00	0.00	
CaO	56.28	2.08	62.40	51.37	45.63	0.32	0.33	36.97
SrO	0.06							
Cl			0.02	0.01	0.02	0.01	0.00	0.00
SO ₃		0.22	0.02	0.04		0.03	0.00	0.00
CO ₂	(43.64)		(10.81)					
H ₂ O		(36.49)						
Total	100.00	100.00	100.00	100.44	96.25	100.30	99.42	100.82
Si apfu	0.00	0.01	1.95	1.99	0.00	0.00	0.00	1.00
Ti	0.00	0.00	0.00	0.00	0.06	0.00	0.00	0.00
Al	0.00	0.02	0.00	0.00	0.59	0.00	1.97	0.00
Fe	0.00	0.02	0.00	0.01	1.20	0.02	0.03	0.03
Mg	0.00	0.94	0.01	0.99	0.05	0.98	1.00	0.94
Mn	0.00					0.00	0.00	
Ca	1.01	0.02	4.91	3.00	2.12	0.00	0.01	1.03
Cl	0.00		0.00	0.00	0.00	0.00	0.00	0.00
Sr	0.00							
S	0.00	0.00	0.00	0.00	0.00	0.00	0.00	0.00
C	(1.00)		(1.08)	0.00				0.00
H		(1.91)						
Total	2.01	2.93	7.96	6.00	4.04	1.00	3.01	3.00

In parentheses, calculated amounts according to stoichiometry. Symbols: Cal: calcite, Brc: brucite, Spu: spurrite, Mer: merwinite, Srb: srebrodolskite, Per: periclase, Spl: spinel, Mtc: monticellite. The compositions were acquired with an electron microprobe. The complete set of analytical data is available in Rosa (2004).

Spurrite, Ca₅(SiO₄)₂(CO₃), a monoclinic nesosilicate typical of contact metamorphism of siliceous limestone in the sanidinite facies (Spear 1993), is present in all the carbonate samples examined in our investigation (Fig. 3). It usually occurs as tiny (1 µm across or less) xenoblastic inclusions in calcite, but it also forms irregularly shaped partially altered poikiloblasts up to 2 mm across containing numerous round inclusions of calcite. In sample DR-09, which comes from the smaller xenolith, we encountered an idiomorphic crystal of spurrite 0.24 by 0.5 mm. The electron-microprobe analysis of fresh spurrite crystals (e.g., Table 2) gave overall compositions similar to those observed in other high-grade skarns, for example at Crestmore, California (Rogers 1929, Wiechmann 1995). The most abundant

pattern of spurrite alteration involves a loss of Ca and the neoformation of new Al-bearing phases. These new minerals appear as very small grainy black inclusions along thin dark grey cracks, or as black cracks in dark grey areas on microprobe scans. Under the microscope, the alteration causes a general darkening of the crystal, especially along fractures (Fig. 3).

The orthorhombic nesosilicate *monticellite*, CaMgSiO_4 , has been observed in a single large crystal of spurrite that partially envelops a grain of brucite in sample DR-02 (Figs. 4, 5). The monticellite fills a roughly radial network of small cracks in the spurrite crystal, which indicates that it is probably the result of yet another type of alteration of spurrite. The monticellite contains a small amount of Fe^{2+} (1.46 wt%), indicating partial Fe-for-Mg substitution. The source of the Fe may well have been ferroan periclase, considered to have been the precursor to the brucite.

Merwinite, $\text{Ca}_3\text{Mg}(\text{SiO}_4)_2$, another monoclinic nesosilicate (Figs. 3, 4), is quite common in samples DR-01, DR-02, DR-07 and DR-08, but absent in all other samples. It invariably occurs as small xenoblastic inclusions in grains of calcite. These inclusions are typically quite small (10 μm or less) and granular or slightly ovoid. The merwinite is close to being ideal in composition (Table 2).

Kamiskutanikaw Island is the site of the first Canadian occurrence of *srebrodolskite*, $\text{Ca}_2(\text{Fe}^{3+}, \text{Al})_2\text{O}_5$.

This orthorhombic oxide is the Fe^{3+} -dominant analogue of brownmillerite, $\text{Ca}_2(\text{Al}, \text{Fe}^{3+})_2\text{O}_5$, a phase commonly found in Portland cement clinker. At West Clearwater Lake, srebrodolskite occurs as squarish reddish brown platelets up to 5 to 20 μm across embedded in a dark, glassy material that forms the contact of centrimetric veins that cut through sample DR-09 (Figs. 6, 7). The composition of this glassy matrix, 25.77% SiO_2 , 1.22% $\text{FeO}_{\text{total}}$, 67.92% CaO , 3.14% SO_3 , total 100.93%, is close to that of artificially produced Portland cement clinker, *i.e.*, a partially fused product of a cement kiln obtained from the rapid heating of impure limestone (a representative composition of clinker is: 23.73% SiO_2 , 4.31% Al_2O_3 , 2.55% Fe_2O_3 , 65.60% CaO , 2.21% MgO , 1.00% SO_3 ; Lea 1970). Two crystals of srebrodolskite from thin section DR-09 were analyzed. Their composition is Al-rich, approaching 13 wt% Al_2O_3 , whereas the material from the type locality contains no detectable Al (Chesnokov & Bazhenova 1985, Chesnokov *et al.* 2008). Type-locality srebrodolskite occurs in petrified wood baked by burning coal in mines near Kopayska in the Chelyabinskiy coal basin in the southern Urals. There, srebrodolskite is derived from the calcining of ankerite. Srebrodolskite is known from only a handful of localities in the world.

With the exception of a few relict crystals, *periclase* no longer exists in the main xenolith. Periclase is an expected product of the high-grade metamorphism of

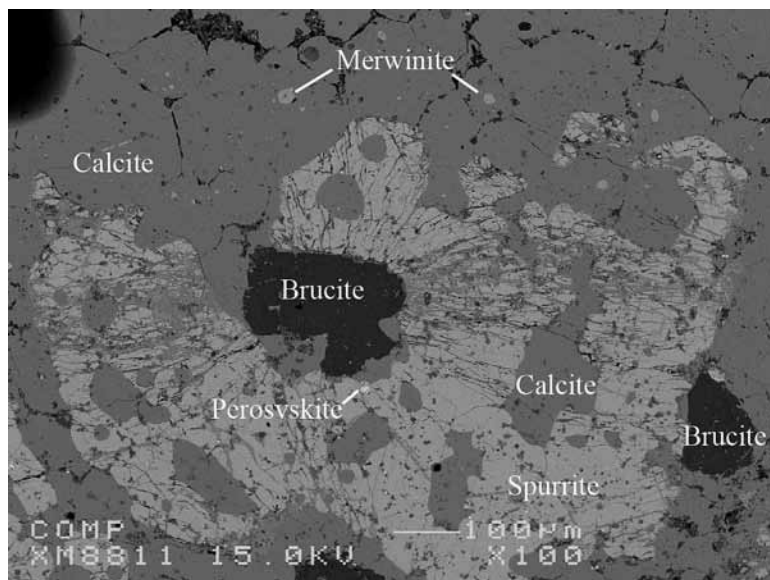


FIG. 4. Back-scattered electron image of sample DR-02. Monticellite fills the cracks in the crystal of spurrite. Local stresses related to the conversion of periclase (molar volume 11.25 cm^3) to brucite (molar volume 24.63 cm^3) forced open radial hairline fractures in the spurrite host, thus allowing aqueous fluids to carry Mg and Fe away from the site of the ferroan periclase to form the monticellite.

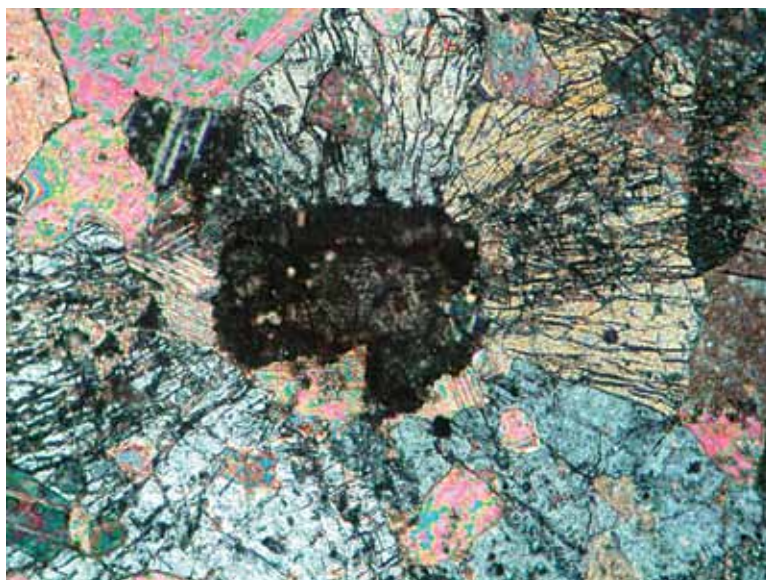


FIG. 5. Image of sample DR-02 under crossed polars (width of field of view: 0.8 mm). The dark mineral, which replaced ferroan periclase, is brucite. Radial fissures in the surrounding spurrite are lined with monticellite.

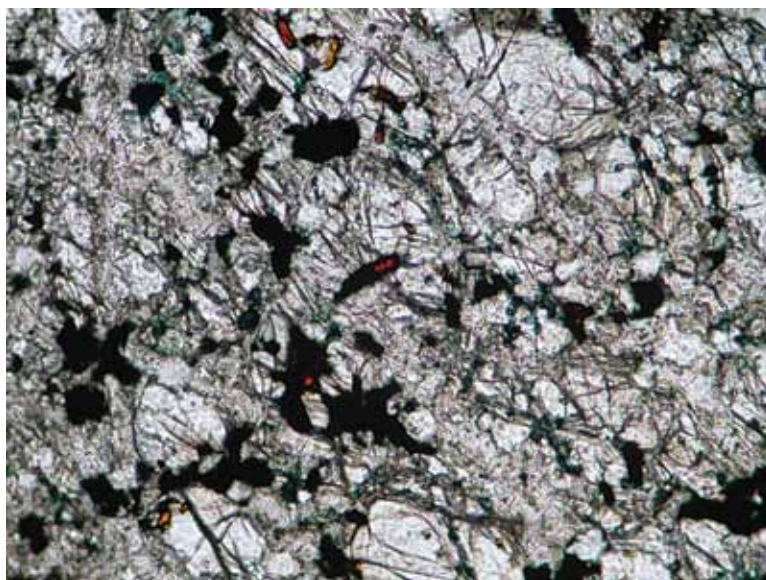


FIG. 6. Polished thin section of sample DR-09 (plane-polarized light, width of field of view 0.8 mm). The small dark brown to opaque crystals are aluminian srebrodolskite, each 15 to 20 μm across. Also present are sparse orange crystals of ferroan periclase. They are in a material with a composition similar to Portland cement clinker, which takes on a greenish color where altered.

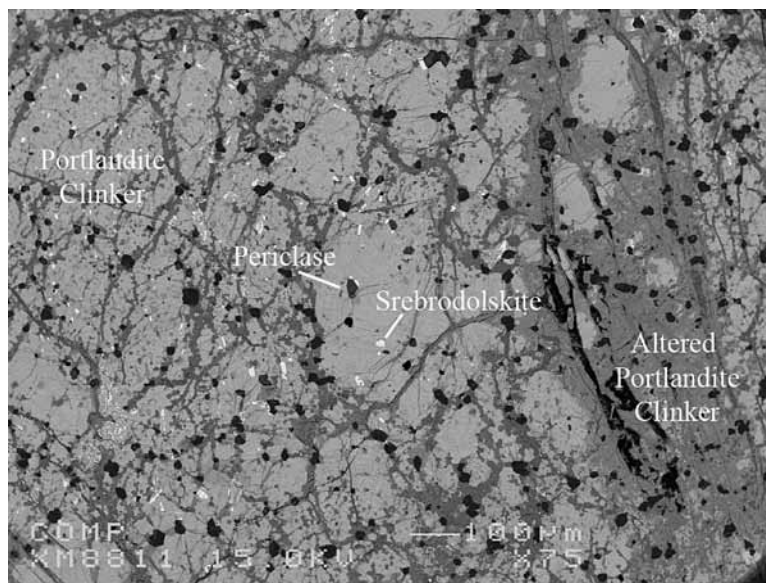


FIG. 7. BSE image of sample DR-09. Ferroan pericase and aluminian srebrodolskite are enclosed in material similar to Portland cement clinker.

dolomitic limestone (Bowen 1940). We interpret the radial cracks around a grain of brucite in Figures 4 and 5 as a result of a hydration reaction that consumed pericase, and caused a local increase in volume. The smaller enclave (DR-09) still contains pristine euhedral crystals of pericase 10 to 50 μm across embedded in the dark, glassy material with a composition similar to Portland cement clinker. These grains of pericase are generally closely associated with srebrodolskite (Fig. 7). They have an orange to pale yellow color in plane-polarized light, which is probably indicative of their relatively high iron content (about 3 wt% FeO).

The *brucite* grains encountered in the marble, 50 μm across (Figs. 4, 5), commonly show the typical “scaly-concentric” structure described by Rogers (1929). The composition of brucite are slightly cation-deficient (Table 2). In some grains, very small point-like Fe-rich inclusions can be seen in microprobe scans of crystals of brucite and of pericase partially transformed to brucite. These inclusions are too small to be analyzed, but they are probably magnetite, which is generally associated with brucite that originates from the retrograde alteration of ferroan pericase. In this respect, Rogers (1929) reported minute inclusions of magnetite in pericase at Crestmore, California. The appearance of this nonstoichiometric brucite at the expense of ferroan pericase may indicate that Fe^{3+} is present in this portion of the pericase–wüstite solid-solution series at the conditions of crystallization, just as it is in more iron-rich examples (McCammon & Liu 1984).

Sample DR-03 contains large interstitial masses of *pyrite*, surrounded by massive *spurrite*, with abundant inclusions of *spinel*, MgAlO_4 . *Spinel* is also present in the *spurrite*, and some grains even straddle the contact between sulfide and *spurrite*. *Pyrite* in reflected light in DR-03 has an irregular surface with abundant relief giving it a bumpy, cell-like aspect. In secondary electron images, the surface of these *pyrite* masses seems irregular and heterogeneous: most of the sulfide surface is taken by bright spots of *pyrite*, the rest being occupied by a grey compound seemingly made of a mixture of fine-grained minerals with the following general composition: 20.10 wt.% SiO_2 , 1.76% Al_2O_3 , 25.67% $\text{FeO}_{\text{total}}$, 35.93% CaO , 1.26% SO_3 , for a total of 84.85%. The scale of these features is much smaller than that of the cell-like bumps seen in reflected light. Because of its close association with the sulfide, the low sulfur content of this compound is surprising, but the only places where there was enough of this material for a quantitative analysis were invariably at the periphery of the *pyrite* mass. It is therefore possible that some oxidation involving a loss of sulfur has occurred. The *pyrite* presumably replaced *pyrrhotite*, the sulfide expected to be stable at conditions of the sanidinite facies of contact metamorphism.

The *spinel* forms small (30 μm or less) subhedral grains evenly distributed in the sulfide and the neighboring *spurrite*. A very thin dark rim surrounds most grains. The mineral is very close to the end-member composition, and contains about 1.25 wt% FeO.

Portlandite, $\text{Ca}(\text{OH})_2$, was detected in the X-ray powder-diffraction pattern of the sample obtained of the small enclave (DR-09). It was not detected with an optical microscope or in energy-dispersion scans, either because the thin section of DR-09 does not contain any, or because it is intermixed with other phases (probably calcite and lime).

Like portlandite, *lizardite*, $\text{Mg}_3\text{Si}_2\text{O}_5(\text{OH})_4$, was only detected by X-ray powder diffraction, and this only after dissolution of most of the carbonate. The thin section prepared of sample DR-01 contains globular low-relief areas that are colorless in plane-polarized light, and almost isotropic with crossed polars. These areas generally contain small inclusions of calcite, and they usually have a shape and distribution similar to those of the scaly globular brucite observed in other samples, but are generally smaller in size. The variable compositions of these areas suggest that they may be made of a mixture of fine-grained lizardite, an Al-bearing fine-grained phase (chlorite? kaolinite?) and calcite. It is also possible that the lizardite might contain Al in its structure.

Perovskite, CaTiO_3 , is usually present as barely discernible anhedral grains included in spurrite or altered spurrite. It is a rare phase, and it was only detected because of its characteristic brightness in back-scattered electron images.

Finally, we observed a few fine-grained assemblages that probably correspond to mixtures of a variety of

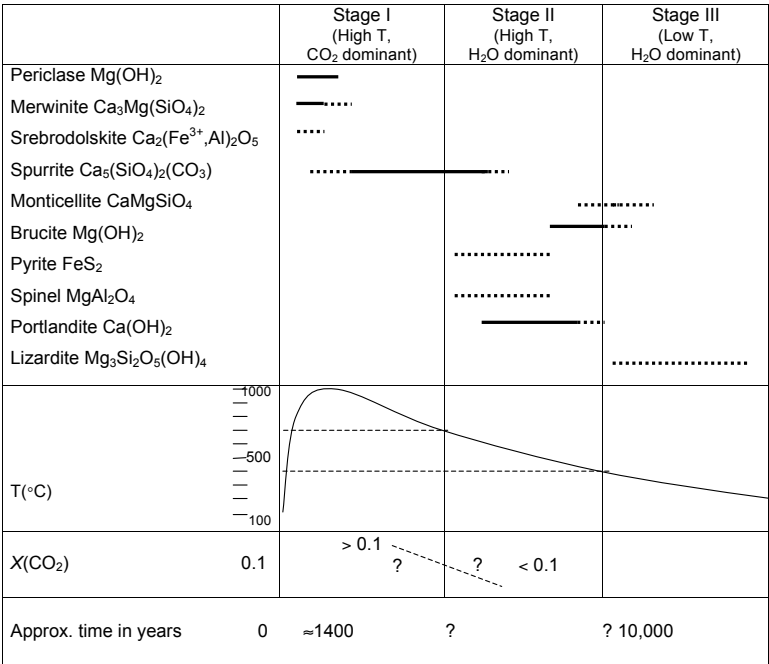
volatile-rich minerals (possibly hydrated calc-silicates) that have not been properly identified, either because of their small size and rarity, or because of devolatilization under the electron beam.

DISCUSSION

Carbonates do not show any real shock-metamorphic effects, besides shatter cones, until relatively high pressures are reached, at which point they start to melt (Osinski *et al.* 2008). Therefore, the effects of the impact event are not recorded in the thin veneer of limestone that covered the West Clearwater area at the time of impact. Instead, the enclaves seem to have been subjected only to post-impact static recrystallization, pseudomorphism and *in situ* retrograde effects. The enclaves might have become embedded in the sheet of impact-generated melt either by landing on it after a short flight, or by becoming engulfed in flowing impact-generated melt within the transient cavity. The smaller enclave seems to have begun melting, but at very low pressure, whereas in the large enclave, a steep thermal gradient evidently developed, to judge from the superficial nature of the contact-metamorphism demonstrated by the preservation of fossil fragments in the bulk of the enclave.

We contend that the carbonate xenoliths went through three distinct stages of metamorphism (Table 3). Stage I corresponds to the main prograde event, when the

TABLE 3. PARAGENESES OF MINERALS OBSERVED IN CARBONATE ENCLAVES AS A FUNCTION OF TEMPERATURE AT DRILLERS ISLAND, WEST CLEARWATER LAKE



sheet of impact-generated melt heated the blocks of limestone. During Stage II, high-temperature hydration took place during early cooling. Stage III corresponds to the formation of low-temperature hydrated phases during later stages of cooling. Note that this reconstruction does not imply a series of separate events.

Stage I: prograde metamorphism

Stage I is responsible for the major high-T phases (periclase, merwinite, spurrite), which formed "instantaneously" from the original impure limestone. The metamorphic reactions are grossly similar to the steps recognized in the industrial production of highly porous cement clinker by rapid heating of a clay-limestone mixture.

With rising temperatures, calcite was increasingly able to accommodate MgCO_3 in solid solution as it stably coexisted with sedimentary dolomite. But because of the low confining pressure (and CO_2 pressure) in the environment, the position of the calcite – dolomite – periclase triple point (680°C at a pressure of 100 bars) dictates that the magnesian calcite can contain at most 10 mol.% MgCO_3 . As the CO_2 was allowed to escape, most of the dolomite, or all of it, would quickly destabilize according to the reaction $\text{dolomite} \rightarrow \text{periclase} + \text{magnesian calcite} + \text{CO}_2$ at temperatures near or above the triple point. The solubility trend of Mg incorporation into calcite is expected to reverse upon continued heating, which favors the sustained production of periclase and effectively keeps the Mg content

in the calcite of the main enclave very low. At even higher temperatures, the formation of merwinite, which is generally present as small inclusions in calcite, may also have contributed to the extraction of any remaining Mg from the calcite structure (Graf & Goldsmith 1955, Goldsmith 1960, Wiechmann 1995).

The lowest possible temperature for the prograde metamorphic phase in the main enclave is constrained by the lower limit of stability of the assemblage merwinite + calcite, which is defined by the reaction $2 \text{ monticellite} + 2 \text{ spurrite} \rightarrow 2 \text{ merwinite} + \text{calcite}$ (Fig. 8). Walter (1965) showed experimentally that the stabilization of the assemblage merwinite + calcite requires, at pressures below 65 bars, a temperature of at least $820 \pm 10^\circ\text{C}$. However, the presence of portlandite, a common product of the hydration of lime (CaO), in the sample extracted from the small enclave indicates that temperatures near the contact with the sheet of impact melt were adequate to dissociate calcite into its CaO and CO_2 components. In the presence of excess CO_2 , the dissociation temperature of calcite at 1 bar is 894°C ; at pressures of 7 bar and 34 bar, it increases to 985° and 1100°C , respectively (Wyllie & Tuttle 1960, Deer *et al.* 1962). We ran an average composition of the impact melt through the MELTS program (Ghiorso & Sack 1995), and we obtained a liquidus temperature of 1134°C , but it should be noted that the impact melt was undoubtedly initially superheated to much higher temperatures, possibly of the order of $1500^\circ\text{--}1700^\circ\text{C}$.

The synthesis of spurrite has been achieved at geological relevant temperatures and pressures by

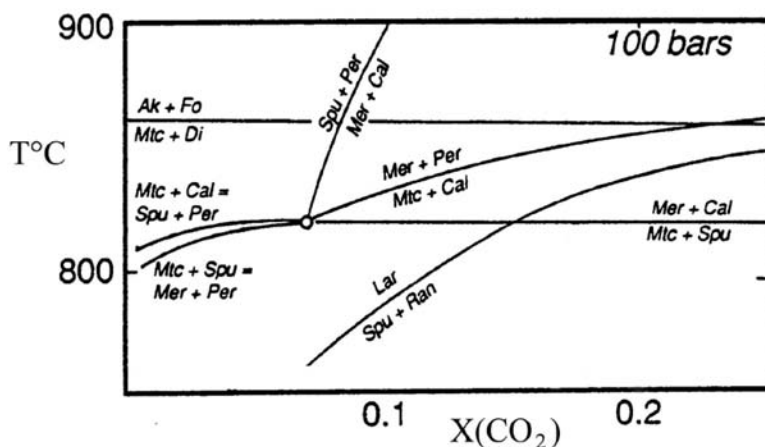


FIG. 8. Phase relations involving calcite, periclase and other relevant phases as a function of $X(\text{CO}_2)$. This diagram applies only to the peak conditions of metamorphism (stage I) observed in the main xenolith. Symbols: Ak: åkermanite, Cal: calcite, Di: diopside, Fo: forsterite, Lar: larnite, Mer: merwinite, Mtc: monticellite, Per: periclase, Ran: rankinite, Spu: spurrite. The diagram is based on experimental data of Harker & Tuttle (1955), Goldsmith (1960), Goldsmith & Heard (1961) and Goldsmith & Newton (1969). Adapted from Wiechmann (1995).

Tuttle & Harker (1957), Zharikov & Shmulovich (1969) and Henmi & Henmi (1978). The variety of conditions under which the synthesis of spurrite can take place shows that the formation of this mineral is highly dependent on fluid composition and pressures: for instance, at 1 kbar, with $P(\text{CO}_2) = P_{\text{total}}$, the reaction calcite + wollastonite = spurrite + CO_2 takes place at about 1200°C (Wyllie & Haas 1966); at 0.5 kbar, this reaction takes place at about 1000°C (Tuttle & Harker 1957). Kurdowski (1968) synthesized spurrite from its components plus 3% CaCl_2 and CO_2 at a pressure of 1 bar; spurrite began to appear at 650°C and was the only solid phase obtained in the range 840 to 920°C. Also, according to Treiman & Essene (1983), no lower-temperature limit has been established for the formation of spurrite. In Si-poor environments, the upper boundary of the stability field of spurrite is determined by melting (Zharikov & Shmulovich 1969).

During Stage I, the rapid heating of the calcareous rock by contact with the enclosing impact-generated melt caused the fluid pressure within the enclave to rapidly increase owing to the decarbonation reactions related to the formation of phases like spurrite. This devolatilization of the marble block caused the fluid pressure within the enclave to reach or even exceed the fluid pressure in the surrounding impact-melt. The solid assemblages buffered the fluid composition in the enclave, and the massive emission of CO_2 prevented exterior fluids from infiltrating the carbonate. The CO_2 content of the metamorphic fluids progressively rose as the enclave approached peak conditions of temperature.

Because none of the reactions involved in Stage I is useful for geobarometry, the pressure at the time of metamorphism can only be estimated. As the density of the impact melt is of about 2500 kg/m³ (Plante *et al.* 1990), and the amount of solidified impact melt above the main enclave removed by erosion probably did not exceed a thickness of about 100 meters (Rondot 1985, Rondot *et al.* 1993), we estimate that the lithostatic pressure on the carbonate enclaves was probably about 25–30 bars. It is unlikely that the overlying impact-melt was sufficiently impermeable to contain and pressurize the CO_2 produced by devolatilization of the carbonates: the purity of the calcite and the absence of retrograde reactions with CO_2 as a reactant show that the fluid phase resulting from decarbonation could easily escape the vicinity of the enclaves.

In this particular geological setting, where a large block of impure limestone was embedded in a high-temperature impact-generated melt, it would be unlikely that the metasedimentary rock would follow a path of prograde reaction similar to that predicted from an equilibrium phase-diagram or a petrogenetic grid. The observed porphyroblasts of spurrite and the small inclusions of merwinite are more readily explained by rapid breakdown of reactants than by prograde reactions along a buffered T - $X(\text{CO}_2)$ path, which would have led to the formation of intermediate minerals such as

wollastonite. Such intermediate products have not been observed, even in the apparently less strongly metamorphosed samples of the main enclave.

Stage II: high-temperature retrograde metamorphism

The loss of volatile species associated with Stage-I metamorphism certainly caused a decrease in the overall solid volume of the enclaves. It is unlikely that at the lithostatic pressures involved, the loss of volume was accommodated by compaction. Instead, the reduction in volume likely made the enclaves more permeable to the influx of externally derived fluids. Once the intensity of the decarbonation reactions diminished owing to the decreasing temperature, the escaping CO_2 -rich fluids could not counteract the influx of H_2O -rich fluids into the permeable enclaves. The H_2O influx also preserved periclase, spurrite and merwinite: the assemblage periclase + calcite quickly reverts to dolomite if it is kept at about 700°C in a CO_2 -rich environment (Graf & Goldsmith 1955). Furthermore, if sufficient CO_2 is present, wollastonite starts to form at the expense of spurrite according to the reaction spurrite + 2 CO_2 → 2 wollastonite + 3 calcite (a carbonation reaction) when temperatures drop below about 650°C (Tuttle & Harker 1957). Finally, in an H_2O - CO_2 fluid mixture, merwinite is stable at low P_{fluid} (e.g., 0.5–1.0 kbar) and $X(\text{CO}_2)$ [e.g., 0.02 < $X(\text{CO}_2)$ < 0.1] and high T (e.g., above 700°C) (Zhou & Hsu 1992). Therefore, the preservation of merwinite indicates that the metasomatic fluid present in the Clearwater Lake carbonates had, in all likelihood, a value of $X(\text{CO}_2)$ less than 0.1 when temperatures in the enclave had dropped to about 700°C. In other words, CO_2 became scarce early at the stage of retrograde metamorphism.

One could propose that the system experienced a rapid decrease in temperature, effectively “quenching in” the high-temperature compositions of the minerals. However, if this were the case, calcite would have probably preserved a higher content of Mg in its structure: the purity of the calcite in the main enclave seems to preclude a thermal quench (Graf & Goldsmith 1955, Goldsmith 1960, Wiechmann 1995).

The formation of the hydrous minerals brucite and portlandite during Stage II reflects lower-temperature, CO_2 -poor, H_2O -dominant conditions. Because of the impact origin of the enclosing melt, most of the fluid phase (if not all) must have had a meteoric origin, with little or no magmatic contribution (Naumov 2005). The impacted country-rock was essentially composed of granulite- and amphibolite-facies rocks of the Canadian Shield, i.e., a relatively dry rock assemblage (Simard *et al.* 2004). The flash melting and vaporization of the impact event probably contributed to make the resulting impact-melt even drier than the target country-rock. The samples of impact rock do contain 1 to 2 wt.% volatiles (Rosa 2004), but much of this was probably introduced by post-impact hydrothermal activity. The relatively

permeable fragmental breccias and fractured basement would provide a conduit for the expected influx from the hydrostatic head developed between the bottom of the excavated crater and the groundwater level in the surrounding rocks (Phinney *et al.* 1978).

Stage III: Progressive cooling-off

Stage III is associated with the formation of the numerous veins and veinlets that cross the carbonate enclaves. At this stage, the hydrothermal system that was set in place shortly after the impact was still active, albeit slowly declining. Thermal contraction led to major fracturing and more localized and easy access of meteoric fluids. This access probably helped to generate, as products of alteration, the lizardite detected in sample DR-01, the calcite-filled veins visible in most of the carbonate samples, and most of the fine-grained, hard-to-identify, hydrated phases (probably hydrated calc-silicates).

CONCLUSIONS

1. We describe here the first example of a high-metamorphic-grade skarn formed by contact of limestone with an impact-generated melt, likely superheated.

2. The formation of merwinite indicates that temperatures of at least 820°C were reached in some parts of the main carbonate enclave during the prograde stage of metamorphism.

3. The presence of portlandite, a product of the hydration of CaO, suggests that during the prograde phase of metamorphism, temperatures at the contact between the limestone and the impact melt were adequate to dissociate calcite into its CaO and CO₂ components. The dissociation of calcite indicates that the highest temperatures registered in the carbonate xenoliths were close to 1000°C. By implication, the impact-generated melt may well have been superheated.

4. The presence of srebrodolskite could well result from the destabilization of an ankeritic component of the original dolomite, just like at the type locality.

5. The preservation of merwinite, spurrite and periclase shows that retrograde reactions were not possible owing to loss of a CO₂-rich gas phase. When temperatures in the carbonate enclaves reached about 700°C, vigorous hydrothermal activity must already have been taking place in and around the contact between the xenoliths and the melt. The X(CO₂) likely was less than 0.1 by this time.

6. The minerals brucite and portlandite, created during the higher-temperature retrograde stage, reflect CO₂-poor, H₂O-dominant conditions in the temperature range 700°C ≤ T ≤ 400°C.

7. As indicated by presence of lizardite, of calcite-filled veins, and of fine-grained, probably hydrated calc-silicates, the hydrothermal system (Stage II) efficiently

dissipated heat, which allowed reactions expected below 350°C to proceed in the xenoliths.

ACKNOWLEDGEMENTS

We acknowledge the valuable assistance of Drs. R.A.F. Grieve and H.H. Bostock of the Geological Survey of Canada. Martin Parent (Ministère des Ressources Naturelles du Québec) provided the logistical help necessary to work in such a remote location. The electron microprobe, geochemical and X-ray powder-diffraction analyses were performed at the Earth & Planetary Sciences Department of McGill University with the assistance of Shi Lang and Glenna Keating. Research and travel costs were covered by a Discovery Grant to RFM. We are most grateful to Associate Editor Tassos Grammatikopoulos and to referees G.R. Osinski and W.H. Peck for their valuable comments.

REFERENCES

- BOSTOCK, H.H. (1969): The Clearwater Complex, New Quebec. *Geol. Surv. Can., Bull.* **178**.
- BOWEN, N.L. (1940): Progressive metamorphism of siliceous limestone and dolomite. *J. Geol.* **48**, 225-274.
- CARD, K.D. & CIESIELSKI, A. (1986): Subdivision of the Superior Province of the Canadian Shield. *Geoscience Can.* **13**, 5-13.
- CHESNOKOV, B.V. & BAZHENOVA, L.F. (1985): Srebrodolskite Ca₂Fe₂O₅ – a new mineral. *Zap. Vses. Mineral. Obshchest.* **114**, 195-199 (in Russian).
- CHESNOKOV, B.V., SCHERBAKOVA, E.P. & NISHANBAEV, T.P. (2008): *Minerals from Burned Dumps of Chelyabinsk Coal Basin*. Institute of Mineralogy, UrO RAS, Miass, Russia (in Russian).
- CIESIELSKI, A. & PLANTE, L. (1990): Archean granulites in the Lac à l'Eau Claire area, north Bienville Subprovince, Superior Province, Quebec. *Geol. Surv. Can., Pap.* **90-1C**, 59-67.
- DEER, W.A., HOWIE, R.A. & ZUSSMAN, J. (1962): *Rock-Forming Minerals. 5. Non-Silicates*. Longman Scientific and Technical, London, U.K.
- DENCE, M.R., INNES, M.J.S. & BEALS, C.S. (1965): On the probable meteorite origin of the Clearwater lakes, Quebec. *J. R. Astron. Soc. Can.* **59**, 13-22.
- FLEISCHER, R.L., VIERTL, J.R.M. & PRICE, P.B. (1969): Age of the Manicouagan and Clearwater lakes craters. *Geochim. Cosmochim. Acta* **33**, 523-527.
- GHIORSO, M.S. & SACK, R.O. (1995): Chemical mass transfer in magmatic processes. IV. A revised and internally consistent thermodynamic model for the interpolation and extrapolation of liquid–solid equilibria in magmatic

- systems at elevated temperatures and pressures. *Contrib. Mineral. Petrol.* **119**, 197-212.
- GOLDSMITH, J.R. (1960): Exsolution of dolomite from calcite. *J. Geol.* **68**, 103-109.
- GOLDSMITH, J.R. & HEARD, H.C. (1961): Subsolidus phase relations in the system $\text{CaCO}_3\text{-MgCO}_3$. *J. Geol.* **69**, 45-74.
- GOLDSMITH, J.R. & NEWTON, R.C. (1969): P-T-X relations in the system $\text{CaCO}_3\text{-MgCO}_3$. *Am. J. Sci.* **267-A**, 160-190.
- GOSSELIN, C., SIMARD, M. & DAVID, J. (2001): Géologie de la région des lacs des Loups Marins (34A). *Ministère des Ressources Naturelles du Québec, Rapport Géologique RG 2001-10*.
- GRAF, D.L. & GOLDSMITH, J.R. (1955): Dolomite – magnesian calcite relations at elevated temperatures and CO_2 pressures. *Geochim. Cosmochim. Acta* **7**, 109-128.
- GRIEVE, R.A.F. (1978): Meteoritic component and impact melt composition at the Lac à l'Eau Claire, Quebec. *Geochim. Cosmochim. Acta* **42**, 429-431.
- GRIEVE, R.A.F. (2006): *Impact Structures in Canada*. Geological Association of Canada, GEOText **5**.
- GRIEVE, R.A.F., DENCE, M.R. & ROBERTSON, P.B. (1977): Cratering processes, as interpreted from the occurrence of impact melts. In *Impact and Explosion Cratering* (D.J. Roddy, R.O. Pepin & R.B. Merrill, eds.). Pergamon, New York, N.Y. (791-814).
- HARKER, R.I. & TUTTLE, O.F. (1955): Studies in the system CaO-MgO-CO_2 . 2. Limits of solid solution along the binary join, $\text{CaCO}_3\text{-MgCO}_3$. *Am. J. Sci.* **253**, 274-282.
- HENMI, C. & HENMI, K. (1978): Synthesis of spurrite and tilleyite at low CO_2 partial pressure. *Mineral. J.* **9**, 106-110.
- KRANCK, S.H. & SINCLAIR, G.W. (1963): Clearwater Lake, New Quebec. *Geol. Surv. Can., Bull.* **100**.
- KURDOWSKI, W. (1968): The synthesis of spurrite. *Polska Akad. Nauk, Prace Mineral.* **14**, 45-68 (in Polish).
- LEA, F.M. (1970): *The Chemistry of Cement and Concrete*. Edward Arnold (Publishers) Ltd., London, U.K.
- MCCAMMON, C. & LIU, LIN-GUN (1984): The effects of pressure and temperature on nonstoichiometric wüstite, Fe_xO : the iron-rich phase boundary. *Phys. Chem. Minerals* **10**, 106-113.
- NAUMOV, M.V. (2005): Principal features of impact-generated hydrothermal circulation systems: mineralogical and geochemical evidence. *Geofluids* **5**, 165-184.
- OSINSKI, G.R., SPRAY, J.G. & GRIEVE, R.A.F. (2008): Impact melting in sedimentary target rocks: an assessment. *Geol. Soc. Am., Spec. Pap.* **437**, 1-18.
- PERCIVAL, J.A., MORTENSEN, J.K., STERN, R.A., CARD, K.D. & BÉGIN, N.J. (1992): Giant granulite terranes of northwestern Superior Province: the Ashuanipi Complex and Minto Block. *Can. J. Earth Sci.* **29**, 2287-2308.
- PHINNEY, W.C., SIMONDS, C.H., COCHRAN, A. & MCGEE, P. (1978): West Clearwater, Quebec impact structure. II. Petrology. *Proc. Lunar Planet. Sci. Conf.* **9**, 2659-2693.
- PLANTE, L. (1986): *Modélisation géophysique des cratères météoritiques du lac à l'Eau-Claire, Nouveau-Québec*. Thèse de maîtrise, Université Laval, Québec, Québec.
- PLANTE, L., SÉGUIN, M.-K. & RONDOT, J. (1990): Étude gravimétrique des astroblièmes du Lac à l'Eau Claire, Nouveau-Québec. *Geoexploration* **26**, 303-323.
- REIMOLD, W.U., GRIEVE, R.A.F. & PALME, H. (1981): Rb-Sr dating of the impact melt from East Clearwater, Quebec. *Contrib. Mineral. Petrol.* **76**, 73-76.
- ROGERS, A.F. (1929): Periclase from Crestmore near Riverside, California, with a list of minerals from this locality. *Am. Mineral.* **14**, 462-469.
- RONDOT, J. (1985): Post-impact modification is a deep (0.2D) gravity compensation. *Meteoritics* **20**, 747-748.
- RONDOT, J., PLANTE, L. & SÉGUIN, M.-K. (1993): Géologie postarchéenne de la partie centrale du lac à l'Eau Claire ouest (Nouveau-Québec). *Gouvernement du Québec, Direction générale de l'exploration géologique et minérale ET92-06* (carte no. 2157).
- ROSA, D.F. (2004): *Marble Enclaves in the Melt Sheet at the West Clearwater Lake Impact Crater, Northern Quebec*. M.Sc. thesis, McGill University, Montreal, Quebec, Canada.
- SANFORD, B.V., NORRIS, A.W. & BOSTOCK, H.H. (1968): Geology of the Hudson Bay Lowlands (Operation Winisk). *Geol. Surv. Can., Pap.* **67-60**.
- SIMARD, M., PARENT, M., THÉRIAULT, R., DAVID, J., LACOSTE, P. & SHARMA, K.N.M. (2004): Géologie de la région du lac à l'Eau Claire (34B et 34C). *Ministère des Ressources Naturelles du Québec, Rapport Géologique RG 2003-8*.
- SIMONDS, C.H., PHINNEY, W.C., MCGEE, P. & COCHRAN, A. (1978): West Clearwater, Quebec impact structure. I. Field geology, structure and bulk chemistry. *Proc. Lunar Planet. Sci. Conf.* **9**, 2633-2658.
- SPEAR, F.S. (1993): *Metamorphic Phase Equilibria and Pressure – Temperature – Time Paths*. Mineralogical Society of America, Washington, D.C.
- STORZER, D. & WAGNER, G.A. (1977): Fission track dating of meteorite impacts. *Meteoritics* **12**, 368-369.
- TREIMAN, A.H. & ESSENE, E.J. (1983): Phase equilibria in the system $\text{CaO-SiO}_2\text{-CO}_2$. *Am. J. Sci.* **283-A**, 97-120.

- TUTTLE, O.F. & HARKER, R.I. (1957): Synthesis of spurrite and the reaction wollastonite + calcite = spurrite + carbon dioxide. *Am. J. Sci.* **255**, 226-234.
- WALTER, L.S. (1965): Experimental studies on Bowen's decarbonation series. III. P-T univariant equilibrium of the reaction spurrite + monticellite = merwinite + calcite and analysis of assemblages found at Crestmore, California. *Am. J. Sci.* **263**, 64-77.
- WANLESS, R.K., STEVENS, R.D., LACHANCE, G.R. & RIMSAITE, J.Y.H. (1964) : Age determinations and geologic studies. I. Isotopic ages, Report 5. *Geol. Surv. Can., Pap.* **64** (17).
- WIECHMANN, M.J. (1995): *Contact Metamorphism and Skarn Formation at Crestmore, California*. Ph.D. thesis, the Johns Hopkins University, Baltimore, Maryland, U.S.A.
- WYLLIE, P.J. & HAAS, J.L., JR. (1966): The system CaO-SiO₂-CO₂-H₂O. II. The petrogenetic model. *Geochim. Cosmochim. Acta* **30**, 525-543.
- WYLLIE, P.J. & TUTTLE, O.F. (1960): The system CaO-CO₂-H₂O and the origin of carbonatites. *J. Petrol.* **1**, 1-46.
- ZHARIKOV, V.A. & SHMULOVICH, K.I. (1969): High temperature mineral equilibria in the system CaO-SiO₂-CO₂. *Geochim. Int.* **6**, 853-869.
- ZHOU, JINCHENG & HSU, L.C. (1992): The stability of merwinite in the system CaO-MgO-SiO₂-H₂O-CO₂ with CO₂-poor fluids. *Contrib. Mineral. Petrol.* **112**, 385-392.

Received March 17, 2010, revised manuscript accepted December 10, 2010.

APPENDIX 1. METHODS OF ANALYSIS

Polished thin sections were investigated using wavelength-dispersion spectroscopy (WDS) with a JEOL 8900 electron microprobe; we used the ZAF correction method. The minerals in all thin sections were analyzed for the following elements: Ca, Al, Mg, Fe, Ti, S and Si. Both whole-rock chemical analyses by X-ray fluorescence (XRF) methods and rapid, semi-quantitative, preliminary energy-dispersion scans of the mineral assemblages of each thin section revealed that elements other than those listed above are not present in significant quantities in the carbonate samples. Natural and synthetic standards were selected to minimize the

correction factors. The estimated precision is $\pm 1\%$ for major elements. The accelerating voltage was 15 keV for all analyzes, and the beam current was 20 nA. Counting intervals were 20 seconds, and the beam diameter was kept mostly in the 10 to 15 μm range, with some analyses done at 5 μm on small grains. X-ray powder-diffraction analyses (XRD) were carried out on both whole-rock samples and on samples in which the non-carbonate components were concentrated by dissolution in a weak acetic acid solution. We used a Rigaku D/MAX 2400 diffractometer operated at 40 kV and 160 mA.